

# **Exotic Neutrino Interactions as a Probe of Physics Beyond the Standard Model**

*Patrick Douglas John Bolton*

A dissertation submitted in partial fulfillment  
of the requirements for the degree of  
**Doctor of Philosophy**  
of  
**University College London.**

Department of Physics and Astronomy  
University College London

October 21, 2021

I, Patrick Douglas John Bolton, confirm that the work presented in this thesis is my own. Where information has been derived from other sources, I confirm that this has been indicated in the work.

# Abstract

This thesis examines the unique window neutrinos provide to physics beyond the Standard Model. Unlike the other fermions of the Standard Model, the question remains as to why the neutrinos are so light and whether they are Dirac or Majorana fermions. If there is some mechanism generating the small neutrino masses that is related to New Physics (NP) at a high energy scale (or weakly-coupled physics at a low energy scale), measuring the properties of the neutrinos such as their interactions is crucial to constrain such models. It is then important to survey the range of experiments probing neutrinos and to gauge their ability to constrain NP. This thesis takes both an agnostic approach to the identity of NP by considering effective neutrino interactions as well as a model-specific approach.

Several topics are considered, firstly the ability of neutrino oscillation experiments to constrain effective lepton number violating ( $|\Delta L| = 2$ ) neutrino non-standard interactions (NSIs) if the far detector is sensitive to the charge of the outgoing lepton. This novel probe is contrasted to neutrinoless double beta decay and other  $|\Delta L| = 2$  processes. Close attention is also given to the theoretical description of neutrino oscillations in the quantum field theory picture and how this can be extended to include neutrino NSIs. A similar study examines the novel ability of atomic spectroscopy experiments to probe long-range forces mediated by neutrinos interacting via effective interactions. An explicit model explored in detail is the so-called inverse seesaw mechanism. A characteristic prediction of this model is the presence of two heavy sterile neutrinos with a small mass splitting, the consequences of which are examined for a range of experiments. We compare these to constraints derived from neutrinoless and two neutrino double beta decay.

# Impact Statement

This work is a study of the nature of neutrinos, which are fundamental building blocks of the universe. Understanding their properties (e.g. masses and interactions) is vital to piece together the evolution of the cosmos to the present day and the events leading up to our existence. Without neutrinos, the nuclear fusion of hydrogen in stars into heavy elements such as carbon, a necessary component of Earth-based life, would be impossible. As they are still poorly understood, neutrinos provide a tantalising window to physics beyond the Standard Model, which could help us understand the earliest moments after the Big Bang.

These fundamental questions and the drive to better understand neutrinos has motivated the building of experiments paving the way in technological innovation. From experimental particle physics as a whole, numerous technologies have made a large impact in medicine, communication, power generation and energy storage. The manipulation of matter on the smallest scales has also fueled progress in other academic disciplines such as the biological, computer and climate sciences. It is difficult to overstate the benefits these fields have brought to society.

This thesis in particular develops the theory of neutrinos and examines how exotic neutrino interactions can be probed in a variety of experiments, for example, neutrino oscillation, atomic spectroscopy and neutrinoless double beta decay search experiments. It is hoped that both experimentalists and theorists in the field find the results useful, motivating further research into the topics covered.

# Acknowledgements

I have several people to thank for making this thesis possible. Firstly, Professor Frank Deppisch for providing clear and consistent guidance for the duration of my time in the High Energy Physics (HEP) group at UCL. Numerous opportunities for travel, collaboration, and personal development were made aware to me that I would not have necessarily found and taken advantage of myself, which I am hugely grateful for. Next, those who I met and hosted me on those travels; the diverse group of PhD students at summer schools, the researchers at Wright Laboratory, Yale University, Professor Bhupal Dev at Washington University in St. Louis, and Sofianne Boucenna at KTH Stockholm. I would like to thank Lukáš Gráf, Fedor Šimkovic, Chandan Hati, Suchita Kulkarni, Julia Harz, and Kåre Fridell for collaboration during the PhD. I would also like to thank my fellow HEP UCL group members for providing a warm and encouraging environment for research. Lastly, I would like to thank my parents for providing ample patience and support over the course of the PhD and without whom this thesis could not have been written.

# Contents

<b>1</b>	<b>Introduction and Overview</b>	<b>21</b>
<b>2</b>	<b>Neutrinos in the Standard Model and Beyond</b>	<b>31</b>
2.1	The Standard Model of Particle Physics . . . . .	31
2.1.1	Field Content and Symmetries . . . . .	32
2.1.2	Gauge and Kinetic Terms . . . . .	35
2.1.3	Higgs Mechanism . . . . .	39
2.1.4	Fermion Masses . . . . .	44
2.2	Neutrino Masses . . . . .	47
2.2.1	Dirac Neutrinos . . . . .	48
2.2.2	Majorana Neutrinos and Seesaw Mechanisms . . . . .	52
2.2.3	Radiative Neutrino Masses . . . . .	62
2.3	Effective Field Theories . . . . .	64
2.3.1	Standard Model Effective Field Theory . . . . .	67
2.3.2	Low Energy Effective Field Theory . . . . .	69
2.3.3	Adding Right-Handed Neutrinos . . . . .	75
<b>3</b>	<b>Lepton Number and Neutrino Oscillations</b>	<b>79</b>
3.1	Theory of Neutrino Oscillations . . . . .	82
3.1.1	Quantum Mechanics . . . . .	82
3.1.2	Quantum Field Theory . . . . .	85
3.2	Neutrino Oscillations with LNV Neutrino NSIs . . . . .	91
3.3	Constraints on LNV Neutrino NSIs . . . . .	97

3.3.1	MINOS Constraints	97
3.3.2	KamLAND Constraints	105
3.4	Other Constraints on LNV Neutrino NSIs	108
<b>4</b>	<b>Neutrino-Mediated Long-Range Forces</b>	<b>115</b>
4.1	Deriving a Long-Range Potential	118
4.2	Neutral-Current Neutrino NSIs	121
4.3	Standard Model Neutrino Potential	128
4.4	Non-Standard Neutrino Potentials	134
4.4.1	Right-Handed Vector Interactions	135
4.4.2	Scalar Interactions	139
4.4.3	Tensor Interactions	142
4.4.4	Neutrino Magnetic and Electric Dipole Moments	146
4.5	Atomic Spectroscopy Constraints	150
<b>5</b>	<b>Probes of the Inverse Seesaw Mechanism</b>	<b>164</b>
5.1	Phenomenological Parametrisation	166
5.1.1	Consistency Relations	167
5.1.2	CP Phases	169
5.2	Constraints on Heavy Sterile Neutrinos	181
5.2.1	Collider Searches	182
5.2.2	Meson Decays and Beam-Dump Experiments	186
5.2.3	Beta Decays and Nuclear Processes	188
5.2.4	Active-Sterile Neutrino Oscillations	189
5.2.5	Indirect Laboratory Constraints	190
5.2.6	Cosmological and Astrophysical Constraints	191
5.3	Neutrinoless Double Beta Decay Constraints	194
5.4	Two-Neutrino Double Beta Decay Constraints	207
5.4.1	Effective Interactions with Sterile Neutrinos	208
5.4.2	Double Beta Decay Rate with a Sterile Neutrino	209
5.4.3	Sensitivity to Sterile Neutrino Parameters	217

<i>Contents</i>	8
<b>6 Conclusions</b>	<b>229</b>
<b>Appendices</b>	<b>233</b>
<b>A Neutrino NSI Parametrisation</b>	<b>233</b>
<b>B Additional Formulae for Long-Range Potentials</b>	<b>235</b>
B.1 Spinor Identities and Non-Relativistic Limits . . . . .	235
B.2 Integrals for Long-Range Potentials . . . . .	238
<b>C Statistical Method</b>	<b>240</b>
<b>Bibliography</b>	<b>244</b>

# List of Figures

2.1	(Left) Dirac neutrino mass generated after EWSB by a Yukawa-type interaction. (Right) Majorana neutrino mass generated by a Type-1 (or extended, e.g. ISS) seesaw mechanism. . . . .	52
2.2	(Left) Two-loop diagram generating Dirac neutrino masses in a left-right symmetric model with a global $U(1)_{B-L}$ symmetry. (Centre and right) Radiative corrections to the Type-I and ISS mechanisms. .	63
2.3	(Left) Effective Majorana mass for the left-handed neutrino fields $\nu_L$ from a dim- $\bar{3}$ LEFT operator. (Right) Majorana neutrino dipole moment interaction from a dim- $\bar{5}$ LEFT operator. . . . .	71
3.1	Feynman diagrams depicting the $\nu_\alpha \rightleftarrows \nu_\beta$ (left) and $\nu_\alpha \rightleftarrows \bar{\nu}_\beta$ (right) oscillation processes. The latter requires a helicity-flip if SM charged-currents are at the interaction vertices. . . . .	86
3.2	(Left) Feynman diagram depicting the neutrino oscillation process with an LNV neutrino NSI at the interaction vertex. (Right) A possible UV completion in a left-right symmetric scenario. . . . .	95
3.3	(Left) Allowed regions in the $(\epsilon_{\mu\mu}, \epsilon_{\mu\tau})$ plane for fixed $L/E_{\mathbf{q}} = 735 \text{ km}/3 \text{ GeV}$ and four values of $\eta$ in the $2\nu$ mixing approximation of the $\nu_\mu - \nu_\tau$ sector. (Right) Allowed regions in $(\epsilon_{\mu\mu}, \epsilon_{\mu\tau})$ for fixed $L = 735 \text{ km}$ and four values of $\eta$ , found by integrating over the NuMI beam neutrino energies. . . . .	99
3.4	Allowed regions in the $(\epsilon_{\mu\mu}, \epsilon_{\mu\tau})$ plane for values of the Majorana phase $\eta = 0$ (left) and $\eta = \pi/2$ (right) and for four different values of the baseline $L$ . . . . .	101

3.5	Allowed values of $\varepsilon_{\mu\mu}$ with $\varepsilon_{\mu\tau} = 0$ (left) and $\varepsilon_{\mu\tau}$ with $\varepsilon_{\mu\mu} = 0$ (right) as a function of the baseline $L$ for three values of the Majorana phase $\eta$ . The baseline of MINOS is indicated by the dashed line. . . . .	102
3.6	(Left) Elliptical allowed regions in the $(\varepsilon_{\mu\mu}, \varepsilon_{\mu\tau})$ plane for $\varepsilon_{\mu e} = 0$ , $L = 735$ km, $\alpha_2 = 0$ and three values of the Majorana phase $\alpha_3$ . (Centre) Eccentricity $e$ of the ellipse as a function of $(\alpha_2, \alpha_3)$ . (Right) Angle $\Theta$ from the positive $\varepsilon_{\mu\mu}$ axis to the semi-major axis of the ellipse as a function of $(\alpha_2, \alpha_3)$ . . . . .	104
3.7	Upper bounds on the NSI coefficients $\varepsilon_{\mu e}$ (left), $\varepsilon_{\mu\mu}$ (centre) and $\varepsilon_{\mu\tau}$ (right), as a function of the Majorana phases $\alpha_2$ and $\alpha_3$ , derived from the MINOS limit $\mathcal{S}_\mu < 0.026$ . Best fit values for the mixing parameters $\theta_{12}$ , $\theta_{13}$ and $\theta_{23}$ , $\Delta m_{21}^2$ and $\Delta m_{32}^2$ and $\delta$ are taken in the NO. . . . .	105
3.8	Microscopic $ \Delta L  = 2$ processes sensitive to the neutrino NSI coefficients. (Left) $0\nu\beta\beta$ decay. (Centre) $\mu^- - e^+$ conversion in a nucleus. (Right) Kaon decay $K^+ \rightarrow \pi^- \mu^+ \mu^+$ . . . . .	108
3.9	Upper bounds on the NSI coefficients $\varepsilon_{ee} \times 10^9$ (left), $\varepsilon_{e\mu} \times 10^9$ (centre) and $\varepsilon_{e\tau} \times 10^9$ (right) as a function of the Majorana phases $(\alpha_2, \alpha_3)$ , found from the ${}^{76}\text{Ge}$ $0\nu\beta\beta$ decay limit $T_{1/2}^{0\nu} > 5.3 \times 10^{25}$ y. Best fit values for the neutrino mixing parameters in the NO scheme are chosen, with $m_1 = 0$ eV. . . . .	110
3.10	Contributions of the $ \Delta L  = 2$ neutrino NSIs at dim-6 to the light neutrino mass at two loops. The diagrams are for operators with coefficients $\varepsilon_{RL}^V$ (left), $\varepsilon_{RL}^S$ (centre) and $\varepsilon_{RR}^S/\varepsilon_{RR}^T$ (right). . . . .	112

4.1 (Left) Long-range force mediated between fermions $\psi_\alpha$ and $\psi'_\beta$ by virtual mediators carrying the momentum $q = p_\alpha - p'_\alpha = p'_\beta - p_\beta$ . (Right) The exchange of two mass-eigenstate neutrinos between fermions $\psi_\alpha$ and $\psi'_\beta$ . The interaction vertices are four-fermion interactions with coefficients $(c_{XY}^\psi)_{ij;\alpha\alpha}$ and $(c_{XY}^{\psi'})_{ij;\beta\beta}$ respectively, where the superscripts $X, Y \in \{L, R\}$ refer to the chirality of the neutrino and fermion currents. . . . .	119
4.2 The exchange of two massive neutrinos $\nu_i$ and $\nu_j$ between fermions $\psi_\alpha$ and $\psi'_\beta$ with SM charged- and neutral-current interactions at each vertex. The charged-current interactions are only possible for $\psi = \ell$ . . . . .	129
4.3 The exchange of two massive neutrinos between fermions $\psi_\alpha$ and $\psi'_\beta$ with SM charged- and neutral-current interactions at one vertex and a neutral-current neutrino NSI at the other. In our framework the effective interaction may be of vector ( $c_{XY}$ ), scalar ( $g_{XY}$ ) or tensor ( $h_{XX}$ ) type. . . . .	136
4.4 (Left) Spin-independent parts of the vector-vector potentials $V_{\alpha\beta}^{LL}$ , $V_{\alpha\beta}^{LR}$ and $V_{\alpha\beta}^{RR}$ for positronium ( $e^-e^+$ ) and three Dirac (D) or Majorana (M) neutrinos with $m_1 = 0.1$ eV and NO mixing parameters, taking $(c_{RL})_{ij;e} = 10^{-2}\delta_{ij}$ . The solid (dashed) lines indicate positive (negative) potentials. (Right) Spin-independent parts of the potentials $V_{ee}^{SS}$ in the Dirac and Majorana cases compared to $V_{ee}^{LL}$ , using $(g_{XY})_{ij;e} = 10^{-2}\delta_{ij}$ and for $X = Y \in \{L, R\}$ . In both plots the neutrino-mediated potentials are compared with the gravitational potential $V_G$ between the electron and positron. . . . .	145

4.5 (Left and centre) Diagrams depicting the exchange of two massive neutrinos between fermions $\psi_\alpha$ and $\psi'_\beta$ with SM interactions at one vertex and the exchange of a photon via a neutrino magnetic moment $\mu_{ij}$ at the other, leading to the vector-dipole potential $V_{\alpha\beta}^{V\gamma}$ . (Right) Diagram when $\mu_{ij}$ is present at both vertices, resulting in the dipole-dipole potential $V_{\alpha\beta}^{\gamma\gamma}$ . . . . .	147
4.6 Neutrino-mediated potentials $V_{ee}^{V\gamma}$ and $V_{ee}^{\gamma\gamma}$ compared to the SM potential $V_{ee}^{LL}$ , plotted for positronium ( $e^-e^+$ ) and three Dirac neutrinos with $m_1 = 0.1$ eV and NO mixing parameters, setting $\mu_{ij} \equiv \mu_\nu = 10^{-12} \mu_B$ . These potentials are compared with the gravitational potential $V_G$ between the electron and positron. . . . .	149
5.1 Visualisation of the $(M_\nu)_{11} = 0$ constraint in Eq. (5.4) in the complex plane. The sides are given in terms of the dimensionless ratios $r_\nu$ and $r_\Delta$ and the squared sines and cosines of the active-sterile neutrino mixing angles $\vartheta_{e1}$ , $\vartheta_{e2}$ . . . . .	168
5.2 (Left) Values of the squared active-sterile mixing strengths $s_{e1}^2$ and $s_{e2}^2$ satisfying the tree-level condition $(M_\nu)_{11} = 0$ in Eq. (5.4) for different combinations of the light and heavy neutrino masses in the ratios $r_\nu = m_\nu/m_{N_1}$ , and $r_\Delta = \Delta m_N/m_{N_1}$ , as shown by the shaded regions. (Right) Equivalent regions in the $s_{e2}^2/s_{e1}^2$ and $s_{e1}^2 + s_{e2}^2$ parameter space. . . . .	170
5.3 (Left) Heavy neutrino CP phase difference $\Delta\phi$ as a function of the normalised active-sterile mixings $s_{e1}^2$ and $s_{e2}^2$ . The edges of the allowed region are determined by the limiting values for $(\phi_1, \phi'_2)$ as indicated. (Right) Sterile-sterile neutrino mixing strength $s_{12}^2$ as a function of $s_{e1}^2$ and $s_{e2}^2$ , setting $\delta = 0$ . . . . .	173

5.4 (Left) Absolute magnitude of the one-loop neutrino mass contribution  $|\delta m_\nu^{1\text{-loop}}|$  as a function of the lighter sterile mass  $m_{N_1}$  and mixing strength  $s_{e1}^2$  for indicated values of the other parameters. The canonical seesaw case with  $s_{e1}^2 = r_\nu$  is indicated by the diagonal grey line. (Right) Maximally allowed value of  $s_{e1}^2 + s_{e2}^2$  from the condition  $|\delta m_\nu^{1\text{-loop}}| < 0.1m_\nu$ , as a function of  $m_{N_1}$  for different values of the heavy neutrino splitting ratio  $r_\Delta = \frac{\Delta m_N}{m_{N_1}}$ . Solid lines are found by using the exact formula Eq. (2.79), while the dashed lines use this same formula but in the limit  $\mu_{R,S} \ll m_S$ . . . . . 179

5.5 Modified allowed regions for the active-sterile mixing strengths satisfying the tree-level constraint  $(M_\nu)_{11} = 0$  and the condition for the one-loop contribution to be small,  $|\delta m_\nu^{1\text{-loop}}| < 0.1m_\nu$ . . . . . 180

5.6 Current constraints on the mixing squared  $|V_{eN}|^2$  between the electron neutrino and sterile neutrino  $N$  as a function of the sterile neutrino mass  $m_N$ . The shaded regions are excluded by the searches and observations discussed in Sec. 5.2. For  $m_N < 10$  MeV, constraints are derived from neutrino oscillation, beta decay and reactor neutrino experiments. For  $m_N > 10$  MeV, constraints are set by meson decay, beam dump and collider measurements. Cosmological and astrophysical bounds from CMB, BBN, Hubble constant, supernovae and X-ray observations are relevant for  $m_N \lesssim 10$  GeV. The grey diagonal line labelled *Seesaw* indicates the seesaw relation  $|V_{eN}|^2 = m_\nu/m_N$  with  $m_\nu = 0.05$  eV. . . . . 182

5.7 Future constraints on the mixing squared $ V_{eN} ^2$ between the electron neutrino and sterile neutrino $N$ as a function of the sterile neutrino mass $m_N$ . The bounds are based on the sensitivities of future beta decay, meson decay, beam dump and collider experiments, as detailed in the main text. The blue shaded region indicates the parameter space already excluded by current experiments, as shown in Fig. 5.6. The red shaded region further specifies the current limits from searches for LNV signals (e.g. from meson decays and collider searches). . . . .	184
5.8 Normalised $0\nu\beta\beta$ decay NMEs for $^{76}\text{Ge}$ (left) and $^{136}\text{Xe}$ (right) as a function of the exchanged sterile neutrino mass $m_{N_i}$ using the interpolating formula Eq. (5.35). We make use of the light and heavy NMEs shown in Table 5.1. The bands indicate the NME uncertainties arising from the choice of quenched $g_A$ and short-range correlations. . . . .	199
5.9 Upper limits on $ V_{eN_1} ^2 +  V_{eN_2} ^2$ for three small values of $r_\Delta \ll 1$ . We show the limits from $^{136}\text{Xe}$ (solid) and $^{76}\text{Ge}$ (dashed) experiments with the bands indicating the NME uncertainties. The red curves highlight the limit in which $0\nu\beta\beta$ decay is driven by a single sterile neutrino. The curves sloping down to the lower right indicate the upper bounds by enforcing $ \delta m_v^{1\text{-loop}}  < 0.1m_v$ . These constraints are compared with the current and future sensitivities of $ \Delta L  = 0$ (blue shaded) and $ \Delta L  = 2$ (red shaded) searches, cf. Figs. 5.6 and 5.7. . . . .	201
5.10 As for Fig. 5.9, but showing the current $^{136}\text{Xe}$ $0\nu\beta\beta$ decay bounds (dashed) and future bounds (solid) assuming a future half-life lower limit $T_{1/2}^{0\nu} = 10^{28}$ y. . . . .	203

5.11 Upper limits on the sum of squared active-sterile mixing for the sterile neutrino mass splitting ratio  $r_\Delta = \frac{\Delta m_N}{m_{N_1}} = 10^{-2}$  derived from  $0\nu\beta\beta$  decay and loop constraints. We show the limits from  $^{136}\text{Xe}$  for different values of  $\phi_1$  (left) and  $m_\nu$  (right). . . . . 205

5.12 Upper limits on  $|V_{eN_1}|^2$  for three large values of  $r_\Delta \geq 1$ . We show the limits for  $^{136}\text{Xe}$  with shaded bands indicating the NME uncertainties. The red curve highlights the limit in which  $0\nu\beta\beta$  decay is driven by a single sterile neutrino. The curves sloping down to the lower right indicate the upper bounds by enforcing  $|\delta m_\nu^{1-\text{loop}}| < 0.1m_\nu$ . These constraints are compared with the current and future sensitivities of  $|\Delta L| = 0$  (blue shaded) and  $|\Delta L| = 2$  (red shaded) searches, cf. Figs. 5.6 and 5.7. . . . . 206

5.13 (Left) Standard  $2\nu\beta\beta$  decay process with the emission of two electrons and two electron antineutrinos. (Right) Non-standard  $\nu N\beta\beta$  process, where the active-sterile mixing  $V_{eN}$  or a right-handed current  $\varepsilon_{RX}$  creates a  $m_N \sim 1$  MeV sterile neutrino  $N$  instead of an antineutrino at one of the vertices. . . . . 209

5.14 Total differential  $2\nu\beta\beta$  decay rate (solid) and the sterile neutrino contribution (dashed) with  $m_N = 1.0$  MeV and  $|V_{eN}|^2 = 0.5$  for the two isotopes  $^{100}\text{Mo}$  (purple) and  $^{136}\text{Xe}$  (blue). Both distributions are normalised to the SM decay rate. The vertical dotted lines indicate the respective  $Q$ -values and the panel at the bottom shows the corresponding percentage deviations from the SM rate. . . . . 219

5.15 The factor  $\alpha(m_N)$  multiplying the right-handed current coefficient  $|\varepsilon_{RX}|^2$  yielding the sterile neutrino contribution to the angular correlation factor  $K^{2\nu}$  for  $^{82}\text{Se}$  (red) and  $^{100}\text{Mo}$  (blue). . . . . 221

5.16 Upper limits and sensitivities at 90% CL on  $|V_{eN}|^2$  as a function of  $m_N$  from  $2\nu\beta\beta$  decay in current (left) and future (right) experiments. We show the individual constraints (as indicated in the legend) as well as a combined constraint (black dashed). The bands in the right plot correspond to the range of possible future exposures in Table 5.3. The combined future sensitivity uses the maximum forecasted exposure of each experiment. . . . . 223

5.17 Current upper limits and future sensitivities at 90% CL on  $|\epsilon_{RX}|^2$  as a function  $m_N$ . The solid (dashed) blue line shows the combined constraint from current (future)  $2\nu\beta\beta$  decay experiments measuring the total kinetic energy distribution. The solid red line is the upper limit derived from the angular distribution measurement of NEMO-3. The dashed red band indicates the range of upper limits expected from the angular distribution measurement of SuperNEMO. The dot-dashed red line shows the upper limit from a future  $^{82}\text{Se}$  experiment with an exposure of  $10^7$  events. . . . . 224

5.18 Current upper limits (solid blue) and future sensitivities (dashed blue) on the mixing strength  $|V_{eN}|^2$  between the electron and sterile neutrino as a function of the sterile mass  $m_N$ . Likewise, the red curves give the current limit and future sensitivity on the right-handed coefficient  $|\epsilon_{RX}|^2$  using a measurement of the angular distribution in  $2\nu\beta\beta$  decay. The shaded regions are excluded by existing searches in single beta decay and sterile decays in reactor and solar neutrino oscillation experiments. . . . . 225

# List of Tables

2.1	Matter and gauge fields of the SM. Given in the columns are the transformation properties of the fields under the SM gauge group $SU(3)_c \times SU(2)_L \times U(1)_Y$ , i.e. either as a triplet or singlet under $SU(3)_c$ , a doublet or singlet under $SU(2)_L$ and their hypercharge $Y$ . Also given are the transformation properties of the fields under the restricted Lorentz group $SO^+(1,3)$ . Fields are given in the flavour basis, i.e. $v \in \{v_e, v_\mu, v_\tau\}$ , $\ell \in \{e, \mu, \tau\}$ , $u \in \{u, c, t\}$ and $d \in \{d, s, b\}$ . . . . .	33
2.2	Transformation properties of the SM fermion fields under the Abelian gauge group $U(1)_Q$ , i.e. the value of the QED charge generator $Q = T^3 + Y$ , and the global $U(1)_L$ lepton number and $U(1)_B$ baryon number. Also shown are the values of $(T^3 - s_W^2 Q)$ which determine the neutral-current interaction of the fields. . . . .	44
2.3	Current global best fit values for the three-neutrino flavour oscillation mixing angles $\theta_{12}$ , $\theta_{13}$ and $\theta_{23}$ , mass-squared splittings $\Delta m_{21}^2$ and $\Delta m_{31}^2$ and CP phase $\delta_{CP}$ . Values are given for Normal Ordering (NO) and Inverted Ordering (IO) of the light neutrino mass eigenstates. . . . .	51
2.4	$ \Delta L  = 0$ (left) and $ \Delta L  = 2$ (right) dim- $\bar{6}$ charged-current LEFT operators, of vector, scalar and tensor type. . . . .	72
2.5	$ \Delta L  = 0$ (left) and $ \Delta L  = 2$ (right) dim- $\bar{6}$ neutral-current LEFT operators, of vector type for the former and scalar and tensor type for the latter. The fermion fields can be $\psi \in \{\ell, u, d\}$ . . . . .	73

2.6	Combinations of Dirac matrices appearing in the standard parametrisation of charged- and neutral-current type neutrino NSIs. . . . .	74
2.7	$ \Delta L  = 0$ (left) and $ \Delta L  = 2$ (right) dim- $\bar{6}$ charged-current LEFT + $N_R$ operators, of vector, scalar and tensor type. Assumes the lepton number assignment $L(N_R) = +1$ . . . . .	76
2.8	$ \Delta L  = 0$ (left) and $ \Delta L  = 2$ (right) dim- $\bar{6}$ neutral-current LEFT + $N_R$ operators, of vector, scalar and tensor type and for fermion fields $\psi \in \{\ell, u, d\}$ . Assumes the lepton number assignment $L(N_R) = +1$ . . . . .	77
3.1	Upper bounds from the MINOS experiment on the LNV NSI coefficients in the $2\nu$ mixing approximation. The range indicates the best and worst upper bound depending on the choice of the Majorana phase. (Left) Bounds derived at a fixed neutrino energy of 3 GeV. (Right) Bounds derived by integrating over the energy-dependent NuMI flux, probability and cross section. . . . .	103
3.2	Upper bounds on the LNV NSI flavour coefficients $ \epsilon_{\alpha\beta} $ in the $e$ and $\mu$ sectors. Left: bounds derived from conventional microscopic LNV processes, with $0\nu\beta\beta$ decay ( $^{76}\text{Ge}$ ) being the most effective the $e$ sector and $\mu^- - e^+$ conversion loosely constraining the $\mu$ sector. Right: bounds from LBL oscillation experiments MINOS and KamLAND. Two values indicate the variation in the upper bound as $(\alpha_2, \alpha_3)$ are varied. . . . .	107
4.1	Bounds on neutral-current neutrino NSI coefficients $c_{LY}^\psi$ for $\psi \in \{\ell, u, d\}$ and $Y \in \{L, R\}$ from the current best limits from cLFV experiments. For the bottom two coefficients $q \in \{u, d\}$ . . . . .	127

4.2	Predicted shifts to the $1S - 2S$ and hyperfine splittings of two-body systems ( $\psi_\alpha, \psi'_\beta$ ) due to the SM-induced neutrino-mediated potential $V_{\alpha\beta}^{LL}$ for three active neutrinos with $m_1 = 0.1$ eV and the other masses and mixings determined in the NO case. Where possible we compare these to the differences between the experimental and theoretical values for these splittings. Uncertainties are calculated by adding the experimental and theoretical uncertainties in quadrature. . . . .	158
4.3	(Left) Upper limits on $c_{RX}$ (for $X \in \{L, R\}$ ) from the right-handed current potential $V_{\alpha\beta}^{LR}$ , probed by the hyperfine splittings of the systems ( $\psi_\alpha, \psi'_\beta$ ). We assume three light active Majorana neutrinos with $m_1 = 0.1$ eV and NO masses and mixings and $(c_{RX}^\ell)_{\alpha;ij} = c_{RX}^\alpha \delta_{ij}$ . (Right) Upper limits on $(g_{XY})_{ij;\alpha} = g_{XY}^\alpha \delta_{ij}$ (for $X, Y \in \{L, R\}$ ) from the scalar-scalar potential $V_{\alpha\beta}^{SS}$ , probed by the $1S - 2S$ splittings of the same systems. . . . .	159
4.4	Upper limits on the magnetic moment $\mu_\nu$ in units of the Bohr magneton probed by the dipole-dipole potential $V_{\alpha\beta}^{\gamma\gamma}$ , derived from the $1S - 2S$ splittings of the systems ( $\psi_\alpha, \psi'_\beta$ ). Equivalent limits apply for the electric dipole moment $\varepsilon_\nu$ . We assume three light active neutrinos with $m_1 = 0.1$ eV and NO masses and mixings. For Dirac neutrinos we take $(\mu_D)_{ij} = \mu_\nu$ , while for Majorana neutrinos $(\mu_M)_{ij} = \mu_\nu(1 - \delta_{ij})$ for $i \leq j$ and $(\mu_M)_{ij} = -\mu_\nu$ for $i > j$ . We also derive upper limits on the transition magnetic moments between two heavy sterile neutrinos $(\mu_M)_{45} = -(\mu_M)_{54} = \mu_N$ . Active and active-sterile neutrino magnetic moments are neglected. . . . .	160

5.1	Light $ \mathcal{M}_v^{0\nu} $ and heavy $ \mathcal{M}_N^{0\nu} $ NMEs and associated fractional uncertainties $\delta \mathcal{M}_v^{0\nu} $ and $\delta \mathcal{M}_N^{0\nu} $ for $^{76}\text{Ge}$ and $^{136}\text{Xe}$ used in this work, taken from QRPA, IBM and ISM calculations in the literature, which are the only available methods quoting both light and heavy neutrino NMEs. When not explicitly given in the reference we estimate the uncertainties from the variation of NMEs with $g_A$ and the choice of short-range correlations. . . . .	197
5.2	Gamow-Teller NMEs for four $2\nu\beta\beta$ decay isotopes calculated within the pn-QRPA with partial isospin restoration assuming the axial vector coupling $g_A = 1$ . . . . .	213
5.3	A selection of current and future $0\nu\beta\beta$ decay search experiments measuring the $2\nu\beta\beta$ decay spectrum of the four isotopes considered in this chapter. Shown are the current and forecasted exposures, total number of events $N_{\text{events}}$ , energy resolutions $\Delta E$ and parameters $(\sigma_\eta, \sigma_f)$ estimating the effect of systematic errors on the log-likelihood function. . . . .	222
B.1	Exact values of the dimensionless integrals $J_{ij}^X(r)$ for $N = \{\text{D, M, } V, \Delta, S, T\}$ derived from the potentials $I_{ij}^X(r) \approx 1$ in the limit of vanishing neutrino masses, $m_i \approx 0$ . These appear in the potentials $V_{\alpha\beta}^{LL}, V_{\alpha\beta}^{LR}, V_{\alpha\beta}^{RR}, V_{\alpha\beta}^{VS}$ and $V_{\alpha\beta}^{VT}$ in this work. . . . .	238

## Chapter 1

# Introduction and Overview

*“I don’t say that the neutrino is going to be a practical thing, but it has been a time-honored pattern that science leads, and then technology comes along, and then, put together, these things make an enormous difference in how we live.”*

- Frederick Reines

Wolfgang Pauli, having introduced a light, neutral, and weakly-interacting fermion, or *neutrino*, to explain the observed continuous energy spectrum of beta decay, declared a few years later: “*I have done a terrible thing, I have postulated a particle that cannot be detected*” [1]. The information available at the time justified his pessimism. The weak interaction, as described by Fermi’s theory of beta decay, predicted an antineutrino scattering cross section with the proton of order  $10^{-44}$  cm<sup>2</sup> [2]. A back-of-the-envelope calculation by Bethe and Peierls showed neutrinos possess a penetrating power of around 10<sup>16</sup> km in solid matter [3]. They therefore concluded that it is “*impossible to observe processes of this kind*”.

Theoretical interest in neutrinos nevertheless remained strong in the following years. In 1935 Goeppert-Mayer proposed the second-order weak process of two-neutrino double beta ( $2\nu\beta\beta$ ) decay [4]. Though suppressed, this process is *a priori* possible for an isotope with an even atomic number  $A$  and an energetically forbidden beta decay channel. In order to account for beta decays in which the spin of the nucleus changes by one unit, Gamow and Teller extended the Fermi theory in 1936 to include axial vector currents [5]. In 1937 Majorana suggested

that neutrinos can be their own antiparticles [6]. This led Furry to postulate the neutrinoless double beta ( $0\nu\beta\beta$ ) decay process in 1939, which is only allowed if neutrinos are so-called Majorana fermions [7]. Fermi's theory of weak interactions also successfully described the observed decay rate of the muon, discovered in 1937 as secondary cosmic rays [8,9]. Hints of new particles beyond the electron, photon, proton and neutron shed little light on the neutrino however.

It was the remarkable insight of Reines and Cowan in 1952 to take advantage of the  $10^{12} - 10^{13} \text{ s}^{-1} \text{ cm}^{-2}$  flux of antineutrinos being produced by the first fission nuclear reactors [10]. Their initial plan had been to use a greater flux of antineutrinos emitted in a controlled nuclear explosion. Their detector, 'El Monstro', would use the liquid scintillation technique to detect antineutrinos via the inverse beta decay process  $\bar{\nu} + p \rightarrow e^+ + n$ . It proved more reliable however to use a smaller but constant flux of reactor antineutrinos, first at the Hanford site, then at the Savannah River site. Their Cd-doped detector aimed to detect both the outgoing positron (via  $e^+ + e^- \rightarrow \gamma$ , followed by Compton scattering and electron cascades) and neutron by absorption. On June 14 1956, Reines and Cowan sent a telegram to Pauli: "*We are happy to inform you that we have definitely detected neutrinos... Observed cross section agrees well with expected six times ten to minus forty-four square centimeters*" [11].

The observation of parity (P) violation in kaon decays and Wu's measurement of the beta decay of polarised  $^{60}\text{Co}$  [12], a test suggested by Lee and Yang [13], suggested that Fermi's theory needed to be extended in some way. By 1958 a range of authors had settled on the vector minus axial vector, or ( $V - A$ ), theory of weak interactions [14–16]. Neutrinos were assumed to be very light, possibly massless, and therefore only a two-component left-handed neutrino field  $\nu_L$  was needed in the theory [17–20]. The absence of processes such as  $\bar{\nu} + ^{37}\text{Cl} \rightarrow e^- + ^{37}\text{Ar}$  (searched for by Davis) also led to the suggestion of a conserved universal lepton number [21]. Furthermore, the absence of the radiative decay mode  $\mu \rightarrow e\gamma$  implied a conserved lepton number for each lepton family. Pontecorvo proposed the existence of a *muon* neutrino,  $\nu_\mu$ , distinct from the previously detected *electron* neutrino,  $\nu_e$ , and pro-

duced alongside muons in weak interactions [22]. This was confirmed by Lederman, Schwartz and Steinberger at Brookhaven National Laboratory (BNL) in 1962 via  $\nu_\mu + n \rightarrow \mu^- + p$  scattering [23].

While the  $(V - A)$  correction had significantly improved the Fermi theory, it was clear in the language of quantum field theory (QFT) that the model was an *effective* field theory (EFT). The model was expected to break down at energies  $E \sim 1/\sqrt{G_F} \sim 100$  GeV, where  $G_F$  is the effective Fermi coupling constant. In 1967, Weinberg and Salam constructed a theory combining the  $SU(2)_L \times U(1)_Y$  electroweak gauge group of Glashow and the spontaneous symmetry breaking mechanism of Brout, Englert and Higgs to explain both the origin of the fermion masses and short-range nature of the weak interaction [24–28]. The theory was proven to be renormalisable and thus highly predictive by ‘t Hooft and Veltman in 1971 [29]. Confirmation of the theory came in 1973 with the discovery of the predicted weak neutral current at the CERN Gargamelle experiment [30]. The  $W^\pm$  and  $Z$  bosons were produced directly a decade later at the CERN Super Proton Synchrotron [31, 32].

The veritable *particle zoo* that emerged after the discovery of the kaon in 1947 led to a chaotic period in the field. In order to make sense of the long lifetimes of the kaon and  $\Lambda^0$  particle, Gell-Mann, Nakano and Nishijima introduced the *strangeness* quantum number  $S$  [33, 34]. In a further bid to categorise and recognise emerging patterns between the different mesons and baryons (particles known to interact strongly, or *hadrons*), Gell-Mann and Ne’eman arranged the known particles into singlets, octets and decuplets in 1961 [35, 36]. This *eightfold way* established group theory as a useful tool for characterising flavour symmetries in particle physics. The long-lived nature of the *strange* hadrons was also examined by Cabibbo, who introduced a mixing angle  $\theta_C$  to parametrise the difference between the observed  $\Delta S = 0$  and  $\Delta S = 1$  weak currents [37]. In 1964 Gell-Mann and Zweig announced a simplification to the picture; the known hadrons are composite particles made up of elementary *quarks* [38–40]. Three were needed to explain the known *zoo* (up, down and strange), but a fourth (charm) was first postulated by Glashow and Bjorken to

match the known number of leptons [41]. Glashow, Iliopoulos and Maiani also invoked a fourth quark to account for the non-observation of flavour-changing neutral currents (FCNCs) [42]. The charm quark was discovered at BNL and the Stanford Linear Accelerator Center (SLAC) during a period known as the ‘November revolution’ of 1974 [43, 44].

A year earlier Kobayashi and Maskawa had already put forward the existence of a third generation of quarks [45]. In 1964 charge and parity (CP) violation had been observed in the decays of neutral kaons by Christenson, Cronin, Fitch and Turlay [46]. A complex phase was needed in the mixing matrix between the flavour and mass eigenstate down-type quark fields; this was not possible for two generations. In addition, the third generation of leptons was established with the discovery of the  $\tau$  lepton by Perl et al. at SLAC in 1975 [47]. While the bottom quark was discovered soon after by the E288 experiment at Fermilab in 1977 [48], the corresponding top quark remained elusive in the following years. The collisions of protons and antiprotons detected by the CDF and D $\emptyset$  experiments at the Fermilab Tevatron collider could only set lower limits on the top quark mass [49, 50]. It was realised, however, that the top quark, if present, contributes to loop corrections of electroweak observables. In particular *oblique corrections* to  $W^\pm$  and  $Z$  propagators, parametrised by the  $S$ ,  $T$  and  $U$  parameters, could be sensitive to both the top quark and Higgs boson masses [51]. Hints of the top quark finally became evidence in 1995, when the CDF and D $\emptyset$  collaborations announced a mass of  $m_t = 176 \pm 18$  GeV, in agreement with the range of masses implied by the  $T$  parameter [52, 53].

The theory of strong interactions also progressed considerably in this time. The  $\Delta^{++}$  and  $\Omega^-$  baryons, composed of three up and strange quarks with parallel spins respectively, were seen as evidence of an additional quantum number possessed by quarks [54]. This observation was quickly developed in a theory with an  $SU(3)_c$  gauge symmetry with a quark *color* charge, quantum chromodynamics (QCD) [55]. The octet of gauge mediators for this symmetry group, also possessing color charge, were named *gluons*. The impact of gluon self-interactions was soon discovered by

Gross, Wilczek and Politzer in 1973; the asymptotic freedom of the strong coupling constant  $\alpha_s$  [56, 57]. This explained both the confinement of quarks in hadrons at low energies and Bjorken and Feynman’s perturbative treatment of *partons* used to quantify deep inelastic scattering at high energies [58–60].

The *Standard Model* (SM) of quarks and leptons interacting via the strong and electroweak forces was convincingly confirmed by the ALEPH, OPAL, DELPHI and L3 detectors at the Large Electron Positron (LEP) collider at CERN [61–64]. Through measurements of the invisible  $Z$  boson decay width, LEP experiments confirmed there to be no more than three generations of neutrinos lighter than  $m_Z$  [65]. The *tau* neutrino,  $\nu_\tau$ , was ultimately discovered by the DONUT collaboration at Fermilab in 2000 [66]. The culmination of the story came in 2012 with the discovery of the Higgs boson by the ATLAS and CMS experiments at the CERN Large Hadron Collider (LHC) [67, 68].

The SM contains only three two-component left-handed neutrino fields. Hence the neutrinos cannot gain masses via the Higgs mechanism. While massless neutrinos remained (and still remain) compatible with beta decay and neutrino scattering measurements, hints nevertheless began to emerge suggesting non-zero neutrinos masses. A spurious detection of reactor antineutrinos by Davis via the process  $\bar{\nu} + {}^{37}\text{Cl} \rightarrow e^- + {}^{36}\text{Ar}$  supported Pontecorvo’s proposal of  $\nu \leftrightarrows \bar{\nu}$  oscillations in 1957 [69], analogous to the  $K^0 \leftrightarrows \bar{K}^0$  phenomenon predicted by Gell-Mann and Pais [70]. However, the subsequent development of the  $(V - A)$  theory made it apparent that a ‘helicity flip’ is necessary for the process; for ultra-relativistic neutrinos this induces a strong suppression.

Moving on to the Homestake experiment, Davis famously saw a deficit of solar  $\nu_e$  compared to the expected flux from contemporary solar models [71, 72]. The persistence of the solar anomaly led to the suggestion of neutrino *flavour* oscillations. Building on the work of Maki, Nakagawa and Sakata, in 1969 Gribov and Pontecorvo raised the possibility of  $\nu_e \leftrightarrows \nu_\mu$  oscillations if neutrinos are massive and there is a mismatch between the (interacting) flavour and (propagating) mass eigenstates, similar to down-type quarks [73–76]. This mixing framework

was soon extended to include a third neutrino flavour and mass eigenstate, i.e.  $\nu_e \leftrightarrows \nu_\tau$  and  $\nu_\mu \leftrightarrows \nu_\tau$  oscillations, raising the possibility of CP violation in the lepton sector [77]. Tantalising hints at the Kamiokande and IMB experiments soon became a conclusive confirmation of the neutrino oscillation hypothesis in 1997, when the Super-Kamiokande experiment observed a disappearance of atmospheric muon neutrinos [78–80]. Not long after the Sudbury Neutrino Observatory (SNO) verified the disappearance of  ${}^8\text{B}$  solar neutrinos [81].

The parameters controlling neutrino oscillations in the three-neutrino picture are two mass-squared splittings, three mixing angles and a CP phase. These have since been probed by a variety of experiments. For example, long-baseline (LBL) accelerator oscillation experiments MINOS, K2K, NOvA and T2K and searches for atmospheric neutrinos at Super-Kamiokande and IceCube (DeepCore) have pinned down the so-called atmospheric mass-squared splitting  $\Delta m_{\text{atm}}^2$  and mixing angle  $\theta_{23}$  [82–86]. Combined measurements of solar neutrino disappearance by GALLEX, SAGE, Super-Kamiokande and Borexino, and also the LBL reactor antineutrino experiment KamLAND, have determined the solar mass-squared splitting  $\Delta m_{\text{sol}}^2$  and angle  $\theta_{12}$  [87–91]. The so-called Large Mixing Angle (LMA) solution verified the resonant enhancement effect of neutrinos propagating through a medium, pioneered by Mikheyev, Smirnov and Wolfenstein [92, 93]. Finally, the LBL accelerator experiments MINOS and T2K and short baseline (SBL) reactor experiments such as Double CHOOZ, RENO and Daya Bay have been able to measure the small angle  $\theta_{13}$  [94–99]. By comparing  $\nu_\mu \leftrightarrows \nu_e$  and  $\bar{\nu}_\mu \leftrightarrows \bar{\nu}_e$  oscillations, the next-generation LBL oscillation experiments DUNE and Hyper-Kamiokande aim to determine the octant of the mixing angle  $\theta_{12}$ , the sign of  $\Delta m_{\text{atm}}^2$  (and hence the ordering of neutrino mass eigenstates) and the CP phase  $\delta_{\text{CP}}$  [100, 101].

Unfortunately, neutrino oscillations are only sensitive to neutrino mass-squared splittings, not to their absolute mass scale. It is nevertheless possible to infer that the two heaviest neutrinos have masses greater than  $\sqrt{\Delta m_{\text{sol}}^2} \simeq 9 \times 10^{-3}$  eV and  $\sqrt{\Delta m_{\text{atm}}^2} \simeq 0.05$  eV, respectively. Precision kinematical measurements at the endpoint of the  ${}^3\text{H}$  beta decay spectrum have instead been able to constrain the *ef*-

fective mass of the electron neutrino,  $m_\beta$ . The Mainz and Troitsk experiments combined to enforce a limit  $m_\beta < 2.2$  eV, while a recent analysis by the KATRIN experiment set  $m_\beta < 1.1$  eV at 90% CL [102–104]. The forecasted future sensitivities of the KATRIN and Project 8 experiments are, respectively,  $m_\beta < 0.1$  eV and  $m_\beta < 0.04$  eV [105, 106].

Neutrinos are also known to have played a crucial role in the evolution of the universe [107, 108]. It is thought that neutrinos remained in thermal equilibrium with the primordial SM bath via scattering processes such as  $e^+ + e^- \rightarrow \nu + \bar{\nu}$ . However, they decoupled when the temperature of the universe dropped below  $T \sim \text{MeV}$ , i.e. when the number density of neutrinos  $n_\nu$  multiplied by the thermally-averaged cross section  $\langle \sigma v \rangle$  fell below the Hubble expansion rate,  $n_\nu \langle \sigma v \rangle \lesssim H(T)$  [109, 110]. When the electrons subsequently decoupled, they injected entropy into the photon bath, increasing its temperature with respect to the neutrinos. Probes of the expansion of the universe during the radiation dominated era, such as the Cosmic Microwave Background (CMB) and matter density fluctuations, are sensitive to  $N_{\text{eff}}$  (the effective number of relativistic fermionic degrees of freedom) and  $\sum m_\nu$  (the sum of neutrino masses). The SM prediction for the former, taking into account that the neutrinos underwent oscillations and were not fully decoupled when the electrons and positron annihilated, is  $N_{\text{eff}} = 3.046$  [111–113]. The current best fit value from the Planck collaboration is  $N_{\text{eff}} = 2.99 \pm 0.17$  [114]. The abundances of light elements in the universe, particularly  ${}^4\text{He}$ , also offer a complementary probe of  $N_{\text{eff}}$ . The abundances are set during the Big Bang Nucleosynthesis (BBN), when free protons and neutrons are bound into nuclei up to  ${}^7\text{Li}$  [115]. The  ${}^4\text{He}$  mass fraction  $Y_p$  is controlled by the proton to neutron ratio, which is in turn determined by the neutrino decoupling temperature and  $N_{\text{eff}}$  [116, 117]. Non-zero neutrino masses,  $\sum m_\nu \neq 0$ , result in small distortions to the power spectra of the CMB and matter distribution of the universe [118]. The current upper bound from the Planck collaboration combining all available data is  $\sum m_\nu < 0.12$  eV [114].

We have seen how neutrinos have been critical in improving our understanding of the fundamental interactions and indeed the history of the universe. We now

know that the neutrinos are massive and mixed, but this is not accounted for in the SM. The SM must be extended in some way to incorporate the light neutrino masses, i.e. a  $\nu$ SM. A plethora of models since the 1980s have attempted to answer this question. Suffice to say, these models can be placed in two main categories; those that predict *Dirac* neutrinos (i.e. similar in nature to the other fermions of the SM) or *Majorana* neutrinos (the neutrino is its own antiparticle).

The phenomenology of the two scenarios is different. In the former case, lepton number remains a valid global symmetry of the  $\nu$ SM; processes that are lepton number violating ( $|\Delta L| = 2$ ) are forbidden. In the latter case,  $|\Delta L| = 2$  processes such as  $0\nu\beta\beta$  decay are possible but usually suppressed due to a correlation with the light neutrino masses. An important point to make is related to the so-called *black box* theorem. Any positive signal of an  $|\Delta L| = 2$  process implies that at least one neutrino is of Majorana nature<sup>1</sup> [120–122]. The process may have been induced by new physics (NP) unrelated to neutrinos, but this NP is guaranteed to contribute to a Majorana neutrino mass at the loop level. Another way of thinking about this is to use the EFT approach. Just as the Fermi weak interaction had been constructed from SM fields to describe the exchange of the  $W^\pm$  boson, effective operators can be used to describe the low energy effects of any physics beyond the SM. The lowest dimensional operator in the Standard Model Effective Field Theory (SMEFT), i.e. operators constructed from SM fields respecting the SM gauge symmetries (but not necessarily the SM accidental global symmetries) is the Weinberg operator at dimension-5 [123]. This operator is  $|\Delta L| = 2$  and generates a Majorana mass for the neutrinos.

As the nature of neutrinos and mechanism generating their masses is still unknown, it is important to utilise both the model-dependent and model-independent approaches for considering NP related to the neutrino sector. Measurements of the SM are now entering a precision era. With the high-luminosity LHC now taking a data-intensive approach, ATLAS and CMS are probing the parameters of the Yukawa and Higgs sector and excluding large areas of NP model parameter

---

<sup>1</sup>More specifically  $|\Delta L| = 2$  processes, where  $L$  is lepton number. The neutrinoless ‘quadruple’ beta decay process, which is  $|\Delta L| = 4$ , is compatible with Dirac neutrinos [119].

space [124–127], while precision measurements of flavour observables at LHCb are seeing anomalies in  $B$  meson decays [128]. The discrepancy between the expected and observed muon anomalous magnetic moment,  $\Delta a_\mu$ , first seen at BNL, has recently persisted at the Fermilab Muon g-2 experiment [129, 130].

Measurements of the  $\nu$ SM still need to pin down a few essential parameters, but it is already known that the neutrino sector must be a window to NP, related in some way to the origin of the neutrino masses. A number of unexplained oscillation anomalies have been seen at SBL accelerator experiments LSND and MiniBooNE, reactor experiments DANSS and NEOS, and gallium experiments GALLEX and SAGE [131–137]. All point to an oscillation between an active and sterile (gauge singlet) neutrino with a mass-squared splitting  $\Delta m^2 \sim 1$  eV. Despite this, the light sterile neutrino hypothesis remains in strong tension with MINOS+ and IceCube observations [138, 139]. The same region of parameter space will be tested in future by the Short Baseline Neutrino (SBN) oscillation programme at Fermilab [140].

This thesis is a review of a number of topics worked on by the author in relation to the  $\nu$ SM. Chapter 2 presents an overview of the SM field content, gauge symmetries and accidental global symmetries. Possible  $\nu$ SM extensions are examined. The EFT approach for parametrising new physics is summarised. In Chapters 3 and 4, a model-independent effective approach is taken to examine the sensitivity of neutrino oscillations and precision atomic spectroscopy measurements to general neutrino Non-Standard Interactions (NSIs), based on work of Refs. [141, 142]. In Chapter 5 a model-dependent approach is used; based on work of Refs. [143, 144], it studies a phenomenological *inverse seesaw* (ISS) mechanism parametrising the mixing between an active and sterile neutrino. Constraints derived from  $0\nu\beta\beta$  and  $2\nu\beta\beta$  decay are compared to astrophysical, cosmological, beta decay, beam dump and collider measurements. Chapter 6 summarises the work of this thesis and presents an outlook for the future of the field.

Throughout this thesis the natural units system of particle physics will be used, i.e.  $c = \hbar = k_B = 1$ , where  $c$  is the speed of light in vacuum,  $\hbar$  is the reduced Planck constant, and  $k_B$  is the Boltzmann constant. We use the Heaviside-Lorentz units for

electromagnetism,  $\alpha = \frac{e^2}{4\pi} \approx \frac{1}{137}$ . Finally, the metric tensor is taken to be mostly minus, i.e.  $g_{\mu\nu} = \text{diag}(1, -1, -1, -1)$ , such that  $p \cdot x = g_{\mu\nu} p^\mu x^\nu = p^0 x^0 - \mathbf{p} \cdot \mathbf{x}$ . A particle with mass  $m$  therefore has  $p^2 = p_\mu p^\mu = (p^0)^2 - |\mathbf{p}|^2 = m^2$ .

## Chapter 2

# Neutrinos in the Standard Model and Beyond

In order to describe the electron ( $\nu_e$ ), muon ( $\nu_\mu$ ) and tau ( $\nu_\tau$ ) flavour neutrinos (or equivalently their three massive counterparts  $\nu_1$ ,  $\nu_2$  and  $\nu_3$ ), this thesis will first cover their representation as fermions in the Standard Model (SM) of particle physics. At the time of writing the neutrinos (along with the Higgs boson, the only known fundamental scalar particle) are the least well quantified fundamental particles. As explained in this chapter, the origin and nature of their small and still-undetermined masses remain unknown. The SM therefore also acts as a foundation on which to build extensions describing exotic interactions of the neutrinos (which, as we will see, are most commonly related to the dynamic mechanism generating their light masses).

### 2.1 The Standard Model of Particle Physics

As discussed in the previous chapter, the SM has gradually emerged as one of the most successful theories in the history of modern science. The SM provides a unified description of the electromagnetic, weak and strong interactions among the three generations of quarks and leptons; thought to constitute roughly 5% of the observed matter in the universe<sup>1</sup>. Using its general framework one can make stunningly precise predictions for the binding energies of electrons in atoms, the scatter-

---

<sup>1</sup>The remaining  $\sim 95\%$  is composed of non-baryonic dark matter and dark energy in the standard  $\Lambda$ CDM model of cosmology.

ing of protons in high-energy collisions and the abundances of light elements across the observable universe.

The description of gravity as the bending of space-time in general relativity is the second pillar of modern physics; it is nonetheless predicted to break down at energies larger than  $1.22 \times 10^{19}$  GeV, when matter is crushed into a singularity at the centre of a black hole. The continuing validity of the SM at higher energies remains unclear. There are outstanding issues such as the hierarchy and strong CP problems which boil down to a tolerance for fine-tuning. Other, more fundamental problems are the abundance of matter over antimatter in the universe, the identity of dark matter and dark energy, the driver of cosmic inflation  $10^{-36}$  seconds after the Big Bang and the aforementioned origin of neutrino masses. For a long time it has been thought that each issue can be explained if the particles and forces of the SM unify as a more symmetric theory at higher energies, combining finally with gravity just below the Planck scale. There has been intense work in the theoretical community to elucidate this theory since supersymmetry (SUSY), Grand Unified Theories (GUTs) and higher-dimensional string theories were first developed in the 1970s. At present there is no high-energy theory that uniquely reproduces the SM at low energies and also predicts the fine-structure constant  $\alpha$  and electron mass  $m_e$ .

### 2.1.1 Field Content and Symmetries

The Standard Model of particle physics is a relativistic quantum field theory (QFT) based on the product of gauge groups  $SU(3)_c \times SU(2)_L \times U(1)_Y$ . The non-abelian group  $SU(3)_c$  describes the strong interaction between colored quarks via the exchange of gluons, also known as quantum chromodynamics (QCD). The non-abelian and abelian groups  $SU(2)_L \times U(1)_Y$  collectively describe the electroweak (EW) interaction distinguishing left- and right-handed fermion fields. The EW symmetry is spontaneously broken via the Higgs mechanism<sup>2</sup> to  $U(1)_Q$ , which describes the electromagnetic interactions between electrically charged particles via the exchange of photons, i.e. quantum electrodynamics (QED).

The dynamics of the SM can be understood by writing a Lagrangian invariant

---

<sup>2</sup>More correctly the Brout–Englert–Higgs–Guralnik–Hagen–Kibble mechanism [27, 145, 146].

SM Field	$SU(3)_c$	$SU(2)_L$	$U(1)_Y$	Lorentz Group
$L_L = \begin{pmatrix} v_L \\ \ell_L \end{pmatrix}$	<b>1</b>	<b>2</b>	$-\frac{1}{2}$	$(\frac{1}{2}, 0)$
$\ell_R$	<b>1</b>	<b>1</b>	$-1$	$(0, \frac{1}{2})$
$Q_L = \begin{pmatrix} u_L \\ d_L \end{pmatrix}$	<b>3</b>	<b>2</b>	$\frac{1}{6}$	$(\frac{1}{2}, 0)$
$u_R$	<b>3</b>	<b>1</b>	$\frac{2}{3}$	$(0, \frac{1}{2})$
$d_R$	<b>3</b>	<b>1</b>	$-\frac{1}{3}$	$(0, \frac{1}{2})$
$H = \begin{pmatrix} H^+ \\ H^0 \end{pmatrix}$	<b>1</b>	<b>2</b>	$\frac{1}{2}$	$(0, 0)$
$G_\mu^a$	<b>8</b>	<b>1</b>	0	$(\frac{1}{2}, \frac{1}{2})$
$W_\mu^i$	<b>1</b>	<b>3</b>	0	$(\frac{1}{2}, \frac{1}{2})$
$B_\mu^a$	<b>1</b>	<b>1</b>	0	$(\frac{1}{2}, \frac{1}{2})$

**Table 2.1:** Matter and gauge fields of the SM. Given in the columns are the transformation properties of the fields under the SM gauge group  $SU(3)_c \times SU(2)_L \times U(1)_Y$ , i.e. either as a triplet or singlet under  $SU(3)_c$ , a doublet or singlet under  $SU(2)_L$  and their hypercharge  $Y$ . Also given are the transformation properties of the fields under the restricted Lorentz group  $SO^+(1,3)$ . Fields are given in the flavour basis, i.e.  $v \in \{v_e, v_\mu, v_\tau\}$ ,  $\ell \in \{e, \mu, \tau\}$ ,  $u \in \{u, c, t\}$  and  $d \in \{d, s, b\}$ .

under the symmetries discussed above. One must first introduce the matter fields in Table 2.1; the left- and right-handed charged lepton, up-type and down-type quark fields  $\ell_{L(R)}$ ,  $u_{L(R)}$ ,  $d_{L(R)}$ , respectively, the left-handed neutrino field  $v_L$  and two complex scalar fields  $H^+$  and  $H^0$ . The two-component Weyl spinor fermion fields can be written as components of the four-component Dirac field  $\psi$

$$\psi_L = P_L \psi, \quad \psi_R = P_R \psi, \quad \psi = \begin{pmatrix} \chi_\alpha \\ \eta^{+\alpha} \end{pmatrix}, \quad (2.1)$$

where the spinor indices  $\alpha, \dot{\alpha} \in \{1, 2\}$  and

$$P_L = \frac{1}{2} (1 - \gamma_5), \quad P_R = \frac{1}{2} (1 + \gamma_5), \quad (2.2)$$

are left- and right-handed projection operators, respectively, with  $\gamma^5 = i\gamma^0\gamma^1\gamma^2\gamma^3$ . The  $\gamma^\mu$  are the standard four-dimensional Dirac matrices with the anticommutation relation  $\{\gamma^\mu, \gamma^\nu\} = 2g^{\mu\nu}$ , where  $g_{\mu\nu} = \text{diag}(1, -1, -1, -1)$  is the flat Minkowski metric, so that they generate a matrix representation of the Clifford

algebra  $C\ell_{1,3}(\mathbb{R})$  [147]. The fields  $\psi_L$  and  $\psi_R$  defined in this way are technically four-component spinors, but there is a one-to-one correspondence between these and the two Weyl spinors  $\chi$  and  $\eta^\dagger$  in  $\psi$  if one assumes  $\gamma^\mu$  to be in the Weyl or chiral basis [148].

The fermion fields in Table 2.1 are repeated over  $n_f = 3$  generations;  $v_\alpha, \ell_\alpha, u_\alpha$  and  $d_\alpha$  with  $\alpha \in \{1, 2, 3\}$ <sup>3</sup>, though we will often omit this flavour index in the text for simplicity. The quark fields transform as triplets under  $SU(3)_c$  transformations, while the charged lepton and neutrino fields transform as singlets. The left-handed charged lepton and neutrino, up- and down-quark and two scalar fields are arranged in doublets  $L_L, Q_L$  and  $H$ , respectively, under  $SU(2)_L$  transformations. Each field has a hypercharge quantum number  $Y$  under  $U(1)_Y$  transformations.

It should also be noted that, per Wigner's classification, each field is an unitary irreducible representation of the Poincaré group (the combination of the Lorentz group  $O(1, 3)$  and space-time translations) [149]. Each representation is infinite-dimensional and labelled by eigenvalues of the Casimir invariants  $P^2 = P_\mu P^\mu$  and  $W^2 = W_\mu W^\mu$ . Here  $P_\mu = (E, \mathbf{P})$  is the four-momentum and  $W_\mu = \frac{1}{2}\epsilon_{\mu\nu\rho\sigma}J^{\nu\rho}P^\sigma$  is the Pauli-Lubanski pseudovector, where  $\epsilon_{\mu\nu\rho\sigma}$  is the four-dimensional Levi-Civita symbol and  $J^{\nu\rho}$  is the relativistic angular-momentum tensor. The first invariant defines the mass  $m$  of the particle and the latter its spin  $J$ , where  $m$  is a non-negative real number and  $J$  is a non-negative half-integer ( $J = 0, \frac{1}{2}, 1, \frac{3}{2}, \dots$ ). For each three-momentum eigenvalue of  $\mathbf{P}$  there are respectively 2 and  $2J + 1$  independent states for  $m = 0$  and  $m > 0$ <sup>4</sup>. A convenient quantity is the projection of the spin  $\mathbf{S}$  along the direction of motion of the particle, called the helicity. This can be constructed from

$$\hat{h} = \frac{W^0}{s|\mathbf{P}|} = \frac{\mathbf{S} \cdot \mathbf{P}}{s|\mathbf{P}|}. \quad (2.3)$$

The degrees of freedom of spin-0, spin- $\frac{1}{2}$  and spin-1 fields can be embedded in the fields  $\phi(x)$ ,  $\psi(x)$  and  $V_\mu(x)$  respectively.

---

<sup>3</sup>We note that the flavour index  $\alpha$  is different from the spinor index in Eq. (2.1).

<sup>4</sup>*A priori*, massless states with continuous spin and so-called tachyonic states with  $m < 0$  can also exist, but are not observed in nature [150–152].

The full Lorentz group (including boosts, rotations, parity flips and time reversals) is a Lie group, and its Lie algebra can be written as the sum of two commuting sub-algebras,  $\mathfrak{so}(1, 3) = \mathfrak{su}(2) \oplus \mathfrak{su}(2)$ . It follows that any irreducible representation of the Lorentz group is characterised by two irreducible representations of  $\mathfrak{su}(2)$  (the algebra of the Pauli matrices generating the  $\text{SO}(3)$  rotation group), or two non-negative half-integers  $(a, b)$ . These are given in the final column of Table 2.1 for the left- and right-handed Weyl spinor fermion fields and scalar doublet. It is often conventional to consider the charge conjugate  $\psi_R^c \equiv \mathcal{C} \bar{\psi}_R^\top$  of the right-handed fields, where  $\mathcal{C} = i\gamma^2\gamma^0$  is the charge conjugation matrix, so that all the fermion fields transform like left-handed fields. The  $u_R^c$  field for example also transforms with opposite hypercharge to  $u_R$  and as an antitriplet  $\bar{\mathbf{3}}$  under  $\text{SU}(3)_c$ .

### 2.1.2 Gauge and Kinetic Terms

We now require a Lagrangian that is Lorentz-invariant and unitary (probabilities for processes are well-defined and add to unity). Such a Lagrangian is also CPT symmetric [153]. For massive fermions  $\psi$  this can naively be achieved with

$$\mathcal{L}_\psi = i\bar{\psi}_L \not{\partial} \psi_L + i\bar{\psi}_R \not{\partial} \psi_R - m\bar{\psi}_L \psi_R - m\bar{\psi}_R \psi_L = \bar{\psi}(i\not{\partial} - m)\psi, \quad (2.4)$$

where  $\not{\partial} = \gamma^\mu \partial_\mu$  and  $\bar{\psi} \equiv \psi^\dagger \gamma^0$ . Applying the Euler-Lagrange equations of motion,

$$\partial_\mu \frac{\partial \mathcal{L}_\psi}{\partial (\partial_\mu \bar{\psi})} - \frac{\partial \mathcal{L}_\psi}{\partial \bar{\psi}} = 0, \quad (2.5)$$

recovers the relativistic free-field Dirac equation  $(i\not{\partial} - m)\psi = 0$ .

Unfortunately there are problems with Eq. (2.4) arising from the requirement of gauge invariance. Under the SM gauge transformations the fields transform under representations of the groups as

$$\psi \xrightarrow{\text{SU}(3)_c} \psi' = e^{i\theta^a(x)t^a} \psi, \quad (2.6)$$

$$\psi \xrightarrow{\text{SU}(2)_L} \psi' = e^{i\theta^i(x)T^i} \psi, \quad (2.7)$$

$$\psi \xrightarrow{\text{U}(1)_Y} \psi' = e^{i\theta(x)Y} \psi, \quad (2.8)$$

where  $t^a \equiv \frac{\lambda^a}{2}$  ( $a = 1, \dots, 8$ ) and  $T^i \equiv \frac{\sigma^i}{2}$  ( $i = 1, 2, 3$ ) are the generators of the  $SU(3)_c$  and  $SU(2)_L$  groups, respectively. These satisfy the Lie group algebras

$$[t^a, t^b] = i f_{abc} t^c, \quad [T^i, T^j] = i \epsilon_{ijk} T^k, \quad (2.9)$$

where  $\epsilon_{ijk}$  (the three-dimensional Levi-Civita symbol) and  $f_{abc}$  are the group structure constants. Since the SM gauge groups are unitary (and special for  $SU(3)_c$  and  $SU(2)_L$ , such that their determinant is unity), all of their representations  $U(x)$  are unitary. Thus the fermion bilinear  $\bar{\psi} \psi \rightarrow \bar{\psi}' \psi' = \bar{\psi} U^\dagger U \psi = \bar{\psi} \psi$  is in principle gauge invariant. However, the mass terms of Eq. (2.4) combine  $\psi_L$  and  $\psi_R$  which transform under different representations of  $SU(2)_L \times U(1)_Y$ . These cross-terms are therefore prohibited if SM gauge invariance is to be conserved.

Furthermore, the kinetic term transforms as

$$\bar{\psi} \partial_\mu \psi \rightarrow \bar{\psi}' \partial_\mu \psi' = \bar{\psi} U^\dagger \partial_\mu (U \psi) = \bar{\psi} \partial_\mu \psi + \bar{\psi} U^\dagger (\partial_\mu U) \psi, \quad (2.10)$$

i.e., in an inhomogeneous way. We require a derivative that transforms covariantly under the gauge transformation, i.e.  $D_\mu \psi \rightarrow D'_\mu \psi' = U D_\mu \psi$ . This derivative can be obtained by defining

$$D_\mu = \partial_\mu + i g_s G_\mu^a t^a + i g W_\mu^i T^i + i g' B_\mu Y, \quad (2.11)$$

i.e., adding an extra term for each gauge group. We have introduced a number of so-called gauge fields equal to the number of generators for each group. The arbitrary real constants  $g_s$ ,  $g$  and  $g'$  will come to be associated with the coupling strengths of the matter fields to the gauge fields. For the derivative to be covariant it must equivalently satisfy  $D'_\mu = U D_\mu U^{-1}$ . We then observe (for just the  $U(1)_Y$  gauge group)

$$\begin{aligned} D_\mu \xrightarrow{U(1)_Y} D'_\mu &= \partial_\mu + i g' B'_\mu Y = U(\partial_\mu + i g' B_\mu Y) U^{-1} \\ &= \partial_\mu + U(\partial_\mu U^{-1}) + U i g' B_\mu Y U^{-1}. \end{aligned} \quad (2.12)$$

For the left- and right-hand sides of the Eq. (2.12) to be equal, the  $U(1)_Y$  gauge field  $B_\mu$  must transform as

$$B_\mu Y \xrightarrow{U(1)_Y} B'_\mu Y = U \left( B_\mu Y - \frac{i}{g'} \partial_\mu \right) U^{-1} = \left( B_\mu - \frac{1}{g'} \partial_\mu \theta(x) \right) Y, \quad (2.13)$$

where in the second equality we have expanded the infinitesimal transformation around unity, i.e.  $U(x) \approx 1 + i\theta(x)Y$ . The same procedure is slightly more involved for the non-Abelian gauge groups due to the multiple gauge fields and group generators satisfying the commutator relations of Eq. (2.9). Nevertheless one can find that the fields transform as

$$G_\mu^a \xrightarrow{\text{SU}(3)_c} G'_\mu^a = G_\mu^a - \frac{1}{g_s} \partial_\mu \theta^a(x) + f^{abc} G_\mu^b \theta^c(x), \quad (2.14)$$

$$W_\mu^i \xrightarrow{\text{SU}(2)_L} W'_\mu^i = W_\mu^i - \frac{1}{g} \partial_\mu \theta^i(x) + \epsilon^{ijk} W_\mu^j \theta^k(x). \quad (2.15)$$

Equipped with the covariant derivative  $D_\mu$  we can now write the kinetic part of the SM Lagrangian for the fermions,

$$\mathcal{L}_\psi = i\bar{\psi} \not{D} \psi, \quad (2.16)$$

where  $\psi \in \{L_L, \ell_R, Q_L, u_R, d_R\}$ . This not only describes the kinetic evolution of the (currently massless) matter fields, but also their couplings to the SM gauge fields.

We now proceed to determine the kinetic part of the Lagrangian for the gauge fields, which, represented by the fields  $G_\mu^a$ ,  $W_\mu^i$  and  $B_\mu$ , we know to be spin-1 vector bosons. We wish the Lagrangian to be positive definite, i.e. give energy densities that are bounded from below. To ensure this one can write for a massive spin-1 field  $A_\mu$  the so-called Proca Lagrangian

$$\mathcal{L}_A = -\frac{1}{4} F_{\mu\nu} F^{\mu\nu} + \frac{1}{2} m^2 A_\mu A^\mu, \quad (2.17)$$

where  $F_{\mu\nu} = \partial_\mu A_\nu - \partial_\nu A_\mu$  is the usual field strength tensor. The equation of motion for this Lagrangian is  $(\partial_\mu \partial^\mu + m^2) A_\nu = 0$ ; identical to the relativistic Klein-Gordon

equation for a scalar field. It also implies the constraint  $\partial_\mu A^\mu = 0$  which eliminates one of the four degrees of freedom of the vector field. The three remaining degrees of freedom correspond to the two transverse polarisations and one longitudinal polarisation of the spin-1 field.

The flaw in Eq. (2.17) is that the mass term cannot be invariant under gauge transformations  $A_\mu \rightarrow A'_\mu$ . The gauge fields  $G_\mu^a$ ,  $W_\mu^i$  and  $B_\mu$  are thus massless, and indeed the gauge symmetry cancels an additional degree of freedom corresponding to the longitudinal polarisation states of these fields. The kinetic term in Eq. (2.17) is also only gauge invariant for  $U(1)_Y$ ; generalisations of the field strength tensor must be used for  $SU(3)_c$  and  $SU(2)_L$ . To find these, notice that the second-order tensors  $[D_\mu^G, D_\nu^G]$  and  $[D_\mu^W, D_\nu^W]$  transform as

$$[D_\mu^G, D_\nu^G] \xrightarrow{SU(3)_c} [D_\mu^G, D_\nu^G]' = U[D_\mu^G, D_\nu^G]U^{-1}, \quad (2.18)$$

$$[D_\mu^W, D_\nu^W] \xrightarrow{SU(2)_L} [D_\mu^W, D_\nu^W]' = U[D_\mu^W, D_\nu^W]U^{-1}, \quad (2.19)$$

where the superscripts denote the gauge fields included in the derivative, i.e.  $D_\mu^G = \partial_\mu + ig_s G_\mu^a t^a$  and  $D_\mu^W = \partial_\mu + ig W_\mu^i T^i$ . The traces  $\text{Tr}([D_\mu^G, D_\nu^G]^2)$  and  $\text{Tr}([D_\mu^W, D_\nu^W]^2)$  are therefore gauge invariant. We can then define the field strength tensors as

$$G_{\mu\nu}^a t^a = -\frac{i}{g_s} [D_\mu^G, D_\nu^G] = (\partial_\mu G_\nu^a - \partial_\nu G_\mu^a - g_s f_{abc} G_\mu^b G_\nu^c) t^a, \quad (2.20)$$

$$W_{\mu\nu}^i T^i = -\frac{i}{g} [D_\mu^W, D_\nu^W] = (\partial_\mu W_\nu^i - \partial_\nu W_\mu^i - g \epsilon_{ijk} W_\mu^j W_\nu^k) T^i, \quad (2.21)$$

and the kinetic part of the SM Lagrangian for the gauge fields becomes

$$\mathcal{L}_A = -\frac{1}{4} G_{\mu\nu}^a G^{a\mu\nu} - \frac{1}{4} W_{\mu\nu}^i W^{i\mu\nu} - \frac{1}{4} B_{\mu\nu} B^{\mu\nu}, \quad (2.22)$$

where we have chosen the conventional normalisations of the generators  $\text{Tr}(t^a t^b) = \frac{1}{2} \delta^{ab}$  and  $\text{Tr}(T^i T^j) = \frac{1}{2} \delta^{ij}$ . Again this does not only describe the kinetic evolution of the (massless) gauge fields; due to the more complicated field strength tensors for the non-Abelian gauge symmetries, it also describes trilinear and quadrilinear self-interactions between the  $G_\mu^a$  and  $W_\mu^i$  fields. This self-coupling property is of

fundamental importance to QCD, leading to the color confinement of the quarks in hadrons and the asymptotic freedom of the strong coupling  $\alpha_s = \frac{g_s^2}{4\pi}$ .

### 2.1.3 Higgs Mechanism

While we now have an interacting theory of fermions and gauge bosons, it is still not sufficient to explain the observed masses of the fermions and the  $W^\pm$  and  $Z$  bosons. It is clear that SM gauge symmetry must be broken in some way. The Higgs mechanism introduces the  $SU(2)_L$  doublet  $H$  so additional dimension-four, gauge-invariant terms can be written in the SM Lagrangian. The kinetic term and quadratic and quartic terms involving just the Higgs doublet are

$$\mathcal{L}_H = (D_\mu H)^\dagger (D^\mu H) - V(H), \quad (2.23)$$

$$V(H) = -\mu^2 H^\dagger H + \lambda (H^\dagger H)^2, \quad (2.24)$$

where (for gauge invariance) the kinetic term uses the covariant derivative and we define the Higgs potential  $V(H)$ . The signs of the parameters  $\mu^2$  and  $\lambda$  are crucial to understanding the properties of the Higgs doublet and whether the theory is physical. If  $\lambda < 0$ , the potential function  $V(H)$  is not bounded from below and is thus unphysical. For  $\mu^2 < 0$  and  $\lambda > 0$  the potential has a minimum at  $|H| = \sqrt{H^\dagger H} = 0$ , while for  $\mu^2 > 0$  and  $\lambda > 0$  the potential has a minimum away from  $|H| = 0$ .

The vacuum expectation value (VEV) of a field or operator is the lowest energy field configuration satisfying the classical equations of motion. Barring exotic vacua predicted by some string theories, VEVs must be Lorentz-invariant and symmetric under the observed quantum numbers of the vacuum (net-zero electric and color charge). There is no requirement, however, for a VEV to respect the EW symmetry  $SU(2)_L \times U(1)_Y$ . Defining

$$v \equiv \sqrt{\frac{\mu^2}{\lambda}}, \quad (2.25)$$

it is possible to rewrite the Higgs potential (up to constant terms) as

$$V(H) = \lambda \left( H^\dagger H - \frac{v^2}{2} \right)^2. \quad (2.26)$$

It is then clear that in the  $\mu^2 > 0$  and  $\lambda > 0$  case the minimum of the potential is at  $|H| = \frac{v}{\sqrt{2}}$ . We now choose the VEV of the Higgs doublet to be  $\langle H \rangle = \frac{1}{\sqrt{2}}(0 \ v)^\top$  which is apparently no longer invariant under the EW symmetry because  $T^i \langle H \rangle \neq 0$  and  $Y \langle H \rangle \neq 0$ . When a symmetry of the Lagrangian is no longer respected by the vacuum it is *spontaneously broken*.

The spontaneous breaking of a symmetry by the vacuum implies the existence of massless modes called Goldstone bosons. These modes are nothing other than fluctuations of the field around the VEV; for the Higgs doublet this can be written as

$$H = \frac{1}{\sqrt{2}} \begin{pmatrix} \Re(h^+) + i\Im(h^+) \\ v + \Re(h^0) + i\Im(h^0) \end{pmatrix}. \quad (2.27)$$

The  $\Re(h^+)$ ,  $\Im(h^+)$  and  $\Im(h^0)$  modes are massless because the Higgs potential  $V(H)$  is flat in the directions of these excitations;  $\Re(h^0)$  on the other hand gets a mass term, i.e.

$$V(H) \supset \frac{1}{2}m_h^2 \Re(h^0)^2, \quad (2.28)$$

where  $m_h = \sqrt{2\lambda v^2}$ . If the broken symmetry is local, as is the case for EW symmetry breaking (EWSB), these extra degrees of freedom can be rotated away. For example, a gauge transformation can rotate the massless Goldstone bosons into the longitudinal polarisation states of the  $SU(2)_L \times U(1)_Y$  gauge bosons, giving them mass. Importantly, it can be shown via the Goldstone boson equivalence theorem that physical observables are not affected by the choice of gauge; the scattering of massless Goldstone bosons is identical to the scattering of longitudinal vector boson polarisation states at high energies.

One can consider a generic gauge by adding the gauge-fixing terms to the SM

Lagrangian (à la 't Hooft),

$$\mathcal{L}_{\text{fix}} = -\frac{1}{2\xi_G}(\partial^\mu G_\mu^a)^2 - \frac{1}{2\xi_W} \left[ \partial^\mu W_\mu^i + ig\xi_W \left( \langle H \rangle^\dagger T^i H - H^\dagger T^i \langle H \rangle \right) \right]^2 - \frac{1}{2\xi_B} \left[ \partial^\mu B_\mu + ig'\xi_B \left( \langle H \rangle^\dagger Y H - H^\dagger Y \langle H \rangle \right) \right]^2, \quad (2.29)$$

which gives the Lagrangian in the so-called  $R_\xi$  gauge. Inserting the Higgs doublet in Eq. (2.27) into Eq. (2.29), the  $\Re(h^+)$ ,  $\Im(h^+)$  and  $\Im(h^0)$  modes obtain mass terms proportional to the gauge-fixing parameters  $\xi_W$  and  $\xi_B$ . With  $\xi_W = \xi_B = 1$ , known as the 't Hooft–Feynman gauge, the masses are the same as the  $W^\pm$  and  $Z$  bosons. For  $\xi_W, \xi_B \rightarrow \infty$ , or the unitary gauge, the masses tend to infinity and the modes decouple from the theory. In this second gauge we write  $H = \frac{1}{\sqrt{2}}(0, v+h)^\top$ , where  $h \equiv \Re(h^0)$ , and inserting into the Higgs kinetic term gives

$$(D_\mu H)^\dagger (D^\mu H) = \frac{1}{2}(\partial_\mu h)^\dagger (\partial^\mu h) + \frac{g^2}{4}(v+h)^2 W_\mu^+ W^{-\mu} + \frac{(g^2+g'^2)}{8}(v+h)^2 Z_\mu Z^\mu, \quad (2.30)$$

where we have defined the fields

$$W_\mu^+ = \frac{1}{\sqrt{2}}(W_\mu^1 - iW_\mu^2), \quad W_\mu^- = \frac{1}{\sqrt{2}}(W_\mu^1 + iW_\mu^2), \quad (2.31)$$

$$Z_\mu = \frac{1}{\sqrt{g^2+g'^2}}(gW_\mu^3 - g'B_\mu) \equiv \cos \theta_W W_\mu^3 - \sin \theta_W B_\mu, \quad (2.32)$$

where  $\sin \theta_W = \frac{g'}{\sqrt{g^2+g'^2}}$  and  $\cos \theta_W = \frac{g}{\sqrt{g^2+g'^2}}$  are the sine and cosine of the weak mixing angle  $\theta_W$  [25]. It can be seen from Eq. (2.30) that the masses of the  $W^\pm$  and  $Z$  bosons are given (at tree-level) by

$$m_W = \frac{gv}{2}, \quad m_Z = \frac{\sqrt{g^2+g'^2} v}{2} = \frac{m_W}{\cos \theta_W}, \quad (2.33)$$

respectively. The three linear combinations of the fields  $W_\mu^i$  ( $i = 1, 2, 3$ ) and  $B_\mu$  above become massive, while the orthonormal combination  $A_\mu = s_W W_\mu^3 + c_W B_\mu$  (where  $s_W \equiv \sin \theta_W$  and  $c_W \equiv \cos \theta_W$ ) remains massless.

It should be noted that due to the gauge-fixing terms in Eq. (2.29) the theory violates unitarity via the presence of unphysical gauge boson polarisation states. In order to account for this one must introduce the Faddeev–Popov ghost and antighost fields  $c^a$  and  $\bar{c}^a$  respectively for each gauge field,

$$\begin{aligned}\mathcal{L}_{\text{gh}} = & (\partial_\mu \bar{c}_G^a) (\delta^{ac} \partial_\mu - g_s f^{abc} G_\mu^b) c_G^c \\ & + (\partial_\mu \bar{c}_W^i) (\delta^{ij} \partial_\mu - g \epsilon^{ijk} W_\mu^j) c_W^k + (\partial_\mu \bar{c}_B) (\partial_\mu c_B).\end{aligned}\quad (2.34)$$

These ghost fields are unphysical because they violate the spin-statistics theorem (the requirement that states with identical particles spin of integer and non-integer spin are symmetric and antisymmetric under the exchange of particles respectively) [154]. More specifically, they are Lorentz scalar fields that anticommute (i.e. Grassmann-valued fields). However, there is nothing stopping them appearing in loop diagrams of physical scattering matrix elements. The ghost Lagrangian in Eq. (2.34) is written in such a way that the unphysical ghost fields exactly cancel the unphysical gauge boson polarisation states. Remarkably, when the ghost fields  $c^a$  and  $\bar{c}^a$  are included the SM Lagrangian exhibits an additional global invariance, called the Becchi–Rouet–Star–Tyutin (BRST) symmetry, e.g.

$$G_\mu^a \xrightarrow{\text{BRST}} G'_\mu^a = G_\mu^a - \frac{\epsilon}{g_s} \partial_\mu c_G^a + \epsilon f^{abc} G_\mu^b c_G^c, \quad (2.35)$$

$$\psi \xrightarrow{\text{BRST}} \psi' = \psi + i \epsilon c_G^a t^a \psi, \quad (2.36)$$

$$c_G^a \xrightarrow{\text{BRST}} c'_G^a = c_G^a + \frac{\epsilon}{2} f^{abc} c_G^b c_G^c, \quad (2.37)$$

$$\bar{c}_G^a \xrightarrow{\text{BRST}} \bar{c}'_G^a = \bar{c}_G^a + \frac{\epsilon}{g_s} \left( \frac{1}{\xi_G} \partial^\mu G_\mu^a \right), \quad (2.38)$$

where  $\epsilon$  is a Grassmann number [155, 156]. It can be seen that the above transformations are similar to a gauge transformation with  $\theta^a = \epsilon c^a$ . Under this transformation the gauge-fixing terms in Eq. (2.29) are also now invariant.

Associated with BRST invariance are the so-called Slavnov–Taylor identities; generalisations of the Ward–Takahashi identity for non-Abelian theories. The Ward–Takahashi identity puts a certain requirement on the off-shell matrix elements in any

Abelian theory [157, 158]. It can then be used to show that the infinities encountered in loop diagrams can always be cancelled by appropriate counterterms that also respect the gauge invariance. The Slavnov-Taylor identities also permit this for non-Abelian theories; for example, it can be shown that the non-Abelian QCD gauge coupling  $g_s$  can always be rescaled by the same factor in order to remove the infinities.

After EWSB it is possible to rewrite the covariant derivative in the form

$$D_\mu = \partial_\mu + ig_s G_\mu^a t^a + ie A_\mu Q + ig W_\mu, \quad (2.39)$$

where  $e = g_s c_W = g' c_W$  and  $Q = T^3 + Y$  (the Gell-Mann–Nishijima relation) [33, 34]. It is straightforward to show that the vacuum remains invariant under the Abelian gauge group  $U(1)_Q$ , because  $Q \langle H \rangle = 0$ . The values of  $Q$  for the SM matter fields are shown in Table 2.2; it can be seen that (by construction) these correspond to the electric charges of the SM particles. Through EWSB the SM therefore undergoes a phase transition  $SU(3)_c \times SU(2)_L \times U(1)_Y \xrightarrow{\text{EWSB}} SU(3)_c \times U(1)_Q$ , where  $U(1)_Q$  is the gauge symmetry of QED and the  $A_\mu$  field corresponds to the photon. In Eq. (2.39), the charged- and neutral-current weak interactions are contained in

$$W_\mu = \frac{1}{\sqrt{2}} (W_\mu^+ T^+ + W_\mu^- T^-) + \frac{1}{c_W} (T^3 - s_W^2 Q) Z_\mu, \quad (2.40)$$

where  $T^\pm = T^1 \pm iT^2$  are the  $SU(2)_L$  raising and lowering operators. Inserting Eq. (2.40) into Eq. (2.39) and subsequently into Eq. (2.16), gives

$$\mathcal{L}_\psi \supset \mathcal{L}_{W^\pm} + \mathcal{L}_Z = -\frac{g}{\sqrt{2}} \bar{\psi} (W^+ T^+ + W^- T^-) \psi - \frac{g}{c_W} \bar{\psi} (T^3 - s_W^2 Q) Z \psi. \quad (2.41)$$

The charged-current weak interactions connect the two fields in each  $SU(2)_L$  doublet (separated in electric charge by one unit) with the appropriate absorption or emission of a  $W^\pm$  boson. The NC weak interaction connects identical fields, with a strength depending on the value of  $(T^3 - s_W^2 Q)$  for the field, listed in the fifth column of Table 2.2.

SM Fermion Field	$U(1)_Q$	$U(1)_L$	$U(1)_B$	$T^3 - s_W^2 Q$
$L_L = \begin{pmatrix} v_L \\ \ell_L \end{pmatrix}$	0 -1	-1 -1	0 0	$\frac{1}{2}$ $-\frac{1}{2} + s_W^2$ $s_W^2$
$\ell_R$	-1	-1	0	$s_W^2$
$Q_L = \begin{pmatrix} u_L \\ d_L \end{pmatrix}$	$\frac{2}{3}$ $-\frac{1}{3}$	0	$\frac{1}{3}$	$\frac{1}{2} - \frac{2}{3}s_W^2$ $-\frac{1}{2} + \frac{1}{3}s_W^2$
$u_R$	$\frac{2}{3}$	0	$\frac{1}{3}$	$-\frac{2}{3}s_W^2$
$d_R$	$-\frac{1}{3}$	0	$\frac{1}{3}$	$\frac{1}{3}s_W^2$

**Table 2.2:** Transformation properties of the SM fermion fields under the Abelian gauge group  $U(1)_Q$ , i.e. the value of the QED charge generator  $Q = T^3 + Y$ , and the global  $U(1)_L$  lepton number and  $U(1)_B$  baryon number. Also shown are the values of  $(T^3 - s_W^2 Q)$  which determine the neutral-current interaction of the fields.

### 2.1.4 Fermion Masses

At dimension-four it is possible to construct additional SM gauge-invariant terms with the fermion fields and Higgs doublet,

$$\mathcal{L}_Y = -\bar{\ell}_R Y_\ell H^\dagger L_L - \bar{u}_R Y_u \tilde{H}^\dagger Q_L - \bar{d}_R Y_d H^\dagger Q_L + \text{h.c.}, \quad (2.42)$$

where  $\tilde{H} \equiv i\sigma^2 H^*$  transforms in the fundamental representation of  $SU(2)_L$  and has a hypercharge of  $Y = -\frac{1}{2}$ . We have introduced the Yukawa couplings  $Y_\ell$ ,  $Y_u$  and  $Y_d$  which are  $3 \times 3$  matrices for three generations. Note that due to the absence of a right-handed neutrino field  $v_R$  it is not possible to write a similar term with a Yukawa coupling for the neutrino. Eq. (2.42) reduces after EWSB to

$$\mathcal{L}_Y = -\frac{1}{\sqrt{2}}(v+h) \{ \bar{\ell}_R Y_\ell \ell_L + \bar{u}_R Y_u u_L + \bar{d}_R Y_d d_L \} + \text{h.c.}, \quad (2.43)$$

where it is possible to identify the  $3 \times 3$  fermion mass matrices as  $M_\ell = \frac{v}{\sqrt{2}} Y_\ell$ ,  $M_u = \frac{v}{\sqrt{2}} Y_u$  and  $M_d = \frac{v}{\sqrt{2}} Y_d$ . It is not guaranteed that the mass matrices are diagonal in the basis of fields interacting according to the Lagrangian in Eq. (2.16) and the covariant derivative in Eq. (2.39), i.e. the *weak eigenstate* basis.

In general it is possible to diagonalise an arbitrary  $N \times N$  matrix  $M$  through a *biunitary* transformation,  $V_L^\dagger M V_R = M'$ , where  $V_L$  and  $V_R$  are unitary  $N \times N$  matrices

and  $M'$  is a diagonal matrix with real and positive elements [76]. Following this procedure for the fermion mass matrices above gives

$$V_L^{\ell\dagger} M_\ell V_R^\ell = M'_\ell, \quad V_L^{u\dagger} M_u V_R^u = M'_u, \quad V_L^{d\dagger} M_d V_R^d = M'_d, \quad (2.44)$$

where  $M'_\ell = \text{diag}(m_e, m_\mu, m_\tau)$ ,  $M'_u = \text{diag}(m_u, m_c, m_t)$  and  $M'_d = \text{diag}(m_d, m_s, m_b)$ . Redefining the charged lepton and quark fields as

$$\ell_{L(R)} = V_{L(R)}^\ell \ell'_{L(R)}, \quad u_{L(R)} = V_{L(R)}^u u'_{L(R)}, \quad d_{L(R)} = V_{L(R)}^d d'_{L(R)}, \quad (2.45)$$

therefore brings Eq. (2.43) into the *mass eigenstate* basis. This redefinition of fields also affects the charged-current weak interaction part of the Lagrangian,

$$\mathcal{L}_{W^\pm} = -\frac{g}{\sqrt{2}} \bar{v}_L \not{W}^+ V_L^\ell \ell'_L - \frac{g}{\sqrt{2}} \bar{u}'_L \not{W}^+ (V_L^{u\dagger} V_L^d) d'_L + \text{h.c.} \quad (2.46)$$

It is now conventional to define the charged lepton and up-type quark weak eigenstate fields to be equivalent to the mass eigenstate fields, requiring the redefinitions of the neutrino and down-type quark fields  $v_L = V_L^\ell v'_L$  and  $d_L = (V_L^{u\dagger} V_L^d) d'_L$ . The redefinition of the neutrino fields is trivial because the neutrinos are massless in this scheme. The matrix  $V = V_L^{u\dagger} V_L^d$  is the famous Cabibbo–Kobayashi–Maskawa (CKM) matrix characterising the observed phenomenon of quark mixing [37, 45].

To determine the number of free parameters in  $V$ , we note that any  $N \times N$  unitary matrix can be parametrised with  $N(N - 1)/2$  mixing angles and  $N(N + 1)/2$  phases; three mixing angles ( $\vartheta_{12}$ ,  $\vartheta_{13}$  and  $\vartheta_{23}$ ) and six phases ( $\eta_{12}$ ,  $\eta_{13}$ ,  $\eta_{23}$ ,  $\omega_1$ ,  $\omega_2$  and  $\omega_3$ ) in the case of the CKM matrix [159]. However, there is a residual global  $U(1)^6$  symmetry in the arbitrary rephasing of the mass eigenstate quark fields,  $u_\alpha \rightarrow e^{i\phi_\alpha} u_\alpha$  and  $d'_i \rightarrow e^{i\phi_i} d'_i$ , which can eliminate five of the six phases in  $V$ . It is conventional to eliminate  $\eta_{12}$ ,  $\eta_{23}$ ,  $\omega_1$ ,  $\omega_2$  and  $\omega_3$  leaving the phase  $\eta_{13} \equiv -\delta$  associated with rotations in the (1, 3) sector. This last phase is of fundamental importance to the presence of CP violation in the quark sector. If  $\delta \neq 0$ , direct and indirect CP violation will be seen in the mixing and decays of  $K$ ,  $D$  and  $B$  mesons,

proportional to the rephasing-invariant quantity

$$\det C = (m_t^2 - m_c^2)(m_t^2 - m_u^2)(m_c^2 - m_u^2)(m_b^2 - m_s^2)(m_b^2 - m_d^2)(m_s^2 - m_d^2) J, \quad (2.47)$$

where  $C = -\frac{1}{2}\Im[\mathbf{M}_u \mathbf{M}_u^\dagger, \mathbf{M}_d \mathbf{M}_d^\dagger]$  and the Jarlskog invariant  $J$  is defined by [160–163]

$$J \sum_{\gamma, k} \epsilon_{\alpha\beta\gamma} \epsilon_{ijk} = \Im \left[ V_{\alpha i}^* V_{\beta i} V_{\alpha j} V_{\beta j}^* \right]. \quad (2.48)$$

The remaining universal rephasing freedom of the quark fields corresponds to the accidental global symmetry of baryon number  $U(1)_B$ . The baryon numbers of the SM matter fields are given in Table 2.2; the quark (antiquark) fields are customarily given values  $B = +\frac{1}{3}$  ( $-\frac{1}{3}$ ) in order to give the baryons (antibaryons)  $B = +1$  ( $-1$ ). Another method of determining the number of free parameters in the theory is to notice that the Yukawa Lagrangian breaks a global  $U(3)_{Q_L} \times U(3)_{u_R} \times U(3)_{d_R}$  flavour symmetry down to  $U(1)_B$ . Thus the 36 free parameters in the complex mass matrices  $\mathbf{M}_u$  and  $\mathbf{M}_d$  can be reduced by 26 broken group generators down to ten free parameters; the six quark masses, three mixing angles and one phase.

Given the freedom to rotate the charged lepton and neutrino weak eigenstate fields to remove the rotation matrix  $V_L^\ell$ , Eq. (2.46) (by definition) connects leptonic fields of the same flavour. There is thus a global  $U(1)_{L_e} \times U(1)_{L_\mu} \times U(1)_{L_\tau}$  symmetry corresponding to each of the lepton flavour numbers. While each of the lepton flavour numbers  $L_e$ ,  $L_\mu$  and  $L_\tau$  is conserved, so is the *total* lepton number  $L = L_e + L_\mu + L_\tau$ , corresponding to the diagonal subgroup  $U(1)_L$ . We see that the global  $U(3)_{L_L} \times U(3)_{\ell_R}$  flavour symmetry is broken down to  $U(1)_{L_e} \times U(1)_{L_\mu} \times U(1)_{L_\tau}$ ; the 18 free parameters in the complex mass matrix  $\mathbf{M}_\ell$  are reduced to three (the charged lepton masses) by the 15 broken group generators.

While  $U(1)_B$ ,  $U(1)_{L_e}$ ,  $U(1)_{L_\mu}$  and  $U(1)_{L_\tau}$  (and thus  $U(1)_L$ ) are symmetries of the classical action, they are broken by non-perturbative quantum effects in the path integral measure (with physical effects such as instantons and sphalerons). It is then not possible for any theory preserving unitarity to have gauged versions of these symmetries. The combination  $n_B B + n_e L_e + n_\mu L_\mu + n_\tau L_\tau$  however is non-

anomalous if either  $n_B = 0$  and  $n_e + n_\mu + n_\tau = 0$  or  $n_B = 1$  and  $n_e + n_\mu + n_\tau = -3$  [164–168]. This has led, for example, to the consideration of gauged  $U(1)_{B-L}$  and  $U(1)_{L_\mu - L_\tau}$  symmetries in the literature [169–172].

To conclude this section, the SM Lagrangian can be written as

$$\mathcal{L}_{\text{SM}} = \mathcal{L}_A + \mathcal{L}_\psi + \mathcal{L}_Y + \mathcal{L}_H + \mathcal{L}_{\text{fix}} + \mathcal{L}_{\text{gh}} + \mathcal{L}_{\text{ct}}, \quad (2.49)$$

where the first six contributions are given in Eqs. (2.22), (2.16), (2.23), (2.43), (2.29) and (2.29), respectively. The 18 free parameters in Eq. (2.49) are: the masses of the leptons and quarks,  $m_e$ ,  $m_\mu$ ,  $m_\tau$ ,  $m_u$ ,  $m_c$ ,  $m_t$ ,  $m_d$ ,  $m_s$  and  $m_b$ ; the CKM mixing matrix angles and phase  $\vartheta_{12}$ ,  $\vartheta_{13}$ ,  $\vartheta_{23}$  and  $\delta$ ; the Higgs self-coupling  $\lambda$  and VEV  $v$ ; the weak mixing angle  $\theta_W$ ; and the QED and strong coupling constants  $e = \sqrt{4\pi\alpha}$  and  $g_s = \sqrt{4\pi\alpha_s}$ . The strong CP phase  $\bar{\theta}$  is also sometimes included as an additional parameter, though is often dropped because its experimental upper limit is tiny ( $\bar{\theta} < 10^{-9}$ ) and a dynamical mechanism is usually invoked to set  $\bar{\theta} = 0$ . For example, a broken global Peccei–Quinn symmetry  $U(1)_{\text{PQ}}$  with an axion as a Goldstone boson [173, 174].

The parameters and fields in the SM Lagrangian above are assumed to be bare, tree-level quantities; not taking into account the infinities introduced by higher-order loop Feynman diagrams. At each order in perturbation theory the infinities can be absorbed into redefinitions of the couplings, masses and fields. This is equivalent to adding counterterms  $\mathcal{L}_{\text{ct}}$  to the SM Lagrangian which can be defined to subtract the divergent integrals from the loop diagrams. With the notable exception of the  $-\mu^2 H^\dagger H$  term in the Higgs potential, all terms in the SM Lagrangian are by construction dimension-four. For dimension-four operators it is always possible to cancel the divergences with dimension-four counterterms.

## 2.2 Neutrino Masses

The observation of oscillations ( $\nu_\alpha \leftrightarrows \nu_\beta$ ) between the three known flavours of neutrino has confirmed that neutrinos are *massive* and *mixed*. This can be taken as conclusive evidence of physics beyond the SM. In the SM, there are only three two-

component left-handed neutrino fields  $\nu_{\alpha L}$  with  $\alpha \in \{e, \mu, \tau\}$ . It is therefore not possible to construct a Yukawa-type term similar to those for the charged leptons and quarks in Eq. (2.43), and the neutrinos remain massless after EWSB.

In this section we will explore a selection of neutrino mass models put forward in the literature. Any model must make a few key predictions. Firstly, it must reproduce the observed neutrino mixing and oscillation phenomena. Secondly, it should explain why the neutrinos are so much lighter than the other SM fermions. This issue is often taken as a hint that New Physics (NP) related to the neutrino masses, or vSM, is at a very high scale,  $\Lambda_{\text{NP}} \gtrsim 10^{16}$  GeV. Finally, it must predict either *Dirac* or *Majorana* neutrinos. This distinction is closely related to the global  $U(1)_L$  lepton number symmetry discussed in the previous section. It can be shown that neutrino masses imply the breaking of the residual global  $U(1)_{L_e} \times U(1)_{L_\mu} \times U(1)_{L_\tau}$  symmetry of the SM Lagrangian. Its diagonal subgroup  $U(1)_L$  may or may not remain a symmetry at high energies. If broken, lepton number violating (LNV) phenomena become possible at low energies, but are usually suppressed due to a correlation with the small neutrino masses. If an LNV process is observed, it would imply that at least one of the light neutrinos is Majorana via the *black box* theorem.

### 2.2.1 Dirac Neutrinos

The minimal vSM extension is the addition of three right-handed neutrino fields  $\nu_{\alpha R}$  with  $\alpha \in \{e, \mu, \tau\}$ . It is then possible to write the Yukawa term

$$\mathcal{L}_{\text{vSM}} = \mathcal{L}_{\text{SM}} - \bar{\nu}_R Y_\nu \tilde{H}^\dagger L_L + \text{h.c.}, \quad (2.50)$$

where we have introduced a  $3 \times 3$  Yukawa matrix  $Y_\nu$ . In order to preserve the SM gauge symmetry, the  $\nu_R$  fields must be singlets under  $SU(3)_c \times SU(2)_L \times U(1)_Y$ . The generation of neutrino masses then proceeds identically to the charged leptons and quarks; after EWSB Eq. (2.50) reduces to

$$\mathcal{L}_{\text{vSM}} = \mathcal{L}_{\text{SM}} - \frac{1}{\sqrt{2}} (v + h) \bar{\nu}_R Y_\nu \nu_L + \text{h.c.}, \quad (2.51)$$

where it is possible to identify the  $3 \times 3$  neutrino mass matrix as  $M_\nu = \frac{v}{\sqrt{2}} Y_\nu$ .

It is again necessary to diagonalise this mass matrix through a biunitary transformation,

$$V_L^{v\dagger} M_\nu V_R^v = M'_\nu, \quad (2.52)$$

where  $V_L^v$  and  $V_R^v$  are  $3 \times 3$  unitary matrices and  $M'_\nu = \text{diag}(m_1, m_2, m_3)$  contains the masses of the neutrino mass eigenstates. Making the field redefinitions  $v_{L(R)} = V_{L(R)}^v v'_{L(R)}$  in addition to those in Eq. (2.45) now gives for the charged-current interactions

$$\mathcal{L}_{W^\pm} = -\frac{g}{\sqrt{2}} \bar{v}_L' \not{W}^+ (V_L^{v\dagger} V_L^\ell) \ell'_L - \frac{g}{\sqrt{2}} \bar{u}_L' \not{W}^+ (V_L^{u\dagger} V_L^d) d'_L + \text{h.c.}, \quad (2.53)$$

where the combination  $U = (V_L^{v\dagger} V_L^\ell)^\dagger = V_L^{e\dagger} V_L^v$  is the so-called Pontecorvo–Maki–Nakagawa–Sakata (PMNS) mixing matrix, directly analogous to the CKM matrix. It is conventional to define the neutrino flavour eigenstates as  $V_L^{e\dagger} v_L$ ; the flavour eigenstate charged leptons are then equivalent to their mass eigenstates. The PMNS mixing matrix then simply rotates from the flavour to mass eigenstate neutrinos,  $v_L = U v'_L$ . If this field redefinition is now made for the neutral-current neutrino interaction,

$$\mathcal{L}_Z \supset -\frac{g}{2c_W} \bar{v}_L \not{Z} v_L = -\frac{g}{2c_W} \bar{v}_L' \not{Z} \underbrace{(U^\dagger U)}_1 v'_L, \quad (2.54)$$

we see that it remains diagonal in the mass basis due to the unitarity of  $U$ .

It is relatively straightforward to observe that the term in Eq. (2.51) implies the non-conservation of the individual lepton numbers  $L_e$ ,  $L_\mu$  and  $L_\tau$ . One can write

$$\mathcal{L}_{\nu\text{SM}} \supset -\bar{v}_R' M'_\nu v'_L - \bar{\ell}_R' M'_\ell \ell'_L + \text{h.c.} = -\bar{v}_R' M'_\nu U^\dagger v_L - \bar{\ell}_R' M'_\ell \ell_L + \text{h.c.}, \quad (2.55)$$

where in the second equality we have made use of the defined equivalence between the flavour and mass eigenstate charged lepton fields and used  $v'_L = U^\dagger v_L$ . Because

$M_\ell$  is a diagonal matrix it is possible to rotate the left- and right-handed charged lepton fields by

$$\ell_L \rightarrow D\ell_L, \quad \ell_R \rightarrow D\ell_R, \quad D = \text{diag}(e^{i\phi_e}, e^{i\phi_\mu}, e^{i\phi_\tau}), \quad (2.56)$$

(i.e. a different phase for each flavour) and Eq. (2.55) remains invariant. In addition, the kinetic part of the Lagrangian

$$\mathcal{L}_{\text{vSM}} \supset i\bar{\ell}_L \not{\partial} \ell_L + i\bar{\ell}_R \not{\partial} \ell_R + i\bar{\nu}_L \not{\partial} \nu_L + i\bar{\nu}_R \not{\partial} \nu_R, \quad (2.57)$$

remains invariant. However, if the left-handed neutrino  $\nu_L$  also transform as  $\nu_L \rightarrow D\nu_L$ , the product  $U M'_\nu \nu'_R$  must transform as  $U M'^{\dagger}_\nu \nu'_R \rightarrow D U M'^{\dagger}_\nu \nu'_R$  for Eq. (2.55) to be invariant. The kinetic term for  $\nu_R$  is in general not invariant under this rotation, apart from two special cases; the mixing matrix  $U$  is unity or  $m_1 = m_2 = m_3$  in  $M'_\nu$ . As the individual lepton numbers are not seen to be conserved by neutrino oscillations,  $\nu_\alpha \rightleftharpoons \nu_\beta$ , it is must be true that  $U \neq \mathbb{1}$  (the neutrinos are mixed) and  $m_1 \neq m_2 \neq m_3$  (at least two of the neutrinos are massive).

The rotation with  $\phi_e = \phi_\mu = \phi_\tau$  (i.e. global lepton number  $L$ ) *does* correspond to a symmetry of the neutrino mass and kinetic terms in Eqs. (2.55) and (2.57). By Noether's theorem, the invariance of Lagrangian corresponds to a *conserved* current and charge. The conserved charge in this case is nothing but the lepton number, with neutrinos (and negatively charged leptons) assigned  $L = +1$  and antineutrinos (and positively charged leptons) assigned  $L = -1$ . The neutrinos in this picture are called *Dirac* neutrinos because the left- and right-handed two-component neutrino fields can be combined into a four-component Dirac spinor like the other SM fermions. The Dirac spinor contains four degrees of freedom; a neutrino and antineutrino with positive or negative helicity.

The mixing matrix  $U$  can be parametrised in the same way as the CKM matrix in the previous section. As a  $3 \times 3$  unitary matrix, it must contain three mixing angles and six phases. Similar to the quark sector, a residual  $U(1)^6$  symmetry allows a rephasing of the mass eigenstate charged lepton and neutrino fields as  $\ell_{\beta L(R)} \rightarrow$

Mixing Parameter	Best Fit $\pm 1\sigma$ [175]	
	NO	IO
$\sin^2 \theta_{12}/10^{-1}$	$3.04^{+0.13}_{-0.12}$	$3.04^{+0.12}_{-0.16}$
$\sin^2 \theta_{13}/10^{-2}$	$2.211^{+0.068}_{-0.062}$	$2.240^{+0.062}_{-0.062}$
$\sin^2 \theta_{23}/10^{-1}$	$5.70^{+0.18}_{-0.24}$	$5.75^{+0.17}_{-0.21}$
$\delta_{\text{CP}}/\pi$	$1.08^{+0.28}_{-0.14}$	$1.59^{+0.15}_{-0.18}$
$\Delta m_{21}^2 / (10^{-5} \text{ eV}^2)$	$7.42^{+0.21}_{-0.20}$	$7.42^{+0.21}_{-0.20}$
$ \Delta m_{31}^2  / (10^{-3} \text{ eV}^2)$	$2.514^{+0.028}_{-0.027}$	$2.497^{+0.028}_{-0.028}$

**Table 2.3:** Current global best fit values for the three-neutrino flavour oscillation mixing angles  $\theta_{12}$ ,  $\theta_{13}$  and  $\theta_{23}$ , mass-squared splittings  $\Delta m_{21}^2$  and  $\Delta m_{31}^2$  and CP phase  $\delta_{\text{CP}}$ . Values are given for Normal Ordering (NO) and Inverted Ordering (IO) of the light neutrino mass eigenstates.

$e^{i\phi_\beta} \ell_{\beta L(R)}$  and  $v'_{jL(R)} \rightarrow e^{i\phi_j} v'_{jL(R)}$  so that we are left with a single phase  $\eta_{13} \equiv -\delta_{\text{CP}}$ . The standard parametrisation of  $U$  is

$$U = R_{23}W_{13}R_{12} = \begin{pmatrix} 1 & 0 & 0 \\ 0 & c_{23} & s_{23} \\ 0 & -s_{23} & c_{23} \end{pmatrix} \cdot \begin{pmatrix} c_{13} & 0 & s_{13}e^{-i\delta_{\text{CP}}} \\ 0 & 1 & 0 \\ -s_{13}e^{i\delta_{\text{CP}}} & 0 & c_{13} \end{pmatrix} \cdot \begin{pmatrix} c_{12} & s_{12} & 0 \\ -s_{12} & c_{12} & 0 \\ 0 & 0 & 1 \end{pmatrix}, \quad (2.58)$$

where  $c_{ij} = \cos \theta_{ij}$  and  $s_{ij} = \sin \theta_{ij}$ . As shown in Chapter 3, oscillations between the three neutrino flavours are sensitive to these mixing angles, the mass-squared splittings  $\Delta m_{21}^2 = m_2^2 - m_1^2$  and  $\Delta m_{31}^2 = m_3^2 - m_1^2$  (corresponding to the solar and atmospheric splittings  $\Delta m_{\text{sol}}^2$  and  $\Delta m_{\text{atm}}^2$  respectively) and finally the phase  $\delta_{\text{CP}}$ .

The phase  $\delta_{\text{CP}}$  induces CP violation in neutrino oscillations and is being probed by current oscillation experiments NOvA and T2K and in future by DUNE and T2HK. The size of CP violation is proportional to an equivalent Jarlskog invariant to Eq. (2.48), replacing  $V$  with  $U$ . The sign of  $\Delta m_{31}^2$ , still to be determined, controls the ordering of the neutrino mass eigenstates; Normal Ordering (NO) for  $m_1 < m_2 < m_3$  and Inverted Ordering (IO) for  $m_3 < m_1 < m_2$ . In Table 2.3 we show the current global best fit values for the PMNS mixing matrix angles and phase and mass-squared splittings from Ref. [175]. Other global fits can be found in Refs. [176, 177].

Before moving on to the next subsection, we comment on the prediction for the neutrino mass matrix,  $M_\nu = \frac{v}{\sqrt{2}} Y_\nu$ . In order to produce neutrino masses below

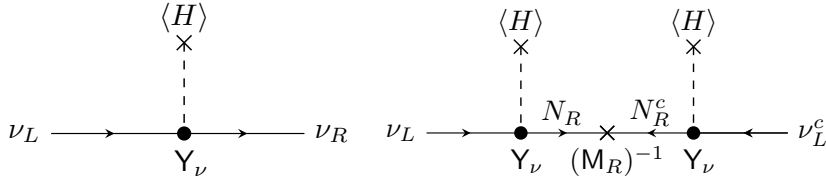


**Figure 2.1:** (Left) Dirac neutrino mass generated after EWSB by a Yukawa-type interaction. (Right) Majorana neutrino mass generated by a Type-1 (or extended, e.g. ISS) seesaw mechanism.

the upper limit  $m_\nu \lesssim 1$  eV from the KATRIN experiment, this result implies that the Yukawa matrix must have entries  $Y_\nu \sim 10^{-12}$ . This suggests a degree of fine-tuning with respect to the other SM fermion Yukawa couplings. As we will see in the next subsection, dynamic mechanisms can instead be invoked to generate the small neutrino masses, avoiding an arbitrary fine-tuning.

## 2.2.2 Majorana Neutrinos and Seesaw Mechanisms

So far we have assumed that the global  $U(1)_L$  lepton number symmetry still applies for the vSM Lagrangian. The global  $U(1)_L$  symmetry of the SM Lagrangian is often called an *accidental* symmetry; lepton number is preserved by all renormalisable dimension-four (or below) terms that respect the SM gauge symmetry. There is no fundamental reason for this in the theory; furthermore, lepton number is broken by non-perturbative effects (and is expected to be broken by quantum gravitational effects above the Planck scale) [178–181].

If the condition of lepton number conservation is relaxed for the particular vSM considered in the previous subsection (three additional SM-singlet right-handed neutrinos  $\nu_R$ ), it becomes possible to write

$$\mathcal{L}_{vSM} = \mathcal{L}_{SM} - \bar{\nu}_R Y_\nu \tilde{H}^\dagger L_L - \frac{1}{2} \bar{\nu}_R^c M_R \nu_R + \text{h.c.}, \quad (2.59)$$

where  $\nu_R^c = \mathcal{C} \bar{\nu}_R^\top$ . Along with the Yukawa term we have an additional *Majorana* (and LNV) mass term for  $\nu_R$ , where  $M_R$  is a complex symmetric  $3 \times 3$  matrix. An equivalent Majorana mass term for  $\nu_L$  is not possible as this would violate the conservation of hypercharge.

Thus far we have only introduced three SM-singlet (or *sterile*) neutrinos  $\nu_R$ ;

one for each SM generation. The number of generations in the SM is not technically fixed at three however. The SM gauge symmetry must be *anomaly free* for the theory to be consistent; the  $U(1)_Y^3$ ,  $SU(3)_c^2 U(1)_Y$  and  $SU(2)_L^2 U(1)_Y$  anomalies (and also  $\text{grav}^2 U(1)_Y$  anomaly if a graviton is included) are all cancelled by different combinations of the hypercharges in each generation. An additional generation with the same hypercharge assignments will also satisfy the anomaly cancellation conditions. On a practical level, however, a fourth generation is heavily constrained by electroweak precision observables and the lack of production at colliders [182–184]. The invisible  $Z$  boson decay width constrains the number of neutrinos lighter than  $m_Z/2$  to be  $N_\nu = 2.92 \pm 0.05$ . This rules out additional light active neutrinos, but light sterile neutrinos  $\nu_R$  which mix with the active neutrinos (via the Yukawa term in Eq. (2.59)) are still allowed. Furthermore, because the sterile neutrinos have zero hypercharge, *a priori* any number can be added without disrupting the anomaly cancellation among the other SM fields. It is customary to replace the symbol  $\nu_R$  with  $N_R$  to indicate that the sterile states may be unrelated to the left-handed SM neutrino fields  $\nu_L$ .

It is nevertheless convenient to combine the  $\nu_L$  and  $N_R$  fields so that Eq. (2.59) can be written in the following form after EWSB

$$\mathcal{L}_{\nu\text{SM}} = \mathcal{L}_{\text{SM}} - \frac{1}{2} n_L^\top C M_\nu n_L + \text{h.c.}, \quad M_\nu = \begin{pmatrix} 0 & M_D^\top \\ M_D & M_R \end{pmatrix}, \quad n_L = \begin{pmatrix} \nu_L \\ N_R^c \end{pmatrix}, \quad (2.60)$$

where we have used  $N_R^c$  as it transforms like a left-handed field and the so-called Dirac mass matrix is  $M_D = \frac{v}{\sqrt{2}} Y_\nu$ . If  $n_S$  sterile states are present,  $M_D$  will be an  $n_S \times 3$  complex matrix and  $M_R$  will be an  $n_S \times n_S$  complex symmetric matrix. The combined matrix  $M_\nu$  is a complex symmetric  $N \times N$  matrix (where  $N = 3 + n_S$ ). It can be shown that such a matrix can be diagonalised with a single unitary  $N \times N$  matrix as  $V_L^\top M_\nu V_L = M'_\nu$ , where  $M'_\nu$  is a diagonal matrix with real and positive elements. Thus the transformation

$$V_L^{\nu\top} M_\nu V_L^\nu = M'_\nu \quad (2.61)$$

can be used to diagonalise the combined Majorana mass matrix in Eq. (2.60). The field redefinition  $n_L = V_L^\nu n'_L$  now gives

$$\mathcal{L}_{\nu\text{SM}} = \mathcal{L}_{\text{SM}} - \frac{1}{2} \bar{n}' (\mathbb{M}'_\nu P_L + \mathbb{M}'_\nu^\dagger P_R) n', \quad n' = (v_1 \ v_2 \ v_3 \ N_1 \ \cdots)^\top, \quad (2.62)$$

where  $n'$  contains  $N$  mass eigenstate neutrino fields. We label the first three massive states  $v$  anticipating that they will be mostly an admixture of the active neutrinos, or *mostly*-active. Likewise, we anticipate the  $n_S$  states being *mostly*-sterile.

The neutrinos in this picture are *Majorana* fermions. In the *Dirac* scenario, neutrinos are described by independent left- and right-handed fields  $v_L$  and  $v_R$  which make up a four-component Dirac spinor,  $v = v_L + v_R$ . In this scenario, the neutrinos are instead described by a single left-handed field  $v_L$ , with the equivalent of the right-handed field being  $v_L^c = \mathcal{C} \bar{v}_L^\top$ . A four-component spinor  $v = v_L + v_L^c$  can then be constructed, from which it is clear that the Majorana condition  $v = v^c$  holds. This condition reduces the number of degrees of freedom for a single Majorana neutrino to two; one for each helicity state. Majorana neutrinos and antineutrinos are equivalent, but it is conventional to refer to a Majorana neutrino with negative or positive helicity as a *neutrino* or *antineutrino* respectively. In a model where three right-handed fields  $v_R$  with a Majorana mass term are present, the theory produces six Majorana mass eigenstates as opposed to three mass eigenstates in the Dirac case. The number of degrees of freedom is the same in each case.

We can again examine the charged-current interactions after transforming the neutrino fields to the mass basis

$$\mathcal{L}_{W^\pm} = -\frac{g}{\sqrt{2}} \bar{n}'_L W^+ (V_L^{v\dagger} \Big|_{N \times 3} V_L^e) \ell'_L - \frac{g}{\sqrt{2}} \bar{u}'_L W^+ (V_L^{u\dagger} V_L^d) d'_L + \text{h.c.}, \quad (2.63)$$

where, because only three active left-handed fields  $v_L$  appear in the interaction, we take the  $3 \times N$  submatrix of  $V_L^\nu$ . To simplify the following discussion, we again redefine the active neutrino flavour eigenstates to be  $V_L^{\ell\dagger} v_L$  so that the weak and mass eigenstate charged leptons are equivalent. A  $3 \times N$  matrix  $\Omega$  is then defined to connect the active neutrinos to the mass eigenstate neutrinos,  $v_L = \Omega n'_L$ . We also

write  $V_L^\nu$  as

$$V_L^\nu = \begin{pmatrix} \Omega \\ \Xi \end{pmatrix} = \begin{pmatrix} U_\nu & V_{\ell N} \\ V_{N\ell} & U_N \end{pmatrix}, \quad (2.64)$$

where  $U_\nu$ ,  $V_{\ell N}$ ,  $V_{N\ell}$  and  $U_N$  are  $3 \times 3$ ,  $3 \times n_S$ ,  $n_S \times 3$  and  $n_S \times n_S$  sub-blocks of  $V_L^\nu$  respectively. It can be seen that the charged-current interaction in Eq. (2.63) connects the charged leptons to *all* neutrino mass eigenstates, which are admixtures of the flavour fields  $v_L$  and  $N_R^c$ , i.e.

$$v' = U_\nu^\dagger v_L + V_{N\ell}^\dagger N_R^c, \quad N' = V_{\ell N}^\dagger v_L + U_N^\dagger N_R^c, \quad (2.65)$$

where  $v' = (v_1 \ v_2 \ v_3)^\top$  and  $N' = (N_1 \ N_2 \ \dots)^\top$ . Similarly, the neutral-current interaction can be written as

$$\mathcal{L}_Z \supset -\frac{g}{2c_W} \bar{v}_L \not{Z} v_L = -\frac{g}{2c_W} \bar{n}'_L \not{Z} \underbrace{(\Omega^\dagger \Omega)}_{\neq 1} n'_L, \quad (2.66)$$

which is now non-diagonal in the mass basis.

The neutral-current interaction of the  $Z$  boson with more than three massive neutrinos appears to be in contradiction with measurements of the invisible  $Z$  decay width, i.e.  $Z \rightarrow v\bar{v}$ . However, we are interested in the limit where the mixings between the active and sterile states are small, i.e.  $V_{\ell N}, V_{N\ell} \ll 1$  in Eq. (2.64). This is naturally obtained in the famous Type-I seesaw limit,  $\|\mathbf{M}_D\| \ll \|\mathbf{M}_R\|$  (where  $\|\mathbf{M}\| \equiv \sqrt{\text{Tr}(\mathbf{M}^\dagger \mathbf{M})}$  is the norm of the matrix  $\mathbf{M}$ ) [185–189]. If the above condition holds, it is possible to diagonalise  $\mathbf{M}_\nu$  up to corrections of order  $\mathbf{M}_D^\dagger \mathbf{M}_R^{-1}$  as

$$V_L^{\nu T} \cdot \begin{pmatrix} 0 & \mathbf{M}_D^T \\ \mathbf{M}_D & \mathbf{M}_R \end{pmatrix} \cdot V_L^\nu = \begin{pmatrix} m_\nu & 0 \\ 0 & m_N \end{pmatrix}, \quad (2.67)$$

where  $m_\nu \approx -\mathbf{M}_D^T \mathbf{M}_R^{-1} \mathbf{M}_D$ ,  $m_N \approx \mathbf{M}_R$  and we have assumed without loss of generality that the matrix  $\mathbf{M}_R$  is diagonal (this can be ensured by an arbitrary rotation

among the sterile states). The sub-blocks of  $V_L^\nu$  are given by

$$\begin{aligned} U_\nu &\approx \left( \mathbb{1} - \frac{1}{2} M_D^\dagger M_R^{-2} M_D \right) U, & V_{\ell N} &\approx M_D^\dagger M_R^{-1}, \\ V_{N\ell} &\approx -M_R^{-1} M_D U, & U_N &\approx \mathbb{1} - \frac{1}{2} M_R^{-1} M_D M_D^\dagger M_R^{-1}, \end{aligned} \quad (2.68)$$

where  $U$  is the standard  $3 \times 3$  PMNS mixing matrix.

The main advantage of the seesaw limit is that it produces small masses for the mostly-active mass eigenstates  $\nu$ . Because they have no connection to the scale of EWSB, the masses in  $M_R$  are *a priori* arbitrary. For example, if we take Yukawa couplings  $Y_\nu \sim 1$  and therefore Dirac matrices  $M_D \sim 100$  GeV, sterile masses  $M_R \sim 10^{16}$  GeV produce light neutrino masses of order  $m_\nu \sim 10^{-3}$  eV, below the current upper limits from beta decay and cosmology. The scale  $\Lambda \sim 10^{16}$  GeV often appears as the scale of gauge coupling unification in GUTs, and right-handed neutrinos are naturally incorporated in such theories [190–194]. Heavy neutrinos at this scale cannot be produced at colliders, but they are key components for the thermal leptogenesis mechanism [195]. In this scenario, heavy neutrinos undergo out-of-equilibrium decays in the early universe, generating a primordial lepton asymmetry which is converted into a baryon asymmetry by EW sphaleron processes [196–200]. All of the so-called Sakharov conditions for producing the observed matter-antimatter asymmetry of the universe are met [201].

A potential issue with GUT-scale sterile neutrinos is that they naively contribute to radiative corrections to the Higgs mass and can thus destabilise the EW scale [202]. A possible solution, known as the *neutrino option*, suggests that the Higgs mass parameter  $\mu = 0$  at tree-level due to classical scale invariance at high energies. A non-zero value is then induced entirely by heavy sterile neutrino threshold corrections [203–205].

Because the sterile neutrino masses in  $M_R$  are arbitrary, they can be made much smaller as long as there is a corresponding change to the Yukawa matrix  $Y_\nu$  to produce the absolute neutrino mass scale  $m_\nu \lesssim 1$  eV and the observed mass-squared splittings. If the relation  $\|M_D\| \ll \|M_R\|$  still holds then the seesaw diagonalisation

of Eq. (2.64) remains valid. Then, depending on what is an acceptable degree of fine-tuning for the Yukawa coupling  $Y_\nu$ , the sterile neutrino masses in  $M_R$  can range anywhere from an eV to the Planck scale. One of the most studied of these *low-scale* seesaw scenarios is the neutrino Minimal Standard Model (vMSM) [206]. This introduces three sterile states; a keV-scale neutrino which contributes to dark matter and a heavier neutrino pair with masses in the range  $1 - 100$  GeV [207, 208]. It was first shown in Ref. [209] (the Akhmedov-Rubakov-Smirnov or ARS mechanism) that CP-violating oscillations between the sterile neutrino pair can generate a baryon asymmetry. Alternatively, the sterile pair can be at the TeV-scale but possess a mass-splitting comparable to their decay widths; thermal leptogenesis can produce a lepton asymmetry via a resonant enhancement [210]. The seesaw limit has even been shown to reproduce the light neutrino masses down to  $M_R \sim 1$  eV, known as the *mini-seesaw* [211, 212].

Low-scale Type-I seesaws (e.g. those with sterile neutrinos in the TeV range) unfortunately predict very small active-sterile mixings,

$$V_{\ell N} \simeq \sqrt{\frac{m_\nu}{m_N}} \lesssim 10^{-6} \sqrt{\frac{100 \text{ GeV}}{m_N}}. \quad (2.69)$$

Even though the sterile neutrinos are kinematically accessible at colliders, their mixings are too suppressed to be produced in sufficient quantities.

The limit  $||M_D|| \gg ||M_R||$  is also possible for the Lagrangian of Eq. (2.60). Setting all elements in  $M_R$  to zero is of course equivalent to the Dirac scenario considered in the previous subsection if  $n_S = 3$ . The six massive Majorana fields are arranged into three degenerate-mass pairs with opposite CP parities, i.e. three Dirac neutrinos. Non-zero elements in  $M_R$  will now perturb the mass spectrum; at least one of the pairs will develop a small mass splitting. The nearly-degenerate neutrino pairs are called *quasi-Dirac* neutrinos. If the splittings are very small, oscillations between the Majorana neutrinos in each pair are too fast to resolve and they are indistinguishable from a single Dirac neutrino [213]. Solar neutrino data have excluded values in  $M_R$  above  $\sim 10^{-9}$  eV in the quasi-Dirac scenario [214]. Finally, it is worth noting that small sterile neutrino masses do not suggest an un-

natural fine-tuning as can be the case for the Yukawa coupling  $Y_V$ . Global lepton number symmetry is restored as  $M_R \rightarrow \mathbf{0}$  and therefore the radiative corrections to the Majorana neutrino masses (which will be examined in the next subsection) are also proportional to the Majorana masses. It is then *technically natural* for  $M_R$  to be small [215]. A baryon asymmetry can be generated for quasi-Dirac (or pure Dirac) neutrinos via the *neutrinoogenesis* mechanism [216].

Returning again to the Type-1 seesaw mechanism, it has been known for some time that there exists a class of models which produce the light neutrino masses *and* a sizeable active-sterile mixing  $V_{\ell N}$ . These extended models assign specific textures to the Dirac and Majorana mass matrices in Eq. (2.60), with the stability of these textures enforced by extra symmetries in the lepton sector [217–222]. In these scenarios the Majorana mass matrix can be written in the generic form

$$M_V = \begin{pmatrix} 0 & M_D^T \\ M_D & M_R \end{pmatrix} = \begin{pmatrix} 0 & (M_D)_1 & (M_D)_2 \\ (M_D)_1 & (M_R)_{11} & (M_R)_{12} \\ (M_D)_2 & (M_R)_{21} & (M_R)_{22} \end{pmatrix}, \quad (2.70)$$

where, as before, the (1,1) sub-block corresponding to the  $\nu_L$  Majorana mass matrix is zero in order to preserve the SM gauge symmetry. Two sets of sterile neutrino fields  $N_{R,1}$  and  $N_{R,2}$  have also been introduced; the mass matrix in Eq. (2.70) then specifies the Dirac and Majorana-like mass matrices of these fields.

We will now examine the different extended seesaw scenarios contained in Eq. (2.70). The *minimal* Inverse Seesaw (ISS) [223–225] sets the sub-blocks to  $(M_R)_{22} = \mu_S$  and  $(M_D)_2 = (M_R)_{11} = 0$ , giving in the basis  $n_L = (\nu_L \ N_{R,1}^c \ N_{R,2}^c)^T$

$$M_V = \begin{pmatrix} 0 & M_D^T & 0 \\ M_D & 0 & M_S \\ 0 & M_S^T & \mu_S \end{pmatrix}. \quad (2.71)$$

For  $\|M_D\|, \|\mu_S\| \ll \|M_S\|$ , this extended mass matrix can be diagonalised by a unitary matrix as in Eq. (2.67) to give a light neutrino mass matrix

$$m_V = M_D^T (M_S^T)^{-1} \mu_S M_S^{-1} M_D. \quad (2.72)$$

This approximate result is also true for the *generalised* ISS which additionally sets  $(M_R)_{11} = \mu_R$  [226, 227]. The matrix  $\mu_R$  does not contribute at tree-level, but does generate a one-loop correction which we will discuss in Subsection 2.2.3 [226, 228]. Finally, the so-called *minimal* Linear Seesaw [229–232] sets  $(M_R)_{11} = (M_R)_{22} = 0$  and  $(M_D)_2 = \mu_F$ , giving

$$M_V = \begin{pmatrix} 0 & M_D^T & \mu_F^T \\ M_D & 0 & M_S \\ \mu_F & M_S^T & 0 \end{pmatrix}. \quad (2.73)$$

With  $||\mu_F||, ||M_D|| \ll ||M_S||$ , the light neutrino mass matrix is given by

$$m_V \approx M_D^T M_S^{-1} \mu_F + \mu_F^T M_S^{-1} M_D. \quad (2.74)$$

Note that if there is no symmetry forbidding a rotation between the sterile states, the mass matrix of Eq. (2.73) can always be transformed to the generalised ISS mass matrix with appropriately defined  $\mu_R$  and  $\mu_S$  [233].

In the above scenarios we have not specified the source of LNV, which is necessary for the light neutrinos to be Majorana fermions. Whether the sub-blocks in Eq. (2.71) and (2.73) violate lepton number depends on the  $L$  assignment of the two sterile neutrinos  $N_{R,1}$ ,  $N_{R,2}$ . For example, making the choice  $L(v_L) = L(N_{R,1}) = L(N_{R,2}) = +1$  (i.e. treating the sterile neutrinos as right-handed counterparts to the left-handed active neutrinos) will mean that both terms in  $M_D$  conserve  $L$  while all terms in  $M_R$  violate  $L$  by two units. On the other hand, if  $L(v_L) = L(N_{R,1}) = +1$ ,  $L(N_{R,2}) = -1$ , the  $|\Delta L| = 2$  terms are  $(M_D)_2$  and  $(M_R)_{12} = (M_R)_{21}$ . While the origin of LNV is important to describe the underlying model, from a phenomenological point of view the assignment of lepton number does not need to be fixed. Also, any observable  $|\Delta L| = 2$  effect will depend on the relative CP phase between  $N_{R,1}$  and  $N_{R,2}$ .

Regardless, the smallness the matrices  $\mu_{R,S,F}$  is again technically natural in the 't Hooft sense [234], i.e. in the limit of  $\mu_{R,S,F} \rightarrow \mathbf{0}$ , lepton number symmetry is restored and the light neutrinos  $\nu$  are exactly massless to all orders in perturba-

tion theory. An advantage of these extended seesaw mechanisms over the standard Type-I seesaw is that the light neutrino masses are now the result of a small (but *technically natural*) parameter instead of a large scale  $M_R$ . The active-sterile mixings  $V_{\ell N}$  can now be sizeable while still satisfying the light neutrino oscillation data. However, for small  $\mu$ , the theory predicts that the massive Majorana sterile states form *pseudo*-Dirac pairs if they have opposite CP phases. This will be the focus of Chapter 5.

It is also worth mentioning that light active neutrino masses can be induced in models without sterile neutrino states. The most studied are the so-called Type-II and Type-III seesaw mechanisms. The former introduces a heavy Higgs field  $\Delta$  that is a triplet under  $SU(2)_L$  [189, 235–239]. The latter introduces three heavy  $SU(2)_L$  triplet fermions  $\Sigma$  [240]. We will see in the next section that these heavy states can be *integrated out* to give an effective light neutrino mass at low energies. One can instead remain agnostic about the source of the light neutrino masses and start from an effective approach. This can be included in the previous discussion by assuming that the Majorana mass matrix takes the form

$$M_V = \begin{pmatrix} M_L & M_D^\top \\ M_D & M_R \end{pmatrix}, \quad (2.75)$$

after EWSB, i.e. some new physics unrelated to the sterile neutrinos  $N_R$  generates a Majorana mass  $M_L$  for the active neutrinos at low energies.

To conclude this subsection we briefly examine the parametrisation of the PMNS mixing matrix  $U$  in the Majorana case. We saw in Eq. (2.63) that, after introducing  $n_S$  sterile neutrino fields, the charged-current interaction contains the  $3 \times N$  mixing matrix  $\Omega$ . This rectangular matrix is not unitary, but nevertheless we have the condition  $\Omega^\dagger \Omega \neq \Omega \Omega^\dagger = \mathbb{1}$ . As such, we can parametrise it in the following way: a general complex  $N_1 \times N_2$  rectangular matrix contains  $2N_1N_2$  free parameters. The condition  $\Omega \Omega^\dagger = \mathbb{1}$  enforces  $N_1^2$  constraints to give  $N_1(2N_2 - N_1)$  free parameters. In this particular case  $N_1 = 3$  and  $N_2 = 3 + n_S$ , and it can be shown that the  $3(3 + 2n_S)$  free parameters can be split up into  $3 + 3n_S$  angles and  $6 + 3n_S$  phases. Fi-

nally, an arbitrary rephasing of the charged lepton fields  $\ell_{\beta L(R)} \rightarrow e^{i\phi_\beta} \ell_{\beta L(R)}$  makes it possible to eliminate three phases to give  $3 + 3n_S$  phases in total. The effective Majorana mass term for the mass eigenstate neutrinos forbids an equivalent rephasing  $n'_{jL(R)} \rightarrow e^{i\phi_j} n'_{jL(R)}$ .

This general prescription is simplified further in the seesaw limit of Eqs. (2.67) and (2.68). Here we now see that the  $3 \times 3$  and  $3 \times n_S$  sub-blocks of  $\Omega$  are correlated; the  $V_{\ell N}$  sub-block contains  $6n_S$  arbitrary parameters. We can now separate out three mixing angles and three phases in the unitary matrix  $U$ , which is now defined to diagonalise the light Majorana mass matrix  $m_V \approx -M_D^T M_R M_D$ . One of these is the Dirac phase  $\delta_{CP}$  and the other two are the so-called Majorana phases  $\alpha_2$  and  $\alpha_3$  situated along the diagonal of the matrix, i.e.  $U = R_{23}W_{13}R_{12}D$  where  $D = \text{diag}(1, e^{i\frac{\alpha_2}{2}}, e^{i\frac{\alpha_3}{2}})$ . Processes that conserve the total lepton number (e.g. neutrino oscillations) are not sensitive to these two phases. This is because the total rate always depends on the PMNS mixing matrix elements multiplied by their complex conjugates. This is not the case for LNV phenomena such as  $0\nu\beta\beta$  decay, which we will see in Chapter 3 is sensitive to  $\alpha_2$  and  $\alpha_3$ .

The Type-I seesaw limit predicts that the mixing between the charged leptons and light neutrinos appearing in the charged-current interaction,  $U_V \approx (1 - \eta)U$ , is not unitary. The deviation from unitarity is encoded by the small parameter

$$\eta = \frac{1}{2} M_D^\dagger M_R^{-2} M_D, \quad (2.76)$$

though  $\eta$  may also be generated by unrelated new physics. Non-unitarity has been extensively examined in the context of neutrino oscillations [241–248].

Finally, it can also be shown that in the  $n_S = 3$  Dirac limit,

$$\Omega = \frac{1}{\sqrt{2}} \begin{pmatrix} \cdot & \cdot & \cdot & \cdot & \cdot & \cdot \\ \cdot & U & \cdot & \cdot & \cdot & \cdot \\ \cdot & \cdot & iU & \cdot & \cdot & \cdot \\ \cdot & \cdot & \cdot & iU & \cdot & \cdot \\ \cdot & \cdot & \cdot & \cdot & iU & \cdot \\ \cdot & \cdot & \cdot & \cdot & \cdot & U \end{pmatrix}, \quad (2.77)$$

where now the absence of the Majorana mass term permits a rephasing of  $\nu$  to remove the Majorana phases from  $U$ . The number of free parameters has been

dramatically reduced from 24 to three angles and one phase [213].

### 2.2.3 Radiative Neutrino Masses

We have so far considered mechanisms that generate the light neutrino masses at tree-level. Neutrino masses can also be generated at higher orders in perturbation theory, i.e. diagrams containing one or more loops [249, 250]. An useful property of these contributions is that they are suppressed by a factor of  $1/16\pi^2$  for each loop; the scale of new physics  $\Lambda_{\text{NP}}$  generating the light neutrino masses can therefore be much lower. Furthermore, loop or *radiative* diagrams can induce either Dirac or Majorana neutrino masses depending on the field content of the theory. The loop diagrams may be the dominant contribution to the light neutrino masses if tree-level Feynman diagrams are forbidden by some symmetry.

A variety of radiative mechanisms have been investigated in the literature. Well-known examples that generate Majorana neutrino masses at one-loop are the Zee and scotogenic models [251, 252]. The latter introduces three fermions  $N$  and an  $SU(2)_L$  doublet Higgs  $(\eta^+, \eta^0)$ , both of which are negatively charged under a discrete  $Z_2$  symmetry (the SM fields are positively charged, thereby forbidding a seesaw diagram at tree-level). Because the  $Z_2$  symmetry forbids it decaying to SM particles, the lightest of the new particles is a suitable DM candidate. At two-loops an example is the so-called Zee-Babu model, which introduces singly- and doubly-charged scalar fields  $h^+$  and  $k^{++}$  [253, 254]. At three-loops the number of possible diagram topologies increases greatly, and the loop integrals themselves are difficult to evaluate. Nevertheless, classes of models studied in the literature include Krauss-Nasri-Trodden (KNT), Aoki-Kanemura-Seto (AKS) and cocktail models [255–257]. Minimal radiative models that do not introduce additional global or gauge symmetries to the SM have been considered in Ref. [258]. A radiative mechanism that instead generates Dirac neutrino masses at one-loop (and provides a possible DM candidate) has been considered in Ref. [259].

More recently, Dirac neutrino masses generated at two-loops have been studied the context of the left-right symmetric model [260]. Here, the SM gauge group is assumed to be the low energy limit of an  $SU(3)_c \times SU(2)_L \times SU(2)_R \times U(1)_X$  gauge

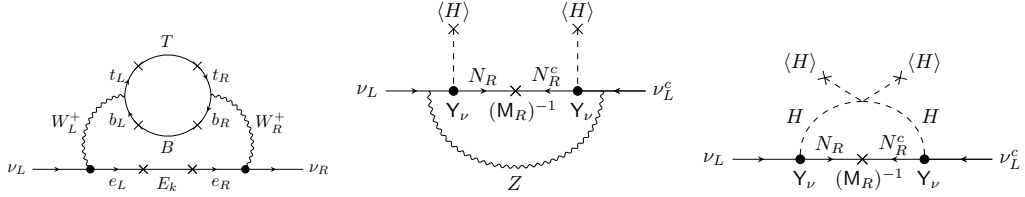


**Figure 2.2:** (Left) Two-loop diagram generating Dirac neutrino masses in a left-right symmetric model with a global  $U(1)_{B-L}$  symmetry. (Centre and right) Radiative corrections to the Type-I and ISS mechanisms.

symmetry at high energies. This gauge group, and in particular the quantum number  $X$ , is usually assumed to be broken by the VEV of a  $SU(2)_R$  triplet Higgs. It is then possible to identify  $X$  as the non-anomalous combination  $B - L$ . As a result of  $B - L$  being broken, Majorana neutrino masses are generated. On the other hand, the precise pattern of symmetry breaking can be changed if the field content of the model is altered. Crucially, if a new quantum number  $\zeta$  is introduced, the  $U(1)_X$  symmetry can correspond to  $X = (B - L) + \zeta$ . For  $\zeta \neq 0$ , the combination  $B - L$  remains a global symmetry at low energies and neutrinos must be Dirac fermions.

The field content of the left-right symmetry model can be considered with or without the presence of a bi-doublet (under  $SU(2)_L$  and  $SU(2)_R$ ) Higgs field, which conventionally gives Dirac masses to the SM fermions after EWSB. If it is not present, one can add new vector-like states for the charged leptons, up-type and down-type quarks;  $E$ ,  $U$  and  $D$  respectively. The left- and right-handed components of these fields transform identically under the left-right gauge group. If these vector-like states are then much heavier than the EW scale, the SM fermion mass matrices  $M_e$ ,  $M_u$  and  $M_d$  are generated via a Dirac seesaw mechanism [261–266]. Most importantly, small Dirac neutrino masses are produced by the two-loop diagram to the left of Fig. 2.2. In order to produce the observed light neutrino mass-squared splittings, Ref. [260] found that the scale of left-right symmetry breaking must be  $\Lambda_{NP} \sim 100$  TeV and that a hierarchy is required between the generations of vector-like charged leptons  $E_k$  (for a single generation of vector-like quarks,  $B$  and  $T$ ).

We finally return to the generalised ISS mechanism, i.e. the Majorana mass matrix in Eq. (2.70) with the (2,2) sub-block set to  $\mu_R$ . It can be shown that the light neutrino Majorana matrix in Eq. (2.72) acquires a one-loop radiative correction

from the diagrams in the centre and right of Fig. 2.2 [228, 267, 268]. This is the standard tree-level ISS diagram with either a  $Z$  loop or a closed Higgs loop (and a quartic Higgs interaction). In terms of the  $3 \times n_S$  matrix  $M_D$  and the  $n_S \times n_S$  matrix  $M_R$  defined as,

$$M_R = \begin{pmatrix} \mu_R & M_S \\ M_S^T & \mu_S \end{pmatrix}, \quad (2.78)$$

the finite loop contribution can be written as

$$\delta m_\nu^{1\text{-loop}} = \frac{\alpha_W M_D M_R}{16\pi m_W^2} \left[ \frac{3m_Z^2}{M_R^2 - m_Z^2 \mathbb{1}} \ln \left( \frac{M_R^2}{m_Z^2} \right) + \frac{m_H^2}{M_R^2 - m_H^2 \mathbb{1}} \ln \left( \frac{M_R^2}{m_H^2} \right) \right] M_D^T, \quad (2.79)$$

with  $\alpha_W = g^2/4\pi$ , where the first and second terms correspond to the  $Z$  and Higgs loop diagrams, respectively [226]. In the limit  $||\mu_{R,S}|| \ll ||M_S||$ , and assuming  $M_S = m_S \mathbb{1}$ , the expression can be simplified to

$$\delta m_\nu^{1\text{-loop}} \approx \frac{\alpha_W M_D \mu_R}{16\pi m_W^2} \left[ \frac{3m_Z^2}{m_S^2 - m_Z^2} \ln \left( \frac{m_S^2}{m_Z^2} \right) + \frac{m_H^2}{m_S^2 - m_H^2} \ln \left( \frac{m_S^2}{m_H^2} \right) \right] M_D^T, \quad (2.80)$$

which we now see depends on the matrix  $\mu_R$ , not  $\mu_S$  [226]. Therefore, in the case  $\mu_S = \mathbf{0}$  but  $\mu_R \neq \mathbf{0}$ , neutrinos are massless at tree-level but acquire a Majorana mass matrix directly proportional to  $\mu_R$ . Because it does not require any additional field content beyond that already present in the ISS, this scenario is called the *minimal radiative* ISS. We will also examine this contribution in Chapter 5.

## 2.3 Effective Field Theories

In this section we will summarise the *effective* approach for parametrising physics beyond the SM. In the previous section we examined specific models (introducing new field content and symmetries) that generate the light neutrino masses, whether they be Dirac or Majorana. Since the 1970s, a plethora of extensions to the SM have been suggested as solutions to other outstanding problems. For example, SUSY was first developed as a means of explaining the seemingly ‘fine-tuned’ Higgs mass. The theory predicts a spectrum of heavy SUSY partners, the lightest of which may be

a Weakly Interacting Massive Particle (WIMP) DM candidate. However, in order to stabilise the Higgs mass the theory needs SUSY partners in the TeV regime; no evidence of such particles has been seen at colliders. Furthermore, the non-observation of proton decay and FCNCs has heavily constrained couplings in the theory.

It is therefore important to complement the study of specific models with a *model-independent* approach. Ideally, this second approach will not be biased by criteria used in the past to develop new theories; namely, notions of naturalness and increased symmetry (or unification) at high energies. While we have observed the unification of the electromagnetic and weak forces at the EW scale, this may not be true for the EW and strong forces. It is nevertheless important to explore all possibilities for new physics, especially those that make experimental predictions (and are thus falsifiable).

The most useful tools for the model-independent approach are Effective Field Theories (EFTs). So-called *effective* theories of nature have been highly useful as our knowledge of the fundamental interactions has improved. They are based on the concept that physics at some high energy  $\Lambda$  in the *ultraviolet* (UV) does not significantly affect phenomena at low energies  $E$  in the *infrared* (IR); the small impact in the IR can be described by an expansion in  $E/\Lambda$ . For example, the non-relativistic approximation can be regarded as an expansion in  $v/c$ , where  $v \ll c$ .

The EFT framework is a systematic procedure for quantifying the effect of UV physics in QFTs. At a given order in the expansion parameter  $E/\Lambda$ , one can construct all operators (from the available degrees of freedom) that satisfy the symmetries of the theory. For powers  $(E/\Lambda)^n$  where  $n > 0$ , the operators are of mass dimension greater than four and are therefore non-renormalisable. Renormalisable theories such as QED can, in principle, compute an infinite number of observables with a finite number of parameters; these can absorb all the UV divergences from loop diagrams. Conversely, a non-renormalisable theory requires an infinite number of counterterms to cancel all UV divergences. On the other hand, these divergences *can* be absorbed by a finite number of parameters order by order by the expansion

parameter. In this way, EFTs are still predictive to a given accuracy.

An EFT can be considered from a *top-down* or *bottom-up* perspective. The former constructs an EFT from a known UV-complete theory where an effective approach may simplify difficult calculations. This is achieved by *integrating out* the degrees of freedom heavier than  $\Lambda$ . For example, Chiral Perturbation Theory ( $\chi$ PT) and Heavy Quark Effective Field Theory (HQEFT) are low energy EFTs of QCD. The former describes the low energy interactions of light hadronic degrees of freedom (such as protons, neutrons and pions) below the chiral symmetry breaking scale of QCD,  $\Lambda_\chi \sim 1$  GeV. The latter describes the low energy dynamics of hadrons containing a charm or bottom quark.

Fermi's effective theory of weak interactions can also be derived from the full description of weak interactions by integrating out the  $W^\pm$  and  $Z$  bosons. This can be achieved by approximating the propagators of the bosons as, e.g.

$$\frac{i(-g_{\mu\nu} + \frac{p_\mu p_\nu}{m_W^2})}{p^2 - m_W^2} \approx \frac{ig_{\mu\nu}}{m_W^2} \left( 1 + \frac{p^2}{m_W^2} + \frac{p^4}{m_W^4} + \dots \right), \quad (2.81)$$

which, when contracted with  $(V - A)$  fermion currents at each vertex gives the dimension-six operator (for the leading-order term in Eq. (2.81))

$$\mathcal{L}_{\text{CC}} \approx -\frac{4G_F}{\sqrt{2}} (\bar{\psi} \gamma^\mu T^+ \psi) (\bar{\psi}' \gamma_\mu T^- \psi'), \quad (2.82)$$

where  $\psi, \psi' \in \{L_L, \ell_R, Q_L, u_R, d_R\}$  and the Fermi coupling constant is defined as  $\frac{G_F}{\sqrt{2}} \equiv \frac{g^2}{8m_W^2}$ . Doing the same for the neutral-current gives

$$\mathcal{L}_{\text{NC}} \approx -\frac{4G_F}{\sqrt{2}} (\bar{\psi} \gamma^\mu (T^3 - s_W^2 Q) \psi) (\bar{\psi}' \gamma_\mu (T^3 - s_W^2 Q) \psi'), \quad (2.83)$$

where we have used the relation  $c_W = m_W/m_Z$  (valid at tree-level). Evaluating  $(T^3 - s_W^2 Q)$  for the fields makes it possible to write the effective neutral-current in the conventional form

$$\mathcal{L}_{\text{NC}} \approx -\frac{4G_F}{\sqrt{2}} g_X^\psi g_Y^{\psi'} (\bar{\psi} \gamma^\mu P_X \psi) (\bar{\psi}' \gamma_\mu P_Y \psi'), \quad (2.84)$$

where  $\psi, \psi' \in \{v, \ell, u, d\}$  and  $X, Y \in \{L, R\}$ . The  $g_X^\psi$  factors correspond to the values of  $(T^3 - s_W^2 Q)$  in Table 2.2. We additionally set  $g_R^v = 0$ .

Of course, the UV-complete theory of weak interactions was not known when the effective Lagrangian of Eq. (2.82) was first written. This is the bottom-up approach; at a given dimension, one constructs all operators from the known degrees of freedom that respect the symmetries of the low-energy theory. New physics at some high scale  $\Lambda_{\text{NP}}$  may contribute to any one of these operators, but we would expect the lowest orders (the least suppressed by powers of  $\Lambda_{\text{NP}}$ ) to contribute the most. For physics beyond the SM, the useful EFT is therefore the Standard Model Effective Field Theory (SMEFT), which we will now present.

For the vSM, we are interested in the operators that contain the left-handed neutrino fields  $v_L$  and therefore contribute to observables such as the neutrino masses, neutrino oscillations, beta decay and  $0\nu\beta\beta$  decay. Because these processes take place at low energies (below the EW scale), the relevant SMEFT operators can be matched onto a more useful Low Energy Effective Field Theory (LEFT). We will also outline the operators that will be used in the subsequent chapters of this thesis.

### 2.3.1 Standard Model Effective Field Theory

In general, physics beyond the SM (at some high energy scale  $\Lambda_{\text{NP}}$ ) will induce higher-dimensional local operators containing all possible permutations of SM fields respecting the  $SU(3)_c \times SU(2)_L \times U(1)_Y$  gauge symmetry of the SM. This can be written as the expansion

$$\mathcal{L}_{\text{SMEFT}} = \mathcal{L}_{\text{SM}} + \sum_{d \geq 5} \sum_i \frac{\hat{C}_i^{(d)}}{\Lambda_{\text{NP}}^{d-4}} \mathcal{O}_i^{(d)}, \quad (2.85)$$

where  $\mathcal{L}_{\text{SM}}$  is the SM Lagrangian,  $\mathcal{O}_i^{(d)}$  are dimension- $d$  (dim- $d$ ) combinations of SM fields and  $\hat{C}_i^{(d)}$  are associated dimensionless Wilson coefficients. The scale of NP can be absorbed into the dimensionful coefficients  $C_i^{(d)} = \hat{C}_i^{(d)} / \Lambda_{\text{NP}}^{d-4}$ . The index  $i$  sums over all Lorentz and gauge-invariant combinations of fields.

The SMEFT does not necessarily impose the conservation of lepton or baryon number, which are accidental symmetries of  $\mathcal{L}_{\text{SM}}$ . It can be shown that an oper-

ator will have even (or odd) dimension if the combination  $(\Delta B - \Delta L)/2$  is even (or odd) [269]. For example, baryon and lepton number violating operators with  $(\Delta B, \Delta L) = (\pm 1, \pm 1)$  arise at dim-6. The dimensionful coefficients  $C_{\beta}^{(6)}$  of these operators are heavily constrained by the non-observation of proton decay. For  $\mathcal{O}(1)$  Wilson coefficients  $\hat{C}_{\beta}^{(6)}$ , the scale of NP must be high,  $\Lambda_{\text{NP}} \gtrsim 10^{16}$  GeV. If NP is instead at the TeV scale, the Wilson coefficients will be highly suppressed,  $\hat{C}_{\beta}^{(6)} \lesssim 10^{-26}$ . The (non-)conservation of lepton number is closely linked to the Dirac or Majorana nature of neutrinos. The presence of *any*  $|\Delta L| = 2$  operator implies that the light neutrinos are Majorana fermions; a Majorana mass term for the left-handed neutrino fields  $\nu_L$  can be constructed from one of these operators at tree-level or radiatively. All operators with  $|\Delta B| = 0$  and  $|\Delta L| = 2$  must be of odd dimension; therefore, operators that induce Majorana neutrino masses and LNV phenomena are of dim-5, dim-7 and dim-9 [270]. It can be shown that the only dim-5 operator in the SMEFT is the well-known Weinberg operator

$$\mathcal{L}^{(5)} = C_V^{(5)} (\ell_L^T \mathcal{C} \tilde{H}^*) (\tilde{H}^\dagger \ell_L) + \text{h.c.}, \quad (2.86)$$

where  $C_V^{(5)} = \hat{C}_V^{(5)} / \Lambda_{\text{NP}}$ ,  $\tilde{H} = i\sigma_2 H^*$  and  $\sigma_2$  the second Pauli matrix [123].

A complete basis of SMEFT operators has been classified in the literature up to dim-9. At dim-6 there are 63 non-redundant, linearly-independant operators, first derived in Refs. [271, 272]. It was shown that 59 of these operators are baryon number conserving, while the remaining four violate baryon and lepton number as  $(\Delta B, \Delta L) = (\pm 1, \pm 1)$ . When  $n_f = 3$  generations of fermions are included, this amounts to 2499 instances of the former operator and 273 of the latter. To determine the behaviour of these operators beyond the tree-level, their renormalisation group (RG) evolution must be characterised. This is the *running* and *mixing* of the Wilson coefficients from the high scale  $\Lambda_{\text{NP}}$  to the low scale  $\mu$ , which can be quantified by the anomalous dimension matrix  $\gamma$ ,

$$\mu \frac{dC_i^{(6)}}{d\mu} = \gamma_{ij} C_j^{(6)}. \quad (2.87)$$

The  $59 \times 59$  anomalous dimension matrix for the dim-6 baryon number conserving operators has been computed at one-loop in Refs. [273–275]. The equivalent  $4 \times 4$  matrix for the  $(\Delta B, \Delta L) = (\pm 1, \pm 1)$  operators has likewise been summarised in Ref. [276]. Mixing is not permitted between operators with different quantum numbers.

At dim-7 there are known to be 18 linearly-independent SMEFT operators; 12 violating lepton number by two units,  $(\Delta B, \Delta L) = (0, \pm 2)$ , and six violating baryon and lepton number by one unit,  $(\Delta B, \Delta L) = (\pm 1, \mp 1)$  [277, 278]. The anomalous dimension matrices for these two classes of operators have been computed in Refs. [278, 279]. The SMEFT operators at dim-8 and dim-9 are listed in Refs. [280] and [281] respectively. For operators with  $\text{dim-}d > 6$ , it is increasingly difficult to count the number of operators for  $n_f$  generations, as some operators vanish when flavour structure is included. However, there has been recent progress with Hilbert series techniques [282, 283]. Furthermore, thorough studies of the RG runnings and mixings of  $\text{dim-}d > 7$  operators have yet to be conducted.

### 2.3.2 Low Energy Effective Field Theory

For phenomena taking place at energies below the EW scale, it is more practical to use the previously-mentioned LEFT. This is an expansion similar to Eq. (2.85), except  $\mathcal{L}_{\text{SM}}$  is now in the broken phase. Additionally, one must add all possible permutations of fields (lighter than the EW scale) respecting the  $\text{SU}(3)_c \times \text{U}(1)_Q$  gauge symmetry of the spontaneously-broken SM. We will introduce the notation  $\text{dim-}\bar{d}$  for the mass dimension of LEFT operators.

It is possible to *match* the SMEFT operators onto the LEFT at the EW scale. To do this, one must expand the Higgs doublet around its VEV (for example, in the unitary gauge,  $H = \frac{1}{\sqrt{2}}(0 \ v + h)^T$ ) and then integrate out the degrees of freedom heavier than the EW scale ( $W^\pm$  and  $Z$  bosons, top quark  $t$  and Higgs boson  $h$ ). Matching can take place at tree-level at multiple loops. At tree-level,  $\text{dim-}\bar{d}$  LEFT operators can be matched to  $\text{dim-}d$  SMEFT operators with  $(d - \bar{d})$  Higgs insertions. As  $d$  increases, the number of SMEFT operators that can be matched to a given LEFT operator increases dramatically; the matching is usually restricted to a given

mass dimension  $d$  and number of loops.

A complete basis of LEFT operators has been specified up to  $\text{dim-}\bar{7}$  [284, 285]. In Ref. [284], LEFT operators up to  $\text{dim-}\bar{6}$  were matched at tree-level to SMEFT operators up to  $\text{dim-6}$ . This was extended to a matching to  $\text{dim-6}$  SMEFT operators at one-loop in Ref. [286] and  $\text{dim-7}$  SMEFT operators at tree-level in Ref. [285]. In Ref. [287], the anomalous dimension matrix was computed for the complete basis of  $\text{dim-}\bar{6}$  LEFT operators. This provides a method for determining the effect of NP above the EW scale at a low energy  $\mu$ . The RG running and mixing of SMEFT Wilson coefficients in Eq. (2.87) is used to evolve the coefficients from  $\Lambda_{\text{NP}}$  down to the EW scale. There, the coefficients are matched onto the equivalent LEFT coefficients, and these coefficients are finally evolved down to the scale  $\mu$ .

The only operator at  $\text{dim-}\bar{3}$  in the LEFT, shown in Fig. 2.3 (left), is

$$\mathcal{L}^{(\bar{3})} = -\frac{1}{2} v_L^\top \mathcal{C} M_L v_L + \text{h.c.}, \quad (2.88)$$

i.e. a Majorana mass term for  $v_L$ . This is induced by the  $\text{dim-5}$  Weinberg operator in Eq. (2.86) after EWSB and therefore the matching  $M_L = v^2 \hat{C}_v^{(5)} / \Lambda_{\text{NP}}$  is possible. After rotating to the mass basis, this mass matrix can be compared to the prediction from the Type-I seesaw,  $m_\nu \approx -M_D M_R^{-1} M_D = -\frac{v^2}{2} Y_\nu M_R^{-1} Y_\nu$ . It is then clear that  $\Lambda_{\text{NP}}$  corresponds to the right-handed neutrino masses in  $M_R$ . However, models such as the Type-II and Type-III seesaw mechanisms also induce this operator. From a model-independent point of view, the small active neutrino masses put a stringent bound on the dimensionful coefficient  $C_v^{(5)}$ . For  $\hat{C}_v^{(5)} \sim 1$ , the scale of NP must be high,  $\Lambda_{\text{NP}} \gtrsim 10^{15}$  GeV. Conversely, for  $\Lambda_{\text{NP}} \sim 1$  TeV the Wilson coefficient must be suppressed,  $\hat{C}_v^{(5)} \lesssim 10^{-12}$ .

At  $\text{dim-}\bar{5}$  is the neutrino dipole operator (shown in Fig. 2.3, right)

$$\mathcal{L}^{(\bar{5})} \supset -\frac{1}{2} v_L^\top \mathcal{C} \mu_L \sigma_{\mu\nu} v_L F^{\mu\nu} + \text{h.c.}, \quad (2.89)$$

which describes magnetic and electric dipole moments of the light active Majorana neutrinos. The lowest dimension SMEFT operators this operator can be matched

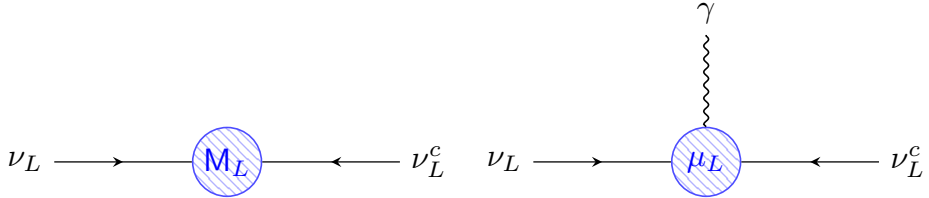


**Figure 2.3:** (Left) Effective Majorana mass for the left-handed neutrino fields  $\nu_L$  from a dim-3 LEFT operator. (Right) Majorana neutrino dipole moment interaction from a dim-5 LEFT operator.

to are at dim-7. Eq. (2.89) is antisymmetric in the exchange of neutrino fields and therefore vanishes when the flavour of the two neutrino fields are the same ( $\alpha = \beta$ ), but not when they are different ( $\alpha \neq \beta$ ). For  $n_f = 3$  generations,  $\mu_L$  is a  $3 \times 3$  antisymmetric matrix and Eq. (2.89) can only describe transition dipole moments.

It is always possible that the same NP contributes to the neutrino mass and dipole operators. For example, the effective neutrino dipole interaction shown in Fig. (2.3) may be a loop process containing a charged particle. One can immediately generate the Majorana mass operator by removing the photon. In this case the Majorana mass and dipole moment are given approximately by

$$m_\nu \sim G\Lambda_{\text{NP}}, \quad \mu_\nu \sim \frac{eG}{\Lambda_{\text{NP}}} \quad \Rightarrow \quad \frac{\mu_\nu}{\mu_B} = \frac{2m_e m_\nu}{\Lambda_{\text{NP}}^2} \quad (2.90)$$

where  $G$  contains coupling constants and loop factors. Above we have rearranged to find a naive relation between the dipole moment (in units of the Bohr magneton  $\mu_B = \frac{e}{2m_e}$ ) and the neutrino masses; the small neutrino masses imply very small neutrino magnetic and electric dipole moments. The situation is complicated by the fact that  $m_\nu$  is symmetric and  $\mu_\nu$  antisymmetric in flavour space. The correlation between the two is examined in detail by Ref. [288], which sets model-independent bounds on the Majorana transition dipole moments as a function of  $\Lambda_{\text{NP}}$ .

The primary focus of Chapters 3 and 4 of this thesis will be to assess novel probes of Non-Standard Interactions (NSIs) of neutrinos with matter. Generically, these kinds of interaction arise at dim-6 in the LEFT; those that involve a single left-handed neutrino field  $\nu_L$  in a charged-current type interaction (shown in Table 2.4) or two  $\nu_L$  fields in a neutral-current type interaction (Table 2.5). As shown to the left

Charged-Current LEFT Operators	
$ \Delta L  = 0 + \text{h.c.}$	$ \Delta L  = 2 + \text{h.c.}$
$(\bar{v}_L \gamma^\mu \ell_L)(\bar{d}_L \gamma_\mu u_L)$	$(v_L^\top \mathcal{C} \gamma^\mu \ell_R)(\bar{d}_L \gamma_\mu u_L)$
$(\bar{v}_L \gamma^\mu \ell_L)(\bar{d}_R \gamma_\mu u_R)$	$(v_L^\top \mathcal{C} \gamma^\mu \ell_R)(\bar{d}_R \gamma_\mu u_R)$
$(\bar{v}_L \ell_R)(\bar{d}_L u_R)$	$(v_L^\top \mathcal{C} \ell_L)(\bar{d}_L u_R)$
$(\bar{v}_L \ell_R)(\bar{d}_R u_L)$	$(v_L^\top \mathcal{C} \ell_L)(\bar{d}_R u_L)$
$(\bar{v}_L \sigma^{\mu\nu} \ell_R)(\bar{d}_L \sigma_{\mu\nu} u_R)$	$(v_L^\top \mathcal{C} \sigma^{\mu\nu} \ell_L)(\bar{d}_R \sigma_{\mu\nu} u_L)$

**Table 2.4:**  $|\Delta L| = 0$  (left) and  $|\Delta L| = 2$  (right) dim-6 charged-current LEFT operators, of vector, scalar and tensor type.

and right of each table, each type of interaction can either be  $|\Delta L| = 0$  or  $|\Delta L| = 2$ . For charged-current type interactions it can be seen that vector-, scalar- and tensor-type currents are possible for both  $|\Delta L| = 0$  or  $|\Delta L| = 2$  operators. The difference is purely the replacements  $v_L \leftrightarrow \mathcal{C} \bar{v}_L^\top$  and  $\ell_L \leftrightarrow \ell_R$ . For the neutral-current type interactions only  $|\Delta L| = 0$  vector-type and  $|\Delta L| = 2$  scalar- and tensor-type currents are possible. If the replacement  $v_L \leftrightarrow \mathcal{C} \bar{v}_L^\top$  is made for any one of the neutrino fields in these operators it will vanish. The  $(\bar{v}_L \gamma^\mu \ell_L)(\bar{d}_L \gamma_\mu u_L)$ ,  $(\bar{v}_L \gamma^\mu v_L)(\bar{\psi}_L \gamma_\mu \psi_L)$  and  $(\bar{v}_L \gamma^\mu v_L)(\bar{\psi}_R \gamma_\mu \psi_R)$  operators all receive contributions from the SM charged- and neutral-current interactions (as seen at the start of this section).

The  $|\Delta L| = 0$  charged-current type operators can be matched onto operators in the SMEFT at dim-6, while  $|\Delta L| = 2$  operators can only be matched onto dim-7 and above operators. For example, the lower four  $|\Delta L| = 2$  operators in Table 2.4 can be matched to dim-7 SMEFT operators with an additional Higgs doublet in order to conserve hypercharge. The operator  $(v_L^\top \mathcal{C} \gamma^\mu \ell_R)(\bar{d}_L \gamma_\mu u_L)$  can only be matched to the SMEFT at dim-9, with three Higgs doublets needed to keep hypercharge invariant. Likewise, the  $|\Delta L| = 0$  neutral-current operators are matched to dim-6 SMEFT operators while  $|\Delta L| = 2$  operators are matched to dim-7 or dim-9.

The standard parametrisation for the dim-6 neutrino NSIs (normalised to the

Neutral-Current LEFT Operators	
$ \Delta L  = 0$	$ \Delta L  = 2 + \text{h.c.}$
$(\bar{v}_L \gamma^\mu v_L)(\bar{\psi}_L \gamma_\mu \psi_L)$	$(v_L^\top \mathcal{C} v_L)(\bar{\psi}_L \psi_R)$
$(\bar{v}_L \gamma^\mu v_L)(\bar{\psi}_R \gamma_\mu \psi_R)$	$(v_L^\top \mathcal{C} v_L)(\bar{\psi}_R \psi_L)$
	$(v_L^\top \mathcal{C} \sigma^{\mu\nu} v_L)(\bar{\psi}_R \sigma_{\mu\nu} \psi_L)$

**Table 2.5:**  $|\Delta L| = 0$  (left) and  $|\Delta L| = 2$  (right) dim-6 neutral-current LEFT operators, of vector type for the former and scalar and tensor type for the latter. The fermion fields can be  $\psi \in \{\ell, u, d\}$ .

Fermi coupling constant  $G_F$ ) is

$$\mathcal{L}_{CC}^{(6)} = -\frac{G_F}{\sqrt{2}} \varepsilon (\bar{v} \Gamma \ell) (\bar{d} \Gamma' u) + \text{h.c.}, \quad (2.91)$$

$$\mathcal{L}_{NC}^{(6)} = -\frac{G_F}{\sqrt{2}} \varepsilon' (\bar{v} \Gamma v) (\bar{\psi} \Gamma' \psi), \quad (2.92)$$

where the possible combinations of Dirac matrices is shown in Table 2.6 [289]. The  $\varepsilon$  and  $\varepsilon'$  are non-standard coefficients with four flavour indices.

Because the LEFT and SMEFT operators are constructed from SM degrees of freedom, they only contain the left-handed neutrino fields  $v_L$ ; no assumption is made about the Dirac or Majorana nature. We have seen that the SMEFT contains  $|\Delta L| = 2$  operators at  $\text{dim-}d > 5$  which generate a Majorana mass term for the light active neutrinos. However, it is still possible that the active neutrinos are Dirac fermions if  $U(1)_L$  is an exact global symmetry of the Lagrangian and the Wilson coefficients of  $|\Delta L| = 2$  operators vanish, i.e.  $\hat{C}_v^{(5)} = 0$ . As the right-handed (Dirac) neutrino fields  $v_R$  are sterile under the gauge symmetry of the SM (and its broken phase), they are usually omitted from the SMEFT (and LEFT).

However, it may be the case that the  $v_R$  fields are involved in  $V+A$  interactions (arising for example in a left-right symmetric model) at high energies. Both the Dirac and Majorana cases are possible in Eqs. (2.91) and (2.92). When the Dirac matrix  $\Gamma$  picks out the right-handed part of the four-component neutrino field  $v$  (and the associated non-standard coefficient is  $\tilde{\varepsilon}$ ), we obtain  $v_R$  in the Dirac case and  $v_L^c$  in the Majorana case. In the Dirac case, all interactions in Eqs. (2.91) and (2.92) are  $|\Delta L| = 0$ . In the Majorana case, the charged-current coefficients  $\varepsilon$  and  $\tilde{\varepsilon}$  indicate

$\epsilon$	$\Gamma$	$\Gamma'$
$\overset{\sim}{\epsilon}_L$	$\gamma^\mu(1 \mp \gamma_5)$	$\gamma_\mu(1 - \gamma_5)$
$\overset{\sim}{\epsilon}_R$	$\gamma^\mu(1 \mp \gamma_5)$	$\gamma^\mu(1 + \gamma_5)$
$\overset{\sim}{\epsilon}_S$	$(1 \pm \gamma_5)$	1
$\overset{\sim}{\epsilon}_P$	$(1 \pm \gamma_5)$	$-\gamma_5$
$\overset{\sim}{\epsilon}_T$	$\sigma^{\mu\nu}(1 \pm \gamma_5)$	$\sigma_{\mu\nu}(1 \pm \gamma_5)$

**Table 2.6:** Combinations of Dirac matrices appearing in the standard parametrisation of charged- and neutral-current type neutrino NSIs.

$|\Delta L| = 0$  and  $|\Delta L| = 2$  interactions respectively. The vector-type neutral-current interactions are  $|\Delta L| = 0$  while scalar and tensor-type interactions are  $|\Delta L| = 2$ . It is also possible that the right-handed fields  $N_R$  are completely unrelated to the light active neutrino fields, but have their own Majorana masses below the EW scale. For full consistency both possibilities should be included, which we outline in the next subsection.

For the ten charged-current  $\epsilon$  coefficients it can be shown (in both the Dirac and Majorana cases) that there are  $2 \times 3^4 \times 10 = 1620$  free parameters. The form of Eq. (2.92) allows to eliminate half of these parameters (810) for the neutral-current  $\epsilon'$  coefficients. Finally, in the Majorana case there are additional constraints in the  $\epsilon'$  coefficients, for example a relationship between  $\epsilon'_L$  and  $\tilde{\epsilon}'_L$  (depending on the flavour indices). These are summarised in Appendix A. This can reduce the number of free parameters in the  $\epsilon'$  coefficients down to 432 [289].

The phenomenology of the non-standard charged-current and neutral-current neutrino interactions in Eqs. (2.91) and (2.92) have been studied extensively in the literature [290–303]. To summarise this line of research very briefly, neutrino NSIs involve all of the same fields as the charged- and neutral-current SM interactions. Their impact will be to induce corrections to observables such as neutrino oscillations and beta decay. As outlined in Ref. [301] for example, the scalar and tensor charged-current interactions alter the electron angular distribution in beta decay.

Finally, we note that the fields in the operators above have been written in the flavour basis. When computing their effect on physical observables it will be

convenient to work in the mass basis. Assuming the charged lepton and up-type quark mass matrices are diagonal in the flavour basis, one can make the rotations  $d_L = V d'_L$ ,  $d_R = \tilde{V} d'_R$  and  $v_L = U v'_L$ , where  $V$  and  $U$  are the usual CKM and PMNS mixing matrices and we have defined a new matrix  $\tilde{V}$ . However, it is always possible to redefine the  $\varepsilon$  and  $\varepsilon'$  coefficients so that  $\tilde{V}$  is the identity matrix,  $\tilde{V} = \mathbb{1}$ . The treatment of right-handed fields  $N_R$  will be examined in the next subsection.

### 2.3.3 Adding Right-Handed Neutrinos

In the previous subsections we reviewed the SMEFT and LEFT, in which only the left-handed neutrino fields  $v_L$  is present. The question of whether neutrinos are Dirac or Majorana is therefore not addressed. One may take a slightly less model-independent approach by introducing  $n_S$  SM gauge-singlet fields  $N_R$  to the theory. It is then possible to construct more operators at each dimension of the EFT. These have been studied in the literature up to operators at dim-9 in the SMEFT and dim- $\bar{9}$  in the LEFT [304–306]. For example, at dim- $\bar{3}$  in the so-called LEFT +  $N_R$  it is now possible to write

$$\mathcal{L}^{(\bar{3})} \supset -\bar{N}_R M_D v_L - \frac{1}{2} N_R^T \mathcal{C} M_R N_R + \text{h.c.}, \quad (2.93)$$

i.e. a Dirac-like mass term and a Majorana mass term for  $N_R$ . The first term can be matched to a Yukawa-like term at dim-4 in the SMEFT +  $N_R$ . This is identical to the Type-I seesaw Lagrangian in Eq. (2.60). There are therefore two important scenarios. The first is if  $U(1)_L$  is a global symmetry, forbidding the Majorana mass term in Eq. (2.93). For  $n_S = 3$ , the  $N_R$  (or  $v_R$ ) fields are then the right-handed counterparts to  $v_L$ . The second is if lepton number is not conserved; depending on the parameters of the theory, this will then generate three light active Majorana neutrinos and  $n_S$  additional states. Subtleties such as the CP phases of the sterile states can add additional complexity to the spectrum of states; for example, some sterile states can form pseudo-Dirac pairs.

Rotating from the flavour to mass basis is therefore more involved with the inclusion of  $N_R$ . In the Dirac case, one can make the rotation  $v_R = V_R^v v'_R \equiv \tilde{U} v'_R$ .

Charged-Current LEFT + $N_R$ Operators	
$ \Delta L  = 0 + \text{h.c.}$	$ \Delta L  = 2 + \text{h.c.}$
$(\bar{N}_R \gamma^\mu \ell_R)(\bar{d}_L \gamma_\mu u_L)$	$(N_R^\top \mathcal{C} \gamma^\mu \ell_L)(\bar{d}_L \gamma_\mu u_L)$
$(\bar{N}_R \gamma^\mu \ell_R)(\bar{d}_R \gamma_\mu u_R)$	$(N_R^\top \mathcal{C} \gamma^\mu \ell_L)(\bar{d}_R \gamma_\mu u_R)$
$(\bar{N}_R \ell_L)(\bar{d}_L u_R)$	$(N_R^\top \mathcal{C} \ell_R)(\bar{d}_L u_R)$
$(\bar{N}_R \ell_L)(\bar{d}_R u_L)$	$(N_R^\top \mathcal{C} \ell_R)(\bar{d}_R u_L)$
$(\bar{N}_R \sigma^{\mu\nu} \ell_L)(\bar{d}_R \sigma_{\mu\nu} u_L)$	$(N_R^\top \mathcal{C} \sigma^{\mu\nu} \ell_R)(\bar{d}_L \sigma_{\mu\nu} u_R)$

**Table 2.7:**  $|\Delta L| = 0$  (left) and  $|\Delta L| = 2$  (right) dim- $\bar{5}$  charged-current LEFT +  $N_R$  operators, of vector, scalar and tensor type. Assumes the lepton number assignment  $L(N_R) = +1$ .

Instead of absorbing  $\tilde{U}$  into the definition of the  $\epsilon$  and  $\epsilon'$  coefficients, we will keep it explicit in the following discussion. In the Majorana case, the transformation of the three left-handed fields  $v_L$  and  $n_S$  right-handed fields  $N_R$  becomes  $v_L = \Omega P_L n'$  and  $N_R = \Xi^* P_R n'$  where  $n' = (v_1 \ v_2 \ v_3 \ N_1 \ \dots)^\top$ . However, we saw in the seesaw limit that the mixings between the active and sterile neutrinos become negligible. Therefore,  $v_L \approx U_V P_L v' \approx U P_L v'$  and  $N_R \approx U_N P_R N' \equiv P_R N'$  where  $U_N = \mathbb{1}$  and  $v' = (v_1 \ v_2 \ v_3)^\top, N' = (N_1 \ N_2 \ \dots)^\top$ .

Keeping the different interpretations of  $N_R$  in mind, it is possible to write at dim- $\bar{5}$  in the LEFT +  $N_R$ ,

$$\mathcal{L}^{(\bar{5})} \supset -\bar{N}_R \mu_D \sigma_{\mu\nu} v_L F^{\mu\nu} - \frac{1}{2} N_R^\top \mathcal{C} \mu_R \sigma_{\mu\nu} N_R F^{\mu\nu} + \text{h.c.}, \quad (2.94)$$

i.e. a Dirac dipole operator between  $v_L$  and  $N_R$  and a Majorana dipole operator for  $N_R$ . The former can be matched to a dim-6 in the SMEFT +  $N_R$  and the latter a dim-5 operator. In the Dirac case the second term is forbidden while the first term describes magnetic and dipole moments of light active Dirac neutrinos. The fields can then be rotated to the mass basis to write,

$$\mathcal{L}^{(\bar{5})} \supset -\bar{v}'_R \mu'_D \sigma_{\mu\nu} v'_L F^{\mu\nu} + \text{h.c.}, \quad (2.95)$$

where  $\mu'_D = \tilde{U}^\dagger \mu_D U$ . In the Majorana case, the combination of the terms in

Neutral-Current LEFT + $N_R$ Operators	
$ \Delta L  = 0$	$ \Delta L  = 2 + \text{h.c.}$
$(\bar{N}_R \gamma^\mu N_R)(\bar{\psi}_L \gamma_\mu \psi_L)$	$(N_R^\top \mathcal{C} \gamma^\mu v_L)(\bar{\psi}_L \gamma_\mu \psi_L)$
$(\bar{N}_R \gamma^\mu N_R)(\bar{\psi}_R \gamma_\mu \psi_R)$	$(N_R^\top \mathcal{C} \gamma^\mu v_L)(\bar{\psi}_R \gamma_\mu \psi_R)$
$(\bar{N}_R v_L)(\bar{\psi}_L \psi_R) + \text{h.c.}$	$(N_R^\top \mathcal{C} N_R)(\bar{\psi}_L \psi_R)$
$(\bar{N}_R v_L)(\bar{\psi}_R \psi_L) + \text{h.c.}$	$(N_R^\top \mathcal{C} N_R)(\bar{\psi}_R \psi_L)$
$(\bar{N}_R \sigma^{\mu\nu} v_L)(\bar{\psi}_R \sigma_{\mu\nu} \psi_L) + \text{h.c.}$	$(N_R^\top \mathcal{C} \sigma^{\mu\nu} N_R)(\bar{\psi}_R \sigma_{\mu\nu} \psi_L)$

**Table 2.8:**  $|\Delta L| = 0$  (left) and  $|\Delta L| = 2$  (right) dim-6 neutral-current LEFT +  $N_R$  operators, of vector, scalar and tensor type and for fermion fields  $\psi \in \{\ell, u, d\}$ . Assumes the lepton number assignment  $L(N_R) = +1$ .

Eqs. (2.89) and (2.94) may be written as

$$\mathcal{L}^{(\bar{5})} \supset -\frac{1}{2}(n_L^\top \mathcal{C} \mu_M \sigma^{\mu\nu} n_L) F_{\mu\nu} + \text{h.c.}, \quad \mu_M = \begin{pmatrix} \mu_L & \mu_D^\top \\ \mu_D & \mu_R \end{pmatrix}. \quad (2.96)$$

Rotating the neutrino fields to the mass basis and making the assumption that the active-sterile mixings to be small gives

$$\mathcal{L}^{(\bar{5})} \supset -\frac{1}{2}\bar{n}' \sigma^{\mu\nu} (\mu_M' P_L - \mu_M'^* P_R) n' F_{\mu\nu}, \quad \mu_M' = \begin{pmatrix} U^\top \mu_L U & U^\top \mu_D^\top \\ \mu_D U & \mu_R \end{pmatrix}. \quad (2.97)$$

The antisymmetric  $N \times N$  matrix  $\mu_M'$  describes transition magnetic and electric dipole moments between the  $N = 3 + n_S$  Majorana states. In both the Dirac and Majorana cases the magnetic and electric dipole moments correspond to the real and imaginary parts of  $\mu_D'$  and  $\mu_M'$  respectively,  $\mu_{D(M)}' = \hat{\mu}_{D(M)}' - i\hat{\varepsilon}_{D(M)}'$ .

The inclusion of  $n_S$  fields  $N_R$  will also enable additional charged-current and neutral-current type interactions at dim-6 in the LEFT. The new charged- and neutral-current type interactions are shown in Tables 2.7 and Table 2.8 respectively. If the  $N_R$  (or  $v_R$ ) are simply the right-handed components of a Dirac neutrino, then the  $|\Delta L| = 2$  operators in Tables 2.7 and 2.8 must vanish and the  $|\Delta L| = 0$  operators are implicitly included in Eqs. (2.91) and (2.92). If they instead have a Majorana mass term and mix with the active neutrinos fields  $v_L$  making  $N = 3 + n_S$  Majorana states, Eqs. (2.91) and (2.92) do not encapsulate all possible interactions. One must

also write

$$\mathcal{L}_{\text{CC}}^{(\bar{6})} \supset -\frac{G_F}{\sqrt{2}} \epsilon_N (\bar{N} \Gamma \ell) (\bar{d} \Gamma' u) + \text{h.c.}, \quad (2.98)$$

$$\mathcal{L}_{\text{NC}}^{(\bar{6})} \supset -\frac{G_F}{\sqrt{2}} \epsilon'_N (\bar{N} \Gamma N) (\bar{\psi} \Gamma' \psi) - \left( \frac{G_F}{\sqrt{2}} \epsilon'_{vN} (\bar{N} \Gamma v) (\bar{\psi} \Gamma' \psi) + \text{h.c.} \right), \quad (2.99)$$

where  $\Gamma$  and  $\Gamma'$  are the same combinations of Dirac matrices in Table 2.6. Similar to Eqs. (2.91) and (2.92), the Dirac matrices pick out either the fields  $N_R$  or their complex conjugates  $N_R^c$ . The flavour basis fields can again be rotated to the mass basis using  $v_L = \Omega P_L n'$  and  $N_R = \Xi^* P_R n'$ .

In the preceding discussion we have demonstrated two possibilities for the production of sterile neutrinos (with arbitrary masses). The first is the so-called *neutrino portal*; the Yukawa-like term  $\bar{N}_R Y_v \tilde{H}^\dagger v_L$  induces a mixing between  $v_L$  and  $N_R^c$  and therefore mostly-sterile states can be produced in SM charged-current, neutral-current and Higgs boson interactions. A small active-sterile mixing implies that their production via this portal is suppressed. The second is the so-called *dipole portal*; the Lagrangian in Eq. (2.97) describes the transition magnetic moments between light mostly-active neutrinos and mostly-sterile neutrinos. Mostly-sterile neutrinos can then be produced via an upscattering process. We emphasise that, generically, the sterile states are Majorana fermions. However, particular choices for their CP phases ensure that in certain limits (such as the ISS mechanism seen in Subsection 2.2.2) the sterile states form pseudo-Dirac pairs. In this limit,  $|\Delta L| = 2$  processes are suppressed and a pseudo-Dirac pair, for small enough splitting, appears to be a single Dirac fermion.

## Chapter 3

# Lepton Number and Neutrino Oscillations

In this chapter we will examine how neutrino oscillation ( $\nu_\alpha \rightleftharpoons \nu_\beta$ ) experiments are sensitive to lepton number. More specifically, we will assess how oscillation experiments which are able to measure the charge of the outgoing lepton at the far detector are sensitive to Lepton Number Violating (LNV) neutrino non-standard interactions (NSIs). We will compare these sensitivities to those of conventional  $|\Delta L| = 2$  probes such as  $0\nu\beta\beta$  decay and rare meson decays.

Neutrino NSIs were summarised in the previous chapter; if the light active neutrinos are Majorana fermions, one can write down the effective charged-current interactions in Eq. (2.91). The SM charged-current interactions correspond the choice of Dirac matrices  $\Gamma = \gamma^\mu(1 - \gamma_5)$  and  $\Gamma' = \gamma_\mu(1 - \gamma_5)$ . However, Eq. (2.91) also includes scalar and tensor charged-currents. In addition, if the Dirac matrix for the leptonic current is right-handed, this selects the charge-conjugate of the neutrino field  $\nu_L^c = \mathcal{C}\bar{\nu}_L^\top$  and the interaction is  $|\Delta L| = 2$ .

As mentioned in Chapter 1, neutrino-antineutrino oscillations ( $\nu \rightleftharpoons \bar{\nu}$ ) were first suggested (for Majorana neutrinos) by Pontecorvo in direct analogy to  $K^0 \rightleftharpoons \bar{K}^0$  oscillations [69, 70]. With the development of the ( $V - A$ ) theory of weak interactions however, it was realised that a charged-current at the production and detection of oscillating neutrinos induces a helicity suppression of approximately  $(m_\nu/E_\nu)^2$ . For neutrinos with masses  $m_\nu \lesssim 1$  eV and typical reactor or accelerator energies

$E_\nu \sim 1 \text{ MeV} - 1 \text{ GeV}$  (ultrarelativistic neutrinos) this factor is highly suppressed.

This can be explained as follows; Majorana neutrinos and antineutrinos are by definition equivalent ( $\nu = \nu^c$ ). As a result, what we label as a ‘neutrino’ and an ‘antineutrino’ in the Majorana case is a neutrino with negative or positive helicity respectively. The  $(V - A)$  charged-current interaction at the production process yields an admixture of negative and positive helicity neutrinos; the positive helicity component with a suppressed amplitude  $(m_\nu/E_\nu)$ . Helicity is a conserved quantum number and therefore the same admixture of helicities is present at the detection process. The  $(V - A)$  charged-current at detection now proceeds with a suppressed amplitude  $(m_\nu/E_\nu)$  for the negative helicity neutrinos but not for positive helicity neutrinos. The overall amplitude squared, needed to compute the  $\nu \leftrightarrows \bar{\nu}$  oscillation probability, is thus proportional to the square of this suppression factor. The term ‘helicity-flip’ has often been used in the literature to describe this scenario. We stress however that the helicities of oscillating neutrinos remain constant and the suppression is induced entirely by the interactions at production and detection.

In this chapter we explore the consequences of replacing either the production or detection interaction with a charged-current neutrino NSI; namely, one that has a right-handed combination of Dirac matrices in the leptonic current. We assume that the light active neutrinos are Majorana fermions, and hence the overall production, oscillation and detection process is now  $|\Delta L| = 2$ . For example, if the neutrino is produced by the decay of a pion as  $\pi \rightarrow \ell^+ \nu$ , it can undergo oscillations and induce the process  $\bar{\nu} + p \rightarrow \ell^+ + n$  (if a right-handed neutrino NSI is present at detection). Measuring the charge of the outgoing lepton at detection, this appears to be the oscillation process  $\nu \leftrightarrows \bar{\nu}$ . Now, instead of being suppressed by the helicity-flip factor squared  $(m_\nu/E_\nu)^2$ , the process is suppressed by the non-standard coefficient squared,  $|\tilde{\epsilon}|^2$ . We will see that oscillations provide a unique way of probing the  $\epsilon$  coefficients, and in particular, their flavour structure.

Much of the literature has so far only considered the effect of  $|\Delta L| = 0$  charged-current neutrino NSIs on neutrino oscillations. This is usually justified; oscillation experiments are often only concerned with the neutrino *flavour* at production and

detection, inferring the process  $\nu_\alpha \leftrightarrows \nu_\beta$  (or  $\bar{\nu}_\alpha \leftrightarrows \bar{\nu}_\beta$ ) from the accompanying charged lepton  $\ell_\alpha^+$  ( $\ell_\alpha^-$ ) at production and  $\ell_\beta^-$  ( $\ell_\beta^+$ ) at detection. There is often no detector at the neutrino source to identify the initial composition of flavours; this and the associated energy spectrum must be inferred from separate measurements and Monte Carlo simulations [307–309]. Also, it is usually not possible to determine the charge of the outgoing lepton  $\ell_\beta^\pm$  at the far detector (and therefore to discern an incoming neutrino or antineutrino). A sensitivity to charge (and therefore lepton number) is not a priority for oscillation experiments because, as we have discussed,  $\nu_\alpha \leftrightarrows \bar{\nu}_\beta$  is heavily suppressed in the SM. However, this suppression can be an advantage; if an experiment sees an excess of *wrong*-signed charged leptons at the far detector, this would strongly imply NP. The long-baseline (LBL) accelerator experiment MINOS and the LBL reactor/solar oscillation experiment KamLAND *were* able to distinguish outgoing leptonic charge, so they will be the focus of this chapter.

We begin this chapter by reviewing the derivation of neutrino oscillations in Quantum Mechanics (QM) and Quantum Field Theory (QFT). Using the latter (more rigorous) formalism, we will study the  $|\Delta L| = 2$   $\nu_\alpha \leftrightarrows \bar{\nu}_\beta$  oscillation process for Majorana neutrinos in the SM, obtaining the anticipated  $(m_\nu/E_\nu)^2$  suppression of the total rate. Furthermore, we show that the total rate cannot be factorised into a production rate, oscillation probability and detection cross section as is commonly done for  $\nu_\alpha \leftrightarrows \nu_\beta$  oscillations. In Section 3.2 we will consider the impact of  $|\Delta L| = 2$  charged-current neutrino NSIs (rather than the well-studied  $|\Delta L| = 0$  NSI) on neutrino oscillations. We will show that the total rate is no longer helicity-suppressed and can be factorised. We then write down a general expression for the non-standard oscillation probability and a simplified expression in the two-neutrino (2ν) mixing approximation, specifically for the  $(\nu_\mu, \nu_\tau)$  sector. In Section 3.3, this allows us to use a limit from the MINOS experiment on the  $\nu_\mu \rightarrow \bar{\nu}_\mu$  appearance process to place bounds on the simplified 2ν parameter space. We then generalise to the complete three-neutrino (3ν) mixing scheme, re-evaluating the constraints from MINOS and also using those from the KamLAND experiment. We compare

these constraints to those from microscopic  $|\Delta L| = 2$  processes such as  $0\nu\beta\beta$  decay,  $\mu^- - e^+$  conversion in nuclei and radiative neutrino masses in Section 3.4, putting particular emphasis on the different flavour structures being probed. Finally, we review the results and briefly outline the potential for future oscillation experiments to improve on these bounds. This chapter is based on the work of Ref. [141].

## 3.1 Theory of Neutrino Oscillations

### 3.1.1 Quantum Mechanics

A quantum description of neutrino oscillations  $\nu_\alpha \rightleftharpoons \nu_\beta$  was first developed using the plane wave approximation of QM [310–312]. We will now briefly summarise the derivation of the oscillation probability  $P_{\nu_\alpha \rightarrow \nu_\beta}$  in this framework.

The origin of neutrino oscillation lies in the mismatch between the kinetic and charged-current interaction terms in the SM Lagrangian,

$$\mathcal{L}_{\text{SM}} \supset \left( \frac{1}{2} \right) \bar{\nu}_{iL}' (i\cancel{d} - m_i) \nu_{iL}' - \frac{g}{\sqrt{2}} \left( \bar{\nu}_{\alpha L} \cancel{W}_\mu^+ \ell_{\alpha L} + \text{h.c.} \right), \quad (3.1)$$

The kinetic term is diagonal in the mass basis of fields (labelled by the index  $i$ ) while the interaction term is diagonal in the flavour basis, i.e. in which the neutrino and associated charged lepton have the same flavour (labelled by the index  $\alpha$ ).

The Lagrangian in Eq. (3.1) is valid for both Dirac and Majorana neutrinos (up to a factor of  $\frac{1}{2}$  in front of the Majorana kinetic and mass term). For Dirac neutrinos, the SM charged-current interaction term shown explicitly in Eq. (3.1) creates negative helicity neutrinos  $|\nu(q, -)\rangle$  and annihilates positive helicity antineutrinos  $|\bar{\nu}(q, +)\rangle$ . The creation and annihilation of the other two degrees of freedom, i.e.  $|\nu(q, +)\rangle$  and  $|\bar{\nu}(q, -)\rangle$ , are suppressed by  $\sim (m_\nu/E_\nu)$  at the amplitude level [313]. For the hermitian conjugate of the charged-current term shown, the suppression is reversed. For Majorana neutrinos,  $|\bar{\nu}(q, +)\rangle$  is equivalent to  $|\nu(q, +)\rangle$ . Therefore, the creation of the *wrong*-helicity degrees of freedom by the explicit charged-current term in Eq. (3.1) is suppressed by  $\sim (m_\nu/E_\nu)$  in the Majorana case.

The kinetic and mass terms in Eq. (3.1) describes the propagation of neutrino

states with *definite masses* and therefore well-defined energy-momentum dispersion relations. On the other hand, the neutrino states produced by charged-currents interactions have *definite flavours*. From the diagonalisation of the neutrino mass matrix in the previous chapter, we know that the flavour basis fields are related those in the mass basis by a unitary rotation (in the basis where the charged lepton flavours have definite masses). This is a rotation by the PMNS mixing matrix  $U$ , i.e.

$$v_\alpha(x) = \sum_i U_{\alpha i} v'_i(x). \quad (3.2)$$

Thus, charged-current interactions produce a coherent superposition of neutrino mass eigenstates, which then go on to propagate as physical states. The time and space evolution of the massive states is naively governed by the time-dependent Schrödinger equation, resulting in the flavour composition from time  $t_0$  to  $t$

$$|v_\alpha(t)\rangle = \sum_i U_{\alpha i}^* e^{-iE_{\mathbf{q}}t} |v'_i(t_0)\rangle = \sum_i \sum_\beta U_{\alpha i}^* e^{-iE_{\mathbf{q}}t} U_{\beta i} |v_\beta(t_0)\rangle, \quad (3.3)$$

where  $E_{\mathbf{q}} = \sqrt{|\mathbf{q}|^2 + m_i^2} \approx |\mathbf{q}| + \frac{m_i^2}{2|\mathbf{q}|}$  is the energy of each ultrarelativistic massive neutrino with mass  $m_i$  and three-momentum  $\mathbf{q}$ , which is assumed to be equal for the different mass eigenstates. States with definite momentum are not localised in space and are therefore characterised by *plane-wave* wavefunctions.

An oscillation probability can now be derived by evaluating the square of the *overlap* between the time-evolved initial flavour state  $|v_\alpha(T)\rangle$  and an arbitrary final flavour state  $|v_\beta\rangle$ ,

$$\begin{aligned} P_{v_\alpha \rightarrow v_\beta}(L, E_{\mathbf{q}}) &= |\langle v_\beta | v_\alpha(T) \rangle|^2 = \left| \sum_i U_{\alpha i}^* U_{\beta i} e^{-iE_{\mathbf{q}}L} \right|^2 \\ &= \sum_i |U_{\alpha i}|^2 |U_{\beta i}|^2 + 2\Re \sum_{i>j} U_{\alpha i}^* U_{\beta i} U_{\alpha j} U_{\beta j}^* e^{-i\frac{\Delta m_{ij}^2}{2E_{\mathbf{q}}}L}, \end{aligned} \quad (3.4)$$

where  $\Delta m_{ij}^2 = m_i^2 - m_j^2$  and we have approximated  $T \simeq L$  (with  $L$  the oscillation baseline). Expanding the absolute square gives a sum over two mass eigenstate indices  $i$  and  $j$ ; the second line splits this into two sums, one with  $i = j$  and the

other  $i > j$  (which must be made real and be multiplied by a factor of two to include  $i < j$  terms). The oscillation probability in Eq. (3.4) can be brought into a more convenient form if we take advantage of the unitarity of  $U$ , i.e.

$$\begin{aligned} U^\dagger U = \mathbb{1} \quad \Rightarrow \quad \sum_i U_{\alpha i}^* U_{\beta i} &= \delta_{\alpha \beta} \\ \Rightarrow \quad \sum_i |U_{\alpha i}|^2 |U_{\beta i}|^2 &= \delta_{\alpha \beta} - 2 \sum_{i>j} \Re[U_{\alpha i}^* U_{\beta i} U_{\alpha j} U_{\beta j}^*]. \end{aligned} \quad (3.5)$$

Plugging this result for  $\sum_i |U_{\alpha i}|^2 |U_{\beta i}|^2$  into Eq. (3.4) and expanding out the real and imaginary parts of the second term (and retaining only the real parts) gives

$$\begin{aligned} P_{\nu_\alpha \rightarrow \nu_\beta}(L, E_{\mathbf{q}}) &= \delta_{\alpha \beta} - 4 \sum_{i>j} \Re[U_{\alpha i}^* U_{\beta i} U_{\alpha j} U_{\beta j}^*] \sin^2 \left( \frac{\Delta m_{ij}^2}{2E_{\mathbf{q}}} L \right) \\ &\quad + 2 \sum_{i>j} \Im[U_{\alpha i}^* U_{\beta i} U_{\alpha j} U_{\beta j}^*] \sin \left( \frac{\Delta m_{ij}^2}{2E_{\mathbf{q}}} L \right), \end{aligned} \quad (3.6)$$

which shows the deviation of the oscillation probability  $\nu_\alpha \rightleftharpoons \nu_\beta$  from unity (for  $\alpha = \beta$ ) or zero (for  $\alpha \neq \beta$ ). The real part of the product of PMNS mixing matrix elements  $\Re[U_{\alpha i}^* U_{\beta i} U_{\alpha j} U_{\beta j}^*]$  will depend on the mixing angles  $\theta_{12}$ ,  $\theta_{13}$  and  $\theta_{23}$ , but not a possible CP violating Dirac phase  $\delta_{\text{CP}}$  (which is present for both Dirac and Majorana neutrinos). Conversely, the imaginary part is sensitive to  $\delta_{\text{CP}}$ , and in a similar manner to the CKM mixing matrix is proportional (up to a sign) to a Jarlskog invariant,

$$J \sum_{\gamma, k} \epsilon_{\alpha \beta \gamma} \epsilon_{i j k} = \Im \left[ U_{\alpha i}^* U_{\beta i} U_{\alpha j} U_{\beta j}^* \right], \quad (3.7)$$

where for the standard  $U$  parametrisation,  $J = s_{12} s_{13} s_{23} c_{12} c_{13}^2 c_{23} \sin \delta_{\text{CP}}$ . The sign in front of the imaginary part in Eq. (3.6) is opposite for antineutrino oscillations, and therefore the difference between neutrino and antineutrino oscillations has been the key observable for determining the size of CP violation in the lepton sector.

This canonical derivation was the first attempt in the literature to understand neutrino oscillations as a purely quantum phenomenon. The approach however

is reliant on a number of unphysical assumptions, namely the use of plane-wave states. The assumption that the propagating  $|v'_i(t)\rangle$  eigenstates are plane waves of equal momenta  $\mathbf{q}$  forces the external particles at production (e.g. a decaying pion and an outgoing charged lepton) to have definite energies and momenta. Energy-momentum conservation at production is then in tension with the creation of three  $|v'_i(t_0)\rangle$  states with different energies  $E_{\mathbf{q}} = \sqrt{|\mathbf{q}|^2 + m_i^2}$  [314]. It is possible to derive Eq. (3.4) without the equal momentum assumption, but an overall uncertainty in the energy and momentum of the neutrino mass eigenstates is still a necessary component for oscillations [315, 316].

A rigorous treatment of neutrino oscillations in QM must therefore describe the  $|v'_i(t)\rangle$  states with *wave packets* [317–319]. While this introduces an uncertainty in the neutrino momenta, their position in space becomes more localised. As in Eq. (3.4), the oscillation probability is proportional to the overlap of the wave packets. The loss of coherence seen at long distance in oscillation experiments is now qualitatively ascribed to the dispersion of the wave packets, which propagate at different group velocities  $\mathbf{v} = \frac{\partial E_{\mathbf{q}}}{\partial \mathbf{q}}|_{\mathbf{q}=\mathbf{Q}}$  (where  $\mathbf{Q}$  the mean momentum) [320–323].

There are still fundamental issues with the QM derivation after the conceptual improvements of the wave packet treatment. Firstly, the neutrino wave packets are an *ad-hoc* addition to the framework, and their specific shape is arbitrary. Secondly, an uncertainty in both the energy and momentum of the propagating neutrino mass eigenstates requires the localisation in space and time of the production/detection processes [322]. Finally, the QM approach does not consider possible entanglement between the outgoing  $\nu$  and  $\ell^{\pm}$  at the production process [324].

### 3.1.2 Quantum Field Theory

A more consistent framework for characterising neutrino oscillations is the external wave packet model [325]. In this formalism the entire production, propagation and detection process can be described by a macroscopic Feynman diagram, as shown in Fig. 3.1 (left). The external interacting particles (for example, pions, charged leptons and nucleons in the detector) are wave packets centred on the production and detection points  $x_P$  and  $x_D$  respectively, while the intermediate neutrinos are

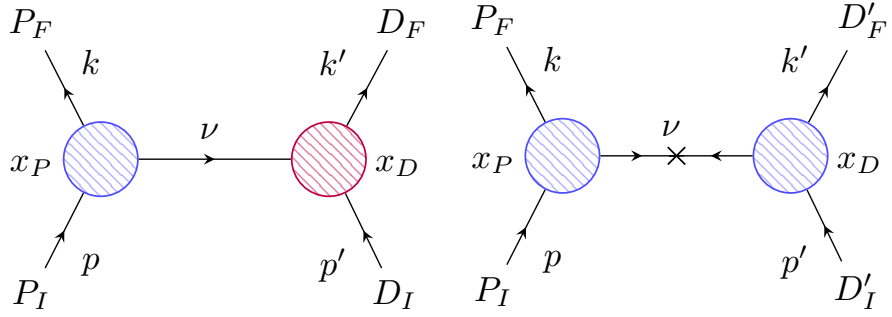


**Figure 3.1:** Feynman diagrams depicting the  $\nu_\alpha \rightleftarrows \nu_\beta$  (left) and  $\nu_\alpha \rightleftarrows \bar{\nu}_\beta$  (right) oscillation processes. The latter requires a helicity-flip if SM charged-currents are at the interaction vertices.

described by an internal propagator. The neutrino wave packets used to describe the propagating neutrinos in the QM approach can be derived from the external particle wave packets in QFT. In the QFT approach, however, the coherence conditions at each stage in the process are explicit [323, 326, 327]. For example, the energy and momentum uncertainties required for the process to produce a coherent superposition of massive neutrinos are well specified. The shapes of the external wave packets are still technically *ad-hoc*, but their form is not important for the following discussion.

To calculate the oscillation probability  $P_{\nu_\alpha \rightarrow \nu_\beta}$  in QFT it is first necessary to determine the overall rate. To do this, one constructs the time-ordered *S*-matrix element (at first order in the Fermi coupling  $G_F$ ),

$$i\mathcal{A}_{\nu_\alpha \rightarrow \nu_\beta}(T, \mathbf{L}) = \langle P_F, D_F | \hat{T} \left\{ \int d^4 x_1 \int d^4 x_2 \mathcal{O}_P(x_1) \mathcal{O}_D(x_2) \right\} | P_I, D_I \rangle, \quad (3.8)$$

where  $P_I, D_I, P_F$  and  $D_F$  represent the initial and final state particles at production and detection, respectively, and  $x_1$  and  $x_2$  are space-time points in the vicinity of  $x_P$  and  $x_D$ . This tree-level process is depicted in Fig. 3.1 (left). The external asymptotic states  $\psi \in \{P_I, D_I, P_F, D_F\}$  are described by the wave packets

$$|\psi\rangle = \int [d\mathbf{p}] f_{\mathbf{P}_\psi}^{(\psi)}(\mathbf{p}) |\psi(p)\rangle; \quad [d\mathbf{p}] = \frac{d^3 \mathbf{p}}{(2\pi)^3 \sqrt{2E}}, \quad (3.9)$$

where  $f_{\mathbf{P}_\psi}^{(\psi)}(\mathbf{p})$  is the momentum distribution function of the external particle  $\psi$

with mean momentum  $\mathbf{P}_\psi$ . In order to create and annihilate an internal neutrino, the production and detection terms must take the general form

$$\mathcal{O}_P(x) = \sum_i U_{\alpha i}^* \bar{v}'_i(x) \tilde{\mathcal{O}}_P(x), \quad \mathcal{O}_D(x) = \sum_i \tilde{\mathcal{O}}_D(x) U_{\beta i} v'_i(x), \quad (3.10)$$

where  $\tilde{\mathcal{O}}_P(x)$  and  $\tilde{\mathcal{O}}_D(x)$  are the *reduced* production and detection interaction terms with the neutrino fields and PMNS matrix elements removed. Note that in order to produce and annihilate a (Dirac or Majorana) neutrino, the SM charged-current and its hermitian conjugate are needed at production and detection respectively. Thus, opposite sign charged leptons are produced at production and detection.

The total rate for the combined production, oscillation and detection process can now be computed by taking the spin average of the  $S$ -matrix element squared (i.e. averaging over the incoming particle spins and summing over the outgoing particle spins),  $\Gamma_{v_\alpha \rightarrow v_\beta}^{\text{tot}} \propto \langle |\mathcal{A}_{v_\alpha \rightarrow v_\beta}(T, \mathbf{L})|^2 \rangle$ . This can be expanded as

$$\begin{aligned} \langle |\mathcal{A}_{v_\alpha \rightarrow v_\beta}|^2 \rangle &= \text{Tr} \left| \sum_i U_{\alpha i}^* U_{\beta i} \mathcal{A}_i \right|^2 \\ &= \sum_i |U_{\alpha i}|^2 |U_{\beta i}|^2 \text{Tr} |\mathcal{A}_i|^2 + 2\Re \sum_{i>j} U_{\alpha i}^* U_{\beta i} U_{\alpha j} U_{\beta j}^* \text{Tr} [\mathcal{A}_i \mathcal{A}_j^\dagger], \end{aligned} \quad (3.11)$$

where  $\text{Tr}$  denotes the Dirac trace. The  $\mathcal{A}_i$  factors are defined as

$$\mathcal{A}_i = \int \frac{d^4 q}{(2\pi)^4} \tilde{\Phi}_D(q) \frac{(\not{q} + m_i)}{q^2 - m_i^2 + i\epsilon} \tilde{\Phi}_P(q) e^{-iq \cdot (x_D - x_P)}, \quad (3.12)$$

where  $\tilde{\Phi}_P$  and  $\tilde{\Phi}_D$  are integrals quantifying the *overlap* of external wave packets at production and detection respectively, explicitly written as

$$\tilde{\Phi}_P(q) = \int d^4 x'_1 e^{iq \cdot x'_1} \int [d\mathbf{p}][d\mathbf{k}] f_{\mathbf{p}}^{(P_I)}(\mathbf{p}) f_{\mathbf{k}}^{(P_F)*}(\mathbf{k}) e^{-i(p-k) \cdot x'_1} \tilde{\mathcal{M}}_P, \quad (3.13)$$

$$\tilde{\Phi}_D(q) = \int d^4 x'_2 e^{-iq \cdot x'_2} \int [d\mathbf{p}'][d\mathbf{k}'] f_{\mathbf{p}'}^{(D_I)}(\mathbf{p}') f_{\mathbf{k}'}^{(D_F)*}(\mathbf{k}') e^{-i(p'-k') \cdot x'_2} \tilde{\mathcal{M}}_D, \quad (3.14)$$

where  $x'_1 = x_1 - x_P$ ,  $x'_2 = x_2 - x_D$  and  $\tilde{\mathcal{M}}_P$ ,  $\tilde{\mathcal{M}}_D$  are *reduced* matrix elements defined as  $\tilde{\mathcal{M}}_P = \langle P_F, \mathbf{k} | \tilde{\mathcal{O}}_P(x_1) | P_I, \mathbf{p} \rangle$  and  $\tilde{\mathcal{M}}_D = \langle D_F, \mathbf{k}' | \tilde{\mathcal{O}}_D(x_2) | D_I, \mathbf{p}' \rangle$ . The trace

appearing in the interference term of Eq. (3.11) is then

$$\begin{aligned} \text{Tr}[\mathcal{A}_i \mathcal{A}_j^\dagger] &= \int \frac{d^4 q}{(2\pi)^4} \int \frac{d^4 q'}{(2\pi)^4} \frac{e^{-i(q-q') \cdot (x_D - x_P)}}{(q^2 - m_i^2 + i\epsilon)(q'^2 - m_j^2 + i\epsilon)} \\ &\quad \times \text{Tr}[\bar{\tilde{\Phi}}_D \tilde{\Phi}_D(q + m_i) \tilde{\Phi}_P \bar{\tilde{\Phi}}_P(q' + m_j)], \end{aligned} \quad (3.15)$$

where  $\bar{\tilde{\Phi}}_{P,D} = \tilde{\Phi}_{P,D}^\dagger \gamma^0$ . To proceed, we now evaluate the  $d^3 \mathbf{q}$  integrals of the above expression in the limit  $L \rightarrow \infty$  [328]. If  $\psi(\mathbf{q})$  is a twice differentiable function, for large  $L = |\mathbf{L}|$  and  $A_i > 0$ , we have

$$\int \frac{d^3 \mathbf{q}}{(2\pi)^3} \frac{\psi(\mathbf{q}) e^{i\mathbf{q} \cdot \mathbf{L}}}{A_i - \mathbf{q}^2 + i\epsilon} = -\frac{1}{4\pi L} \psi\left(\sqrt{A_i} \frac{\mathbf{L}}{L}\right) e^{i\sqrt{A_i} L} + \mathcal{O}\left((\sqrt{A_i} L)^{-\frac{3}{2}}\right). \quad (3.16)$$

For  $A_i < 0$  the integral falls off as  $L^{-2}$  and can be neglected. Applying Eq. (3.16) to Eq. (3.15) with  $A_i = E_{\mathbf{q}}^2 - m_i^2$  gives

$$\begin{aligned} \text{Tr}[\mathcal{A}_i \mathcal{A}_j^\dagger] &= \frac{1}{64\pi^4 L^2} \int dE_{\mathbf{q}} \int dE'_{\mathbf{q}} e^{i(|\mathbf{q}_i| - |\mathbf{q}_j|)L} \\ &\quad \times \text{Tr}[\bar{\tilde{\Phi}}_{jD} \tilde{\Phi}_{iD}(q_i + m_i) \tilde{\Phi}_{iP} \bar{\tilde{\Phi}}_{jP}(q_j + m_j)], \end{aligned} \quad (3.17)$$

which has effectively set the virtual neutrinos to be on their mass shell. As has been elaborated before in the literature [329, 330], if the production and detection processes are of the same chirality (e.g. both are left-handed SM charged-current interactions), the trace in Eq. (3.17) can be factorised in the ultrarelativistic limit ( $m_i \approx 0$ ) into  $\text{Tr}[\tilde{\Phi}_{iD}(q_i + m_i) \bar{\tilde{\Phi}}_{jD}] \text{Tr}[\bar{\tilde{\Phi}}_{jP}(q_j + m_j) \tilde{\Phi}_{iP}]$ . For each of these factors (one corresponding to production, the other detection),  $(q + m_i)$  can be written as the spinor sum  $\sum_{h=\pm} u_i(q, h) \bar{u}_i(q, h)$ . Then, taking the chirality projectors out of the overlap integrals on each side of the spinor sum gives

$$\begin{aligned} P_L(q + m_i) P_R &= u_{iL}(q, -) \bar{u}_{iL}(q, -) + u_{iL}(q, +) \bar{u}_{iL}(q, +) \\ &= (q^0 + |\mathbf{q}|) \begin{pmatrix} 0 & 0 & 0 & 0 \\ 0 & 0 & 0 & 1 \\ 0 & 0 & 0 & 0 \\ 0 & 0 & 0 & 0 \end{pmatrix} + (q^0 - |\mathbf{q}|) \begin{pmatrix} 0 & 0 & 1 & 0 \\ 0 & 0 & 0 & 0 \\ 0 & 0 & 0 & 0 \\ 0 & 0 & 0 & 0 \end{pmatrix}. \end{aligned} \quad (3.18)$$

Expanding  $|\mathbf{q}| = \sqrt{E_{\mathbf{q}}^2 - m_i^2}$  for the small neutrino masses  $m_i$  gives for the different

combinations of energy and momentum in Eq. (3.18),

$$(q^0 + |\mathbf{q}|) \approx 2E_{\mathbf{q}} \left\{ 1 - \left( \frac{m_i}{2E_{\mathbf{q}}} \right)^2 \right\}, \quad (q^0 - |\mathbf{q}|) \approx 2E_{\mathbf{q}} \left( \frac{m_i}{2E_{\mathbf{q}}} \right)^2. \quad (3.19)$$

We therefore see that for  $\nu_{\alpha} \leftrightarrows \nu_{\beta}$ , the propagation of positive helicity neutrinos (the second term in Eq. (3.18)) is doubly suppressed by  $(m_i/2E_{\mathbf{q}})^2$  compared to the propagation of negative helicity neutrinos (the first term in Eq. (3.18)).

Neglecting the positive helicity neutrino contribution to the spinor sum in Eq. (3.18), i.e.  $P_L(\not{q} + m_i)P_R \approx u_{iL}(q, -)\bar{u}_{iL}(q, -)$ , we now absorb the negative helicity spinors into the overlap integrals on each side of  $\text{Tr}[\bar{\Phi}_{jP}(q_j + m_j)\tilde{\Phi}_{iP}]$  as

$$\Phi_P^* \equiv \bar{\Phi}_{jP} \frac{u_{jL}(q, -)}{\sqrt{2E_{\mathbf{q}}}}, \quad \Phi_P \equiv \frac{\bar{u}_{jL}(q, -)}{\sqrt{2E_{\mathbf{q}}}} \tilde{\Phi}_{iP}, \quad (3.20)$$

where we have normalised the spinors by the factor  $\sqrt{2E_{\mathbf{q}}}$  so that the resulting ratio is dimensionless. In Eq. (3.20) the mass indices have also been neglected, which is a suitable approximation in the ultrarelativistic limit [323]. After these simplifications the trace appearing in the interference term Eq. (3.17), can now be expressed as

$$\text{Tr}[\mathcal{A}_j^{\dagger}\mathcal{A}_i] = \frac{1}{64\pi^4 L^2} \int dE_{\mathbf{q}} \int dE'_{\mathbf{q}} 4E_{\mathbf{q}} E'_{\mathbf{q}} \langle |\Phi_P|^2 \rangle e^{i(|\mathbf{q}_i| - |\mathbf{q}_j|)L} \langle |\Phi_D|^2 \rangle, \quad (3.21)$$

where  $\langle |\Phi_P|^2 \rangle = \text{Tr}[\Phi_P^* \Phi_P]$  and  $\langle |\Phi_D|^2 \rangle = \text{Tr}[\Phi_D \Phi_D^*]$ . From Eq. (3.21) it can be seen that the contributions from the production, propagation and detection processes have factorised at the squared amplitude level. It is now a straightforward step to show that the total rate for the  $\nu_{\alpha} \leftrightarrows \nu_{\beta}$  process is related to the differential production flux, oscillation probability and detection cross section as

$$\Gamma_{\nu_{\alpha} \rightarrow \nu_{\beta}}^{\text{tot}}(L, E_{\mathbf{q}}) = \frac{1}{4\pi L^2} \int dE_{\mathbf{q}} \frac{d\Gamma_{\nu_{\alpha}}^{\text{prod}}(E_{\mathbf{q}})}{dE_{\mathbf{q}}} \cdot P_{\nu_{\alpha} \rightarrow \nu_{\beta}}(L, E_{\mathbf{q}}) \cdot \sigma_{\nu_{\beta}}^{\text{det}}(E_{\mathbf{q}}), \quad (3.22)$$

where we have neglected experimental parameters such as the detection efficiency and fiducial volume [331].

The final aim of this QFT approach is to derive an expression for the oscil-

lation probability  $P_{\nu_\alpha \rightarrow \nu_\beta}$ ; this can now be isolated by rearranging Eq. (3.22). As demonstrated in Ref. [323], when the flux of incoming neutrinos is continuous the differential production flux and detection cross section take the forms

$$\frac{d\Gamma_{\nu_\alpha}^{\text{prod}}}{dE_{\mathbf{q}}} \propto \sum_i |U_{\alpha i}|^2 \langle |\Phi_P|^2 \rangle E_{\mathbf{q}} |\mathbf{q}_i|, \quad \sigma_{\nu_\beta}^{\text{det}} \propto \sum_j |U_{\beta j}|^2 \langle |\Phi_D|^2 \rangle E_{\mathbf{q}} |\mathbf{q}_j|^{-1}. \quad (3.23)$$

Making use of the fact that  $\langle |\Phi_P|^2 \rangle$  and  $\langle |\Phi_D|^2 \rangle$  are independent of the mass  $m_i$ , while also taking  $|\mathbf{q}_i| \approx |\mathbf{q}_j|$  in the ultrarelativistic limit, any dependence that  $P_{\nu_\alpha \rightarrow \nu_\beta}$  has on the specific form of the wave packets is cancelled [323]. In this limit  $P_{\nu_\alpha \rightarrow \nu_\beta}$  is given exactly by Eq. (3.4), confirming the result of the naive QM approach. We note that the same result holds in the quasi-degenerate mass limit  $||\mathbf{q}_i| - |\mathbf{q}_j|| \ll |\mathbf{q}_i|, |\mathbf{q}_j|$ , a property of the  $K^0 - \bar{K}^0$  system for example.

We will now show that for Majorana neutrinos the  $|\Delta L| = 2$  process  $\nu_\alpha \rightleftarrows \bar{\nu}_\beta$  is possible but suppressed by the factor  $(m_i/2E_{\mathbf{q}})^2$  with respect to  $|\Delta L| = 0$  oscillations. This process is described by an amplitude like Eq. (3.8) where now the production and detection interactions are the same, i.e.

$$\mathcal{O}_P(x) = \mathcal{O}_D(x) = \sum_i U_{\alpha i}^* \bar{\nu}'_i(x) \tilde{\mathcal{O}}(x), \quad (3.24)$$

which is non-zero for Majorana neutrinos because the field  $\bar{\nu}'_i(x)$  both creates and annihilates neutrinos. The Feynman diagram for this process is depicted in Fig. 3.1 (right).

As before, this amplitude can be written as a sum of amplitudes  $\mathcal{A}_i$  and squared as in Eq. (3.11). Using the Feynman rules for a Majorana fermion in Ref. [332], the amplitudes  $\mathcal{A}_i$  are identical to Eq. (3.12) but with the overlap integral for the detection process  $\Phi_D$  replaced with  $\Phi_D^M$ . For  $\Phi_D$  the reduced matrix element is  $\tilde{\mathcal{M}}_D \propto \bar{u}_\beta(p_\beta)\Gamma$ , while for  $\Phi_D^M$  it is  $\tilde{\mathcal{M}}_D \propto \bar{u}_\beta(p_\beta)\mathcal{C}\Gamma^\top\mathcal{C}^{-1}$ , where  $i\Gamma$  is the vertex factor for the detection process. This transformation has the effect of flipping the chirality of the detection process; for left-handed SM charged-current interactions we have  $P_L \rightarrow P_R$ . Now in the trace  $\text{Tr}[\tilde{\Phi}_{iD}^M(q_i + m_i)\tilde{\Phi}_{iP}\bar{\tilde{\Phi}}_{jP}(q_j + m_j)\bar{\tilde{\Phi}}_{jD}^M]$  we have the same chiralities on either side of the  $(q + m_i)$  factors. Thus, the mass terms are

retained and the  $\not{q}$  terms vanish. To see this explicitly, we again write the  $(\not{q} + m_i)$  as the spinor sum  $\sum_{h=\pm} u_i(q, h) \bar{u}_i(q, h)$ . Then extracting the chirality projectors from the overlap integrals and placing them on either side,

$$\begin{aligned} P_R(\not{q}_i + m_i) P_R &= u_{iR}(q, -) \bar{u}_{iL}(q, -) + u_{iR}(q, +) \bar{u}_{iL}(q, +) \\ &= 2E_{\mathbf{q}} \left( \frac{m_i}{2E_{\mathbf{q}}} \right) \begin{pmatrix} 0 & 0 & 0 & 0 \\ 0 & 0 & 0 & 0 \\ 0 & 0 & 0 & 0 \\ 0 & 0 & 0 & 1 \end{pmatrix} + 2E_{\mathbf{q}} \left( \frac{m_i}{2E_{\mathbf{q}}} \right) \begin{pmatrix} 0 & 0 & 0 & 0 \\ 0 & 0 & 0 & 0 \\ 0 & 0 & 1 & 0 \\ 0 & 0 & 0 & 0 \end{pmatrix} \end{aligned} \quad (3.25)$$

where we have normalised with respect to  $2E_{\mathbf{q}}$  to compare to Eq. (3.19). The propagation of negative and positive helicity neutrinos in  $|\Delta L| = 2$  oscillations are therefore singly suppressed by  $(m_i/2E_{\mathbf{q}})^2$  with respect to the propagation of negative helicity neutrinos in  $|\Delta L| = 0$  oscillations [333–335].

Because the trace is proportional to the neutrino masses, it must vanish in the ultrarelativistic limit instead of factorising into components corresponding to the production, oscillation, and detection processes. Technically, it is therefore not impossible to define an oscillation probability if a ‘helicity-flip’ is the dominant mechanism contributing to  $\nu_{\alpha} \rightleftharpoons \bar{\nu}_{\beta}$ , only a rate for the entire process [329].

## 3.2 Neutrino Oscillations with LNV Neutrino NSIs

We will now consider the presence of interactions at production and detection which are different from the usual SM charged-current interaction. Charged- and neutral-current type neutrino NSIs (reviewed in Chapter 2) which conserve lepton number, but introduce a new source of lepton flavour violation (LFV), have been long been studied in the literature [295, 296, 299]. Results from LBL accelerator experiments such as MINOS, NOvA and T2K and short-baseline (SBL) reactor experiments such as Daya Bay, RENO and Double Chooz have have been used to probe the flavour structure of the  $\epsilon$  coefficients controlling the magnitude of the NSIs [297, 336–341]. The sensitivities of next-generation experiments such as DUNE, Hyper-Kamiokande and JUNO have also been explored [342–353]. Only the flavours of the outgoing charged leptons at production and detection are required for these constraints to be made; their charge is irrelevant for these analyses.

However, if an experiment is sensitive to the signs of the outgoing charged

leptons  $\ell_\alpha^\pm$  and  $\ell_\beta^\pm$  at production and detection, it could in principle be sensitive to lepton number. This has in fact been possible in the past; a magnetised far detector was used by the MINOS experiment to determine charges from the curvature of tracks in the steel scintillator near and far detectors. In addition, the KamLAND experiment used the prompt energy deposit from an outgoing  $\ell_\beta^+$  (and a coincident neutron capture on hydrogen) as a distinct signal from the  $\ell_\beta^-$  case [354]. The non-observation of an excess of *wrong*-signed charged leptons by these experiments is in line with the highly-suppressed Majorana neutrino oscillation  $\nu_\alpha \rightleftharpoons \bar{\nu}_\beta$ . In this section, we will explore how the presence of a  $|\Delta L| = 2$  neutrino NSI at production or detection will induce an altered oscillation probability, and use the null results of MINOS and KamLAND to place constraints on the associated  $\varepsilon$  coefficients.

In this chapter we will adopt the following notation for the charged-current type neutrino NSIs (introduced in Eq. (2.91))

$$\mathcal{L}_{\text{CC}}^{(6)} = -\frac{4G_F V_{ud}}{\sqrt{2}} \left\{ j_L J_L^\dagger + \sum_{\circ} \sum_{X,Y} \varepsilon_{XY}^\circ j_X^\circ J_Y^{\circ\dagger} \right\} + \text{h.c.}, \quad (3.26)$$

i.e., separating the left-handed SM charged-current term with the leptonic and hadronic currents  $j_L = \bar{\ell}_\alpha \gamma^\mu P_L \nu_\alpha$  and  $J_L = \bar{d}' \gamma_\mu P_L u$ , respectively. We have rotated the down quark field to the mass basis, picking up the CKM mixing matrix element  $V_{ud}$ . The sum includes all possible Lorentz contractions of the leptonic current  $j_X^\circ = \bar{\ell}_\beta \Gamma^\circ P_X \nu_\alpha$  and hadronic current  $J_Y^\circ = \bar{d}' \Gamma^\circ P_Y u$ , where  $X, Y \in \{L, R\}$ ,  $\circ \in \{S, V, T\}$  and  $\Gamma^\circ \in \{\mathbb{1}, \gamma^\mu, \sigma^{\mu\nu}\}$ . These terms then run over the possible combinations of scalar, vector and tensor currents proportional to the left- and right-handed chirality projectors, i.e.  $(S \pm P)$ ,  $(V \pm A)$  and  $(T \pm \tilde{T})$ , where  $\tilde{T}$  corresponds to  $\sigma^{\mu\nu} \gamma_5 = \frac{i}{2} \varepsilon^{\mu\nu\rho\sigma} \sigma_{\rho\sigma}$ . The  $\varepsilon_{XY}^\circ$  coefficients control the strength of the charged-current neutrino NSIs with respect to  $G_F$ . For the tensor currents we must have  $X = Y$ . We note that the form of Eq. (3.26) is different from the parametrisation of Eq. (2.91) where the scalar and pseudoscalar quark currents are treated separately. We relate the two parametrisations in Appendix A.

We will now assume that the light active neutrinos are Majorana fermions. The terms with right-handed ( $X = R$ ) leptonic currents are therefore  $|\Delta L| = 2$  and those

with left-handed ( $X = L$ ) leptonic currents are  $|\Delta L| = 0$ . We can now consider the scenario where, for example, Majorana neutrinos are produced by the left-handed SM charged-current, propagate over a macroscopic distance  $L$ , and interact at the detector via a  $|\Delta L| = 2$  neutrino NSI. In the QFT framework, the total rate can again be written as the absolute square of a sum of amplitudes  $\mathcal{A}_i$ , but again we use the Feynman rules for Majorana fermions, replacing the detection overlap integral  $\Phi_D$  with  $\Phi_D^M$  (which contains the vertex factor  $\mathcal{C}\Gamma^T\mathcal{C}^{-1}$ ). Now that the chirality of the detection NSI is right-handed, the chiralities extracted from the overlap integrals on each side of the factor  $(\not{q} + m_i)$  are opposite. Analogous to the expression in Eq. (3.18), the chirality projectors retain the  $\not{q}$  term and the  $m_i$  term vanishes. In the same way, we can neglect the oscillation of positive helicity neutrinos and factorise the rate (in the ultrarelativistic limit) into production, oscillation and detection terms. Well-studied models in which right-handed currents arise are left-right symmetric theories, which has an additional broken  $SU(2)_R$  gauge symmetry [355].

We see that instead of being suppressed by the factor  $(m_i/2E_{\mathbf{q}})^2$ , the process is now accompanied by a factor  $\sim |\varepsilon|^2$ . Before moving on, we note that while we have rotated the quark fields to the mass basis in Eq. (3.26), the lepton fields are still in flavour basis. The  $\varepsilon$  coefficients are therefore defined in the flavour basis. If we rotate the neutrino fields to the mass basis using  $\nu_L = U\nu'_L$ , we can absorb the PMNS mixing matrix into  $\varepsilon_{XY}^\circ$  and define a non-standard coefficient in the mass basis  $\gamma_{XY}^\circ$ ,

$$(\varepsilon_{XY}^\circ)_{\beta\alpha} \equiv \sum_i U_{\alpha i} (\gamma_{XY}^\circ)_{\beta i}. \quad (3.27)$$

where  $\alpha$  and  $i$  are the neutrino flavour and mass indices and  $\beta$  is the charged lepton flavour index. This redefinition will be convenient in the following discussion.

We now consider a neutrino oscillation experiment which is sensitive to the charge of the outgoing charged lepton  $\ell_\beta^\pm$  at the far detector (but does not observe the outgoing charged lepton  $\ell_\alpha^\pm$  in the beam pipe). If the far detector observes a positively charged lepton  $\ell_\beta^+$ , this would imply either the standard antineutrino oscillation process  $\bar{\nu}_\alpha \rightarrow \bar{\nu}_\beta$  or the non-standard process  $\nu_\alpha \rightarrow \bar{\nu}_\beta$  (via a  $|\Delta L| = 2$

neutrino NSI). Likewise, a negatively charged lepton  $\ell_\beta^-$  would suggest either the standard  $\nu_\alpha \rightarrow \nu_\beta$  or the non-standard  $\bar{\nu}_\alpha \rightarrow \nu_\beta$  process. Despite not measuring the outgoing charged lepton at production, the initial flux of neutrinos is usually well-known. Accelerator experiments, for example, pass charged pions  $\pi^+$  through a magnetic field to select the intended charge, which then decay via  $\pi^\pm \rightarrow \overset{(-)}{\nu}_\alpha \ell_\alpha^\pm$ . A beam selected for neutrinos may still contain a small background of antineutrinos however. Comparing the number of positive to negative charged leptons in the far detector ( $N_{\ell_\beta^+}$  and  $N_{\ell_\beta^-}$ ) an experiment can ultimately infer the ratio

$$\mathcal{R}_\beta \equiv \frac{N_{\ell_\beta^+}}{N_{\ell_\beta^-}} = \sum_\alpha \frac{\Gamma_{\nu_\alpha \rightarrow \bar{\nu}_\beta} + \Gamma_{\bar{\nu}_\alpha \rightarrow \bar{\nu}_\beta}}{\Gamma_{\nu_\alpha \rightarrow \nu_\beta} + \Gamma_{\bar{\nu}_\alpha \rightarrow \nu_\beta}}. \quad (3.28)$$

If we assume that a  $|\Delta L| = 2$  neutrino NSI contributes to the total rates  $\Gamma_{\bar{\nu}_\alpha \rightarrow \nu_\beta}$  and  $\Gamma_{\nu_\alpha \rightarrow \bar{\nu}_\beta}$ , these rates are *factorisable* and  $\mathcal{R}_\beta$  can be decomposed as

$$\mathcal{R}_\beta = \sum_\alpha \sum_{\circ, Y} \frac{\int dE_{\mathbf{q}} \left( \frac{d\Gamma_{\nu_\alpha}}{dE_{\mathbf{q}}} \cdot P_{\nu_\alpha \rightarrow \bar{\nu}_\beta}^{\circ Y} \cdot \sigma_{\bar{\nu}_\beta} + \frac{d\Gamma_{\bar{\nu}_\alpha}}{dE_{\mathbf{q}}} \cdot P_{\bar{\nu}_\alpha \rightarrow \bar{\nu}_\beta}^{\circ Y} \cdot \sigma_{\bar{\nu}_\beta} \right)}{\int dE_{\mathbf{q}} \left( \frac{d\Gamma_{\nu_\alpha}}{dE_{\mathbf{q}}} \cdot P_{\nu_\alpha \rightarrow \nu_\beta}^{\circ Y} \cdot \sigma_{\nu_\beta} + \frac{d\Gamma_{\bar{\nu}_\alpha}}{dE_{\mathbf{q}}} \cdot P_{\bar{\nu}_\alpha \rightarrow \nu_\beta}^{\circ Y} \cdot \sigma_{\nu_\beta} \right)}. \quad (3.29)$$

The non-standard probabilities  $P_{\nu_\alpha \rightarrow \bar{\nu}_\beta}^{\circ Y}$  and  $P_{\bar{\nu}_\alpha \rightarrow \bar{\nu}_\beta}^{\circ Y}$  are given the superscript  $\circ Y$  to indicate that they are induced by the NSI with coefficient  $\epsilon_{RY}^\circ$ . We have assumed that the processes  $\nu_\alpha \rightarrow \nu_\beta$  and  $\bar{\nu}_\alpha \rightarrow \bar{\nu}_\beta$  are induced by SM interactions. However, the non-standard process  $\nu_\alpha \rightarrow \bar{\nu}_\beta$  reduces the number of neutrinos that undergo  $\nu_\alpha \rightarrow \nu_\beta$ . From the unitarity of the PMNS mixing matrix we have  $\sum_\beta P_{\nu_\alpha \rightarrow \nu_\beta} = 1$ , but this no longer applies. To ensure instead that the probabilities of the two processes  $\nu_\alpha \rightarrow \nu_\beta$  and  $\nu_\alpha \rightarrow \bar{\nu}_\beta$  adds to unity, we must normalise both probabilities by an appropriate factor. The corrected probabilities are

$$P_{\nu_\alpha \rightarrow \nu_\beta}^{\circ Y} = \frac{1}{\mathcal{N}_\alpha^{\circ Y}} \left| \sum_i U_{\alpha i}^* U_{\beta i} e^{-i \frac{m_i^2}{2E_{\mathbf{q}}} L} \right|^2, \quad (3.30)$$

$$P_{\nu_\alpha \rightarrow \bar{\nu}_\beta}^{\circ Y} = \frac{1}{\mathcal{N}_\alpha^{\circ Y}} \left| \sum_i U_{\alpha i}^* (\gamma_{RY}^\circ)_{\beta i} e^{-i \frac{m_i^2}{2E_{\mathbf{q}}} L} \right|^2, \quad (3.31)$$

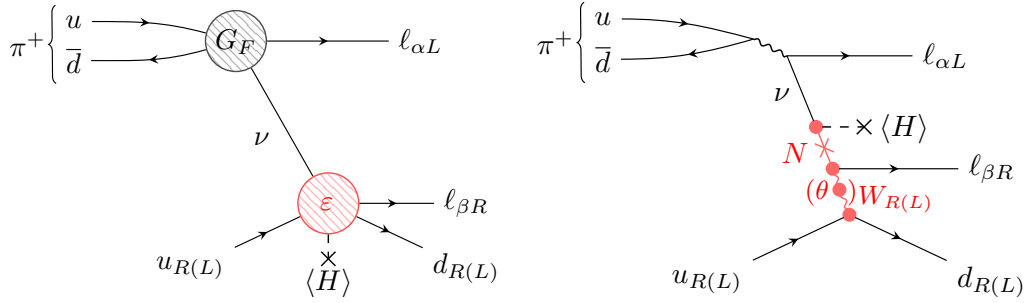


**Figure 3.2:** (Left) Feynman diagram depicting the neutrino oscillation process with an LNV neutrino NSI at the interaction vertex. (Right) A possible UV completion in a left-right symmetric scenario.

where the normalisation factor  $\mathcal{N}_\alpha^{\circ Y}$  is found from the unitarity condition  $\sum_\beta (P_{v_\alpha \rightarrow v_\beta}^{\circ Y} + P_{v_\alpha \rightarrow \bar{v}_\beta}^{\circ Y}) = 1$ ,

$$\mathcal{N}_\alpha^{\circ Y} = 1 + \sum_\beta \left| \sum_i U_{\alpha i}^* (\gamma_{RY}^\circ)_{\beta i} e^{-i \frac{m_i^2}{2E_\mathbf{q}} L} \right|^2. \quad (3.32)$$

If we expand the normalisation factor in the denominators of Eqs. (3.30) and (3.31), it can be seen that  $\sum_\beta P_{v_\alpha \rightarrow v_\beta}^{\circ Y} \approx 1 - \mathcal{O}(\varepsilon_{RY}^{\circ 4})$  and  $\sum_\beta P_{v_\alpha \rightarrow \bar{v}_\beta}^{\circ Y} \approx \mathcal{O}(\varepsilon_{RY}^{\circ 2}) - \mathcal{O}(\varepsilon_{RY}^{\circ 6})$ . Setting  $\varepsilon_{RY}^{\circ} = 0$  therefore recovers the SM prediction. If we assume that  $\varepsilon_{RY}^{\circ} \ll 1$ , to good approximation  $\mathcal{N}_\alpha^{\circ Y} \approx 1$ . However, the normalisation factor  $\mathcal{N}_\alpha^{\circ Y}$  cancels in the ratio  $\mathcal{R}_\beta$  regardless. We will also assume in the following that the neutrino NSI coefficients are real.

Assuming that  $\mathcal{N}_\alpha^{\circ Y} \approx 1$ , the absolute square in the non-standard probability  $P_{v_\alpha \rightarrow \bar{v}_\beta}^{\circ Y}$  in Eq. (3.31) can be expanded to give

$$\begin{aligned}
P_{v_\alpha \rightarrow \bar{v}_\beta}^{\circ Y} &\approx \left| \sum_i U_{\alpha i}^* (\gamma_{RY}^\circ)_{\beta i} e^{-i \frac{m_i^2}{2E_\mathbf{q}} L} \right|^2 \\
&= \sum_\lambda F_{\alpha \lambda} (\varepsilon_{RY}^\circ)_{\beta \lambda}^2 + \sum_{\lambda > \lambda'} G_{\alpha \lambda \lambda'} (\varepsilon_{RY}^\circ)_{\beta \lambda} (\varepsilon_{RY}^\circ)_{\beta \lambda'}, \quad (3.33)
\end{aligned}$$

where we have rotated  $(\gamma_{RY}^\circ)_{\beta i}$  back to the flavour basis using Eq. (3.27) and the indices  $\lambda, \lambda'$  sum over flavour. The number of flavour and mass indices has been kept general and could also include sterile states. The effective Lagrangian we have considered in this chapter is equivalent to the LEFT Lagrangian in Eq. (2.91). It is

also possible to include  $n_S$  sterile states and write the LEFT +  $N_R$  charged-current in Eq. (2.98); these states can be light and contribute to oscillations. A full analysis of this scenario is beyond the scope of this chapter.

In Eq. (3.33), the factors  $F_{\alpha\lambda}$  and  $G_{\alpha\lambda\lambda'}$  are functions of the baseline, neutrino energy and relevant mixing parameters. These functions take the form

$$F_{\alpha\lambda} = \sum_i |U_{\alpha i}|^2 |U_{\lambda i}|^2 + 2\Re \sum_{i>j} U_{\alpha i}^* U_{\lambda i}^* U_{\alpha j} U_{\lambda j} e^{-i \frac{\Delta m_{ij}^2}{2E_\mathbf{q}} L}, \quad (3.34)$$

$$G_{\alpha\lambda\lambda'} = 2\Re \sum_i |U_{\alpha i}|^2 U_{\lambda i}^* U_{\lambda' i} \\ + 2\Re \sum_{i>j} (U_{\alpha i}^* U_{\lambda i}^* U_{\alpha j} U_{\lambda' j} + U_{\alpha i}^* U_{\lambda' i}^* U_{\alpha j} U_{\lambda j}) e^{-i \frac{\Delta m_{ij}^2}{2E_\mathbf{q}} L}, \quad (3.35)$$

where  $U$  is the PMNS mixing matrix. For three generations (i.e. the 3 $\nu$  mixing scheme) these are complicated functions of the three mixing angles and Dirac CP phase ( $\theta_{12}$ ,  $\theta_{13}$ ,  $\theta_{23}$  and  $\delta$ ), three mass-squared splittings ( $\Delta m_{21}^2$ ,  $\Delta m_{31}^2$  and  $\Delta m_{32}^2$ ) and two Majorana phases ( $\alpha_2$  and  $\alpha_3$ ). This dependence on the Majorana phases is in contrast to the standard neutrino oscillation probability.

For the purposes of atmospheric and accelerator oscillations ( $\nu_\mu \rightleftharpoons \nu_\tau$ ), the two generation or 2 $\nu$  mixing approximation is justified due to the dominance of the atmospheric mass-squared splitting with respect to the solar mass-squared splitting,  $\Delta m_{\text{atm}}^2 \gg \Delta m_{\text{sol}}^2$ . The  $2 \times 2$  mixing matrix in this case is

$$U^{(2\nu)} = \begin{pmatrix} \cos \vartheta & \sin \vartheta e^{i\eta} \\ -\sin \vartheta e^{-i\eta} & \cos \vartheta \end{pmatrix}, \quad (3.36)$$

where  $\vartheta$  is the single mixing angle (corresponding approximately to  $\theta_{23}$ ) and  $\eta$  is the Majorana phase. The mass-squared splitting is  $\delta m^2$ , corresponding to  $\Delta m_{32}^2$ . The functions  $F_{\mu\lambda}$  and  $G_{\mu\lambda\lambda'}$  take the simplified forms,

$$F_{\mu\mu}^{(2\nu)} = 1 - \sin^2(2\vartheta) \sin^2 \varphi, \\ F_{\mu\tau}^{(2\nu)} = \sin^2(2\vartheta) \sin^2 \varphi, \\ G_{\mu\mu\tau}^{(2\nu)} = 2 \sin(2\vartheta) \sin^2 \varphi (\sin \eta \cot \varphi - \cos \eta \cos(2\vartheta)), \quad (3.37)$$

where  $\varphi = \eta - \frac{\delta m^2 L}{4E_{\mathbf{q}}}$ . For  $\eta = 0$ ,  $F_{\mu\mu}^{(2\nu)}$  and  $F_{\mu\tau}^{(2\nu)}$  are equal to the  $2\nu$  oscillation probabilities  $P_{\nu_{\mu} \rightarrow \nu_{\mu}}$  and  $P_{\nu_{\mu} \rightarrow \nu_{\tau}}$  respectively, therefore

$$P_{\nu_{\mu} \rightarrow \bar{\nu}_{\mu}} = P_{\nu_{\mu} \rightarrow \nu_{\mu}} (\varepsilon_{RY}^{\circ})_{\mu\mu}^2 + P_{\nu_{\mu} \rightarrow \nu_{\tau}} (\varepsilon_{RY}^{\circ})_{\mu\tau}^2 - \sin(4\vartheta) \sin^2 \left( \frac{\delta m^2 L}{4E_{\mathbf{q}}} \right) (\varepsilon_{RY}^{\circ})_{\mu\mu} (\varepsilon_{RY}^{\circ})_{\mu\tau}. \quad (3.38)$$

### 3.3 Constraints on LNV Neutrino NSIs

We will now use the parametrisation of  $|\Delta L| = 2$  neutrino NSIs in Eq. (3.26) and the predictions for the non-standard  $\nu_{\alpha} \rightarrow \bar{\nu}_{\beta}$  process in Eqs. (3.29), (3.30) and (3.31) to put constraints on the  $\varepsilon$  coefficient parameter space. We will first derive constraints from the MINOS experiment in the  $2\nu$  mixing approximation, moving on to examine both MINOS and KamLAND in the  $3\nu$  mixing scheme. We will then compare these constraints to the more common limits from  $\Delta L = 2$  processes such as  $0\nu\beta\beta$  decay,  $\mu^- - e^+$  conversion in nuclei, rare meson decays and radiative neutrino masses. We summarise all derived limits in Table 3.2.

#### 3.3.1 MINOS Constraints

The MINOS experiment first took data from 2005 to 2012, detecting neutrinos from the low-energy NuMI beam with a near detector at Fermilab and a far detector (at a baseline of  $L = 735$  km) at the Soudan mine [356]. The experiment resumed from 2013 to 2016 as MINOS+, using the medium-energy NuMI beam [357]. Over this time the experiment observed the disappearance of  $\nu_{\mu}$  produced from the decay of pions  $\pi^+$  (in the focusing beam configuration) and  $\bar{\nu}_{\mu}$  from  $\pi^-$  decays (defocusing), allowing the atmospheric mixing parameters dominating the  $\nu_{\mu} \rightarrow \nu_{\mu}$  disappearance channel to be probed. The experiment also confirmed  $\nu_e$  and  $\bar{\nu}_e$  appearance, constraining the reactor mixing angle  $\theta_{13}$ . Most importantly for this analysis, charged lepton sign identification was possible in the near and far detectors through the use of 1.3 T toroidal magnetic fields. As a result,  $\nu_{\mu}$ ,  $\bar{\nu}_{\mu}$ ,  $\nu_e$  and  $\bar{\nu}_e$  events could be distinguished from the curvature of outgoing  $\mu^-$ ,  $\mu^+$ ,  $e^-$  and  $e^+$  tracks, respectively.

Before the first MINOS run, the expected fluxes of  $\nu_\mu$  and  $\bar{\nu}_\mu$  in the focusing and defocusing configurations of the NuMI beam were determined from hadron production data and *in situ* measurements. An improved flux model was provided by Ref. [309]. In the focusing configuration the background of  $\bar{\nu}_e$  (produced by  $\pi^-$  avoiding deflection by the magnetic field) were non-negligible and an important systematic error to correct [358]. There were also  $\bar{\nu}_e$  produced downstream from secondary interactions in the beam pipe wall [359]. We neglect this  $\nu_e$  and  $\bar{\nu}_e$  background and assume all the incoming neutrinos are either  $\nu_\mu$  or  $\bar{\nu}_\mu$ . By measuring outgoing muons or antimuons, the MINOS experiment therefore constrained the ratio  $\mathcal{R}_\mu$  in Eq. (3.28).

We now split the ratio  $\mathcal{R}_\mu$  in Eq. (3.28) into a signal part  $\mathcal{S}_\mu$  arising from the non-standard  $\nu_\mu \rightarrow \bar{\nu}_\mu$  process and a background part  $\mathcal{B}_\mu$  arising from the standard oscillation of background antineutrinos  $\bar{\nu}_\mu \rightarrow \bar{\nu}_\mu$ . The MINOS analysis of Ref. [359] removes the predicted energy-dependent value of the background  $\mathcal{B}_\mu$  from the total measured ratio  $\mathcal{R}_\mu$  and derives the constraint  $\mathcal{S}_\mu \lesssim 0.026$ , i.e.

$$\mathcal{S}_\mu \approx \sum_{\circ, Y} \frac{\int dE_{\mathbf{q}} \frac{d\Gamma_{\nu_\mu}}{dE_{\mathbf{q}}} \cdot P_{\nu_\mu \rightarrow \bar{\nu}_\mu}^{\circ Y} \cdot \sigma_{\bar{\nu}_\mu}}{\int dE_{\mathbf{q}} \frac{d\Gamma_{\nu_\mu}}{dE_{\mathbf{q}}} \cdot P_{\nu_\mu \rightarrow \nu_\mu}^{\circ Y} \cdot \sigma_{\nu_\mu}} \lesssim 0.026. \quad (3.39)$$

We can use this limit to put corresponding constraints on  $(\varepsilon_{RY}^{\circ})_{\mu\lambda}$ . We repeat that the factorised form of Eq. (3.39) assumes the chirality of the production and detection processes to be opposite. For a left-handed SM charged-current at production there must a right-handed leptonic current at detection ( $X = R$ ). However, the quark current can be left- or right-handed ( $Y = L, R$ ). In left-right symmetric models the latter corresponds to the exchange of a  $W_R$  boson and the former to  $W_L - W_R$  mixing (if the masses of the gauge bosons are different), as depicted in Fig. 3.2 [313].

To simplify this work we will only consider two cases; a SM charged-current at production and a vector-type neutrino NSI with a right-handed leptonic current (therefore  $|\Delta L| = 2$ ) and either a left- or right-handed quark current at detection. In other words, we will retain the terms in Eq. (3.26) with the coefficients  $\varepsilon_{RY}^V$  and set all other  $\varepsilon_{XY}^{\circ}$  to zero. We also set  $(\varepsilon_{RL}^V)_{\beta\alpha} = (\varepsilon_{RR}^V)_{\beta\alpha} \equiv \varepsilon_{\beta\alpha}$  to simplify the

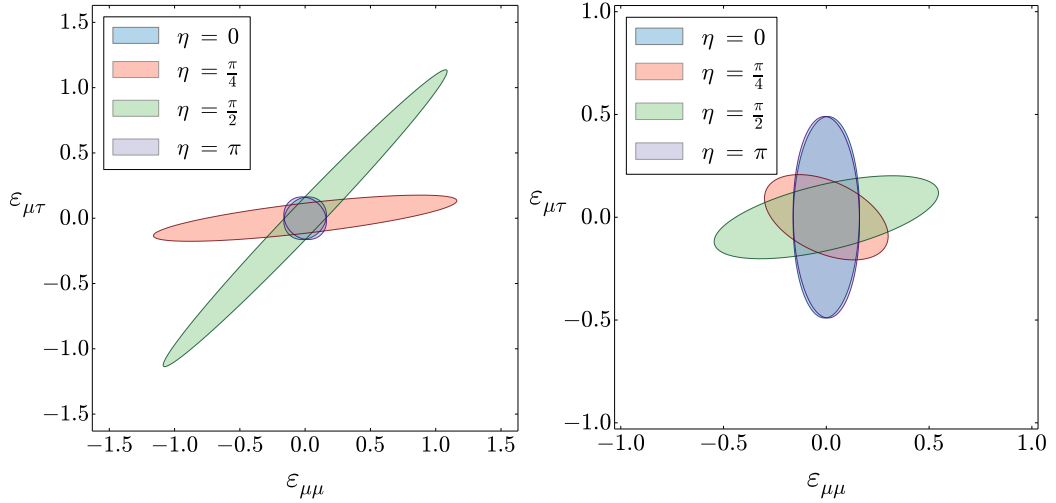


**Figure 3.3:** (Left) Allowed regions in the  $(\varepsilon_{\mu\mu}, \varepsilon_{\mu\tau})$  plane for fixed  $L/E_{\mathbf{q}} = 735 \text{ km}/3 \text{ GeV}$  and four values of  $\eta$  in the  $2\nu$  mixing approximation of the  $\nu_{\mu} - \nu_{\tau}$  sector. (Right) Allowed regions in  $(\varepsilon_{\mu\mu}, \varepsilon_{\mu\tau})$  for fixed  $L = 735 \text{ km}$  and four values of  $\eta$ , found by integrating over the NuMI beam neutrino energies.

notation. It is worth remarking that there is a subtle difference between the neutrino NSI being present at production and detection. Because the outgoing lepton  $\ell_{\alpha}^{\pm}$  at production is not measured, one must sum over the different initial flavours in Eq. (3.28). For the MINOS experiment, however, it is kinematically forbidden for pions in the NuMI beam to decay to  $\tau^{\pm}$  (ruling out any sensitivity to the coefficient  $\varepsilon_{\tau\lambda}$ ), and their decays to electrons are helicity-suppressed with respect to muons (so that the  $\nu_{\mu}$  or  $\bar{\nu}_{\mu}$  flux dominates). We therefore neglect this detail and assume that a neutrino NSI at production is probed in the same way as an NSI at detection.

We will first examine the MINOS limit on  $\mathcal{S}_{\mu}$  in Eq. (3.39) using the  $2\nu$  mixing approximation. As mentioned previously, the baseline and neutrino energies of the MINOS experiment were such that  $L/E_{\mathbf{q}} \sim 2\pi/\Delta m_{\text{atm}}^2$ . Because a hierarchy exists between the atmospheric and solar mass-squared splittings,  $\Delta m_{\text{atm}}^2 \gg \Delta m_{\text{sol}}^2$ , the oscillations  $\nu_{\mu} \rightleftharpoons \nu_{\tau}$  are accurately described by a  $2\nu$  oscillation probability. We therefore insert the  $2\nu$  mixing expressions for the functions  $F_{\alpha\lambda}$  and  $G_{\alpha\lambda\lambda'}$  in Eq. (3.37) into the non-standard probability  $P_{\nu_{\mu} \rightarrow \bar{\nu}_{\mu}}$  in Eq. (3.33). Plugging this into Eq. (3.39) then allows to place bounds on the  $(\varepsilon_{\mu\mu}, \varepsilon_{\mu\tau})$  parameter space. The sensitivity to these two parameters is clear from dependence on  $\varepsilon_{\beta\lambda}$  in Eq. (3.33); the first index of  $\varepsilon_{\beta\lambda}$  corresponds to the flavour of the outgoing charged lepton, in

this case  $\beta = \mu$ . The second index is summed over all other flavours, so in the  $2\nu$  mixing approximation  $\lambda = \{\mu, \tau\}$ .

To derive constraints in the  $(\varepsilon_{\mu\mu}, \varepsilon_{\mu\tau})$  plane we must perform the integrals over the neutrino energy in the numerator and denominator of Eq. (3.39). For the differential neutrino flux  $\frac{d\Gamma_{\nu_\mu}}{dE_{\mathbf{q}}}$  we will either assume a fixed neutrino energy or use the NuMI  $\nu_\mu$  differential flux of Ref. [309]. For the cross sections we will use the quasi-elastic scattering result

$$\sigma_{\nu_\mu}(E_{\mathbf{q}}) \simeq \sigma_{\bar{\nu}_\mu}(E_{\mathbf{q}}) \simeq \frac{G_F^2 |V_{ud}|^2}{\pi} (g_V^2 + 3g_A^2) E_{\mathbf{q}}^2, \quad (3.40)$$

where  $g_V$  and  $g_A$  are the vector and axial vector couplings of the nucleon current respectively [360]. We then perform each integral over the flux, normalised probability and cross section numerically, splitting the integration region  $0 - 20$  GeV into bins of 500 MeV width. The result of this procedure is

$$\mathcal{S}_\mu \approx x_\mu F_{\mu\mu}^{(2\nu)} \varepsilon_{\mu\mu}^2 + y_\mu F_{\mu\tau}^{(2\nu)} \varepsilon_{\mu\tau}^2 + z_\mu G_{\mu\mu\tau}^{(2\nu)} \varepsilon_{\mu\mu} \varepsilon_{\mu\tau} \lesssim 0.026. \quad (3.41)$$

where  $x_\mu$ ,  $y_\mu$  and  $z_\mu$  are numerical constants depending on the choice of flux and integration method. This inequality excludes the area outside an ellipse in the  $(\varepsilon_{\mu\mu}, \varepsilon_{\mu\tau})$  plane.

In Fig. 3.3 (left) we plot the allowed regions in the  $(\varepsilon_{\mu\mu}, \varepsilon_{\mu\tau})$  plane for fixed  $L/E_{\mathbf{q}} = 735$  km/(3 GeV). We use best fit values for  $\delta m^2 \approx \Delta m_{23}^2$  and  $\vartheta \approx \theta_{23}$  in the NO scheme (shown in Table 2.3),  $G_F = 1.166 \times 10^{-5}$  GeV $^{-2}$ ,  $|V_{ud}| = 0.974$ ,  $g_V = 1$ ,  $g_A = 1.269$  and four different values of the Majorana phase  $\eta$  [361]. The choice of a fixed neutrino energy is equivalent to assuming the  $\nu_\mu$  flux to be sharply peaked at 3 GeV and evaluating the oscillation probability and cross section at this energy. The constraints are most stringent for  $\eta = 0, \pi$ , of order  $|\varepsilon_{\mu\mu}| \lesssim 0.2$  and  $|\varepsilon_{\mu\tau}| \lesssim 0.1$ . For values  $\eta = (n + \frac{1}{2})\pi$  where  $n \in \mathbb{Z}$ , a specific direction in the parameter space appears to alleviate the constraints. This is because  $F_{\mu\tau}^{(2\nu)} \ll 1$  for the best fit parameters and these particular values of  $\eta$ . In Fig. 3.3 (right) we instead depict the allowed regions after the full numerical integration of the numerator and

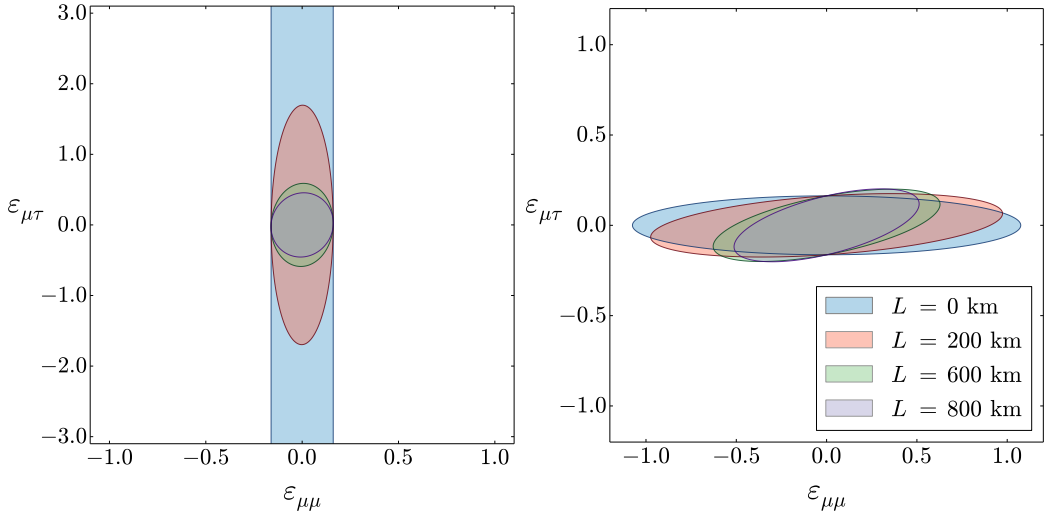


**Figure 3.4:** Allowed regions in the  $(\varepsilon_{\mu\mu}, \varepsilon_{\mu\tau})$  plane for values of the Majorana phase  $\eta = 0$  (left) and  $\eta = \pi/2$  (right) and for four different values of the baseline  $L$ .

denominator of  $\mathcal{S}_\mu$ . For  $\eta = \frac{\pi}{4}, \frac{\pi}{2}$ , the allowed values are now ellipses more similar to those for  $\eta = 0, \pi$ . The orientations of the ellipses have also changed marginally. Upper bounds are now in the ranges  $|\varepsilon_{\mu\mu}| \lesssim 0.2 - 0.5$  and  $|\varepsilon_{\mu\tau}| \lesssim 0.2 - 0.6$ .

The baseline of the MINOS experiment was fixed at  $L = 735$  km. We will now briefly consider a hypothetical experiment similar in design to MINOS but at a different baseline. In Fig. 3.4 (left) we set  $\eta = 0$  and examine the allowed regions in the  $(\varepsilon_{\mu\mu}, \varepsilon_{\mu\tau})$  plane for different values of the baseline  $L$ , derived using the MINOS limit  $\mathcal{S}_\mu \lesssim 0.026$ . We see that at  $L = 0$  km this sets the bound  $|\varepsilon_{\mu\mu}| \lesssim 0.16$ , while  $\varepsilon_{\mu\tau}$  remains unbounded. This is because the factors  $F_{\mu\tau}^{(2\nu)}$  and  $G_{\mu\mu\tau}^{(2\nu)}$  are directly proportional to  $\sin\varphi$  which vanishes at  $L = 0$  km, while the first term in  $F_{\mu\mu}^{(2\nu)}$  is always non-zero. At  $L = 0$  km, only the term containing  $\varepsilon_{\mu\mu}^2$  remains in Eq. (3.41) and it is therefore the only coefficient that can be constrained. At larger baselines of 200, 600 and 800 km the functions  $F_{\mu\tau}^{(2\nu)}$  and  $G_{\mu\mu\tau}^{(2\nu)}$  are non-zero and the allowed regions again become ellipses. As  $L$  increases it can be seen that the bounded area becomes more circular, i.e. improving the bound in the  $\varepsilon_{\mu\tau}$  direction. For  $\eta = \frac{\pi}{2}$ , shown in Fig. 3.4 (right),  $F_{\mu\tau}^{(2\nu)}$  and  $G_{\mu\mu\tau}^{(2\nu)}$  are non-zero even at  $L = 0$  km and the bound is an ellipse at zero distance. The bound now improves in the  $\varepsilon_{\mu\mu}$  direction as  $L$  increases.

Finally, it is interesting to examine the bounds on  $\varepsilon_{\mu\mu}$  as a function of  $L$  when

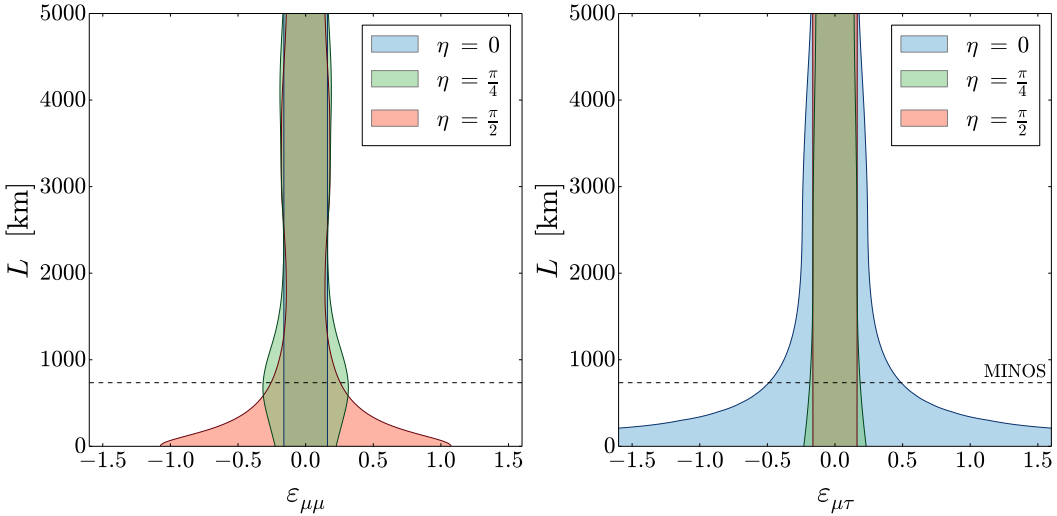


**Figure 3.5:** Allowed values of  $\varepsilon_{\mu\mu}$  with  $\varepsilon_{\mu\tau} = 0$  (left) and  $\varepsilon_{\mu\tau}$  with  $\varepsilon_{\mu\mu} = 0$  (right) as a function of the baseline  $L$  for three values of the Majorana phase  $\eta$ . The baseline of MINOS is indicated by the dashed line.

$\varepsilon_{\mu\tau} = 0$ . In Fig. 3.5 (left) we show the allowed values of  $\varepsilon_{\mu\mu}$  (along the  $x$ -axis) as a function of  $L$  (along the  $y$ -axis) for a fixed neutrino energy  $E_{\mathbf{q}} = 3$  GeV. For  $\eta = 0$  (and  $\eta = n\pi$  where  $n \in \mathbb{Z}$ ),  $F_{\mu\mu}^{(2\nu)}$  in the numerator of  $\mathcal{S}_\mu$  is exactly cancelled by the standard probability  $P_{\nu_\alpha \rightarrow \nu_\beta}$  in the denominator. The bound on  $\varepsilon_{\mu\mu}$  is therefore constant as a function of the baseline. For  $\eta = \frac{\pi}{2}$  the constraint at  $L = 0$  km is less stringent, but improves as  $L$  is increased to 1000 km. For  $\eta = \frac{\pi}{4}$ , the constraint worsens as  $L$  reaches  $\sim 800$  km but improves for larger baselines. For  $L \gtrsim 2000$  km the constraints for non-zero  $\eta$  values slowly oscillate but are roughly equivalent to the  $\eta = 0$  bound,  $|\varepsilon_{\mu\mu}| \lesssim 0.15$ . We show in Fig. 3.5 (right) a similar plot for  $\varepsilon_{\mu\tau}$ , setting  $\varepsilon_{\mu\mu} = 0$  and plotting the bounds as a function of the baseline. At  $L = 0$  km,  $\varepsilon_{\mu\tau}$  is unbounded for  $\eta = 0$ , as discussed previously. For large  $L$  the upper limits converge to  $|\varepsilon_{\mu\tau}| \lesssim 0.16$ .

We summarise the  $2\nu$  mixing approximation constraints on the coefficients  $\varepsilon_{\mu\mu}$  and  $\varepsilon_{\mu\tau}$  in Table 3.1. We allow one coefficient at a time to be non-zero, computing an upper bound for fixed neutrino energy  $E_{\mathbf{q}} = 3$  GeV (left) and integrating over the NuMI flux (right). The lower and upper values are the most and least stringent upper bounds, respectively, as the Majorana phase  $\eta$  is varied. For a fixed energy, one can see that  $\varepsilon_{\mu\tau}$  is unbounded for a specific value of  $\eta$ . We note that so far in

NSI Coefficient	$>  \epsilon_{\beta\alpha} $	
	Fixed Energy	NuMI Flux
$\epsilon_{\mu\mu}$	$0.11 - 0.76$	$0.15 - 0.55$
$\epsilon_{\mu\tau}$	$0.12 - \infty$	$0.16 - 0.66$

**Table 3.1:** Upper bounds from the MINOS experiment on the LNV NSI coefficients in the  $2\nu$  mixing approximation. The range indicates the best and worst upper bound depending on the choice of the Majorana phase. (Left) Bounds derived at a fixed neutrino energy of 3 GeV. (Right) Bounds derived by integrating over the energy-dependent NuMI flux, probability and cross section.

in this analysis we have taken the best fit values of the standard mixing parameters to be fixed. For a rigorous fit to the data it would be necessary to let these parameters vary alongside the  $\epsilon$  coefficients, as is commonly done for the  $|\Delta L| = 0$  neutrino NSIs [296, 299, 338, 362]. We leave this for a future complete analysis.

We now examine the constraints that can be made from the MINOS experiment in the full  $3\nu$  mixing scheme. Instead of Eq. (3.36), we now use the standard parametrisation of the PMNS mixing matrix  $U = R_{23}W_{13}R_{12}D$  shown explicitly in Eq. (2.58). As the neutrinos are Majorana fermions, we must include the diagonal matrix  $D$  containing the two Majorana phases  $\alpha_2$  and  $\alpha_3$ . We now hope to be able to probe the three generation flavour structure of the non-standard coefficients  $\epsilon_{\beta\alpha}$  (which are taken to be real).

To do this, we again expand the effective non-standard oscillation probability  $P_{\nu_\alpha \rightarrow \bar{\nu}_\beta}$  as in Eq. (3.33), where now the flavour indices run over  $\lambda, \lambda' \in \{e, \mu, \tau\}$ . The factors  $F_{\alpha\lambda}$  and  $G_{\alpha\lambda\lambda'}$  are now functions of the baseline  $L$ , neutrino energy  $E_{\mathbf{q}}$ , three-generation mixing parameters and Majorana phases  $\alpha_2$  and  $\alpha_3$ . We use the best fit values for the mixing parameters  $\theta_{12}, \theta_{23}, \theta_{13}, \Delta m_{21}^2, \Delta m_{32}^2$  and  $\delta$  in the NO scheme (shown in Table 2.3), while  $L, E_{\mathbf{q}}, \alpha_2$  and  $\alpha_3$  are again free parameters. It is informative to compare the two Majorana phases used here to the single Majorana phase  $\eta$  in the  $2\nu$  mixing approximation. If we take the expression for  $F_{\mu\mu}$  in the  $3\nu$  scheme and take the limits  $\Delta m_{21}^2 \rightarrow 0$  and  $\Delta m_{31}^2 \rightarrow \Delta m_{32}^2$ , we can compare to  $F_{\mu\mu}^{(2\nu)}$  in Eq. (3.37) and find the correspondences  $\vartheta \approx \theta_{23}, \delta m^2 \approx \Delta m_{32}^2$  and  $\eta \approx (\alpha_3 - \alpha_2)/2$ .

In the three generation picture, the limit  $\mathcal{S}_\mu < 0.026$  can be projected onto an

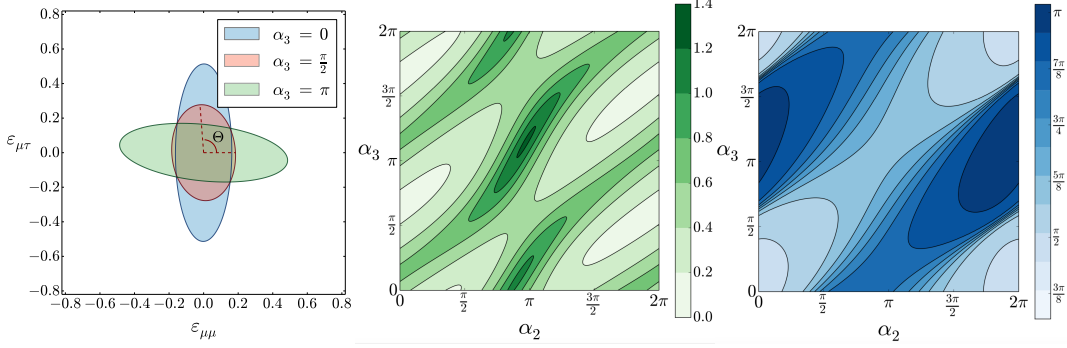


**Figure 3.6:** (Left) Elliptical allowed regions in the  $(\varepsilon_{\mu\mu}, \varepsilon_{\mu\tau})$  plane for  $\varepsilon_{\mu e} = 0$ ,  $L = 735$  km,  $\alpha_2 = 0$  and three values of the Majorana phase  $\alpha_3$ . (Centre) Eccentricity  $e$  of the ellipse as a function of  $(\alpha_2, \alpha_3)$ . (Right) Angle  $\Theta$  from the positive  $\varepsilon_{\mu\mu}$  axis to the semi-major axis of the ellipse as a function of  $(\alpha_2, \alpha_3)$ .

allowed region in the  $(\varepsilon_{\mu e}, \varepsilon_{\mu\mu}, \varepsilon_{\mu\tau})$  parameter space. For values of the baseline  $L$  and Majorana phases  $(\alpha_2, \alpha_3)$  we can again perform the integrals in  $\mathcal{S}_\mu$  numerically. Firstly, in order to compare with the bounds from the 2ν mixing approximation, we set  $\varepsilon_{\mu e} = 0$  and depict in Fig. 3.6 (left) the allowed regions in the  $(\varepsilon_{\mu\mu}, \varepsilon_{\mu\tau})$  plane for  $\alpha_2 = 0$  and three different values of  $\alpha_3$ . The elliptical allowed regions are of similar size to those for the 2ν mixing approximation but generally have different shapes and orientations (which we can define as an eccentricity  $e$  and anticlockwise angle  $\Theta$  from the positive  $\varepsilon_{\mu\mu}$  axis to the semi-major axis, shown in Fig. 3.6). We show how the eccentricities and orientations depend on the Majorana phases in Fig. 3.6 (centre and right). We can see that the angle  $\Theta$  is roughly constant along lines  $\alpha_3 = \alpha_2 + C$ , suggesting that it can approximately be taken as a single-valued function of  $\eta \approx (\alpha_3 - \alpha_2)/2$ . For example, at  $(\alpha_2, \alpha_3) = (0, 0)$  we see that the bound is more stringent in the  $\varepsilon_{\mu\mu}$  direction; this is also the case for  $\eta = 0$  in the 2ν approximation. Likewise, for  $(\alpha_2, \alpha_3) = (0, \pi)$ , the bound is more constraining in the  $\varepsilon_{\mu\tau}$  direction which is similar to  $\eta = \pi$ . We see that the largest eccentricity occurs at  $(\alpha_2, \alpha_3) \approx (\pi, \pi)$ , coinciding with the semi-major axis pointing in the  $\varepsilon_{\mu\tau}$  direction.

We will now allow each of the non-standard coefficients  $(\varepsilon_{\mu e}, \varepsilon_{\mu\mu}, \varepsilon_{\mu\tau})$  to be non-zero. In Fig. 3.7, we plot the upper bounds on coefficients as a function of  $(\alpha_2, \alpha_3)$ , setting the other coefficients to zero. For  $\varepsilon_{\mu e}$  (left), we can see that the

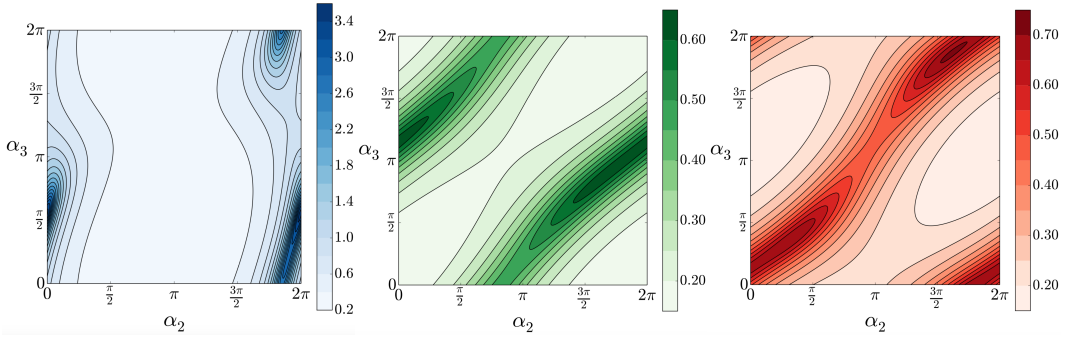


**Figure 3.7:** Upper bounds on the NSI coefficients  $\epsilon_{\mu e}$  (left),  $\epsilon_{\mu \mu}$  (centre) and  $\epsilon_{\mu \tau}$  (right), as a function of the Majorana phases  $\alpha_2$  and  $\alpha_3$ , derived from the MINOS limit  $S_\mu < 0.026$ . Best fit values for the mixing parameters  $\theta_{12}$ ,  $\theta_{13}$  and  $\theta_{23}$ ,  $\Delta m_{21}^2$  and  $\Delta m_{32}^2$  and  $\delta$  are taken in the NO.

upper bound is of order  $|\epsilon_{\mu e}| \lesssim 1$  for most values of  $(\alpha_2, \alpha_3)$ , but increases for specific values of the phases to around  $|\epsilon_{\mu e}| \lesssim 3.4$ . On the other hand, upper bounds on the other two coefficients are in the ranges  $|\epsilon_{\mu \mu}| \lesssim 0.2 - 0.6$  and  $|\epsilon_{\mu \tau}| \lesssim 0.2 - 0.7$ . We summarise these constraints (along with constraints derived in the next section) to the right of Table 3.2. The lower and upper values are the most and least stringent upper bounds depending on the value of the Majorana phases  $(\alpha_2, \alpha_3)$ .

OPERA was another LBL accelerator experiment which employed a magnetic field in the far detector [363, 364]. Unlike MINOS, OPERA searched for neutrinos from the CNGS beam at CERN with energies above the production threshold for  $\tau^\pm$ . The main aim of the experiment was to confirm  $\nu_\tau$  appearance; around ten  $\tau^\pm$  events were recorded over four years of data taking [365]. Unfortunately, the experiment was only able to distinguish the charge of a single  $\tau^-$  event at  $5\sigma$  significance (the other charges were undetermined). In theory, a future high-statistics OPERA-like experiment could be able to probe the neutrino NSI coefficients  $\epsilon_{\tau e}$ ,  $\epsilon_{\tau \mu}$  and  $\epsilon_{\tau \tau}$ .

### 3.3.2 KamLAND Constraints

The LBL reactor experiment KamLAND operated for 185.5 days between March 4 and December 1 2002 and conducted a search for solar  $\nu_e$  with the characteristic flux of  ${}^8\text{B}$  neutrinos. The analysis of Ref. [354] instead searched for  $\bar{\nu}_e$ , assumed to have been produced via the spin precession of  $\nu_e$  in the solar magnetic field (due to a non-zero neutrino magnetic moment) or via sterile neutrino decays. The experiment

did not see an excess of  $\bar{\nu}_e$  above the background and therefore enforced the bound  $\mathcal{S}_e \lesssim 2.8 \times 10^{-4}$  at 90% C.L.. We will instead use this bound to place constraints on the coefficients of the  $|\Delta L| = 2$  neutrino NSIs.

We assume that the initial solar  $\nu_e$  are produced from the beta decays of  ${}^8\text{B}$  and propagate from the solar core to the solar surface and then on to the KamLAND detector. The oscillation probability must therefore take into account the resonant conversion of solar  $\nu_e$  to  $\nu_\mu$  and  $\nu_\tau$  through the MSW effect, a consequence of the decreasing matter potential from the Sun's core to surface. We approximate the conversion as adiabatic and utilise the  $\Delta m_{21}^2 \ll \Delta m_{32}^2$  hierarchy to write the standard  $\nu_\alpha \rightarrow \nu_\beta$  oscillation probability in a similar form to that in Ref. [299],

$$P_{\nu_\alpha \rightarrow \nu_\beta}^{\text{MSW}} \approx \left| \sum_{i,j}^2 (R_{23}W_{13})_{\alpha i}^* (R_{23}W_{13})_{\beta j} \mathcal{U}_{ij}(x) \right|^2 + |U_{\alpha 3}|^2 |U_{\beta 3}|^2, \quad (3.42)$$

where  $R_{23}$  and  $W_{13}$  are Euler rotations in standard parametrisation of the PMNS matrix and  $\mathcal{U}(x)$  is a  $2 \times 2$  unitary matrix satisfying the equation

$$i \frac{d}{dx} \mathcal{U}(x) = \frac{\hat{M}_{2 \times 2}^2}{2E_{\mathbf{q}}} \mathcal{U}(x), \quad (3.43)$$

where  $x$  is the distance from the source. The matrix  $\hat{M}_{2 \times 2}^2$  is the  $2 \times 2$  effective squared mass matrix

$$\hat{M}_{2 \times 2}^2 = \frac{\Delta m_{12}^2 + c_{13}^2 A_{\text{CC}}}{2} + \frac{1}{2} \begin{pmatrix} -\cos 2\theta_{12} \Delta m_{12}^2 + c_{13}^2 A_{\text{CC}} & \sin 2\theta_{12} \Delta m_{12}^2 \\ \sin 2\theta_{12} \Delta m_{12}^2 & \cos 2\theta_{12} \Delta m_{12}^2 - c_{13}^2 A_{\text{CC}} \end{pmatrix}, \quad (3.44)$$

where  $A_{\text{CC}} = 2\sqrt{2}G_F E_{\mathbf{q}} N_e$  and  $N_e$  is the electron number density in the Sun. In order to construct  $\mathcal{S}_e$  we now require the non-standard oscillation equivalent of Eq. (3.42). This can be derived from Eq. (3.33), but an exact formula taking into account the MSW effect, even in the  $\Delta m_{21}^2 \ll \Delta m_{32}^2$  limit, is beyond the scope of this chapter. The possibility that the neutrino NSI occurs at production also complicates the derivation, because  $\bar{\nu}_e$  experience a different matter effect while propagating through the Sun. We therefore concentrate on the neutrino NSI being at detection.

$ \epsilon_{\alpha\beta} $	Previous Upper Bound	Process	LBL Upper Bound	LBL Experiment
$ \epsilon_{ee} $	$2.1 \times 10^{-9} - 6.3 \times 10^{-9}$		0.017	
$ \epsilon_{e\mu} $	$2.9 \times 10^{-9} - \infty$	$0\nu\beta\beta$	0.017	KamLAND
$ \epsilon_{e\tau} $	$2.6 \times 10^{-9} - \infty$		0.015	
$ \epsilon_{\mu e} $	$\sim 4 \times 10^3 - 1 \times 10^4$		0.22 – 3.47	
$ \epsilon_{\mu\mu} $	$\sim 6 \times 10^3 - \infty$	$\mu^- - e^+$	0.16 – 0.63	MINOS
$ \epsilon_{\mu\tau} $	$\sim 5 \times 10^3 - \infty$		0.16 – 0.71	

**Table 3.2:** Upper bounds on the LNV NSI flavour coefficients  $|\epsilon_{\alpha\beta}|$  in the  $e$  and  $\mu$  sectors. Left: bounds derived from conventional microscopic LNV processes, with  $0\nu\beta\beta$  decay ( $^{76}\text{Ge}$ ) being the most effective the  $e$  sector and  $\mu^- - e^+$  conversion loosely constraining the  $\mu$  sector. Right: bounds from LBL oscillation experiments MINOS and KamLAND. Two values indicate the variation in the upper bound as  $(\alpha_2, \alpha_3)$  are varied.

It is safe to assume that, by the time the solar neutrinos reach Earth and the KamLAND detector, they make up an incoherent admixture of flavour eigenstates. Naively, this has the effect of washing out any dependence on the Majorana phases, and we can approximate the non-standard oscillation probability  $P_{\nu_e \rightarrow \bar{\nu}_\beta}^{\text{MSW}}$  as the MSW oscillation probability  $P_{\nu_e \rightarrow \nu_\beta}^{\text{MSW}}$  in Eq. (3.42) multiplied by the neutrino NSI coefficient  $\epsilon_{e\beta}^2$  (the incoming neutrino can be of any flavour  $\nu_\beta$  as long as the neutrino NSI produces an outgoing positron  $e^+$ ). KamLAND is therefore sensitive to the coefficients  $\epsilon_{ee}$ ,  $\epsilon_{e\mu}$  and  $\epsilon_{e\tau}$ .

The signal ratio  $\mathcal{S}_e$  can be written as

$$\mathcal{S}_e \approx \sum_{\beta} \frac{\int dE_{\mathbf{q}} \frac{d\Gamma_{\nu_e}}{dE_{\mathbf{q}}} \cdot P_{\nu_e \rightarrow \bar{\nu}_\beta}^{\text{MSW}} \cdot \epsilon_{e\beta}^2 \cdot \sigma_{\bar{\nu}_\beta}}{\int dE_{\mathbf{q}} \frac{d\Gamma_{\nu_e}}{dE_{\mathbf{q}}} \cdot P_{\nu_e \rightarrow \nu_e}^{\text{MSW}} \cdot \sigma_{\nu_e}} \lesssim 2.8 \times 10^{-4}, \quad (3.45)$$

where  $\frac{d\Gamma_{\nu_e}}{dE_{\mathbf{q}}}$  is the  $^{8}\text{B}$  solar  $\nu_e$  flux of Ref. [366] while  $\sigma_{\bar{\nu}_\beta}$ ,  $\sigma_{\nu_e}$  are the quasi-elastic scattering cross sections for the  $\bar{\nu}_\beta + p \rightarrow \ell_\beta^+ + n$  and  $\nu_e + n \rightarrow e^- + p$  processes, respectively. We again numerically integrate the numerator and denominator of Eq. (3.45), dividing the energy range  $8.3 - 14.8$  MeV into bins of 0.02 MeV width. The left-hand side of the inequality is a function of the neutrino NSI coefficients, and therefore an allowed region can be projected on to the  $(\epsilon_{ee}, \epsilon_{e\mu}, \epsilon_{e\tau})$  parameter space.

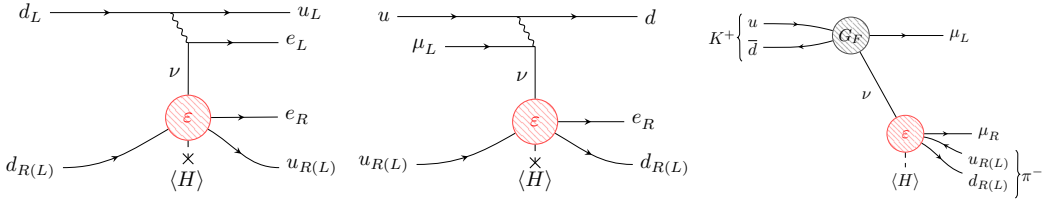


**Figure 3.8:** Microscopic  $|\Delta L| = 2$  processes sensitive to the neutrino NSI coefficients. (Left)  $0\nu\beta\beta$  decay. (Centre)  $\mu^- - e^+$  conversion in a nucleus. (Right) Kaon decay  $K^+ \rightarrow \pi^- \mu^+ \mu^+$ .

For each of these non-standard coefficients, we set the others to zero and derive an upper bound; these are shown in Table 3.2. Because the dependence on the Majorana phases is washed out, Eq. (3.45) can only set a single upper bound on each coefficient. For the coefficient  $\epsilon_{ee}$ , the numerator and denominator of  $\mathcal{S}_e$  in Eq. (3.45) are identical except for the factor of  $\epsilon_{ee}^2$  in the numerator; the upper bound on  $|\epsilon_{ee}|$  (for  $\epsilon_{e\mu} = \epsilon_{e\tau} = 0$ ) is simply the square root of  $2.8 \times 10^{-4}$ . For  $\epsilon_{e\mu}$  and  $\epsilon_{e\tau}$ , the ratio  $\mathcal{S}_e$  will contain different oscillation probabilities in the numerator and denominator, giving different upper bounds.

### 3.4 Other Constraints on LNV Neutrino NSIs

We will now compare the constraints derived from MINOS and KamLAND to those from conventional searches for  $|\Delta L| = 2$  processes. The most promising probe of the Majorana nature of the active neutrinos continues to be  $0\nu\beta\beta$  decay. However, light Majorana neutrino exchange may not be the dominant contribution to the process. The contribution of non-standard  $|\Delta L| = 2$  mechanisms to  $0\nu\beta\beta$  decay have also been studied in the literature, including the dimension-six charged-current neutrino NSI considered in this chapter [367–370]. We will now extend these results to the  $3 \times 3$  flavour structure of the  $\epsilon$  coefficient in order to compare with the MINOS and KamLAND constraints.

From Ref. [371], we use the general expression for the inverse half-life of the  $0\nu\beta\beta$  decay process when a right-handed leptonic current is present at one of the

interaction vertices (as shown in Fig. 3.8),

$$(T_{1/2}^{0\nu})^{-1} = \frac{G_{mm}}{m_e^2} \left| \sum_i^3 U_{ei}^2 m_i \right|^2 + G_{\gamma\gamma} \left| \sum_i^3 U_{ei} \gamma_{ei}^* \right|^2 + G_{m\gamma} \Re \left[ \sum_{i,j}^3 U_{ei}^2 m_i U_{ej}^* \gamma_{ej} \right], \quad (3.46)$$

where  $G_{mm}$ ,  $G_{\gamma\gamma}$  and  $G_{m\gamma}$  contain phase space factors and nuclear matrix elements, given by Ref. [371]. We can now expand this inverse half-life in a similar manner to the oscillation probability,

$$(T_{1/2}^{0\nu})^{-1} = X + \sum_{\lambda} Y_{\lambda} \varepsilon_{e\lambda} + \sum_{\lambda} F_{e\lambda} \varepsilon_{e\lambda}^2 + \sum_{\lambda > \lambda'} G_{e\lambda\lambda'} \varepsilon_{e\lambda} \varepsilon_{e\lambda'}, \quad (3.47)$$

where  $F_{e\lambda}$  and  $G_{e\lambda\lambda'}$  are the functions in Eq. (3.34) with  $L = 0$  km. The contribution from light neutrino exchange is contained in the factor  $X$ , which is a function of the Majorana phases  $(\alpha_2, \alpha_3)$  and lightest neutrino mass  $m_0$  ( $m_1$  or  $m_3$  in the NO or IO scenarios respectively). The interference between light neutrino exchange and the non-standard mechanism is described by the factor  $Y_{\lambda}$ , again a function of  $(\alpha_2, \alpha_3)$  and  $m_0$ . The inverse half-life depends on the coefficients  $\varepsilon_{ee}$ ,  $\varepsilon_{e\mu}$  and  $\varepsilon_{e\tau}$  (the same as KamLAND).

We now set  $T_{1/2}^{0\nu} > 5.3 \times 10^{25}$  y from the  $^{76}\text{Ge}$   $0\nu\beta\beta$  decay experiment GERDA-II [372, 373]. We may also make use of the lower bound from the  $^{136}\text{Xe}$  experiment KamLAND-Zen,  $T_{1/2}^{0\nu} > 1.07 \times 10^{26}$  y, but the exact lower bound is not crucial for the following discussion [374]. For  $^{76}\text{Ge}$  we have  $G_{mm} = 1.12 \times 10^{-13}$ ,  $G_{\gamma\gamma} = 4.44 \times 10^{-9}$  and  $G_{m\gamma} = 2.19 \times 10^{-11}$ . The lower bound from GERDA-II can now be projected onto an allowed region in the  $(\varepsilon_{ee}, \varepsilon_{e\mu}, \varepsilon_{e\tau})$  parameter space. For each coefficient we set the others to zero and solve Eq. (3.47) for an upper bound on  $\varepsilon$  as a function of  $(\alpha_2, \alpha_3)$ .

These upper bounds are displayed in the contour plots of Fig. 3.9 for a lightest neutrino mass of  $m_1 = 0$  eV in the NO scheme. The associated most and least stringent of these upper bounds are shown in Table 3.2. The upper bound on  $|\varepsilon_{ee}|$  is of order  $10^{-9}$  for all values of  $(\alpha_2, \alpha_3)$ . The upper bound on  $|\varepsilon_{e\mu}|$  and  $|\varepsilon_{e\tau}|$  can be of similar size, but for very finely tuned values of  $(\alpha_2, \alpha_3)$  this bound tends to infinity. This occurs when  $F_{e\mu}$  and  $F_{e\tau}$  vanish. Comparing these bounds to those

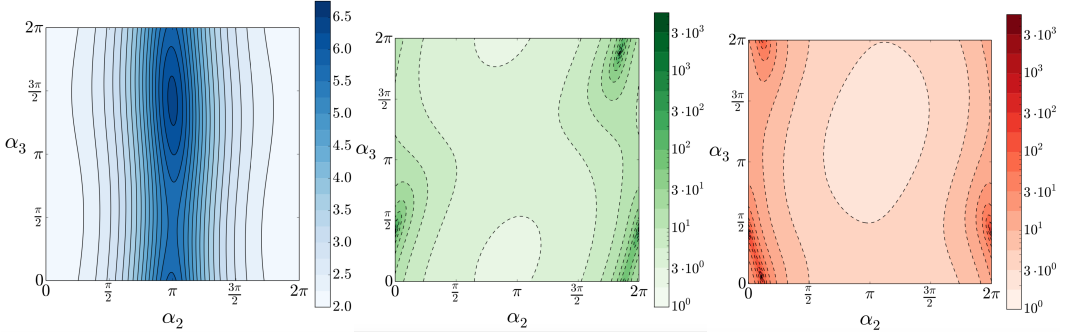


**Figure 3.9:** Upper bounds on the NSI coefficients  $\epsilon_{ee} \times 10^9$  (left),  $\epsilon_{e\mu} \times 10^9$  (centre) and  $\epsilon_{e\tau} \times 10^9$  (right) as a function of the Majorana phases  $(\alpha_2, \alpha_3)$ , found from the  $^{76}\text{Ge}$   $0\nu\beta\beta$  decay limit  $T_{1/2}^{0\nu} > 5.3 \times 10^{25}$  y. Best fit values for the neutrino mixing parameters in the NO scheme are chosen, with  $m_1 = 0$  eV.

from KamLAND, we see that  $0\nu\beta\beta$  decay is unequivocally the best method of probing  $\epsilon_{ee}$ . For a large portion of the  $(\alpha_2, \alpha_3)$  parameter space it is also better at constraining  $\epsilon_{e\mu}$  and  $\epsilon_{e\tau}$ . However, for certain fine-tuned values of the phases these coefficients not bounded and KamLAND can provide a better constraint.

While searches for  $0\nu\beta\beta$  decay remain the most sensitive probes of  $|\Delta L| = 2$  processes, they can only probe NP in the electron sector (as there must be two outgoing electrons). In the context of the non-standard charged-current neutrino NSIs,  $0\nu\beta\beta$  decay is only sensitive to  $(\epsilon_{ee}, \epsilon_{e\mu}, \epsilon_{e\tau})$ , but not the other flavour coefficients. Other  $|\Delta L| = 2$  processes involving SM fermions not in the first generation may instead shed light on different NP scenarios. An interesting process which may provide complementary sensitivity is the LFV and  $|\Delta L| = 2$  conversion of captured muons in nuclei,  $\mu^- + (Z, A) \rightarrow e^+ + (Z - 2, A)$ . Proposed by Pontecorvo in Ref. [74], it has gained recent interest due to the upcoming searches for the  $|\Delta L| = 0$  muon conversion  $\mu^- + (Z, A) \rightarrow e^- + (Z, A)$  by the COMET and Mu2e experiments, which aim to increase the experimental sensitivity by  $\mathcal{O}(10^4)$  [375, 376]. While it is doubtful that the current limit  $R_{\mu e}^{\text{Ti}} \lesssim 10^{-11}$  [377] on the alternative  $|\Delta L| = 2$  rate can also be improved due to different background considerations [378],  $\mu^- - e^+$  conversion is an important complementary probe to  $0\nu\beta\beta$  decay.

To estimate the sensitivity of the  $\mu^- - e^+$  conversion process on the neutrino NSI coefficients considered in this chapter, we follow the estimate in Ref. [370]. In

this approach, and using our notation, the conversion rate is approximated as

$$R_{\mu e} \approx |\xi_{\mu e}|^2 \frac{G_F^2 Q^6}{2 q^2}; \quad |\xi_{\mu e}|^2 \equiv \left| \sum_i (U_{ei}^* \gamma_{ui} + U_{\mu i}^* \gamma_{ei}) \right|^2, \quad (3.48)$$

where  $q \approx 100$  MeV is the momentum scale of the intermediate neutrino in the process and  $Q \approx 15.6$  MeV is the energy release of the emitted positron [379]. The effective parameter  $\xi_{\mu e}$  can be expanded as

$$\begin{aligned} |\xi_{\mu e}|^2 = & \sum_{\lambda} \left( F_{e\lambda} \varepsilon_{\mu\lambda}^2 + F_{\mu\lambda} \varepsilon_{e\lambda}^2 \right) \\ & + \sum_{\lambda > \lambda'} \left( G_{e\lambda\lambda'} \varepsilon_{\mu\lambda} \varepsilon_{\mu\lambda'} + G_{\mu\lambda\lambda'} \varepsilon_{e\lambda} \varepsilon_{e\lambda'} \right). \end{aligned} \quad (3.49)$$

The two terms in the first line of Eq. (3.49) account for the neutrino NSI being at the interaction vertex of the incoming  $\mu^-$  or the outgoing  $e^+$  (the latter being shown in Fig. 3.8). The difference between the two diagrams is the exchange  $U_{ei}^* \gamma_{\mu i} \leftrightarrow U_{\mu i}^* \gamma_{ei}$ .

Because the process is incoherent and can result in excited nuclear final states,  $Q$  also approximately includes the nuclear matrix element of this transition. The relevant nuclear matrix elements have not been calculated in detail and Eq. (3.48) can only be regarded as an estimate of the conversion rate. Nevertheless, using the experimental limit  $R_{\mu e}^{\text{Ti}} \lesssim 10^{-11}$ , we estimate a limit on  $|\xi_{\mu e}|$  of order  $|\xi_{\mu e}| \lesssim 10^4$ . This limit corresponds to a LEFT effective operator scale of  $\Lambda_{\text{NP}} = (|\xi_{\mu e}| G_F)^{-1/2} \approx 3 \text{ GeV} > q$ , pushing the validity of the EFT approach. Even with the most optimistic future sensitivity of  $R_{\mu e} \lesssim 10^{-16}$  [379], the coefficient  $|\xi_{\mu e}|$  will only be probed at  $|\xi_{\mu e}| \sim 30$  which corresponds to a scale  $\Lambda_{\text{NP}} \sim 50 \text{ GeV}$ .

We summarise the constraints on the coefficients  $\varepsilon_{\mu e}$ ,  $\varepsilon_{\mu\mu}$  and  $\varepsilon_{\mu\tau}$  (with each of the other coefficients is set to zero) in Table 3.2. These limits are also of order  $|\varepsilon_{\mu\lambda}| \lesssim 10^4$ . However, we see that the coefficients  $\varepsilon_{\mu\mu}$  and  $\varepsilon_{\mu\tau}$  are unbounded for particular values of  $(\alpha_2, \alpha_3)$ . The factors preceding  $\varepsilon_{\mu\lambda}^2$  in Eq. (3.49) are  $F_{e\lambda}$ , and therefore the dependences on  $(\alpha_2, \alpha_3)$  for the  $\mu^- - e^+$  upper bounds are identical to those from  $0\nu\beta\beta$  decay in Fig. 3.9 (except being weaker by a factor of  $\sim 10^{12}$ ). We can see from Eq. (3.49) that  $\mu^- - e^+$  conversion also probes the coefficients  $\varepsilon_{ee}$ ,

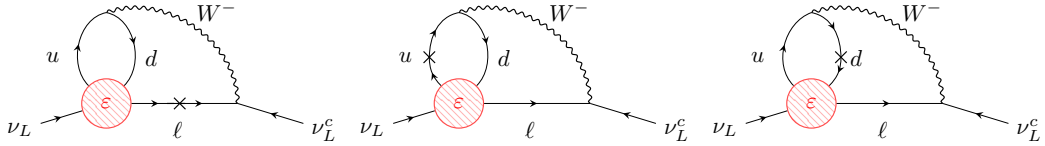


**Figure 3.10:** Contributions of the  $|\Delta L| = 2$  neutrino NSIs at dim-6 to the light neutrino mass at two loops. The diagrams are for operators with coefficients  $\epsilon_{RL}^V$  (left),  $\epsilon_{RL}^S$  (centre) and  $\epsilon_{RR}^S/\epsilon_{RR}^T$  (right).

$\epsilon_{e\mu}$  and  $\epsilon_{e\tau}$ , but sets bounds weaker than  $0\nu\beta\beta$  decay by a factor of  $10^{12}$ .

Searches for rare  $|\Delta L| = 2$  meson decays such as  $K^\pm \rightarrow \pi^\mp \mu^\pm \mu^\pm$  and  $B^+ \rightarrow D^- \mu^+ \mu^+$  and rare  $\tau$  decays such as  $\tau^- \rightarrow \pi^- \pi^- \mu^+$  are also able to probe the neutrino NSI coefficients considered in this chapter, as well as  $\epsilon_{\tau e}$ ,  $\epsilon_{\tau \mu}$  and  $\epsilon_{\tau \tau}$  [329, 380, 381]. However, at present the bounds on the rates of these processes are similar or worse than the bounds on  $\mu^- - e^+$  conversion. We then emphasise the main result of this chapter; comparing the constraints on the coefficients  $\epsilon_{\mu e}$ ,  $\epsilon_{\mu \mu}$  and  $\epsilon_{\mu \tau}$  in Table 3.2, we see that the constraints from MINOS (and similar future LBL oscillation experiments) are currently far more stringent than searches for microscopic  $|\Delta L| = 2$  processes.

So far we have only focused on the constraints from the non-observation of  $|\Delta L| = 2$  processes; in general, however,  $|\Delta L| = 2$  neutrino NSIs can be constrained alongside the  $|\Delta L| = 0$  NSIs by processes that are insensitive to lepton number, such as the beta decays of neutrons and nuclei,  $2\nu\beta\beta$  decay and charged pion decays (where the outgoing neutrinos are not detected). For these processes, the angular distributions for left- and right-handed currents can be different. Limits are set on the electron flavour coefficients of order  $|(\epsilon_{XY}^V)_{e\lambda}|, |(\epsilon_{XY}^S)_{e\lambda}|, |(\epsilon_{XX}^T)_{e\lambda}| \lesssim 10^{-3} - 10^{-2}$  [300–303]. Both  $|\Delta L| = 0$  and  $|\Delta L| = 2$  charged-current neutrino NSIs can also lead to single electron and missing energy signatures at colliders and deviations from CKM unitarity [382–384].

To conclude this discussion, we briefly mention the contribution of the dim-6  $|\Delta L| = 2$  charged-current neutrino NSIs in Eq. (3.26) to the light active neutrino masses. In Ref. [270], the radiative contributions of odd-dimensional operators in the SMEFT to the left-handed neutrino Majorana mass matrix  $M_L$  were estimated.

In Refs. [385, 386], the two-loop radiative contributions of the  $|\Delta L| = 2$  operators in Eq. (3.26) to the light Majorana neutrino masses was found to be

$$\delta m_\nu^{\text{2-loop}} \approx \frac{3g^2 G_F \epsilon_{RY}^{\circ}}{(16\pi^2)^2} m_\psi m_W^2 \ln^2 \left( \frac{\mu^2}{m_W^2} \right), \quad (3.50)$$

where  $\epsilon_{RY}^{\circ} \in \{\epsilon_{RL}^V, \epsilon_{RL}^S, \epsilon_{RR}^S, \epsilon_{RR}^T\}$ . The corresponding two-loop diagrams are shown in Fig. 3.10. For each operator, a mass insertion  $m_\psi$  is required for one of the quark or charged lepton legs. For example, the vector-type operator with coefficient  $\epsilon_{RL}^V$  contains a right-handed charged-lepton field. A mass insertion is needed to connect this with a left-handed charged lepton field which couples with the  $W^\pm$  boson. The vector-type operator with coefficient  $\epsilon_{RR}^V$  requires a mass insertion on all internal fermion lines and therefore its contribution to  $\delta m_\nu^{\text{2-loop}}$  is suppressed. A limit can be placed on the neutrino NSI coefficients by requiring that the radiative neutrino mass not exceed the cosmological upper bound on the sum of neutrino masses  $\sum m_\nu \lesssim 0.12$  eV. This conservatively gives the bounds  $|\epsilon_{RL}^V| \lesssim 10^{-2}$  and  $|\epsilon_{RL}^S|, |\epsilon_{RR}^S|, |\epsilon_{RR}^T| \lesssim 10^{-3}$  [387].

To conclude this chapter, we have studied the effect of  $|\Delta L| = 2$  charged-current neutrino NSIs on long-baseline neutrino oscillations. If the light active neutrinos are of Majorana fermions the  $|\Delta L| = 2$  oscillation process  $\nu_\alpha \rightleftharpoons \bar{\nu}_\beta$  become possible, either via the standard ‘helicity-flip’ process or a  $|\Delta L| = 2$  right-handed interaction at production or detection. These dim-6 LEFT operators can be matched to dim-7 (and above) operators in the SMEFT.

We first reviewed the derivations of neutrino oscillations  $\nu_\alpha \rightleftharpoons \nu_\beta$  in QM and QFT; the latter framework takes into account the coherence of overlapping wave packets at production and detection. We showed that there is a stringent  $(m_\nu/E_\nu)^2$  suppression for the helicity-flip of Majorana neutrinos, and that the total rate in this case cannot be factorised into a production flux, oscillation probability and detection cross section. With a non-standard right-handed leptonic current at one of the interaction vertices, we demonstrated that a non-standard oscillation probability  $P_{\nu_\alpha \rightarrow \bar{\nu}_\beta}$  can be factorised out from the total rate of the process. We derived this probability in Eq. (3.33) and showed that the  $(m_\nu/E_\nu)^2$  suppression is replaced by

a factor of  $|\varepsilon|^2$ , where  $\varepsilon$  parametrises the strength of the  $|\Delta L| = 2$  neutrino NSI compared to the Fermi coupling  $G_F$ .

Using a bound made by the MINOS experiment on the  $\nu_\mu \rightarrow \bar{\nu}_\mu$  process, we put limits on the  $\varepsilon$  flavour coefficients in the case of right-handed vector leptonic current at detection. In the  $2\nu$  mixing approximation (which is roughly valid for accelerator LBL experiments such as MINOS) we derived upper bounds on the absolute values of the coefficients  $(\varepsilon_{\mu\mu}, \varepsilon_{\mu\tau})$ , shown in Table 3.1. The upper bounds depend on the value of the single Majorana phase  $\eta$ . We also studied the sensitivity of a future MINOS-like experiment at a different baseline. We next generalised the to the full  $3\nu$  scheme, using the best fit values for the mixing parameters and the MINOS bound to constrain the  $(\varepsilon_{\mu e}, \varepsilon_{\mu\mu}, \varepsilon_{\mu\tau})$  parameter space as a function of the Majorana phases  $(\alpha_2, \alpha_3)$ . Similarly, we used a KamLAND bound on the number of solar  $\bar{\nu}_e$  from the source of solar  ${}^8\text{B}$   $\nu_e$  to place constraints on the  $(\varepsilon_{ee}, \varepsilon_{e\mu}, \varepsilon_{e\tau})$  parameter space. We raised the possibility of a future OPERA-like experiment constraining the  $(\varepsilon_{\tau e}, \varepsilon_{\tau\mu}, \varepsilon_{\tau\tau})$  parameter space.

We discussed some of the constraints on these coefficients derived from the non-observation of other  $|\Delta L| = 2$  processes. We compared the KamLAND constraints to those from  $0\nu\beta\beta$  decay ( ${}^{76}\text{Ge}$ ). While  $0\nu\beta\beta$  decay still provides the most stringent bound on  $|\varepsilon_{ee}|$ , for particular values of the Majorana phases  $(\alpha_2, \alpha_3)$  the coefficients  $|\varepsilon_{e\mu}|$  and  $|\varepsilon_{e\tau}|$  become unbounded. Similarly,  $\mu^- - e^+$  conversion sets very loose bounds on the same coefficients as MINOS. The upper bounds from MINOS are more stringent for all values of the Majorana phases  $(\alpha_2, \alpha_3)$ .

## Chapter 4

# Neutrino-Mediated Long-Range Forces

In this chapter we will investigate the impact of neutral-current neutrino NSIs on long-range forces. Four fundamental forces have been observed so far in nature, corresponding to the strong, weak and electromagnetic forces of the broken SM gauge group  $SU(3)_c \times SU(2)_L \times U(1)_Y \xrightarrow{\text{EWSB}} SU(3)_c \times U(1)_Q$ , and gravity. In QFT, the first three of these forces are understood as the exchange of virtual particles (gluons,  $W^\pm$ ,  $Z$  bosons and photons, respectively) between interacting states. The *graviton* is the postulated spin-2 mediator of gravity [388–391].

Forces are characterised by their potentials  $V(r)$ , which can be derived in QFT and depend on the mass and gauge interactions of the mediator. For example, the photon is massless and neutral under  $U(1)_Q$  and thus the Coulomb potential falls off with the distance  $r$  as  $V_C(r) = \frac{q_1 q_2}{4\pi r}$  where  $q_i = eQ_i$  are the particle charges. The theorised graviton is likewise massless which reproduces the observed gravitational potential  $V_G(r) = -\frac{Gm_1 m_2}{r}$  where  $m_i$  are the particle masses and  $G$  is Newton's gravitational constant. Potentials that scale with an inverse power of the distance between interacting states describe *long-range* forces. The gluons, on the other hand, are charged under  $SU(3)_c$  and therefore self-interacting, leading to the confinement of quarks in hadrons. The associated potential increases with the distance as  $V_{\text{QCD}}(r) \propto r$ . The  $W^\pm$  and  $Z$  bosons are massive and usually much heavier than the energy exchange between the interacting states. The result is a potential

$V_{\text{weak}}(r) \propto \frac{1}{r} e^{-mr}$ , which scales as  $\frac{1}{r}$  at distances below the Compton wavelength of the mediator  $r \sim \frac{1}{m}$ , but is exponentially-suppressed above this distance. These are often called *short-range* forces.

There may exist *additional* forces beyond the four fundamental forces. These are generically induced by the exchange of a new spin-0 or spin-1 boson between SM fermions. For example, axions (spin-0), dark photons and light  $Z'$  bosons (both spin-1) are potential candidates for the mediator of an exotic *fifth* force. A variety of experimental methods, which we will review later in this chapter, are being used to search for the effects of such a fifth force [392–431]. The exchange of a fermion (spin- $\frac{1}{2}$ ) between two interacting states is forbidden by Lorentz invariance and the conservation of angular momentum. However, the exchange of *two* fermions can ensure that the quantum numbers of the interacting particles are unchanged, and can potentially lead to a long-range force if the fermions are light.

The neutrinos in the SM are massless and can only interact with the other SM fermions via the charged- and neutral-current weak interactions, described at low energy by Fermi’s effective interaction. Thus, the long-range force mediated by two *massless* neutrinos was first mooted by Feynman to be gravity [432]. However, the neutrino-mediated force was studied in proper in Ref. [433] which found a long-range potential of the form  $V(r) = \frac{G_F^2}{4\pi^3 r^5}$ , falling off too fast with the distance to be the gravitational potential. This work only considered the charged-current neutrino interaction, which must be Fierz-transformed to bring it into an useful form for the calculation. The contribution of SM neutral-current interactions was included in Ref. [434] and the dependence on the interacting particle velocity  $v$  (calculated to first order) in Ref. [435]. In all of these calculations the neutrinos were assumed to be massless.

In Ref. [436], the neutrino-mediated potential was determined for either Dirac or Majorana massive neutrinos, where now the potential falls off exponentially as  $V(r) \propto e^{-2m_\nu r}$  above a distance  $r \sim \frac{1}{2m_\nu}$  (for a single neutrino of mass  $m_\nu = 0.1$  eV,  $r \sim 1$   $\mu\text{m}$ ). Below this cut-off, the Dirac and Majorana neutrino potentials both scale as  $V(r) \propto \frac{1}{r^5}$ . Above the cut-off the Dirac and Majorana neutrino potentials

depend differently on the distance (in addition to the exponential suppression). This picture was extended to the mixing of three neutrinos in Refs. [437, 438] for the spin-independent part of the force.

Recently, improvements in the precision of atomic and nuclear spectroscopy experiments has encouraged studies of their sensitivity to fifth forces [439–443]. Ref. [444] in particular examines the ability of spectroscopy measurements to probe the neutrino-mediated force. In Refs. [442, 445], it was discussed how the Dirac and Majorana neutrino-mediated potentials can be distinguished at long distances. In order to make this distinction, the former suggests tests (specifically, searches for violations) of the weak equivalence principle (the notion that the only long-range force felt by an electrically neutral object is gravity) and the latter measurements of a neutrino-induced Casimir force between two plates.

Given the significant progress made in the literature, it seems desirable to have a systematic analysis of all possible realisations of the neutrino-mediated force. In particular, a model-independent approach for parametrising both the SM prediction for the neutrino-mediated potential and also non-standard variations of this exchange. For example, one could consider non-standard right-handed vector, scalar and tensor interactions instead of the SM Fermi interaction. It is also important to characterise the spin-independent and spin-dependent parts of the SM and non-standard neutrino-mediated potentials. This is especially important for atomic and nuclear spectroscopy, where the spin-dependent part of a potential plays a crucial role [444]. To add to this, the model-independent approach should take into account the neutrino masses and mixings, allowing for both Dirac and Majorana neutrinos which are known give different predictions at long distance.

The neutral-current neutrino NSIs of relevance to this chapter are therefore in Tables 2.5 and 2.8, or written in Eq. (2.92) in the usual parametrisation (normalised to  $G_F$ ). The Majorana case corresponds to the operators in Table 2.5; a right-handed current in Eq. (2.92) picks out the charge-conjugate of the left-handed neutrino field  $v_L^c = \mathcal{C}v_L^\top$ . The Dirac case corresponds to the  $|\Delta L| = 0$  operators in Tables 2.5 and 2.8; there are  $n_S = 3$  fields  $N_R$  (or  $v_R$ ) corresponding to the right-handed

component of a Dirac spinor  $\nu$ . One could also include the neutral-currents of additional heavy Majorana neutrinos  $N = N^c$ , described by Eq. (2.99), but these will not be considered further in this chapter.

We begin this chapter by reviewing in Section 4.1 the derivation of a potential in QFT, setting up a framework to derive the long-range potential mediated by a pair of neutrinos. We next outline our parametrisation for neutral-current type neutrino NSIs in Section 4.2 and discuss the necessary steps to go from quark fields to hadronic fields using chiral perturbation theory. We will also outline the current bounds on the NSI coefficients from charged Lepton Flavour Violation (cLFV), neutrino-electron scattering, neutrino-nucleon scattering, beta decays and LEP data. In Section 4.3 we derive the neutrino-mediated potential for SM charged- and neutral-current interactions. In Section 4.4.1 derive the potentials when one or both of the neutrino currents are right-handed. In Section 4.4.2 we introduce scalar interactions and derive the vector-scalar and scalar-scalar potentials. In Section 4.4.3 we consider tensor interactions, determining the vector-tensor potential. We will also examine in Section 4.4.4 the potential when the neutrinos have non-standard electromagnetic properties. We derive each potential for Dirac and Majorana neutrinos, examining the dependence on the distance in the short and long-range limits and on the spins of the external states. Finally, we will study the phenomenology of the spin-independent and spin-dependent terms in atomic and nuclear laboratory experiments, setting upper bounds on the coefficients of NSIs and comparing these to those from other processes such as cLFV. This chapter is based on the work of Ref. [142].

## 4.1 Deriving a Long-Range Potential

In the QFT framework, a force resulting in the scattering of two on-shell particles can be interpreted as the exchange of one (or multiple) virtual mediator(s). As depicted to the left of Fig. 4.1, one or more mediators are required to exchange the momentum  $q = p_\alpha - p'_\alpha = p'_\beta - p_\beta$  between two interacting particles  $\psi_\alpha$  and  $\psi'_\beta$  with initial momenta  $p_\alpha$  and  $p_\beta$  and final momenta  $p'_\alpha$  and  $p'_\beta$ , respectively.

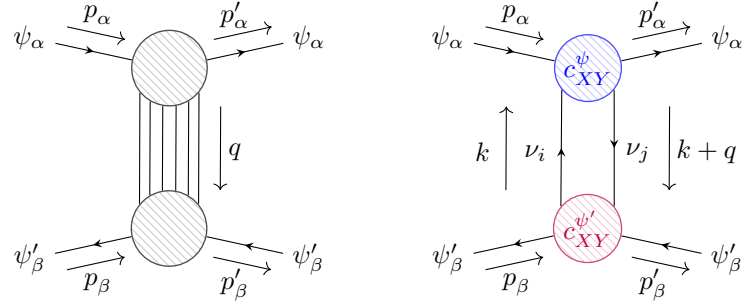


**Figure 4.1:** (Left) Long-range force mediated between fermions  $\psi_\alpha$  and  $\psi'_\beta$  by virtual mediators carrying the momentum  $q = p_\alpha - p'_\alpha = p'_\beta - p_\beta$ . (Right) The exchange of two mass-eigenstate neutrinos between fermions  $\psi_\alpha$  and  $\psi'_\beta$ . The interaction vertices are four-fermion interactions with coefficients  $(c_{XY}^\psi)_{ij;\alpha\alpha}$  and  $(c_{XY}^{\psi'})_{ij;\beta\beta}$  respectively, where the superscripts  $X, Y \in \{L, R\}$  refer to the chirality of the neutrino and fermion currents.

In the Feynman-diagrammatic approach it is possible to derive a long-range potential  $V(\mathbf{r}, \mathbf{v})$  for an interaction, which is generally a function of the relative displacement between the particles  $\mathbf{r}$  and the average velocity of the system,

$$\mathbf{v} = \frac{1}{2} \left( \frac{\mathbf{p}_\alpha}{m_\alpha} + \frac{\mathbf{p}_\beta}{m_\beta} \right). \quad (4.1)$$

The potential can be computed by taking the Fourier transform of the invariant amplitude  $\mathcal{A}$  of the scattering process [446],

$$V(\mathbf{r}, \mathbf{v}) = \int \frac{d^3 \mathbf{q}}{(2\pi)^3} e^{i\mathbf{q} \cdot \mathbf{r}} \mathcal{A}(s, t), \quad (4.2)$$

where the invariant amplitude  $\mathcal{A}(s, t)$  is an analytic function of the Mandelstam variables  $s = P^2 = (p_\alpha + p_\beta)^2 = (p'_\alpha + p'_\beta)^2$  and  $t = q^2 = (p_\alpha - p'_\alpha)^2 = (p'_\beta - p_\beta)^2$ . The potential  $V(\mathbf{r}, \mathbf{v})$  is time-independent in the static limit of momentum transfer,  $q \approx (0, \mathbf{q})$  and  $t \approx -\mathbf{q}^2$ , which is a good approximation for particles interacting at a distance. Furthermore, one can also make use of the analyticity properties of  $\mathcal{A}(s, t)$  which enable the so-called spectral decomposition [434]

$$\mathcal{A}(s, -\mathbf{q}^2) = - \int_0^\infty dt' \frac{\rho(s, t')}{t' + \mathbf{q}^2}, \quad (4.3)$$

where  $\rho(s, t)$  is the *spectral function* of the process. The spectral function is related to the imaginary part of the *discontinuity* along the real  $t$ -axis of  $\mathcal{A}(s, t)$ ,

$$\rho(s, t) = \frac{1}{\pi} \Im[\mathcal{A}(s, t)] = \frac{1}{2\pi i} \text{dsc}[\mathcal{A}(s, t)], \quad (4.4)$$

where the discontinuity is defined as

$$\text{dsc}[\mathcal{A}(s, t)] = \mathcal{A}(s, t + i\epsilon) - \mathcal{A}(s, t - i\epsilon), \quad (4.5)$$

for  $\epsilon \rightarrow 0$ . It is now possible to insert the spectral decomposition of Eq. (4.3) into Eq. (4.2) and integrate over the angular variables  $d\Omega = \sin \theta d\theta d\phi$  contained in  $d^3\mathbf{q}$ . This integration is non-trivial if  $\mathcal{A}(s, t)$  and therefore  $\rho(s, t)$  are functions of  $\theta$  and  $\phi$ . For example, the angular dependence is non-trivial if there are spin-dependent terms containing the dot product of  $\mathbf{q}$  and a particle spin  $\boldsymbol{\sigma}$ . Such terms arise after taking the non-relativistic limit of the scattering amplitude. The non-relativistic limit is convenient when examining the long-range interactions between two particles in, for example, an atomic system, and we will make use of it later in this chapter.

We therefore follow the approach of Ref. [447] and decompose the general spectral function  $\rho(t)$  (omitting the  $s$  dependence) according to a complete basis of 16 spin-dependent operators that may arise when the non-relativistic limit of the scattering amplitude is taken,

$$\rho(t) = \sum_{k=1}^{16} \rho_k(t) O_k(\mathbf{q}, \mathbf{P}) f_k(\mathbf{v}^2), \quad (4.6)$$

where  $f_k(\mathbf{v}^2)$  are polynomials in powers of  $\mathbf{v}^2$  corresponding to higher order terms in the non-relativistic expansion. The operators  $O_k(\mathbf{q}, \mathbf{P})$  are a complete basis of operators constructed from the three-momenta  $\mathbf{q}$  and  $\mathbf{P}$  and the interacting particle spins  $\mathbf{s}_\alpha = \boldsymbol{\sigma}_\alpha/2$  and  $\mathbf{s}_\beta = \boldsymbol{\sigma}_\beta/2$  (where  $\boldsymbol{\sigma}$  is a vector of Pauli matrices) given in Appendix B. Combining Eqs. (4.2), (4.3) and (4.6), the potential  $V(\mathbf{r}, \mathbf{v})$  can also be

written as

$$V(\mathbf{r}, \mathbf{v}) = \sum_{k=1}^{16} \mathcal{V}_k(\mathbf{r}, \mathbf{v}) f_k(\mathbf{v}^2), \quad (4.7)$$

where the spin-dependent potentials are

$$\mathcal{V}_k(\mathbf{r}, \mathbf{v}) = - \int \frac{d^3 \mathbf{q}}{(2\pi)^3} e^{i\mathbf{q} \cdot \mathbf{r}} \int_0^\infty dt' \frac{\rho_k(t') O_k(\mathbf{q}', \mathbf{P})}{t' + \mathbf{q}^2}, \quad (4.8)$$

and the variable  $t' = -(\mathbf{q}')^2$  is integrated over  $dt'$  while  $\mathbf{q}$  is integrated over  $d^3 \mathbf{q}$ .

The potentials  $\mathcal{V}_k(\mathbf{r}, \mathbf{v})$  can be computed by first evaluating the integral in Eq. (4.8) without the spin operator  $O_k$  and multiplying by a single power of  $r$ ,

$$\mathcal{V}'_k(r) \equiv -r \int \frac{d^3 \mathbf{q}}{(2\pi)^3} e^{i\mathbf{q} \cdot \mathbf{r}} \int_0^\infty dt' \frac{\rho_k(t')}{t' + \mathbf{q}^2} = \frac{1}{4\pi} \int_0^\infty dt \rho_k(t) e^{-r\sqrt{t}}, \quad (4.9)$$

where in the second equality we have integrated over  $|\mathbf{q}|$ ,  $\theta$  and  $\phi$  and relabelled the dummy variable  $t'$  as  $t$ . As outlined in Ref. [447], the potentials  $\mathcal{V}_k(r)$  are finally computed by applying derivatives to the  $\mathcal{V}'_k(r)$  functions. We have for the operators  $O_1 = \mathbb{1}$ ,  $O_2 = \boldsymbol{\sigma}_\alpha \cdot \boldsymbol{\sigma}_\beta$  and  $O_3 = (\boldsymbol{\sigma}_\alpha \cdot \mathbf{q})(\boldsymbol{\sigma}_\beta \cdot \mathbf{q})$  which will be the most important in this chapter,

$$\begin{aligned} \mathcal{V}_1(r) &= \frac{1}{r} O_1 \mathcal{V}'_1(r), \\ \mathcal{V}_2(r) &= \frac{1}{r} O_2 \mathcal{V}'_2(r), \\ \mathcal{V}_3(r) &= \frac{1}{r^3} \left[ O_2 \left( 1 - r \frac{d}{dr} \right) - 3O_3 \left( 1 - r \frac{d}{dr} + \frac{r^2}{3} \frac{d^2}{dr^2} \right) \right] \mathcal{V}'_3(r). \end{aligned} \quad (4.10)$$

## 4.2 Neutral-Current Neutrino NSIs

We will now outline the parametrisation of neutral-current neutrino NSIs to be used in this chapter, which arise at  $\text{dim-6}$  in the LEFT. We write Eq. (2.92) as

$$\begin{aligned} \mathcal{L}_{\text{NC}}^{(6)} = -\frac{4G_F}{\sqrt{2}} \Big\{ & c_{XY}^\psi (\bar{v} \gamma^\mu P_X v) (\bar{\psi} \gamma_\mu P_Y \psi) + g_{XY}^\psi (\bar{v} P_X v) (\bar{\psi} P_Y \psi) \\ & + h_{XX}^\psi (\bar{v} \sigma^{\mu\nu} P_X v) (\bar{\psi} \sigma_{\mu\nu} P_X \psi) \Big\}, \end{aligned} \quad (4.11)$$

where  $c_{XY}^\psi$ ,  $g_{XY}^\psi$  and  $h_{XX}^\psi$  are the coefficients of the vector-, scalar- and tensor-type neutral-currents, with  $X, Y \in \{L, R\}$  and  $\psi \in \{\ell, u, d\}$ . In the following we drop the superscripts  $\psi$  when they are not needed explicitly. The currents in Eq. (4.11) are thus the combinations  $(V \pm A)$ ,  $(S \pm P)$  and  $(T \pm \tilde{T})$ , rather than separating out the scalar and pseudoscalar currents as in the standard parametrisation. The relations between the  $\varepsilon'$  coefficients and  $c_{XY}$ ,  $g_{XY}$  and  $h_{XX}$  are given in Appendix A. The fields in Eq. (4.11) are written in the flavour basis and so the coefficients have four flavour indices, i.e.  $(c_{XY}^\psi)_{\rho\sigma;\alpha\beta} (\bar{v}_\rho \gamma^\mu P_X v_\sigma) (\bar{\psi}_\alpha \gamma_\mu P_Y \psi_\beta)$ . As mentioned previously, the right-handed projector  $P_R$  selects out  $v_R$  in the Dirac case and  $v_L^c$  in the Majorana case. As stated below Eq. (2.92), the Dirac or Majorana scenario determines the number of free parameters contained in the NSI coefficients. The relationships between  $c_{XY}$ ,  $g_{XY}$  and  $h_{XX}$  summarised in Appendix A.

In the Majorana case there are the important relations

$$(c_{LL})_{\rho\sigma;\alpha\beta} = -(c_{RL})_{\sigma\rho;\alpha\beta}, \quad (c_{LR})_{\rho\sigma;\alpha\beta} = -(c_{RR})_{\sigma\rho;\alpha\beta}, \quad (4.12)$$

which mean that the  $c_{RL}$  and  $c_{RR}$  coefficients can be eliminated. Thus, the vector-type neutral-current neutrino NSIs can only be  $|\Delta L| = 0$ . Conversely, the relations  $(g_{LL})_{\rho\sigma;\alpha\beta} = (g_{RR})_{\sigma\rho;\alpha\beta}^*$ ,  $(g_{LR})_{\rho\sigma;\alpha\beta} = (g_{RL})_{\sigma\rho;\alpha\beta}^*$  and  $(h_{LL})_{\rho\sigma;\alpha\beta} = (h_{RR})_{\sigma\rho;\alpha\beta}^*$  imply that the scalar- and tensor-type neutral-current neutrino NSIs can only be  $|\Delta L| = 2$ . The additional Majorana neutrino relations  $(g_{XY})_{\rho\sigma;\alpha\beta} = (g_{XY})_{\sigma\rho;\alpha\beta}$  and  $(h_{XX})_{\rho\sigma;\alpha\beta} = -(h_{XX})_{\sigma\rho;\alpha\beta}$  imply that there are six independent  $(g_{XY})_{\rho\sigma;\alpha\beta}$  coefficients and three independent  $(h_{XX})_{\rho\sigma;\alpha\beta}$  coefficients (the diagonal elements vanish).

Unlike our parametrisation of the charged-current neutrino NSIs in Eq. (3.26), where we explicitly isolated the SM charged-current interaction, in Eq. (4.11) the SM contributions are contained implicitly in the coefficients  $c_{LL}$  and  $c_{LR}$ . For charged leptons ( $\psi = \ell$ ) both charged- and neutral-current SM weak interactions contribute to  $c_{LL}$  (through an appropriate Fierz transformation of the charged-current term), while only the neutral-current interaction contributes to  $c_{LR}$ . For the up- and down-type quarks ( $\psi = u, d$ ) only the neutral-current SM interaction

contributes to  $c_{LL}$  and  $c_{LR}$ . We will write down these contributions shortly.

So far we have kept the coefficients  $c_{XY}$ ,  $g_{XY}$  and  $h_{XX}$  in the flavour basis of neutrino and fermion fields. We will follow the convention that the charged lepton and up-type quark Yukawa matrices  $Y_\ell$  and  $Y_u$  are diagonal. In the Dirac case, the diagonalisation of the neutrino and down-type quark Yukawa matrices proceed via the biunitary transformations  $V_L^{V^\dagger} Y_v V_R^V = Y'_v$  and  $V_L^{d^\dagger} Y_d V_R^d = Y'_d$ . The  $V_L^V$ ,  $V_R^V$ ,  $V_L^d$  and  $V_R^d$ , matrices rotate the left- and right-handed up-type quark and neutrino fields according to

$$d_L = V_L^d d'_L, \quad d_R = V_R^d d'_R, \quad v_L = V_L^V v'_L, \quad v_R = V_R^V v'_R, \quad (4.13)$$

where the unprimed fields denote flavour eigenstates and the primed fields mass eigenstates. Neutrino mass eigenstates are labelled with the indices  $i$  or  $j$ . The matrices  $V_L^V \equiv U$  and  $V_L^d \equiv V$  then correspond to the PMNS and CKM mixing matrices, respectively. The matrices  $V_R^V \equiv \tilde{U}$  and  $V_R^d \equiv \tilde{V}$  do not appear in any SM interaction; while the right-handed fields  $d_R$  are present in the SM neutral-current, the matrix  $\tilde{V}$  cancels in the bilinear  $\bar{u}_R \gamma^\mu u_R$  if it is unitary. Furthermore, the fields  $v_R$  are sterile under the SM and  $\tilde{V}$  and  $\tilde{U}$  are usually taken to be unphysical. They will, on the other hand, make an appearance for some of the operators in Eq. (4.11) after rotating from the flavour to mass basis. In the Majorana case we instead have the redefinition  $U^\top M_L U = m_v$  for the neutrino fields (assuming the  $3 \times 3$  effective Majorana mass matrix  $M_L$  is generated by physics at a high scale). For example, in the seesaw scenario we have  $v_L = \Omega P_L n'$ , where  $n' = (v_1 \ v_2 \ v_3 \ N_1 \ \dots)^\top$  can contain heavy Majorana states. For simplicity, we can assume that the active-sterile mixings are negligible and  $v_L \approx U P_L v'$  where  $v' = (v_1 \ v_2 \ v_3)^\top$ .

In the Dirac case, one can choose to define the coefficients  $c_{XY}$ ,  $g_{XY}$  and  $h_{XX}$  in the mass basis by absorbing the  $U$ ,  $V$ ,  $\tilde{U}$  and  $\tilde{V}$  matrices into the flavour basis coefficients. For example, the coefficient  $c_{LL}$  is given in the mass basis by

$$(c_{LL}^\psi)_{ij;\alpha\beta} = \sum_{\rho,\sigma} \sum_{\gamma,\delta} U_{\rho i}^* U_{\sigma j} V_{\gamma\alpha}^* V_{\delta\beta} (c_{LL}^\psi)_{\rho\sigma;\gamma\delta} \quad (4.14)$$

where the  $V_{\gamma\alpha}^* V_{\delta\beta}$  factor is only present for  $\psi = d$ . On the other hand the coefficient  $c_{RR}$  is written in the mass basis as

$$(c_{RR}^\psi)_{ij;\alpha\beta} = \sum_{\gamma,\delta} \sum_{\rho,\sigma} \tilde{U}_{\rho i}^* \tilde{U}_{\sigma j} \tilde{V}_{\gamma\alpha}^* \tilde{V}_{\delta\beta} (c_{RR}^\psi)_{\rho\sigma;\gamma\delta}, \quad (4.15)$$

which now contains the right-handed rotation matrices  $\tilde{U}$  and  $\tilde{V}$  (the  $\tilde{V}$  factors are again only present for  $\psi = d$ ). However, there is a redundancy in Eq. (4.15) because there is more than one unknown parameter on the right-hand side. The unknown mixing angles and phases in  $\tilde{V}$  and  $\tilde{U}$  can instead be absorbed into the  $c_{RR}$  matrix in the flavour basis, which is equivalent to setting  $\tilde{U} = \tilde{V} = \mathbb{1}$  from the start. In the Majorana case the transformation of the coefficients  $c_{LL}$  and  $c_{LR}$  is similar to that above. For the scalar and tensor coefficients, e.g.  $g_{LL}$ ,

$$(g_{LL}^\psi)_{ij;\alpha\beta} = \sum_{\rho,\sigma} \sum_{\gamma,\delta} U_{\rho i} U_{\sigma j} V_{\gamma\alpha}^* V_{\delta\beta} (g_{LL}^\psi)_{\rho\sigma;\gamma\delta}, \quad (4.16)$$

where now the combination of PMNS mixing matrix elements  $U_{\rho i} U_{\sigma j}$  can contain Majorana phases. However, these can also be absorbed into the coefficient  $g_{LL}$  on the right-hand side. If we are considering a seesaw mechanism, the active-sterile mixings have been neglected in Eq. (4.16). However,  $U$  can in principle be replaced with the  $3 \times N$  matrix  $\Omega$  and  $i, j \in \{1, \dots, N\}$ .

In both the Dirac and Majorana cases, the coefficients  $c_{LL}$  and  $c_{RL}$  (in the mass basis) get contributions from the SM charged- and neutral-current interactions of

$$\begin{aligned} (c_{LL}^\ell)_{ij;\alpha\beta} &= U_{\alpha i}^* U_{\beta j} + 2\delta_{ij} \delta_{\alpha\beta} g_L^v g_L^\ell, & (c_{LR}^\ell)_{ij;\alpha\beta} &= 2\delta_{ij} \delta_{\alpha\beta} g_L^v g_R^\ell, \\ (c_{LL}^u)_{ij;\alpha\beta} &= 2\delta_{ij} \delta_{\alpha\beta} g_L^v g_L^u, & (c_{LR}^u)_{ij;\alpha\beta} &= 2\delta_{ij} \delta_{\alpha\beta} g_L^v g_R^u, \\ (c_{LL}^d)_{ij;\alpha\beta} &= 2\delta_{ij} \delta_{\alpha\beta} g_L^v g_L^d, & (c_{LR}^d)_{ij;\alpha\beta} &= 2\delta_{ij} \delta_{\alpha\beta} g_L^v g_R^d. \end{aligned} \quad (4.17)$$

where the  $g_{L(R)}^\psi$  are the combinations  $(T^3 - s_W^2 Q)$  given in Table 2.2 and we have assumed the unitarity of the matrices  $U$ ,  $V$  and  $\tilde{V}$ . We have neglected possible active-sterile mixings in the Majorana case, but in general we can make the replacements  $U \rightarrow \Omega$  and  $\delta_{ij} \rightarrow C_{ij}$  where  $C_{ij} = \sum_\rho \Omega_{\rho i}^* \Omega_{\rho j}$  and  $i, j \in \{1, \dots, N\}$ . The

matrices  $c_{LL}$  and  $c_{LR}$  are now  $N \times N$  matrices in the mass basis.

For the low energies relevant to long-range neutrino exchange, the quarks are confined within non-relativistic nucleons (protons and neutrons), which are in turn bound within nuclei. The quark currents in the neutral-current NSI Lagrangian of Eq. (4.11) can be matched onto non-relativistic nucleon currents using heavy baryon Chiral Perturbation Theory ( $\chi$ PT) as detailed in Refs. [297, 448, 449]. This is a general framework to match the quark-level coefficients (e.g.  $c_{LL}^u$  and  $c_{LL}^d$ ) to non-relativistic nucleon coefficients at some order in the power counting scheme, i.e. a power of the ratio  $q/\Lambda_\chi$  where  $\Lambda_\chi \sim 1$  GeV is the chiral symmetry breaking scale. The effective theory is therefore only viable when the relevant momentum exchange  $q$  of the long-range force is below the cut-off scale  $\Lambda_\chi \sim 1$  GeV. At leading order in  $\chi$ PT, the light pseudoscalar meson masses are of order  $m_\pi \sim O(q)$  and neutrinos only interact with a single nucleon. Interactions of neutrinos with more than one nucleon (for example, both the proton and neutron in deuterium) are suppressed by powers of  $q/\Lambda_\chi$ .

Following the approach of Ref. [297], we write the coefficients for the neutrino NSIs at the nucleon-level in terms of the quark-level coefficients as

$$\begin{aligned} c_{LL}^{\mathcal{N}} &= \frac{1}{2} \sum_q \left\{ F_1^{q/\mathcal{N}}(q^2) (c_{LL}^q + c_{LR}^q) + F_A^{q/\mathcal{N}}(q^2) (c_{LL}^q - c_{LR}^q) \right\}, \\ c_{LR}^{\mathcal{N}} &= \frac{1}{2} \sum_q \left\{ F_1^{q/\mathcal{N}}(q^2) (c_{LL}^q + c_{LR}^q) - F_A^{q/\mathcal{N}}(q^2) (c_{LL}^q - c_{LR}^q) \right\}, \end{aligned} \quad (4.18)$$

where the sum is over the  $q \in \{u, d, s\}$  quarks and  $F_1^{q/\mathcal{N}}(q^2)$  and  $F_A^{q/\mathcal{N}}(q^2)$  are respectively the neutral-current vector and axial vector form factors for the quark  $q$  within the nucleon or nucleus  $\mathcal{N}$ . For the proton, the following linear combinations at zero-momentum exchange ( $q^2 = 0$ ) are given in the SM by

$$(c_{LL}^p)_{ij} + (c_{LR}^p)_{ij} \equiv g_V^p \delta_{ij}, \quad (c_{LL}^p)_{ij} - (c_{LR}^p)_{ij} \equiv g_A^p \delta_{ij}, \quad (4.19)$$

where  $g_V^p \approx (2g_V^u + g_V^d)$  and  $g_A^p \approx g_A(2g_A^u + g_A^d)$ . Here  $g_V^\psi = g_L^\psi + g_R^\psi$ ,  $g_A^\psi = g_L^\psi - g_R^\psi$  and  $g_A \approx 1.27$  is the nucleon axial vector coupling. To derive Eq. (4.19) we have

used that  $F_1^{u/p}(0) = 2$ ,  $F_1^{d/p}(0) = 1$ ,  $F_A^{u/p}(0) = 2g_A$  and  $F_A^{d/p}(0) = g_A$  and neglected the small contribution from non-valence quarks. Likewise we have for the deuteron

$$(c_{LL}^D)_{ij} + (c_{LR}^D)_{ij} \equiv g_V^D \delta_{ij}, \quad (c_{LL}^D)_{ij} - (c_{LR}^D)_{ij} \equiv g_A^D \delta_{ij}, \quad (4.20)$$

where  $g_V^D \approx 3(g_V^u + g_V^d)$  and  $g_A^D \approx F_A^{s/D}(0)g_A^d$ . To derive this we have used that the vector form factors for the valence quarks in the deuteron are  $F_1^{u/D}(0) = F_1^{d/D}(0) = 3$ . The equivalent axial form factors vanish,  $F_1^{u/D}(0) = F_1^{d/D}(0) = 0$ , and the main contribution arises from strange quarks. The strange quark deuteron form factor is determined in  $\chi$ PT to be

$$F_A^{s/D}(0) \approx 2\Delta s \left( 1 - \frac{g_A^2 m_D m_\pi^2}{4\pi f_\pi^2 (m_\pi + 2\gamma)} \right) - \frac{8\gamma(\mu - \gamma)^2}{m_D \mu^2} \sim -0.09, \quad (4.21)$$

where  $\gamma = \sqrt{m_D E_D}$  [450]. Here  $\Delta s$  is the strange axial moment of the deuteron,  $m_D$  is the deuteron mass,  $E_D$  is the deuteron binding energy,  $m_\pi$  is the neutral pion mass and  $f_\pi$  is the pion decay constant. We take the renormalisation scale  $\mu$  to be at the neutral pion mass  $m_\pi$ .

In the SM, the left-handed neutrino fields  $\nu_L$  are components of the  $SU(2)_L$  doublets  $L_L = (\nu_L \ \ell_L)^\top$ , with the charged leptons as their partners. The neutrino NSIs in Eq. (4.11) containing  $\nu_L$  must therefore be matched onto SMEFT operators containing  $L_L$  doublets. For NP at some high scale  $\Lambda_{\text{NP}}$ , the resulting SMEFT operators that generate the neutral-current neutrino NSIs (and thus the neutrino-mediated potentials studied in this chapter) can also induce cLFV processes, which are highly constrained [291, 451–453]. The cLFV decays  $\mu \rightarrow e\gamma$ ,  $\mu \rightarrow 3e$  and  $\tau \rightarrow 3e$ , and  $\mu^- - e^-$  conversion in nuclei are particularly relevant probes as they are subject to precision searches at ongoing and upcoming experiments. The decays of tau leptons into a lepton and light mesons,  $\tau \rightarrow e\rho$  and  $\tau \rightarrow e\eta$ , are also relevant because the associated bounds are expected to be improved by Belle II [454]. It should be noted that the neutrino NSIs can be generated by higher-dimensional SMEFT operators that do not induce cLFV at tree-level. For example, the neutrino NSI with coefficient  $c_{LL}$  can be matched to dim-6 or dim-8 SMEFT operators. However, even if

NSI Coefficient	cLFV Process	> $ c_{LY}^{\psi} $	
		$Y = L$	$Y = R$
$(c_{LY}^{\ell})_{\mu e;ee}$	$\mu \rightarrow 3e$	$7.8 \times 10^{-7}$	$9.3 \times 10^{-7}$
$(c_{LY}^u)_{\mu e;uu}$	$\mu^- - e^-$ , Au	$6.0 \times 10^{-8}$	$6.3 \times 10^{-8}$
$(c_{LY}^d)_{\mu e;dd}$	$\mu^- - e^-$ , Au	$5.3 \times 10^{-8}$	$5.4 \times 10^{-8}$
$(c_{LY}^{\ell})_{\tau e;ee}$	$\tau \rightarrow 3e$	$2.8 \times 10^{-4}$	$4.0 \times 10^{-4}$
$(c_{LY}^{\ell})_{\tau \mu;ee}$	$\tau \rightarrow \mu e \bar{e}$	$3.2 \times 10^{-4}$	$3.2 \times 10^{-4}$
$(c_{LY}^q)_{\tau e;qq}$	$\tau \rightarrow e \rho$ , $\tau \rightarrow e \eta$	$7.1 \times 10^{-4}$	$7.1 \times 10^{-4}$
$(c_{LY}^q)_{\tau \mu;qq}$	$\tau \rightarrow \mu \rho$ , $\tau \rightarrow \mu \eta$	$5.9 \times 10^{-4}$	$5.9 \times 10^{-4}$

**Table 4.1:** Bounds on neutral-current neutrino NSI coefficients  $c_{LY}^{\psi}$  for  $\psi \in \{\ell, u, d\}$  and  $Y \in \{L, R\}$  from the current best limits from cLFV experiments. For the bottom two coefficients  $q \in \{u, d\}$ .

the chosen SMEFT operator does not induce tree-level cLFV, the RG runnings and mixings of operators at one-loop (from  $\Lambda_{\text{NP}}$  down to the EW scale) ensures that tree-level cLFV operators are always present. In Table 4.1 we display the limits on the vector-type neutral-current neutrino NSI coefficients  $c_{LY}$  that can be derived from the non-observation of cLFV processes [453].

One point to note regarding these limits is that the relevant cLFV processes occur at the energy scales of the decaying muon and tau lepton masses. The LEFT framework (or neutrino NSI Lagrangian in Eq. (4.11)) must therefore be valid at these energy scales; the NSI coefficients are sensitive to NP scales heavier than  $m_{\mu}$  and  $m_{\tau}$ . The neutrino-mediated exchange process considered in this chapter can take place at an energy scale corresponding to the inverse Bohr radius  $a_0^{-1} = \alpha m_e \approx \mathcal{O}(10)$  keV (for atomic-scale measurements) or scales as small as the neutrino masses  $m_{\nu} \sim \mathcal{O}(\text{eV})$  (for macroscopic forces). The LEFT framework, in this case, is sensitive to much lighter NP scales. It is then possible to explore NP scenarios where new light degrees of freedom couple to neutrinos and other SM fermions.

The neutrino NSI coefficients of first and second-generation leptons are also also subject to direct bounds from scattering processes such as  $\nu_{\mu} e$  scattering in CHARM-II [455, 456] (which will be improved by an order of magnitude at

the DUNE near detector [353]) and neutrino-nucleon scattering at CHARM and CDHS [296, 455, 456]. The NSI coefficients for tau leptons are bounded by  $e\bar{e} \rightarrow \nu\bar{\nu}\gamma$  data at LEP where the flavour of the outgoing neutrino is not measured [457]. These bounds are unfortunately orders of magnitude weaker compared to the cLFV bounds [292, 301, 457–460]. In addition, the observation of Coherent Elastic Neutrino-Nucleus Scattering (CEvNS) at COHERENT [461, 462] can also place bounds on the scalar and tensor coefficients  $g_{XY}$  and  $h_{XX}$  [289].

### 4.3 Standard Model Neutrino Potential

We start by deriving the potential  $V_{\alpha\beta}^{LL}(r)$  arising from the exchange of two neutrinos between the interacting fermions  $\psi_\alpha$  and  $\psi'_\beta$ . We restrict the interactions to SM charged- and neutral-currents, as shown in Fig. 4.2. We determine the amplitude  $\mathcal{A}_{\alpha\beta}$  (and the corresponding spectral function  $\rho_{\alpha\beta}$ ) by integrating out the  $W^\pm$  and  $Z$  bosons and using the neutrino NSI Lagrangian of Eq. (4.11). The exchange of a  $W^\pm$  boson can only occur for interacting charged leptons while  $Z$  boson exchange is possible for both charged leptons and quarks (within a nucleon/nucleus  $\mathcal{N}$ ). Both  $W^\pm$  and  $Z$  exchange contribute to the coefficient  $c_{LL}$  while only  $Z$  exchange contributes to  $c_{LR}$ . The SM values for these were given in Eq. (4.17).

Using the appropriate Feynman rules from the neutrino NSI Lagrangian of Eq. (4.11), we can write the invariant amplitude of the scattering process in Fig. 4.1 (right) as

$$-i\mathcal{A}_{\alpha\beta} = \frac{1}{4m_\alpha m_\beta} \left( -i \frac{4G_F}{\sqrt{2}} \right)^2 \sum_{i,j} \sum_{X,Y} (c_{LX}^\psi)_{ij;\alpha} (c_{LY}^{\psi'})_{ij;\beta} \mathcal{H}_{\mu\nu}^{\alpha\beta} \mathcal{N}_{ij}^{\mu\nu}, \quad (4.22)$$

where  $\frac{1}{4m_\alpha m_\beta}$  is a normalisation factor commonly used in the non-relativistic limit [434]. The amplitude contains the sum over the neutrino mass eigenstates,  $i, j \in \{1, 2, 3\}$  (or  $i, j \in \{1, \dots, N\}$  if there are  $n_S$  additional Dirac or Majorana states). It also contains the sum over the possible chiralities  $X, Y \in \{L, R\}$  of the interacting fermions. We are interested in scattering processes where the flavours of the interacting fermions do not change, i.e  $(c_{XY}^\psi)_{ij;\alpha\alpha} \equiv (c_{XY}^\psi)_{ij;\alpha}$ .

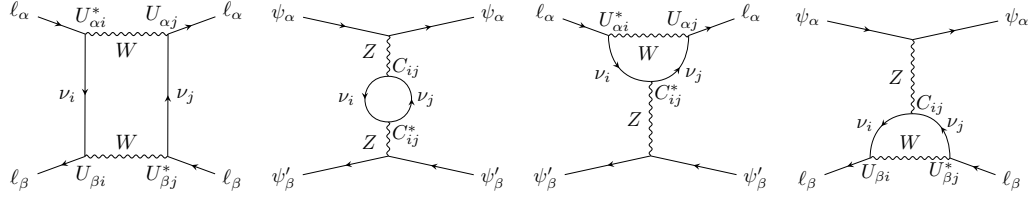


**Figure 4.2:** The exchange of two massive neutrinos  $\nu_i$  and  $\nu_j$  between fermions  $\psi_\alpha$  and  $\psi'_\beta$  with SM charged- and neutral-current interactions at each vertex. The charged-current interactions are only possible for  $\psi = \ell$ .

The amplitude in Eq. (4.22) is split conveniently into the factors  $\mathcal{H}_{\mu\nu}^{\alpha\beta}$  and  $\mathcal{N}_{ij}^{\mu\nu}$ . The first factor is the product of external fermion bilinears

$$\mathcal{H}_{\mu\nu}^{\alpha\beta} = [\bar{u}_{s'_\alpha}(\mathbf{p}'_\alpha) \gamma_\mu P_X u_{s_\alpha}(\mathbf{p}_\alpha)][\bar{u}_{s'_\beta}(\mathbf{p}'_\beta) \gamma_\nu P_Y u_{s_\beta}(\mathbf{p}_\beta)] \equiv [\gamma_\mu P_X]_\alpha [\gamma_\nu P_Y]_\beta, \quad (4.23)$$

where  $u_{s_\alpha}(\mathbf{p}_\alpha)$  and  $u_{s_\beta}(\mathbf{p}_\beta)$  are the incoming four-component Dirac spinors for the fermions  $\psi_\alpha$  and  $\psi'_\beta$  (or nucleon  $\mathcal{N}$ ) and  $P_X$  and  $P_Y$  are the usual chirality projection operators with  $X, Y \in \{L, R\}$ . The Dirac spinors  $u_{s'_\alpha}(\mathbf{p}'_\alpha)$  and  $u_{s'_\beta}(\mathbf{p}'_\beta)$  are for the outgoing fermions.

The second factor is a loop integral over the product of massive neutrino propagators. For Dirac neutrinos,

$$\mathcal{N}_{ij}^{\mu\nu} = \int \frac{d^4 k}{(2\pi)^4} \frac{\text{Tr}[\gamma^\mu P_L(\not{q} + \not{k} + m_j) \gamma^\nu P_L(\not{k} + m_i)]}{(k^2 - m_i^2)((q + k)^2 - m_j^2)}, \quad (4.24)$$

where  $k$  is the loop momentum. For Majorana neutrinos the vector part of the neutrino current vanishes and the axial vector is a factor of two larger than in the Dirac case. The neutrino loop factor  $\mathcal{N}_{ij}^{\mu\nu}$  is now

$$\mathcal{N}_{ij}^{\mu\nu} = \frac{1}{2} \times 4 \int \frac{d^4 k}{(2\pi)^4} \frac{\text{Tr}[\gamma^\mu \gamma_5(\not{q} + \not{k} + m_j) \gamma^\nu \gamma_5(\not{k} + m_i)]}{(k^2 - m_i^2)((q + k)^2 - m_j^2)}, \quad (4.25)$$

where the factor of  $\frac{1}{2}$  takes into account the permutation symmetry of the Majorana neutrinos in the loop.

We will now use the method of Section 4.1 to calculate the potential for this exchange process. Using Eq. (4.4), we first compute the spectral function by taking

the discontinuity of  $\mathcal{A}_{\alpha\beta}$ . The discontinuity for the Dirac loop integral,

$$\text{dsc}(\mathcal{N}_{ij}^{\mu\nu}) = \frac{\Lambda^{1/2}(q^2, m_i^2, m_j^2)}{12\pi} \left\{ -\left(1 - \frac{\overline{m_{ij}^2}}{q^2} - \frac{(\Delta m_{ij}^2)^2}{2q^4}\right) g^{\mu\nu} \right. \\ \left. + \left(1 + \frac{2\overline{m_{ij}^2}}{q^2} - \frac{2(\Delta m_{ij}^2)^2}{q^4}\right) \frac{q^\mu q^\nu}{q^2} \right\} \Theta(q^2 - (m_i + m_j)^2), \quad (4.26)$$

where  $\Theta(x)$  is the Heaviside step function,  $\overline{m_{ij}^2} = (m_i^2 + m_j^2)/2$  is the average of the squares of the neutrino masses,  $\Delta m_{ij}^2 = m_i^2 - m_j^2$  is mass-squared difference and  $\Lambda(x, y, z)$  is the Källén function,  $\Lambda(x, y, z) = x^2 + y^2 + z^2 - 2xy - 2yz - 2zx$ . To compute the spectral function we must now contract  $\mathcal{H}_{\mu\nu}^{\alpha\beta}$  with  $\text{dsc}(\mathcal{N}_{ij}^{\mu\nu})$ . The Lorentz indices of  $\mathcal{H}_{\mu\nu}^{\alpha\beta}$  either contract with  $g^{\mu\nu}$  in  $\text{dsc}(\mathcal{N}_{ij}^{\mu\nu})$  to give  $[\gamma_\mu P_X]_\alpha [\gamma^\mu P_Y]_\beta$  or with  $q^\mu q^\nu$  to give  $[\not{q} P_X]_\alpha [\not{q} P_Y]_\beta$ .

We now assume that the external fermions are *non-relativistic*. In this limit it is possible to replace  $[\gamma_\mu P_X]_\alpha [\gamma^\mu P_Y]_\beta$  and  $[\not{q} P_X]_\alpha [\not{q} P_Y]_\beta$  with the lowest-order terms in the non-relativistic expansion in  $\mathbf{q}/m_\alpha$  and  $\mathbf{q}/m_\beta$ . Appendix B.1 lists the lowest-order terms for bilinear products such as  $[\gamma_\mu]_\alpha [\gamma^\mu]_\beta$ ,  $[\gamma_\mu]_\alpha [\gamma^\mu \gamma_5]_\beta$  and  $[\not{q} \gamma_5]_\alpha [\not{q} \gamma_5]_\beta$ . The terms that dominate the spectral function are proportional to  $4m_\alpha m_\beta$ , therefore cancelling the  $\frac{1}{4m_\alpha m_\beta}$  normalisation factor in the amplitude. Higher-order terms in the expansion are suppressed by powers of  $\mathbf{q}/m_\alpha$  and can be neglected.

Assembling these different components, we can now write the spectral function

$$\rho_{\alpha\beta}^{LL}(t) = -\frac{G_F^2}{\pi m_\alpha m_\beta} \sum_{i,j} \sum_{X,Y} (c_{LX}^\psi)_{ij;\alpha} (c_{LY}^{\psi'})_{ij;\beta} \mathcal{H}_{\mu\nu}^{\alpha\beta} \text{dsc}(\mathcal{N}_{ij}^{\mu\nu}). \quad (4.27)$$

Inserting Eqs. (4.26) and (4.23) into Eq. (4.27) and taking the non-relativistic limit, we obtain to lowest-order

$$\rho_{\alpha\beta}^{LL, D(M)}(t) = \frac{G_F^2}{12\pi^2} \sum_{i,j} \Theta(t - (m_i + m_j)^2) \Lambda^{\frac{1}{2}}(t, m_i^2, m_j^2) \\ \times \left\{ \left[ (X_{LL}^{\psi\psi'})_{ij;\alpha\beta} - (Y_{LL}^{\psi\psi'})_{ij;\alpha\beta} (\boldsymbol{\sigma}_\alpha \cdot \boldsymbol{\sigma}_\beta) \right] F_{ij}^{D(M)}(t) \right. \\ \left. - (Y_{LL}^{\psi\psi'})_{ij;\alpha\beta} (\boldsymbol{\sigma}_\alpha \cdot \mathbf{q}) (\boldsymbol{\sigma}_\beta \cdot \mathbf{q}) F_{ij}^V(t) \right\}, \quad (4.28)$$

where we explicitly see spin-independent and spin-dependent terms. This spectral function is valid for both Dirac (D) and Majorana (M) neutrinos. The factors  $X_{LL}^{\psi\psi'}$  and  $Y_{LL}^{\psi\psi'}$  are the following combinations of the NSI coefficients,

$$(X_{LL}^{\psi\psi'})_{ij;\alpha\beta} = (c_{LL}^{\psi} + c_{LR}^{\psi})_{ij;\alpha} (c_{LL}^{\psi'} + c_{LR}^{\psi'})_{ij;\beta}^*, \quad (4.29)$$

$$(Y_{LL}^{\psi\psi'})_{ij;\alpha\beta} = (c_{LL}^{\psi} - c_{LR}^{\psi})_{ij;\alpha} (c_{LL}^{\psi'} - c_{LR}^{\psi'})_{ij;\beta}^*, \quad (4.30)$$

Inserting the SM values of the coefficients in Eq. (4.17) and assuming a unitary light neutrino mixing matrix  $U$  such that  $C_{ij} = \delta_{ij}$ , these factors for charged leptons ( $\psi, \psi' = \ell$  and  $\alpha, \beta \in \{e, \mu, \tau\}$ ) are for example

$$(X_{LL}^{\ell\ell})_{ij;\alpha\beta} = (U_{\alpha i}^* U_{\alpha j} + g_V^\ell \delta_{ij}) (U_{\beta i}^* U_{\beta j} + g_V^\ell \delta_{ij})^*, \quad (4.31)$$

$$(Y_{LL}^{\ell\ell})_{ij;\alpha\beta} = (U_{\alpha i}^* U_{\alpha j} + g_A^\ell \delta_{ij}) (U_{\beta i}^* U_{\beta j} + g_A^\ell \delta_{ij})^*. \quad (4.32)$$

The functions  $F_{ij}^D$ ,  $F_{ij}^M$  and  $F_{ij}^V$  in Eq. (4.28) are given by

$$F_{ij}^D(t) = 1 - \frac{\overline{m_{ij}^2}}{t} - \frac{(\Delta m_{ij}^2)^2}{2t^2}, \quad (4.33)$$

$$F_{ij}^M(t) = 1 - \frac{\overline{m_{ij}^2} + 3m_i m_j}{t} - \frac{(\Delta m_{ij}^2)^2}{2t^2}, \quad (4.34)$$

$$F_{ij}^V(t) = \frac{1}{t} \left( 1 + \frac{2\overline{m_{ij}^2}}{t} - \frac{2(\Delta m_{ij}^2)^2}{t^2} \right). \quad (4.35)$$

The distinction between the Dirac (D) and Majorana (M) cases is reflected in the different functions  $F_{ij}^{D(M)}$  multiplying the term in square brackets in Eq. (4.28). The Majorana function  $F_{ij}^M$  contains an additional term  $\frac{-3m_i m_j}{t}$ . This corresponds to the helicity-suppressed process of two neutrinos (with negative helicity) being created and two ‘antineutrinos’ (neutrinos with positive helicity) being annihilated, usually referred to as a ‘helicity-flip’. This process is not possible for Dirac neutrinos as the right-handed fields  $\nu_R$  are sterile under the SM gauge group; one would need to introduce a right-handed current to make the process possible.

As in Eq. (4.6), the spectral function of Eq. (4.28) can be split into terms mul-

tiplying the spin operators  $O_1 = \mathbb{1}$ ,  $O_2 = \boldsymbol{\sigma}_\alpha \cdot \boldsymbol{\sigma}_\beta$  and  $O_3 = (\boldsymbol{\sigma}_\alpha \cdot \mathbf{q})(\boldsymbol{\sigma}_\beta \cdot \mathbf{q})$ . To determine the overall potential  $V_{\alpha\beta}^{LL}(r)$ , we evaluate the integral over  $t$  in Eq. (4.9) for each of these three terms. We then take the appropriate derivatives in Eq. (4.10) to derive the three potentials  $\mathcal{V}_k^{LL}(r)$  ( $k = 1, 2, 3$ ) and add these to obtain

$$V_{\alpha\beta}^{LL, D(M)}(r) = \frac{G_F^2}{4\pi^3 r^5} \sum_{i,j} \left\{ (X_{LL}^{\psi\psi'})_{ij;\alpha\beta} I_{ij}^{D(M)}(r) - (Y_{LL}^{\psi\psi'})_{ij;\alpha\beta} \left[ (\boldsymbol{\sigma}_\alpha \cdot \boldsymbol{\sigma}_\beta) J_{ij}^{D(M)}(r) - (\boldsymbol{\sigma}_\alpha \cdot \hat{\mathbf{r}})(\boldsymbol{\sigma}_\beta \cdot \hat{\mathbf{r}}) J_{ij}^V(r) \right] \right\}, \quad (4.36)$$

where  $\hat{\mathbf{r}} = \mathbf{r}/|\mathbf{r}|$  is the unit displacement vector between the interacting fermions and the integral functions  $I_{ij}^{D(M)}(r)$ ,  $J_{ij}^{D(M)}(r)$  and  $J_{ij}^V(r)$  are given in Appendix B.2. These functions are defined to be dimensionless so that the dimensionful factor  $\frac{G_F^2}{4\pi^3 r^5}$  can be taken out of the sum. The potential therefore naively scales with the distance as  $\frac{1}{r^5}$ , though we will see that this behaviour changes in the long-range limit. The variation between the Dirac and Majorana cases is reflected in the functions  $I_{ij}^{D(M)}(r)$  and  $J_{ij}^{D(M)}(r)$  appearing in Eq. (4.36).

The SM neutrino-mediated potential in Eq. (4.36) is simplified when only a single massive neutrino  $\nu$  of mass  $m_\nu$  is considered. Firstly, the mixing factors in  $(X_{LL}^{\psi\psi'})_{ij;\alpha\beta}$  and  $(Y_{LL}^{\psi\psi'})_{ij;\alpha\beta}$  have the replacements  $U_{\alpha i}^* U_{\alpha j} \rightarrow 1$  and  $\delta_{ij} \rightarrow 1$ ; in the case of two interacting charged leptons we have  $(X_{LL}^{\ell\ell})_{\nu;\alpha\beta} = (1 + g_V^\ell)^2$  and  $(Y_{LL}^{\ell\ell})_{\nu;\alpha\beta} = (1 + g_A^\ell)^2$ . Secondly, the integral functions  $I_{ij}^D(r)$ ,  $I_{ij}^M(r)$  and  $I_{ij}^V(r)$  take the closed-forms

$$I_\nu^D(r) = m_\nu^3 r^3 K_3(2m_\nu r), \quad (4.37)$$

$$I_\nu^M(r) = 2m_\nu^2 r^2 K_2(2m_\nu r), \quad (4.38)$$

$$I_\nu^V(r) = 2m_\nu r K_1(2m_\nu r) + \frac{\pi^2}{2} m_\nu^2 r^2 G_{2,4}^{2,0} \left( m_\nu^2 r^2 \left| \begin{smallmatrix} \frac{1}{2}, \frac{3}{2} \\ 0, 0, \frac{1}{2}, \frac{1}{2} \end{smallmatrix} \right. \right) + 2\pi m_\nu^3 r^3, \quad (4.39)$$

where the  $K_n(x)$  are modified Bessel functions of the second kind and  $G_{p,q}^{m,n}$  is the Meijer G-function [463, 464]. Using the relations in Appendix B.2, the functions  $J_\nu^D(r)$ ,  $J_\nu^M(r)$  and  $J_\nu^V(r)$  can also be determined. For interacting charged leptons, the

spin-independent parts of the Dirac and Majorana potentials become

$$V_{\alpha\beta}^{LL,D}(r) = \frac{G_F^2 m_\nu^3 (1 + g_V^\ell)^2}{4\pi^3 r^2} K_3(2m_\nu r), \quad (4.40)$$

$$V_{\alpha\beta}^{LL,M}(r) = \frac{G_F^2 m_\nu^2 (1 + g_V^\ell)^2}{2\pi^3 r^3} K_2(2m_\nu r), \quad (4.41)$$

respectively, in agreement with previous results [438].

The functions in Eqs. (4.37)–(4.39) depend on the product  $2m_\nu r$ ; therefore, given the behaviour of the modified Bessel functions  $K_n(x)$  in the limits  $x \ll 1$  and  $x \gg 1$ , the potential  $V_{\alpha\beta}^{LL}(r)$  displays contrasting behaviour in the limits  $r \ll r_\nu$  and  $r \gg r_\nu$ , where  $r_\nu = \frac{1}{2m_\nu}$  is half the Compton wavelength of the neutrino. In the *short-range* limit ( $r \ll r_\nu$ ) the exchanged neutrinos are relativistic and their masses can be neglected. Therefore the Dirac or Majorana nature of neutrinos cannot be probed. Explicitly, this is because the  $\frac{-3m_i m_j}{t}$  in the function  $F_{ij}^M(t)$  is suppressed, and so  $F_{ij}^D(t) \approx F_{ij}^M(t)$  and  $V_{\alpha\beta}^{LL,D}(r) \approx V_{\alpha\beta}^{LL,M}(r)$ . In the *long-range* limit ( $r \gg r_\nu$ ) the neutrinos are now non-relativistic and the Dirac and Majorana potentials become exponentially suppressed as  $V_{\alpha\beta}^{LL,D(M)}(r) \propto e^{-2m_\nu r}$ . The additional term  $\frac{-3m_i m_j}{t}$  in the function  $F_{ij}^M(t)$  due to the ‘helicity-flip’ process is no longer suppressed and thus the Dirac and Majorana potentials can in theory be distinguished.

To verify these statements quantitatively, we write the SM potential (4.36) for a single neutrino  $\nu$ . We then expand the functions in Eqs. (4.37)–(4.39) in the opposing limits  $r \ll r_\nu$  and  $r \gg r_\nu$ . For  $r \ll r_\nu$  we find to lowest order

$$V_{\alpha\beta}^{LL,D(M)}(r) \approx \frac{G_F^2}{4\pi^3 r^5} \left\{ (X_{LL}^{\psi\psi'})_{\nu;\alpha\beta} - (Y_{LL}^{\psi\psi'})_{\nu;\alpha\beta} \left[ \frac{3}{2}(\boldsymbol{\sigma}_\alpha \cdot \boldsymbol{\sigma}_\beta) - \frac{5}{2}(\boldsymbol{\sigma}_\alpha \cdot \hat{\mathbf{r}})(\boldsymbol{\sigma}_\beta \cdot \hat{\mathbf{r}}) \right] \right\}, \quad (4.42)$$

in both the Dirac and Majorana cases, confirming that the potentials are degenerate in this limit. The potentials scale with the distance as  $\frac{1}{r^5}$  up to half the neutrino Compton wavelength  $r_\nu$ . In the limit  $r \ll r_\nu$  we can also approximate the potential  $V_{\alpha\beta}^{LL,D(M)}(r)$  for three generations by neglecting the neutrino masses  $m_i$  and  $m_j$  in the integral functions  $I_{ij}^{D(M)}(r)$ ,  $J_{ij}^{D(M)}(r)$  and  $J_{ij}^V(r)$ . In this limit the functions tend

to the constant values  $I_{ij}^{\text{D(M)}}(r) \approx 1$ ,  $J_{ij}^{\text{D(M)}}(r) \approx \frac{3}{2}$  and  $J_{ij}^V(r) \approx \frac{5}{2}$  as outlined in Appendix B.2. It is then possible to relate the single and three generation parameters as

$$(X_{LL}^{\psi\psi'})_{v;\alpha\beta} = \sum_{i,j} (X_{LL}^{\psi\psi'})_{ij;\alpha\beta}, \quad (Y_{LL}^{\psi\psi'})_{v;\alpha\beta} = \sum_{i,j} (Y_{LL}^{\psi\psi'})_{ij;\alpha\beta}. \quad (4.43)$$

Expanding the potential in the opposing limit  $r \gg r_v$  gives in the Dirac case

$$V_{\alpha\beta}^{LL,\text{D}}(r) \approx \frac{G_F^2 m_v^{5/2} e^{-2m_v r}}{8\pi^{5/2} r^{5/2}} \left\{ (X_{LL}^{\psi\psi'})_{v;\alpha\beta} - (Y_{LL}^{\psi\psi'})_{v;\alpha\beta} \left[ (\boldsymbol{\sigma}_\alpha \cdot \boldsymbol{\sigma}_\beta) - 2(\boldsymbol{\sigma}_\alpha \cdot \hat{\mathbf{r}})(\boldsymbol{\sigma}_\beta \cdot \hat{\mathbf{r}}) \right] \right\}, \quad (4.44)$$

while in the Majorana case

$$V_{\alpha\beta}^{LL,\text{M}}(r) \approx \frac{G_F^2 m_v^{3/2} e^{-2m_v r}}{4\pi^{5/2} r^{7/2}} \left\{ (X_{LL}^{\psi\psi'})_{v;\alpha\beta} - (Y_{LL}^{\psi\psi'})_{v;\alpha\beta} \left[ \frac{3}{2}(\boldsymbol{\sigma}_\alpha \cdot \boldsymbol{\sigma}_\beta) - m_v r (\boldsymbol{\sigma}_\alpha \cdot \hat{\mathbf{r}})(\boldsymbol{\sigma}_\beta \cdot \hat{\mathbf{r}}) \right] \right\}. \quad (4.45)$$

In the Dirac case both the spin-independent and spin-dependent terms scale as  $\frac{e^{-2m_v r}}{r^{5/2}}$ . In the Majorana case the spin-independent and  $\boldsymbol{\sigma}_\alpha \cdot \boldsymbol{\sigma}_\beta$  terms scale as  $\frac{e^{-2m_v r}}{r^{7/2}}$ , while the  $(\boldsymbol{\sigma}_\alpha \cdot \hat{\mathbf{r}})(\boldsymbol{\sigma}_\beta \cdot \hat{\mathbf{r}})$  term scales as  $\frac{e^{-2m_v r}}{r^{5/2}}$ .

## 4.4 Non-Standard Neutrino Potentials

We will now consider neutrino-mediated potentials where the interactions between the neutrinos and interacting fermions can be any of the neutral-current neutrino NSIs in Eq. (4.11), i.e of vector type ( $c_{XY}$ ), scalar type ( $g_{XY}$ ) or tensor type ( $h_{XX}$ ). Assuming that the non-standard coefficients are suppressed by small couplings or physics at a high scale  $\Lambda_{\text{NP}}$ , we examine the first-order effect of a SM interaction ( $c_{LL}$  and  $c_{LR}$ ) at one vertex and a neutrino NSI at the other.

Finally, we note that the operators with coefficients  $(c_{LL})_{ij;\alpha\beta}$  and  $(c_{LR})_{ij;\alpha\beta}$  may also include the effects of new physics, which can be parametrised as small corrections  $(\delta c_{LL})_{ij;\alpha\beta}$  and  $(\delta c_{LR})_{ij;\alpha\beta}$  to the SM values of  $(c_{LL})_{ij;\alpha}$  and  $(c_{LR})_{ij;\alpha}$ .

We will assume that the NP does not change the flavour of the fermion, i.e.  $\alpha = \beta$ . Deviations from the SM potential  $V_{\alpha\beta}^{LL}(r)$  will therefore arise as corrections to the factors  $X_{LL}^{\psi\psi'}$  and  $Y_{LL}^{\psi\psi'}$ ,

$$(\delta X_{LL}^{\psi\psi'})_{ij;\alpha\beta} = (c_{LL}^\psi + c_{LR}^\psi)_{ij;\alpha} (\delta c_{LL}^{\psi'} + \delta c_{LR}^{\psi'})_{ij;\beta}^* + (\psi_\alpha \leftrightarrow \psi'_\beta), \quad (4.46)$$

$$(\delta Y_{LL}^{\psi\psi'})_{ij;\alpha\beta} = (c_{LL}^\psi - c_{LR}^\psi)_{ij;\alpha} (\delta c_{LL}^{\psi'} - \delta c_{LR}^{\psi'})_{ij;\beta}^* + (\psi_\alpha \leftrightarrow \psi'_\beta), \quad (4.47)$$

where we take into account that the correction will be at both the interaction vertices of  $\psi_\alpha$  and  $\psi'_\beta$  by adding  $(\psi_\alpha \leftrightarrow \psi'_\beta)$ .

#### 4.4.1 Right-Handed Vector Interactions

Motivated by theories such as left-right symmetric models, we now introduce the vector-type neutral-current neutrino NSIs with a right-handed neutrino current. In other words, we will now allow the coefficients  $c_{RL}$  and  $c_{RR}$  to be non-zero in Eq. (4.11). We will first derive the neutrino-mediated potential  $V_{\alpha\beta}^{LR}(r)$  induced by SM weak interactions at one vertex and a right-handed neutrino current at the other, shown in Fig. 4.3.

The spectral function  $\rho_{\alpha\beta}^{LR}(t)$  in this case is the same as Eq. (4.28) but with one coefficient replaced as  $c_{LX} \rightarrow c_{RX}$  and one chirality projection operator replaced as  $P_L \rightarrow P_R$  in the neutrino loop factor  $\mathcal{N}_{ij}^{\mu\nu}$ . We also add an identical contribution with  $(\psi_\alpha \leftrightarrow \psi'_\beta)$  to account for the right-handed current being either interaction vertex. If the external fermions are identical ( $\psi_\alpha = \psi'_\beta$ ) we must then multiply the spectral function by an additional factor of  $\frac{1}{2}$  to avoid double counting. We can account for this with the factor  $\mathcal{D}_{\alpha\beta} \equiv \frac{1}{(1 + \delta_{\psi\psi'} \delta_{\alpha\beta})}$ .

The discontinuity of the neutrino loop factor  $\mathcal{N}_{ij}^{\mu\nu}$  in the Dirac case is now

$$\text{dsc}(\mathcal{N}_{ij}^{\mu\nu}) = -\frac{\Lambda^{1/2}(t, m_i^2, m_j^2)}{4\pi} \frac{m_i m_j}{q^2} g^{\mu\nu} \Theta(q^2 - (m_i + m_j)^2), \quad (4.48)$$

which is now helicity-suppressed by the factor  $\frac{m_i m_j}{q^2}$  with respect to the SM case. This is because a negative helicity neutrino  $\nu_i$  created by the left-handed current will be annihilated by the right-handed current with an associated factor  $\frac{m_i}{q}$ . For

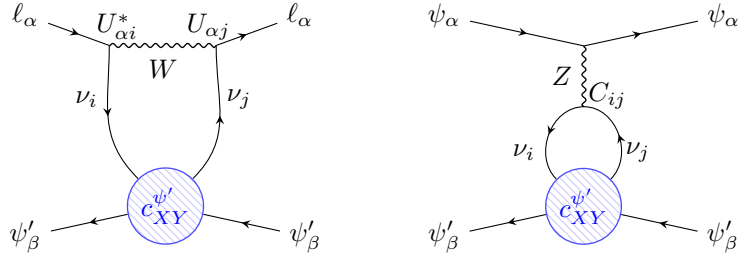


**Figure 4.3:** The exchange of two massive neutrinos between fermions  $\psi_\alpha$  and  $\psi'_\beta$  with SM charged- and neutral-current interactions at one vertex and a neutral-current neutrino NSI at the other. In our framework the effective interaction may be of vector ( $c_{XY}$ ), scalar ( $g_{XY}$ ) or tensor ( $h_{XX}$ ) type.

both neutrinos this results in  $\frac{m_i m_j}{q^2}$ .

Contracting the  $g^{\mu\nu}$  factor in Eq. (4.48) with the product of external fermion bilinears  $\mathcal{H}_{\mu\nu}^{\alpha\beta}$  we now obtain  $[\gamma_\mu P_X]_\alpha [\gamma^\mu P_Y]_\beta$ . Taking again the non-relativistic limit of the fermion bilinears, the following spectral function can be written in the Dirac case

$$\begin{aligned} \rho_{\alpha\beta}^{LR, D}(t) &= \frac{G_F^2}{4\pi^2} \mathcal{D}_{\alpha\beta} \sum_{i,j} \Theta(t - (m_i + m_j)^2) \Lambda^{1/2}(t, m_i^2, m_j^2) \\ &\quad \times \frac{m_i m_j}{t} \left\{ (X_{LR}^{\psi\psi'})_{ij;\alpha\beta} - (Y_{LR}^{\psi\psi'})_{ij;\alpha\beta} (\boldsymbol{\sigma}_\alpha \cdot \boldsymbol{\sigma}_\beta) \right\}, \end{aligned} \quad (4.49)$$

where the prefactors  $X_{LR}^{\psi\psi'}$  and  $Y_{LR}^{\psi\psi'}$  are

$$(X_{LR}^{\psi\psi'})_{ij;\alpha\beta} = (c_{LL}^\psi + c_{LR}^\psi)_{ij;\alpha} (c_{RL}^{\psi'} + c_{RR}^{\psi'})_{ij;\beta}^* + (\alpha, \beta), \quad (4.50)$$

$$(Y_{LR}^{\psi\psi'})_{ij;\alpha\beta} = (c_{LL}^\psi - c_{LR}^\psi)_{ij;\alpha} (c_{RL}^{\psi'} - c_{RR}^{\psi'})_{ij;\beta}^* + (\alpha, \beta). \quad (4.51)$$

where  $(\alpha, \beta)$  is shorthand for  $(\psi_\alpha \leftrightarrow \psi'_\beta)$ . Using the same approach as the previous section to derive the potential from the spectral function, we find in the Dirac scenario

$$\begin{aligned} V_{\alpha\beta}^{LR, D}(r) &= \frac{G_F^2}{8\pi^3 r^3} \mathcal{D}_{\alpha\beta} \sum_{i,j} m_i m_j \left\{ (X_{LR}^{\psi\psi'})_{ij;\alpha\beta} \right. \\ &\quad \left. - (Y_{LR}^{\psi\psi'})_{ij;\alpha\beta} (\boldsymbol{\sigma}_\alpha \cdot \boldsymbol{\sigma}_\beta) \right\} I_{ij}^{LR}(r), \end{aligned} \quad (4.52)$$

where the dimensionless function  $I_{ij}^{LR}(r)$  is given in Appendix B.2.

In the Majorana case we must be careful about the relations between coefficients  $c_{XY}$  discussed below Eq. (4.11). The right-handed neutrino current operator with coefficient  $(c_{RL})_{ij;\alpha\beta}$  is equivalent to the left-handed current operator with coefficient  $(c_{LL})_{ji;\alpha\beta}$ . This is also why vector currents vanish for Majorana neutrinos. The coefficient  $(c_{RL})_{ij;\alpha\beta}$  therefore gets the same contributions from the SM weak interactions as  $(c_{LL})_{ij;\alpha\beta}$  and the potential we derive is identical to Eq. (4.36). This is true only for  $i, j \in \{1, 2, 3\}$  and not for additional Majorana states.

It therefore makes sense to consider the corrections  $(\delta c_{LL})_{ij;\alpha} = -(\delta c_{RL})_{ji;\alpha}$  to the SM-valued coefficients  $(c_{LL})_{ij;\alpha} = -(c_{RL})_{ji;\alpha}$  from NP, as discussed at the start of this section. The correction to the spectral function is

$$\begin{aligned} \rho_{\alpha\beta}^{LR,M}(t) = & -\frac{G_F^2}{12\pi^2} \mathcal{D}_{\alpha\beta} \sum_{i,j=1}^3 \Theta(t - (m_i + m_j)^2) \Lambda^{1/2}(t, m_i^2, m_j^2) \\ & \times \left\{ \left[ (\delta X_{LR}^{\psi\psi'})_{ij;\alpha\beta} - (\delta Y_{LR}^{\psi\psi'})_{ij;\alpha\beta} (\boldsymbol{\sigma}_\alpha \cdot \boldsymbol{\sigma}_\beta) \right] F_{ij}^M(t) \right. \\ & \left. - (\delta Y_{LR}^{\psi\psi'})_{ij;\alpha\beta} (\boldsymbol{\sigma}_\alpha \cdot \mathbf{q}) (\boldsymbol{\sigma}_\beta \cdot \mathbf{q}) F_{ij}^V(t) \right\}, \end{aligned} \quad (4.53)$$

where  $(\delta X_{LR}^{\psi\psi'})_{ij;\alpha\beta} = -(\delta X_{LL}^{\psi\psi'})_{ji;\alpha\beta}$  and  $(\delta Y_{LR}^{\psi\psi'})_{ij;\alpha\beta} = -(\delta Y_{LL}^{\psi\psi'})_{ji;\alpha\beta}$  are given in Eq. (4.46). This gives the following potential

$$\begin{aligned} V_{\alpha\beta}^{LR,M}(r) = & -\frac{G_F^2}{4\pi^3 r^5} \mathcal{D}_{\alpha\beta} \sum_{i,j} \left\{ (\delta X_{LR}^{\psi\psi'})_{ij;\alpha\beta} I_{ij}^M(r) \right. \\ & \left. - (\delta Y_{LR}^{\psi\psi'})_{ij;\alpha\beta} \left[ (\boldsymbol{\sigma}_\alpha \cdot \boldsymbol{\sigma}_\beta) J_{ij}^M(r) - (\boldsymbol{\sigma}_\alpha \cdot \hat{\mathbf{r}}) (\boldsymbol{\sigma}_\beta \cdot \hat{\mathbf{r}}) J_{ij}^V(r) \right] \right\}. \end{aligned} \quad (4.54)$$

In order to study the properties of the potentials in Eqs. (4.52) and (4.54) we again use the single neutrino simplification. In this case the function  $I_{ij}^{LR}(r)$  takes the closed form

$$I_v^{LR}(r) = 2m_v r K_1(2m_v r). \quad (4.55)$$

In the short-range limit ( $r \ll r_\nu$ ) we can write the Dirac potential in Eq. (4.52) as

$$V_{\alpha\beta}^{LR,D}(r) = \frac{G_F^2 m_\nu^2}{8\pi^3 r^3} \mathcal{D}_{\alpha\beta} \left\{ (X_{LR}^{\psi\psi'})_{v;\alpha\beta} - (X_{LR}^{\psi\psi'})_{v;\alpha\beta} (\boldsymbol{\sigma}_\alpha \cdot \boldsymbol{\sigma}_\beta) \right\}. \quad (4.56)$$

For  $r \ll r_\nu$  we also have that  $I_{ij}^{LR}(r) \approx 1$  in Eq. (4.52) which enables the relations  $(X_{LR}^{\psi\psi'})_{v;\alpha\beta} = \sum_{i,j} (X_{LR}^{\psi\psi'})_{ij;\alpha\beta}$  and  $(Y_{LR}^{\psi\psi'})_{v;\alpha\beta} = \sum_{i,j} (Y_{LR}^{\psi\psi'})_{ij;\alpha\beta}$ . In the long-range limit ( $r \gg r_\nu$ ) we instead obtain

$$V_{\alpha\beta}^{LR,D}(r) = \frac{G_F^2 m_\nu^{5/2} e^{-2m_\nu r}}{8\pi^{5/2} r^{5/2}} \mathcal{D}_{\alpha\beta} \left\{ (X_{LR}^{\psi\psi'})_{v;\alpha\beta} - (Y_{LR}^{\psi\psi'})_{v;\alpha\beta} (\boldsymbol{\sigma}_\alpha \cdot \boldsymbol{\sigma}_\beta) \right\}. \quad (4.57)$$

For Majorana neutrinos, the single neutrino simplification for the potential in Eq. (4.54) takes the same form as Eqs. (4.42) and (4.45) in the short and long-range limits respectively.

We finish this subsection by considering the case where both of the interaction vertices have right-handed neutrino currents. Now the potential takes the same form as Eq. (4.36),

$$V_{\alpha\beta}^{RR,D(M)}(r) = \frac{G_F^2}{4\pi^3 r^5} \sum_{i,j=1}^N \left\{ (X_{RR}^{\psi\psi'})_{ij;\alpha\beta} I_{ij}^{D(M)}(r) - (Y_{RR}^{\psi\psi'})_{ij;\alpha\beta} \left[ (\boldsymbol{\sigma}_\alpha \cdot \boldsymbol{\sigma}_\beta) J_{ij}^{D(M)}(r) - (\boldsymbol{\sigma}_\alpha \cdot \hat{\mathbf{r}})(\boldsymbol{\sigma}_\beta \cdot \hat{\mathbf{r}}) J_{ij}^V(r) \right] \right\}, \quad (4.58)$$

where

$$(X_{RR}^{\psi\psi'})_{ij;\alpha\beta} = (c_{RL}^\psi + c_{RR}^\psi)_{ij;\alpha} (c_{RL}^{\psi'} + c_{RR}^{\psi'})_{ij;\beta}^*, \quad (4.59)$$

$$(Y_{RR}^{\psi\psi'})_{ij;\alpha\beta} = (c_{RL}^\psi - c_{RR}^\psi)_{ij;\alpha} (c_{RL}^{\psi'} - c_{RR}^{\psi'})_{ij;\beta}^*. \quad (4.60)$$

Consequently, the short and long-range limits of the potential in Eq. (4.58) are given by Eqs. (4.42) and (4.45) respectively with the replacements  $(X_{LL}^{\psi\psi'})_{ij;\alpha\beta} \rightarrow (X_{RR}^{\psi\psi'})_{ij;\alpha\beta}$  and  $(Y_{LL}^{\psi\psi'})_{ij;\alpha\beta} \rightarrow (Y_{RR}^{\psi\psi'})_{ij;\alpha\beta}$ .

## 4.4.2 Scalar Interactions

We now derive the neutrino-mediated potential when a *scalar* neutrino NSI is present. In our Lagrangian Eq. (4.11) these are the operators with the coefficients  $g_{XY}$  where  $X, Y \in \{L, R\}$ . We first focus on the case where a scalar interaction is at one vertex and a SM charged- or neutral-current interaction at the other, as shown Fig. 4.3. The spectral function can be determined in this scenario according to

$$\rho_{\alpha\beta}^{VS}(t) = \frac{-G_F^2}{\pi m_\alpha m_\beta} \sum_{i,j} \sum_{X,Y,Z} \left\{ (c_{LX}^\psi)_{ij;\alpha} (g_{YZ}^{\psi'})_{ij;\beta} \mathcal{H}_\mu^{\alpha\beta} \text{dsc}(\mathcal{N}_{ij}^\mu) + (\alpha, \beta) \right\}, \quad (4.61)$$

where  $X, Y, Z \in \{L, R\}$ . We have taken into account that the scalar interaction may either be at the interaction vertex of  $\psi_\alpha$  or  $\psi'_\beta$  by adding an identical contribution with  $(\psi_\alpha \leftrightarrow \psi'_\beta)$ . If the interacting fermions are identical we must multiply by the factor  $\mathcal{D}_{\alpha\beta}$  to avoid double counting. For Majorana neutrinos we only retain twice the SM axial vector current and multiply by a factor of  $\frac{1}{2}$  due to the permutation symmetry of the neutrinos in the loop.

The discontinuity of the neutrino loop factor  $\mathcal{N}_{ij}^\mu$  in the Dirac case is

$$\text{dsc}(\mathcal{N}_{ij}^\mu) = \frac{\mp \Lambda^{1/2}(q^2, m_i^2, m_j^2)}{8\pi} \frac{m_i q^\mu}{q^2} \left( 1 - \frac{m_i^2 - m_j^2}{q^2} \right) \Theta(q^2 - (m_i + m_j)^2), \quad (4.62)$$

where the minus (positive) sign is for  $Y = L$  ( $R$ ) and the product of external fermion bilinears is  $\mathcal{H}_\mu^{\alpha\beta} = [\gamma_\mu P_X]_\alpha [P_Y]_\beta$ . Contracting  $\mathcal{H}_\mu^{\alpha\beta}$  with  $\text{dsc}(\mathcal{N}_{ij}^\mu)$  and making use of the non-relativistic limits of the fermion bilinear products given in Appendix B.1, we obtain in the Dirac case

$$\begin{aligned} \rho_{\alpha\beta}^{VS,D}(t) &= \frac{G_F^2}{8\pi^2} \mathcal{D}_{\alpha\beta} \sum_{i,j} \Theta(t - (m_i + m_j)^2) m_i \Lambda^{1/2}(t, m_i^2, m_j^2) \\ &\quad \times \left\{ (X_{VS}^{\psi\psi'})_{ij;\alpha\beta} (\boldsymbol{\sigma}_\alpha \cdot \mathbf{q}) + (\alpha, \beta) \right\} F_{ij}^\Delta(t), \end{aligned} \quad (4.63)$$

while in the Majorana case we obtain

$$\begin{aligned} \rho_{\alpha\beta}^{VS,M}(t) &= \frac{G_F^2}{8\pi^2} \mathcal{D}_{\alpha\beta} \sum_{i,j} \Theta(t - (m_i + m_j)^2) (m_i + m_j) \Lambda^{1/2}(t, m_i^2, m_j^2) \\ &\quad \times \left\{ (X_{VS}^{\psi\psi'})_{ij;\alpha\beta} (\boldsymbol{\sigma}_\alpha \cdot \mathbf{q}) + (\alpha, \beta) \right\} F_{ij}^S(t). \end{aligned} \quad (4.64)$$

The factor  $X_{VS}^{\psi\psi'}$  contains the scalar coefficients as

$$(X_{VS}^{\psi\psi'})_{ij;\alpha\beta} = (c_{LL}^\psi - c_{LR}^\psi)_{\alpha;ij} (g_{LL}^{\psi'} + g_{LR}^{\psi'} - g_{RL}^{\psi'} - g_{RR}^{\psi'})_{\beta;ij}^*, \quad (4.65)$$

while the functions  $F_{ij}^\Delta$  and  $F_{ij}^S$  are given by

$$F_{ij}^\Delta(t) = \frac{1}{t} \left( 1 - \frac{\Delta m_{ij}^2}{t} \right), \quad (4.66)$$

$$F_{ij}^S(t) = \frac{1}{t} \left( 1 - \frac{(m_i - m_j)^2}{t} \right). \quad (4.67)$$

The above spectral functions only contain terms proportional to the parity (P) violating spin operators  $O'_9 = \boldsymbol{\sigma}_\alpha \cdot \mathbf{q}$  and  $O'_{10} = \boldsymbol{\sigma}_\beta \cdot \mathbf{q}$ , which are proportional to linear combinations of the operators  $O_9$  and  $O_{10}$  in Eq. (B.2). Splitting the spectral functions into terms multiplying these spin operators, we can compute the functions  $\mathcal{V}'_9(r)$  and  $\mathcal{V}'_{10}(r)$  in Eq. (4.9) and from these the components of the overall potential using

$$\begin{aligned} \mathcal{V}_9(r) &= \frac{i}{r^2} (\boldsymbol{\sigma}_\alpha \cdot \hat{\mathbf{r}}) \left( 1 - r \frac{d}{dr} \right) \mathcal{V}'_9(r), \\ \mathcal{V}_{10}(r) &= \frac{i}{r^2} (\boldsymbol{\sigma}_\beta \cdot \hat{\mathbf{r}}) \left( 1 - r \frac{d}{dr} \right) \mathcal{V}'_{10}(r), \end{aligned} \quad (4.68)$$

as outlined in Ref. [447].

By adding these factors we derive the following *vector-scalar* potentials for

the Dirac and Majorana cases

$$V_{\alpha\beta}^{VS,D}(r) = \frac{iG_F^2}{16\pi^3 r^4} \mathcal{D}_{\alpha\beta} \sum_{i,j} m_i \left\{ (X_{VS}^{\psi\psi'})_{ij;\alpha\beta} (\boldsymbol{\sigma}_\alpha \cdot \hat{\mathbf{r}}) + (\alpha, \beta) \right\} J_{ij}^\Delta(r), \quad (4.69)$$

$$V_{\alpha\beta}^{VS,M}(r) = \frac{iG_F^2}{16\pi^3 r^4} \mathcal{D}_{\alpha\beta} \sum_{i,j} (m_i + m_j) \left\{ (X_{VS}^{\psi\psi'})_{ij;\alpha\beta} (\boldsymbol{\sigma}_\alpha \cdot \hat{\mathbf{r}}) + (\alpha, \beta) \right\} J_{ij}^S(r), \quad (4.70)$$

respectively, where the dimensionless integral functions  $J_{ij}^\Delta(r)$  and  $J_{ij}^S(r)$  are given in Appendix B.2.

The first thing to note is that these potentials depend on the distance as  $\frac{1}{r^4}$  and contain a single power of the neutrino masses in the numerator. Due to the small neutrino masses, this is more suppressed than the SM potential in Eq. (4.36) which scales as  $\frac{1}{r^5}$  but less suppressed than the right-handed current potential for Dirac neutrinos in Eq. (4.52), which scales as  $\frac{1}{r^3}$  but is suppressed by two powers of the neutrino masses.

We now consider the situation where scalar neutral-current NSIs are at both interaction vertices. We now obtain the potential via the spectral function

$$\rho_{\alpha\beta}^{SS}(t) = \frac{-G_F^2}{\pi m_\alpha m_\beta} \sum_{i,j} \sum_{W,X,Y,Z} \left\{ (g_{WX}^\psi)_{ij;\alpha} (g_{YZ}^{\psi'})_{ij;\beta} \mathcal{H}^{\alpha\beta} \text{dsc}(\mathcal{N}_{ij}) + (\alpha, \beta) \right\}, \quad (4.71)$$

where  $W, X, Y, Z \in \{L, R\}$ . The discontinuity of the neutrino loop factor  $\mathcal{N}_{ij}$  is given in the Dirac case by

$$\text{dsc}(\mathcal{N}_{ij}) = -\frac{\Lambda^{1/2}(q^2, m_i^2, m_j^2)}{4\pi} \frac{m_i m_j}{q^2} \Theta(q^2 - (m_i + m_j)^2), \quad (4.72)$$

if the chirality of the neutrino currents are the same ( $W = Y$ ) and

$$\text{dsc}(\mathcal{N}_{ij}) = \frac{\Lambda^{1/2}(q^2, m_i^2, m_j^2)}{8\pi} \left( 1 - \frac{2\overline{m_{ij}^2}}{q^2} \right) \Theta(q^2 - (m_i + m_j)^2), \quad (4.73)$$

if the chiralities of the neutrino currents are opposite ( $W \neq Y$ ). The external fermion bilinear product is now  $\mathcal{H}^{\alpha\beta} = [P_W]_\alpha [P_Y]_\beta$  and after taking the non-relativistic limit

we obtain the following *scalar-scalar* potential in the Dirac case

$$V_{\alpha\beta}^{SS,D}(r) = \frac{-G_F^2}{8\pi^3 r^5} \sum_{i,j} \left\{ 3(X_{SS}^{\psi\psi'})_{ij;\alpha\beta} I_{ij}^{SD}(r) - m_i m_j r^2 (Y_{SS}^{\psi\psi'})_{ij;\alpha\beta} I_{ij}^{LR}(r) \right\}, \quad (4.74)$$

where the combination of scalar coefficients are given by

$$(X_{SS}^{\psi\psi'})_{ij;\alpha\beta} = (g_{LL}^\psi + g_{LR}^\psi)_{ij;\alpha} (g_{RL}^{\psi'} + g_{RR}^{\psi'})_{ij;\beta} + (\alpha, \beta), \quad (4.75)$$

$$\begin{aligned} (Y_{SS}^{\psi\psi'})_{ij;\alpha\beta} = & (g_{LL}^\psi + g_{LR}^\psi)_{ij;\alpha} (g_{LL}^{\psi'} + g_{LR}^{\psi'})_{ij;\beta} \\ & + (g_{RL}^\psi + g_{RR}^\psi)_{ij;\alpha} (g_{RL}^{\psi'} + g_{RR}^{\psi'})_{ij;\beta}, \end{aligned} \quad (4.76)$$

and the dimensionless functions  $I_{ij}^{SD}(r)$  and  $I_{ij}^{LR}(r)$  are given in Appendix B.2. For Majorana neutrinos we instead obtain

$$V_{\alpha\beta}^{SS,M}(r) = \frac{3G_F^2}{8\pi^3 r^5} \sum_{i,j} (Z_{SS}^{\psi\psi'})_{ij;\alpha\beta} I_{ij}^{SM}(r), \quad (4.77)$$

where the combination of scalar coefficients is

$$(Z_{SS}^{\psi\psi'})_{ij;\alpha\beta} = (g_{LL}^\psi + g_{LR}^\psi - g_{RL}^\psi - g_{RR}^\psi)_{ij;\alpha} (g_{LL}^{\psi'} + g_{LR}^{\psi'} - g_{RL}^{\psi'} - g_{RR}^{\psi'})_{ij;\beta}, \quad (4.78)$$

and the function  $I_{ij}^{SM}(r)$  is also given in Appendix B.2.

We see that the Dirac potential depends on the distance as  $\frac{1}{r^5}$  only when the neutrino currents are of opposite chirality (the first term in Eq. (4.74)). When they are the both left or right-handed the potential becomes suppressed as  $\frac{m_i m_j}{r^3}$  (the second term in Eq. (4.74)). For Majorana neutrinos the potential scales as  $\frac{1}{r^5}$  for any combination of the coefficients  $g_{XY}$ .

#### 4.4.3 Tensor Interactions

We next examine the neutrino-mediated potential when a *tensor* neutrino NSI is present. In our framework these are the operators in Eq. (4.11) with the coefficients  $h_{XX}$  where  $X \in \{L, R\}$ . We first focus on the case of a tensor interaction at one vertex and a SM charged or neutral-current interaction at the other, shown Fig. 4.3.

The spectral function can be determined in this scenario according to

$$\rho_{\alpha\beta}^{VT}(t) = \frac{-G_F^2}{\pi m_\alpha m_\beta} \sum_{i,j} \sum_{X,Y,Z} \left\{ (c_{LX}^\psi)_{ij;\alpha} (h_{YZ}^{\psi'})_{ij;\beta} \mathcal{H}_{\mu\nu\rho}^{\alpha\beta} \text{dsc}(\mathcal{N}_{ij}^{\mu\nu\rho}) + (\alpha, \beta) \right\}, \quad (4.79)$$

where  $X, Y, Z \in \{L, R\}$ . We take into account that the tensor interaction may be at either interaction vertex by adding an identical contribution with  $(\psi_\alpha \leftrightarrow \psi'_\beta)$ . The Dirac and Majorana cases are treated in the same way as previous subsections.

The discontinuity of  $\mathcal{N}_{ij}^{\mu\nu\rho}$  in the Dirac case is

$$\begin{aligned} \text{dsc}(\mathcal{N}_{ij}^{\mu\nu\rho}) &= \frac{\Lambda^{1/2}(q^2, m_i^2, m_j^2)}{8\pi} \frac{im_i}{q^2} (g^{\mu\nu} q_\rho - g^{\mu\rho} q_\nu \mp i\epsilon^{\mu\nu\rho\sigma} q_\sigma) \\ &\quad \times \left( 1 - \frac{m_i^2 - m_j^2}{q^2} \right) \Theta(q^2 - (m_i + m_j)^2), \end{aligned} \quad (4.80)$$

and the external fermion bilinear product is  $\mathcal{H}_{\mu\nu\rho}^{\alpha\beta} = [\gamma_\mu P_X]_\alpha [\sigma_{\nu\rho} P_Y]_\beta$ .

Contracting these factors and using the non-relativistic limits in Appendix B.1, we obtain the spectral function for Dirac neutrinos

$$\begin{aligned} \rho_{\alpha\beta}^{VT,D}(t) &= -\frac{G_F^2}{2\pi^2} \mathcal{D}_{\alpha\beta} \sum_{i,j=1}^3 \Theta(t - (m_i + m_j)^2) m_i \Lambda^{1/2}(t, m_i^2, m_j^2) \\ &\quad \times \left\{ (X_{VT}^{\psi\psi'})_{ij;\alpha\beta} (\boldsymbol{\sigma}_\beta \cdot \mathbf{q}) + i(Y_{VT}^{\psi\psi'})_{ij;\alpha\beta} (\boldsymbol{\sigma}_\alpha \times \boldsymbol{\sigma}_\beta) \cdot \mathbf{q} + (\alpha, \beta) \right\} F_{ij}^\Delta(t), \end{aligned} \quad (4.81)$$

while in the Majorana case we obtain

$$\begin{aligned} \rho_{\alpha\beta}^{VT,M}(t) &= -\frac{G_F^2}{2\pi^2} \mathcal{D}_{\alpha\beta} \sum_{i,j=1}^N \Theta(t - (m_i + m_j)^2) (m_i - m_j) \Lambda^{1/2}(t, m_i^2, m_j^2) \\ &\quad \times \left\{ (X_{VT}^{\psi\psi'})_{ij;\alpha\beta} (\boldsymbol{\sigma}_\beta \cdot \mathbf{q}) + i(Y_{VT}^{\psi\psi'})_{ij;\alpha\beta} (\boldsymbol{\sigma}_\alpha \times \boldsymbol{\sigma}_\beta) \cdot \mathbf{q} + (\alpha, \beta) \right\} F_{ij}^T(t), \end{aligned} \quad (4.82)$$

where the prefactors  $X_{VT}^{\psi\psi'}$  and  $Y_{VT}^{\psi\psi'}$  are

$$(X_{VT}^{\psi\psi'})_{ij;\alpha\beta} = (c_{LL}^\psi + c_{RL}^\psi)_{ij;\alpha} (h_{LL}^{\psi'} - h_{RR}^{\psi'})_{ij;\beta}^*, \quad (4.83)$$

$$(Y_{VT}^{\psi\psi'})_{ij;\alpha\beta} = (c_{LL}^\psi - c_{RL}^\psi)_{ij;\alpha} (h_{LL}^{\psi'} + h_{RR}^{\psi'})_{ij;\beta}^*. \quad (4.84)$$

The function  $F_{ij}^\Delta$  remains the same as Eq. (4.66) and  $F_{ij}^T$  is given by

$$F_{ij}^T(t) = \frac{1}{t} \left( 1 - \frac{(m_i + m_j)^2}{t} \right). \quad (4.85)$$

The spectral functions above contain terms proportional to the P violating spin operators  $O'_9 = \boldsymbol{\sigma}_\alpha \cdot \mathbf{q}$ ,  $O'_{10} = \boldsymbol{\sigma}_\beta \cdot \mathbf{q}$  and  $O_{11} = (\boldsymbol{\sigma}_\alpha \times \boldsymbol{\sigma}_\beta) \cdot \mathbf{q}$ . We can again split the spectral functions into terms multiplying these operators and evaluate the functions  $\mathcal{V}'_9(r)$ ,  $\mathcal{V}'_{10}(r)$  and  $\mathcal{V}'_{11}(r)$  of Eq. (4.9). From these we use Eq. (4.68) and

$$\mathcal{V}_{11}(r) = \frac{i}{r^2} (\boldsymbol{\sigma}_\alpha \times \boldsymbol{\sigma}_\beta) \cdot \hat{\mathbf{r}} \left( 1 - r \frac{d}{dr} \right) \mathcal{V}'_{11}(r), \quad (4.86)$$

to derive the full *vector-tensor* potential in the Dirac case

$$V_{\alpha\beta}^{VT,D}(r) = -\frac{G_F^2}{4\pi^3 r^4} \mathcal{D}_{\alpha\beta} \sum_{i,j} m_i \left\{ i(X_{VT}^{\psi\psi'})_{ij;\alpha\beta} (\boldsymbol{\sigma}_\beta \cdot \hat{\mathbf{r}}) \right. \\ \left. - (Y_{VT}^{\psi\psi'})_{ij;\alpha\beta} (\boldsymbol{\sigma}_\alpha \times \boldsymbol{\sigma}_\beta) \cdot \hat{\mathbf{r}} + (\alpha, \beta) \right\} J_{ij}^\Delta(r), \quad (4.87)$$

and in the Majorana case

$$V_{\alpha\beta}^{VT,M}(r) = -\frac{G_F^2}{4\pi^3 r^4} \mathcal{D}_{\alpha\beta} \sum_{i,j} (m_i - m_j) \left\{ i(X_{VT}^{\psi\psi'})_{ij;\alpha\beta} (\boldsymbol{\sigma}_\beta \cdot \hat{\mathbf{r}}) \right. \\ \left. - (Y_{VT}^{\psi\psi'})_{ij;\alpha\beta} (\boldsymbol{\sigma}_\alpha \times \boldsymbol{\sigma}_\beta) \cdot \hat{\mathbf{r}} + (\alpha, \beta) \right\} J_{ij}^T(r), \quad (4.88)$$

where the dimensionless functions  $J_{ij}^\Delta(r)$  and  $J_{ij}^T(r)$  are given in Appendix B.2.

We note that these two potentials, similar to the vector-scalar potentials of the previous subsection, scale as  $\frac{m_i}{r^4}$ . They also contain only P violating spin operators. The difference between the potentials for Dirac and Majorana neutrinos arises from the different distance dependence of the functions  $J_{ij}^\Delta(r)$  and  $J_{ij}^T(r)$ . Finally, we observe that the diagonal elements in the  $i, j$  sum vanish for Majorana neutrinos.

We will now compare the neutrino-mediated potentials derived in the previous subsections. To the left of Fig. 4.4 we plot the spin-independent parts of the vector-vector potentials  $V_{\alpha\beta}^{LL}$ ,  $V_{\alpha\beta}^{LR}$  and  $V_{\alpha\beta}^{RR}$  for positronium  $e^- e^+$  ( $\alpha = \beta = e$ ) and three

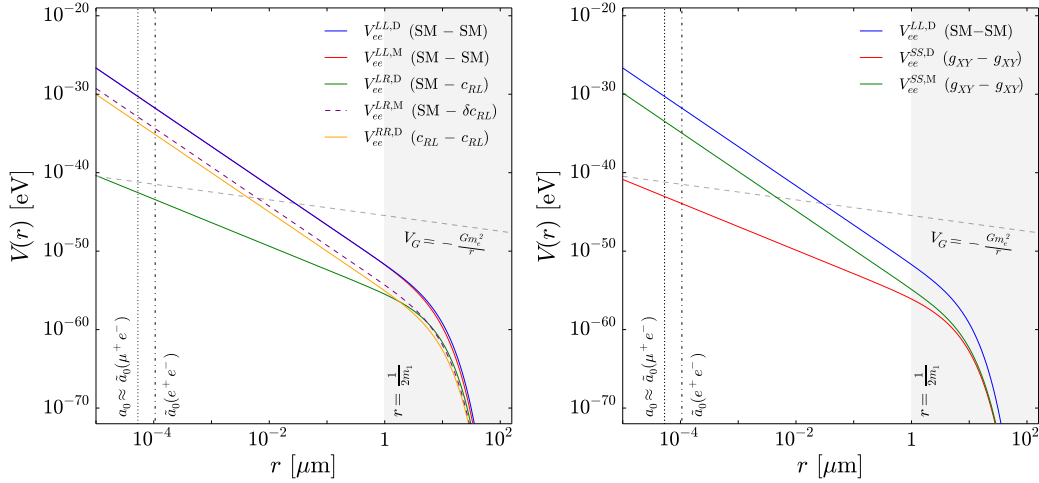


**Figure 4.4:** (Left) Spin-independent parts of the vector-vector potentials  $V_{\alpha\beta}^{LL}$ ,  $V_{\alpha\beta}^{LR}$  and  $V_{\alpha\beta}^{RR}$  for positronium ( $e^- e^+$ ) and three Dirac (D) or Majorana (M) neutrinos with  $m_1 = 0.1$  eV and NO mixing parameters, taking  $(c_{RL})_{ij;e} = 10^{-2} \delta_{ij}$ . The solid (dashed) lines indicate positive (negative) potentials. (Right) Spin-independent parts of the potentials  $V_{ee}^{SS}$  in the Dirac and Majorana cases compared to  $V_{ee}^{LL}$ , using  $(g_{XY})_{ij;e} = 10^{-2} \delta_{ij}$  and for  $X = Y \in \{L, R\}$ . In both plots the neutrino-mediated potentials are compared with the gravitational potential  $V_G$  between the electron and positron.

massive Dirac or Majorana neutrinos. The potentials  $V_{ee}^{LL,D}$  and  $V_{ee}^{LL,M}$  (blue and red lines, respectively) are calculated using SM values for the prefactors  $(X_{LL}^{\ell\ell})_{ij;ee}$  and  $(Y_{LL}^{\ell\ell})_{ij;ee}$  in Eq. (4.31). In the Dirac case, the potential  $V_{ee}^{LR,D}$  (green line) has a single SM interaction and a non-standard  $c_{RL}$  interaction. In the Majorana case, the coefficient  $c_{RL}$  is equivalent to  $c_{LL}$  and the potential  $V_{ee}^{LR,M}$  is instead interpreted as a correction to the SM potential  $V_{ee}^{LL,M}$ , though we plot this contribution separately (purple dashed line). The potential  $V_{ee}^{RR,D}$  is derived assuming both interactions have coefficients  $c_{RL}$ . We set the lightest neutrino mass to  $m_1 = 0.1$  eV and use the best fit normal-ordered (NO) values of the mixing angles, Dirac CP phase and mass-squared splittings in Table 2.3. We set the non-standard coefficients to be  $(c_{RL}^{\ell})_{ij;e} = 10^{-2} \delta_{ij}$  (or  $(\delta c_{RL}^{\ell})_{ij;e} = 10^{-2} \delta_{ij}$  in the Majorana case).

We first compare Dirac and Majorana SM potentials  $V_{ee}^{LL,D}$  and  $V_{ee}^{LL,M}$ . In the short-range limit  $r \ll \frac{1}{2m_1}$  the potentials are identical, while in the long-range limit  $r \gg \frac{1}{2m_1}$  the Majorana potential is smaller than the Dirac potential, confirming with the results of Ref. [442]. The potentials both fall off as  $\frac{1}{r^5}$  until the neutrinos become

non-relativistic around  $r \sim \frac{1}{2m_1}$ , and the potentials are exponentially suppressed. In the long-range limit the potentials are many orders of magnitude smaller than the gravitational potential  $V_G = -\frac{Gm_e^2}{r}$  between the electron and positron. We also note the large difference between the Dirac and Majorana potentials  $V_{ee}^{LR,D}$  and  $V_{ee}^{LR,M}$ . While the Dirac potential is slightly larger than the Majorana potential in the long-range limit, in the short-range limit the former scales as  $\frac{1}{r^3}$  and is suppressed by two powers of the neutrino masses while the latter scales as  $\frac{1}{r^5}$  and is unsuppressed. As stated before, this is because the Majorana potential is interpreted as a correction to the SM potential  $V_{ee}^{LL,M}$  and thus scales in the same way. Due to the suppression from  $c_{RL}$ ,  $V_{ee}^{LR,M}$  is around two orders of magnitude smaller than  $V_{ee}^{LL,D(M)}$ . It can be seen that the potential  $V_{ee}^{RR,D}$  is further suppressed because it contains two factors of  $c_{RL}$ .

To the right of Fig. 4.4 we plot the scalar-scalar potentials for  $e^-e^+$  and Dirac and Majorana neutrinos,  $V_{ee}^{SS,D}$  and  $V_{ee}^{SS,M}$ , and compare them to the spin-independent part of  $V_{ee}^{LL,D}$  and the gravitational potential  $V_G$ . We choose a scalar coefficient  $(g_{XY})_{ij;e} = 10^{-2} \delta_{ij}$  for  $X = Y$ . Looking at Eqs. (4.74) and (4.77) we see that the surviving terms of the Dirac potential scale in the short-range limit as  $\frac{1}{r^3}$  while for the Majorana potential as  $\frac{1}{r^5}$ , as can be seen in the diagram. As the vector-scalar and vector-tensor potentials  $V_{\alpha\beta}^{VS}$  and  $V_{\alpha\beta}^{VT}$  only contain spin-dependent terms, we do not plot them here. However, these potentials depend on the distance as  $\frac{1}{r^4}$  and will therefore have a slope between the  $V_{\alpha\beta}^{LL,D}$  and  $V_{\alpha\beta}^{LR,D}$  potentials.

#### 4.4.4 Neutrino Magnetic and Electric Dipole Moments

In this final subsection we will derive the long-range potentials generated by non-zero neutrino magnetic and electric dipole moments. Long-range potentials induced by neutrino electromagnetic properties have been studied before, for example in Ref. [437].

In Section 2.3 we reviewed how magnetic and electric dipole moments can be parametrised for Dirac and Majorana neutrinos. For Dirac neutrinos one introduces three right-handed fields  $N_R$  (or  $\nu_R$ ) and writes the dim- $\bar{5}$  LEFT operator in Eq. (2.94). The neutrino flavour fields are transformed to the mass basis by the

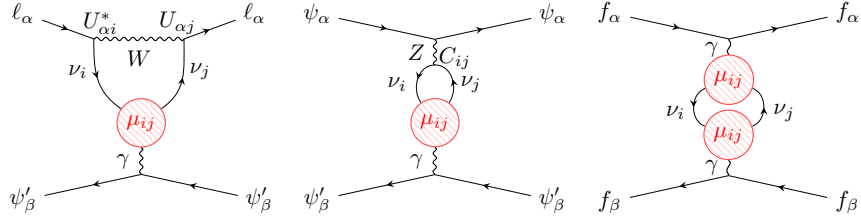


**Figure 4.5:** (Left and centre) Diagrams depicting the exchange of two massive neutrinos between fermions  $\psi_\alpha$  and  $\psi'_\beta$  with SM interactions at one vertex and the exchange of a photon via a neutrino magnetic moment  $\mu_{ij}$  at the other, leading to the vector-dipole potential  $V_{\alpha\beta}^{V\gamma}$ . (Right) Diagram when  $\mu_{ij}$  is present at both vertices, resulting in the dipole-dipole potential  $V_{\alpha\beta}^{\gamma\gamma}$ .

PMNS matrix  $U$  and a matrix  $\tilde{U}$  rotating the right-handed fields. The coefficient of the operator in the mass basis is  $\mu'_D = \tilde{U}^\dagger \mu_D U$ . Dipole moments for the light Majorana neutrinos are produced by the dim-5 LEFT operator in Eq. (2.89), assumed to be generated by NP at a high energy scale. Neglecting possible active-sterile mixings if  $n_S$  right-handed states  $N_R$  are also included in the theory, the operator coefficient can be rotated to the mass basis as  $\mu'_M \equiv \mu'_L = U^\dagger \mu_L U$ . The mass basis coefficients can then be split up into  $\mu'_{D(M)} = \hat{\mu}'_{D(M)} - i\hat{\epsilon}'_{D(M)}$  to write the Lagrangian

$$\mathcal{L}^{(\bar{5})} = -\frac{1}{2} \bar{v}' \sigma^{\mu\nu} (\hat{\mu}'_{D(M)} + i\hat{\epsilon}'_{D(M)} \gamma_5) v' F_{\mu\nu} + \text{h.c.}, \quad (4.89)$$

where  $\hat{\mu}'_{D(M)}$  and  $\hat{\epsilon}'_{D(M)}$  correspond to the magnetic and electric dipole moments of the Dirac (Majorana) neutrinos respectively. We will drop the hats on these quantities in the following discussion.

We now compute the long-range potential corresponding to the two-neutrino exchange diagrams to the left and centre of Fig. 4.5. In these diagrams a pair of mass eigenstate neutrinos interacts via SM charged- or neutral-current interactions at one vertex and via a photon at the other, coupled to the magnetic or electric dipole moment of the neutrino. The amplitude for this process is given by

$$-i\mathcal{A}_{\alpha\beta} = \frac{(-ie)}{4m_\alpha m_\beta} \left( -i \frac{4G_F}{\sqrt{2}} \right) \sum_{i,j} \sum_X \left\{ (c_{LX}^\psi)_{ij;\alpha} \frac{1}{q^2} \mathcal{H}_{\mu\nu}^{\alpha\beta} \mathcal{N}_{ij}^{\mu\nu} + (\alpha, \beta) \right\}, \quad (4.90)$$

where  $\mathcal{H}_{\mu\nu}^{\alpha\beta} = [\gamma_\mu P_X]_\alpha [\gamma_\nu]_\beta$  with  $X \in \{L, R\}$  and the neutrino loop factor  $\mathcal{N}_{ij}^{\mu\nu}$  is

$$\mathcal{N}_{ij}^{\mu\nu} = \int \frac{d^4 k}{(2\pi)^4} \frac{\text{Tr}[-i\sigma^{\mu\rho} q_\rho (\mu'_{ij} + i\epsilon'_{ij}\gamma_5)(q + k + m_j)\gamma^\nu P_L(k + m_i)]}{(k^2 - m_i^2)((q + k)^2 - m_j^2)}. \quad (4.91)$$

Taking the non-relativistic limit of  $\mathcal{H}_{\mu\nu}^{\alpha\beta} = [\gamma_\mu P_X]_\alpha [\gamma_\nu]_\beta$  and the discontinuity of Eq. (4.90), we can construct a spectral function  $\rho_{\alpha\beta}^{V\gamma}(t)$ . Using the method of Section 4.1, from this the following *vector-dipole* potential can be derived in the Dirac case

$$V_{\alpha\beta}^{V\gamma, D}(r) = \frac{\alpha G_F}{8\sqrt{2}\pi^2 r^3} \frac{1}{m_e \mu_B} \mathcal{D}_{\alpha\beta} \sum_{i,j} \left\{ (m_i + m_j) (X_{V\gamma}^{\psi\psi'})_{ij;\alpha} I_{ij}^S(r) - i(m_i - m_j) (Y_{V\gamma}^{\psi\psi'})_{ij;\alpha} I_{ij}^T(r) + (\alpha, \beta) \right\}, \quad (4.92)$$

where we have normalised by the Bohr magneton  $\mu_B = \frac{e}{2m_e}$  and the  $\mathcal{D}_{\alpha\beta}$  factor again takes into account double counting if  $\psi_\alpha = \psi'_\beta$ . The prefactors are given by

$$(X_{V\gamma}^{\psi\psi'})_{ij;\alpha\beta} = (c_{LL}^\psi + c_{LR}^\psi)_{ij;\alpha} (\mu_D')_{ij}, \quad (4.93)$$

$$(Y_{V\gamma}^{\psi\psi'})_{ij;\alpha\beta} = (c_{LL}^\psi + c_{LR}^\psi)_{ij;\alpha} (\epsilon'_D)_{ij}, \quad (4.94)$$

In the Majorana case we instead have

$$V_{\alpha\beta}^{V\gamma, M}(r) = \frac{-i\alpha G_F}{8\sqrt{2}\pi^2 r^3} \frac{1}{m_e \mu_B} \mathcal{D}_{\alpha\beta} \sum_{i,j} \left\{ (m_i - m_j) (Z_{V\gamma}^{\psi\psi'})_{ij;\alpha\beta} I_{ij}^T(r) + (\alpha, \beta) \right\}, \quad (4.95)$$

where the prefactor is

$$(Z_{V\gamma}^{\psi\psi'})_{ij;\alpha\beta} = (c_{LL}^\psi + c_{LR}^\psi)_{ij;\alpha} (\epsilon'_M)_{ij}. \quad (4.96)$$

where it can be seen that the magnetic dipole moment does not contribute. The first thing to observe in these potentials is that the distance dependence is  $\frac{1}{r^3}$ , similar to the right-handed current potential  $V_{\alpha\beta}^{LR}$  in the Dirac case. However, there is now a factor of  $\alpha G_F$  instead of  $G_F^2$  and the potential is proportional to a single power of the neutrino masses instead of two. For  $\mu_{ij} \sim \mu_B$  and noting that  $G_F^2 m_\nu^2 \ll \frac{\alpha G_F m_\nu}{m_e}$  for

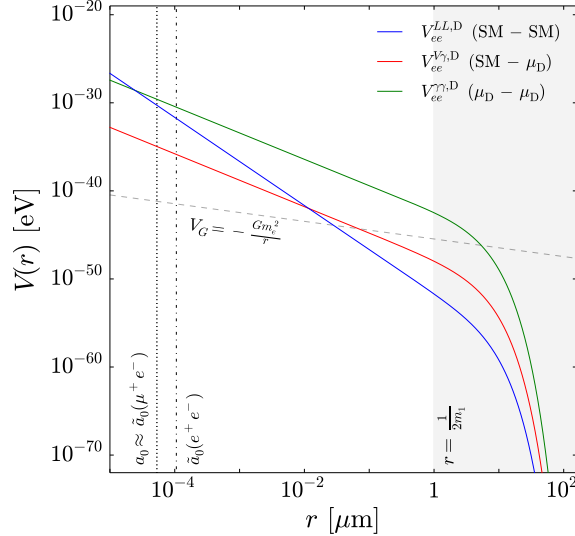


**Figure 4.6:** Neutrino-mediated potentials  $V_{ee}^{V\gamma}$  and  $V_{ee}^{\gamma\gamma}$  compared to the SM potential  $V_{ee}^{LL}$ , plotted for positronium ( $e^-e^+$ ) and three Dirac neutrinos with  $m_1 = 0.1$  eV and NO mixing parameters, setting  $\mu_{ij} \equiv \mu_\nu = 10^{-12} \mu_B$ . These potentials are compared with the gravitational potential  $V_G$  between the electron and positron.

$m_\nu \sim 0.1$  eV, we see that the potential is far less suppressed than  $V_{\alpha\beta}^{LR}$  in the Dirac case.

We can also consider the process depicted by the Feynman diagram to the right of Fig. 4.5, where the two neutrinos are both coupled to the interacting fermions by their magnetic or electric dipole moment. The *dipole-dipole* potential obtained in this case (valid for both Dirac and Majorana neutrinos) is

$$V_{\alpha\beta}^{\gamma\gamma}(r) = \frac{\alpha^2}{12\pi r^3} \frac{1}{m_e^2 \mu_B^2} \sum_{i,j} \left\{ (X_{\gamma\gamma})_{ij} I_{ij}^{M\gamma}(r) - (Y_{\gamma\gamma})_{ij} I_{ij}^{E\gamma}(r) \right\}, \quad (4.97)$$

where  $(X_{\gamma\gamma})_{ij} = (\mu_{D(M)})_{ij} (\mu_{D(M)})_{ij}^*$  and  $(Y_{\gamma\gamma})_{ij} = (\epsilon_{D(M)})_{ij} (\epsilon_{D(M)})_{ij}^*$  and the integral functions  $I_{ij}^{M\gamma}(r)$  and  $I_{ij}^{E\gamma}(r)$  are given in Appendix B.2. The two terms correspond to the presence of magnetic and electric dipole moments respectively. The cross-term (i.e. a magnetic dipole moment at one vertex and electric dipole moment at the other) vanishes.

In Fig. 4.6 we compare for positronium  $e^-e^+$  the spin-independent potentials  $V_{ee}^{V\gamma}$  (red) and  $V_{ee}^{\gamma\gamma}$  (green) to the spin-independent part of SM potential  $V_{ee}^{LL}$  (blue). We take non-zero values of the magnetic dipole moment entries  $\mu'_{ij} = 10^{-12} \mu_B$  and

let the electric dipole moment vanish. As expected we see that the potentials scale as  $\frac{1}{r^3}$  in the short-range limit  $r \ll \frac{1}{2m_1}$ . However, unlike the potentials  $V_{ee}^{LR}$  and  $V_{ee}^{SS}$  it is possible for  $V_{ee}^{V\gamma}$  and  $V_{ee}^{\gamma\gamma}$  to be greater than the SM potential  $V_{ee}^{LL}$  over a wide range of distances.

## 4.5 Atomic Spectroscopy Constraints

There are a number of ways to test for the presence of non-standard (or *fifth*) forces over a range of distances. At the macroscopic scale, precision torsion balance experiments have adapted the method first used by Cavendish to measure Newton's gravitational constant  $G$ . Theories looking to resolve the discrepancy between the observed dark energy density  $\rho_\Lambda \approx 3.8 \text{ keV/cm}^3$  and the theoretical prediction from QFT ( $\sim 10^{120}$  larger) predict power-law modifications of the gravitational force at length-scales of  $r \sim 1 \text{ }\mu\text{m}$  to  $1 \text{ mm}$  [465]. These theories can involve extra time [466] and space [467] dimensions and mediators such the axion [468], dilaton [469], dark photon and  $Z'$  boson [470], all of which can change the typical  $\frac{1}{r}$  scaling of the gravitational potential and violate the so-called weak equivalence principle. Torsion balance experiments have been able to exclude a large region in the parameter space of the Yukawa-type parametrisation of deviations from the  $\frac{1}{r}$  potential [471–479]. Other novel techniques for probing macroscopic forces include optical levitation [480, 481] and atom interferometry [482]. Finally, experiments with polarised electrons have been able to constrain macroscopic *spin-dependent* potentials [483, 484].

In Fig. 4.2, the neutrino-mediated potentials can be seen to fall off sharply for  $r \gtrsim 1 \text{ }\mu\text{m}$ , corresponding to the Compton wavelength of the lightest neutrino with  $m_1 = 0.1 \text{ eV}$ . For interacting electrons and positrons, the associated forces are many orders of magnitude smaller than their gravitational attraction. In theory, however, this suppression can be overcome by using neutral matter with a coherent weak charge, boosting the strength of the neutrino-mediated force with respect to the gravitational force [442]. Another suggested method is to measure the pressure exerted on two parallel plates by the Casimir-like force induced by the neutrino

potential [445]. However, current experimental sensitivities are around 20 orders of magnitude below what is required to measure the neutrino contribution.

To be sensitive to the neutrino-mediated potentials it is therefore necessary to go to smaller distances, where the potentials can result in forces exceeding the gravitational force. The most stringent measurements come from nuclear and atomic spectroscopy probing distance scales of  $r \sim 1$  fm and  $r \sim 1$  Å respectively. We will outline some of the methods explored in the literature.

Naively, atomic spectroscopy of heavy atoms ( $Z \gg 1$ ) is useful for probing the spin-independent part of a neutrino-mediated potential because the force scales coherently with the number of neutrons  $N$  in the nucleus. The spin-dependent part on the other hand will be cancelled out because nuclear pairing interactions leave the ground-state nucleus with at most two unpaired nucleon spins. Unfortunately, the complexity of many-electron interactions makes the theoretical predictions for atomic transition frequencies inadequate for current experimental precisions. One can instead measure *isotope shifts* (the differences in splittings between isotopes) in systems such as  $\text{Ca}^+$  by observing a non-linearity in the King plot [485]. In the literature this has been used to constrain models with  $Z'$  bosons, exotic Higgs bosons and chameleon particles [486–489] and recently the neutrino-mediated potential [444].

A useful probe at nuclear scales is the binding energy of the deuteron  $D^+$ , a bound state of a proton and a neutron. It is possible to model the binding energy as a spherical potential well with an infinitely repulsive inner hard core in order to find the radial wavefunction of the system. This can then be used to calculate the expectation value of the neutrino-mediated potential and the predicted shift to the binding energy. The difference in the measured [490] and predicted [491, 492] binding energies has been used to constrain the neutrino-mediated potential [444].

The sensitivity of atomic-like leptonic systems such as positronium ( $e^-e^+$ ) and muonium ( $e^-\mu^+$ ) to the neutrino-mediated potential could be more promising than the deuteron and other nuclear probes. As we will see, the characteristic cut-off scale (below which the distance dependence of the potential no longer holds) of

these systems is the cut-off of validity of the EFT, not the charge-radius  $\langle r_N \rangle$  of the nucleon/nucleus in semi-leptonic systems like hydrogen ( $e^- p$ ), deuterium ( $e^- D^+$ ) or their muonic counterparts ( $\mu^- p$  and  $\mu^- D^+$ ). The best measured splittings of these systems at present are the  $1S - 2S$  and ground state hyperfine splittings. These splittings have already been predicted to high accuracy and used as precision tests of QED. For example, QED corrections to the ground state hyperfine splitting  $E_F$  in atomic systems have been calculated up to orders  $\alpha^2(Z\alpha)^2 E_F$  [493–495]. Much smaller weak [496, 497] and hadronic corrections [498] have also been calculated.

We will now follow the same approach as Ref. [444], which derives the shifts to energy levels using the expectation value of the position-space potential  $V(r)$ . With the experimental and SM-predicted values for the  $1S - 2S$  and hyperfine splittings of positronium and muonium, we will also examine the contributions from the non-standard neutrino-mediated potentials to put upper bounds on the coefficients  $c_{XY}$ ,  $g_{XY}$ ,  $h_{XX}$  and neutrino dipole moments.

The small shift  $\delta E$  to an atomic energy level due to a non-standard force can be computed to first order in perturbation theory as the expectation value of the associated potential  $V(r)$ ,

$$\delta E = -\langle V(r) \rangle = -\langle n^{2S+1}L_J | V(r) | n^{2S+1}L_J \rangle, \quad (4.98)$$

where  $n^{2S+1}L_J$  labels the atomic state.  $n$  is the principal quantum number,  $S$  the total spin,  $L \in \{S, P, D, \dots\}$  the total orbital angular momentum and  $J$  the total angular momentum. Shifts to the  $1S - nS$  and  $n$ -hyperfine splittings are, respectively,

$$\begin{aligned} \delta E^{1S-nS} &= \delta E(n^3S_1) - \delta E(1^3S_1), \\ \delta E^{n\text{-hfs}} &= \delta E(n^3S_1) - \delta E(n^1S_0). \end{aligned} \quad (4.99)$$

The average of the potential over the atomic quantum numbers is the following position-space integral

$$\langle V(r) \rangle_{n,\ell,m} = \int d^3 \mathbf{r} \Psi_{n,\ell,m}^*(\mathbf{r}) V(r) \Psi_{n,\ell,m}(\mathbf{r}), \quad (4.100)$$

where  $\Psi_{n,\ell,m}(r) = R_{n,\ell}(r)Y_{\ell,m}(\theta, \phi)$  is the atomic wave-function. For the two-body systems we are considering this is the separable solution of the Schrödinger equation with the Coulomb potential  $V_C(r) = -\frac{Ze^2}{4\pi r} = -\frac{Z\alpha}{r}$ . Assuming that  $V(r)$  is only a function of  $r$  (and not  $\theta$  and  $\phi$ ), the integration over the spherical harmonic  $Y_{\ell,m}(\theta, \phi)$  is unity and the average for general distance dependence  $\frac{1}{r^d}$  is,

$$\langle V(r) \rangle_{n,\ell,m} \propto \left\langle \frac{1}{r^d} \right\rangle_{n,\ell} = \int_{r_c}^{\infty} dr \, r^{2-d} \, (R_{n,\ell}(r))^2, \quad (4.101)$$

where  $R_{n,\ell}(r)$  is a hydrogen-like radial wave-function and  $r_c$  is a distance cut-off corresponding to an upper cut-off of validity for the EFT. For Fermi's effective theory of the SM weak interactions this distance is around the inverse  $Z$  boson mass (or reduced Compton wavelength), i.e.  $r_c = \frac{1}{m_Z} = 2.16 \times 10^{-3}$  fm. We can write the Fermi coupling constant in terms of this length scale as

$$G_F = \frac{\pi\alpha}{\sqrt{2}s_W^2 c_W^2 m_Z^2} \equiv A^2 r_c^2, \quad A \equiv \left( \frac{\pi\alpha}{\sqrt{2}s_W^2 c_W^2} \right)^{1/2}, \quad (4.102)$$

This cut-off scale could be different for a non-standard interaction mediated by a particle with a different mass, for example a  $Z'$  boson. In this case the distance cut-off will be  $r'_c = \frac{1}{m_{Z'}}$ . If this mediator interacts with the SM via a coupling  $g'$ , for large  $m_{Z'}$  we can match this onto the vector neutrino NSI normalised to the Fermi coupling constant,

$$G_F c_{XY} = \frac{g'^2}{m_{Z'}^2} \equiv g'^2 r'_c^2. \quad (4.103)$$

Regardless of the new physics being above or below the EW scale, or strongly or weakly coupled, the lower distance scale of validity  $r'_c$  compares to the SM Fermi interaction cut-off  $r_c$  as

$$r'_c^2 = \frac{A^2}{g'^2} c_{XY} r_c^2 = \frac{m_Z^2}{m_{Z'}^2} r_c^2. \quad (4.104)$$

While this discussion is valid for an EFT with point-like particles, for semi-leptonic

systems the cut-off  $r_c$  must take into account the finite size of the nucleon or nucleus. For a nucleus,  $r_c = \langle r_N \rangle \approx R_A = r_0 A^{1/3}$  with  $r_0 \approx 1.2$  fm.

Eq. (4.101) can now be integrated using the hydrogen-like radial wavefunction,

$$R_{n,l}(r) = \sqrt{\frac{(n-l-1)!}{2n(n+l)!}} \left(\frac{2Z}{n\tilde{a}_0}\right)^3 e^{-\frac{2Zr}{n\tilde{a}_0}} \left(\frac{2Zr}{n\tilde{a}_0}\right)^l L_{n-l-1}^{2l+1} \left(\frac{2Zr}{n\tilde{a}_0}\right), \quad (4.105)$$

where  $L_k^j(x)$  is the associated Laguerre function and  $\tilde{a}_0$  is the reduced Bohr radius of a system with reduced mass  $m_r$ ,

$$\tilde{a}_0 = \frac{1}{m_r \alpha} = \left(\frac{m_{\psi_\alpha} + m_{\psi'_\beta}}{m_{\psi_\alpha} m_{\psi'_\beta}}\right) \frac{1}{\alpha}. \quad (4.106)$$

For hydrogen this is the standard Bohr radius  $\tilde{a}_0 \approx a_0 = \frac{1}{m_e \alpha}$ . For different values of the power  $d$  in Eq. (4.101) and expanding in  $r_c$  we obtain

$$\begin{aligned} \left\langle \frac{1}{r^3} \right\rangle_{n,\ell=0} &= \frac{4Z^3}{n^3 \tilde{a}_0^3} \left[ A_n - \gamma_E - \ln \left( \frac{2Zr_c}{na_0} \right) \right] + \mathcal{O} \left( \frac{r_c}{\tilde{a}_0^4} \right), \\ \left\langle \frac{1}{r^4} \right\rangle_{n,\ell=0} &= \frac{4Z^3}{n^3 r_c \tilde{a}_0^3} + \mathcal{O} \left( \frac{1}{\tilde{a}_0^4} \right), \\ \left\langle \frac{1}{r^5} \right\rangle_{n,\ell=0} &= \frac{2Z^3}{n^3 r_c^2 \tilde{a}_0^3} + \mathcal{O} \left( \frac{1}{r_c \tilde{a}_0^4} \right). \end{aligned} \quad (4.107)$$

Here the parameter  $A_n$  is given by

$$A_n = \sum_{j=1}^{n-1} C_{jj}^n (2j-1)! + \sum_{k>j=0}^{n-1} C_{jk}^n (j+k-1)!, \quad (4.108)$$

with

$$C_{jk}^n = \frac{1}{j!k!} \frac{(-1)^{j+k} [(n-1)!]^2}{(n-1-j)!(1+j)!(n-1-k)!(1+k)!}. \quad (4.109)$$

It is possible that the potential in Eq. (4.100) contains spin-dependent terms. For example, the factors  $\boldsymbol{\sigma}_\alpha \cdot \boldsymbol{\sigma}_\beta$  and  $(\boldsymbol{\sigma}_\alpha \cdot \hat{\mathbf{r}})(\boldsymbol{\sigma}_\beta \cdot \hat{\mathbf{r}})$  appear in  $V_{\alpha\beta}^{LL}$  and  $V_{\alpha\beta}^{LR}$ . Firstly, as we will be only considering  $n^{2S+1}S_J$  states for the  $1S - nS$  and  $n$ -hyperfine

splittings, the following equality holds for  $\ell = 0$

$$\langle (\boldsymbol{\sigma}_\alpha \cdot \hat{\mathbf{r}}) (\boldsymbol{\sigma}_\beta \cdot \hat{\mathbf{r}}) \rangle_{\ell=0} = \frac{1}{3} \langle \boldsymbol{\sigma}_\alpha \cdot \boldsymbol{\sigma}_\beta \rangle_{\ell=0}. \quad (4.110)$$

In order to determine the hyperfine splittings between the singlet ( $s = 0$ ) and triplet ( $s = 1$ ) configurations of interacting particle spins, we also need to evaluate the average of the spin dot-product  $\langle \boldsymbol{\sigma}_\alpha \cdot \boldsymbol{\sigma}_\beta \rangle_s$  in these cases. From the properties of the Pauli matrices, these averages are  $\langle \boldsymbol{\sigma}_\alpha \cdot \boldsymbol{\sigma}_\beta \rangle_{s=0} = -3$  and  $\langle \boldsymbol{\sigma}_\alpha \cdot \boldsymbol{\sigma}_\beta \rangle_{s=1} = 1$  respectively.

The averages of the P violating potentials  $V_{\alpha\beta}^{VS}$  and  $V_{\alpha\beta}^{VT}$ , which depend on the spin operators  $\boldsymbol{\sigma}_\alpha \cdot \hat{\mathbf{r}}$ ,  $\boldsymbol{\sigma}_\beta \cdot \hat{\mathbf{r}}$  and  $(\boldsymbol{\sigma}_\alpha \times \boldsymbol{\sigma}_\beta) \cdot \hat{\mathbf{r}}$ , vanish. However, the potentials can induce transitions between different  $\ell$  states similar to an electric dipole moment. While not the focus of this section, atomic and molecular electric dipole moment experiments have constrained spin-dependent, P- and T-violating potentials induced by axion exchange in Ref. [424]. In the context of the neutrino-mediated force, Ref. [441] has suggested probing atomic P violation by measuring the optical rotation of light as it passes through vaporised atoms.

We now wish to compute the shifts to energy levels brought about by the SM neutrino-mediated potential  $V_{\alpha\beta}^{LL}$ . The expectation value of the SM-induced potential  $V_{\alpha\beta}^{LL}$  can be written as

$$\begin{aligned} \langle V_{\alpha\beta}^{LL}(r) \rangle &= \frac{G_F^2}{4\pi^3} \sum_{i,j} \left\{ (X_{LL}^{\psi\psi'})_{ij;\alpha\beta} \left\langle \frac{I_{ij}^{D(M)}(r)}{r^5} \right\rangle \right. \\ &\quad \left. - (Y_{LL}^{\psi\psi'})_{ij;\alpha\beta} \left[ \left\langle \frac{(\boldsymbol{\sigma}_\alpha \cdot \boldsymbol{\sigma}_\beta) J_{ij}^{D(M)}(r)}{r^5} \right\rangle - \left\langle \frac{(\boldsymbol{\sigma}_\alpha \cdot \hat{\mathbf{r}})(\boldsymbol{\sigma}_\beta \cdot \hat{\mathbf{r}}) J_{ij}^V(r)}{r^5} \right\rangle \right] \right\}. \end{aligned} \quad (4.111)$$

To evaluate these averages, recall that the functions  $I_{ij}^{D(M)}(r)$ ,  $J_{ij}^{D(M)}(r)$  and  $J_{ij}^V(r)$  are exponentially suppressed for distances greater than the Compton wavelength of the neutrinos  $r \gg \frac{1}{2m_i}$ . For  $r \ll \frac{1}{2m_i}$  the neutrino masses can instead be neglected ( $m_i \approx m_j \approx 0$ ) and the functions take constant values, discussed in Appendix B.2. For atomic spectroscopy measurements the relevant distance scale (the reduced Bohr

radius  $\tilde{a}_0$ ) is within this regime. The averages in Eq. (4.111) therefore become

$$\left\langle \frac{I_{ij}^{\text{D(M)}}(r)}{r^5} \right\rangle_{n,\ell=0} \approx \frac{2Z^3}{n^3 r_c^2 \tilde{a}_0^3}, \quad (4.112)$$

$$\left\langle \frac{(\boldsymbol{\sigma}_\alpha \cdot \boldsymbol{\sigma}_\beta) J_{ij}^{\text{D(M)}}(r)}{r^5} \right\rangle_{n,\ell=0} \approx \frac{3}{2} \frac{2Z^3}{n^3 r_c^2 \tilde{a}_0^3} \langle \boldsymbol{\sigma}_\alpha \cdot \boldsymbol{\sigma}_\beta \rangle, \quad (4.113)$$

$$\left\langle \frac{(\boldsymbol{\sigma}_\alpha \cdot \hat{\mathbf{r}})(\boldsymbol{\sigma}_\beta \cdot \hat{\mathbf{r}}) J_{ij}^V(r)}{r^5} \right\rangle_{n,\ell=0} \approx \frac{5}{6} \frac{2Z^3}{n^3 r_c^2 \tilde{a}_0^3} \langle \boldsymbol{\sigma}_\alpha \cdot \boldsymbol{\sigma}_\beta \rangle, \quad (4.114)$$

giving the average for the potential

$$\langle V_{\alpha\beta}^{LL}(r) \rangle_{n,\ell=0} \approx \frac{G_F^2}{2\pi^3} \frac{Z^3}{n^3 r_c^2 \tilde{a}_0^3} \left\{ (X_{LL}^{\psi\psi'})_{v;\alpha\beta} - \frac{2}{3} (Y_{LL}^{\psi\psi'})_{v;\alpha\beta} \langle \boldsymbol{\sigma}_\alpha \cdot \boldsymbol{\sigma}_\beta \rangle \right\}, \quad (4.115)$$

where  $(X_{LL}^{\psi\psi'})_{v;\alpha\beta} = \sum_{i,j} (X_{LL}^{\psi\psi'})_{ij;\alpha\beta}$  and  $(Y_{LL}^{\psi\psi'})_{v;\alpha\beta} = \sum_{i,j} (Y_{LL}^{\psi\psi'})_{ij;\alpha\beta}$ .

Calculating the average of the potential  $V_{\alpha\beta}^{LR}$  for Dirac neutrinos in Eq. (4.52) requires evaluating the average of the factor  $\frac{m_i m_j I_{ij}^{LR}(r)}{r^3}$ . For distances  $r \ll \frac{1}{2m_i}$ ,

$$\left\langle \frac{m_i m_j I_{ij}^{LR}(r)}{r^3} \right\rangle_{n,\ell=0} \ll \left\langle \frac{I_{ij}^{\text{D(M)}}(r)}{r^5} \right\rangle_{n,\ell=0}, \quad (4.116)$$

which shows that the potential is too suppressed to be a useful probe of the non-standard coefficients  $c_{RL}$  and  $c_{RR}$ . In the Majorana case the potential  $V_{\alpha\beta}^{LR}$  has the same distance dependence as  $V_{\alpha\beta}^{LL}$  and so

$$\langle V_{\alpha\beta}^{LR}(r) \rangle_{n,\ell=0} \approx -\frac{G_F^2}{2\pi^3} \frac{Z^3}{n^3 r_c^2 \tilde{a}_0^3} \left\{ (X_{LR}^{\psi\psi'})_{v;\alpha\beta} - \frac{2}{3} (Y_{LR}^{\psi\psi'})_{v;\alpha\beta} \langle \boldsymbol{\sigma}_\alpha \cdot \boldsymbol{\sigma}_\beta \rangle \right\}, \quad (4.117)$$

where  $(X_{LR}^{\psi\psi'})_{v;\alpha\beta} = \sum_{i,j} (X_{LR}^{\psi\psi'})_{ij;\alpha\beta}$  and  $(Y_{LR}^{\psi\psi'})_{v;\alpha\beta} = \sum_{i,j} (Y_{LR}^{\psi\psi'})_{ij;\alpha\beta}$ . Recall that  $(X_{LR}^{\psi\psi'})_{ij;\alpha\beta} = -(X_{LL}^{\psi\psi'})_{ji;\alpha\beta}$  and  $(Y_{LR}^{\psi\psi'})_{ij;\alpha\beta} = -(Y_{LL}^{\psi\psi'})_{ji;\alpha\beta}$  for Majorana neutrinos, so any NP contribution to  $c_{RL}$  is added to the SM contributions.

Computing the shifts to the  $1S - 2S$  and  $n$ -hfs splittings in Eq. (4.99) due to

$V_{\alpha\beta}^{LL}$  now gives

$$\delta E_{\psi_\alpha\psi'_\beta}^{1S-nS} = \frac{G_F^2}{2\pi^3} \frac{Z^3}{r_c^2 \tilde{a}_0^3} \left(1 - \frac{1}{n^3}\right) \left\{ (X_{LL}^{\psi\psi'})_{v;\alpha\beta} - \frac{2}{3} (Y_{LL}^{\psi\psi'})_{v;\alpha\beta} \langle \boldsymbol{\sigma}_\alpha \cdot \boldsymbol{\sigma}_\beta \rangle_{s=1} \right\}, \quad (4.118)$$

$$\delta E_{\psi_\alpha\psi'_\beta}^{n-\text{hfs}} = \frac{G_F^2}{3\pi^3} \frac{Z^3}{n^3 r_c^2 \tilde{a}_0^3} (Y_{LL}^{\psi\psi'})_{v;\alpha\beta} \left\{ \langle \boldsymbol{\sigma}_\alpha \cdot \boldsymbol{\sigma}_\beta \rangle_{s=1} - \langle \boldsymbol{\sigma}_\alpha \cdot \boldsymbol{\sigma}_\beta \rangle_{s=0} \right\}, \quad (4.119)$$

which can be written as

$$\delta E_{\psi_\alpha\psi'_\beta}^{1S-nS} = \frac{\alpha G_F}{2\sqrt{2}\pi^2 c_W^2 s_W^2} \frac{Z^3}{\tilde{a}_0^3} \left(1 - \frac{1}{n^3}\right) \left\{ (X_{LL}^{\psi\psi'})_{v;\alpha\beta} - \frac{2}{3} (Y_{LL}^{\psi\psi'})_{v;\alpha\beta} \right\}, \quad (4.120)$$

$$\delta E_{\psi_\alpha\psi'_\beta}^{n-\text{hfs}} = \frac{2\sqrt{2}\alpha G_F}{3\pi^2 c_W^2 s_W^2} \frac{Z^3}{n^3 \tilde{a}_0^3} (Y_{LL}^{\psi\psi'})_{v;\alpha\beta}. \quad (4.121)$$

where we have made use of Eq. (4.102). Recalling that  $\tilde{a}_0 = \frac{1}{m_r \alpha}$ , the shifts to the splittings are of order  $\alpha^4 G_F m_r^3$ . As a particular example, the shift to the hyperfine splitting of the  $n = 1$  energy level for two charged leptons  $\ell_\alpha^-$  and  $\ell_\beta^+$  is

$$\delta E_{\ell_\alpha \ell_\beta}^{1-\text{hfs}} = \frac{2\sqrt{2}\alpha^4 G_F m_r^3}{3\pi^2 c_W^2 s_W^2} \sum_{i,j}^3 (U_{\alpha i}^* U_{\alpha j} + g_A^\ell \delta_{ij}) (U_{\beta i} U_{\beta j}^* + g_A^\ell \delta_{ij}), \quad (4.122)$$

while the same shift for a charged lepton  $\ell_\alpha^\pm$  and nucleon/nucleus  $\mathcal{N}$  is

$$\delta E_{\ell_\alpha \mathcal{N}}^{1-\text{hfs}} = \frac{4Z^2 \alpha^3 G_F^2 m_r^3}{3\pi^3 r_c^2} \sum_i^3 (|U_{\alpha i}|^2 + g_A^\ell) g_A^{\mathcal{N}}, \quad (4.123)$$

where the cut-off  $r_c = \langle r_{\mathcal{N}} \rangle$  corresponds to the size of the nucleon/nucleus.

With Eqs. (4.122) and (4.123) we list in Table 4.2 the predicted shifts to the  $1S - 2S$  and  $n$ -hyperfine splittings (specific  $n$  values are given in the table) due to the SM-induced potential  $V_{\alpha\beta}^{LL}$  for a range of leptonic and semi-leptonic two-body systems. For both the  $1S - 2S$  and hyperfine splittings we compare the predicted shift in units of mHz to the differences between experimental and theoretical values (from QED, hadronic and first-order weak contributions). References for these are provided in the table.

System	$\delta E_{\alpha\beta}^{1S-2S}$ [mHz]		$\delta E_{\alpha\beta}^{n-\text{hfs}}$ [mHz]	
	$V_{\alpha\beta}^{LL}$	exp – theory	$V_{\alpha\beta}^{LL}$	exp – theory
$(e, e)$	10	$-5.8(3.3) \cdot 10^9$ <sup>(1)</sup>	57	$2.2(1.9) \cdot 10^9$ <sup>(a)</sup>
$(e, \mu)$	13	$5.2(9.9) \cdot 10^9$ <sup>(2)</sup>	-150	$-1.1(5.2) \cdot 10^5$ <sup>(b)</sup>
$(e, p)$	$-4.1 \cdot 10^{-4}$	$-1.4(0.5) \cdot 10^7$ <sup>(3)</sup>	$-1.2 \cdot 10^{-3}$	$-1.1(0.1) \cdot 10^7$ <sup>(c)</sup>
$(e, D^+)$			$-1.7 \cdot 10^{-6}$	$1.4(0.1) \cdot 10^6$ <sup>(d)</sup>
$(\mu, p)$	$2.2 \cdot 10^3$	-	$-1.0 \cdot 10^3$	$-9.4(1.5) \cdot 10^{12}$ <sup>(e)</sup>
$(\mu, D^+)$	-550	-	-13	$-1.1(2.1) \cdot 10^{12}$ <sup>(f)</sup>

<sup>(1)</sup> [499], [500], <sup>(2)</sup> [501], [502], <sup>(3)</sup> [503] (Deuterium–Hydrogen 1S – 2S Isotope Shift)  
<sup>(a)</sup> [504], [500] (1S-hfs), <sup>(b)</sup> [505], [493] (1S-hfs), <sup>(c)</sup> [506], [507] (1S-hfs)  
<sup>(d)</sup> [508, 509], [510–512] (2S-hfs), <sup>(e)</sup> [513], [512, 514] (2S-hfs), <sup>(f)</sup> [515], [516] (2S-hfs)

**Table 4.2:** Predicted shifts to the 1S – 2S and hyperfine splittings of two-body systems  $(\psi_\alpha, \psi'_\beta)$  due to the SM-induced neutrino-mediated potential  $V_{\alpha\beta}^{LL}$  for three active neutrinos with  $m_1 = 0.1$  eV and the other masses and mixings determined in the NO case. Where possible we compare these to the differences between the experimental and theoretical values for these splittings. Uncertainties are calculated by adding the experimental and theoretical uncertainties in quadrature.

We see that the expected shifts from  $V_{\alpha\beta}^{LL}$  are much smaller than the discrepancy between experiment and theory; the leptonic systems provide larger shifts in relation to the discrepancy compared to the semi-leptonic systems. This is mainly due to the cut-off  $r_c = \frac{1}{m_Z}$  being two orders of magnitude smaller than the charge radii of the proton and deuteron. Of the leptonic systems we see muonium has the most precise experimental measurements. The predicted shift due to neutrino-exchange  $\delta E_{e\mu}^{n-\text{hfs}} \approx -150$  mHz is three orders of magnitude smaller than the experiment–theory difference. This makes the hyperfine splitting of muonium the most stringent probe at present.

The shift to the hyperfine splitting for a leptonic system from the potential  $V_{\alpha\beta}^{LR}$  (in the Majorana case) can be found from Eq. (4.117) to be

$$\delta E_{\ell\alpha\ell\beta}^{1-\text{hfs}} = \frac{4G_F^2}{3\pi^3 r_c^2 \tilde{a}_0^3} \mathcal{D}_{\alpha\beta} \sum_{i,j}^3 \left\{ (U_{\alpha i}^* U_{\alpha j} + g_A^\ell \delta_{ij}) (c_{RL}^\ell - c_{RR}^\ell)_{ij;\beta} + (\alpha, \beta) \right\}, \quad (4.124)$$

which depends linearly on the coefficient  $c_{RX}^\ell$  ( $X \in \{L, R\}$ ). In theory the potential relies on two effective interactions, an effective SM Fermi interaction and a neutrino

System	$c_{RX}^{\psi} (V_{\alpha\beta}^{LR, M})$	$g_{XY}^{\psi} (V_{\alpha\beta}^{SS, M})$
$(e, e)$	$c_{RX}^e < 5.7 \cdot 10^7$	$g_{XY}^e < 7.2 \cdot 10^3$
$(e, \mu)$	$c_{RX}^e < 3.6 \cdot 10^2$	$g_{XY}^e \cdot g_{XY}^{\mu} < 5.9 \cdot 10^6$
	$c_{RX}^{\mu} < 3.6 \cdot 10^2$	
$(e, p) / (e, D^+)$	$c_{RX}^e < 1.5 \cdot 10^9$ $c_{RX}^p < 5.5 \cdot 10^9$	$g_{XY}^e \cdot (g_{XY}^D - 6.48 g_{XY}^p) < 1.6 \cdot 10^{10}$

**Table 4.3:** (Left) Upper limits on  $c_{RX}$  (for  $X \in \{L, R\}$ ) from the right-handed current potential  $V_{\alpha\beta}^{LR}$ , probed by the hyperfine splittings of the systems  $(\psi_{\alpha}, \psi'_{\beta})$ . We assume three light active Majorana neutrinos with  $m_1 = 0.1$  eV and NO masses and mixings and  $(c_{RX}^{\ell})_{\alpha;ij} = c_{RX}^{\alpha} \delta_{ij}$ . (Right) Upper limits on  $(g_{XY})_{ij;\alpha} = g_{XY}^{\alpha} \delta_{ij}$  (for  $X, Y \in \{L, R\}$ ) from the scalar-scalar potential  $V_{\alpha\beta}^{SS}$ , probed by the  $1S - 2S$  splittings of the same systems.

NSI, which in general have different cut-offs  $r_c$  and  $r'_c$ . The cut-off appearing in Eq. (4.124) must therefore be the larger of these two scales. For simplicity we assume that the NP arises around the EW scale  $m_Z$  and therefore  $r'_c \approx r_c = \frac{1}{m_Z}$  regardless of the exotic coupling strength  $g'$ . For the equivalent shift of a semi-leptonic system,  $\delta E_{\ell_{\alpha}\mathcal{N}}^{1\text{-hfs}}$ , we instead set  $r'_c = \langle r_{\mathcal{N}} \rangle$  and replace  $c_{RX}^{\ell}$  with  $c_{RX}^{\mathcal{N}}$ .

We now use Eq. (4.124) to compute the predicted hyperfine splitting shift as a function of the non-standard coefficient  $c_{RX}$ . To simplify the sum over mass eigenstates  $i, j$ , we take the coefficients to be diagonal in the mass basis, i.e.  $(c_{RX}^{\ell})_{ij;\alpha} = c_{RX}^{\alpha} \delta_{ij}$ . We now write the following inequality relating this predicted shift to the difference between experimental and theoretical values,

$$|\delta E_{\ell_{\alpha}\ell_{\beta}(\ell_{\alpha}\mathcal{N})}^{1\text{-hfs}}| < |\delta E_{\text{exp}}^{1\text{-hfs}} - \delta E_{\text{theory}}^{1\text{-hfs}}| \quad (4.125)$$

and rearrange to put an upper bound on the value of  $c_{RX}^{\alpha}$ . We note that  $(c_{RX}^{\ell})_{ij;\alpha}$  gets a contribution from the SM weak interactions for Majorana neutrinos. Even if we include this contribution, it is too small to alter the upper bound derived for the correction  $(\delta c_{RX}^{\ell})_{ij;\alpha}$  to the coefficient. In Table 4.3 we give the constraints from positronium on  $c_{RX}^e$ , muonium on  $c_{RX}^e$  and  $c_{RX}^{\mu}$  and hydrogen on  $c_{RX}^e$  and  $c_{RX}^p$ . The constraints from muonium are five orders of magnitude better than those from positronium and hydrogen.

System	$\mu_v/\mu_B$ ( $V_{\alpha\beta}^{\gamma\gamma, D(M)}$ )	$\mu_N/\mu_B$ ( $V_{\alpha\beta}^{\gamma\gamma, M}$ , two $N$ )
$(e, e)$	$3.6 \cdot 10^{-2}$ ( $4.4 \cdot 10^{-2}$ )	$7.6 \cdot 10^{-2}$
$(e, \mu)$	$1.3 \cdot 10^{-2}$ ( $1.5 \cdot 10^{-2}$ )	$2.6 \cdot 10^{-2}$
$(e, p) / (e, D^+)$	$2.7 \cdot 10^{-3}$ ( $3.3 \cdot 10^{-3}$ )	$5.7 \cdot 10^{-3}$

**Table 4.4:** Upper limits on the magnetic moment  $\mu_v$  in units of the Bohr magneton probed by the dipole-dipole potential  $V_{\alpha\beta}^{\gamma\gamma}$ , derived from the  $1S - 2S$  splittings of the systems  $(\psi_\alpha, \psi'_\beta)$ . Equivalent limits apply for the electric dipole moment  $\varepsilon_v$ . We assume three light active neutrinos with  $m_1 = 0.1$  eV and NO masses and mixings. For Dirac neutrinos we take  $(\mu_D)_{ij} = \mu_v$ , while for Majorana neutrinos  $(\mu_M)_{ij} = \mu_v(1 - \delta_{ij})$  for  $i \leq j$  and  $(\mu_M)_{ij} = -\mu_v$  for  $i > j$ . We also derive upper limits on the transition magnetic moments between two heavy sterile neutrinos  $(\mu_M)_{45} = -(\mu_M)_{54} = \mu_N$ . Active and active-sterile neutrino magnetic moments are neglected.

We now consider the scalar-scalar potential  $V_{\alpha\beta}^{SS}$  in Eq. (4.64) which does not depend on the spins of the interacting particles. We must instead use the  $1S - 2S$  splitting to derive upper bounds on the coefficients  $g_{XY}$ . The shift to the  $1S - 2S$  splitting is found to be (for leptonic systems)

$$\delta E_{\ell_\alpha \ell_\beta}^{1S-2S} = \frac{21G_F^2}{32\pi^3 r_c^2 \tilde{a}_0^3} \sum_{i,j}^3 (g_{XY}^\ell)_{ij;\alpha} (g_{XY}^\ell)_{ij;\beta} . \quad (4.126)$$

where we take  $r_c = \frac{1}{m_Z}$ . For semi-leptonic systems we find the equivalent  $\delta E_{\ell_\alpha \mathcal{N}}^{1S-2S}$  by setting  $r_c = \langle r_{\mathcal{N}} \rangle$  replacing one  $g_{XY}^\ell$  with  $g_{XY}^{\mathcal{N}}$ .

Examining again the differences in the experimental and theoretical values for the splittings, we derive the upper bounds on the coefficients in Table 4.3. We assume that  $(g_{XY})_{ij;\alpha} = g_{XY}^\alpha \delta_{ij}$  for  $X, Y \in \{L, R\}$ . Positronium can put an upper bound on  $g_{XY}^\ell$ , while muonium can only constrain the product of coefficients  $g_{XY}^\ell \cdot g_{XY}^\mu$ . We also use the experimental and theoretical values of the difference between the  $1S - 2S$  splittings of deuterium and hydrogen,  $\delta E_{eD^+}^{1S-2S} - \delta E_{ep}^{1S-2S}$ . This can only constrain the combination  $g_{XY}^\ell \cdot (g_{XY}^D - 6.48g_{XY}^p)$ . The limits from positronium and muonium are roughly comparable while those from hydrogen/deuterium remain less stringent.

We now examine the constraints on neutrino electromagnetic properties from the neutrino-mediated potentials of Eqs. (4.92), (4.95) and (4.97). The vector-dipole

potential  $V_{\alpha\beta}^{V\gamma}$  is proportional to the neutrino masses and therefore suppressed in the short-range limit, so we will only focus on the shifts induced by the dipole-dipole potential  $V_{\alpha\beta}^{\gamma\gamma}$ . Using the procedure outlined above, we find the expectation value of the potential,

$$\langle V_{\alpha\beta}^{\gamma\gamma} \rangle_{n,\ell=0} \approx \frac{\alpha^2}{12\pi} \frac{1}{m_e^2 \mu_B^2} \frac{4Z^3}{n^3 \tilde{a}_0^3} \left[ A_n - \gamma_E - \ln\left(\frac{2Zr_c}{na_0}\right) \right] \{ (Y_{\gamma\gamma})_v - (X_{\gamma\gamma})_v \}, \quad (4.127)$$

where  $(X_{\gamma\gamma})_v = \sum_{i,j} (\mu_{D(M)})_{ij} (\mu_{D(M)})_{ij}^*$  and  $(Y_{\gamma\gamma})_v = \sum_{i,j} (\varepsilon_{D(M)})_{ij} (\varepsilon_{D(M)})_{ij}^*$ . The potential is spin-independent so we can only use the  $1S - 2S$  splitting to put an upper bound on the neutrino magnetic and electric dipole moments. This is found from Eq. (4.127) as  $\delta E_{\psi_\alpha \psi'_\beta}^{1S-2S} = \langle V_{\alpha\beta}^{\gamma\gamma} \rangle_{n=1,\ell=0} - \langle V_{\alpha\beta}^{\gamma\gamma} \rangle_{n=2,\ell=0}$ .

In Table 4.4 (left) we show the upper bounds on the magnetic moments when we assume  $(\mu_D)_{ij} = \mu_v$  such that  $(X_{\gamma\gamma})_v = 9\mu_v^2$  (for three light Dirac neutrinos) derived from the positronium, muonium and hydrogen/deuterium  $1S - 2S$  splittings. In brackets is the upper bound when we assume there to be three light Majorana neutrinos with  $(\mu_M)_{ij} = \mu_v(1 - \delta_{ij})$  for  $i \leq j$  and  $(\mu_M)_{ij} = -\mu_v$  for  $i > j$ , such that  $(X_{\gamma\gamma})_v = 6\mu_v^2$ . These limits also apply for the Dirac and Majorana electric dipole moments.

In Table 4.4 (right) we consider the scenario where two right-handed neutrinos  $N_R$  are introduced in the Type-I seesaw. We neglect the magnetic moments of the light active neutrinos and the transition magnetic dipole moments between active and sterile states, taking  $(\mu_M)_{ij} = 0$  except for  $(\mu_M)_{45} = -(\mu_M)_{54} = \mu_N$ , where  $\mu_N$  is the transition dipole moment between the two sterile states. We again use the  $1S - 2S$  splittings of the different systems to put an upper bound on this parameter in units of the Bohr magneton, shown in Table 4.4.

To conclude this chapter, the interpretation of forces as the exchange of virtual particles is key to our understanding of nature. On scales larger than nuclei, the long-range electromagnetic force is induced by the exchange of photons in QED. Gravity is also experienced by massive bodies. A number of experiments have searched for a so-called *fifth* force, mediated by new particles. However, within the SM, it is technically possible for two neutrinos to be exchanged between fermions

and induce a long-range force. This corresponds to a one-loop Feynman diagram, shown in Fig. 4.2. Due to the weakness of neutrino interactions and the loop suppression, the effect is small but nevertheless possible to be probed by spectroscopy measurements of (exotic) atoms, especially muonium [444].

In this chapter we have used an EFT approach to parametrise the effect of neutral-current neutrino NSIs on the long-range potential induced by the exchange of two neutrinos. This includes all possible Dirac structures (e.g. vector, scalar and tensor) for effective interactions between two neutrinos and fermions. We have calculated the spin-independent and spin-dependent long-range potentials between interacting fermions  $\psi_\alpha$  and  $\psi'_\beta$  assuming a SM interaction at one vertex and an NSI at the other. We have also considered an NSI at both interaction vertices and the presence of neutrino magnetic moments. We have kept the discussion general to allow for both Dirac or Majorana neutrinos.

Using our results, we discussed how the NSI couplings and magnetic moments can be probed using state-of-the-art atomic and nuclear spectroscopy experiments and high precision QED calculations. Normalising the NSI coefficients to the Fermi coupling constant, we have found that the current precision in atomic spectroscopy is sensitive to coefficients as low as  $c_{XY} = \mathcal{O}(10^2)$  for muonium. If the exchange is induced by a neutrino magnetic  $\mu_\nu$  or electric dipole moment  $\epsilon_\nu$ , values of order  $\mu_\nu$  ( $\epsilon_\nu$ ) =  $\mathcal{O}(10^{-2}) \mu_B$  are being probed.

The limits on neutrino NSIs from atomic spectroscopy can be used to constrain NP scales. For example, the muonium  $n = 1$  hyperfine splitting energy shift in the SM is of order

$$|\delta E_{e\mu}^{1-\text{hfs}}| \approx 0.14 \alpha^4 m_e^3 G_F \approx 6 \times 10^{-16} \text{ eV} \approx 150 \text{ mHz}. \quad (4.128)$$

This compares with the current sensitivity of  $|\delta E^{1-\text{hfs}}| \lesssim 7 \times 10^{-14} \text{ eV}$  [493, 505]. On the other hand, NP at a scale  $\Lambda_{\text{NP}}$  would also induce a shift of order

$$|\delta E_{e\mu}^{1-\text{hfs}}| \approx \frac{\alpha^4 m_e^3}{\Lambda_{\text{NP}}^2} \approx 10^{-13} \left( \frac{60 \text{ GeV}}{\Lambda_{\text{NP}}} \right)^2 \text{ eV}. \quad (4.129)$$

Thus, NP at the EW scale is currently being probed. Experimental advancements in muonium spectroscopy [497] and QED precision calculations [517, 518] are expected to improve the sensitivity to  $|\delta E_{e\mu}^{1\text{-hfs}}| \approx 10 \text{ Hz} \approx 5 \times 10^{-15} \text{ eV}$ .<sup>1</sup> While this will not improve on the existing limits from other (e.g. cLFV) processes, atomic-scale probes have the advantage that the effective operator treatment is valid down to very low energy scales corresponding to the Bohr radius,  $\Lambda_{\text{NP}} \gtrsim \alpha m_e \approx 3 \text{ keV}$ , and therefore could be sensitive to much lighter NP.

---

<sup>1</sup>The sensitivity in atomic systems involving nuclei is expected to be much weaker as the larger distance cut-off  $r'_c \gtrsim 1 \text{ fm}$  only makes it possible to probe NP at scales  $\Lambda_{\text{NP}} \gtrsim 100 \text{ MeV}$ .

## Chapter 5

# Probes of the Inverse Seesaw Mechanism

In this chapter we will return to a specific model (reviewed in Chapter 2) generating Majorana masses for the light active neutrinos. The *inverse seesaw mechanism* (ISS) introduces two sets of sterile neutrinos,  $N_{R,1}$  and  $N_{R,2}$ , which makes it possible to write the general Majorana mass matrix in Eq. (2.70). In the canonical Type-I seesaw mechanism, light active neutrino masses  $m_\nu \approx -M_D^T M_R^{-1} M_D$  are induced by large Majorana masses  $M_R$  of the right-handed neutrinos  $N_R$ . However, the mixings between active and sterile states are small,  $V_{\ell N} \approx M_D^\dagger M_R^{-1}$ . In the ISS, the small active neutrino masses  $m_\nu = M_D^T (M_S^T)^{-1} \mu_S M_S^{-1} M_D$  are instead the result of small Majorana masses  $\mu_S$  of the  $N_{R,2}$  fields. It is *technically natural* for these masses to be small, because global lepton number is conserved when  $\mu_S \rightarrow \mathbf{0}$ . *A priori*, the active-sterile mixings  $V_{\ell N}$  in this scenario can be large. This feature of ISS models is of phenomenological interest, because heavy sterile states  $N$  which have masses kinematically accessible to collider experiments can have large enough mixings to be produced in sufficient quantities. Conversely, the non-observation of sterile states in a variety of experiments allows to constrain the ISS parameter space.

Another characteristic of the ISS mechanism is the suppression of  $|\Delta L| = 2$  processes. If the sterile fields  $N_{R,1}$  and  $N_{R,2}$  have opposite CP parities, then in the small  $\mu_S$  limit they will form *pseudo-Dirac* neutrino pairs (with mass splittings proportional to  $\mu_S$ ). In the limit  $\mu_S \rightarrow \mathbf{0}$ , the active neutrinos are exactly massless

and the pseudo-Dirac pairs become Dirac fermions. Furthermore, lepton number is conserved and  $|\Delta L| = 2$  processes are forbidden. If the ISS mechanism is to describe the observed non-zero active neutrino masses,  $\mu_S$  must indeed be small and as a consequence  $|\Delta L| = 2$  processes are suppressed. In the Type-I seesaw the heavy sterile neutrinos are purely Majorana fermions. However, this distinction between the Type-I seesaw and ISS mechanisms may not be as clear in the presence of additional CP phases in the sterile sector, which can depend on the sterile neutrino mass spectrum [519–521].

In this chapter, we aim to show that the Majorana and pseudo-Dirac cases can be understood as opposite limits in a general model containing left-handed neutrino fields  $v_L$  and sterile neutrino fields  $N_{R,1}$  and  $N_{R,2}$ . The two limits depend on the *a priori* measurable masses, mixing angles and CP phases of the model. To study these limits analytically, in Section 5.1 we will work in a simplified single-generation picture (involving only the electron flavour) and two SM-singlet Weyl fermions  $N_{R,1}$  and  $N_{R,2}$ . In this case, the unitary matrix  $V_L^V$  diagonalising the  $3 \times 3$  Majorana neutrino mass matrix  $M_V$  contains three mixing angles and three CP phases. We will identify the regions of parameter space allowed by consistency relations among the neutrino mass matrix elements. Most importantly, we will examine how the Majorana and pseudo-Dirac limits depend on the CP phases. These phases are completely determined by the active-sterile mixings as a result of the condition  $(M_V)_{11} = 0$ , i.e. that the  $v_L^T \mathcal{C} v_L$  Majorana mass term is forbidden due to  $SU(2)_L$  invariance in the SM.

In Section 5.2 we will review the experimental constraints on the parameter space of a sterile neutrino ( $N$ ) mass  $m_N$  and active-sterile mixing  $|V_{eN}|^2$  (with the electron flavour). The majority of these are searches for the direct production of  $N$ , and so are insensitive to the Majorana or pseudo-Dirac nature. We also note the searches for  $|\Delta L| = 2$  processes and put particular emphasis on the most promising probe of lepton number,  $0\nu\beta\beta$  decay. In Section 5.3, we re-evaluate the constraints from  $0\nu\beta\beta$  decay on the simple parametrisation discussed above and show how these bounds are affected by the sterile neutrino mass splitting and

CP phases. Under certain conditions (close to the pure Dirac limit), we find that the  $0\nu\beta\beta$  decay constraints are *weaker* than the direct search limits, reinforcing the importance of independent searches for sterile neutrinos in all flavours. On the other hand, for the theoretically interesting (e.g., for leptogenesis) mass range  $0.1 \text{ GeV} < m_N < 10 \text{ GeV}$ ,  $0\nu\beta\beta$  decay is still competitive to current and future collider searches. As we work in a single-generation framework containing an the electron neutrino, we cannot model the coherent contribution of the other two light states to  $0\nu\beta\beta$  decay. However, our main focus is on the constraints on sterile neutrinos in a simplified yet consistent seesaw picture. In Section 5.4 we will finally take the agnostic view on the nature of  $N$  and derive constraints on the active-sterile mixings from  $2\nu\beta\beta$  decay, complementing the other direct searches reviewed in Section 5.2. This chapter is based on Refs. [143, 144].

## 5.1 Phenomenological Parametrisation

For simplicity, we neglect the flavour structure of the lepton sector and work in a single-generation picture with a left-handed (electron flavour) neutrino field and two sterile fields;  $\nu_{eL}$ ,  $N_{R,1}^c$  and  $N_{R,2}^c$ . In this scenario the general neutrino mass matrix  $M_\nu$  in Eq. (2.71) can be diagonalised by a  $3 \times 3$  unitary matrix  $V_L^\nu$  as described in Eq. (2.61). It is straightforward to reverse this diagonalisation to express  $M_\nu$  in terms of the *a priori* measurable mixing angles, CP phases and mass eigenvalues,

$$M_\nu = \begin{pmatrix} 0 & M_D^T \\ M_D & M_R \end{pmatrix} = \begin{pmatrix} 0 & m_D & 0 \\ m_D & \mu_R & m_S \\ 0 & m_S & \mu_S \end{pmatrix} = V_L^\nu \cdot \begin{pmatrix} m_\nu & 0 & 0 \\ 0 & m_{N_1} & 0 \\ 0 & 0 & m_{N_2} \end{pmatrix} \cdot V_L^{\nu T}, \quad (5.1)$$

where  $m_\nu$ ,  $m_{N_1}$  and  $m_{N_2}$  are the masses of the mostly-active and (two) mostly-sterile mass eigenstates respectively. The mixing angles and CP phases are contained in  $V_L^\nu$  and so we must choose a suitable parametrisation for this matrix.

The parametrisation of  $V_L^\nu$  chosen for this analysis is analogous to that of the PMNS mixing matrix  $U$ . Just as for three flavour neutrinos,  $V_L^\nu$  must contain three mixing angles and three CP phases (one Dirac and two Majorana phases). We write

it as

$$\begin{aligned}
V_L^\nu &= \begin{pmatrix} U_\nu & V_{eN} \\ V_{Ne} & U_N \end{pmatrix} = \begin{pmatrix} 1 & 0 & 0 \\ 0 & c_{12} & s_{12} \\ 0 & -s_{12} & c_{12} \end{pmatrix} \cdot \begin{pmatrix} c_{e2} & 0 & s_{e2}e^{-i\delta} \\ 0 & 1 & 0 \\ -s_{e2}e^{i\delta} & 0 & c_{e2} \end{pmatrix} \cdot \begin{pmatrix} c_{e1} & s_{e1} & 0 \\ -s_{e1} & c_{e1} & 0 \\ 0 & 0 & 1 \end{pmatrix} \cdot D \\
&= \begin{pmatrix} c_{e1}c_{e2} & s_{e1}c_{e2} & s_{e2}e^{-i\delta} \\ -s_{e1}c_{12} - c_{e1}s_{e2}s_{12}e^{i\delta} & c_{e1}c_{12} - s_{e1}s_{e2}s_{12}e^{i\delta} & c_{e2}s_{12} \\ s_{e1}s_{12} - c_{e1}s_{e2}c_{12}e^{i\delta} & -c_{e1}s_{12} - s_{e1}s_{e2}c_{12}e^{i\delta} & c_{e2}c_{12} \end{pmatrix} \cdot D \quad (5.2) \\
&\approx \begin{pmatrix} 1 & s_{e1} & s_{e2}e^{-i\delta} \\ -s_{e1}c_{12} - s_{e2}s_{12}e^{i\delta} & c_{12} & s_{12} \\ s_{e1}s_{12} - s_{e2}c_{12}e^{i\delta} & -s_{12} & c_{12} \end{pmatrix} \cdot D + \mathcal{O}(s_{ei}^2),
\end{aligned}$$

where  $c_{ij} \equiv \cos \vartheta_{ij}$  and  $s_{ij} \equiv \sin \vartheta_{ij}$ . The mixing angles  $\vartheta_{e1}$ ,  $\vartheta_{e2}$  and  $\vartheta_{12}$  control the active-sterile mixings between the *mostly-active* neutrino mass eigenstate  $\nu_e$  and the *mostly-sterile* mass eigenstates  $N_1$  and  $N_2$  and the sterile-sterile mixing between  $N_1$  and  $N_2$ . The angles can lie in the range  $\vartheta_{ij} \in [0, \frac{\pi}{2}]$  and the Dirac CP phase in the range  $\delta \in [0, 2\pi]$ . The matrix  $D$  is diagonal and contains the remaining two Majorana phases  $\phi_{1,2} \in [0, 2\pi]$ ,

$$D = \text{diag}(1, e^{i\frac{\phi_1}{2}}, e^{i\frac{\phi_2}{2}}). \quad (5.3)$$

Only two Majorana phases are physical because an overall phase can be rotated away by a redefinition of the neutrino fields.

### 5.1.1 Consistency Relations

Without a triplet Higgs extending the SM field content, the active neutrinos cannot acquire a mass of the form  $\nu_L^\top \mathcal{C} \nu_L$  and therefore the  $(1, 1)$  entry of  $M_\nu$  in Eq. (5.1) is strictly zero at tree-level. This requirement must be satisfied irrespective of the remaining mass matrix structure (i.e. Type-I seesaw or ISS). Written in terms of the phenomenological parameters this condition may be written as

$$(M_\nu)_{11} = 0 \Rightarrow c_{e1}^2 c_{e2}^2 \frac{m_\nu}{m_{N_1}} + s_{e1}^2 c_{e2}^2 e^{i\phi_1} + s_{e2}^2 \frac{m_{N_2}}{m_{N_1}} e^{i(\phi_2 - 2\delta)} = 0, \quad (5.4)$$

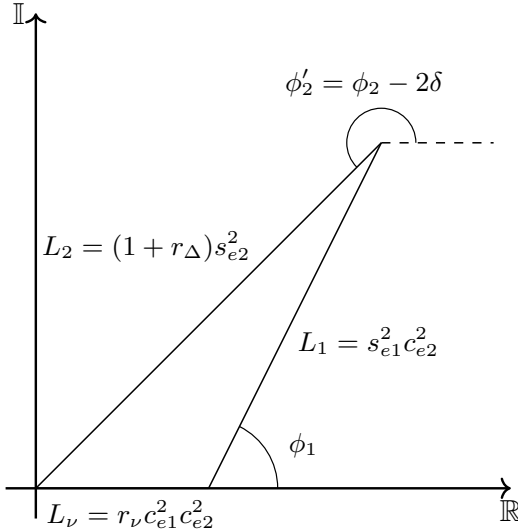


**Figure 5.1:** Visualisation of the  $(M_\nu)_{11} = 0$  constraint in Eq. (5.4) in the complex plane. The sides are given in terms of the dimensionless ratios  $r_\nu$  and  $r_\Delta$  and the squared sines and cosines of the active-sterile neutrino mixing angles  $\vartheta_{e1}$ ,  $\vartheta_{e2}$ .

where we have divided by the heavy neutrino mass  $m_{N_1}$ . We first note that this constraint has no dependence on the sterile-sterile mixing angle  $\vartheta_{12}$ . It can also be seen that such a constraint is equivalent to the vanishing of the effective  $0\nu\beta\beta$  decay mass  $m_{\beta\beta} = \sum_i U_{ei}^2 m_i$ , where the summation is over the three light neutrino mass eigenstates. This would need to be an accidental cancellation (for particular values of the Majorana phases), while the condition in Eq. (5.4) must always be satisfied at tree-level, putting requirements on the values of the three masses, three mixing angles and three CP phases. Instead of the mass  $m_{N_2}$  we can define the system with mass splitting  $\Delta m_N = m_{N_2} - m_{N_1}$ .

As depicted in Fig. 5.1, the condition in Eq. (5.4) can be visualised as a triangle in the complex plane, formed by three sides with lengths  $L_\nu = r_\nu c_{e1}^2 c_{e2}^2$ ,  $L_1 = s_{e1}^2 c_{e2}^2$  and  $L_2 = (1 + r_\Delta) s_{e2}^2$ . The dimensionless ratios are defined as  $r_\nu = \frac{m_\nu}{m_{N_1}}$  and  $r_\Delta = \frac{\Delta m_N}{m_{N_1}}$ . The angles between these sides are determined by the phase  $\phi_1$  and the linear combination  $\phi'_2 \equiv \phi_2 - 2\delta$ . Not all combinations of the masses and mixings allow a triangle to be formed with sides of lengths  $L_\nu$ ,  $L_1$  and  $L_2$ . Specifically, the triangle can only be closed (for some values of  $\phi_1$  and  $\phi'_2$ ) if the longest length is less than

or equal to the sum of the shorter lengths, i.e.

$$\max(L_v, L_1, L_2) \leq \min(L_v, L_1, L_2) + \text{med}(L_v, L_1, L_2). \quad (5.5)$$

From this requirement we can find allowed regions for the squared active-sterile mixing strengths  $s_{e1}^2$  and  $s_{e2}^2$ . These are shown in Fig. 5.2 (left) for different choices of  $r_v$  and  $r_\Delta$ . The light blue region corresponds to the choice  $r_v = 10^{-10}$  and  $r_\Delta = 10^{-2}$ . This could correspond to a light neutrino mass  $m_v = 10^{-3}$  eV and heavy neutrino masses  $m_{N_1} = 10$  MeV and  $m_{N_2} = 10.01$  MeV. The allowed mixings can be seen to form a region centred around  $s_{e1}^2 \approx s_{e2}^2 \approx r_v$ . However, thin extensions to large  $s_{e1}^2 \approx s_{e2}^2$  and small  $s_{e1}^2$  or  $s_{e2}^2$  are also possible.

As can be seen from the dark blue and green regions, increasing (decreasing)  $r_v$  will move the bulk of the region along the diagonal to higher (smaller) mixings. As demonstrated by the yellow region, increasing the splitting in  $r_\Delta$  shifts the allowed region to smaller values of  $s_{e2}^2$  but not  $s_{e1}^2$ . The red region, on the other hand, shows the scenario in which  $r_\Delta$  (i.e.  $\Delta m_N$ ) becomes negative (when  $m_{N_2} < m_{N_1}$ ). The allowed region now moves to larger  $s_{e2}^2$  values for the same  $s_{e1}^2$ . We will study this behaviour more quantitatively below. In Fig. 5.2 (right), we show the same regions but with the axes given by the ratio and sum of the mixing strengths,  $\frac{s_{e2}^2}{s_{e1}^2}$  and  $s_{e1}^2 + s_{e2}^2$ , respectively. This illustrates that there is a lower limit on the total active-sterile mixing strength  $s_{e1}^2 + s_{e2}^2$  for specific choices of  $r_v$  or  $r_\Delta$ .

### 5.1.2 CP Phases

We will now demonstrate that particular limits of the mixings correspond to the CP-conserving cases  $e^{i\phi_1} = \pm 1$ ,  $e^{i\phi_2'} = \pm 1$ , which control the relative CP parity of the sterile fields (the CP parity of the  $m_v$  state is conventionally defined as +1). Keeping the dependence on the parameters  $m_v$ ,  $m_{N_1}$  and  $\Delta m_N$  explicit, three possibilities emerge:

- (i)  $e^{i\phi_1} = e^{i\phi_2'} = +1$ : In this case, the condition  $(M_v)_{11} = 0$  in Eq. (5.4) cannot be satisfied (unless  $m_v = m_{N_1} = m_{N_2} = 0$ ) as all three contributions add up constructively,  $L_v + L_1 + L_2 > 0$ .

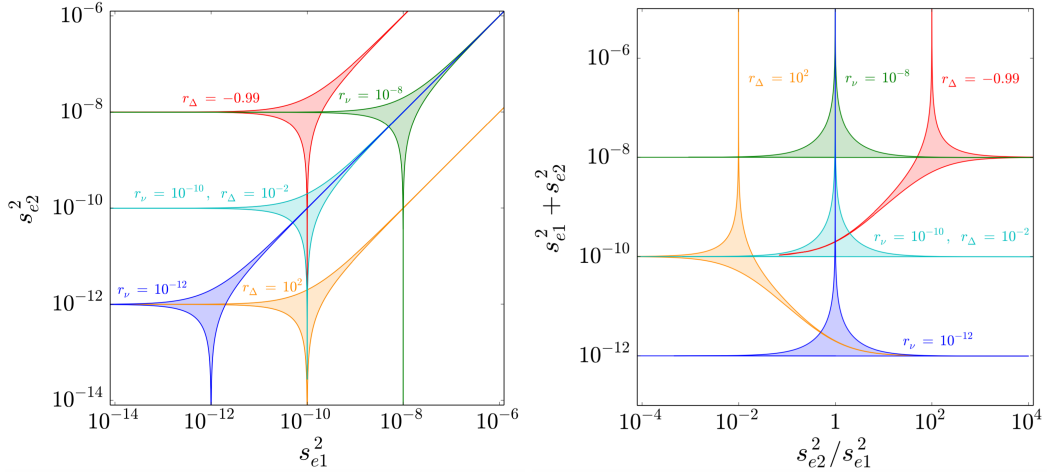


**Figure 5.2:** (Left) Values of the squared active-sterile mixing strengths  $s_{e1}^2$  and  $s_{e2}^2$  satisfying the tree-level condition  $(M_{\nu})_{11} = 0$  in Eq. (5.4) for different combinations of the light and heavy neutrino masses in the ratios  $r_{\nu} = m_{\nu}/m_{N_1}$ , and  $r_{\Delta} = \Delta m_N/m_{N_1}$ , as shown by the shaded regions. (Right) Equivalent regions in the  $s_{e2}^2/s_{e1}^2$  and  $s_{e1}^2 + s_{e2}^2$  parameter space.

(ii)  $e^{i\phi_1} = e^{i\phi_2} = -1$ : Here, the contributions of the states  $N_1$  and  $N_2$  are negative and cancel the active neutrino contribution,  $L_{\nu} - (L_1 + L_2) = 0$ . Now, Eq. (5.4) can be solved for one of the active-sterile mixing angles as

$$\begin{aligned} s_{e2}^2 &= \frac{m_{\nu} - (m_{N_1} + m_{\nu})s_{e1}^2}{m_{N_1} + \Delta m_N + m_{\nu} - (m_{N_1} + m_{\nu})s_{e1}^2} \\ &\approx \frac{m_{\nu}/m_{N_1} - s_{e1}^2}{1 + \Delta m_N/m_{N_1}} \quad \text{for } m_{\nu} \ll m_{N_1} \text{ and } s_{e1}^2 \ll 1. \end{aligned} \quad (5.6)$$

Because  $s_{e2}^2 \geq 0$  this can only be satisfied if  $s_{e1}^2 \leq \frac{m_{\nu}}{m_{N_1} + m_{\nu}} \lesssim \frac{m_{\nu}}{m_{N_1}}$ , i.e. for  $s_{e1}^2$  values up to the ordinary seesaw mixing  $s_{e1}^2 = m_{\nu}/m_{N_1}$ . Consequently,  $s_{e2}^2$  can range from  $s_{e2}^2 = 0$  (when  $s_{e1}^2 = \frac{m_{\nu}}{m_{N_1}}$ ) to  $s_{e2}^2 \approx \frac{m_{\nu}}{m_{N_2}}$  (when  $s_{e1}^2 = 0$ ). This scenario case therefore corresponds to the *canonical seesaw* with two heavy Majorana states. The active state can mix with either of them with adjustable strength. In Fig. 5.2 (left), this limit corresponds to the line-like extensions of the allowed regions towards vanishing  $s_{e2}^2$  at the bottom ( $N_2$  decouples,  $s_{e1}^2 \rightarrow \frac{m_{\nu}}{m_{N_1}}$ ) and vanishing  $s_{e1}^2$  to the left ( $N_1$  decouples,  $s_{e2}^2 \rightarrow \frac{m_{\nu}}{m_{N_2}}$ ). Intermediate solutions lie on the lower left edge of the allowed regions. Rearranging Eq. (5.6) for small  $\Delta m_N$  gives  $s_{e1}^2 + s_{e2}^2 \approx \frac{m_{\nu}}{m_{N_1}}$ , a behaviour that

can be seen in Fig. 5.2 (right).

(iii)  $e^{i\phi_1} = +1, e^{i\phi'_2} = -1$ : Now, it is possible that the contributions of the heavy states can (partially) cancel each other,  $L_V + (L_1 - L_2) = 0$ . We can again solve for the mixing  $s_{e2}^2$ ,

$$\begin{aligned} s_{e2}^2 &= \frac{m_V + (m_{N_1} - m_V)s_{e1}^2}{m_{N_1} + \Delta m_N + m_V + (m_{N_1} - m_V)s_{e1}^2} \\ &\approx \frac{s_{e1}^2}{1 + \Delta m_N/m_{N_1}} \quad \text{for } m_V \ll m_{N_1} \text{ and } s_{e1}^2 \ll 1. \end{aligned} \quad (5.7)$$

In this case, no upper bound on  $s_{e1}^2$  exists and it can in principle take values between  $0 \leq s_{e1}^2 \leq 1$ . For a small mass splitting  $\Delta m_N \ll m_{N_1}$  this corresponds to the ISS scenario where the two heavy Majorana states form a pseudo-Dirac pair. In Fig. 5.2 (left), this limit is equivalent to the thin extension of the allowed region to large mixing strengths (in the top right). It should be noted that this parametrisation does not enforce a small mass splitting and  $\Delta m_N$  can be arbitrarily large for a given light neutrino mass  $m_V$ . As we will discuss below, however, this will induce large loop corrections to  $m_V$ .

For arbitrary values of the phases  $\phi_1$  and  $\phi'_2$  the interior of the shaded regions in Fig. 5.2 is covered. For arbitrary phases, Eq. (5.4) in fact represents two conditions;  $\Re\{(M_V)_{11}\} = 0$  and  $\Im\{(M_V)_{11}\} = 0$ . These relations can be rearranged to find two equivalent expressions for  $s_{e2}^2$ ,

$$1 - \frac{1}{s_{e2}^2} = \frac{(1 + r_\Delta) \cos \phi'_2}{r_V + (\cos \phi_1 - r_V)s_{e1}^2} = \frac{(1 + r_\Delta) \sin \phi'_2}{\sin \phi_1 s_{e1}^2}, \quad (5.8)$$

where the first equality is derived from the real condition and second equality from the imaginary. We can also rearrange Eq. (5.8) to find the tangent of  $\phi'_2$ ,

$$\tan \phi'_2 = \frac{\sin \phi_1 s_{e1}^2}{r_V + (\cos \phi_1 - r_V)s_{e1}^2} \approx \begin{cases} \sin \phi_1 \frac{s_{e1}^2}{r_V} + \mathcal{O}(s_{e1}^4) & \text{for } s_{e1}^2 \ll r_V \\ \tan(\phi_1/2) & \text{for } s_{e1}^2 = r_V \\ \tan \phi_1 + \mathcal{O}(r_V) & \text{for } s_{e1}^2 \gg r_V \end{cases}, \quad (5.9)$$

where we also show the approximate solutions for the different limits of  $s_{e1}^2$ .

In effect, the  $(M_V)_{11} = 0$  condition has allowed us to eliminate two parameters:  $s_{e2}^2$  and  $\phi'_2$ . These are now a function of the other free parameters  $r_V$ ,  $r_\Delta$ ,  $s_{e1}^2$  and  $\phi_1$ . The freedom to divide  $(M_V)_{11} = 0$  by  $m_{N_1}$  and using the ratios  $r_V$  and  $r_\Delta$  also effectively removes a mass degree of freedom. This is evident from the behaviour of the allowed regions in Fig. 5.2; a shift in the  $(s_{e1}^2, s_{e2}^2)$  plane only occurs when  $r_V$  and  $r_\Delta$  are changed. To be fully consistent, the other elements of  $M_V$  (e.g.  $m_D$ ,  $m_S$ ,  $\mu_R$ ,  $\mu_S$ ) must also be divided by  $m_{N_1}$ , so this factor must be taken into account when writing these flavour-basis parameters as functions of the mass-basis parameters.

Alternatively, one can solve for  $\cos \phi_1$  and  $\cos \phi'_2$  by using the cosine rule on the  $(M_V)_{11} = 0$  constraint triangle in Fig. 5.1, i.e.

$$\cos \phi_1 = \frac{(1+r_\Delta)^2 s_{e2}^4 - r_V^2 c_{e1}^4 c_{e2}^4 - s_{e1}^4 c_{e2}^4}{2r_V s_{e1}^2 c_{e1}^2 c_{e2}^4} \approx \frac{(1+r_\Delta)^2 s_{e2}^4 - r_V^2 - s_{e1}^4}{2r_V s_{e1}^2}, \quad (5.10)$$

$$\cos \phi'_2 = \frac{s_{e1}^4 c_{e2}^4 - r_V^2 c_{e1}^4 c_{e2}^4 - (1+r_\Delta)^2 s_{e2}^4}{2r_V (1+r_\Delta) c_{e1}^2 s_{e2}^2 c_{e2}^2} \approx \frac{s_{e1}^4 - r_V^2 - (1+r_\Delta)^2 s_{e2}^4}{2r_V (1+r_\Delta) s_{e2}^2}, \quad (5.11)$$

where the approximate expressions hold for small mixings  $s_{e1}^2, s_{e2}^2 \ll 1$ . In this way the phases  $\phi_1$  and  $\phi'_2$  are determined (up to a pair of solutions in the range  $[0, 2\pi]$ , modulo  $\pi$ ) by the ratios  $r_V$  and  $r_\Delta$  and the mixing strengths  $s_{e1}^2$  and  $s_{e2}^2$ , all of which are in principle measurable. If the solution for  $\phi_1$  lies in the first or second quadrant (i.e.  $\phi_1 \in [0, \pi]$ ), in order to close the triangle in Fig. 5.1 it is a requirement for  $\phi'_2$  to be in the third or fourth quadrants ( $\phi'_2 \in [\pi, 2\pi]$ ) and vice versa.

An important parameter in determining the nature of the two heavy states is the phase difference  $\Delta\phi = \phi_1 - \phi'_2 = \phi_1 - \phi_2 + 2\delta$  between  $N_1$  and  $N_2$ . If  $\Delta\phi \approx 0$ , the heavy states should behave like Majorana fermions, while for  $\Delta\phi \approx \pm\pi$  they should form a pseudo-Dirac pair with an associated suppression of  $|\Delta L| = 2$  effects. Using the solutions Eqs. (5.10) and (5.11), or alternatively using the cosine rule for the third angle of the triangle in Fig. 5.1,  $\Delta\phi$  is given in terms of the other parameters

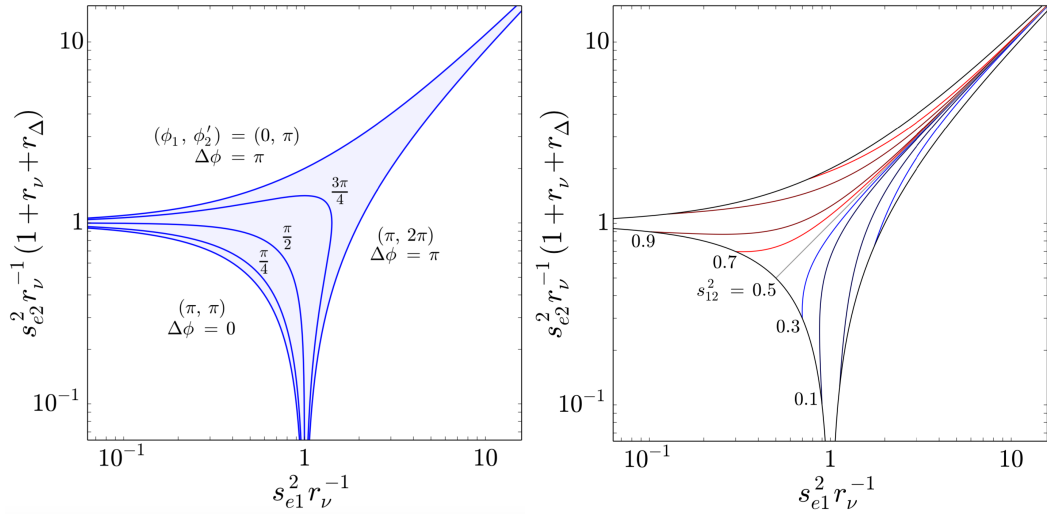


**Figure 5.3:** (Left) Heavy neutrino CP phase difference  $\Delta\phi$  as a function of the normalised active-sterile mixings  $s_{e1}^2$  and  $s_{e2}^2$ . The edges of the allowed region are determined by the limiting values for  $(\phi_1, \phi'_2)$  as indicated. (Right) Sterile-sterile neutrino mixing strength  $s_{12}^2$  as a function of  $s_{e1}^2$  and  $s_{e2}^2$ , setting  $\delta = 0$ .

by

$$\cos(\Delta\phi) = \frac{r_v^2 c_{e1}^4 c_{e2}^4 - s_{e1}^4 c_{e2}^4 - (1 + r_\Delta)^2 s_{e2}^4}{2(1 + r_\Delta)s_{e1}^2 c_{e2}^2 s_{e2}^2} \approx \frac{r_v^2 - s_{e1}^4 - (1 + r_\Delta)^2 s_{e2}^4}{2(1 + r_\Delta)s_{e1}^2 s_{e2}^2}. \quad (5.12)$$

This phase difference is plotted in Fig. 5.3 (left) as a function of the mixing strengths  $s_{e1}^2$  and  $s_{e2}^2$  within the region allowed by the  $(M_V)_{11} = 0$  constraint. Note that the active-sterile mixing strengths  $s_{e1}^2$  and  $s_{e2}^2$  are normalised by  $r_\nu$  and  $r_\nu/(1 + r_\nu + r_\Delta)$  respectively, making the plot valid for an arbitrary choice of the light and heavy neutrino masses. The edges of the allowed region again correspond to the CP-conserving combinations of phases: (i)  $\phi_1 = \phi'_2 = \pi$  to the lower left corresponding to the *canonical seesaw* with two Majorana heavy states and (ii)  $\phi_1 = 0(\pi)$ ,  $\phi'_2 = \pi(2\pi)$  on the top (lower right) edge, corresponding to an ISS-like scenario. Intermediate scenarios between these limiting cases are characterised by the phase difference  $|\Delta\phi|$  increasing from 0 to  $\pi$ , as shown.

We have seen that it is possible to eliminate the two phases  $\phi_1$  and  $\phi'_2$  from the nine initial phenomenological parameters. Further parameters can be eliminated if we can make convenient choices for the remaining parameters in  $M_V$ . For example, without lack of generality we can assume that the (1,3) element of  $M_V$  in Eq. (5.1)

is zero. This can always be achieved by performing a rotation among the sterile states [233]. In our phenomenological parametrisation this is

$$\begin{aligned} (\mathbf{M}_v)_{13} = & r_v c_{e1} c_{e2} \left( s_{e1} s_{12} - e^{i\delta} c_{e1} s_{e2} c_{12} \right) \\ & - e^{i\phi_1} s_{e1} c_{e2} \left( c_{e1} s_{12} + e^{i\delta} s_{e1} s_{e2} c_{12} \right) \\ & + e^{i(\phi_2 - \delta)} (1 + r_\Delta) c_{e2} s_{e2} c_{12} = 0. \end{aligned} \quad (5.13)$$

The linear combination  $\phi'_2 = \phi_2 - 2\delta$  does not appear explicitly in this condition. As we would like to continue using the relations for  $\cos \phi_1$  and  $\cos \phi'_2$  in Eqs. (5.10) and (5.11), we introduce the linear combination  $\delta' = 2\phi_2 + \delta$  orthogonal to  $\phi'_2$ . The phases  $\phi_1$ ,  $\phi_2$  and  $\delta$  can thus be written as linear combinations of  $\phi_1$ ,  $\phi'_2$  and  $\delta'$ . Similar to the  $(\mathbf{M}_v)_{11} = 0$  constraint, we can take both the real and imaginary part of Eq. (5.13) and rearrange for  $s_{12}^2$  as a function of  $s_{e1}^2$ ,  $s_{e2}^2$  and the phases,

$$\frac{1}{s_{12}^2} = 1 + C_R \frac{s_{e1}^2 c_{e1}^2}{s_{e2}^2} = 1 + C_I \frac{s_{e1}^2 c_{e1}^2}{s_{e2}^2}, \quad (5.14)$$

where

$$\begin{aligned} C_R &= \frac{(r_v - \cos \phi_1)^2}{((1 + r_\Delta) \cos(\phi_2 - \delta) - r_v \cos \delta + (r_v \cos \delta - \cos(\phi_1 + \delta)) s_{e1}^2)^2}, \\ C_I &= \frac{\sin^2 \phi_1}{((1 + r_\Delta) \sin(\phi_2 - \delta) - r_v \sin \delta + (r_v \sin \delta - \cos(\phi_1 + \delta)) s_{e1}^2)^2}. \end{aligned} \quad (5.15)$$

where the first and second equalities in Eq. (5.14) are derived from the real and imaginary conditions respectively.

The sterile-sterile mixing  $s_{12}^2$  is shown in Fig. 5.3 (right) in the normalised  $(s_{e1}^2, s_{e2}^2)$  plane for  $\delta = 0$ . Furthermore, we can equate the real and imaginary solutions of  $s_{12}^2$  in Eq. (5.14), i.e.  $C_R = C_I$ . Rewriting these in terms of the phases  $\phi_1$ ,  $\phi'_2$  and  $\delta'$  and making use of the solutions for  $\cos \phi_1$  and  $\cos \phi'_2$  allows to solve for the final phase  $\delta'$  in terms of  $r_v$ ,  $r_\Delta$ ,  $s_{e1}^2$  and  $s_{e2}^2$ . In practice it is difficult to do this analytically, but numerically  $\delta'$  can be found by finding the intersecting points of the curves  $C_R(\delta')$  and  $C_I(\delta')$ .

We have therefore demonstrated that, given values of the parameters  $r_v$ ,  $r_\Delta$ ,  $s_{e1}^2$  and  $s_{e2}^2$  and assuming a particular parametrisation of the Majorana mass matrix  $M_v$ , the remaining parameters  $s_{12}^2$ ,  $\phi_1$ ,  $\phi'_2$  and  $\delta'$  are fully determined. Thus, if the absolute neutrino mass scale  $m_v$  is known and an experiment observes two sterile states with a mass splitting  $\Delta m_N$  and mixing strengths  $s_{e1}^2$  and  $s_{e2}^2$ , the sterile-sterile mixing strength  $s_{12}^2$  and CP phases  $\phi_1$ ,  $\phi'_2$  and  $\delta'$  are predicted quantities. We remind the reader that this is true for a *single* generation; if we were to consider the three active states and an arbitrary number of sterile states, an analytical treatment would not be possible. This is because the number of angles and phases between the active and sterile states rapidly increases for additional generations.

As we will see in Section 5.2, direct searches for the production and decay of heavy states can probe (if not sensitive to the lepton numbers of the final states) the mixings  $|V_{eN_1}|^2 \approx s_{e1}^2$  and  $|V_{eN_2}|^2 \approx s_{e2}^2$  for particular values of  $m_{N_1}$  or  $m_{N_2}$ . If the splitting  $\Delta m_N$  is large enough for the two states to be resolved,  $|V_{eN_1}|^2$  and  $|V_{eN_2}|^2$  can be measured independently, constraining the values of the other parameters. If  $\Delta m_N$  is below the energy resolution of an experiment, it will only be sensitive to the sum  $|V_{eN_1}|^2 + |V_{eN_2}|^2$ . An upper bound on  $|V_{eN_1}|^2 + |V_{eN_2}|^2$  excludes a region to the top right of Fig. 5.3 (left), thus placing an upper bound on  $\Delta\phi$ . The parameters  $s_{12}^2$  and  $\delta'$  remain unconstrained. Most current and future direct searches are probing the regime  $|V_{eN_1}|^2 \approx |V_{eN_2}|^2 \gg r_v$  where the phase difference is  $\Delta\phi = \pm\pi$ . Some experiments like the KATRIN upgrade TRISTAN [522] and the future LBL neutrino oscillation experiment DUNE [523] may test mixings  $|V_{eN_1}|^2 \lesssim r_v$ , thus being able to pin down phase differences in the range  $|\Delta\phi| \in [0, \pi]$ , cf. Fig. 5.7.

We next ask whether the parameters  $s_{12}^2$ ,  $\phi_1$ ,  $\phi'_2$  and  $\delta'$  can be measured in order to confirm the predictions of the generalised ISS. The Majorana and pseudo-Dirac limits (governed by  $\phi_1$  and  $\phi'_2$ ) are primarily distinguished by the magnitude of  $|\Delta L| = 2$  processes. In the case where  $\Delta m_N$  is not too small,  $|\Delta L| = 2$  searches are currently probing mixings in the pseudo-Dirac limit. It is unlikely for future  $|\Delta L| = 2$  searches to reach  $|V_{eN_1}|^2 \lesssim r_v$  needed for the Majorana limit. In other words, if an experiment sees two sterile states with mixings  $|V_{eN_1}|^2 \approx |V_{eN_2}|^2 \gg r_v$ ,

but also a large  $|\Delta L| = 2$  signal (e.g. from a large asymmetry in the pseudorapidity distribution at the ILC [524]), it would strongly imply some other source of  $|\Delta L| = 2$  [525]. For example, the states  $N_1$  and  $N_2$  could possess additional strong couplings to SM particles from a TeV-scale Type-III seesaw mechanism, or the light neutrino masses are not generated by the seesaw (e.g. instead, radiatively) [526].

In the small mixing limit  $s_{e1}^2, s_{e2}^2 \ll 1$ , the matrix

$$U_N \approx \begin{pmatrix} c_{12} & s_{12} \\ -s_{12} & c_{12} \end{pmatrix} \cdot \begin{pmatrix} e^{i\phi_1/2} & 0 \\ 0 & e^{i\phi_2/2} \end{pmatrix} \quad (5.16)$$

diagonalises the  $2 \times 2$  submatrix  $M_R$  of  $M_\nu$  as  $U_N^T M_R U_N$  in the basis where the charged lepton Yukawa coupling  $Y_\nu$  is diagonal. In Ref. [527] it was noted that the Dirac submatrix  $M_D$  can always be redefined as  $M'_D = M_D U_N^\dagger$  so that it is impossible to measure the angle  $\vartheta_{12}$ , making it unphysical (see also Ref. [528]). If right-handed interactions are introduced, for example in a left-right symmetric model,  $s_{12}^2$  is an observable because the lower two sub-blocks of  $V_L^\nu$  in Eq. (5.2) (called  $\Xi$  in Chapter 2) rotate the  $W_R$  gauge boson interaction. It becomes possible to observe the sterile neutrino mixing via the ratio of same-sign to opposite-sign charged lepton production rates in colliders [521, 529, 530],

$$\mathcal{R}_{\ell\ell} = \frac{\Delta m_N^2}{2\Gamma_N^2 + \Delta m_N^2}, \quad (5.17)$$

where  $\Gamma_N$  is the average decay width of the sterile neutrinos. The ratio  $\mathcal{R}_{\ell\ell}$  can be between 0 (Dirac limit) and 1 (Majorana limit). The sterile-sterile mixing  $s_{12}^2$  appears in the same-sign and opposite-sign rates in the numerator and denominator of  $\mathcal{R}_{\ell\ell}$ , but cancel for  $\Delta\phi = \pm\pi$ . This is generally not true for  $|\Delta\phi| < \pi$ .

The sterile-sterile mixing  $s_{12}^2$  is nevertheless needed to evaluate the radiatively-generated neutrino mass at one-loop in Eq. (2.79) (exact expression) and Eq. (2.80) (in the limit  $\mu_{R,S} \ll m_S$ ). When written in terms of the masses, mixing angles and CP phases (in the particular parametrisation with  $(M_\nu)_{13} = 0$ ), the flavour-space parameters  $m_D$ ,  $m_S$ ,  $\mu_S$  and  $\mu_R$  are functions of  $s_{12}^2$ . Using these parameters to evaluate  $\delta m_\nu^{1\text{-loop}}$ , we will for simplicity assume  $\delta = 0$  instead of numerically

solving  $C_R = C_I$  for  $s_{12}^2$  and  $\delta'$  for particular values of  $r_V$ ,  $m_{N_1}$ ,  $r_\Delta$ ,  $s_{e1}^2$  and  $s_{e2}^2$ . We reiterate that  $m_{N_1}$  must be chosen independently because an overall factor  $m_{N_1}$  cannot be eliminated from  $m_D$ ,  $m_S$ ,  $\mu_S$  and  $\mu_R$  as for the  $(M_V)_{11} = 0$  and  $(M_V)_{13} = 0$  constraints.

In this scenario we can investigate the value of the sterile-sterile mixing angle  $\vartheta_{12}$  for the limiting cases of  $\phi_1$  and  $\phi'_2 = \phi_2$  along the edges of the allowed region in Fig. 5.3. In the limits  $s_{e1}^2, s_{e2}^2 \ll 1$  and  $r_V \ll 1$ , we find from Eq. (5.14),

(i)  $e^{i\phi_1} = e^{i\phi_2} = +1$ : No solution.

(ii)  $e^{i\phi_1} = e^{i\phi_2} = -1$ : In this case we have

$$\tan \vartheta_{12} = \sqrt{(1+r_\Delta)(r_V/s_{e1}^2 - 1)}, \quad (5.18)$$

where  $s_{e1}^2 \leq r_V$  as discussed before in this case, ensuring that the square root is positive.

(iii)  $e^{i\phi_1} = \pm 1, e^{i\phi_2} = \mp 1$ : Now the sterile-sterile mixing angle is determined as

$$\tan \vartheta_{12} = \sqrt{(1+r_\Delta)(1 \pm r_V/s_{e1}^2)}. \quad (5.19)$$

which is only valid for  $s_{e1}^2 \geq r_V$  in the  $e^{i\phi_1} = -1, e^{i\phi_2} = +1$  case.

The behaviour of  $s_{12}^2$  is shown in Fig. 5.3 (right) as a function of the active-sterile mixing strengths  $s_{e1}^2$  and  $s_{e2}^2$ . At each point in the allowed region the phases  $\phi_1$  and  $\phi'_2 = \phi_2$  ( $\delta$  is set to zero) are calculated according to Eqs. (5.10) and (5.11). We observe that the sterile-sterile mixing angle is  $\vartheta_{12} = \frac{\pi}{2}$  when  $s_{e1}^2 \ll r_V$ . As  $s_{e1}^2$  approaches  $r_V$  along the canonical seesaw side of the allowed region the mixing angle falls to  $\vartheta_{12} = 0$ . These two values represent physically equivalent cases, signifying an exchange in the role of the two heavy states as one state becomes decoupled while mixing of the other state increases to  $r_V$  or  $\frac{r_V}{1+r_V+r_\Delta}$ . In the ISS limit the sterile-sterile mixing angle approaches  $\vartheta_{12} = \pi/4$ , i.e. maximal mixing.

Having quantified the behaviour of  $s_{12}^2$  as a function of the other parameters, we now return to the neutrino mass generated at one-loop. So far in this section we

have worked at tree-level. Due to the gauge invariance of the SM under  $SU(2)_L$ , it is not possible to write a Majorana mass term  $v_L^\top \mathcal{C} v_L$  for the left-handed neutrino fields, and thus  $(M_\nu)_{11} = 0$ . However, the inclusion of loop corrections *will* lead to the appearance of a finite value for  $(M_\nu)_{11}$ , i.e.

$$M_\nu = \begin{pmatrix} \delta m_\nu^{1\text{-loop}} & m_D & 0 \\ m_D & \mu_R & m_S \\ 0 & m_S & \mu_S \end{pmatrix}, \quad (5.20)$$

where  $\delta m_\nu^{1\text{-loop}}$  is given by Eq. (2.79) in the single generation case. This will result in a mass eigenvalue of the lightest state of

$$m_\nu = m_\nu^{\text{tree}} + \delta m_\nu^{1\text{-loop}}, \quad (5.21)$$

where  $m_\nu^{\text{tree}} = \frac{\mu_S m_D^2}{m_S^2}$  for a single generation. When using  $m_\nu$  from now on we assume that the physical mass (measured by an experiments) includes both the tree-level and one-loop contributions.

In Fig. 5.4 (left), we plot the exact formula for  $\delta m_\nu^{1\text{-loop}}$  in Eq. (2.79) as a function of the heavy neutrino mass  $m_{N_1}$  and mixing  $s_{e1}^2$ . The parameters  $m_\nu$ ,  $r_\Delta$ ,  $\phi_1$  and  $\phi_2$  (for  $\delta = 0$ ) are fixed, while  $s_{e2}^2$  and  $s_{12}^2$  are determined according to Eqs. (5.8) and (5.14). Specifically, the tree-level mass and heavy neutrino splitting are set to the benchmark values  $m_\nu = 10^{-3}$  eV and  $r_\Delta = 10^{-2}$  respectively, while the Majorana phases are chosen such that the scenario is located on the right edge of the allowed parameter space in Fig. 5.3 (left). We also plot (in grey) the ‘seesaw’ line  $s_{e1}^2 = r_\nu$ . Below this line  $s_{e2}^2$  tends to the constant value  $\frac{r_\nu}{1+r_\nu+r_\Delta} \approx r_\nu$  while  $s_{12}^2$  tends to  $\frac{\pi}{2}$ . Above this line is the ISS limit with  $s_{e2}^2 = \frac{s_{e1}^2}{1+r_\Delta} \approx s_{e1}^2$  and  $s_{12}^2 = \frac{\pi}{4}$ .

This plot illustrates the strong dependence of  $|\delta m_\nu^{1\text{-loop}}|$  on the parameters  $m_{N_1}$  and  $s_{e1}^2$ . For large  $m_{N_1}$ , the one-loop correction is dangerously large as a result of the large splitting between the heavy states  $\Delta m_N = r_\Delta m_{N_1}$ . Looking at the approximate loop formula in Eq. (2.80) and recalling that  $m_D, m_S, \mu_R$  are functions of  $m_{N_1}$  (when written in terms of the mass-basis parameters and mixing angles), the strong dependence on  $m_{N_1}$  is not surprising because  $\delta m_\nu^{1\text{-loop}}$  naively scales as  $m_{N_1}^3 \ln(m_{N_1})$  for

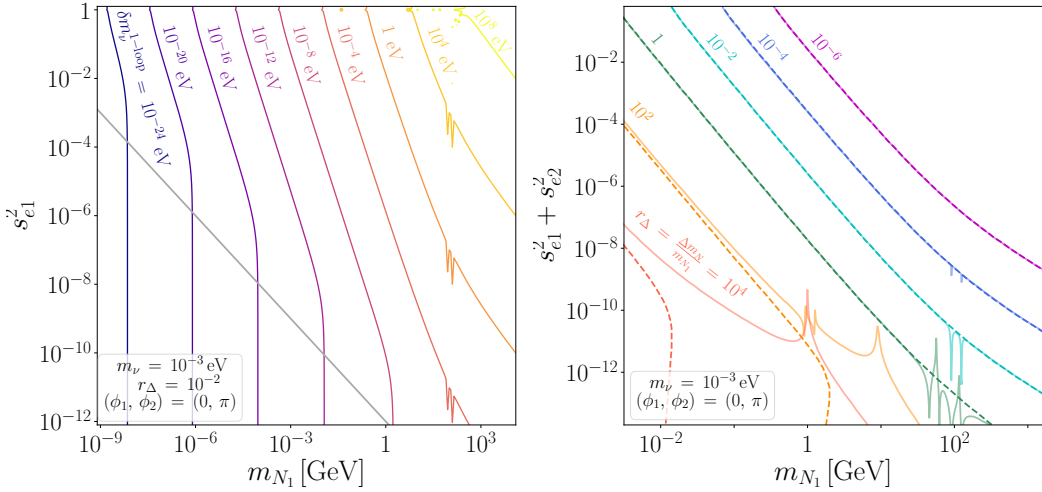


**Figure 5.4:** (Left) Absolute magnitude of the one-loop neutrino mass contribution  $|\delta m_\nu^{1\text{-loop}}|$  as a function of the lighter sterile mass  $m_{N_1}$  and mixing strength  $s_{e1}^2$  for indicated values of the other parameters. The canonical seesaw case with  $s_{e1}^2 = r_\nu$  is indicated by the diagonal grey line. (Right) Maximally allowed value of  $s_{e1}^2 + s_{e2}^2$  from the condition  $|\delta m_\nu^{1\text{-loop}}| < 0.1m_\nu$ , as a function of  $m_{N_1}$  for different values of the heavy neutrino splitting ratio  $r_\Delta = \frac{\Delta m_N}{m_{N_1}}$ . Solid lines are found by using the exact formula Eq. (2.79), while the dashed lines use this same formula but in the limit  $\mu_{R,S} \ll m_S$ .

$m_{N_1} < m_Z, m_h$  and as  $m_{N_1} \ln(m_{N_1})$  for  $m_{N_1} > m_Z, m_h$ . The discontinuities or ‘kinks’ in Fig. 5.4 occur at  $m_{N_1} = m_Z$  and  $m_{N_1} = m_h$ , i.e. when the one-loop contribution is enhanced.

In this analysis, we will require for consistency that the one-loop correction is subdominant compared to the tree-level mass. We choose the benchmark limit of 10% the size of the tree-level mass<sup>1</sup>,

$$|\delta m_\nu^{1\text{-loop}}| \leq 0.1m_\nu. \quad (5.22)$$

Using different benchmark limits will not change our results qualitatively. This limit can now be used to put an upper limit on the active-sterile mixing strengths. The maximally allowed values of  $s_{e1}^2 + s_{e2}^2$  are shown in Fig. 5.4 (right) as a function of the heavy neutrino mass  $m_{N_1}$  for different values of  $r_\Delta$ . The solid and dashed lines correspond to the upper limit derived from the exact formula Eq. (2.79) and the

<sup>1</sup>This condition excludes by construction the scenario where  $\mu_R \neq 0$  and  $\mu_S = 0$  and the neutrino masses are generated purely at one-loop.

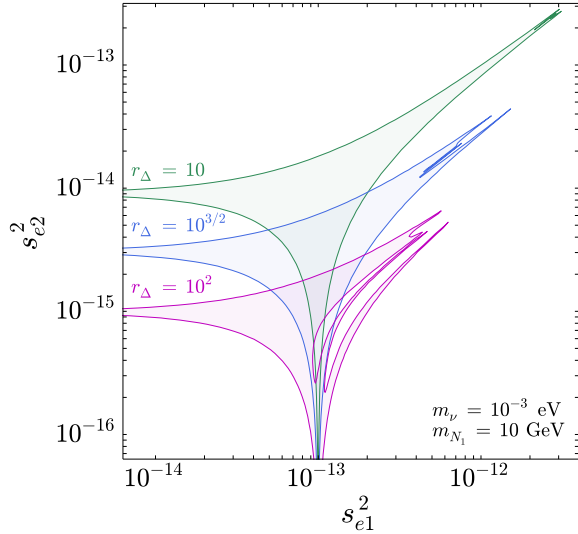


**Figure 5.5:** Modified allowed regions for the active-sterile mixing strengths satisfying the tree-level constraint  $(M_\nu)_{11} = 0$  and the condition for the one-loop contribution to be small,  $|\delta m_\nu^{1\text{-loop}}| < 0.1m_\nu$ .

approximation Eq. (2.80), respectively. It can be seen that as  $r_\Delta$  becomes smaller, the associated upper limits on  $s_{e1}^2 + s_{e2}^2$  become weaker. The exact and approximate upper limits diverge for small  $m_{N_1}$  and  $s_{e1}^2$ ; this is because  $\mu_{R,S} \ll m_S$  no longer holds in this particular region of the parameter space.

In Fig. 5.5 we plot again the allowed region from the tree-level constraint  $(M_\nu)_{11} = 0$ , but now also exclude the region no longer satisfying the inequality in Eq. (5.22) for different values of the relative splitting  $r_\Delta$ . It can be seen that increasing  $r_\Delta$  reduces the size of the allowed region, excluding much of the ISS region. The loop requirement only excludes mixings around  $s_{e1}^2 \sim r_\nu$  for large relative splittings.

While combining the constraints  $(M_\nu)_{11} = 0$  and  $|\delta m_\nu^{1\text{-loop}}| < 0.1m_\nu$  roughly consistent for small  $|\delta m_\nu^{1\text{-loop}}|$  values, it breaks down for larger values. An exact treatment would need to combine the conditions  $(M_\nu)_{11} = \delta m_\nu^{1\text{-loop}}$  and  $|\delta m_\nu^{1\text{-loop}}| < 0.1m_\nu$ . Consequently,

$$c_{e1}^2 c_{e2}^2 \frac{m_\nu^{\text{tree}}}{m_{N_1}} + s_{e1}^2 c_{e2}^2 e^{i\phi_1} + s_{e2}^2 \frac{m_{N_2}}{m_{N_1}} e^{i\phi'_2} = \frac{\delta m_\nu^{1\text{-loop}}}{m_{N_1}}, \quad (5.23)$$

where we approximate the neutrino mass on the left-hand side to be the tree-level

neutrino mass. Substituting  $m_v^{\text{tree}} = m_v - \delta m_v^{\text{1-loop}}$  via Eq. (5.21), Eq. (5.23) can be rearranged to solve for  $s_{e2}^2$  and  $\cos \phi'_2$ , but now as a function of the loop mass. However,  $s_{e2}^2$  and  $\phi'_2$  are themselves required to evaluate the loop mass in Eq. (2.79) as a function of  $m_{N_1}$  and  $s_{e1}^2$ . We must therefore solve for  $s_{e2}^2$  and  $\phi'_2$  iteratively by first setting  $(M_v)_{11} = 0$  and then re-inserting the values of  $s_{e2}^2$  and  $\phi'_2$  back into the one-loop formula. We find that the difference between the initial values of  $s_{e2}^2$  and  $\phi'_2$  (setting  $(M_v)_{11} = 0$ ) and iterated loop values is negligibly small when the inequality in Eq. (5.22) is enforced. This should not then significantly affect the upper bounds on  $s_{e1}^2 + s_{e2}^2$  derived from the loop condition. In other words, we keep the constraints on  $s_{e1}^2 + s_{e2}^2$  derived using  $(M_v)_{11} \approx 0$  and  $|\delta m_v^{\text{1-loop}}| < 0.1 m_v$  (as shown in Fig. 5.4).

## 5.2 Constraints on Heavy Sterile Neutrinos

In this section we will provide a review of the direct searches for sterile neutrinos and hence constraints on the active-sterile mixing  $|V_{\ell N}|^2$  over the sterile neutrino mass range  $1 \text{ eV} < m_N < 10 \text{ TeV}$ . For masses  $m_N < 1 \text{ eV}$  it becomes possible for one of the sterile states to form a *quasi-Dirac* state with an active state. A large portion of this parameter space is excluded by solar neutrino oscillations [214, 531]. For heavier masses  $m_N \gtrsim 10 \text{ TeV}$ , sterile neutrinos can generate the light active neutrino masses via the conventional seesaw mechanism. These neutrinos, however, are not kinematically accessible to direct searches.

The constraints from existing searches and observations in the  $(m_N, |V_{eN}|^2)$  plane are shown in Fig. 5.6 as various shaded regions. The sensitivities of expected future experiments and observations are shown in Fig. 5.7. As our ultimate focus is on a comparison with constraints from  $0\nu\beta\beta$  decay in Section 5.3, we focus on the first generation mixing element  $|V_{eN}|^2$ . The constraints on  $|V_{\mu N}|^2$  and  $|V_{\tau N}|^2$  are depicted in the plots of Ref. [143]<sup>2</sup>. Constraints on sterile neutrinos or heavy neutral leptons have been reviewed before in the literature, e.g. in Refs. [532–535].

---

<sup>2</sup>Furthermore, at the time of writing the current and future constraints are reviewed and provided by the website <http://sterile-neutrino.org/>, produced by the author of this thesis.

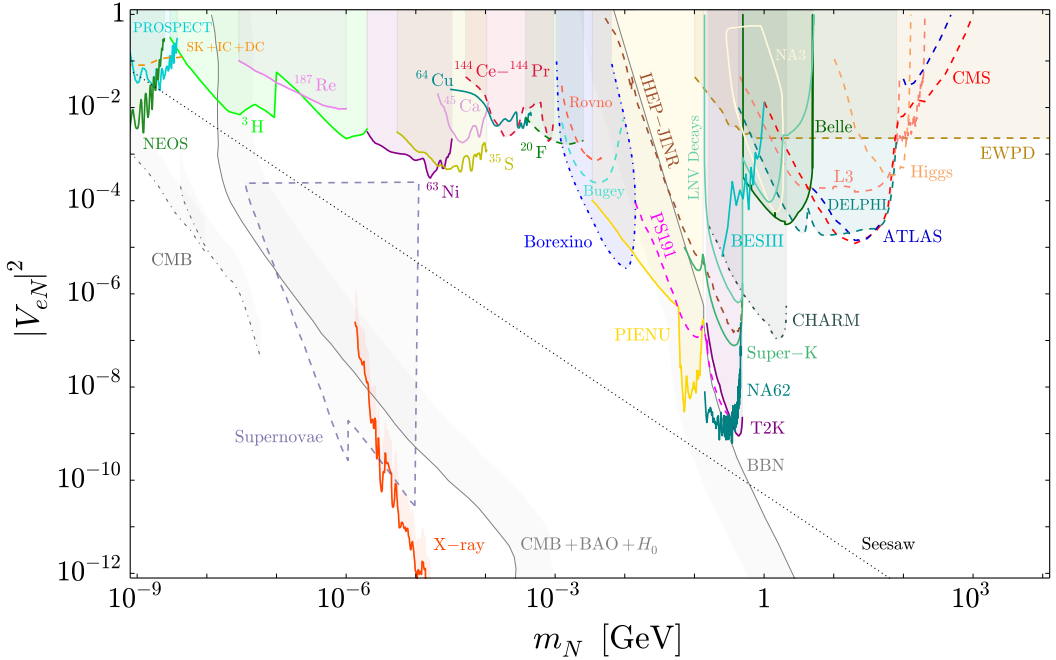


**Figure 5.6:** Current constraints on the mixing squared  $|V_{eN}|^2$  between the electron neutrino and sterile neutrino  $N$  as a function of the sterile neutrino mass  $m_N$ . The shaded regions are excluded by the searches and observations discussed in Sec. 5.2. For  $m_N < 10$  MeV, constraints are derived from neutrino oscillation, beta decay and reactor neutrino experiments. For  $m_N > 10$  MeV, constraints are set by meson decay, beam dump and collider measurements. Cosmological and astrophysical bounds from CMB, BBN, Hubble constant, supernovae and X-ray observations are relevant for  $m_N \lesssim 10$  GeV. The grey diagonal line labelled *Seesaw* indicates the seesaw relation  $|V_{eN}|^2 = m_v/m_N$  with  $m_v = 0.05$  eV.

### 5.2.1 Collider Searches

Heavy states can be produced by SM charged- and neutral-current interactions through their admixture with the active states (the *neutrino portal*), and thus their decay products can be searched for at high-energy colliders. For sufficiently small mixings, the macroscopic decay length of the heavy neutrinos can result in displaced vertices with distinct detector signatures. We consider the following searches (key-words in bold correspond to lines/shaded regions in Figs. 5.6 and 5.7):

- The LHC collaborations **ATLAS** and **CMS** have searched for  $N$  production and decay through a variety of channels. Both have recently searched for decays of  $W$ -produced  $N$  to three charged leptons,  $W^\pm \rightarrow \ell^\pm N$ ,  $N \rightarrow \ell^\pm \ell^\mp \nu_\ell$  ( $\ell = e, \mu$ ), either in the  $|\Delta L| = 0$  or  $|\Delta L| = 2$  mode. ATLAS used the prompt

final state of three isolated leptons and no opposite-charge same-flavour lepton pairs ( $|\Delta L| = 2$  channel) to reject Drell-Yan,  $W$  + jets and  $t\bar{t}$  backgrounds. CMS broadened the search to the  $|\Delta L| = 0$  channel with a sensitivity to displaced decays [536, 537]. ATLAS and CMS have also conducted searches for the  $|\Delta L| = 2$  same-sign dilepton + jets channel,  $W^\pm \rightarrow \ell^\pm N$ ,  $N \rightarrow \ell^\pm jj$  [538, 539]. For  $m_N > m_Z$  the limits can be improved by ATLAS and CMS during the high luminosity ( $\mathcal{L} = 3 \text{ ab}^{-1}$ ) LHC phase (**HL-LHC**) and by a future  $\sqrt{s} = 27$  to 100 TeV Future Circular Collider (**FCC-hh**) [540, 541]. Around  $m_N = m_h$ , limits can also be set from the SM Higgs decay to sterile neutrinos [542].

- In the future, **ATLAS**, **CMS** and **LHCb** will be able to probe smaller mixings  $|V_{\ell N}|^2$  through displaced vertex searches. For a given mixing,  $m_N$  must lie in a specific range in order to avoid  $N$  decaying promptly or outside the detector [536].
- At the LEP collider, the collaborations **L3** [543, 544] and **DELPHI** [545] searched for  $N$  produced through on-shell  $Z$  production,  $e^+e^- \rightarrow Z \rightarrow N\nu_\ell$ , followed by the decays  $N \rightarrow \ell^\mp W^\pm$ ,  $N \rightarrow \nu_\ell Z$  and  $N \rightarrow \nu_\ell h$ . Limits may be improved by future electron-electron colliders such as the **ILC**, **CLIC** and **FCC-ee** colliders [546–549]. The ILC may also be able to distinguish the  $|\Delta L| = 0$  and  $|\Delta L| = 2$   $W^\pm$  exchange channels between the  $e^+e^-$  pair by measuring the asymmetry of the outgoing lepton pseudorapidity distribution [524]. Finally, the proposed Large Hadron-Electron Collider (**LHeC**) LHC upgrade may also provide competitive constraints for  $m_N > m_Z$  [548, 550, 551]. An overview of proposed collider sensitivities is given in Ref. [552].
- Proposed detectors positioned near existing LHC interaction points have been designed specifically to search for displaced vertex signatures. These include **AL3X** [553], **CODEX-b** [554], **FASER2** [555, 556], **MATHUSLA** [557, 558] and the MoEDAL experiment MAPP detector [559].

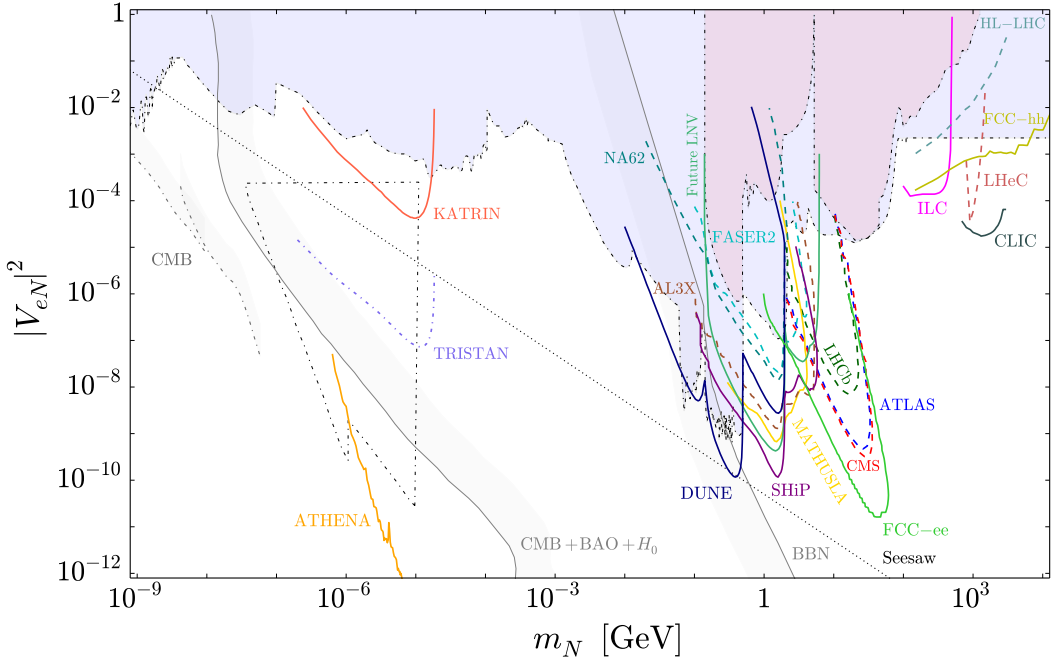


**Figure 5.7:** Future constraints on the mixing squared  $|V_{eN}|^2$  between the electron neutrino and sterile neutrino  $N$  as a function of the sterile neutrino mass  $m_N$ . The bounds are based on the sensitivities of future beta decay, meson decay, beam dump and collider experiments, as detailed in the main text. The blue shaded region indicates the parameter space already excluded by current experiments, as shown in Fig. 5.6. The red shaded region further specifies the current limits from searches for LNV signals (e.g. from meson decays and collider searches).

As for the  $|\Delta L| = 2$  signature at colliders, in a natural seesaw scenario with approximate lepton number conservation, the  $|\Delta L| = 2$  amplitude for the on-shell production of heavy neutrinos can be written as [519, 560]

$$\mathcal{A}_{\text{LNV}} = V_{eN}^2 \frac{2\Delta m_N}{\Delta m_N^2 + \Gamma_N^2} + \mathcal{O}\left(\frac{\Delta m_N}{m_N}\right), \quad (5.24)$$

for  $\Delta m_N \lesssim \Gamma_N$ , i.e. for a small mass splitting  $|\Delta m_N| = |m_{N_2} - m_{N_1}|$  between the heavy neutrinos compared to their average decay width  $\Gamma_N \equiv (\Gamma_{N_1} + \Gamma_{N_2})/2$ . Thus, the  $|\Delta L| = 2$  amplitude in Eq. (5.24) will be suppressed by a small  $\Delta m_N$ , except for the case  $\Delta m_N \simeq \Gamma_N$  when it can be resonantly enhanced [519, 561].

For the  $5 \text{ GeV} < m_N < 50 \text{ GeV}$  range of sterile neutrino masses probed by the ATLAS and CMS same-sign trilepton and dilepton + jets analyses, the total sterile neutrino decay width (if decays only takes to place to SM leptonic and hadronic

degrees of freedom) is given by

$$\Gamma_N = \sum_{\ell} a_{\ell}(m_N) |V_{\ell N}|^2, \quad (5.25)$$

where the expressions for the factors  $a_{\ell}(m_N)$  are given in Refs. [532, 562]. The factors  $a_{\ell}(m_N)$  include the contributions from two-body semi-leptonic and three-body leptonic decays, and are approximately given by

$$a_{\ell}(m_N) \approx N_{1 \rightarrow 2} \Gamma_{1 \rightarrow 2} + N_{1 \rightarrow 3} \Gamma_{1 \rightarrow 3}, \quad (5.26)$$

where  $N_{1 \rightarrow 2}$  and  $N_{1 \rightarrow 3}$  are the number of decay channels open for the two decay topologies. The factors  $\Gamma_{1 \rightarrow 2}$  and  $\Gamma_{1 \rightarrow 3}$  are given roughly by

$$\Gamma_{1 \rightarrow 2} \sim \frac{G_F^2 f_M^2 m_N^3}{5\pi}, \quad \Gamma_{1 \rightarrow 3} \sim \frac{G_F^2 m_N^5}{200\pi^3}, \quad (5.27)$$

where  $f_M$  represents the meson decay constants [532]. For  $m_N \approx 50$  GeV, all three-body leptonic decays and two-body semi-leptonic decays to pseudoscalar and vector mesons are open, and so the total decay width (assuming  $|V_{\mu N}|^2 = |V_{\tau N}|^2 = 0$ ) is approximately

$$\Gamma_N \sim (30 \cdot \Gamma_{1 \rightarrow 2} + 10 \cdot \Gamma_{1 \rightarrow 3}) |V_{e N}|^2 \sim 10^{-4} |V_{e N}|^2 \text{ GeV}. \quad (5.28)$$

For small splittings, e.g.  $r_{\Delta} = 10^{-4}$  and therefore  $\Delta m_N \sim 5$  MeV (for  $m_N \sim 50$  GeV), and the  $|V_{e N}|^2 \sim 10^{-5}$  mixings probed by the  $|\Delta L| = 2$  analyses, Eq. (5.28) implies that  $\frac{\Gamma_N}{\Delta m_N} \sim 10^{-6}$ . Collider searches specifically looking for a  $|\Delta L| = 2$  signal in Fig. 5.7 are therefore still valid for this splitting and also splittings down to  $r_{\Delta} \sim 10^{-10}$ . As will be discussed later, this is important for the comparison with  $0\nu\beta\beta$  decay in this mass range. We finally note that the analysis of Ref. [563] gives an estimate for the regions of the  $(m_N, |V_{\ell N}|^2)$  parameter space where the ratio  $\mathcal{R}_{\ell\ell}$  in Eq. (5.17) is less than or greater than a third. Comparing with Fig. 1 of that work, we again confirm that  $|\Delta L| = 2$  signals below the EW scale remain unsuppressed, particularly for  $\Delta m_N$  of order the light neutrino mass splittings (motivated

by naturalness).

### 5.2.2 Meson Decays and Beam-Dump Experiments

At the intensity frontier  $N$  can be produced in beam-dump experiments and through meson decays. We consider the following limits:

- The TRIUMF **PIENU** experiment [564] conducted a search for  $N$  produced in pion decays at rest. Utilising the helicity suppression of the  $\pi \rightarrow e\nu$  decay channel in comparison to  $\pi \rightarrow \mu\nu$  channel, the presence of  $N$  induces extra peaks in the lower positron energy region. The collaboration improved on previous results limited by the background  $\mu^+ \rightarrow e^+ \nu_e \bar{\nu}_\mu$  [565–567].
- The **NA62** experiment [568] used a secondary 75 GeV hadron beam containing a fraction of kaons, and has been able to probe the decays  $K^+ \rightarrow \ell^+ N$  ( $\ell = e, \mu$ ). For small  $|V_{\ell N}|^2$  the  $N$  decay length is much longer than the 156 m detector volume and the process is characterised by a single detected track; a positive signal is a peak in the missing mass distribution. In future, NA62 will be converted to a beam-dump configuration and will be able to probe hadronic decays to  $N$ , followed by  $N$  decays, up to the  $D$  meson mass [569]. A re-analysis of the impact of sterile neutrinos on kaon decays was conducted in Ref. [570].
- The **Belle** experiment [571] was a  $B$  factory that extended the peak search method to higher energies; using  $B\bar{B}$  pairs collected at the  $\Upsilon(4S)$  resonance, the decay mode  $B \rightarrow (X)\ell N$ , with  $X$  a charmed meson  $D^{(*)}$  or light meson, could be followed by  $N \rightarrow \ell\pi$  ( $\ell = e, \mu$ ). Constraints on  $|V_{\ell N}|^2$  were made between the  $K$  and  $B$  meson masses [572].
- The **NA3** experiment [573] collided a secondary 300 GeV  $\pi^-$  beam with an iron absorber, producing hadronic states which subsequently decayed to leptonic, semi-leptonic or fully hadronic final states.  $N$  decays producing leptonic or semi-leptonic final states could be produced from the decays of  $\pi$ ,  $K$ ,  $D$  and  $B$  mesons. NA3 was most sensitive up to the  $D$  meson mass.

- Accelerator neutrino beam experiments have conducted a variety of parallel searches. The **CHARM** [574, 575] and **PS191** [576] experiments and the **IHEP-JINR** neutrino detector [565, 577] searched for a small fraction of  $N$  in a predominantly  $\nu_\mu$  beam. The beams were produced by colliding a primary beam of protons with an iron or copper fixed target, with the hadronic products decaying as  $\pi/K/D \rightarrow \ell\nu(N)$  ( $\ell = e, \mu$ ). If sufficiently massive,  $N$  may decay before reaching the detector via the channel  $N \rightarrow \ell^+\ell^-\nu_\ell$ . CHARM also used a wide-band neutrino beam to constrain the neutral-current process  $\nu_\mu n(p) \rightarrow NX$  followed by  $N \rightarrow \mu X$  within the detector. IHEP-JINR and PS191 provide constraints up to the kaon mass and CHARM up to the  $D$  meson mass.
- The LBL neutrino oscillation experiment **T2K** [578] searched for an admixture of  $N$  in its initial neutrino beam flux, produced by colliding 30 GeV protons with a graphite target at J-PARC. Daughter  $K^\pm$  of a given charge are focused and decay via  $K \rightarrow \ell\nu(N)$ . The off-axis near-detector at a baseline of 280 m searched for  $N$  decays via the channel  $N \rightarrow \ell\pi$ , improving on the constraints made by PS191. In future, the near detector of the oscillation experiment **DUNE** will be highly sensitive for  $m_N$  up to the  $D_s$  meson mass [579, 580].
- The future beam-dump experiment **SHiP** [581] is purposely designed to look for exotic long-lived particles. Utilising a 400 GeV proton beam from the CERN Super Proton Synchrotron, it is expected to be sensitive to sterile neutrinos with  $m_N$  up to the  $B_c$  meson mass ( $\sim 6$  GeV) [582].
- In parallel with collider searches it is possible to look for  $|\Delta L| = 2$  or **LNV Decays** of tau leptons and pseudoscalar mesons as discussed in Refs. [532, 562, 583, 584]. One issue is that if the  $|\Delta L| = 2$  process is mediated by the light neutrinos the amplitude is proportional to and suppressed by the small  $m_\nu^2$ , while if mediated by heavy neutrinos it is suppressed by  $1/m_N$  and  $|V_{\ell N}|^2$ . However,  $|\Delta L| = 2$  decays can be strongly enhanced if the sterile state is pro-

duced on-shell. The sensitivity of NA62 to three-body  $|\Delta L| = 2$  light meson decays, BESIII to charmed meson decays and BaBar, Belle and LHCb for  $B$  meson decays were estimated most recently in Ref. [584]. The **BESIII** experiment has also conducted its own analysis on the  $(D^+ \rightarrow \ell^+ \ell^+ \pi^- / K^-)$  decay channel [585]. Finally, the **Future LNV** decay sensitivities of NA62, LHCb, Belle-II, MATHUSLA, SHiP and FCC-ee have been explored in Ref. [586]

### 5.2.3 Beta Decays and Nuclear Processes

Active neutrinos are produced in the beta decays of unstable isotopes and in nuclear fission processes. Heavy sterile neutrinos can also be produced via the active-sterile mixing if the sterile mass is smaller than the energy release ( $Q$ -value) of the nuclear process. The production of a sterile state produces a distortion or ‘kink’ in the beta decay spectrum and associated Kurie plot. We consider the following searches:

- Heavy neutrinos produced in beta decays significantly alter the energy spectrum of the emitted  $\beta$  electron. To be kinematically accessible,  $m_N$  must be smaller than the  $Q$ -value of the process. If the sterile states are also considerably more massive than the active states, the beta decay spectrum can be written as the incoherent sum

$$\frac{d\Gamma}{dE} = \left(1 - \sum_i |V_{eN_i}|^2\right) \frac{d\Gamma}{dE}(m_\beta^2) + \sum_i |V_{eN_i}|^2 \frac{d\Gamma}{dE}(m_{N_i}^2) \Theta(Q_\beta - m_{N_i}), \quad (5.29)$$

where  $m_\beta^2 = \sum_k |U_{ek}|^2 m_k^2$  is the usual neutrino mass scale probed by beta decay [587]. This expression can give rise to multiple kinks in the spectrum at energies  $E = Q_\beta - m_{N_i}$  and of relative size  $|V_{eN_i}|^2$ . This effect for a single sterile neutrino has been probed for a variety of isotopes with a range of  $Q$ -values, and therefore sensitive to different  $m_N$ . Isotopes include  $^3\text{H}$  [588–591],  $^{20}\text{F}$  [592],  $^{35}\text{S}$  [593],  $^{45}\text{Ca}$  [594],  $^{63}\text{Ni}$  [595],  $^{64}\text{Cu}$  [596],  $^{144}\text{Ce}$ – $^{144}\text{Pr}$  [597] and  $^{187}\text{Re}$  [598]. In the future, limits will be improved by the operating tritium beta decay experiment **KATRIN** and its upgrade **TRISTAN** [522]. The Project 8 and CRESIDA experiments will instead use the alternative method of cyclotron radiation emission spectroscopy [599, 600].

- Reactor neutrino experiments are sensitive to sterile neutrinos with masses in the range  $1 \text{ MeV} < m_N < 10 \text{ MeV}$ , where it is possible for  $N$  to decay within the detector via the channel  $N \rightarrow e^+ e^- \nu$ . Limits have been set by searches at the **Rovno** [601] and **Bugey** [602] reactors. This effect was also searched for by the **Borexino** experiment [603], which detected neutrinos produced by the fission processes in the Sun; heavy neutrinos with masses up to 14 MeV can be produced in the decay of  ${}^8\text{B}$  and then decay before reaching the terrestrial detector.

### 5.2.4 Active-Sterile Neutrino Oscillations

Anomalies in neutrino oscillation experiments are still providing hints for the existence of an additional mass-squared splitting  $\Delta m^2 \sim 1 \text{ eV}^2$  to the well-established solar and atmospheric mass-squared splittings [139, 176]. This apparent splitting has been established in the measurement of multiple channels, including  $\nu_\mu \rightarrow \nu_e$  accelerator neutrino appearance (LSND anomaly),  $\bar{\nu}_e \rightarrow \bar{\nu}_e$  reactor neutrino disappearance (reactor anomaly) and the  $\nu_e \rightarrow \nu_e$  disappearance of  ${}^{37}\text{Ar}$  and  ${}^{51}\text{Cr}$  electron capture decay neutrinos (gallium anomaly). Attempts have been made to fit the data to models with additional eV-scale neutrinos, e.g. phenomenological (3 + 1) and (3 + 2) models. While recent reactor experiments such as **DANSS** [135] and **NEOS** [134] have improved the statistical significance of an additional eV-scale sterile state, when combined with the  $\nu_e$  appearance data of MiniBooNE they are in strong tension with the observed  $\nu_\mu \rightarrow \nu_\mu$  accelerator neutrino disappearance of the MINOS, NO $\nu$ A and IceCube experiments.

In the context of the single generation model of this chapter, we interpret the mass-squared splitting to be  $\Delta m_{41}^2 = m_N^2 - m_\nu^2$ . As we are focused on the active-sterile mixing with the electron flavour, only experiments sensitive to  $\nu_e \rightarrow \nu_e$  and  $\bar{\nu}_e \rightarrow \bar{\nu}_e$  and measuring  $\sin^2 2\theta_{ee} \approx 4|V_{eN}|^2$  are relevant. For sub-eV sterile neutrino masses the **Daya Bay** [604], **KamLAND** [531] and upcoming **JUNO** [605] experiments can probe the mixing down to  $|V_{eN}|^2 \lesssim 10^{-3}$ . However it should be noted that if one wants to fit the solar and atmospheric mass splittings in a minimal (3 + 1) or (3 + 2) extension, solar data excludes the region  $10^{-9} \text{ eV} < m_N < 0.6 \text{ eV}$  [214, 606].

Below this region is the quasi-Dirac scenario and above the mini-seesaw extending to the conventional high-scale seesaw. Light sterile neutrinos can be implemented in an ISS model as in Refs. [227, 607, 608].

Above the eV-scale, DANSS and NEOS provide limits down to  $|V_{eN}|^2 \lesssim 10^{-2}$  (as both exclusions are similar, Fig. 5.6 shows NEOS only) while the **PROSPECT** [609] experiment provides constraints up to  $m_N = \sqrt{\Delta m_{41}^2 + m_V^2} \sim 5$  eV. Over the same mass range Super-Kamiokande, IceCube and DeepCore (**SK+IC+DC**) provide complementary limits [138].

### 5.2.5 Indirect Laboratory Constraints

As discussed in Chapter 2, any mixing between active and sterile neutrinos induces non-unitarity effects among the active neutrinos which are visible in SM charged and neutral-current processes [610–612]. This is most easily parametrised by a non-unitary light neutrino mixing matrix

$$U_V = (1 - \eta)U, \quad (5.30)$$

where  $U$  is a unitary matrix corresponding to the standard PMNS mixing matrix and the matrix  $\eta$  measures deviations from unitarity. The elements of  $\eta$  are given in a general seesaw model by  $\sqrt{2|\eta_{\ell\ell'}|} = \sum_i \sqrt{V_{\ell N_i} V_{\ell' N_i}^*}$  and alter electroweak precision data (**EWPD**) observables. These include leptonic and hadronic measurements of the weak mixing angle  $s_W^2$ , the  $W$  boson mass  $m_W$ , ratios of fermionic  $Z$  boson decay rates  $R_l$ ,  $R_c$ ,  $R_b$  and  $\sigma_{\text{had}}^0$ , the  $Z$  invisible decay width  $\Gamma_Z^{\text{inv}}$  and ratios of leptonic weak decays testing EW universality  $R_{\ell\ell'}^\pi$ ,  $R_{\ell\ell'}^W$ ,  $R_{\ell\ell'}^K$  and  $R_{\ell\ell'}^l$ . Furthermore, by modifying  $G_F$ , the non-unitarity of  $U_V$  impacts the values of CKM mixing matrix elements extracted from experiments. Numerous weak decays have been used to pin down the CKM elements  $V_{ud}$ ,  $V_{us}$ ,  $V_{ub}$  and the unitarity condition  $|V_{ud}|^2 + |V_{us}|^2 + |V_{ub}|^2 = 1$ . Assuming a single sterile state coupling to just the first generation, all of these measurements enforce a constant bound of  $\sqrt{2|\eta_{ee}|} = |V_{eN}| < 0.050$  for  $m_N \gtrsim 1$  GeV [242, 612–616].

Another indirect measurement of  $\eta_{\ell\ell'}$  and hence different combinations of the

active-sterile mixings comes from the non-observation of lepton flavour violating (LFV) processes  $\ell_\alpha \rightarrow \ell_\beta \gamma$  and  $\mu^- - e^-$  conversion in nuclei [451]. Due to the different flavours of charged leptons involved in these processes, active-sterile mixings to at least two active generations are required. For the purpose of our single active generation picture we therefore do not show the LFV constraints in Fig. 5.6.

### 5.2.6 Cosmological and Astrophysical Constraints

The presence of sterile states with masses  $m_N$  and mixings  $|V_{\ell N}|^2$  can have drastic consequences on early-universe observables and have been explored extensively in the literature [617]. These include the abundances of light nuclei formed during Big Bang Nucleosynthesis (BBN), temperature anisotropies in the Cosmic Microwave Background (CMB) radiation and the large-scale clustering of galaxies. Deviations from the standard smooth, isotropic background evolution (and perturbations around this background) impose severe constraints, especially for sterile states with masses  $m_N \lesssim 100$  MeV. The limits are however highly sensitive to the production and decay mechanism of the sterile state and can be relaxed in extensions to seesaw models. We consider the following:

- Sterile neutrinos with masses  $m_N \lesssim 1$  GeV can be long-lived and disrupt the standard formation of light nuclei  ${}^4\text{He}$ ,  $\text{D}$ ,  ${}^3\text{He}$  and  ${}^7\text{Li}$  during **BBN** [618,619]. For larger masses the decay products from the accessible two-body and three-body decays have enough time to thermalise with the plasma. For decay times  $\tau \gtrsim 1$  s occurring below  $T \lesssim 1$  MeV, i.e. roughly after neutrino decoupling and the onset of BBN, both the modified background expansion due to the presence of non-relativistic  $N$  and the altered weak processes  $n + v \leftrightarrow p + e^-$  and  $p + \bar{v} \leftrightarrow n + e^+$  involving non-thermal decay product neutrinos lead to modified nuclei abundances. To limit the impact of  $N$ , the naive condition  $\tau = \Gamma_N^{-1} \gtrsim 1$  s is commonly used. This translates to a lower limit of  $|V_{eN}|^2 \gtrsim 10^{-11} (\text{GeV}/m_N)^5$  for  $N \rightarrow 3v$ ,  $N \rightarrow ve^+e^-$  and the sub-dominant radiative decay  $N \rightarrow v\gamma$ . Above the pion mass threshold the constraints are made weaker by including the decays  $N \rightarrow v\pi^0$  and  $N \rightarrow e^\pm\pi^\mp$ .

- Sterile neutrinos decaying at later times (with  $\tau \lesssim t_{\text{rec}} \approx 1.2 \times 10^{13}$  s) to non-thermal active neutrinos can modify the amount of dark radiation measured (beyond the usual value including active neutrino oscillations,  $N_{\text{eff}} \simeq 3.046$ ) at recombination,  $\Delta N_{\text{eff}}$ . Decays after recombination but before the current epoch ( $t_{\text{rec}} \lesssim \tau \lesssim t_0 \approx 4.3 \times 10^{17}$  s) can also be important. Useful probes of these effects on the smooth, isotropic expansion history include the CMB shift parameter  $R_{\text{CMB}}$  (related to the position of the first acoustic peak in the CMB temperature power spectrum), the first peak of Baryon Acoustic Oscillation (BAO) sound waves imprinted on the large-scale distribution of galaxies and finally the value of the Hubble parameter  $H$  inferred from Type Ia supernova, BAO and Lyman- $\alpha$  survey data. These exclude values of  $m_N$  and  $|V_{eN}|^2$  corresponding to lifetimes up to  $t_0$ , where the condition that  $N$  does not make up more than the observed matter density  $\Omega_{\text{sterile}} < \Omega_{\text{DM}} \approx 0.12 h^{-2}$  and thus overcloses the Universe also applies. This constraint can be evaded in exotic models [620–623], for example those that inject additional entropy and dilute the dark matter (DM) energy density. We indicate the combined constraints from Ref. [624] in Fig. 5.6 as **CMB+BAO+ $H_0$** .
- Sterile neutrinos with masses  $1 \text{ keV} \lesssim m_N \lesssim 100 \text{ keV}$  can avoid the global constraints above if the active-sterile mixing is sufficiently small, i.e  $10^{-10} \lesssim |V_{eN}|^2 \lesssim 10^{-8}$ . With lifetimes longer than the current age of the Universe, these sterile states are viable DM candidates [599, 625, 626]. Depending on the size of the lepton-antilepton asymmetry  $\eta_L \equiv n_L/n_\gamma$ , production can occur either through resonant ( $\eta_L > 10^6 \eta_b$ ) or non-resonant ( $\eta_L \approx 0$ ) active-sterile oscillations. The former (Shi-Fuller mechanism [627]) is independent of  $|V_{eN}|^2$  while the latter (Dodelson-Widrow mechanism [628]) requires now-excluded  $|V_{eN}|^2$  values. If DM is composed entirely of keV sterile neutrinos, their fermionic nature limits the phase space density of DM-rich dwarf galaxies and imposes the so-called Tremaine-Gunn bound,  $m_N \gtrsim 0.4 \text{ keV}$ .

It is also possible to search for anomalous **X-ray** lines from the radiative decays  $N \rightarrow v\gamma$  in the diffuse X-ray background and from DM-rich astro-

physical objects. An observed signal at  $E \simeq 3.55$  keV may imply a sterile neutrino with a mass of 7.1 keV and has continued to persist in observations of stacked galaxy clusters [629], the Perseus galaxy cluster and Andromeda M31 galaxy [630] and the centre bulge of the Milky Way [631]. In Fig. 5.6 we show the most recent limits from observations of M31 and the Milky Way by NuSTAR [632,633]. In Fig. 5.7 we show the improved future sensitivity of **ATHENA** [634]. These limits assume  $\Omega_{\text{DM}} = \Omega_{\text{sterile}}$  and must be multiplied by  $\frac{\Omega_{\text{sterile}}}{\Omega_{\text{DM}}}$  to account for other DM species [624].

- Mixings can be excluded for sterile neutrinos in the mass range  $10 \text{ eV} \lesssim m_N \lesssim 10 \text{ keV}$  by examining their impact on Type-II **Supernovae**. Active-sterile neutrino oscillations hinder the standard neutrino reheating of the reflected shock wave which becomes stalled in the first fraction of a second after the supernova core bounce. For the explosion to continue and additionally produce the observed SN1987A  $\bar{\nu}_e$  flux at Kamioka [635] and IMB [636], a certain region of the  $(m_N, |V_{\ell N}|^2)$  parameter space must be excluded.

In Refs. [637–643], the resonant conversion  $\nu_e \rightarrow N$  was studied. Meanwhile, Refs. [644–646] have investigated  $\nu_{\mu,\tau} \rightarrow N$  conversions for which the MSW resonance conditions are different. An open question is whether the conditions for  $r$ -process nucleosynthesis (producing heavy elements in the supernova outflows) are met in these scenarios [639,642]. Lastly, sterile neutrinos that escape supernovae can subsequently decay via  $N \rightarrow \nu_e \gamma$  and  $N \rightarrow \nu_e e^+ e^- \gamma$ , producing an excess of gamma rays arriving soon after the detection of the  $\nu_e$ . The non-observation of such an excess for SN1987A provides a stringent limit in the mass range  $1 \text{ MeV} \lesssim m_N \lesssim 30 \text{ MeV}$  [647]. Given the various assumptions and calculational differences of the constraints discussed we show for illustration in Fig. 5.6 the excluded region from Ref. [638].

- Sufficiently stable and light sterile neutrinos with masses  $m_N \lesssim 50 \text{ eV}$  can be produced with quasi-thermal temperatures via active-sterile oscillations be-

fore the neutrino decoupling [599, 648, 649]. While relativistic they continue to contribute towards the extra effective number of light fermionic degrees of freedom  $\Delta N_{\text{eff}}$ . Once non-relativistic they add to the matter density as  $\Omega_{\text{sterile}} h^2 = \frac{m_{\text{eff}}^{\text{sterile}}}{94.1 \text{ eV}}$ , while also damping density perturbations below a mass-dependent free-streaming scale. The most simple case of a single sterile neutrino thermalising through oscillations at the active neutrino temperature has  $\Delta N_{\text{eff}} = 1$  and  $m_{\text{eff}}^{\text{sterile}} \simeq m_N$  [531, 650, 651] which is now excluded [652]. The Planck collaboration has made fits of CMB (TT+lowP+lensing+BAO) data to the parameters  $(\sum m_\nu, N_{\text{eff}})$  and  $(m_{\text{eff}}^{\text{sterile}}, \Delta N_{\text{eff}})$  [114]. In Refs. [624] and [653] these constraints are mapped to the  $(\Delta m_{41}^2, \sin^2 2\theta_{ee})$  parameter space which we plot as grey dot-dashed **CMB** constraints in Fig. 5.6.

### 5.3 Neutrinoless Double Beta Decay Constraints

In this section we will now determine the constraints from  $0\nu\beta\beta$  decay on our phenomenological model. The bounds from  $0\nu\beta\beta$  decay have been covered before in the literature in the context of the Type-I seesaw [654, 655], ISS mechanism [656, 657] and left-right symmetric models [260, 369, 658–664].

Of particular importance will be the dependence of the  $0\nu\beta\beta$  decay constraints on the sterile neutrino mass  $m_N$  and the average momentum exchange  $p_F$  of the process. We will see that for  $m_N \gg p_F$ , the contribution from a heavy sterile neutrino is proportional to  $\frac{|V_{eN}|^2}{m_N}$ ; this is equivalent to integrating out the heavy states. If  $m_N \ll p_F$ , the ‘light’ sterile neutrino contributes much like a light active neutrino in the standard  $0\nu\beta\beta$  decay exchange mechanism. However, in this case the  $(M_\nu)_{11} = 0$  condition suppresses the total  $0\nu\beta\beta$  decay rate because  $(T_{1/2}^{0\nu})^{-1} \sim (M_\nu)_{11}$  in the  $m_N \ll p_F$  regime. Multiple sterile states, some with masses above and some below  $p_F$ , is an intriguing intermediate scenario.

We will also give a broad comparison between  $0\nu\beta\beta$  decay constraints and those from the direct searches discussed in Sec. 5.2, particularly where the  $0\nu\beta\beta$  decay constraints are the most relevant ( $m_N \sim 100$  keV). One of the most interesting aspects of this comparison is the dependence of the  $0\nu\beta\beta$  decay constraints on the

mass splitting  $\Delta m_N$  between the heavy states. Because  $0\nu\beta\beta$  decay is an  $|\Delta L| = 2$  process we know it must vanish in the  $\mu_{R,S} \rightarrow \mathbf{0}$  limit of the ISS mechanism. The  $|\Delta L| = 2$  mass matrices  $\mu_{R,S}$  also control the splitting between the heavy states, so in the limit  $\Delta m_N \rightarrow 0$  (the heavy states form a pseudo-Dirac fermion) the  $0\nu\beta\beta$  decay limits vanish. We will compare this to the suppression of  $|\Delta L| = 2$  collider and meson decay constraints. No such suppression occurs for the  $|\Delta L| = 0$  search constraints discussed in Section 5.2.

However, it is important to consider the effect  $\Delta m_N$  has on the interpretation of the direct search constraints. For example, the analyses of beta decay kink searches and meson decay peak searches assume a single sterile state and constrain the associated mixing  $|V_{eN}|^2$  and mass  $m_N$ . On the other hand, it could also be the case that there are two sterile neutrinos with a splitting  $\Delta m_N$  below the energy resolution of the experiment; the searches are then probing the sum of mixings  $|V_{\ell N_1}|^2 + |V_{\ell N_2}|^2$ . In the single-generation case there is a lower limit on this sum from the  $(M_\nu)_{11} = 0$  condition,

$$|V_{\ell N_1}|^2 + |V_{\ell N_2}|^2 \approx s_{e1}^2 + s_{e2}^2 = s_{e1}^2 + \frac{1}{1 - \frac{(1+r_\Delta)\cos\phi_2}{r_\nu + (\cos\phi_1 - r_\nu)s_{e1}^2}} \gtrsim \frac{m_\nu}{m_{N_1}}, \quad (5.31)$$

where we assume  $r_\Delta \ll 1$ . If  $\Delta m_N$  is instead larger than the energy resolution of direct searches, the non-observation of a sterile state excludes regions in both the  $(m_{N_1}, |V_{\ell N_1}|^2)$  and  $(m_{N_2}, |V_{\ell N_2}|^2)$  parameter spaces. So far, direct searches have only probed mixing strengths in the ISS region of the parameter space, i.e.  $|V_{\ell N_1}|^2 \approx |V_{\ell N_2}|^2(1 + r_\Delta)$ . Thus, the excluded region in  $(m_{N_2}, |V_{\ell N_2}|^2)$  excludes additional portions of  $(m_{N_1}, |V_{\ell N_1}|^2)$  parameter space. This is simply the same excluded region but shifted to smaller  $m_{N_1}$  and larger  $|V_{\ell N_1}|^2$  by the factor  $(1 + r_\Delta)$ .

The  $0\nu\beta\beta$  decay rate or inverse half-life, taking into account the exchange of three active and  $n_S$  sterile neutrinos, can be written as

$$(T_{1/2}^{0\nu})^{-1} = G^{0\nu} g_A^4 m_p^2 \left| \sum_{i=1}^3 U_{ei}^2 m_i \mathcal{M}^{0\nu}(m_i) + \sum_{i=1}^{n_S} V_{eN_i}^2 m_{N_i} \mathcal{M}^{0\nu}(m_{N_i}) \right|^2, \quad (5.32)$$

where  $G^{0\nu}$  is a kinematic phase space factor (PSF) for the outgoing electron pair,  $g_A$  the axial coupling for the nuclear current,  $m_p$  the proton mass and  $\mathcal{M}^{0\nu}(m_i)$  the nuclear matrix element (NME) for the process of an exchanged Majorana neutrino of mass  $m_i$  [665].

The most recent calculations of  $G^{0\nu}$  for relevant  $0\nu\beta\beta$  decay isotopes have included effects such as electron screening and the Coulomb distortion of the electronic wave functions due to the finite size of the daughter nucleus [666–668]. The NMEs are in principle much more difficult to compute as they encode the non-trivial transition between the initial and final state nuclei in the process. The NMEs entering Eq. (5.32) take the form

$$\begin{aligned} \mathcal{M}^{0\nu}(m_i) = & \frac{1}{m_e m_p} \frac{R_A}{g_A(0)^2} \int d^3\mathbf{x} \int d^3\mathbf{y} \int \frac{d\mathbf{p}}{2\pi^2} e^{i\mathbf{p}\cdot(\mathbf{x}-\mathbf{y})} \\ & \times \sum_n \frac{\langle F | J^{\mu\dagger}(\mathbf{x}) | n \rangle \langle n | J_\mu^\dagger(\mathbf{y}) | I \rangle}{\omega_i(\omega_i + \mu)}, \end{aligned} \quad (5.33)$$

where  $J^\mu$  is a hadronic current,  $R_A$  the nuclear radius and  $\omega_i = \sqrt{\mathbf{p}^2 + m_i^2}$  the energy of the exchanged neutrino. It is necessary to sum over all possible intermediate nuclear states  $n$  between the initial and final states  $I$  and  $F$  respectively, and  $\mu = E_n - \frac{1}{2}(E_I + E_F)$  is the relative energy of these virtual states with respect to the average energy of the process. This sum, along with the non-perturbative nature of the hadronic currents, makes the calculation of Eq. (5.33) extremely difficult, and at present there are still large theoretical uncertainties in computed values.

Four common simplifying assumptions are: (i) the closure approximation, (ii) the impulse approximation, (iii)  $J^P = 0^+$  nuclear states and (iv)  $s$ -wave electron wavefunctions. Assumption (i) is that only neutrino momenta  $\mathbf{p}$  of similar size to the nucleon-nucleon spacing contribute to the amplitude; this allows the denominator in Eq. (5.33) to be removed from the sum and cancels the contribution of intermediate odd-odd nuclei. Approximation (ii) allows the hadronic current matrix elements to be expressed in terms of the *nucleon* current form factors associated with the vector ( $g_V$ ), axial vector ( $g_A$ ), weak-magnetic ( $g_M$ ) and pseudoscalar ( $g_P$ ) couplings. Because  $0\nu\beta\beta$  decay parent and daughter isotopes must have even num-

NME Calculation	$\mathcal{M}_v^{0v}$   ( $\delta \mathcal{M}_v^{0v} $ )		$\mathcal{M}_N^{0v}$   ( $\delta \mathcal{M}_N^{0v} $ )	
	$^{76}\text{Ge}$	$^{136}\text{Xe}$	$^{76}\text{Ge}$	$^{136}\text{Xe}$
QRPA Tübingen [669]	4.73 (0.18)	2.05 (0.20)	318.5 (0.36)	168.0(0.36)
QRPA Jyväskylä [670]	5.90 (0.11)	3.21 (0.09)	437.5 (0.08)	202.3 (0.08)
IBM-2 [671]	4.68 (0.32)	3.05 (0.32)	104.0 (0.54)	73.0 (0.54)
ISM [672]	2.79 (0.30)	2.15 (0.30)	132.7 (0.38)	114.9 (0.38)

**Table 5.1:** Light  $|\mathcal{M}_v^{0v}|$  and heavy  $|\mathcal{M}_N^{0v}|$  NMEs and associated fractional uncertainties  $\delta|\mathcal{M}_v^{0v}|$  and  $\delta|\mathcal{M}_N^{0v}|$  for  $^{76}\text{Ge}$  and  $^{136}\text{Xe}$  used in this work, taken from QRPA, IBM and ISM calculations in the literature, which are the only available methods quoting both light and heavy neutrino NMEs. When not explicitly given in the reference we estimate the uncertainties from the variation of NMEs with  $g_A$  and the choice of short-range correlations.

bers of protons and neutrons, their ground state is always  $J^P = 0^+$  (while decays to excited states are suppressed) thus justifying the assumption (iii). Lastly, the emission of  $p$ -wave electrons is also suppressed and the computation of  $G^{0v}$  is greatly simplified in the  $s$ -wave case, as assumed in (iv).

A useful interpolating formula for the NMEs can be derived when considering Eq. (5.33) in the limits  $m_i \ll p_F$  and  $m_i \gg p_F$ ,

$$\mathcal{M}^{0v}(m_i \ll p_F) = \frac{\mathcal{M}_v^{0v}}{m_e m_p}, \quad \mathcal{M}^{0v}(m_i \gg p_F) = \frac{\mathcal{M}_N^{0v}}{m_i^2}, \quad (5.34)$$

where  $\mathcal{M}_v^{0v}$  and  $\mathcal{M}_N^{0v}$  are dimensionless *light* and *heavy* NMEs respectively. It is possible to write the following interpolating formula that includes both of these scaling behaviours,

$$\mathcal{M}^{0v}(m_i) \approx \frac{|\mathcal{M}_N^{0v}|}{\langle \mathbf{p}^2 \rangle + m_i^2}, \quad \langle \mathbf{p}^2 \rangle = m_e m_p \left| \frac{\mathcal{M}_N^{0v}}{\mathcal{M}_v^{0v}} \right|, \quad (5.35)$$

so that the half-life formula Eq. (5.32) including sterile states becomes [583, 669]

$$(T_{1/2}^{0v})^{-1} = G^{0v} g_A^4 m_p^2 |\mathcal{M}_N^{0v}|^2 \left| \sum_{i=1}^3 \frac{U_{ei}^2 m_i}{\langle \mathbf{p}^2 \rangle} + \sum_{i=1}^{n_S} \frac{V_{eN_i}^2 m_{N_i}}{\langle \mathbf{p}^2 \rangle + m_{N_i}^2} \right|^2. \quad (5.36)$$

The values of the NMEs  $|\mathcal{M}_v^{0v}|$  and  $|\mathcal{M}_N^{0v}|$  have been calculated for different

isotopes in a variety of frameworks [673]. These include the Quasiparticle Random Phase Approximation (QRPA) [669, 670], Interacting Boson Model (IBM-2) [671, 674, 675] and Interacting Shell Model (ISM) [672]. In Table 5.1 we show the light and heavy NMEs and their associated uncertainties for the  $0\nu\beta\beta$  decay isotopes  $^{76}\text{Ge}$  and  $^{136}\text{Xe}$ . The QRPA calculations of the Tübingen and Jyväskylä groups and the IBM-2 calculations of the Yale group give NME values for quenched ( $g_A = 1$ ) and non-quenched ( $g_A = 1.269$ ) values of the axial vector coupling and also for the Argonne [676] and CD-Bonn [677] forms of the Jastrow potential (describing two-nucleon short-range correlations). For the purposes of Table 5.1 we take average of these NME values and the uncertainty (when not provided by the reference) to be half of the total range in values.

In Fig. 5.8 we plot the  $^{76}\text{Ge}$  and  $^{136}\text{Xe}$  NMEs as a function of the exchanged neutrino mass  $m_{N_i}$  using the interpolating formula of Eq. (5.35) and the light and heavy NMEs given in Table 5.1. It can be seen that the NMEs are constant below  $\langle \mathbf{p}^2 \rangle \sim 100 \text{ MeV}^2$  and suppressed by  $\frac{1}{m_{N_i}^2}$  above. However, if all the masses are below  $\langle \mathbf{p}^2 \rangle$  we will see that the  $(M_\nu)_{11} = 0$  condition suppresses the  $0\nu\beta\beta$  decay rate regardless of the NME value. To plot the uncertainty bands in Fig. 5.8 we propagate the uncertainties of  $|\mathcal{M}_\nu^{0\nu}|$  and  $|\mathcal{M}_N^{0\nu}|$  through Eq. (5.35) as

$$\delta \mathcal{M}^{0\nu} = \sqrt{\left(\frac{\partial \mathcal{M}^{0\nu}}{\partial |\mathcal{M}_\nu^{0\nu}|}\right)^2 \delta |\mathcal{M}_\nu^{0\nu}|^2 + \left(\frac{\partial \mathcal{M}^{0\nu}}{\partial |\mathcal{M}_N^{0\nu}|}\right)^2 \delta |\mathcal{M}_N^{0\nu}|^2}, \quad (5.37)$$

where the fractional uncertainties for the light and heavy NMEs,  $\delta |\mathcal{M}_\nu^{0\nu}|$  and  $\delta |\mathcal{M}_N^{0\nu}|$  respectively, are given in Table 5.1. These are the uncertainties on the NMEs divided by the NMEs themselves. It can be seen that the IBM-2 NMEs have the largest uncertainties; for illustrative purposes and to give conservative estimates we therefore use these NMEs in the following discussion.

In our single-generation model, the summation appearing in the interpolating formula Eq. (5.35) is approximately

$$\frac{m_\nu}{\langle \mathbf{p}^2 \rangle} + \frac{e^{i\phi_1} m_{N_1} s_{e1}^2}{\langle \mathbf{p}^2 \rangle + m_{N_1}^2} + \frac{e^{i\phi_2} m_{N_1} (1 + r_\Delta) s_{e2}^2}{\langle \mathbf{p}^2 \rangle + m_{N_1}^2 (1 + r_\Delta)^2} \approx \alpha + \beta s_{e1}^2 e^{i\phi_1}, \quad (5.38)$$

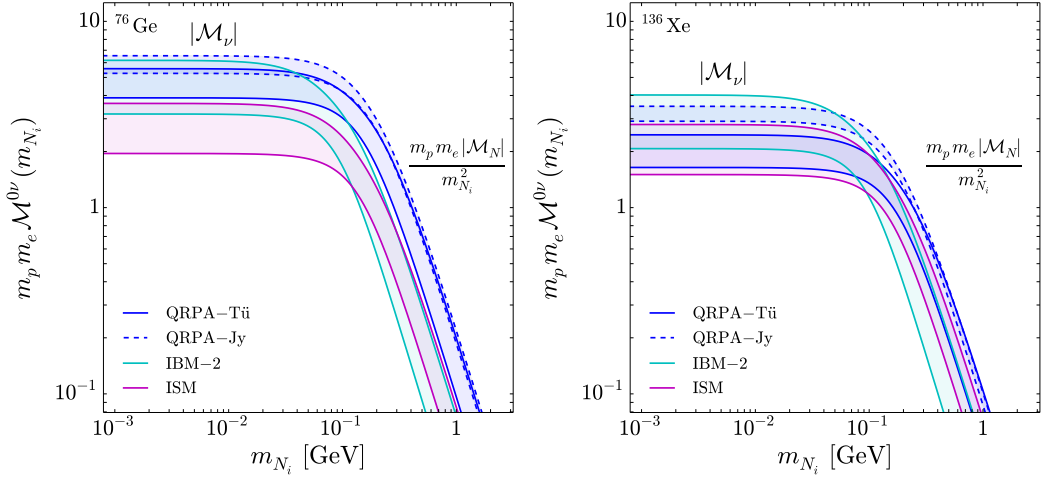


**Figure 5.8:** Normalised  $0\nu\beta\beta$  decay NMEs for  $^{76}\text{Ge}$  (left) and  $^{136}\text{Xe}$  (right) as a function of the exchanged sterile neutrino mass  $m_{N_i}$  using the interpolating formula Eq. (5.35). We make use of the light and heavy NMEs shown in Table 5.1. The bands indicate the NME uncertainties arising from the choice of quenched  $g_A$  and short-range correlations.

where in the equality we have used  $(M_\nu)_{11} = 0$  to eliminate  $s_{e2}^2$  and assumed  $s_{e1}^2, s_{e2}^2 \ll 1$  to rewrite the summation using the factors

$$\begin{aligned} \alpha &\equiv m_\nu \left( \frac{1}{\langle \mathbf{p}^2 \rangle} - \frac{1}{\langle \mathbf{p}^2 \rangle + m_{N_1}^2 (1 + r_\Delta)^2} \right), \\ \beta &\equiv m_{N_1} \left( \frac{1}{\langle \mathbf{p}^2 \rangle + m_{N_1}^2} - \frac{1}{\langle \mathbf{p}^2 \rangle + m_{N_1}^2 (1 + r_\Delta)^2} \right). \end{aligned} \quad (5.39)$$

Alternatively, one can eliminate  $s_{e2}^2$  and  $\phi_2$  using the relations Eqs. (5.8) and (5.9). Taking the square of the summation in Eq. (5.38) and inserting into the inverse  $0\nu\beta\beta$  decay half-life in Eq. (5.36) gives

$$\chi^2 = \alpha^2 + \beta^2 s_{e1}^4 + 2\alpha\beta s_{e1}^2 \cos\phi_1; \quad \chi \equiv \sqrt{\frac{1}{T_{1/2}^{0\nu} G^{0\nu} g_A^4 |\mathcal{M}_N^{0\nu}|^2 m_p^2}}. \quad (5.40)$$

Experimental lower bounds on the  $0\nu\beta\beta$  decay half-life  $T_{1/2}^{0\nu} > (T_{1/2}^{0\nu})_{\text{exp}}$  (or equivalently  $\chi^2 < \chi_{\text{exp}}^2$ ) can therefore be used to put an *upper* bound on  $s_{e1}^2$  as a

function of  $m_{N_1}$ ,  $m_\nu$ ,  $r_\Delta$ ,  $\phi_1$  and the light and heavy NMEs  $|\mathcal{M}_\nu^{0\nu}|$  and  $|\mathcal{M}_N^{0\nu}|$ ,

$$s_{e1}^2 < -\frac{\alpha}{\beta} \cos \phi_1 + \frac{1}{\beta} \sqrt{\chi_{\text{exp}}^2 - \alpha^2 \sin^2 \phi_1}. \quad (5.41)$$

Another limit can be derived from the quadratic inequality  $\chi^2 < \chi_{\text{exp}}^2$  that is a *lower* bound on  $s_{e1}^2$

$$s_{e1}^2 > -\frac{\alpha}{\beta} \cos \phi_1 - \frac{1}{\beta} \sqrt{\chi_{\text{exp}}^2 - \alpha^2 \sin^2 \phi_1}. \quad (5.42)$$

For most of the parameter space this is negative and therefore unphysical. It will be important however when  $\cos \phi_1 < 0$  and  $\alpha > \chi_{\text{exp}}$ .

Because we work in a one-generation model with a single light neutrino  $\nu_L$  which we identify as the electron neutrino, the effective  $0\nu\beta\beta$  decay mass is not the usual coherent sum,

$$m_{\beta\beta} = \left| \sum_{i=1}^3 U_{ei}^2 m_{\nu_i} \right|, \quad (5.43)$$

but simply  $m_{\beta\beta} = m_\nu$ . In our parametrisation,  $m_\nu$  is always real and positive. We calculate the  $0\nu\beta\beta$  decay rate consistently in this framework by including the coherent summation of the light neutrino and the two heavy neutrino contributions as detailed above. In this sense,  $m_\nu$  is a surrogate for the general effective  $0\nu\beta\beta$  decay mass  $m_{\beta\beta}$ , but we cannot include the possible destructive interference between light neutrinos due to the Majorana phases in the PMNS mixing matrix. This effect has been studied extensively in the literature (for a review, see Ref. [678]) whereas our focus is on the constraints on the heavy neutrino parameters.

The precise value of  $m_\nu$  will only be important if it saturates the limit from  $0\nu\beta\beta$  decay searches. This is shown in Fig. 5.11 (right) and the accompanying text where the choice  $m_\nu = 6 \times 10^{-2}$  eV is near the excluded  $m_{\beta\beta}$  limit and thus the constraints on the extra contributions of the heavy neutrinos become overly restrictive. These may instead be relaxed if there is a sizeable cancellation among the light neutrino contributions reducing  $m_{\beta\beta}$ . A full analytic discussion of  $0\nu\beta\beta$

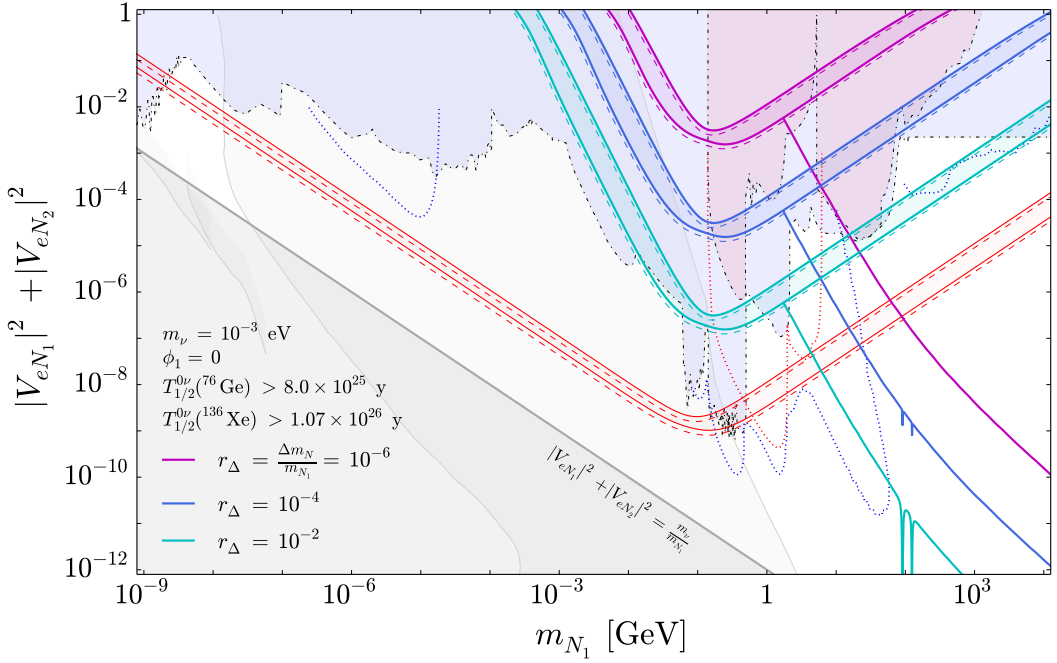


**Figure 5.9:** Upper limits on  $|V_{eN_1}|^2 + |V_{eN_2}|^2$  for three small values of  $r_{\Delta} \ll 1$ . We show the limits from  $^{136}\text{Xe}$  (solid) and  $^{76}\text{Ge}$  (dashed) experiments with the bands indicating the NME uncertainties. The red curves highlight the limit in which  $0\nu\beta\beta$  decay is driven by a single sterile neutrino. The curves sloping down to the lower right indicate the upper bounds by enforcing  $|\delta m_{\nu}^{1-\text{loop}}| < 0.1m_{\nu}$ . These constraints are compared with the current and future sensitivities of  $|\Delta L| = 0$  (blue shaded) and  $|\Delta L| = 2$  (red shaded) searches, cf. Figs. 5.6 and 5.7.

decay in presence of three active neutrinos mixing with sterile neutrinos is beyond the scope of this chapter and is the topic of future work.

In Fig. 5.9 we depict the upper bounds on the sum of squared active-sterile mixings  $|V_{eN_1}|^2 + |V_{eN_2}|^2 \approx s_{e1}^2 + s_{e2}^2$  as a function of the first sterile neutrino mass  $m_{N_1}$  for three *small* values of the sterile neutrino mass splitting ratio  $r_{\Delta} \ll 1$  and benchmark values of the light neutrino mass  $m_{\nu} = 10^{-3}$  eV and Majorana phase  $\phi_1 = 0$ . The sum is used assuming that the energy resolutions of direct searches are larger than  $\Delta m_N$  and can only constrain  $|V_{eN_1}|^2 + |V_{eN_2}|^2$  as a function of  $m_{N_1} \approx m_{N_2}$ . Using  $s_{e1}^2$  inequality in Eq. (5.41), we take the most recent lower limits on  $T_{1/2}^{0\nu}$  from the  $^{136}\text{Xe}$  experiment KamLAND-Zen [374] ( $^{76}\text{Ge}$  experiment GERDA II [373]) and the IBM-2 light and heavy NMEs in Table 5.1 to plot the solid (dashed) curves in the upper right portion of Fig. 5.9. The bands illustrate the uncertainty on the  $|V_{eN_1}|^2 + |V_{eN_2}|^2$  upper bound found by propagating the IBM-2 NME uncertainties

through Eq. (5.41). The red lines in Fig. 5.9 show the upper limits on the sum of mixings when only the contribution of a single sterile neutrino is included (light active neutrino exchange is neglected). Finally, we show for these choices of  $r_\Delta$  the upper limits on  $|V_{eN_1}|^2 + |V_{eN_2}|^2$  from the requirement that  $|\delta m_v^{1\text{-loop}}| < 0.1 m_v$ .

In Fig. 5.9 we compare the  $0\nu\beta\beta$  decay bounds to the direct search limits discussed in Section 5.2. These include the current (blue-shaded) and future (blue dot-dashed line) sensitivities of  $|\Delta L| = 2$  probes. We also display separately the current (red-shaded) and future (red dot-dashed line) sensitivities of other  $|\Delta L| = 2$  probes (e.g. from meson decays and colliders). The faint grey areas correspond to the regions excluded by cosmology. Finally, the dark grey shaded region below the seesaw line  $|V_{eN_1}|^2 + |V_{eN_2}|^2 = \frac{m_v}{m_{N_1}}$  is excluded as shown in Eq. (5.31).

We first observe in Fig. 5.9 that the upper bounds are the most stringent for  $m_{N_1} \sim \sqrt{\langle \mathbf{p}^2 \rangle} \sim 200$  MeV. Towards lower  $m_{N_1}$ , both sterile states are *light* and the  $0\nu\beta\beta$  decay rate is suppressed by  $(M_v)_{11} = 0$  condition. For higher  $m_{N_1}$  both sterile states are *heavy* and the limits become weaker due to the growing suppression of NMEs as  $\frac{1}{m_{N_1}^2}$ . We also see a strong dependence on the sterile mass splitting ratio. Decreasing  $r_\Delta$  by a factor of  $10^2$  weakens the upper bound by a similar magnitude both above and below  $m_{N_1} \sim \sqrt{\langle \mathbf{p}^2 \rangle}$ . This is to be expected, as  $r_\Delta \rightarrow 0$  corresponds to the pseudo-Dirac limit in which lepton number is approximately conserved and the  $0\nu\beta\beta$  decay process is forbidden. Comparing the bounds from  $^{76}\text{Ge}$  and  $^{136}\text{Xe}$  it is interesting to note that the former are slightly more stringent despite the weaker experimental lower bound on the half-life. As seen in Fig. 5.8, this is counteracted by  $^{76}\text{Ge}$  having larger NMEs on average compared to  $^{136}\text{Xe}$ . Comparing with the direct search constraints we see that for  $r_\Delta = 10^{-2}$  the current upper bounds are comparable with non-resonant meson decay limits for  $1 \text{ MeV} \lesssim m_{N_1} \lesssim 1 \text{ GeV}$  and more stringent than collider constraints for  $m_{N_1} > 5 \text{ GeV}$ .

We saw in Section 5.2 that when the sterile mass splitting ratio  $r_\Delta$  is decreased, the  $|\Delta L| = 2$  collider constraints (shaded in red) do not weaken significantly. This is because the amplitude is controlled by the ratio  $\frac{\Gamma_N}{\Delta m_N}$ . Considering the decays of sterile neutrinos to SM particles we found that  $\frac{\Gamma_N}{\Delta m_N} = \frac{\Gamma_N}{r_\Delta m_{N_1}} \ll 1$  in the mass range

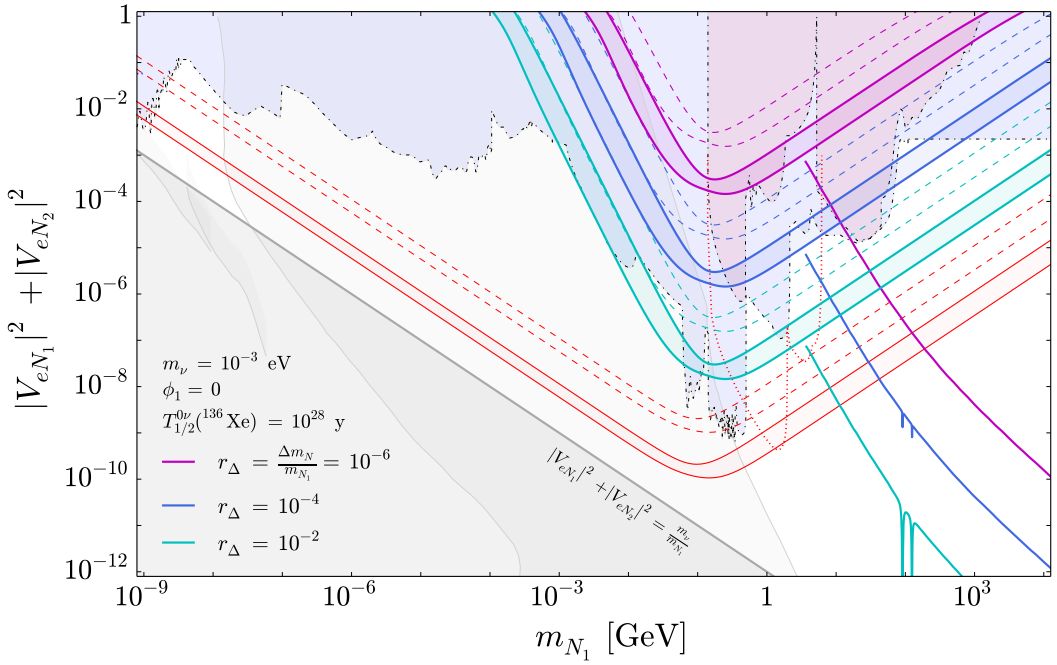


**Figure 5.10:** As for Fig. 5.9, but showing the current  $^{136}\text{Xe}$   $0\nu\beta\beta$  decay bounds (dashed) and future bounds (solid) assuming a future half-life lower limit  $T_{1/2}^{0\nu} = 10^{28}$  y.

$5 \text{ GeV} \lesssim m_{N_1} \lesssim 50 \text{ GeV}$  for  $r_\Delta \gtrsim 10^{-10}$ . As a result, when  $r_\Delta \lesssim 10^{-2}$  the  $0\nu\beta\beta$  decay constraints become less stringent than the  $|\Delta L| = 2$  same-sign dilepton and trilepton collider constraints.

In Fig. 5.10, we similarly show the upper bounds from  $0\nu\beta\beta$  decay and radiatively-induced neutrino masses for the same (small) values of  $r_\nu$  but instead using the forecasted sensitivity of  $T_{1/2}^{0\nu} \gtrsim 10^{28}$  y for future  $^{136}\text{Xe}$  experiments. The current bounds are shown as dashed lines and the future bounds as solid. This reach may be achievable at the proposed  $^{136}\text{Xe}$  experiments PandaX-III [679] and nEXO [680], the  $^{76}\text{Ge}$  experiment LEGEND [681] and the  $^{130}\text{Te}$ ,  $^{100}\text{Mo}$ ,  $^{82}\text{Se}$  and  $^{112}\text{Cd}$  experiment CUPID [682].

The behaviour of the  $0\nu\beta\beta$  decay upper bound in the *light* and *heavy* regimes can be understood by taking the Taylor expansion of Eq. (5.41) in the opposite limits  $\frac{m_{N_1}}{\sqrt{\langle \mathbf{p}^2 \rangle}} \ll 1$  and  $\frac{m_{N_1}}{\sqrt{\langle \mathbf{p}^2 \rangle}} \gg 1$ . In the light regime we derive

$$s_{e1}^2 \lesssim \frac{\langle \mathbf{p}^2 \rangle^2 \chi_{\text{exp}}}{m_{N_1}^3 r_\Delta (2 + r_\Delta)}, \quad (5.44)$$

while in the heavy regime,

$$s_{e1}^2 \lesssim \left( -\frac{m_\nu}{\langle \mathbf{p}^2 \rangle} \cos \phi_1 + \sqrt{\chi_{\text{exp}}^2 - \frac{m_\nu^2 \sin^2 \phi_1}{\langle \mathbf{p}^2 \rangle^2}} \right) \frac{m_{N_1}(1+r_\Delta)^2}{r_\Delta(2+r_\Delta)}. \quad (5.45)$$

The  $m_{N_1}$  dependence of these upper bounds agrees qualitatively with Fig. (5.9); in the light regime the upper bounds scale as  $\frac{1}{m_{N_1}^3}$  and in the heavy regime as  $m_{N_1}$ . The dependence on  $r_\Delta$  is also consistent; for  $r_\Delta \ll 1$  both Eqs. (5.44) and (5.45) are inversely proportional to  $r_\Delta$ . Thus decreasing or increasing  $r_\Delta$  shifts the upper bound to higher or lower mixings respectively for the whole range of  $m_{N_1}$ .

In Fig. 5.11 we examine more closely the  $|V_{eN_1}|^2 + |V_{eN_2}|^2 \approx s_{e1}^2 + s_{e2}^2$  upper bound in the  $r_\Delta = 10^{-2}$  case for different values of the Majorana phase  $\phi_1$  (left) and the light neutrino mass  $m_\nu$  (right). To the left it is clear that changing  $\phi_1$  has little effect on the  $0\nu\beta\beta$  decay bounds. As shown in Eq. (5.44), in the light regime the  $s_{e1}^2$  upper bound is independent of  $\phi_1$ . From Eq. (5.45) we see that in the heavy regime changing  $\phi_1$  also has little effect because  $\frac{m_\nu}{\langle \mathbf{p}^2 \rangle} \ll \chi_{\text{exp}}$ , i.e. the light neutrino contribution is negligible.  $0\nu\beta\beta$  decay is therefore driven by the two heavy states; this is the limit  $\alpha \ll 1$  and  $s_{e1}^2 \lesssim \frac{\chi_{\text{exp}}}{\beta}$  in Eq. (5.41). For  $m_{N_1} \gg \sqrt{\langle \mathbf{p}^2 \rangle}$  we have

$$\beta \approx \frac{r_\Delta(2+r_\Delta)}{m_{N_1}(1+r_\Delta)^2}, \quad (5.46)$$

which gives the expected dependence on  $r_\Delta$  and  $m_{N_1}$  in Eq. (5.45).

To the right we see that increasing  $m_\nu$  for  $\phi_1 = 0$  strengthens the upper bound in the heavy regime. This again is described by Eq. (5.45); there is a cancellation between the two terms in the brackets as  $\frac{m_\nu}{\langle \mathbf{p}^2 \rangle}$  approaches  $\chi_{\text{exp}}$ . In this limit the light active contribution becomes non-negligible compared to the difference between the heavy sterile contributions. For the inverse seesaw region of the parameter space,

$$\chi^2 \approx \left| \frac{m_\nu}{\langle \mathbf{p}^2 \rangle} + \frac{r_\Delta(2+r_\Delta)}{m_{N_1}(1+r_\Delta)^2} s_{e1}^2 e^{i\phi_1} \right|^2 < \chi_{\text{exp}}^2. \quad (5.47)$$

If for example  $(\phi_1, \phi_2) = (0, \pi)$ , the light contribution adds constructively with the difference between the sterile contributions and the upper bound on  $s_{e1}^2$  must be

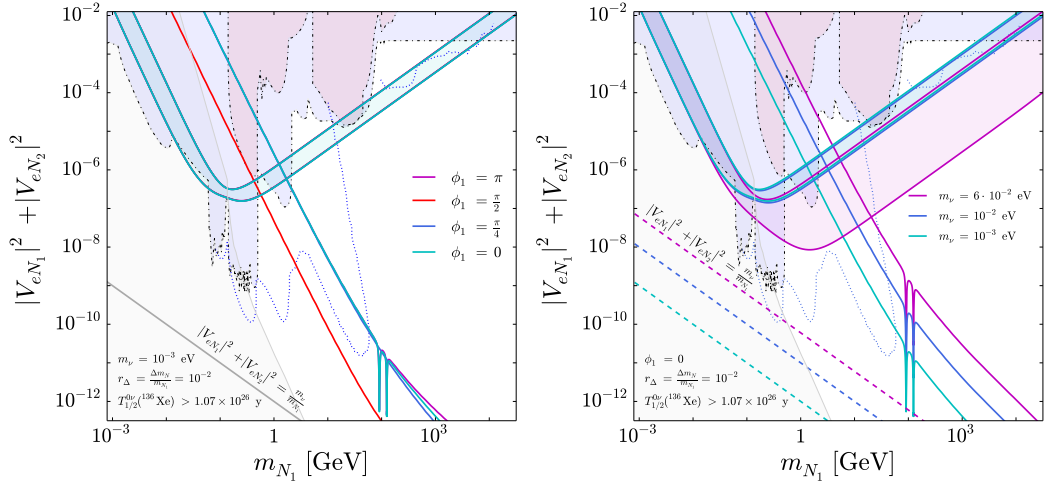


**Figure 5.11:** Upper limits on the sum of squared active-sterile mixing for the sterile neutrino mass splitting ratio  $r_\Delta = \frac{\Delta m_N}{m_{N_1}} = 10^{-2}$  derived from  $0\nu\beta\beta$  decay and loop constraints. We show the limits from  $^{136}\text{Xe}$  for different values of  $\phi_1$  (left) and  $m_\nu$  (right).

smaller to account for the observed half-life lower bound. If on the other hand for  $(\phi_1, \phi_2) = (\pi, 0)$ , the light and heavy contributions add destructively and the  $s_{e1}^2$  upper bound can be less stringent.

If  $\frac{m_\nu}{\langle \mathbf{p}^2 \rangle} > \chi_{\text{exp}}$  (which may be the case for a large lower limit on  $T_{1/2}^{0\nu}$ ), no value of  $s_{e1}^2$  in the heavy regime is permitted for  $\phi_1 = 0$ . This corresponds to  $\alpha > \chi_{\text{exp}}$  and the upper bound in Eq. (5.41) becoming negative and unphysical. Constructive interference between the light active contribution and the difference between the heavy sterile contributions, e.g. for  $(\phi_1, \phi_2) = (0, \pi)$ , now gives a  $T_{1/2}^{0\nu}$  less than the experimental lower limit. Conversely, if the light and heavy contributions interfere destructively, e.g. for  $(\phi_1, \phi_2) = (\pi, 0)$  or  $(\pi, \pi)$ , then  $s_{e1}^2$  multiplying the heavy contributions can be made large enough to meet the condition  $\chi < \chi_{\text{exp}}$  (but not so large as to dominate over the light contribution). As well as an upper bound, this sets a *lower* bound on  $s_{e1}^2$  in the heavy regime. This corresponds to the lower bound in Eq. (5.42) becoming non-negative.

In Fig. 5.11 we also see how the bounds from radiative neutrino masses change when  $\phi_1$  and  $m_\nu$  are varied. For the values  $\phi_1 = 0, \pi$  and  $\frac{\pi}{4}$ , the loop constraints are broadly the same. However for  $\phi_1 = \frac{\pi}{2}$  the upper bound becomes nearly two orders of magnitude more excluding. As  $m_\nu$  is increased by an order of magnitude (we do

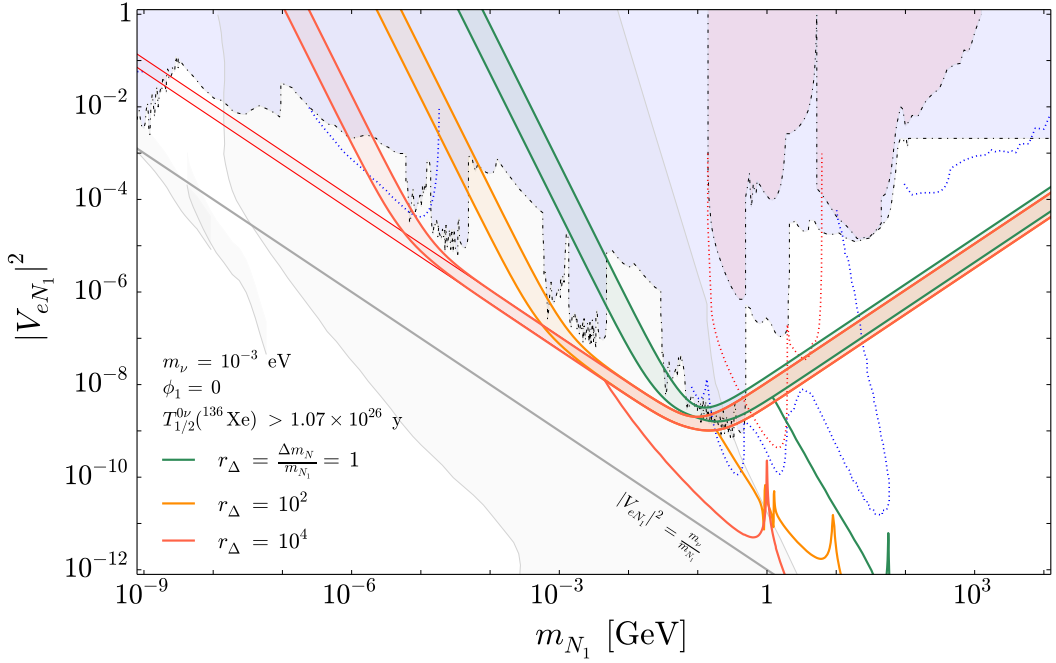


**Figure 5.12:** Upper limits on  $|V_{eN_1}|^2$  for three large values of  $r_\Delta \geq 1$ . We show the limits for  $^{136}\text{Xe}$  with shaded bands indicating the NME uncertainties. The red curve highlights the limit in which  $0\nu\beta\beta$  decay is driven by a single sterile neutrino. The curves sloping down to the lower right indicate the upper bounds by enforcing  $|\delta m_\nu^{1\text{-loop}}| < 0.1m_\nu$ . These constraints are compared with the current and future sensitivities of  $|\Delta L| = 0$  (blue shaded) and  $|\Delta L| = 2$  (red shaded) searches, cf. Figs. 5.6 and 5.7.

not go above  $m_\nu \sim \langle \mathbf{p}^2 \rangle \chi_{\text{exp}} \approx 0.083$  eV for the reasons discussed in the previous paragraph) we can also see that the loop constraints are weakened by an order of magnitude.

In Fig. 5.12, we display the active-sterile mixing  $|V_{eN_1}|^2 \approx s_{e1}^2$  as a function of  $m_{N_1}$  for three *large* values of the sterile neutrino mass splitting  $r_\Delta \geq 1$  and benchmark values of  $m_\nu = 10^{-3}$  eV and  $\phi_1 = 0$ . We do not use the sum  $|V_{eN_1}|^2 + |V_{eN_2}|^2$  in this case because the splittings are assumed to be large enough for the two states to be resolved individually in direct search experiments. We again compare these bounds to the direct search limits discussed in Section 5.2. Due to the large splitting, shifted versions of the excluded region in the  $(m_{N_2}, |V_{eN_2}|^2)$  parameter space now apply in the  $(m_{N_1}, |V_{eN_1}|^2)$  plane. The shift is to smaller  $m_{N_1}$  and to larger  $|V_{eN_1}|^2$  by a factor  $(1 + r_\Delta)$ . For example, if the T2K experiment excludes a neutrino of mass  $m_{N_2}$  and mixing  $|V_{eN_2}|^2$ , it also implies the non-existence a neutrino at  $m_{N_1} \approx \frac{m_{N_2}}{1+r_\Delta}$ .

and  $|V_{eN_1}|^2 \approx |V_{eN_2}|^2(1 + r_\Delta)$  in this model. These particular relations apply because the T2K bounds are in the ISS region of the parameter space. For large splittings we see that the  $0\nu\beta\beta$  decay constraints converge towards the upper bound in the limit of single heavy neutrino exchange, shown by the thin red curves in Figs. 5.9, 5.10 and 5.12.

We have so far neglected the one-loop contribution to the neutrino mass  $\delta m_\nu^{1\text{-loop}}$  in this discussion (other than restricting it to be small). One could ask if this has a large impact in the  $m_{N_i} \ll \sqrt{\langle \mathbf{p}^2 \rangle}$  limit because

$$(T_{1/2}^{0\nu})^{-1} \propto \left| c_{e1}^2 c_{e2}^2 m_\nu^{\text{tree}} + s_{e1}^2 c_{e2}^2 m_{N_1} e^{i\phi_1} + s_{e2}^2 m_{N_2} e^{i\phi_2} \right|^2 \propto \left| \delta m_\nu^{1\text{-loop}} \right|^2, \quad (5.48)$$

which would be expected to alter the suppression and  $\frac{1}{m_{N_1}^3}$  scaling of the upper bound on the mixing. However, examining Fig. 5.4 we see that  $|\delta m_\nu^{1\text{-loop}}| \sim 10^{-12}$  eV in this regime. Thus we safely neglect its effect on the  $0\nu\beta\beta$  decay constraint curves.

## 5.4 Two-Neutrino Double Beta Decay Constraints

Before moving on to the conclusions of this chapter, in this section we will assess the sensitivity of  $0\nu\beta\beta$  decay experiments to kinks in the two-neutrino double beta ( $2\nu\beta\beta$ ) decay spectrum caused by the presence of sterile neutrinos  $N$  with masses  $m_N \lesssim 1$  MeV. This is analogous to the kink searches of single beta decays, discussed around Eq. (5.29), but  $2\nu\beta\beta$  decaying isotopes typically have  $Q$ -values of order  $Q_{\beta\beta} \sim \mathcal{O}(1)$  MeV and are thus expected to probe different values of  $m_N$ . The  $2\nu\beta\beta$  decay process is suppressed and so at first it may seem difficult to achieve high enough statistics. While  $2\nu\beta\beta$  decay does not improve on the limits in the  $0.1 \text{ MeV} \lesssim m_N \lesssim 3 \text{ MeV}$  mass range considerably,  $2\nu\beta\beta$  decay spectra will be measured to high precision in several isotopes as  $0\nu\beta\beta$  decay is searched for in ongoing and future experiments. Generally speaking,  $2\nu\beta\beta$  decay can be used to look for signs of NP in its own right [303, 683].

In addition to a sterile neutrino coupling to the SM charged-current interaction via an active-sterile mixing, we can also consider right-handed current interactions of the ‘sterile’ neutrino, e.g. arising in left-right symmetric models. Right-

handed interactions alter the angular distribution of the electrons emitted in  $2\nu\beta\beta$  decay [303]. For the energy scales relevant to  $2\nu\beta\beta$  decay ( $\sim 10$  MeV), we will therefore parametrise the interactions as LEFT +  $N_R$  operators containing SM fields with a light sterile neutrino  $N$ , as in Eq. (2.98).

### 5.4.1 Effective Interactions with Sterile Neutrinos

We now outline our parametrisation for operators in the LEFT +  $N_R$  framework, i.e. all operators built from the SM degrees of freedom plus a gauge-singlet fermion  $N$  respecting the  $SU(3)_c \times U(1)_Y$  gauge symmetry of the broken SM. However, as we are considering the second-order weak process of  $2\nu\beta\beta$  decay, we restrict ourselves to charged-current type operators and the first generation of SM fermions. We will also only consider left- or right-handed vector-type currents. The effective Lagrangian takes the form

$$\mathcal{L}_{CC}^{(6)} = -\frac{4G_F V_{ud}}{\sqrt{2}} \left\{ j_L J_L^\dagger + V_{eN} j_L^N J_L^\dagger + \varepsilon_{RL} j_R^N J_L^\dagger + \varepsilon_{RR} j_R^N J_R^\dagger \right\} + \text{h.c.}, \quad (5.49)$$

where the leptonic and hadronic currents are  $j_L = \bar{e} \gamma^\mu P_L v$ ,  $j_{L,R}^N = \bar{e} \gamma^\mu P_{L,R} N$  and  $J_{L,R} = \bar{d}^\mu \gamma_\mu P_{L,R} u$ , respectively. The active-sterile mixing described by  $V_{eN}$  and the  $\varepsilon_{XY}$  coefficients encapsulate the impact of integrating out NP giving rise to ( $V+A$ ) currents. We neglect any further effective operators, such as non-standard contributions to the SM charged-current interaction and right-handed currents for the active neutrinos, which has been studied in Ref. [303].

In Eq. (5.49),  $v$  and  $N$  are four-spinor fields of the light electron neutrino and the sterile neutrino. They can either be Majorana fermions,  $v = v_L + v_L^c$  and  $N = N_R^c + N_R$  (i.e. a Majorana spinor constructed from the left-handed Weyl spinor and its charge-conjugate) or Dirac fermions  $v = v_L + v_R$  and  $N = N_R + N_L$  (a Dirac spinor constructed from two different Weyl fields). The calculation of  $2\nu\beta\beta$  decay is not affected by this, i.e. it is insensitive lepton number and therefore to the Dirac or Majorana character.

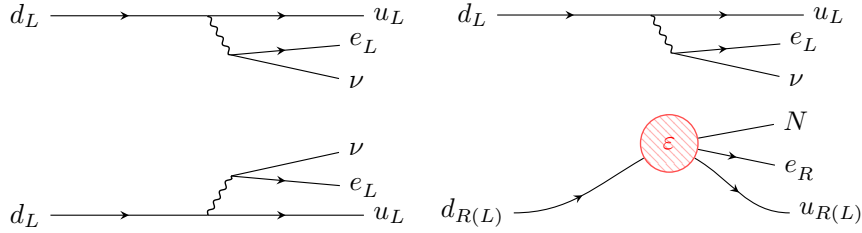


**Figure 5.13:** (Left) Standard  $2\nu\beta\beta$  decay process with the emission of two electrons and two electron antineutrinos. (Right) Non-standard  $\nu N\beta\beta$  process, where the active-sterile mixing  $V_{eN}$  or a right-handed current  $\varepsilon_{RX}$  creates a  $m_N \sim 1$  MeV sterile neutrino  $N$  instead of an antineutrino at one of the vertices.

### 5.4.2 Double Beta Decay Rate with a Sterile Neutrino

We will now outline the derivation of the  $2\nu\beta\beta$  decay rate with the operators in Eq. (5.49). Considering a sterile neutrino  $N$  with a mass  $m_N < Q_{\beta\beta} \lesssim \mathcal{O}(1)$  MeV and an active-sterile mixing strength  $|V_{eN}|^2$ , now a  $\bar{N}$  is emitted instead of a  $\bar{\nu}_e$  in  $2\nu\beta\beta$  decay (we call this new process  $\nu N\beta\beta$ ). We assume that  $N$  is long-lived and does not decay within the detector. The final state is different to the standard  $2\nu\beta\beta$  decay and thus there is no interference between  $\nu N\beta\beta$  and  $2\nu\beta\beta$ . No anti-symmetrisation is needed with respect to the two different neutrinos in  $\nu N\beta\beta$ . Moreover, the sterile neutrino can also be produced via a right-handed current which further affects the  $2\nu\beta\beta$  observables, mainly the angular correlation of the outgoing electrons.

To write down expressions for the  $2\nu\beta\beta$  and  $\nu N\beta\beta$  decay rates (including the possibility of right-handed currents) we start with the general expression [684]

$$d\Gamma^{2\nu} = 2(2 - \delta_{\bar{\nu}_i \bar{\nu}_j})\pi\delta(E_{e_1} + E_{e_2} + E_{\bar{\nu}_1} + E_{\bar{\nu}_2} + E_F - E_I) \times \sum_{\text{spins}} |\mathcal{R}^{2\nu}|^2 d\Omega_{e_1} d\Omega_{e_2} d\Omega_{\bar{\nu}_1} d\Omega_{\bar{\nu}_2}, \quad (5.50)$$

where  $E_I, E_F, E_{e_i} = \sqrt{|\mathbf{p}_{e_i}|^2 + m_e^2}$  and  $E_{\bar{\nu}_i} = \sqrt{|\mathbf{p}_{\bar{\nu}_i}|^2 + m_{\bar{\nu}_i}^2}$  (with  $i = 1, 2$ ) are the energies of the initial and final nuclei, electrons and antineutrinos, respectively. The phase space differentials are  $d\Omega_{e_1} = \frac{d^3 \mathbf{p}_{e_1}}{(2\pi)^3}$  and so on. The symmetry factor in Eq. (5.50) is  $(2 - \delta_{\bar{\nu}_i \bar{\nu}_j}) = 1$  if identical neutrinos are emitted and  $(2 - \delta_{\bar{\nu}_i \bar{\nu}_j}) = 2$  if they are distinguishable, i.e. in the case of  $\nu N\beta\beta$  decay. The amplitude  $\mathcal{R}^{2\nu}$  con-

tains the average contribution of the two diagrams with the neutrinos interchanged, with a relative minus sign if the neutrinos are identical. In our calculations we will neglect the mass of  $\nu$  and retain only the mass  $m_N$  of the sterile neutrino.

After integrating over the phase space of the outgoing neutrinos, the resulting differential  $2\nu\beta\beta$  decay rate can be written in terms of the energies  $0 \leq E_{e_1}, E_{e_2} \leq Q_{\beta\beta} + m_e$  of the two outgoing electrons, with  $Q_{\beta\beta} = E_I - E_F - 2m_e$ , and the angle  $0 \leq \theta \leq \pi$  between the electron momenta  $\mathbf{p}_{e_1}$  and  $\mathbf{p}_{e_2}$  as [684]

$$\frac{d\Gamma^{2\nu}}{dE_{e_1}dE_{e_2}d\cos\theta} = \frac{c_{2\nu}}{2} (A^{2\nu} + B^{2\nu} \cos\theta) |\mathbf{p}_{e_1}|E_{e_1}|\mathbf{p}_{e_1}|E_{e_2}, \quad (5.51)$$

where  $c_{2\nu} = (2 - \delta_{\bar{\nu}_i \bar{\nu}_j}) \frac{G_\beta^4 m_e^9}{8\pi^7}$  with  $G_\beta = G_F V_{ud}$ .

The factors  $A^{2\nu}$  and  $B^{2\nu}$  in Eq. (5.51) are functions of the electron energies  $E_{e_1}$  and  $E_{e_2}$  and include the integration over the neutrino phase space as

$$A^{2\nu} = \int_{m_{\nu_1}}^{E_I - E_F - E_{e_1} - E_{e_2}} \mathcal{A}^{2\nu} \sqrt{E_{\bar{\nu}_1}^2 - m_{\nu_1}^2} \sqrt{(E_I - E_F - E_{e_1} - E_{e_2} - E_{\bar{\nu}_1})^2 - m_{\nu_2}^2} \times E_{\bar{\nu}_1} (E_I - E_F - E_{e_1} - E_{e_2} - E_{\bar{\nu}_1}) dE_{\bar{\nu}_1}, \quad (5.52)$$

$$B^{2\nu} = \int_{m_{\nu_1}}^{E_I - E_F - E_{e_1} - E_{e_2}} \mathcal{B}^{2\nu} \sqrt{E_{\bar{\nu}_1}^2 - m_{\nu_1}^2} \sqrt{(E_I - E_F - E_{e_1} - E_{e_2} - E_{\bar{\nu}_1})^2 - m_{\nu_2}^2} \times E_{\bar{\nu}_1} (E_I - E_F - E_{e_1} - E_{e_2} - E_{\bar{\nu}_1}) dE_{\bar{\nu}_1}, \quad (5.53)$$

where  $E_{\bar{\nu}_2} = E_I - E_F - E_{e_1} - E_{e_2} - E_{\bar{\nu}_1}$  due to energy conservation and we have kept the dependence on the neutrino masses  $m_{\nu_1}$  and  $m_{\nu_2}$ , though in the SM case they can be neglected. The factors  $\mathcal{A}^{2\nu}$  and  $\mathcal{B}^{2\nu}$  are functions of the electron and neutrino energies and are calculated using the nuclear and leptonic matrix elements. The  $\nu N\beta\beta$  decay rate then differs from  $2\nu\beta\beta$  decay rate only by the non-negligible  $m_N$  entering  $\sqrt{E_{\bar{\nu}_1}^2 - m_{\nu_1}^2}$  and the integration bounds. In the standard case with only left-handed lepton currents the quantities  $\mathcal{A}^{2\nu}$  and  $\mathcal{B}^{2\nu}$  do not depend on neutrino masses; hence, the main effect of the sterile neutrino mass is to ‘shrink’ the electron energy distribution according to the smaller  $Q$ -value, now given by  $Q_{\beta\beta} = E_I - E_F - 2m_e - m_N$ .

In these calculations we take the standard  $S_{1/2}$  spherical wave approximation for the outgoing electrons, i.e.

$$\psi_s(\mathbf{p}_e) = \begin{pmatrix} g_{-1}(E_e)\chi_s \\ f_1(E_e)(\boldsymbol{\sigma} \cdot \hat{\mathbf{p}}_e)\chi_s \end{pmatrix}, \quad (5.54)$$

where,  $\hat{\mathbf{p}}_e = \frac{\mathbf{p}_e}{|\mathbf{p}_e|}$  is the direction of the electron momentum,  $\chi_s$  is a two-component spinor and  $g_{-1}(E_e)$  and  $f_1(E_e)$  are the radial electron wave functions depending on the electron energy  $E_e$ . We will approximate them with their values at the surface of the nucleus, i.e. at a distance  $R_A$ . The neutrinos can be simply described as plane waves in the long-wave approximation,

$$\psi(\mathbf{p}_\nu) = \sqrt{\frac{E_\nu + m_\nu}{2E_\nu}} \begin{pmatrix} \chi_s \\ \frac{(\boldsymbol{\sigma} \cdot \hat{\mathbf{p}}_\nu)}{E_\nu + m_\nu} \chi_s \end{pmatrix}. \quad (5.55)$$

The standard contribution from the SM charged-current interaction to  $2\nu\beta\beta$  decay has been studied in great detail [685, 686]. Following the notation of those works and the formalism outlined above, the decay rate is described by the functions

$$\begin{aligned} \mathcal{A}_{\text{SM}}^{2\nu} = & [g_{-1}^2(E_{e1}) + f_1^2(E_{e1})][g_{-1}^2(E_{e2}) + f_1^2(E_{e2})] \\ & \times \left\{ \frac{1}{4} \left[ g_V^2 (\mathcal{M}_F^K + \mathcal{M}_F^L) - g_A^2 (\mathcal{M}_{\text{GT}}^K + \mathcal{M}_{\text{GT}}^L) \right]^2 \right. \\ & \left. + \frac{3}{4} \left[ g_V^2 (\mathcal{M}_F^K - \mathcal{M}_F^L) + \frac{1}{3} g_A^2 (\mathcal{M}_{\text{GT}}^K - \mathcal{M}_{\text{GT}}^L) \right]^2 \right\}, \end{aligned} \quad (5.56)$$

and

$$\begin{aligned} \mathcal{B}_{\text{SM}}^{2\nu} = & 4f_1(E_{e1})f_1(E_{e2})g_{-1}(E_{e1})g_{-1}(E_{e2}) \\ & \times \left\{ \frac{1}{4} \left[ g_V^2 (\mathcal{M}_F^K + \mathcal{M}_F^L) - g_A^2 (\mathcal{M}_{\text{GT}}^K + \mathcal{M}_{\text{GT}}^L) \right]^2 \right. \\ & \left. - \frac{1}{4} \left[ g_V^2 (\mathcal{M}_F^K - \mathcal{M}_F^L) + \frac{1}{3} g_A^4 (\mathcal{M}_{\text{GT}}^K - \mathcal{M}_{\text{GT}}^L) \right]^2 \right\}, \end{aligned} \quad (5.57)$$

where the Fermi and Gamow-Teller NMEs  $\mathcal{M}_F$  and  $\mathcal{M}_{GT}$  are defined as

$$\mathcal{M}_{F,GT}^{K,L} = m_e \sum_n \mathcal{M}_{F,GT} \frac{E_n - (E_I + E_F)/2}{[E_n - (E_I + E_F)/2]^2 - \epsilon_{K,L}^2}, \quad (5.58)$$

with

$$\mathcal{M}_F = \langle 0_F^+ | \sum_m \tau_m^- | 0_n^+ \rangle \langle 0_n^+ | \sum_n \tau_m^- | 0_I^+ \rangle, \quad (5.59)$$

$$\mathcal{M}_{GT} = \langle 0_F^+ | \sum_m \tau_m^- \sigma_m | 1_n^+ \rangle \langle 1_n^+ | \sum_m \tau_m^- \sigma_m | 0_I^+ \rangle. \quad (5.60)$$

Here,  $\tau_m^-$  are nuclear isospin lowering operators,  $\sigma_m$  are Pauli matrices and the sum  $\sum_n$  is over intermediate nuclear states. The electron mass  $m_e$  is inserted in Eq. (5.58) to make the NMEs dimensionless. The lepton energies enter Eq. (5.58) through the terms

$$\epsilon_K = \frac{1}{2} (E_{e_2} + E_{\bar{v}_2} - E_{e_1} - E_{\bar{v}_1}), \quad \epsilon_L = \frac{1}{2} (E_{e_1} + E_{\bar{v}_2} - E_{e_2} - E_{\bar{v}_1}), \quad (5.61)$$

which satisfy  $-\frac{Q_{\beta\beta}}{2} \leq \epsilon_{K,L} \leq \frac{Q_{\beta\beta}}{2}$ . In case of  $2\nu\beta\beta$  decay with energetically forbidden transitions to the intermediate states,  $E_n - E_I > -m_e$ , the quantity  $E_n - (E_I + E_F)/2 = \frac{Q_{\beta\beta}}{2} + m_e + (E_n - E_I)$  is always larger than  $\frac{Q_{\beta\beta}}{2}$ .

The above expressions may be further simplified using several well-motivated approximations:

- (i) Isospin Invariance: Neglecting the isospin non-conservation in the nucleus, the double Fermi nuclear matrix elements vanish, i.e.  $\mathcal{M}_F^K = \mathcal{M}_F^L = 0$ . The factors in Eqs. (5.56) and (5.57) then acquire the approximate forms

$$\begin{aligned} \mathcal{A}_{SM}^{2\nu} \approx & [g_{-1}^2(E_{e_1}) + f_1^2(E_{e_1})][g_{-1}^2(E_{e_2}) + f_1^2(E_{e_2})] \\ & \times \frac{1}{4} g_A^4 \left[ (\mathcal{M}_{GT}^K + \mathcal{M}_{GT}^L)^2 + \frac{1}{3} (\mathcal{M}_{GT}^K - \mathcal{M}_{GT}^L)^2 \right] \end{aligned} \quad (5.62)$$

Isotope	$\mathcal{M}_{\text{GT-1}}^{2\nu}$	$\mathcal{M}_{\text{GT-3}}^{2\nu}$	$\mathcal{M}_{\text{GT-5}}^{2\nu}$
$^{76}\text{Ge}$	0.111	0.0133	0.00263
$^{82}\text{Se}$	0.0795	0.0129	0.00355
$^{100}\text{Mo}$	0.184	0.0876	0.0322
$^{136}\text{Xe}$	0.0170	0.00526	0.00169

**Table 5.2:** Gamow-Teller NMEs for four  $2\nu\beta\beta$  decay isotopes calculated within the pn-QRPA with partial isospin restoration assuming the axial vector coupling  $g_A = 1$ .

and

$$\begin{aligned} \mathcal{B}_{\text{SM}}^{2\nu} \approx & 4f_1(E_{e_1})f_1(E_{e_2})g_{-1}(E_{e_1})g_{-1}(E_{e_2}) \\ & \times \frac{1}{4}g_A^4 \left[ (\mathcal{M}_{\text{GT}}^K + \mathcal{M}_{\text{GT}}^L)^2 + \frac{1}{9}(\mathcal{M}_{\text{GT}}^K - \mathcal{M}_{\text{GT}}^L)^2 \right]. \end{aligned} \quad (5.63)$$

(ii) NME Dependence on the Lepton Energies: If we neglect the dependence of NMEs on  $\varepsilon_{K,L}$ , the nuclear and leptonic parts can be separated and we obtain

$$\mathcal{A}_{\text{SM}}^{2\nu} \approx [g_{-1}^2(E_{e_1}) + f_1^2(E_{e_1})][g_{-1}^2(E_{e_2}) + f_1^2(E_{e_2})]g_A^4\mathcal{M}_{\text{GT}}^2, \quad (5.64)$$

$$\mathcal{B}_{\text{SM}}^{2\nu} \approx 4f_1(E_{e_1})f_1(E_{e_2})g_{-1}(E_{e_1})g_{-1}(E_{e_2})g_A^4\mathcal{M}_{\text{GT}}^2, \quad (5.65)$$

with the Gamow-Teller NME now defined as

$$\mathcal{M}_{\text{GT}} = m_e \sum_n \frac{\langle 0_F^+ | \sum_m \tau_m^+ \sigma_m | 1_n^+ \rangle \langle 1_n^+ | \sum_m \tau_m^+ \sigma_m | 0_I^+ \rangle}{E_n - (E_I + E_F)/2}. \quad (5.66)$$

A more accurate approximation is obtained by Taylor expanding the NMEs in the small parameters  $\varepsilon_{K,L}$  [686]. Retaining terms up to  $\varepsilon_{K,L}^4$  gives

$$\begin{aligned} \mathcal{A}_{\text{SM}}^{2\nu} \approx & [g_{-1}^2(E_{e_1}) + f_1^2(E_{e_1})][g_{-1}^2(E_{e_2}) + f_1^2(E_{e_2})] \\ & \times g_A^4 \left[ (\mathcal{M}_{\text{GT-1}})^2 + (\varepsilon_K^2 + \varepsilon_L^2)\mathcal{M}_{\text{GT-1}}\mathcal{M}_{\text{GT-3}} + \frac{1}{3}\varepsilon_K^2\varepsilon_L^2(\mathcal{M}_{\text{GT-3}})^2 \right. \\ & \left. + (\varepsilon_K^4 + \varepsilon_L^4) \left( \mathcal{M}_{\text{GT-1}}\mathcal{M}_{\text{GT-5}} + \frac{1}{3}(\mathcal{M}_{\text{GT-3}})^2 \right) \right] \end{aligned} \quad (5.67)$$

and

$$\begin{aligned} \mathcal{B}_{\text{SM}}^{2\nu} \approx & 4f_1(E_{e_1})f_1(E_{e_2})g_{-1}(E_{e_1})g_{-1}(E_{e_2}) \\ & \times g_A^4 \left[ (\mathcal{M}_{\text{GT-1}})^2 + (\varepsilon_K^2 + \varepsilon_L^2) \mathcal{M}_{\text{GT-1}} \mathcal{M}_{\text{GT-3}} + \frac{4}{9} \varepsilon_K^2 \varepsilon_L^2 (\mathcal{M}_{\text{GT-3}})^2 \right. \\ & \left. + (\varepsilon_K^4 + \varepsilon_L^4) \left( \mathcal{M}_{\text{GT-1}} \mathcal{M}_{\text{GT-5}} + \frac{5}{18} (\mathcal{M}_{\text{GT-3}})^2 \right) \right]. \end{aligned} \quad (5.68)$$

Here, the introduced NMEs are defined (in the notation of Ref. [686]) as

$$\mathcal{M}_{\text{GT-1}} \equiv \mathcal{M}_{\text{GT}}, \quad (5.69)$$

$$\mathcal{M}_{\text{GT-3}} = 4m_e^3 \sum_n \frac{\mathcal{M}_{\text{GT}}}{(E_n - (E_I + E_F)/2)^3}, \quad (5.70)$$

$$\mathcal{M}_{\text{GT-5}} = 16m_e^5 \sum_n \frac{\mathcal{M}_{\text{GT}}}{(E_n - (E_I + E_F)/2)^5}. \quad (5.71)$$

This is the approximation we employ in our later numerical analyses.

The non-standard contribution to  $2\nu\beta\beta$  decay from the right-handed currents proportional to the  $\varepsilon_{RX}$  coupling, as appearing in the Lagrangian in Eq. (5.49), was

calculated in Ref. [303]. The corresponding functions  $\mathcal{A}^{2\nu}$  and  $\mathcal{B}^{2\nu}$  factors are

$$\begin{aligned}
\mathcal{A}_\epsilon^{2\nu} = & 4|\epsilon_{RX}|^2 \left\{ [g_{-1}^2(E_{e_1}) + f_1^2(E_{e_1})][g_{-1}^2(E_{e_2}) + f_1^2(E_{e_2})] \right. \\
& + [g_{-1}^2(E_{e_1}) - f_1^2(E_{e_1})][g_{-1}^2(E_{e_2}) - f_1^2(E_{e_2})] \frac{m_\nu m_N}{E_{v_1} E_{v_2}} \Big\} \\
& \times \left\{ \left[ g_V^4 (\mathcal{M}_F^K - \mathcal{M}_F^L)^2 + \frac{1}{3} g_A^4 (\mathcal{M}_{\text{GT}}^K - \mathcal{M}_{\text{GT}}^L)^2 \right] \right. \\
& \quad + \left[ g_V^4 (\mathcal{M}_F^K + \mathcal{M}_F^L)^2 + \frac{1}{3} g_A^4 (\mathcal{M}_{\text{GT}}^K + \mathcal{M}_{\text{GT}}^L)^2 \right] \Big\} \\
& + 2|\epsilon_{RX}|^2 \left\{ [g_{-1}^2(E_{e_1}) - f_1^2(E_{e_1})][g_{-1}^2(E_{e_2}) - f_1^2(E_{e_2})] \right. \\
& \quad + [g_{-1}^2(E_{e_1}) + f_1^2(E_{e_1})][g_{-1}^2(E_{e_2}) + f_1^2(E_{e_2})] \frac{m_\nu m_N}{E_{v_1} E_{v_2}} \Big\} \\
& \times \left\{ \left[ g_V^4 (\mathcal{M}_F^K - \mathcal{M}_F^L)^2 - \frac{1}{3} g_A^4 (\mathcal{M}_{\text{GT}}^K - \mathcal{M}_{\text{GT}}^L)^2 \right] \right. \\
& \quad - \left[ g_V^4 (\mathcal{M}_F^K + \mathcal{M}_F^L)^2 - \frac{1}{3} g_A^4 (\mathcal{M}_{\text{GT}}^K + \mathcal{M}_{\text{GT}}^L)^2 \right] \\
& \quad + 2g_V^2 g_A^2 [(\mathcal{M}_F^K - \mathcal{M}_F^L)(\mathcal{M}_{\text{GT}}^K - \mathcal{M}_{\text{GT}}^L) \\
& \quad \quad + (\mathcal{M}_F^K + \mathcal{M}_F^L)(\mathcal{M}_{\text{GT}}^K + \mathcal{M}_{\text{GT}}^L)] \Big\} \quad (5.72)
\end{aligned}$$

and

$$\begin{aligned}
\mathcal{B}_\epsilon^{2\nu} = & 4|\epsilon_{RX}|^2 f_1(E_{e_1}) f_1(E_{e_2}) g_{-1}(E_{e_1}) g_{-1}(E_{e_2}) \\
& \times \left\{ 2g_V^4 [(\mathcal{M}_F^K + \mathcal{M}_F^L)^2 - (\mathcal{M}_F^K - \mathcal{M}_F^L)^2] \frac{m_\nu m_N}{E_{v_1} E_{v_2}} \right. \\
& \quad + \frac{8}{9} g_A^4 [(\mathcal{M}_{\text{GT}}^K - \mathcal{M}_{\text{GT}}^L)^2 + (\mathcal{M}_{\text{GT}}^K + \mathcal{M}_{\text{GT}}^L)^2] \\
& \quad + \frac{10}{9} g_A^4 [(\mathcal{M}_{\text{GT}}^K + \mathcal{M}_{\text{GT}}^L)^2 - (\mathcal{M}_{\text{GT}}^K - \mathcal{M}_{\text{GT}}^L)^2] \frac{m_\nu m_N}{E_{v_1} E_{v_2}} \\
& \quad + \frac{4}{3} g_V^2 g_A^2 [(\mathcal{M}_F^K - \mathcal{M}_F^L)(\mathcal{M}_{\text{GT}}^K - \mathcal{M}_{\text{GT}}^L) \\
& \quad \quad + (\mathcal{M}_F^K + \mathcal{M}_F^L)(\mathcal{M}_{\text{GT}}^K + \mathcal{M}_{\text{GT}}^L)] \frac{m_\nu m_N}{E_{v_1} E_{v_2}} \\
& \quad - \frac{8}{3} g_V^2 g_A^2 [(\mathcal{M}_F^K - \mathcal{M}_F^L)(\mathcal{M}_{\text{GT}}^K - \mathcal{M}_{\text{GT}}^L) \\
& \quad \quad + (\mathcal{M}_F^K + \mathcal{M}_F^L)(\mathcal{M}_{\text{GT}}^K + \mathcal{M}_{\text{GT}}^L)] \Big\}. \quad (5.73)
\end{aligned}$$

In Eqs. (5.72) and (5.73) the terms proportional to  $m_\nu m_N$  are small, as one of the emitted neutrinos is still assumed to be the light with  $m_\nu \lesssim 0.1$  eV. As in the SM case, we estimate the above expressions with their Taylor expansions up to the fourth power in the small parameters  $\varepsilon_{K,L}$ .

The kinematics of the outgoing electrons in the decay is described by the fully differential decay rate in Eq. (5.51) depending on the electron energies  $E_{e_1}, E_{e_2}$  and angle  $\theta$  between the electron momenta. All the information is contained by the quantities  $\mathcal{A}^{2\nu}$  and  $\mathcal{B}^{2\nu}$  presented above for both the SM (Eqs. (5.56) and (5.57)) and right-handed current with sterile state  $N$  (Eqs. (5.67) and (5.68)) cases. The following values of the physical constants are used in our numerical analysis:  $G_\beta = 1.1363 \times 10^{-5}$  GeV $^{-2}$ ,  $\alpha = \frac{1}{137}$ ,  $m_e = 0.511$  MeV,  $m_p = 938$  MeV,  $R_A \approx 1.2A^{1/3}$  fm and  $g_V = 1$ . Since the axial vector coupling  $g_A$  is expected to be quenched in the nucleus [687], we take  $g_A = 1$  instead of the usual value of  $g_A = 1.269$  for a free neutron. Furthermore, we use the  $2\nu\beta\beta$  decay NMEs from Ref. [686] as shown in Table 5.2.

We can now calculate the total  $2\nu\beta\beta$  decay rate and the decay distributions potentially observable in experiments. At present, the  $2\nu\beta\beta$  decay experiments primarily measure the differential rate in the total kinetic energy  $E_K = E_{e_1} + E_{e_2} - 2m_e - m_{\nu_1} - m_{\nu_2}$  of the outgoing electrons,

$$\frac{d\Gamma^{2\nu}}{dE_K} = \frac{E_K}{E_K^{\max}} \int_0^{E_K^{\max}} dE \frac{d\Gamma^{2\nu}}{dE_{e_1} dE_{e_2}}, \quad (5.74)$$

where  $E_K^{\max} = E_I - E_F - 2m_e - m_{\nu_1} - m_{\nu_2}$  and

$$E_{e_1} = E_K - \frac{E_K}{E_K^{\max}} E + m_e, \quad E_{e_2} = \frac{E_K}{E_K^{\max}} E + m_e. \quad (5.75)$$

In the SM  $m_{\nu_{1,2}}$  are negligible, but for a heavy sterile neutrino one of these will be the non-negligible  $m_N$ , i.e.  $m_{\nu_1} = m_N, m_{\nu_2} = 0$ . We will also neglect the recoil of the final state isotope which could shift the endpoint by  $\sim \frac{Q_{\beta\beta}^2}{m_A} \lesssim 0.1$  eV, with the  $Q_{\beta\beta} \lesssim 3$  MeV and the mass of the nucleus is  $m_A \sim 76 - 136$  GeV. Some experiments capture the energies and tracks of individual electrons, therefore allowing to

study the single electron energy distribution  $\frac{d\Gamma^{2\nu}}{dE_{e_1}}$  and double differential distribution  $\frac{d\Gamma^{2\nu}}{dE_{e_1}dE_{e_2}}$ . These are calculated from Eq. (5.51) as

$$\begin{aligned} \frac{d\Gamma^{2\nu}}{dE_{e_1}} &= \int_{m_e}^{E_I - E_F - m_{\nu_1} - m_{\nu_2} - E_{e_1}} dE_{e_2} \frac{d\Gamma^{2\nu}}{dE_{e_1}dE_{e_2}}, \\ \frac{d\Gamma^{2\nu}}{dE_{e_1}dE_{e_2}} &= \int_{-1}^1 d\cos\theta \frac{d\Gamma^{2\nu}}{dE_1 dE_2 d\cos\theta}. \end{aligned} \quad (5.76)$$

Given that most experiments only provide the differential  $2\nu\beta\beta$  decay distribution in the total kinetic energy of the electrons  $E_K$ , in the following analysis we focus primarily on this observable.

The integration over the electron energies in Eq. (5.51) instead leads to the equation

$$\frac{d\Gamma^{2\nu}}{d\cos\theta} = \frac{\Gamma^{2\nu}}{2} (1 + K^{2\nu} \cos\theta), \quad (5.77)$$

describing the differential angular distribution of the decay. Here,  $\Gamma^{2\nu}$  denotes the total  $2\nu\beta\beta$  decay rate and  $K^{2\nu} = \frac{\Lambda^{2\nu}}{\Gamma^{2\nu}}$  stands for the angular correlation factor. The factors  $\Gamma^{2\nu}$  and  $\Lambda^{2\nu}$  are given by

$$\begin{pmatrix} \Gamma^{2\nu} \\ \Lambda^{2\nu} \end{pmatrix} = \frac{c_{2\nu}}{m_e^{11}} \int_{m_e}^{E_I - E_F - m_e} dE_{e_1} |\mathbf{p}_{e_1}| E_{e_1} \int_{m_e}^{E_I - E_F - E_{e_1}} dE_{e_2} |\mathbf{p}_{e_2}| E_{e_2} \begin{pmatrix} A^{2\nu} \\ B^{2\nu} \end{pmatrix} \quad (5.78)$$

The inclusion of right-handed current can result in an opposite sign for the angular correlation of the emitted electrons [303]. The angular distribution is therefore useful for distinguishing the possible contributions, as analysed in the following section.

### 5.4.3 Sensitivity to Sterile Neutrino Parameters

We will now use the differential  $2\nu\beta\beta$  decay rates derived in the previous section to exclude regions of the sterile neutrino parameter space; namely, the sterile neutrino mass  $m_N$  and active-sterile mixing (with the electron flavour)  $|V_{eN}|^2$ . We will use the non-observation of distortions to the SM  $2\nu\beta\beta$  decay spectrum by ( $0\nu\beta\beta$  decay search) experiments such as GERDA II, CUPID-0, NEMO-3 and KamLAND-Zen

to put upper limits on  $|V_{eN}|^2$  as a function of  $m_N$ . We will also estimate upper limits from the forecasted sensitivities of LEGEND, SuperNEMO, CUPID and DARWIN. Finally, we will compare these to bounds in the  $0.1 \text{ MeV} \lesssim m_N \lesssim 3 \text{ MeV}$  range from single beta decay ( $^{64}\text{Cu}$ ,  $^{144}\text{Ce} - ^{144}\text{Pr}$  and  $^{20}\text{F}$ ) and sterile neutrino decays (Borexino) as discussed in Section 5.2.

To obtain upper limits on the mixing  $|V_{eN}|^2$  we follow the standard frequentist approach of Refs. [688, 689] outlined in Appendix C. Firstly, we define the total differential  $2\nu\beta\beta$  decay rate as the incoherent sum of the SM and sterile neutrino rates for a given  $m_N$  and total kinetic energy  $E_K$ ,

$$\frac{d\Gamma^{2\nu}}{dE_K} = (1 - |V_{eN}|^2)^2 \frac{d\Gamma_{\text{SM}}^{2\nu}}{dE_K} + (1 - |V_{eN}|^2) |V_{eN}|^2 \frac{d\Gamma_N^{2\nu}(m_N)}{dE_K}, \quad (5.79)$$

where we have extracted the dependence on the active-sterile mixing  $|V_{eN}|^2$  from the rates. The total differential rate depends on the parameters  $(m_N, |V_{eN}|^2)$  and  $E_K$ . Here, the contribution  $\frac{d\Gamma_N^{2\nu}}{dE_K}$  due to the sterile neutrino includes a factor of two with respect to the SM contribution, as two distinguishable neutrinos are emitted in the process, cf. Eq. (5.50).

In Fig. 5.14, we plot the total differential rate in Eq. (5.79) and compare it to the sterile neutrino contribution  $|V_{eN}|^2 \frac{d\Gamma_N^{2\nu}}{dE_K}$  for the isotopes  $^{100}\text{Mo}$  and  $^{136}\text{Xe}$ . We normalise both to the total SM decay rate  $\Gamma_{\text{SM}}^{2\nu}$ . The respective  $Q$ -values of the isotopes are indicated by the vertical dotted lines and the benchmark values of  $m_N = 1.0 \text{ MeV}$  and  $|V_{eN}|^2 = 0.5$  are chosen. In the panel below we show the percentage deviation of the total differential rate from the SM rate,

$$\left( \frac{d\Gamma^{2\nu}}{dE_K} - \frac{d\Gamma_{\text{SM}}^{2\nu}}{dE_K} \right) \Big/ \frac{d\Gamma_{\text{SM}}^{2\nu}}{dE_K} = |V_{eN}|^2 \left( \frac{d\Gamma_N^{2\nu}}{dE_K} \Big/ \frac{d\Gamma_{\text{SM}}^{2\nu}}{dE_K} - 1 \right). \quad (5.80)$$

It can be seen that the magnitude of  $\frac{d\Gamma^{2\nu}}{dE_K}$  decreases with respect to the  $\frac{d\Gamma_{\text{SM}}^{2\nu}}{dE_K}$  as  $E_K$  increases, eventually plateauing at around  $-10\%$ . This is because the sterile neutrino contribution  $|V_{eN}|^2 \frac{d\Gamma_N^{2\nu}}{dE_K}$  falls when  $E_K$  increases above  $\sim 1.0 \text{ MeV}$ . Eventually its contribution is negligible, but there remains a suppression from the  $(1 - |V_{eN}|^2)$

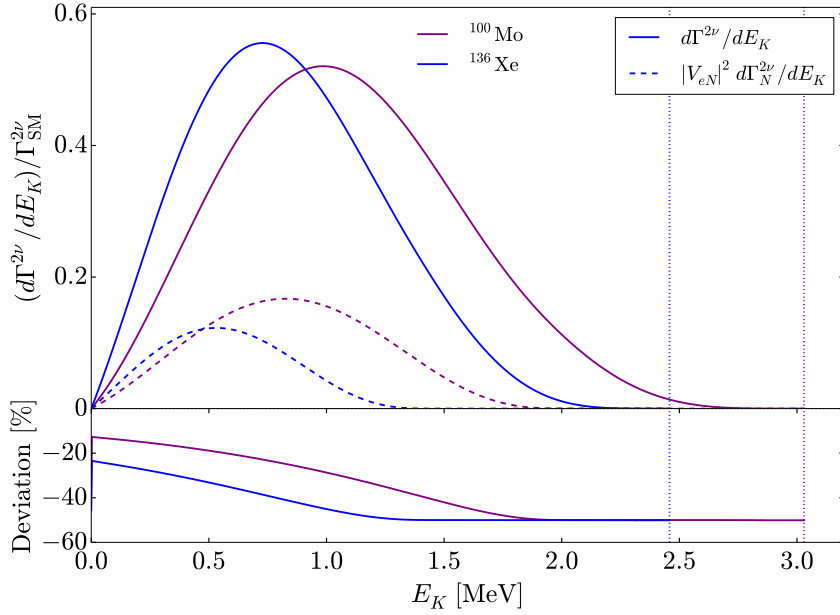


**Figure 5.14:** Total differential  $2\nu\beta\beta$  decay rate (solid) and the sterile neutrino contribution (dashed) with  $m_N = 1.0$  MeV and  $|V_{eN}|^2 = 0.5$  for the two isotopes  $^{100}\text{Mo}$  (purple) and  $^{136}\text{Xe}$  (blue). Both distributions are normalised to the SM decay rate. The vertical dotted lines indicate the respective  $Q$ -values and the panel at the bottom shows the corresponding percentage deviations from the SM rate.

factor multiplying the SM contribution, which is particularly large for  $|V_{eN}|^2 = 0.5$ . It is apparent from Eq. (5.80) that the deviation tends to a factor of  $-|V_{eN}|^2$ . The characteristic signature of the sterile neutrino is a relative increase of the differential rate for  $E_K \lesssim Q_{\beta\beta} - m_N$ .

We note that the main uncertainty is from the experimental measurement of the  $2\nu\beta\beta$  decay rate and not the theoretical calculation of the corresponding NMEs. This is because the SM  $2\nu\beta\beta$  and  $\nu N\beta\beta$  decays approximately have the same NMEs and depend for example on the axial vector coupling  $g_A$  in the same way, at least to very good approximation. Thus, the individual decay rates have large theoretical uncertainties, e.g. considering a range of  $0.7 \lesssim g_A \lesssim 1.27$ , but their ratio is largely unaffected. One may then use the experimental measurement to fix the overall scale.

The sterile neutrino mass  $m_N$  does change the factors in Eq. (5.61), resulting in different NMEs as a sub-leading effect. This will affect the differential decay properties, such as the electron energy spectrum, but is essentially negligible for the

sterile neutrino produced by a left-handed current. This is because the distinctive feature of  $\nu N \beta\beta$  decay, the different energy threshold to  $2\nu\beta\beta$  decay, is practically unaffected. Its location is determined by kinematics and its shape is already smooth,  $\propto (Q_{\beta\beta} - m_N - E)^{7/2}$ . We expect small corrections due the NMEs from  $m_N$  to have little effect within the experimental energy resolutions considered.

The same procedure can be applied to place upper limits on the right-handed current coefficients  $|\epsilon_{RL}|^2$  and  $|\epsilon_{RR}|^2$ . As seen in the previous sections, the right-handed current modifies the total kinetic energy distribution to

$$\frac{d\Gamma^{2\nu}}{dE_K} = \frac{d\Gamma_{\text{SM}}^{2\nu}}{dE_K} + |\epsilon_{RX}|^2 \frac{d\Gamma_N^{2\nu}(m_N)}{dE_K}, \quad (5.81)$$

where the SM contribution is no longer reduced by the sterile neutrino mixing. The right-handed current also changes the total rate  $\Gamma^{2\nu}$  and angular correlation factor  $K^{2\nu}$  in Eq. (5.77) to

$$\Gamma^{2\nu} = A_{\text{SM}}^{2\nu} + A_N^{2\nu}(m_N)|\epsilon_{RX}|^2, \quad K^{2\nu} = \frac{B_{\text{SM}}^{2\nu} + B_N^{2\nu}(m_N)|\epsilon_{RX}|^2}{A_{\text{SM}}^{2\nu} + A_N^{2\nu}(m_N)|\epsilon_{RX}|^2}, \quad (5.82)$$

where  $A_{\text{SM}}^{2\nu}$  and  $B_{\text{SM}}^{2\nu}$  are found by plugging Eqs. (5.67) and (5.68) into Eqs. (5.53) and (5.53). The factors  $A_N^{2\nu}$  and  $B_N^{2\nu}$  are likewise found by inserting Eqs. (5.72) and (5.73) into Eqs. (5.53) and (5.53) and extracting  $|\epsilon_{RX}|^2$ . Assuming  $|\epsilon_{RX}|^2 \ll 1$ ,  $K^{2\nu}$  can now be Taylor expanded as

$$K^{2\nu} \approx K_{\text{SM}}^{2\nu} + \alpha(m_N)|\epsilon_{RX}|^2, \quad (5.83)$$

where the SM and right-handed current contributions, respectively, are

$$K_{\text{SM}}^{2\nu} = \frac{B_{\text{SM}}^{2\nu}}{A_{\text{SM}}^{2\nu}}, \quad \alpha(m_N) = \frac{B_N^{2\nu}(m_N) - K_{\text{SM}}^{2\nu}A_N^{2\nu}(m_N)}{A_{\text{SM}}^{2\nu}}, \quad (5.84)$$

We have the SM values  $K_{\text{SM}}^{2\nu} = -0.627$  for  $^{100}\text{Mo}$  and  $K_{\text{SM}}^{2\nu} = -0.631$  for  $^{82}\text{Se}$  (the isotopes of experiments sensitive to the angular correlation factor, NEMO-3 and SuperNEMO respectively). The  $\alpha(m_N)$  factors are plotted for  $^{82}\text{Se}$  (red) and

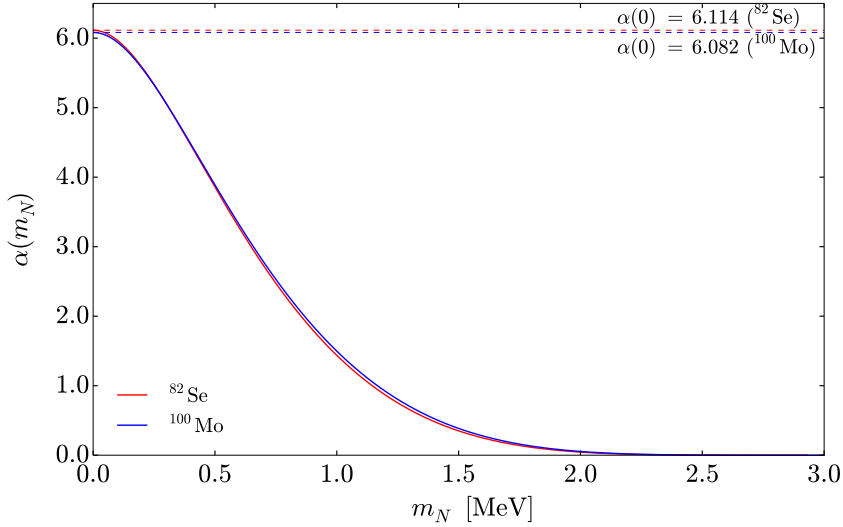


**Figure 5.15:** The factor  $\alpha(m_N)$  multiplying the right-handed current coefficient  $|\varepsilon_{RX}|^2$  yielding the sterile neutrino contribution to the angular correlation factor  $K^{2\nu}$  for  $^{82}\text{Se}$  (red) and  $^{100}\text{Mo}$  (blue).

$^{100}\text{Mo}$  (blue) in Fig. 5.15, which also explicitly shows the values at  $m_N = 0$ . The factor  $\alpha(m_N)$  is positive, indicating a change of the angular distribution away from the back-to-back configuration of electrons in the SM case. It is maximal for  $m_N = 0$  and is suppressed as  $m_N$  approaches the  $Q$ -value.

As outlined in Appendix C, we will now follow the frequentist approach to set bounds on the  $(m_N, |V_{eN}|^2)$  and  $(m_N, |\varepsilon_{RX}|^2)$  parameter spaces. We assume that the  $0\nu\beta\beta$  decay experiments do not see a  $2\nu\beta\beta$  decay spectrum deviating significantly from the SM prediction. For each  $(m_N, |V_{eN}|^2)$ , we use the differential rate in the total kinetic energy  $\frac{d\Gamma^{2\nu}}{dE_K}$  to construct the binned test-statistic  $q$  in Eq. (C.11), quantifying the level of compatibility between the null and sterile neutrino hypothesis. For each  $m_N$ , we exclude at 90% CL the mixings  $|V_{eN}|^2$  which have a test-statistic  $q > 2.71$ . The  $(m_N, |\varepsilon_{RX}|^2)$  parameter space can be similarly constrained by using either  $\frac{d\Gamma^{2\nu}}{dE_K}$  or  $\frac{d\Gamma^{2\nu}}{d\cos\theta}$  to construct a binned test-statistic. The two observables provide complementary limits.

A selection of current and next generation  $0\nu\beta\beta$  decay experiments measuring the  $2\nu\beta\beta$  decay of isotopes  $^{76}\text{Ge}$ ,  $^{82}\text{Se}$ ,  $^{100}\text{Mo}$  and  $^{136}\text{Xe}$  are shown in Table 5.3. This list is not exhaustive; for example, the nEXO and SNO+ experiments will also search for  $0\nu\beta\beta$  decay in  $^{136}\text{Xe}$  and  $^{130}\text{Te}$  respectively [690, 691]. For a review of

Isotope	Experiment	Exposure [kg · y]	$N_{\text{events}}$	$\Delta E$ [keV]	$(\sigma_\eta, \sigma_f)$ [%]
$^{76}\text{Ge}$	GERDA II [693]	103.7	$3.63 \times 10^4$	15	(4.6, 1.9)
	LEGEND [694]	$10^3\text{--}10^4$	$10^5\text{--}10^6$	2.5	(0.5, 0.5)
$^{82}\text{Se}$	CUPID-0 [695]	9.95	$5.8 \times 10^3$	50	(1.5, 1.0)
	SuperNEMO [696]	$10^2\text{--}10^3$	$10^4\text{--}10^5$	50	(0.5, 0.5)
$^{100}\text{Mo}$	NEMO-3 [697]	34.3	$4.95 \times 10^5$	100	(5.4, 1.8)
	CUPID [698]	$10^2\text{--}10^3$	$10^6\text{--}10^7$	5	(0.5, 0.5)
$^{136}\text{Xe}$	KamLAND-Zen [699]	126.3	$9.83 \times 10^4$	50	(3.1, 0.3)
	DARWIN [700]	$(2\text{--}5) \times 10^4$	$10^6\text{--}10^7$	5	(0.5, 0.5)

**Table 5.3:** A selection of current and future  $0\nu\beta\beta$  decay search experiments measuring the  $2\nu\beta\beta$  decay spectrum of the four isotopes considered in this chapter. Shown are the current and forecasted exposures, total number of events  $N_{\text{events}}$ , energy resolutions  $\Delta E$  and parameters  $(\sigma_\eta, \sigma_f)$  estimating the effect of systematic errors on the log-likelihood function.

current and next generation experiments, see Ref. [692]. Listed in Table 5.3 are the exposures, total number of events  $N_{\text{events}}$ , energy resolutions  $\Delta E$  and estimates for the parameters  $\sigma_\eta$  and  $\sigma_f$  quantifying the uncertainties on the nuisance parameter  $\eta$  and from other systematic effects, respectively. Values are taken from the list of references given for the experiments. For each experiment we make use of Eq. (C.11) to set an upper limit on the active-sterile mixing  $|V_{eN}|^2$  as a function of the sterile neutrino mass  $m_N$ .

Fig. 5.16 (left) shows the 90% CL upper limits from the current generation experiments GERDA II (grey), CUPID-0 (red), NEMO-3 (purple) and KamLAND-Zen (blue). We also show a combined constraint (black dashed) found by adding the log-likelihoods of the experiments (each minimised with respect to a separate nuisance parameter  $\eta$ ). It can be seen that the upper limits worsen for smaller and larger values of  $m_N$  in the range  $0.1 \text{ MeV} \lesssim m_N \lesssim 3 \text{ MeV}$ , with the best upper bounds being found at  $m_N$  similar to the peak energy of the spectrum. We compare the constraints to those from single beta decay experiments and sterile neutrino decays (shaded areas). While NEMO-3 and KamLAND-Zen provide the best constraints, they are not as stringent as previous limits. However, it is interesting that  $2\nu\beta\beta$  decay is most sensitive to sterile masses in the range  $0.3 \text{ MeV} \lesssim m_N \lesssim 0.7 \text{ MeV}$

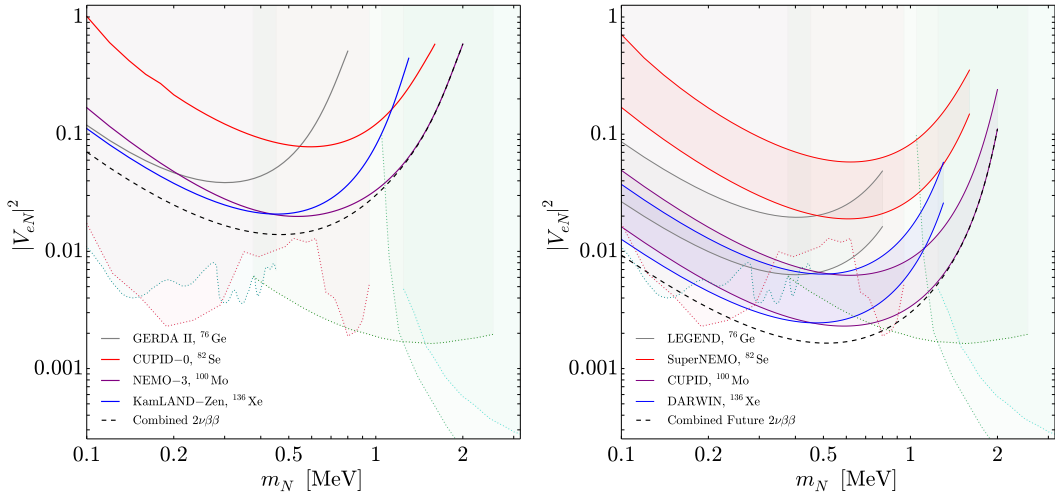


**Figure 5.16:** Upper limits and sensitivities at 90% CL on  $|V_{eN}|^2$  as a function of  $m_N$  from  $2\nu\beta\beta$  decay in current (left) and future (right) experiments. We show the individual constraints (as indicated in the legend) as well as a combined constraint (black dashed). The bands in the right plot correspond to the range of possible future exposures in Table 5.3. The combined future sensitivity uses the maximum forecasted exposure of each experiment.

where existing constraints are less stringent.

Fig. 5.16 (right) shows the corresponding sensitivities of the next generation of  $0\nu\beta\beta$  decay experiments. The forecasted exposures given by the collaborations are often one or two orders of magnitude larger than those of current experiments. We estimate the total number of events  $N_{\text{events}}$  seen in future by multiplying the current number by the ratio of future to current exposures. Energy resolutions are taken from the references in Table 5.3 and we assume an optimistic value of  $\sigma_\eta \sim \sigma_f \sim 0.5\%$  for the systematic uncertainties. We compute the 90% CL sensitivity for both the higher and lower forecasted number of events in Table 5.3, shown as bands for LEGEND (grey), SuperNEMO (red), CUPID (purple) and DARWIN (blue). Also shown is the combined sensitivity (black dashed) using the largest predicted exposure of each experiment. For a given experiment the upper bounds exhibit the same improvement for sterile masses close to the maximum of the total differential decay rate. The most stringent upper limits come from CUPID and DARWIN,  $|V_{eN}|^2 \lesssim 2.5 \times 10^{-3}$ , which would exclude the currently unconstrained region in the  $0.3 \text{ MeV} \lesssim m_N \lesssim 0.7 \text{ MeV}$  range.

Likewise, we estimate the current limits and future sensitivity on the right-

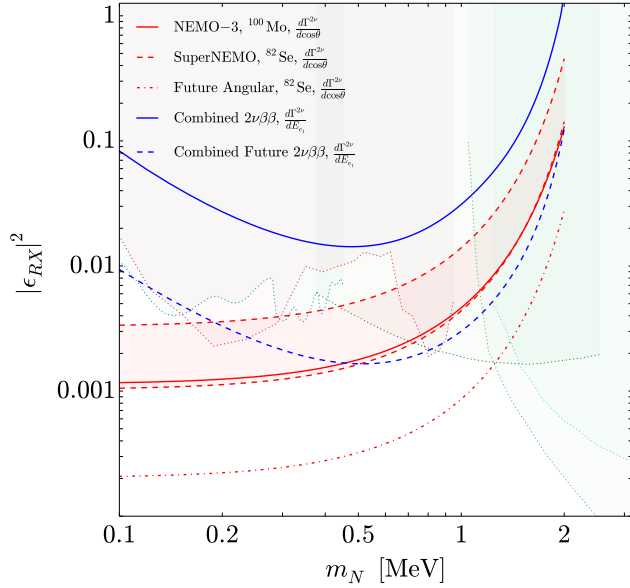


**Figure 5.17:** Current upper limits and future sensitivities at 90% CL on  $|\epsilon_{RX}|^2$  as a function  $m_N$ . The solid (dashed) blue line shows the combined constraint from current (future)  $2\nu\beta\beta$  decay experiments measuring the total kinetic energy distribution. The solid red line is the upper limit derived from the angular distribution measurement of NEMO-3. The dashed red band indicates the range of upper limits expected from the angular distribution measurement of SuperNEMO. The dot-dashed red line shows the upper limit from a future  $^{82}\text{Se}$  experiment with an exposure of  $10^7$  events.

handed current coefficients  $|\epsilon_{RL}|^2$  and  $|\epsilon_{RR}|^2$  from measuring the  $2\nu\beta\beta$  decay energy distribution and angular correlation. In Fig. 5.17 we plot the upper limits at 90% CL on  $|\epsilon_{RL}|^2$  and  $|\epsilon_{RR}|^2$  as a function of the sterile neutrino mass  $m_N$ . The blue solid line is the combined constraint from current  $2\nu\beta\beta$  decay experiments using the total kinetic energy distribution, while the red solid line is the upper limit derived from the angular distribution measurement of NEMO-3. The blue dashed line is the combined sensitivity from future  $2\nu\beta\beta$  decay experiments, while the red dashed band indicates the sensitivity of the SuperNEMO angular measurement. The latter is not a large improvement as SuperNEMO is not expected to have a significantly increased exposure compared to NEMO-3, see Table 5.3. We therefore also indicate the sensitivity of a hypothetical  $^{82}\text{Se}$  angular measurement with an exposure of  $10^7$  events (red dot dashed).

The combined constraints on  $|\epsilon_{RL}|^2$  and  $|\epsilon_{RR}|^2$  (dashed lines) from  $\frac{d\Gamma^{2\nu}}{dE_K}$  are slightly weaker than the equivalent constraints on  $|V_{eN}|^2$ . This is because the SM

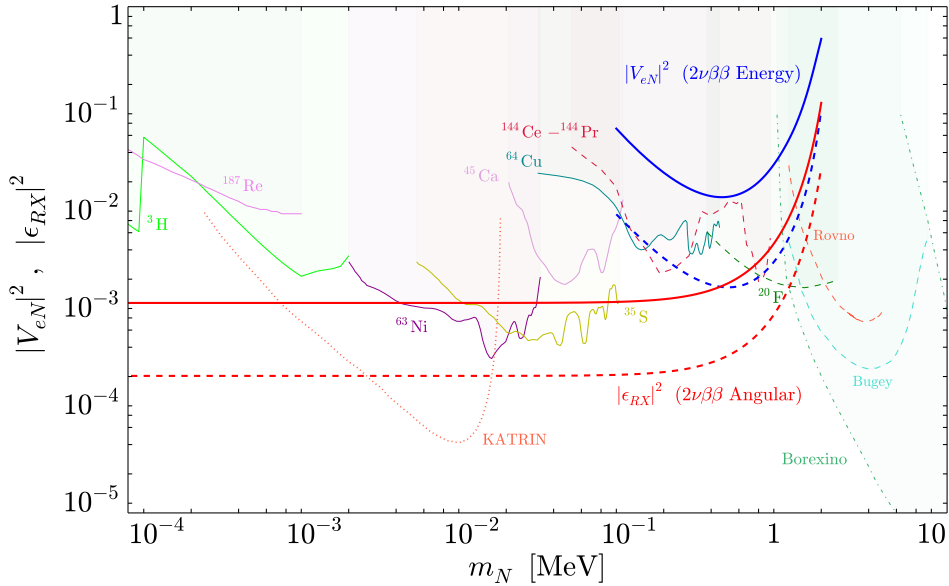


**Figure 5.18:** Current upper limits (solid blue) and future sensitivities (dashed blue) on the mixing strength  $|V_{eN}|^2$  between the electron and sterile neutrino as a function of the sterile mass  $m_N$ . Likewise, the red curves give the current limit and future sensitivity on the right-handed coefficient  $|\epsilon_{RX}|^2$  using a measurement of the angular distribution in  $2\nu\beta\beta$  decay. The shaded regions are excluded by existing searches in single beta decay and sterile decays in reactor and solar neutrino oscillation experiments.

contribution in Eq. (5.81) is not suppressed, as is the case for Eq. (5.79). The constraints from the NEMO-3 angular distribution are generally better, tending to a constant upper bound  $|\epsilon_{RX}|^2 \lesssim 10^{-3}$  for  $m_N \lesssim 0.2$  MeV. This roughly agrees with the result  $\epsilon_{RX} < 2.7 \times 10^{-2}$  in the massless case found in Ref. [303].

To summarise the sensitivity of  $2\nu\beta\beta$  decay, we compare in Fig. 5.18 the current limits on  $|V_{eN}|^2$  from existing  $2\nu\beta\beta$  decay (solid blue) to constraints from single beta decays and sterile neutrino decays over the  $100$  eV  $< m_N < 10$  MeV mass range. The blue curve uses the combined constraints from measurements of  $2\nu\beta\beta$  decay electron energies. The red curve shows the current constraint on the right-handed coefficient  $|\epsilon_{RX}|^2$  using the NEMO-3 angular distribution measurement. The dashed curves indicate the corresponding future sensitivities. At lower masses both the current and future upper limits on  $|V_{eN}|^2$  cannot compete with existing constraints from  $^{64}\text{Cu}$  and  $^{144}\text{Ce} - 144\text{Pr}$  beta decays. At higher masses they are also less stringent than constraints from Borexino, Bugey and Rovno. It is the

$0.3 \text{ MeV} < m_N < 0.7 \text{ MeV}$  range where  $2\nu\beta\beta$  decay can provide competitive constraints in the future, though we expect that similar improvements from  $^{20}\text{F}$  and  $^{144}\text{Ce}-^{144}\text{Pr}$  beta decays are also possible. The constraints on the right-handed coefficient  $|\varepsilon_{RX}|^2$  using an angular distribution measurement in  $2\nu\beta\beta$  decay are most sensitive for light sterile neutrino masses  $m_N \lesssim 0.1 \text{ MeV}$  as the effect is otherwise phase-space suppressed. We note, though, that the limits from single beta decays (and the other processes shown) apply to  $|V_{eN}|^2$  and should be re-evaluated for a sterile neutrino coupling through a right-handed current. However, we expect the upper bounds on  $|\varepsilon_{RX}|^2$  to be different by a factor of  $\mathcal{O}(1)$ .

To conclude this chapter, we reiterate that heavy sterile neutrinos are one of the most interesting candidates for particles beyond the SM. They are conspicuously absent from the SM field content, so that the left-handed neutrinos  $\nu_L$  are the only fermions that do not have right-handed partner fields. Adding  $n_S$  right-handed fields  $N_R$  to the SM field content opens up a number of possibilities, with the two main classes of models either forbidding or allowing  $|\Delta L| = 2$  mass terms for the sterile  $N_R$  fields. The situation may be somewhere inbetween these two limiting cases. For example, two Majorana sterile neutrinos with opposite CP phases may form a pseudo-Dirac states if the source of  $|\Delta L| = 2$  is small. The phenomenology of these scenarios can be vastly different.

In Section 5.1 we introduced a phenomenological parametrisation of a single-generation seesaw model in terms of experimentally measurable quantities, such as active-sterile neutrino mixing angles, CP phases, masses and mass splittings. We have identified the regions of parameter space allowed by consistency conditions for the neutrino mass matrix  $(M_V)_{11}$  in the single-generation case, and have showed how Type-I seesaw and ISS limits can be recovered (cf. Fig. 5.2). Imposing the additional constraint that the radiative contribution to the active neutrino mass must be less than 10% of the tree-level mass further reduces this allowed parameter space, as shown in Fig. 5.5.

There is a strong ongoing and planned effort to search for sterile neutrinos over a wide range of masses and active-sterile mixing strengths. The main focus of this

chapter was to compare direct searches (e.g. direct production at colliders and in meson decays) with constraints from  $0\nu\beta\beta$  decay. The latter is the most important probe of light Majorana neutrino masses, but also of exotic  $|\Delta L| = 2$  processes such as the exchange of heavy sterile Majorana neutrinos. They are therefore constrained by current  $0\nu\beta\beta$  decay searches.

In Section 5.2 we summarised the current and future experimental constraints on the sterile neutrino  $(m_N, |V_{eN}|^2)$  parameter space over a wide mass range, including both  $|\Delta L| = 0$  and  $|\Delta L| = 2$  processes (cf. Figs. 5.6 and 5.7), remarking that the  $|\Delta L| = 2$  constraints are dependent on the relative CP phase and mass splitting between the two sterile states. This is especially true for  $0\nu\beta\beta$  decay searches, which are significantly weakened for quasi-Dirac sterile neutrinos (small  $\Delta m_N$ ), as shown in Fig. 5.9. For large  $\Delta m_N$ , the  $0\nu\beta\beta$  decay constraint remains strong in the electron sector (cf. Fig. 5.12) and it is most stringent heavy neutrino masses in the region  $\mathcal{O}(100) \text{ MeV} \lesssim m_N \lesssim \mathcal{O}(1) \text{ GeV}$ . Future  $0\nu\beta\beta$  decay experiments be able to exclude active-sterile mixings close to the Type-I seesaw prediction.

In this chapter we have also analysed the ability of  $0\nu\beta\beta$  decay experiments to constrain the  $(m_N, |V_{eN}|^2)$  parameter space from precision measurements of the  $2\nu\beta\beta$  decay spectrum. If one of the two emitted neutrinos is heavy, we showed that this changed the differential distribution in the total kinetic energy  $E_K$  of the electrons. The kinematic endpoint is shifted to lower values depending on  $m_N$  and the the usual SM contribution is reduced by  $|V_{eN}|^2$ . The very long  $2\nu\beta\beta$  decay half-lives and small rates compared to single beta decay may appear to hinder this probe. Nevertheless, future searches for  $0\nu\beta\beta$  decay will push the exposure up to  $10^7$  events, making it possible to probe NP with  $2\nu\beta\beta$  decay [683, 683]. We have also extended the analysis to consider a right-handed current for the sterile neutrino. As in Ref. [303], this gives rise to an anomalous angular distribution of the electrons in  $2\nu\beta\beta$  decay which we use to constrain the  $(m_N, |\mathcal{E}_{RX}|^2)$  parameter space. While current limits are not as strong as those from single beta decays, future searches will improve the bounds in the interesting region  $0.3 \text{ MeV} \lesssim m_N \lesssim 0.7 \text{ MeV}$ . We note that sterile neutrinos in this mass range are also constrained by astrophysical and

cosmological bounds (c.f. Fig. 5.6), but these may be relaxed in certain models. It is nonetheless important to use all available data in the search for NP.

## Chapter 6

# Conclusions

*“All truths are easy to understand once they are discovered; the point is to discover them.”*

- Galileo Galilei

To conclude this thesis, we have studied a number of topics related to the light neutrinos ( $\nu_e$ ,  $\nu_\mu$ , and  $\nu_\tau$ ). From the observation of neutrino oscillations, we know that the neutrinos are massive and mixed. However, neutrinos are strictly massless in the Standard Model (SM) of particle physics; this is therefore a hint of physics beyond the SM. We call the SM plus the new physics (NP) generating the light neutrino masses the vSM.

The primary question of whether the neutrinos are Dirac or Majorana fermions is a recurring theme and was reviewed in Chapter 2. There, we outlined how these two scenarios depend on the conservation of the global lepton number symmetry  $U(1)_L$ . We also explored the introduction of  $n_S$  sterile (under the SM gauge group) states  $N_R$  to the SM field content. The resulting phenomenology heavily depends on the *a priori* arbitrary masses and CP phases of these states. Regardless of the many possibilities for the field content of the vSM, we also examined how to parametrise exotic neutrino interactions using effective operators. Constraining the coefficients of these operators is a model-independent approach for probing the effect of NP in low-energy neutrino observables.

In Chapter 3, we investigated the effect of lepton number violating ( $|\Delta L| = 2$ ) charged-current non-standard interactions (NSIs) on long baseline (LBL) neutrino

oscillations. If the neutrinos are Majorana fermions, it is in theory possible for the  $\nu_\alpha \leftrightarrows \bar{\nu}_\beta$  oscillation to occur with SM charged-current interactions. However, this process is highly suppressed by the ‘helicity-flip’ factor  $\sim (m_\nu/E_\nu)^2$ . We showed that a  $|\Delta L| = 2$  neutrino NSI at the production or detection process replaces this suppression with  $|\varepsilon|^2$ , where  $\varepsilon$  is the coefficient of the neutrino NSI normalised to the Fermi coupling constant  $G_F$ . Experiments that are sensitive to the charge of the outgoing  $\ell_\beta^\pm$  are thus able to constrain this parameter. We used the non-observation of an excess of *wrong*-signed charged leptons in MINOS and KamLAND to put bounds on the flavour structure of this coefficient, comparing the constraints from microscopic  $|\Delta L| = 2$  processes such as neutrinoless double beta decay ( $0\nu\beta\beta$ ) decay and  $\mu^- - e^+$  conversion in nuclei.

In Chapter 4 we instead examined the effect of neutral-current neutrino NSIs on the long-range force mediated by a pair of neutrinos. We re-derived the potential between charged leptons and quarks (within nucleons) induced by the exchange of three massive Dirac or Majorana neutrinos with SM charged- and neutral-current interactions. We next studied the dependence of the potential on the separation and spins of the interacting particles when one (or both) of the interactions is a right-handed vector, scalar or tensor interaction. We also introduced a neutrino magnetic and electric dipole moment and derived a corresponding potential with the exchange of a photon between the neutrinos and an interacting fermion. With these potentials, we set out how to derive shifts to the energy levels of atomic and nuclear systems using perturbation theory. We then used the observed and predicted  $1S - 2S$  and hyperfine splittings in systems such as positronium ( $e^-e^+$ ), muonium ( $e^-\mu^+$ ) and hydrogen ( $e^-p$ ) to derive constraints on the NSI coefficients.

Finally, in Chapter 5 we returned to the *inverse seesaw* (ISS) mechanism first outlined in Chapter 2. To study the phenomenology of this extension, we made use of a single-generation model with one active and two sterile neutrinos. We showed how the two sterile states can behave like a pair of Majorana fermions or a single pseudo-Dirac limit depending on the parameters of the model. If the absolute mass scale  $m_\nu$  of the light neutrino is known, and an experiment observes

two sterile states with a splitting  $\Delta m_N$  and mixing strengths  $|V_{eN_1}|^2$  and  $|V_{eN_2}|^2$ , the sterile-sterile mixing and CP phases (and thus the Majorana versus pseudo-Dirac limit) are uniquely determined. We reviewed the constraints on the  $(m_N, |V_{eN}|^2)$  parameter space from a variety of direct search experiments. We compared these to the constraints from  $0\nu\beta\beta$  decay; as a  $|\Delta L| = 2$  probe, these constraints heavily depend on the splitting  $\Delta m_N$  between the sterile states. In this chapter was also derived constraints on the  $(m_N, |V_{eN}|^2)$  parameter space from measurements of the  $2\nu\beta\beta$  decay spectrum in  $0\nu\beta\beta$  decay search experiments. Using the frequentist limit setting approach of Appendix C, we took the non-observation of deviations from the SM differential  $2\nu\beta\beta$  decay rate (in the total electron kinetic energy  $E_K$ ) at experiments to set limits at 90% CL. We also introduced right-handed vector charged-current interactions for the sterile neutrinos. We used both the differential  $2\nu\beta\beta$  decay rate in  $E_K$  and the enclosed angle between the outgoing electrons  $\cos \theta$  to set bounds on the  $(m_N, |\epsilon_{RX}|^2)$  parameter space.

In the near future, the properties of the light neutrinos will be probed to greater precision by astrophysical and cosmological observations, neutrino oscillations, beta decays, and  $0\nu\beta\beta$  decay searches. For example, the Dirac CP phase  $\delta_{\text{CP}}$  and normal or inverted neutrino ordering may become clear at the next-generation oscillation experiments DUNE and Hyper-Kamiokande. Upper limits on the absolute neutrino mass scale will be pushed down to the sub-eV scale by the beta decay experiments KATRIN and Project 8 and cosmological surveys. Entering this precision era, the neutrino sector also provides a complementary window to NP. The mechanism generating the light neutrino masses is still unknown and the related NP may be accessible at future experiments. As reviewed in this thesis, there are a plethora of possible mass-generation models predicting different experimental signatures. Depending on the scale of the NP, signatures can explicitly or implicitly imply the presence of new particles or interactions (e.g. a sub-TeV pseudo-Dirac neutrino or a right-handed current). For heavy NP, it is important to have a systematic framework for parametrising the effective interactions induced in the neutrino sector. In the SM and low energy effective field theories, one can consider the effective operators

generated by a particular model, or alternatively remain model-agnostic and study a certain operator or class of operators. To constrain the coefficients of such operators, it is beneficial to use all the available experimental data, i.e. remain impartial about where the NP can appear. In this thesis, we have seen how the results from a variety of experiments (neutrino oscillation, atomic spectroscopy,  $0\nu\beta\beta$  and  $2\nu\beta\beta$  decay experiments) can be interpreted to constrain non-standard neutrino interactions as well as a specific model, the ISS mechanism. As the precision of these and other experiments improves in the future it will become possible to explore and constrain more of the landscape of physics beyond the SM.

## Appendix A

# Neutrino NSI Parametrisation

As mentioned in Chapter 2, in the low-energy effective field theory (LEFT) the standard parametrisation of charged- and neutral-current type neutrino NSIs in Ref. [289] is

$$\mathcal{L}_{\text{CC}}^{(\bar{6})} = -\frac{G_F}{\sqrt{2}} \epsilon (\bar{v} \Gamma \ell) (\bar{d} \Gamma' u) + \text{h.c.}, \quad (\text{A.1})$$

$$\mathcal{L}_{\text{NC}}^{(\bar{6})} = -\frac{G_F}{\sqrt{2}} \epsilon' (\bar{v} \Gamma v) (\bar{\psi} \Gamma' \psi), \quad (\text{A.2})$$

where  $\psi = \{\ell, u, d\}$  and  $\Gamma$  and  $\Gamma'$  run over the ten combinations of Dirac matrices in Table 2.6. The coefficients  $\epsilon$  and  $\epsilon'$  have the associated subscripts  $L, R, S, P$  or  $T$  and a tilde if the leptonic current is right-handed.

In Chapter 3 we consider the charged-current type operators in the context of long-baseline neutrino oscillations. Our parametrisation for these operators is given in Eq. (3.26). The relations between the coefficients  $\epsilon_{XY}^\circ$  with  $X, Y \in \{L, R\}$  and  $\circ \in \{S, V, T\}$  and the  $\overset{(\sim)}{\epsilon}$  coefficients are

$$\begin{aligned} \epsilon_{LL}^V &= \epsilon_L, & \epsilon_{LR}^V &= \epsilon_R, \\ \epsilon_{RL}^V &= \tilde{\epsilon}_L, & \epsilon_{RR}^V &= \tilde{\epsilon}_R, \\ \epsilon_{LL}^S &= \epsilon_S + \epsilon_P, & \epsilon_{LR}^S &= \epsilon_S - \epsilon_P, \\ \epsilon_{RL}^S &= \tilde{\epsilon}'_S + \tilde{\epsilon}_P, & \epsilon_{RR}^S &= \tilde{\epsilon}_S - \tilde{\epsilon}_P, \\ \epsilon_{LL}^T &= \epsilon'_T, & \epsilon_{RR}^T &= \tilde{\epsilon}_T, \end{aligned} \quad (\text{A.3})$$

where flavour indices have been omitted.

In Chapter 4 we consider the neutral-current type operators in the context of neutrino-mediated potentials. Our parametrisation for these operators is given in Eq. (4.11). The relations between the coefficients  $c_{XY}$ ,  $g_{XY}$  and  $h_{XX}$  with  $X, Y \in \{L, R\}$  and the  $\tilde{\epsilon}'$  coefficients are

$$\begin{aligned} c_{LL} &= \epsilon'_L, & c_{LR} &= \epsilon'_R, \\ c_{RL} &= \tilde{\epsilon}'_L, & c_{RR} &= \tilde{\epsilon}'_R, \\ g_{LL} &= \epsilon'_S + \epsilon'_P, & g_{LR} &= \epsilon'_S - \epsilon'_P, \\ g_{RL} &= \tilde{\epsilon}'_S + \tilde{\epsilon}'_P, & g_{RR} &= \tilde{\epsilon}'_S - \tilde{\epsilon}'_P, \\ h_{LL} &= \epsilon'_T, & h_{RR} &= \tilde{\epsilon}'_T, \end{aligned} \tag{A.4}$$

where flavour indices have again been omitted. Now including flavour indices, the following relations apply for the neutral-current coefficients

$$\begin{aligned} (c_{LL})_{\rho\sigma;\alpha\beta} &= (c_{LL})_{\sigma\rho;\alpha\beta}^*, & (c_{LR})_{\rho\sigma;\alpha\beta} &= (c_{LR})_{\sigma\rho;\alpha\beta}^*, \\ (c_{RL})_{\rho\sigma;\alpha\beta} &= (c_{RL})_{\sigma\rho;\alpha\beta}^*, & (c_{RR})_{\rho\sigma;\alpha\beta} &= (c_{RR})_{\sigma\rho;\alpha\beta}^*, \\ (g_{LL})_{\rho\sigma;\alpha\beta} &= (g_{RR})_{\sigma\rho;\alpha\beta}^*, & (g_{LR})_{\rho\sigma;\alpha\beta} &= (g_{RL})_{\sigma\rho;\alpha\beta}^*, \\ (h_{LL})_{\rho\sigma;\alpha\beta} &= (h_{RR})_{\sigma\rho;\alpha\beta}^*, \end{aligned} \tag{A.5}$$

where  $\rho, \sigma$  are the neutrino flavours and  $\alpha, \beta$  are the flavours of  $\psi$ . If the neutrinos are Majorana fermions, additional relations apply to the neutral-current coefficients

$$\begin{aligned} (c_{LL})_{\rho\sigma;\alpha\beta} &= -(c_{RL})_{\sigma\rho;\alpha\beta}, & (c_{LR})_{\rho\sigma;\alpha\beta} &= -(c_{RR})_{\sigma\rho;\alpha\beta}, \\ (g_{LL})_{\rho\sigma;\alpha\beta} &= (g_{LL})_{\sigma\rho;\alpha\beta}, & (g_{LR})_{\rho\sigma;\alpha\beta} &= (g_{LR})_{\sigma\rho;\alpha\beta}, \\ (g_{RL})_{\rho\sigma;\alpha\beta} &= (g_{RL})_{\sigma\rho;\alpha\beta}, & (g_{RR})_{\rho\sigma;\alpha\beta} &= (g_{RR})_{\sigma\rho;\alpha\beta}, \\ (h_{LL})_{\rho\sigma;\alpha\beta} &= -(h_{LL})_{\sigma\rho;\alpha\beta}, & (h_{RR})_{\rho\sigma;\alpha\beta} &= -(h_{RR})_{\sigma\rho;\alpha\beta}. \end{aligned} \tag{A.6}$$

## Appendix B

# Additional Formulae for Long-Range Potentials

In this appendix we will summarise some of the key formulae for the derivation of neutrino-mediated long-range potentials in Chapter 4.

## B.1 Spinor Identities and Non-Relativistic Limits

A crucial step to take in deriving the spectral functions or absorptive parts  $\rho_{\alpha\beta}$  of the invariant scattering amplitudes  $\mathcal{A}_{\alpha\beta}$  is taking the non-relativistic limit of the external interacting fermion bilinears. This can be done by expanding the bilinears to first order in both the 3-momentum transfer  $\mathbf{q} = \mathbf{p}_\alpha - \mathbf{p}'_\alpha = \mathbf{p}'_\beta - \mathbf{p}_\beta$  and the sum of three-momenta  $\mathbf{P} = \mathbf{p}_\alpha + \mathbf{p}_\beta = \mathbf{p}'_\alpha + \mathbf{p}'_\beta$ ,

$$\begin{aligned} [\Gamma^a]_\alpha &\equiv [\bar{u}_{s'_\alpha}(\mathbf{p}'_\alpha) \Gamma^a u_{s_\alpha}(\mathbf{p}_\alpha)] \\ &\approx \xi_{s'_\alpha}^\dagger \left( 2m_{\psi_\alpha} \Gamma^a - \frac{P_j}{2} \{ \Gamma^a, \gamma_j \} - \frac{q_j}{2} [\Gamma^a, \gamma_j] \right) \xi_{s_\alpha}, \end{aligned} \quad (\text{B.1})$$

where  $\Gamma^a \in \{\mathbb{I}, \gamma_5, \gamma_\mu, \gamma_\mu \gamma_5, \sigma_{\mu\nu}\}$  is one of the 16 irreducible products of  $\gamma$  matrices and  $u_{s_\alpha}(\mathbf{p}_\alpha)$  and  $\xi_{s_\alpha}$  are respectively the four-component Dirac spinor and two-component Weyl spinor for a fermion  $\psi_\alpha$  with mass  $m_{\psi_\alpha}$ , three-momentum  $\mathbf{p}_\alpha$  and spin  $s_\alpha$ .

This expansion must be made for the external fermion bilinear at each of the interaction vertices. Hence the bilinears only appear as the products  $[\Gamma^a]_\alpha [\Gamma^b]_\beta$ .

We retain the higher orders terms in  $\mathbf{P}$  and  $\mathbf{q}$  arising from this product for comparison with the basis of 16 operators in Ref. [447], a complete set of scalar operators constructed from two spins and two momenta. These are

$$O_1 = 1, \quad (\text{B.2})$$

$$O_2 = \boldsymbol{\sigma}_\alpha \cdot \boldsymbol{\sigma}_\beta, \quad (\text{B.3})$$

$$O_3 = (\boldsymbol{\sigma}_\alpha \cdot \mathbf{q})(\boldsymbol{\sigma}_\beta \cdot \mathbf{q}), \quad (\text{B.4})$$

$$O_{4,5} = \frac{i}{2}(\boldsymbol{\sigma}_\alpha \pm \boldsymbol{\sigma}_\beta)(\mathbf{P} \times \mathbf{q}), \quad (\text{B.5})$$

$$O_{6,7} = \frac{i}{2}[(\boldsymbol{\sigma}_\alpha \cdot \mathbf{P})(\boldsymbol{\sigma}_\beta \cdot \mathbf{q}) \pm (\alpha, \beta)], \quad (\text{B.6})$$

$$O_8 = (\boldsymbol{\sigma}_\alpha \cdot \mathbf{P})(\boldsymbol{\sigma}_\beta \cdot \mathbf{P}), \quad (\text{B.7})$$

$$O_{9,10} = \frac{i}{2}(\boldsymbol{\sigma}_\alpha \pm \boldsymbol{\sigma}_\beta) \cdot \mathbf{q}, \quad (\text{B.8})$$

$$O_{11} = i(\boldsymbol{\sigma}_\alpha \times \boldsymbol{\sigma}_\beta) \cdot \mathbf{q}, \quad (\text{B.9})$$

$$O_{12,13} = \frac{1}{2}(\boldsymbol{\sigma}_\alpha \pm \boldsymbol{\sigma}_\beta) \cdot \mathbf{P}, \quad (\text{B.10})$$

$$O_{14} = (\boldsymbol{\sigma}_\alpha \times \boldsymbol{\sigma}_\beta) \cdot \mathbf{P}, \quad (\text{B.11})$$

$$O_{15} = \frac{1}{2}[(\boldsymbol{\sigma}_\alpha \cdot (\mathbf{P} \times \mathbf{q}))(\boldsymbol{\sigma}_\beta \cdot \mathbf{q}) + (\alpha, \beta)], \quad (\text{B.12})$$

$$O_{16} = \frac{i}{2}[(\boldsymbol{\sigma}_\alpha \cdot (\mathbf{P} \times \mathbf{q}))(\boldsymbol{\sigma}_\beta \cdot \mathbf{P}) + (\alpha, \beta)], \quad (\text{B.13})$$

where  $(\alpha, \beta)$  is shorthand for  $(\alpha \leftrightarrow \beta)$ .

The products of scalar-like fermion bilinears are

$$\begin{aligned} [\mathbb{I}]_\alpha [\mathbb{I}]_\beta &\approx 4m_\alpha m_\beta, \\ [\gamma_5]_\alpha [\gamma_5]_\beta &\approx (\boldsymbol{\sigma}_\alpha \cdot \mathbf{q})(\boldsymbol{\sigma}_\beta \cdot \mathbf{q}), \\ [\mathbb{I}]_\alpha [\gamma_5]_\beta &\approx -2m_\alpha (\boldsymbol{\sigma}_\beta \cdot \mathbf{q}), \end{aligned} \quad (\text{B.14})$$

which are proportional to the  $O_1$ ,  $O_3$  and  $O_9 \pm O_{10}$  operators in Ref. [447] respectively. Throughout this work however we consider a SM weak vector interaction at one vertex and an arbitrary scalar, vector or tensor-like interaction at the other. These fermion bilinears are therefore not used in this work, but are relevant for axion-mediated long-range potentials [424, 429, 701].

The products of vector-like fermion bilinears are

$$\begin{aligned}
[\gamma_\mu]_\alpha [\gamma^\mu]_\beta &\approx (4m_\alpha m_\beta - \mathbf{P}^2) + (\boldsymbol{\sigma}_\alpha \cdot \boldsymbol{\sigma}_\beta) \mathbf{q}^2 - (\boldsymbol{\sigma}_\alpha \cdot \mathbf{q})(\boldsymbol{\sigma}_\beta \cdot \mathbf{q}), \\
&\quad - i(\boldsymbol{\sigma}_\alpha + \boldsymbol{\sigma}_\beta) \cdot (\mathbf{P} \times \mathbf{q}), \\
[\gamma_\mu]_\alpha [\gamma^\mu \gamma_5]_\beta &\approx 2im_\beta (\boldsymbol{\sigma}_\alpha \times \boldsymbol{\sigma}_\beta) \cdot \mathbf{q} - 2(m_\alpha - m_\beta)(\boldsymbol{\sigma}_\beta \cdot \mathbf{P}), \\
[\gamma_\mu \gamma_5]_\alpha [\gamma^\mu \gamma_5]_\beta &\approx -(4m_\alpha m_\beta - \mathbf{P}^2)(\boldsymbol{\sigma}_\alpha \cdot \boldsymbol{\sigma}_\beta), \\
[\not{q} \gamma_5]_\alpha [\not{q} \gamma_5]_\beta &\approx 4m_\alpha m_\beta (\boldsymbol{\sigma}_\alpha \cdot \mathbf{q})(\boldsymbol{\sigma}_\beta \cdot \mathbf{q}).
\end{aligned} \tag{B.15}$$

The first of these products contains terms proportional to  $O_1$ ,  $O_2$ ,  $O_3$  and  $O_4$ , the second to  $O_{11}$  and  $O_{12} \pm O_{13}$ , the third to  $O_2$  and finally the fourth to  $O_3$ . These products are relevant in the case of a vector-like current at both interaction vertices. We have not included products containing the bilinear  $[\not{q}]_\alpha$  which vanishes according to the equations of motion.

The relevant products of scalar-like and vector-like (which must be contracted with the momentum exchange  $q^\mu$ ) fermion bilinears are

$$\begin{aligned}
[\not{q}]_\alpha [\not{q} \gamma_5]_\beta &\approx 4m_\alpha m_\beta (\boldsymbol{\sigma}_\beta \cdot \mathbf{q}), \\
[\gamma_5]_\alpha [\not{q} \gamma_5]_\beta &\approx -2m_\beta (\boldsymbol{\sigma}_\alpha \cdot \mathbf{q})(\boldsymbol{\sigma}_\beta \cdot \mathbf{q}),
\end{aligned} \tag{B.16}$$

proportional to  $O_2$  and  $O_3$  respectively. These are used for the case of a scalar interaction at one vertex and a charged or neutral-current interaction at the other.

Finally, we list the relevant products of vector-like and tensor-like (where again the free Lorentz index must be contracted with the momentum exchange  $q^\mu$ ) fermion bilinears,

$$\begin{aligned}
[\gamma_\mu]_\alpha [\sigma^{\mu\nu} q_\nu]_\beta &\approx 2im_\alpha \mathbf{q}^2 - 2im_\beta [(\boldsymbol{\sigma}_\alpha \cdot \boldsymbol{\sigma}_\beta) \mathbf{q}^2 - (\boldsymbol{\sigma}_\alpha \cdot \mathbf{q})(\boldsymbol{\sigma}_\beta \cdot \mathbf{q})] \\
&\quad + 2(m_\alpha - m_\beta)[\boldsymbol{\sigma}_\beta \cdot (\mathbf{P} \times \mathbf{q})], \\
[\gamma_\mu]_\alpha [\sigma^{\mu\nu} q_\nu \gamma_5]_\beta &\approx i(4m_\alpha m_\beta - \mathbf{P}^2)(\boldsymbol{\sigma}_\beta \cdot \mathbf{q}) + [\boldsymbol{\sigma}_\alpha \cdot (\mathbf{P} \times \mathbf{q})](\boldsymbol{\sigma}_\beta \cdot \mathbf{q}), \\
[\gamma_\mu \gamma_5]_\alpha [\sigma^{\mu\nu} q_\nu]_\beta &\approx -4m_\alpha m_\beta (\boldsymbol{\sigma}_\alpha \times \boldsymbol{\sigma}_\beta) \cdot \mathbf{q} - (\boldsymbol{\sigma}_\alpha \cdot \mathbf{P})[i\mathbf{q}^2 + \boldsymbol{\sigma}_\beta \cdot (\mathbf{P} \times \mathbf{q})], \\
[\gamma_\mu \gamma_5]_\alpha [\sigma^{\mu\nu} q_\nu \gamma_5]_\beta &\approx 2i(m_\alpha - m_\beta)(\boldsymbol{\sigma}_\alpha \cdot \mathbf{P})(\boldsymbol{\sigma}_\beta \cdot \mathbf{q}) - 2im_\alpha (\boldsymbol{\sigma}_\alpha \cdot \boldsymbol{\sigma}_\beta)(\mathbf{P} \cdot \mathbf{q}).
\end{aligned} \tag{B.17}$$

$X$	D	M	V	$\Delta$	S	T
$J_{ij}^X(r)$	$\frac{3}{2}$	$\frac{3}{2}$	$\frac{5}{2}$	3	3	3

**Table B.1:** Exact values of the dimensionless integrals  $J_{ij}^X(r)$  for  $N = \{\text{D, M, V, } \Delta, \text{S, T}\}$  derived from the potentials  $I_{ij}^X(r) \approx 1$  in the limit of vanishing neutrino masses,  $m_i \approx 0$ . These appear in the potentials  $V_{\alpha\beta}^{LL}$ ,  $V_{\alpha\beta}^{LR}$ ,  $V_{\alpha\beta}^{RR}$ ,  $V_{\alpha\beta}^{VS}$  and  $V_{\alpha\beta}^{VT}$  in this work.

The first product contains terms proportional to  $O_1, O_2, O_3$  and  $O_4 \pm O_5$ , the second to  $O_9 \pm O_{10}$  and  $O_{15}$ , the third to  $O_{11}, O_{12} \pm O_{13}$  and  $O_{16}$  and finally the fourth to  $O_6 \pm O_7$  and  $O_2$ . These are needed when evaluating the potential for a tensor interaction at one vertex and a charged- or neutral-current interaction at the other.

## B.2 Integrals for Long-Range Potentials

The generic form for the dimensionless integrals appearing in Chapter 4 (functions of the distance  $r$  between the interacting fermions and labelled by the superscript  $X$ ) is

$$I_{ij}^X(r) = \int_{(m_i+m_j)r}^{\infty} dy \Lambda^{1/2}(y^2, m_i^2 r^2, m_j^2 r^2) G_{ij}^X(y, r) e^{-y}, \quad (\text{B.18})$$

where the dimensionless variable  $y = r\sqrt{t}$ , the indices  $i, j$  run over either the three massive Dirac states or  $N = 3 + n_S$  massive Majorana states, and  $\Lambda(x, y, z) = x^2 + y^2 + z^2 - 2xy - 2yz - 2zx$  is the Källén function. The functions  $G_{ij}^X(y, r)$  for the integrals appearing in the SM neutrino-mediated potential are given by

$$\begin{aligned} G_{ij}^{\text{D}}(y, r) &= \frac{y}{6} \left\{ 1 - \frac{\overline{m_{ij}^2} r^2}{y^2} - \frac{(\Delta m_{ij}^2)^2 r^4}{2y^4} \right\}, \\ G_{ij}^{\text{M}}(y, r) &= \frac{y}{6} \left\{ 1 - \frac{(\overline{m_{ij}^2} + 3m_i m_j)r^2}{y^2} - \frac{(\Delta m_{ij}^2)^2 r^4}{2y^4} \right\}, \\ G_{ij}^V(y, r) &= \frac{1}{y} \left\{ 1 + \frac{2\overline{m_{ij}^2} r^2}{y^2} - \frac{2(\Delta m_{ij}^2)^2 r^4}{y^4} \right\}, \end{aligned} \quad (\text{B.19})$$

where  $\overline{m_{ij}^2} = \frac{1}{2}(m_i^2 + m_j^2)$  and  $\Delta m_{ij}^2 = m_i^2 - m_j^2$ .

The functions  $G_{ij}^X(y, r)$  needed for the non-standard potentials are

$$\begin{aligned}
 G_{ij}^{LR}(y, r) &= \frac{1}{y}, \\
 G_{ij}^{\Delta}(y, r) &= \frac{1}{y} \left\{ 1 - \frac{\Delta m_{ij}^2 r^2}{y^2} \right\}, \\
 G_{ij}^S(y, r) &= \frac{1}{y} \left\{ 1 - \frac{(m_i - m_j)^2 r^2}{y^2} \right\}, \\
 G_{ij}^{SD}(y, r) &= \frac{y}{6} \left\{ 1 - \frac{2\overline{m_{ij}^2} r^2}{y^2} \right\}, \\
 G_{ij}^{SM}(y, r) &= \frac{y}{6} \left\{ 1 - \frac{(m_i - m_j)^2 r^2}{y^2} \right\}, \\
 G_{ij}^T(y, r) &= \frac{1}{y} \left\{ 1 - \frac{(m_i + m_j)^2 r^2}{y^2} \right\}, \\
 G_{ij}^{M\gamma}(y, r) &= \frac{1}{y} \left\{ 1 - \frac{(m_i - m_j)^2 r^2}{y^2} \right\} \left\{ 1 + \frac{2(m_i + m_j)^2 r^2}{y^2} \right\}, \\
 G_{ij}^{E\gamma}(y, r) &= \frac{1}{y} \left\{ 1 - \frac{(m_i + m_j)^2 r^2}{y^2} \right\} \left\{ 1 + \frac{2(m_i - m_j)^2 r^2}{y^2} \right\}, \tag{B.20}
 \end{aligned}$$

A second set of dimensionless integrals  $J_{ij}^X(r)$  appear in some of the potentials.

These are derived from the first set by performing the operations

$$\begin{aligned}
 J_{ij}^{D(M)}(r) &= I_{ij}^{D(M)}(r) + \left( \frac{1}{2} - \frac{r}{6} \frac{d}{dr} \right) I_{ij}^V(r), \\
 J_{ij}^V(r) &= \left( \frac{5}{2} - \frac{7r}{6} \frac{d}{dr} + \frac{r^2}{6} \frac{d^2}{dr^2} \right) I_{ij}^V(r), \\
 J_{ij}^{\Delta, S, T}(r) &= \left( 3 - r \frac{d}{dr} \right) I_{ij}^{\Delta, S, T}(r). \tag{B.21}
 \end{aligned}$$

The first set of integrals are normalised such that  $I_{ij}^X(r) \approx 1$  for vanishing neutrino masses  $m_i \approx 0$ . The values of the second set  $J_{ij}^X(r)$  in this limit are given in Table B.1. The functions tend to these constant values in the short-range limit of the potentials in which they appear.

## Appendix C

# Statistical Method

This appendix will review the frequentist limit setting approach used in Chapter 5 to derive constraints on the sterile neutrino mass and mixing from  $2\nu\beta\beta$  decay. We assume that an experiment measuring a differential rate  $\frac{d\Gamma}{dX}$  will count a number of events  $N_{\text{events}}$  distributed over a number of bins  $N_{\text{bins}}$  in the observable  $X$ . In  $2\nu\beta\beta$  decay, for example,  $X$  could be the total kinetic energy  $E_K$  of the outgoing electrons or the enclosed angle  $\cos\theta$  between their momenta. The relevant differential rates are therefore  $\frac{d\Gamma^{2\nu}}{dE_K}$  and  $\frac{d\Gamma^{2\nu}}{d\cos\theta}$ . The expected fraction of events  $\Delta N_{\text{exp}}^{(i)}$  per bin will be the integral of  $\frac{d\Gamma}{dX}$  over the width of the bin  $X_i$  to  $X_{i+1}$ ,

$$\Delta N_{\text{exp}}^{(i)} = \frac{1}{\mathcal{N}} \int_{X_i}^{X_{i+1}} dX \frac{d\Gamma}{dX}; \quad \mathcal{N} = \int_{X_{\min}}^{X_{\max}} dX \frac{d\Gamma}{dX}, \quad (\text{C.1})$$

where the normalisation factor  $\mathcal{N}$  is the total area enclosed by  $\frac{d\Gamma}{dX}$  between limits  $X_{\min}$  and  $X_{\max}$ . In the presence of NP, for example the emission of a sterile neutrino  $N$  in  $2\nu\beta\beta$  decay, we assume that the differential rate can be split into contributions from the SM and NP as

$$\frac{d\Gamma}{dX} \approx \frac{d\Gamma_{\text{SM}}}{dX} + \mu \frac{d\Gamma_{\text{NP}}}{dX}(\zeta), \quad (\text{C.2})$$

where  $\mu$  is a parameter controlling the magnitude of the NP contribution and  $\zeta$  is a set of parameters characterising the shape of the NP distribution.

For example, the differential rate  $\frac{d\Gamma^{2\nu}}{dE_K}$  in Eq. (5.79) can be written as a sum of SM and sterile neutrino (produced by the active-sterile mixing  $|V_{eN}|^2$ ) contributions.

Expanding Eq. (5.79) gives

$$\frac{d\Gamma^{2\nu}}{dE_K} \approx \frac{d\Gamma_{\text{SM}}^{2\nu}}{dE_K} + |V_{eN}|^2 \left( \frac{d\Gamma_N^{2\nu}}{dE_K} - 2 \frac{d\Gamma_{\text{SM}}^{2\nu}}{dE_K} \right), \quad (\text{C.3})$$

neglecting terms proportional to  $|V_{eN}|^4$ . The first and second terms correspond to  $\frac{d\Gamma_{\text{SM}}}{dX}$  and  $\frac{d\Gamma_{\text{NP}}}{dX}$  in Eq. (C.2) and we identify  $\mu = |V_{eN}|^2$ . The mass  $m_N$  of the sterile neutrino changes the shape of the distribution  $\frac{d\Gamma_N^{2\nu}}{dE_K}$  and so it is included in  $\boldsymbol{\zeta}$ . The  $\Gamma^{2\nu}$  and  $K^{2\nu}$  factors in the angular differential rate  $\frac{d\Gamma^{2\nu}}{d\cos\theta}$  of Eq. (5.77) can also be split into contributions from the SM and sterile neutrino emission, where now  $\mu = |\varepsilon_{RX}|^2$ . The SM differential rate constitutes the *background*, while the NP correction is the postulated *signal*. The parameter  $\mu$  is often referred to as the *signal strength*.

We now split up the expected number of events in each bin as

$$N_{\text{exp}}^{(i)}(\boldsymbol{\xi}) = N_{\text{events}} \cdot \Delta N_{\text{exp}}^{(i)}(\boldsymbol{\xi}) = N_{\text{sig}}^{(i)}(\boldsymbol{\xi}) + N_{\text{bkg}}^{(i)}, \quad (\text{C.4})$$

where the expected number of signal and background events per bin are

$$N_{\text{sig}}^{(i)}(\boldsymbol{\xi}) = \mu \frac{N_{\text{events}}}{\mathcal{N}} \int_{X_i}^{X_{i+1}} dX \frac{d\Gamma_{\text{NP}}}{dX}(\boldsymbol{\xi}), \quad (\text{C.5})$$

$$N_{\text{bkg}}^{(i)} = \frac{N_{\text{events}}}{\mathcal{N}} \int_{X_i}^{X_{i+1}} dX \frac{d\Gamma_{\text{SM}}}{dX}. \quad (\text{C.6})$$

and  $\boldsymbol{\xi} \equiv (\boldsymbol{\zeta}, \mu)$ . The probability of an experiment observing  $N_{\text{obs}}^{(i)}$  events per bin given  $N_{\text{exp}}^{(i)}$  expected events per bin is given by the Poisson probability  $P(N_{\text{obs}}^{(i)} | N_{\text{exp}}^{(i)})$ . The *likelihood* of the data  $D$  given the NP hypothesis,  $\mathcal{L}(D|\boldsymbol{\xi})$ , is defined as the product of the Poisson probabilities over all bins. It is convenient to use the log-likelihood

$$\begin{aligned} -2 \log \mathcal{L}(D|\boldsymbol{\xi}) &= 2 \sum_i^{N_{\text{bins}}} \left\{ N_{\text{exp}}^{(i)}(\boldsymbol{\xi}) - N_{\text{obs}}^{(i)} + N_{\text{obs}}^{(i)} \log \left( \frac{N_{\text{obs}}^{(i)}}{N_{\text{exp}}^{(i)}(\boldsymbol{\xi})} \right) \right\} \\ &\approx \sum_i^{N_{\text{bins}}} \frac{\left( N_{\text{obs}}^{(i)} - N_{\text{exp}}^{(i)}(\boldsymbol{\xi}) \right)^2}{N_{\text{exp}}^{(i)}(\boldsymbol{\xi})}, \end{aligned} \quad (\text{C.7})$$

where the second equality holds via Wilks' theorem if there are a large number of events per bin [702]. From this we can construct the *test-statistic*

$$q_{\xi} = -2 \left( \log \mathcal{L}(D|\xi) - \log \mathcal{L}(D|\hat{\xi}) \right), \quad (C.8)$$

where  $\hat{\xi}$  are the values of the NP parameters and  $\mu$  that minimise the log-likelihood function. The quantity  $q_{\xi}$  is expected to follow a  $\chi^2$  distribution with one degree of freedom.

We assume that the experiments do not observe rates deviating significantly from the SM prediction. We therefore set the number of observed events in Eq. (C.7) to  $N_{\text{obs}}^{(i)} = N_{\text{exp}}^{(i)}(\xi)$  with  $\xi = (\zeta, 0)$ . In reality, however, experiments can be repeated many times and record a different value of  $N_{\text{obs}}^{(i)}$  each iteration. This fluctuation can be imitated by running a series of toy Monte Carlo (MC) simulations of the experiment. For every toy MC there is a value of  $q_{\xi}$ , with the mean of these values being the relevant test-statistic. A representative data set is commonly used as a good approximation of the MC method in the large sample limit [703]. This is the so-called Asimov data set  $D_A$  for which the observed number of events per bin  $N_{\text{obs}}^{(i)}$  equals the number of background events  $N_{\text{bkg}}^{(i)}$  [704]. The  $\hat{\xi}$  that minimises the log-likelihood to  $-2 \log \mathcal{L}(D_A|\hat{\xi}) = 0$  is then simply  $\hat{\xi} = (\zeta, 0)$  which matches our initial approach.

The magnitude of the test-statistic  $q_{\xi} = -2 \log \mathcal{L}(D_A|\xi)$  translates to a degree of compatibility between the Asimov data set  $D_A$  and the NP hypothesis with parameters  $\xi = (\zeta, \mu)$ . If  $\zeta$  contains a single parameter, combinations of this parameter and  $\mu$  giving  $q_{\xi} \gtrsim 4.61$  are excluded at 90% confidence level (CL). For  $2\nu\beta\beta$  decay with sterile neutrinos, we will be interested  $\xi = (m_N, |V_{eN}|^2)$  and  $\xi = (m_N, |\varepsilon_{RX}|^2)$  parameter spaces. Rather than performing two-dimensional scans of these parameters, we instead fix  $m_N$  for values over the range  $\sim 0.1 - 3$  MeV and find the value of  $|V_{eN}|^2$  or  $|\varepsilon_{RX}|^2$  for which  $q_{\xi} = 2.71$ , corresponding to the 90% CL upper limit on the mixing/right-handed coefficient.

We finally note that we have not yet included the impact of systematic uncertainties. Systematic errors altering the total number of observed events without

leading to distortions in the spectrum can be accounted for by introducing the *nuisance parameter*  $\eta$

$$-2\log \mathcal{L}(D|\xi, \eta) \approx \sum_i^{N_{\text{bins}}} \frac{\left(N_{\text{bkg}}^{(i)} - (1 + \eta)N_{\text{exp}}^{(i)}(\xi)\right)^2}{(\sigma_{\text{stat}}^{(i)})^2 + (\sigma_{\text{sys}}^{(i)})^2} + \left(\frac{\eta}{\sigma_\eta}\right)^2, \quad (\text{C.9})$$

where  $\sigma_\eta$  is a small associated uncertainty. The remaining systematic uncertainties are included in the quantity  $\sigma_{\text{sys}}^{(i)} = \sigma_f N_{\text{exp}}^{(i)}$  which adds in quadrature with the statistical uncertainty  $(\sigma_{\text{stat}}^{(i)})^2 = N_{\text{exp}}^{(i)}$  in the denominator of Eq. (C.9). The test-statistic becomes

$$q_\xi = -2 \left( \log \mathcal{L}(D|\xi, \hat{\eta}) - \log \mathcal{L}(D|\hat{\xi}, \hat{\eta}) \right), \quad (\text{C.10})$$

where  $\hat{\eta}$  minimises the log-likelihood for a given  $\xi$  while  $\hat{\xi}$  and  $\hat{\eta}$  are the values at the global minimum of the log-likelihood. For the Asimov data set the parameters at the global minimum are  $\hat{\xi} = (m_N, 0)$  and  $\hat{\eta} = 0$  such that  $-2\log \mathcal{L}(D_A|\hat{\xi}, \hat{\eta}) = 0$ .

The test-statistic now reduces to

$$q_\xi = \min_\eta \left[ \sum_i^{N_{\text{bins}}} \frac{\left(N_{\text{bkg}}^{(i)} - (1 + \eta)N_{\text{exp}}^{(i)}(\xi)\right)^2}{(\sigma_{\text{stat}}^{(i)})^2 + (\sigma_{\text{sys}}^{(i)})^2} + \left(\frac{\eta}{\sigma_\eta}\right)^2 \right], \quad (\text{C.11})$$

which will be used to derive constraints from  $2\nu\beta\beta$  decay in Chapter 5.

# Bibliography

- [1] W. Pauli. Dear radioactive ladies and gentlemen. *Phys. Today*, 31N9:27, 1978.
- [2] E. Fermi. An attempt of a theory of beta radiation. 1. *Z. Phys.*, 88:161–177, 1934.
- [3] H. Bethe and R. Peierls. The 'neutrino'. *Nature*, 133:532, 1934.
- [4] M. Goeppert-Mayer. Double beta-disintegration. *Phys. Rev.*, 48:512–516, 1935.
- [5] G. Gamow and E. Teller. Selection rules for the beta-disintegration. *Phys. Rev.*, 49:895–899, 1936.
- [6] Ettore Majorana. Teoria simmetrica dell'elettrone e del positrone. *Nuovo Cim.*, 14:171–184, 1937.
- [7] W.H. Furry. On transition probabilities in double beta-disintegration. *Phys. Rev.*, 56:1184–1193, 1939.
- [8] J. C. Street and E. C. Stevenson. New Evidence for the Existence of a Particle of Mass Intermediate Between the Proton and Electron. *Phys. Rev.*, 52:1003–1004, 1937.
- [9] S. H. Neddermeyer and C. D. Anderson. Note on the Nature of Cosmic Ray Particles. *Phys. Rev.*, 51:884–886, 1937.
- [10] F. Reines and C. L. Cowan. A Proposed experiment to detect the free neutrino. *Phys. Rev.*, 90:492–493, 1953.

- [11] C. L. Cowan, F. Reines, F. B. Harrison, H. W. Kruse, and A. D. McGuire. Detection of the free neutrino: A Confirmation. *Science*, 124:103–104, 1956.
- [12] C. S. Wu, E. Ambler, R. W. Hayward, D. D. Hoppes, and R. P. Hudson. Experimental Test of Parity Conservation in  $\beta$  Decay. *Phys. Rev.*, 105:1413–1414, 1957.
- [13] T. D. Lee and Chen-Ning Yang. Question of Parity Conservation in Weak Interactions. *Phys. Rev.*, 104:254–258, 1956.
- [14] R. P. Feynman and Murray Gell-Mann. Theory of Fermi interaction. *Phys. Rev.*, 109:193–198, 1958.
- [15] E. C. G. Sudarshan and R. e. Marshak. Chirality invariance and the universal Fermi interaction. *Phys. Rev.*, 109:1860–1860, 1958.
- [16] J. J. Sakurai. MASS REVERSAL AND WEAK INTERACTIONS. *Nuovo Cim.*, 7:649–660, 1958.
- [17] L. D. Landau. On the conservation laws for weak interactions. *Nucl. Phys.*, 3:127–131, 1957.
- [18] T. D. Lee and Chen-Ning Yang. Parity Nonconservation and a Two Component Theory of the Neutrino. *Phys. Rev.*, 105:1671–1675, 1957.
- [19] Abdus Salam. On parity conservation and neutrino mass. *Nuovo Cim.*, 5:299–301, 1957.
- [20] M. Goldhaber, L. Grodzins, and A. W. Sunyar. Helicity of Neutrinos. *Phys. Rev.*, 109:1015–1017, 1958.
- [21] E. J. Konopinski and H. M. Mahmoud. The Universal Fermi interaction. *Phys. Rev.*, 92:1045–1049, 1953.
- [22] B. Pontecorvo. Electron and Muon Neutrinos. *Zh. Eksp. Teor. Fiz.*, 37:1751–1757, 1959.

- [23] G. Danby et al. Observation of high-energy neutrino reactions and the existence of two kinds of neutrinos. *Phys. Rev. Lett.*, 9:36–44, 1962.
- [24] S. L. Glashow. Partial symmetries of weak interactions. *Nucl. Phys.*, 22:579–588, 1961.
- [25] S. Weinberg. A model of leptons. *Phys. Rev. Lett.*, 19:1264–1266, 1967.
- [26] A. Salam. Weak and electromagnetic interactions. Originally printed in Proceedings Of The Nobel Symposium, Sweden, Stockholm 1968, Elementary Particle Theory, Ed. Svartholm, pp 367-377.
- [27] F. Englert and R. Brout. Broken Symmetry and the Mass of Gauge Vector Mesons. *Phys. Rev. Lett.*, 13:321–323, 1964.
- [28] Peter W. Higgs. Broken Symmetries and the Masses of Gauge Bosons. *Phys. Rev. Lett.*, 13:508–509, 1964.
- [29] Gerard 't Hooft and M. J. G. Veltman. Regularization and Renormalization of Gauge Fields. *Nucl. Phys. B*, 44:189–213, 1972.
- [30] F. J. Hasert et al. Observation of Neutrino Like Interactions Without Muon Or Electron in the Gargamelle Neutrino Experiment. *Phys. Lett. B*, 46:138–140, 1973.
- [31] M. Banner et al. Observation of Single Isolated Electrons of High Transverse Momentum in Events with Missing Transverse Energy at the CERN anti-p p Collider. *Phys.Lett.*, B122:476–485, 1983.
- [32] G. Arnison et al. Experimental Observation of Lepton Pairs of Invariant Mass Around 95-GeV/c\*\*2 at the CERN SPS Collider. *Phys.Lett.*, B126:398–410, 1983.
- [33] M. Gell-Mann. Isotopic Spin and New Unstable Particles. *Phys. Rev.*, 92:833–834, 1953.

- [34] T. Nakano and K. Nishijima. Charge Independence for V-particles. *Prog. Theor. Phys.*, 10:581–582, 1953.
- [35] Murray Gell-Mann. The Eightfold Way: A Theory of strong interaction symmetry. 3 1961.
- [36] Yuval Ne’eman. Derivation of strong interactions from a gauge invariance. *Nucl. Phys.*, 26:222–229, 1961.
- [37] N. Cabibbo. Unitary symmetry and leptonic decays. *Phys. Rev. Lett.*, 10:531–532, 1963.
- [38] Murray Gell-Mann. A Schematic Model of Baryons and Mesons. *Phys. Lett.*, 8:214–215, 1964.
- [39] G. Zweig. An SU(3) model for strong interaction symmetry and its breaking. Version 1. 1 1964.
- [40] G. Zweig. *An SU(3) model for strong interaction symmetry and its breaking. Version 2.* 2 1964.
- [41] J. D. Bjorken and S. L. Glashow. Elementary Particles and SU(4). *Phys. Lett.*, 11:255–257, 1964.
- [42] S. L. Glashow, J. Iliopoulos, and L. Maiani. Weak interactions with lepton - hadron symmetry. *Phys. Rev.*, D2:1285–1292, 1970.
- [43] J. J. Aubert et al. Experimental Observation of a Heavy Particle *J. Phys. Rev. Lett.*, 33:1404–1406, 1974.
- [44] J. E. Augustin et al. Discovery of a Narrow Resonance in  $e^+e^-$  Annihilation. *Phys. Rev. Lett.*, 33:1406–1408, 1974.
- [45] M. Kobayashi and T. Maskawa. Cp violation in the renormalizable theory of weak interaction. *Prog. Theor. Phys.*, 49:652–657, 1973.
- [46] J. H. Christenson, J. W. Cronin, V. L. Fitch, and R. Turlay. Evidence for the 2 pi decay of the k(2)0 meson. *Phys. Rev. Lett.*, 13:138–140, 1964.

- [47] Martin L. Perl et al. Evidence for Anomalous Lepton Production in e+ - e- Annihilation. *Phys. Rev. Lett.*, 35:1489–1492, 1975.
- [48] S. W. Herb et al. Observation of a Dimuon Resonance at 9.5-GeV in 400-GeV Proton-Nucleus Collisions. *Phys. Rev. Lett.*, 39:252–255, 1977.
- [49] F. Abe et al. A search for the top quark in the reaction  $\bar{p}p \rightarrow e + \text{jets}$  at  $\sqrt{s} = 1.8$  TeV. *Phys. Rev. Lett.*, 64:142–146, 1990.
- [50] S. Abachi et al. Search for the top quark in  $p\bar{p}$  collisions at  $\sqrt{s} = 1.8$  TeV. *Phys. Rev. Lett.*, 72:2138–2142, 1994.
- [51] Michael E. Peskin and Tatsu Takeuchi. Estimation of oblique electroweak corrections. *Phys. Rev.*, D46:381–409, 1992.
- [52] F. Abe et al. Observation of top quark production in  $\bar{p}p$  collisions. *Phys. Rev. Lett.*, 74:2626–2631, 1995.
- [53] S. Abachi et al. Observation of the top quark. *Phys. Rev. Lett.*, 74:2632–2637, 1995.
- [54] Fyodor Tkachov. A Contribution to the history of quarks: Boris Struminsky's 1965 JINR publication. 4 2009.
- [55] H. Fritzsch, Murray Gell-Mann, and H. Leutwyler. Advantages of the Color Octet Gluon Picture. *Phys. Lett. B*, 47:365–368, 1973.
- [56] David J. Gross and Frank Wilczek. Ultraviolet Behavior of Nonabelian Gauge Theories. *Phys. Rev. Lett.*, 30:1343–1346, 1973.
- [57] H. David Politzer. Reliable Perturbative Results for Strong Interactions? *Phys. Rev. Lett.*, 30:1346–1349, 1973.
- [58] Richard P. Feynman. Very high-energy collisions of hadrons. *Phys. Rev. Lett.*, 23:1415–1417, 1969.
- [59] J. D. Bjorken. Asymptotic Sum Rules at Infinite Momentum. *Phys. Rev.*, 179:1547–1553, 1969.

- [60] J. D. Bjorken. Highly Relativistic Nucleus-Nucleus Collisions: The Central Rapidity Region. *Phys. Rev. D*, 27:140–151, 1983.
- [61] D. Decamp et al. ALEPH: A detector for electron-positron annnihilations at LEP. *Nucl. Instrum. Meth. A*, 294:121–178, 1990. [Erratum: Nucl.Instrum.Meth.A 303, 393 (1991)].
- [62] K. Ahmet et al. The OPAL detector at LEP. *Nucl. Instrum. Meth. A*, 305:275–319, 1991.
- [63] P. A. Aarnio et al. The DELPHI detector at LEP. *Nucl. Instrum. Meth. A*, 303:233–276, 1991.
- [64] B. Adeva et al. The Construction of the L3 Experiment. *Nucl. Instrum. Meth. A*, 289:35–102, 1990.
- [65] S. Schael et al. Precision electroweak measurements on the  $Z$  resonance. *Phys. Rept.*, 427:257–454, 2006.
- [66] K. Kodama et al. Observation of tau neutrino interactions. *Phys. Lett. B*, 504:218–224, 2001.
- [67] G. Aad et al. Observation of a new particle in the search for the Standard Model Higgs boson with the ATLAS detector at the LHC. *Phys.Lett.*, B716:1, 2012.
- [68] S. Chatrchyan et al. Observation of a new boson at a mass of 125 GeV with the CMS experiment at the LHC. *Phys.Lett.*, B716:30, 2012.
- [69] B. Pontecorvo. Mesonium and anti-mesonium. *Sov. Phys. JETP*, 6:429, 1957. [Zh. Eksp. Teor. Fiz.33,549(1957)].
- [70] Murray Gell-Mann and A. Pais. Behavior of neutral particles under charge conjugation. *Phys. Rev.*, 97:1387–1389, 1955.
- [71] Raymond Davis, Jr., Don S. Harmer, and Kenneth C. Hoffman. Search for neutrinos from the sun. *Phys. Rev. Lett.*, 20:1205–1209, 1968.

- [72] Bruce T. Cleveland et al. Measurement of the solar electron neutrino flux with the homestake chlorine detector. *Astrophys. J.*, 496:505–526, 1998.
- [73] Ziro Maki, Masami Nakagawa, and Shoichi Sakata. Remarks on the unified model of elementary particles. *Prog. Theor. Phys.*, 28:870–880, 1962.
- [74] B. Pontecorvo. Neutrino Experiments and the Problem of Conservation of Leptonic Charge. *Sov. Phys. JETP*, 26:984–988, 1968. [Zh. Eksp. Teor. Fiz. 53, 1717(1967)].
- [75] V. N. Gribov and B. Pontecorvo. Neutrino astronomy and lepton charge. *Phys. Lett. B*, 28:493, 1969.
- [76] Samoil M. Bilenky and S. T. Petcov. Massive neutrinos and neutrino oscillations. *Rev. Mod. Phys.*, 59:671, 1987.
- [77] L. Wolfenstein. Oscillations Among Three Neutrino Types and CP Violation. *Phys. Rev. D*, 18:958–960, 1978.
- [78] Y. Fukuda et al. Atmospheric muon-neutrino / electron-neutrino ratio in the multigev energy range. *Phys. Lett.*, B335:237–245, 1994.
- [79] W. Gajewski. A search for oscillation of atmospheric neutrinos with the IMB detector. *Nucl. Phys. B Proc. Suppl.*, 28:161–164, 1992.
- [80] Y. Fukuda et al. Evidence for oscillation of atmospheric neutrinos. *Phys. Rev. Lett.*, 81:1562–1567, 1998.
- [81] Q. R. Ahmad et al. Direct evidence for neutrino flavor transformation from neutral-current interactions in the sudbury neutrino observatory. *Phys. Rev. Lett.*, 89:011301, 2002.
- [82] P. Adamson et al. Improved search for muon-neutrino to electron-neutrino oscillations in MINOS. *Phys. Rev. Lett.*, 107:181802, 2011.
- [83] M. H. Ahn et al. Indications of neutrino oscillation in a 250-km long- baseline experiment. *Phys. Rev. Lett.*, 90:041801, 2003.

- [84] M. A. Acero et al. New constraints on oscillation parameters from  $\nu_e$  appearance and  $\nu_\mu$  disappearance in the NOvA experiment. *Submitted to: Phys. Rev. D*, 2018.
- [85] K. Abe et al. Indication of Electron Neutrino Appearance from an Accelerator-produced Off-axis Muon Neutrino Beam. *Phys. Rev. Lett.*, 107:041801, 2011.
- [86] M. G. Aartsen et al. Determining neutrino oscillation parameters from atmospheric muon neutrino disappearance with three years of IceCube DeepCore data. *Phys. Rev. D*, 91(7):072004, 2015.
- [87] W. Hampel et al. Gallex solar neutrino observations: Results for gallex iv. *Phys. Lett.*, B447:127–133, 1999.
- [88] J. N. Abdurashitov et al. Measurement of the solar neutrino capture rate with gallium metal. *Phys. Rev.*, C60:055801, 1999.
- [89] S. Fukuda et al. Solar b-8 and he p neutrino measurements from 1258 days of super-kamiokande data. *Phys. Rev. Lett.*, 86:5651–5655, 2001.
- [90] C. Arpesella et al. Direct Measurement of the Be-7 Solar Neutrino Flux with 192 Days of Borexino Data. *Phys. Rev. Lett.*, 101:091302, 2008.
- [91] K. Eguchi et al. First results from kamland: Evidence for reactor anti- neutrino disappearance. *Phys. Rev. Lett.*, 90:021802, 2003.
- [92] S.P. Mikheev and A.Yu. Smirnov. Resonance Amplification of Oscillations in Matter and Spectroscopy of Solar Neutrinos. *Sov.J.Nucl.Phys.*, 42:913–917, 1985.
- [93] L. Wolfenstein. Neutrino Oscillations and Stellar Collapse. *Phys. Rev. D*, 20:2634–2635, 1979.
- [94] P. Adamson et al. Electron neutrino and antineutrino appearance in the full MINOS data sample. *Phys. Rev. Lett.*, 110(17):171801, 2013.

- [95] K. Abe et al. Observation of Electron Neutrino Appearance in a Muon Neutrino Beam. *Phys. Rev. Lett.*, 112:061802, 2014.
- [96] M. Apollonio et al. Limits on neutrino oscillations from the chooz experiment. *Phys. Lett.*, B466:415–430, 1999.
- [97] Y. Abe et al. Improved measurements of the neutrino mixing angle  $\theta_{13}$  with the Double Chooz detector. *JHEP*, 10:086, 2014. [Erratum: JHEP 02, 074 (2015)].
- [98] J.K. Ahn et al. Observation of Reactor Electron Antineutrino Disappearance in the RENO Experiment. 2012.
- [99] Xinheng Guo et al. A precision measurement of the neutrino mixing angle theta(13) using reactor antineutrinos at daya bay. 2007.
- [100] R. Acciarri et al. Long-Baseline Neutrino Facility (LBNF) and Deep Underground Neutrino Experiment (DUNE). 2015.
- [101] K. Abe et al. Physics potential of a long-baseline neutrino oscillation experiment using a J-PARC neutrino beam and Hyper-Kamiokande. *PTEP*, 2015:053C02, 2015.
- [102] Ch. Kraus et al. Final results from phase II of the Mainz neutrino mass search in tritium beta decay. *Eur.Phys.J.*, C40:447, 2005.
- [103] V. N. Aseev et al. An upper limit on electron antineutrino mass from Troitsk experiment. *Phys.Rev.*, D84:112003, 2011.
- [104] M. Aker et al. Improved Upper Limit on the Neutrino Mass from a Direct Kinematic Method by KATRIN. *Phys. Rev. Lett.*, 123(22):221802, 2019.
- [105] A. Osipowicz et al. Katrin: A next generation tritium beta decay experiment with sub-ev sensitivity for the electron neutrino mass. 2001.
- [106] Ali Ashtari Esfahani et al. Determining the neutrino mass with cyclotron radiation emission spectroscopy—Project 8. *J. Phys. G*, 44(5):054004, 2017.

- [107] P. J. E. Peebles. Primeval Helium Abundance and the Primeval Fireball. *Phys. Rev. Lett.*, 16(10):410–413, 1966.
- [108] G. Steigman, D. N. Schramm, and J. E. Gunn. Cosmological Limits to the Number of Massive Leptons. *Phys. Lett. B*, 66:202–204, 1977.
- [109] A. D. Dolgov and Ya. B. Zeldovich. Cosmology and Elementary Particles. *Rev. Mod. Phys.*, 53:1–41, 1981.
- [110] K. Enqvist, K. Kainulainen, and V. Semikoz. Neutrino annihilation in hot plasma. *Nucl. Phys. B*, 374:392–404, 1992.
- [111] K. Enqvist, K. Kainulainen, and J. Maalampi. Refraction and Oscillations of Neutrinos in the Early Universe. *Nucl. Phys. B*, 349:754–790, 1991.
- [112] Gianpiero Mangano, Gennaro Miele, Sergio Pastor, Teguayco Pinto, Ofelia Pisanti, and Pasquale D. Serpico. Relic neutrino decoupling including flavor oscillations. *Nucl. Phys. B*, 729:221–234, 2005.
- [113] S. Gariazzo, P. F. de Salas, and S. Pastor. Thermalisation of sterile neutrinos in the early Universe in the 3+1 scheme with full mixing matrix. *JCAP*, 07:014, 2019.
- [114] N. Aghanim et al. Planck 2018 results. VI. Cosmological parameters. 2018.
- [115] R. A. Alpher, H. Bethe, and G. Gamow. The origin of chemical elements. *Phys. Rev.*, 73:803–804, 1948.
- [116] Subir Sarkar. Big bang nucleosynthesis and physics beyond the standard model. *Rept. Prog. Phys.*, 59:1493–1610, 1996.
- [117] Keith A. Olive, Gary Steigman, and Terry P. Walker. Primordial nucleosynthesis: Theory and observations. *Phys. Rept.*, 333:389–407, 2000.
- [118] Julien Lesgourgues, Gianpiero Mangano, Gennaro Miele, and Sergio Pastor. *Neutrino Cosmology*. Cambridge University Press, 2 2013.

- [119] Julian Heeck and Werner Rodejohann. Neutrinoless Quadruple Beta Decay. *EPL*, 103(3):32001, 2013.
- [120] J. Schechter and J. W. F. Valle. Neutrinoless Double beta Decay in SU(2) x U(1) Theories. *Phys. Rev. D*, 25:2951, 1982.
- [121] Martin Hirsch, Sergey Kovalenko, and Ivan Schmidt. Extended black box theorem for lepton number and flavor violating processes. *Phys. Lett.*, B642:106, 2006.
- [122] Martin Hirsch, Rahul Srivastava, and José W. F. Valle. Can one ever prove that neutrinos are Dirac particles? *Phys. Lett. B*, 781:302–305, 2018.
- [123] Steven Weinberg. Baryon and Lepton Nonconserving Processes. *Phys. Rev. Lett.*, 43:1566–1570, 1979.
- [124] Georges Aad et al. Measurements of the Higgs boson production and decay rates and constraints on its couplings from a combined ATLAS and CMS analysis of the LHC pp collision data at  $\sqrt{s} = 7$  and 8 TeV. *JHEP*, 08:045, 2016.
- [125] Georges Aad et al. Search for direct production of charginos, neutralinos and sleptons in final states with two leptons and missing transverse momentum in  $pp$  collisions at  $\sqrt{s} = 8$  TeV with the ATLAS detector. *JHEP*, 05:071, 2014.
- [126] Georges Aad et al. Search for squarks and gluinos with the ATLAS detector in final states with jets and missing transverse momentum using  $\sqrt{s} = 8$  TeV proton–proton collision data. *JHEP*, 09:176, 2014.
- [127] Serguei Chatrchyan et al. Search for Supersymmetry at the LHC in Events with Jets and Missing Transverse Energy. *Phys. Rev. Lett.*, 107:221804, 2011.
- [128] Roel Aaij et al. Test of lepton universality in beauty-quark decays. 3 2021.
- [129] G. W. Bennett et al. Final Report of the Muon E821 Anomalous Magnetic Moment Measurement at BNL. *Phys. Rev. D*, 73:072003, 2006.

- [130] B. Abi et al. Measurement of the Positive Muon Anomalous Magnetic Moment to 0.46 ppm. *Phys. Rev. Lett.*, 126(14):141801, 2021.
- [131] A. Aguilar et al. Evidence for neutrino oscillations from the observation of anti-nu/e appearance in a anti-nu/mu beam. *Phys. Rev.*, D64:112007, 2001.
- [132] A. A. Aguilar-Arevalo et al. Improved Search for  $\bar{\nu}_\mu \rightarrow \bar{\nu}_e$  Oscillations in the MiniBooNE Experiment. *Phys. Rev. Lett.*, 110:161801, 2013.
- [133] G. Mention et al. The Reactor Antineutrino Anomaly. *Phys. Rev.*, D83:073006, 2011.
- [134] Y. J. Ko et al. Sterile Neutrino Search at the NEOS Experiment. *Phys. Rev. Lett.*, 118(12):121802, 2017.
- [135] I Alekseev et al. Search for sterile neutrinos at the DANSS experiment. *Phys. Lett.*, B787:56–63, 2018.
- [136] P. Anselmann et al. First results from the Cr-51 neutrino source experiment with the GALLEX detector. *Phys. Lett. B*, 342:440–450, 1995.
- [137] J. N. Abdurashitov et al. Measurement of the response of the Russian-American gallium experiment to neutrinos from a Cr-51 source. *Phys. Rev. C*, 59:2246–2263, 1999.
- [138] Mona Dentler, Alvaro Hernandez-Cabezudo, Joachim Kopp, Pedro A. N. Machado, Michele Maltoni, Ivan Martinez-Soler, and Thomas Schwetz. Updated Global Analysis of Neutrino Oscillations in the Presence of eV-Scale Sterile Neutrinos. *JHEP*, 08:010, 2018.
- [139] A. Diaz, C. A. Argüelles, G. H. Collin, J. M. Conrad, and M. H. Shaevitz. Where Are We With Light Sterile Neutrinos? 2019.
- [140] M. Antonello et al. A Proposal for a Three Detector Short-Baseline Neutrino Oscillation Program in the Fermilab Booster Neutrino Beam. 3 2015.

- [141] Patrick D. Bolton and Frank F. Deppisch. Probing nonstandard lepton number violating interactions in neutrino oscillations. *Phys. Rev. D*, 99(11):115011, 2019.
- [142] Patrick D. Bolton, Frank F. Deppisch, and Chandan Hati. Probing new physics with long-range neutrino interactions: an effective field theory approach. *JHEP*, 07:013, 2020.
- [143] Patrick D. Bolton, Frank F. Deppisch, and P. S. Bhupal Dev. Neutrinoless double beta decay versus other probes of heavy sterile neutrinos. *JHEP*, 03:170, 2020.
- [144] Patrick D. Bolton, Frank F. Deppisch, Lukáš Gráf, and Fedor Šimkovic. Two-Neutrino Double Beta Decay with Sterile Neutrinos. *Phys. Rev. D*, 103(5):055019, 2021.
- [145] Peter W. Higgs. Broken symmetries, massless particles and gauge fields. *Phys. Lett.*, 12:132–133, 1964.
- [146] G. S. Guralnik, C. R. Hagen, and T. W. B. Kibble. Global conservation laws and massless particles. *Phys. Rev. Lett.*, 13:585–587, 1964.
- [147] W. Pauli. Mathematical contributions to the theory of Dirac’s matrices. *Ann. Inst. H. Poincaré Phys. Theor.*, 6:109–136, 1936.
- [148] Herbi K. Dreiner, Howard E. Haber, and Stephen P. Martin. Two-component spinor techniques and Feynman rules for quantum field theory and supersymmetry. *Phys. Rept.*, 494:1–196, 2010.
- [149] Eugene P. Wigner. On Unitary Representations of the Inhomogeneous Lorentz Group. *Annals Math.*, 40:149–204, 1939.
- [150] G. Feinberg. Possibility of Faster-Than-Light Particles. *Phys. Rev.*, 159:1089–1105, 1967.

- [151] Y. Aharonov, A. Komar, and Leonard Susskind. Superluminal behavior, causality, and instability. *Phys. Rev.*, 182:1400–1403, 1969.
- [152] Lars Brink, Abu M. Khan, Pierre Ramond, and Xiao-zhen Xiong. Continuous spin representations of the Poincare and superPoincare groups. *J. Math. Phys.*, 43:6279, 2002.
- [153] R. F. Streater and A. S. Wightman. *PCT, spin and statistics, and all that*. 1989.
- [154] L. D. Faddeev and V. N. Popov. Feynman Diagrams for the Yang-Mills Field. *Phys. Lett. B*, 25:29–30, 1967.
- [155] C. Becchi, A. Rouet, and R. Stora. Renormalization of the Abelian Higgs-Kibble Model. *Commun. Math. Phys.*, 42:127–162, 1975.
- [156] C. Becchi, A. Rouet, and R. Stora. Renormalization of Gauge Theories. *Annals Phys.*, 98:287–321, 1976.
- [157] John Clive Ward. An Identity in Quantum Electrodynamics. *Phys. Rev.*, 78:182, 1950.
- [158] Y. Takahashi. On the generalized ward identity. *Nuovo Cim.*, 6:371, 1957.
- [159] Ling-Lie Chau and Wai-Yee Keung. Comments on the Parametrization of the Kobayashi-Maskawa Matrix. *Phys. Rev. Lett.*, 53:1802, 1984.
- [160] C. Jarlskog. Commutator of the Quark Mass Matrices in the Standard Electroweak Model and a Measure of Maximal CP Violation. *Phys. Rev. Lett.*, 55:1039, 1985.
- [161] C. Jarlskog. A Basis Independent Formulation of the Connection Between Quark Mass Matrices, CP Violation and Experiment. *Z. Phys. C*, 29:491–497, 1985.
- [162] O. W. Greenberg. Rephase Invariant Formulation of CP Violation in the Kobayashi-Maskawa Framework. *Phys. Rev. D*, 32:1841, 1985.

- [163] Dan-di Wu. The Rephasing Invariants and CP. *Phys. Rev. D*, 33:860, 1986.
- [164] Xiao-Gang He, Girish C. Joshi, H. Lew, and R. R. Volkas. Simplest Z-prime model. *Phys. Rev. D*, 44:2118–2132, 1991.
- [165] X. G. He, Girish C. Joshi, H. Lew, and R. R. Volkas. NEW Z-prime PHENOMENOLOGY. *Phys. Rev. D*, 43:22–24, 1991.
- [166] Ernest Ma. Gauged B - 3L(tau) and radiative neutrino masses. *Phys. Lett. B*, 433:74–81, 1998.
- [167] Ernest Ma and Utpal Sarkar. Gauged B - 3L(tau) and baryogenesis. *Phys. Lett. B*, 439:95–102, 1998.
- [168] Ernest Ma and D. P. Roy. Phenomenology of the  $B$  - 3L( $\tau$ ) gauge boson. *Phys. Rev. D*, 58:095005, 1998.
- [169] Paul Langacker. The Physics of Heavy  $Z'$  Gauge Bosons. *Rev.Mod.Phys.*, 81:1199–1228, 2009.
- [170] S. N. Glinenko and N. V. Krasnikov. Probing the muon  $g_\mu - 2$  anomaly,  $L_\mu - L_\tau$  gauge boson and Dark Matter in dark photon experiments. *Phys. Lett. B*, 783:24–28, 2018.
- [171] Ayuki Kamada, Kunio Kaneta, Keisuke Yanagi, and Hai-Bo Yu. Self-interacting dark matter and muon  $g - 2$  in a gauged  $U(1)_{L_\mu - L_\tau}$  model. *JHEP*, 06:117, 2018.
- [172] Miguel Escudero, Dan Hooper, Gordan Krnjaic, and Mathias Pierre. Cosmology with A Very Light  $L_\mu - L_\tau$  Gauge Boson. *JHEP*, 03:071, 2019.
- [173] R. D. Peccei and Helen R. Quinn. CP Conservation in the Presence of Instantons. *Phys. Rev. Lett.*, 38:1440–1443, 1977.
- [174] Frank Wilczek. Problem of Strong  $P$  and  $T$  Invariance in the Presence of Instantons. *Phys. Rev. Lett.*, 40:279–282, 1978.

- [175] Ivan Esteban, M. C. Gonzalez-Garcia, Michele Maltoni, Thomas Schwetz, and Albert Zhou. The fate of hints: updated global analysis of three-flavor neutrino oscillations. *JHEP*, 09:178, 2020.
- [176] P. F. de Salas, D. V. Forero, C. A. Ternes, M. Tortola, and J. W. F. Valle. Status of neutrino oscillations 2018:  $3\sigma$  hint for normal mass ordering and improved CP sensitivity. *Phys. Lett.*, B782:633–640, 2018.
- [177] F. Capozzi, E. Lisi, A. Marrone, and A. Palazzo. Current unknowns in the three neutrino framework. *Prog. Part. Nucl. Phys.*, 102:48–72, 2018.
- [178] Gerard 't Hooft. Symmetry Breaking Through Bell-Jackiw Anomalies. *Phys. Rev. Lett.*, 37:8–11, 1976.
- [179] N. S. Manton. Topology in the Weinberg-Salam Theory. *Phys. Rev. D*, 28:2019, 1983.
- [180] Frans R. Klinkhamer and N. S. Manton. A Saddle Point Solution in the Weinberg-Salam Theory. *Phys. Rev. D*, 30:2212, 1984.
- [181] Sidney R. Coleman. Black Holes as Red Herrings: Topological Fluctuations and the Loss of Quantum Coherence. *Nucl. Phys. B*, 307:867–882, 1988.
- [182] Graham D. Kribs, Tilman Plehn, Michael Spannowsky, and Timothy M. P. Tait. Four generations and Higgs physics. *Phys. Rev. D*, 76:075016, 2007.
- [183] Otto Eberhardt, Alexander Lenz, and Jurgen Rohrwild. Less space for a new family of fermions. *Phys. Rev. D*, 82:095006, 2010.
- [184] Andrzej J. Buras, Bjorn Duling, Thorsten Feldmann, Tillmann Heidsieck, Christoph Promberger, and Stefan Recksiegel. Patterns of Flavour Violation in the Presence of a Fourth Generation of Quarks and Leptons. *JHEP*, 09:106, 2010.
- [185] P. Minkowski.  $\mu \rightarrow e\gamma$  at a Rate of One Out of 1-Billion Muon Decays? *Phys. Lett.*, B67:421, 1977.

- [186] R. N. Mohapatra and G. Senjanović. Neutrino mass and spontaneous parity nonconservation. *Phys. Rev. Lett.*, 44:912, 1980.
- [187] Murray Gell-Mann, Pierre Ramond, and Richard Slansky. Complex Spinors and Unified Theories. *Conf. Proc.*, C790927:315–321, 1979.
- [188] T. Yanagida. Horizontal Symmetry And Masses Of Neutrinos. *Conf. Proc.*, C7902131:95, 1979.
- [189] J. Schechter and J. W. F. Valle. Neutrino masses in  $su(2) \times u(1)$  theories. *Phys. Rev.*, D22:2227, 1980.
- [190] Jogesh C. Pati and Abdus Salam. Unified Lepton-Hadron Symmetry and a Gauge Theory of the Basic Interactions. *Phys. Rev.*, D8:1240–1251, 1973.
- [191] Jogesh C. Pati and Abdus Salam. Lepton Number as the Fourth Color. *Phys. Rev.*, D10:275–289, 1974. [Erratum: *Phys. Rev.* D11, 703 (1975)].
- [192] H. Georgi and S. L. Glashow. Unity of All Elementary Particle Forces. *Phys. Rev. Lett.*, 32:438–441, 1974.
- [193] H. Georgi, H. R. Quinn, and S. Weinberg. Hierarchy of interactions in unified gauge theories. *Phys. Rev. Lett.*, 33:451–454, Aug 1974.
- [194] H. Fritzsch and P. Minkowski. Unified Interactions of Leptons and Hadrons. *Annals Phys.*, 93:193, 1975.
- [195] Sacha Davidson and Alejandro Ibarra. A lower bound on the right-handed neutrino mass from leptogenesis. *Phys. Lett.*, B535:25–32, 2002.
- [196] M. Fukugita and T. Yanagida. Baryogenesis without grand unification. *Phys. Lett.*, B174:45, 1986.
- [197] James M. Cline, Kimmo Kainulainen, and Keith A. Olive. On the erasure and regeneration of the primordial baryon asymmetry by sphalerons. *Phys. Rev. Lett.*, 71:2372–2375, 1993.

- [198] Wilfried Buchmuller and Michael Plumacher. Matter antimatter asymmetry and neutrino properties. *Phys. Rept.*, 320:329–339, 1999.
- [199] Frank F. Deppisch, Julia Harz, and Martin Hirsch. Falsifying High-Scale Leptogenesis at the LHC. *Phys. Rev. Lett.*, 112:221601, 2014.
- [200] Frank F. Deppisch, Lukas Graf, Julia Harz, and Wei-Chih Huang. Neutrinoless Double Beta Decay and the Baryon Asymmetry of the Universe. *Phys. Rev.*, D98(5):055029, 2018.
- [201] A. D. Sakharov. Violation of cp invariance, c asymmetry, and baryon asymmetry of the universe. *Pisma Zh. Eksp. Teor. Fiz.*, 5:32–35, 1967.
- [202] Francesco Vissani. Do experiments suggest a hierarchy problem? *Phys. Rev.*, D57:7027–7030, 1998.
- [203] Ilaria Brivio and Michael Trott. Radiatively Generating the Higgs Potential and Electroweak Scale via the Seesaw Mechanism. *Phys. Rev. Lett.*, 119(14):141801, 2017.
- [204] Ilaria Brivio and Michael Trott. Examining the neutrino option. *JHEP*, 02:107, 2019.
- [205] Vedran Brdar, Alexander J. Helmboldt, Sho Iwamoto, and Kai Schmitz. Type-I Seesaw as the Common Origin of Neutrino Mass, Baryon Asymmetry, and the Electroweak Scale. *Phys. Rev. D*, 100:075029, 2019.
- [206] T. Asaka, S. Blanchet, and M. Shaposhnikov. The nuMSM, dark matter and neutrino masses. *Phys. Lett.*, B631:151, 2005.
- [207] T. Asaka and M. Shaposhnikov. The nuMSM, dark matter and baryon asymmetry of the universe. *Phys. Lett.*, B620:17, 2005.
- [208] Mikhail Shaposhnikov and Igor Tkachev. The nuMSM, inflation, and dark matter. *Phys. Lett. B*, 639:414–417, 2006.

- [209] E. K. Akhmedov, V. A. Rubakov, and A. Yu. Smirnov. Baryogenesis via neutrino oscillations. *Phys.Rev.Lett.*, 81:1359, 1998.
- [210] Apostolos Pilaftsis and Thomas E. J. Underwood. Resonant leptogenesis. *Nucl. Phys.*, B692:303–345, 2004.
- [211] Andre de Gouvea. See-saw energy scale and the LSND anomaly. *Phys.Rev.*, D72:033005, 2005.
- [212] G. C. Branco, J. T. Penedo, Pedro M. F. Pereira, M. N. Rebelo, and J. I. Silva-Marcos. Type-I Seesaw with eV-Scale Neutrinos. *JHEP*, 07:164, 2020.
- [213] G. Anamiati, R. M. Fonseca, and M. Hirsch. Quasi Dirac neutrino oscillations. *Phys. Rev.*, D97(9):095008, 2018.
- [214] A. Donini, P. Hernandez, J. Lopez-Pavon, and M. Maltoni. Minimal models with light sterile neutrinos. *JHEP*, 1107:105, 2011.
- [215] Gerard 't Hooft. Naturalness, chiral symmetry, and spontaneous chiral symmetry breaking. *NATO Sci. Ser. B*, 59:135–157, 1980.
- [216] Karin Dick, Manfred Lindner, Michael Ratz, and David Wright. Leptogenesis with Dirac neutrinos. *Phys. Rev. Lett.*, 84:4039–4042, 2000.
- [217] A. Pilaftsis. Resonant tau-leptogenesis with observable lepton number violation. *Phys.Rev.Lett.*, 95:081602, 2005.
- [218] J. Kersten and A. Yu. Smirnov. Right-Handed Neutrinos at CERN LHC and the Mechanism of Neutrino Mass Generation. *Phys.Rev.*, D76:073005, 2007.
- [219] F. F. Deppisch and A. Pilaftsis. Lepton Flavour Violation and theta(13) in Minimal Resonant Leptogenesis. *Phys.Rev.*, D83:076007, 2011.
- [220] M. Shaposhnikov. A Possible symmetry of the nuMSM. *Nucl.Phys.*, B763:49, 2007.

- [221] C.-H. Lee, P. S. B. Dev, and R. N. Mohapatra. Natural TeV-scale left-right seesaw mechanism for neutrinos and experimental tests. *Phys.Rev.*, D88:093010, 2013.
- [222] Pratik Chattopadhyay and Ketan M. Patel. Discrete symmetries for electroweak natural type-I seesaw mechanism. *Nucl. Phys.*, B921:487–506, 2017.
- [223] R. N. Mohapatra. Mechanism for understanding small neutrino mass in superstring theories. *Phys. Rev. Lett.*, 56:561, 1986.
- [224] S. Nandi and U. Sarkar. A Solution to the Neutrino Mass Problem in Superstring E6 Theory. *Phys.Rev.Lett.*, 56:564, 1986.
- [225] R. N. Mohapatra and J. W. F. Valle. Neutrino mass and baryon-number non-conservation in superstring models. *Phys. Rev.*, D34:1642, 1986.
- [226] P. S. B. Dev and A. Pilaftsis. Minimal Radiative Neutrino Mass Mechanism for Inverse Seesaw Models. *Phys.Rev.*, D86:113001, 2012.
- [227] P. S. B. Dev and Apostolos Pilaftsis. Light and Superlight Sterile Neutrinos in the Minimal Radiative Inverse Seesaw Model. *Phys.Rev.*, D87(5):053007, 2013.
- [228] A. Pilaftsis. Radiatively induced neutrino masses and large Higgs neutrino couplings in the standard model with Majorana fields. *Z.Phys.*, C55:275, 1992.
- [229] D. Wyler and L. Wolfenstein. Massless neutrinos in left-right symmetric models. *Nucl. Phys.*, B218:205, 1983.
- [230] Eugeni K. Akhmedov, Manfred Lindner, Erhard Schnapka, and J. W. F. Valle. Left-right symmetry breaking in njl approach. *Phys. Lett.*, B368:270–280, 1996.

- [231] Evgeny K. Akhmedov, Manfred Lindner, Erhard Schnapka, and J. W. F. Valle. Dynamical left-right symmetry breaking. *Phys. Rev.*, D53:2752–2780, 1996.
- [232] M. Malinsky, J. C. Romao, and J. W. F. Valle. Novel supersymmetric  $so(10)$  seesaw mechanism. *Phys. Rev. Lett.*, 95:161801, 2005.
- [233] Ernest Ma. Deciphering the Seesaw Nature of Neutrino Mass from Unitarity Violation. *Mod.Phys.Lett.*, A24:2161–2165, 2009.
- [234] G. t’Hooft. *Lectures at Cargese Summer Inst. 1979*. World Scientific, Singapore, 1982.
- [235] W. Konetschny and W. Kummer. Nonconservation of Total Lepton Number with Scalar Bosons. *Phys. Lett.*, B70:433, 1977.
- [236] M. Magg and C. Wetterich. Neutrino Mass Problem and Gauge Hierarchy. *Phys. Lett.*, 94B:61–64, 1980.
- [237] T. P. Cheng and L-F. Li. Neutrino Masses, Mixings and Oscillations in  $SU(2) \times U(1)$  Models of Electroweak Interactions. *Phys.Rev.*, D22:2860, 1980.
- [238] G. Lazarides, Q. Shafi, and C. Wetterich. Proton lifetime and fermion masses in an  $so(10)$  model. *Nucl. Phys.*, B181:287, 1981.
- [239] R. N. Mohapatra and G. Senjanovic. Neutrino mass and spontaneous parity nonconservation. *Phys. Rev. Lett.*, 44:91, 1980.
- [240] R. Foot, H. Lew, X. G. He, and G. C. Joshi. Seesaw neutrino masses induced by a triplet of leptons. *Z. Phys.*, C44:441, 1989.
- [241] D.V. Forero, S. Morisi, M. Tortola, and J. W. F. Valle. Lepton flavor violation and non-unitary lepton mixing in low-scale type-I seesaw. *JHEP*, 1109:142, 2011.
- [242] S. Antusch and O. Fischer. Non-unitarity of the leptonic mixing matrix: Present bounds and future sensitivities. *JHEP*, 1410:94, 2014.

- [243] F. J. Escrivuela, D. V. Forero, O. G. Miranda, M. Tortola, and J. W. F. Valle. On the description of nonunitary neutrino mixing. *Phys. Rev. D*, 92(5):053009, 2015. [Erratum: Phys.Rev.D 93, 119905 (2016)].
- [244] Shao-Feng Ge, Pedro Pasquini, M. Tortola, and J. W. F. Valle. Measuring the leptonic CP phase in neutrino oscillations with nonunitary mixing. *Phys. Rev. D*, 95(3):033005, 2017.
- [245] Surender Verma and Shankita Bhardwaj. Probing Non-unitary *CP* Violation effects in Neutrino Oscillation Experiments. *Indian J. Phys.*, 92(9):1161–1167, 2018.
- [246] Chee Sheng Fong, Hisakazu Minakata, and Hiroshi Nunokawa. Non-unitary evolution of neutrinos in matter and the leptonic unitarity test. *JHEP*, 02:015, 2019.
- [247] C. Soumya and Mohanta Rukmani. Non-unitary lepton mixing in an inverse seesaw and its impact on the physics potential of long-baseline experiments. *J. Phys. G*, 45(9):095003, 2018.
- [248] Luis Salvador Miranda, Pedro Pasquini, Ushak Rahaman, and Soebur Razzaque. Searching for non-unitary neutrino oscillations in the present T2K and NOvA data. *Eur. Phys. J. C*, 81(5):444, 2021.
- [249] Yi Cai, Juan Herrero-García, Michael A. Schmidt, Avelino Vicente, and Raymond R. Volkas. From the trees to the forest: a review of radiative neutrino mass models. *Front. in Phys.*, 5:63, 2017.
- [250] Ricardo Cepedello Pérez. *Radiative neutrino masses: A window to new physics*. PhD thesis, Valencia U., IFIC, 2021.
- [251] A. Zee. A Theory of Lepton Number Violation, Neutrino Majorana Mass, and Oscillation. *Phys. Lett. B*, 93:389, 1980. [Erratum: Phys.Lett.B 95, 461 (1980)].

- [252] E. Ma. Verifiable radiative seesaw mechanism of neutrino mass and dark matter. *Phys. Rev.*, D73:077301, 2006.
- [253] A. Zee. Quantum numbers of majorana neutrino masses. *Nucl. Phys.*, B264:99, 1986.
- [254] K. S. Babu. Model of 'calculable' majorana neutrino masses. *Phys. Lett.*, B203:132, 1988.
- [255] Lawrence M. Krauss, Salah Nasri, and Mark Trodden. A Model for neutrino masses and dark matter. *Phys. Rev. D*, 67:085002, 2003.
- [256] Mayumi Aoki, Shinya Kanemura, and Osamu Seto. Neutrino mass, Dark Matter and Baryon Asymmetry via TeV-Scale Physics without Fine-Tuning. *Phys. Rev. Lett.*, 102:051805, 2009.
- [257] Michael Gustafsson, Jose Miguel No, and Maximiliano A. Rivera. Predictive Model for Radiatively Induced Neutrino Masses and Mixings with Dark Matter. *Phys. Rev. Lett.*, 110(21):211802, 2013. [Erratum: *Phys. Rev. Lett.* 112, 259902 (2014)].
- [258] Christiane Klein, Manfred Lindner, and Sebastian Ohmer. Minimal Radiative Neutrino Masses. *JHEP*, 03:018, 2019.
- [259] Ernest Ma and Oleg Popov. Pathways to Naturally Small Dirac Neutrino Masses. *Phys. Lett. B*, 764:142–144, 2017.
- [260] Patrick D. Bolton, Frank F. Deppisch, Chandan Hati, Sudhanwa Patra, and Utpal Sarkar. Alternative formulation of left-right symmetry with  $B - L$  conservation and purely Dirac neutrinos. *Phys. Rev.*, D100(3):035013, 2019.
- [261] Darwin Chang and Rabindra N. Mohapatra. Small and Calculable Dirac Neutrino Mass. *Phys. Rev. Lett.*, 58:1600, 1987.
- [262] Aharon Davidson and Kameshwar C. Wali. Universal seesaw mechanism? *Phys. Rev. Lett.*, 59:393, 1987.

- [263] S. Rajpoot. Seesaw Masses for Quarks and Leptons. *Phys. Rev. D*, 36:1479–1483, 1987.
- [264] B. S. Balakrishna. Fermion Mass Hierarchy From Radiative Corrections. *Phys. Rev. Lett.*, 60:1602, 1988.
- [265] K. S. Babu and Rabindra N. Mohapatra. CP Violation in Seesaw Models of Quark Masses. *Phys. Rev. Lett.*, 62:1079, 1989.
- [266] Biswajoy Brahmachari, Ernest Ma, and Utpal Sarkar. Truly minimal left right model of quark and lepton masses. *Phys. Rev. Lett.*, 91:011801, 2003.
- [267] Walter Grimus and Luis Lavoura. One-loop corrections to the seesaw mechanism in the multi-Higgs-doublet standard model. *Phys. Lett.*, B546:86–95, 2002.
- [268] Enrique Fernandez-Martinez, Josu Hernandez-Garcia, Jacobo Lopez-Pavon, and Michele Lucente. Loop level constraints on Seesaw neutrino mixing. *JHEP*, 10:130, 2015.
- [269] Andrew Kobach. Baryon Number, Lepton Number, and Operator Dimension in the Standard Model. *Phys. Lett. B*, 758:455–457, 2016.
- [270] Andre de Gouvea and James Jenkins. A Survey of Lepton Number Violation Via Effective Operators. *Phys. Rev.*, D77:013008, 2008.
- [271] W. Buchmuller and D. Wyler. Effective Lagrangian Analysis of New Interactions and Flavor Conservation. *Nucl. Phys.*, B268:621–653, 1986.
- [272] B. Grzadkowski, M. Iskrzynski, M. Misiak, and J. Rosiek. Dimension-Six Terms in the Standard Model Lagrangian. *JHEP*, 10:085, 2010.
- [273] Elizabeth E. Jenkins, Aneesh V. Manohar, and Michael Trott. Renormalization Group Evolution of the Standard Model Dimension Six Operators I: Formalism and lambda Dependence. *JHEP*, 10:087, 2013.

- [274] Elizabeth E. Jenkins, Aneesh V. Manohar, and Michael Trott. Renormalization Group Evolution of the Standard Model Dimension Six Operators II: Yukawa Dependence. *JHEP*, 01:035, 2014.
- [275] Rodrigo Alonso, Elizabeth E. Jenkins, Aneesh V. Manohar, and Michael Trott. Renormalization Group Evolution of the Standard Model Dimension Six Operators III: Gauge Coupling Dependence and Phenomenology. *JHEP*, 04:159, 2014.
- [276] Rodrigo Alonso, Hsi-Ming Chang, Elizabeth E. Jenkins, Aneesh V. Manohar, and Brian Shotwell. Renormalization group evolution of dimension-six baryon number violating operators. *Phys. Lett. B*, 734:302–307, 2014.
- [277] Landon Lehman. Extending the Standard Model Effective Field Theory with the Complete Set of Dimension-7 Operators. *Phys. Rev. D*, 90(12):125023, 2014.
- [278] Yi Liao and Xiao-Dong Ma. Renormalization Group Evolution of Dimension-seven Baryon- and Lepton-number-violating Operators. *JHEP*, 11:043, 2016.
- [279] Yi Liao and Xiao-Dong Ma. Renormalization Group Evolution of Dimension-seven Operators in Standard Model Effective Field Theory and Relevant Phenomenology. *JHEP*, 03:179, 2019.
- [280] Christopher W. Murphy. Dimension-8 operators in the Standard Model Effective Field Theory. *JHEP*, 10:174, 2020.
- [281] Yi Liao and Xiao-Dong Ma. An explicit construction of the dimension-9 operator basis in the standard model effective field theory. *JHEP*, 11:152, 2020.
- [282] Landon Lehman and Adam Martin. Low-derivative operators of the Standard Model effective field theory via Hilbert series methods. *JHEP*, 02:081, 2016.

- [283] Brian Henning, Xiaochuan Lu, Tom Melia, and Hitoshi Murayama. 2, 84, 30, 993, 560, 15456, 11962, 261485, ...: Higher dimension operators in the SM EFT. *JHEP*, 08:016, 2017. [Erratum: *JHEP* 09, 019 (2019)].
- [284] Elizabeth E. Jenkins, Aneesh V. Manohar, and Peter Stoffer. Low-Energy Effective Field Theory below the Electroweak Scale: Operators and Matching. *JHEP*, 03:016, 2018.
- [285] Yi Liao, Xiao-Dong Ma, and Quan-Yu Wang. Extending low energy effective field theory with a complete set of dimension-7 operators. *JHEP*, 08:162, 2020.
- [286] Wouter Dekens and Peter Stoffer. Low-energy effective field theory below the electroweak scale: matching at one loop. *JHEP*, 10:197, 2019.
- [287] Elizabeth E. Jenkins, Aneesh V. Manohar, and Peter Stoffer. Low-Energy Effective Field Theory below the Electroweak Scale: Anomalous Dimensions. *JHEP*, 01:084, 2018.
- [288] Nicole F. Bell, Mikhail Gorchein, Michael J. Ramsey-Musolf, Petr Vogel, and Peng Wang. Model independent bounds on magnetic moments of Majorana neutrinos. *Phys. Lett.*, B642:377–383, 2006.
- [289] Ingolf Bischer and Werner Rodejohann. General neutrino interactions from an effective field theory perspective. *Nucl. Phys.*, B947:114746, 2019.
- [290] S. Davidson, C. Pena-Garay, N. Rius, and A. Santamaria. Present and future bounds on non-standard neutrino interactions. *JHEP*, 03:011, 2003.
- [291] Stefan Antusch, Jochen P. Baumann, and Enrique Fernandez-Martinez. Non-Standard Neutrino Interactions with Matter from Physics Beyond the Standard Model. *Nucl. Phys.*, B810:369–388, 2009.
- [292] Carla Biggio, Mattias Blennow, and Enrique Fernandez-Martinez. General bounds on non-standard neutrino interactions. *JHEP*, 08:090, 2009.

[293] Tanmoy Bhattacharya, Vincenzo Cirigliano, Saul D. Cohen, Alberto Filipuzzi, Martin Gonzalez-Alonso, Michael L. Graesser, Rajan Gupta, and Huey-Wen Lin. Probing Novel Scalar and Tensor Interactions from (Ultra)Cold Neutrons to the LHC. *Phys. Rev. D*, 85:054512, 2012.

[294] Tommy Ohlsson. Status of non-standard neutrino interactions. *Rept. Prog. Phys.*, 76:044201, 2013.

[295] O. G. Miranda and H. Nunokawa. Non standard neutrino interactions: current status and future prospects. *New J. Phys.*, 17(9):095002, 2015.

[296] Y. Farzan and M. Tortola. Neutrino oscillations and Non-Standard Interactions. *Front.in Phys.*, 6:10, 2018.

[297] Wolfgang Altmannshofer, Michele Tammari, and Jure Zupan. Non-standard neutrino interactions and low energy experiments. *JHEP*, 09:083, 2019.

[298] Amir N. Khan and Werner Rodejohann. New physics from COHERENT data with an improved quenching factor. *Phys. Rev. D*, 100(11):113003, 2019.

[299] Ivan Esteban, M. C. Gonzalez-Garcia, Michele Maltoni, Ivan Martinez-Soler, and Jordi Salvado. Updated Constraints on Non-Standard Interactions from Global Analysis of Oscillation Data. *JHEP*, 08:180, 2018.

[300] Nathal Severijns, Marcus Beck, and Oscar Naviliat-Cuncic. Tests of the standard electroweak model in beta decay. *Rev. Mod. Phys.*, 78:991–1040, 2006.

[301] Vincenzo Cirigliano, Susan Gardner, and Barry Holstein. Beta Decays and Non-Standard Interactions in the LHC Era. *Prog. Part. Nucl. Phys.*, 71:93–118, 2013.

[302] Martin Gonzalez-Alonso, Oscar Naviliat-Cuncic, and Nathal Severijns. New physics searches in nuclear and neutron  $\beta$  decay. *Prog. Part. Nucl. Phys.*, 104:165–223, 2019.

- [303] Frank F. Deppisch, Lukas Graf, and Fedor Simkovic. Searching for New Physics in Two-Neutrino Double Beta Decay. 2020.
- [304] Francisco del Aguila, Shaouly Bar-Shalom, Amarjit Soni, and Jose Wudka. Heavy Majorana Neutrinos in the Effective Lagrangian Description: Application to Hadron Colliders. *Phys. Lett.*, B670:399–402, 2009.
- [305] Yi Liao and Xiao-Dong Ma. Operators up to Dimension Seven in Standard Model Effective Field Theory Extended with Sterile Neutrinos. *Phys. Rev.*, D96(1):015012, 2017.
- [306] Hao-Lin Li, Zhe Ren, Ming-Lei Xiao, Jiang-Hao Yu, and Yu-Hui Zheng. Operator Bases in Effective Field Theories with Sterile Neutrinos:  $d \leq 9$ . 5 2021.
- [307] A. Ferrari, A. Guglielmi, and Paola R. Sala. CNGS neutrino beam: From CERN to Gran Sasso. *Nucl. Phys. Proc. Suppl.*, 168:169–172, 2007.
- [308] Jun Cao. Determining Reactor Neutrino Flux. *Nucl. Phys. Proc. Suppl.*, 229-232:205–209, 2012.
- [309] L. Aliaga et al. Neutrino Flux Predictions for the NuMI Beam. *Phys. Rev.*, D94(9):092005, 2016. [Addendum: Phys. Rev.D95,no.3,039903(2017)].
- [310] Shalom Eliezer and Arthur R. Swift. Experimental Consequences of electron Neutrino-Muon-neutrino Mixing in Neutrino Beams. *Nucl. Phys.*, B105:45–51, 1976.
- [311] Harald Fritzsch and Peter Minkowski. Vector-Like Weak Currents, Massive Neutrinos, and Neutrino Beam Oscillations. *Phys. Lett.*, 62B:72–76, 1976.
- [312] Samoil M. Bilenky and B. Pontecorvo. Again on Neutrino Oscillations. *Lett. Nuovo Cim.*, 17:569, 1976.
- [313] Paul Langacker and Jing Wang. Neutrino anti-neutrino transitions. *Phys. Rev.*, D58:093004, 1998.

- [314] Evgeny Kh. Akhmedov and Alexei Yu. Smirnov. Paradoxes of neutrino oscillations. *Phys. Atom. Nucl.*, 72:1363–1381, 2009.
- [315] R. G. Winter. NEUTRINO OSCILLATION KINEMATICS. *Lett. Nuovo Cim.*, 30:101–104, 1981.
- [316] C. Giunti, C. W. Kim, and U. W. Lee. When do neutrinos really oscillate?: Quantum mechanics of neutrino oscillations. *Phys. Rev.*, D44:3635–3640, 1991.
- [317] S. Nussinov. Solar Neutrinos and Neutrino Mixing. *Phys. Lett.*, 63B:201–203, 1976.
- [318] Boris Kayser. On the Quantum Mechanics of Neutrino Oscillation. *Phys. Rev.*, D24:110, 1981.
- [319] Ken Kiers, Shmuel Nussinov, and Nathan Weiss. Coherence effects in neutrino oscillations. *Phys. Rev.*, D53:537–547, 1996.
- [320] C. Giunti and C. W. Kim. Coherence of neutrino oscillations in the wave packet approach. *Phys. Rev.*, D58:017301, 1998.
- [321] Marek Zralek. From kaons to neutrinos: Quantum mechanics of particle oscillations. *Acta Phys. Polon.*, B29:3925–3956, 1998.
- [322] Mikael Beuthe. Oscillations of neutrinos and mesons in quantum field theory. *Phys. Rept.*, 375:105–218, 2003.
- [323] Evgeny Kh. Akhmedov and Joachim Kopp. Neutrino oscillations: Quantum mechanics vs. quantum field theory. *JHEP*, 04:008, 2010. [Erratum: *JHEP*10,052(2013)].
- [324] Andrew G. Cohen, Sheldon L. Glashow, and Zoltan Ligeti. Disentangling Neutrino Oscillations. *Phys. Lett.*, B678:191–196, 2009.

- [325] C. Giunti, C. W. Kim, J. A. Lee, and U. W. Lee. On the treatment of neutrino oscillations without resort to weak eigenstates. *Phys. Rev.*, D48:4310–4317, 1993.
- [326] W. Grimus, P. Stockinger, and S. Mohanty. The Field theoretical approach to coherence in neutrino oscillations. *Phys. Rev.*, D59:013011, 1999.
- [327] Christian Y. Cardall. Coherence of neutrino flavor mixing in quantum field theory. *Phys. Rev.*, D61:073006, 2000.
- [328] W. Grimus and P. Stockinger. Real oscillations of virtual neutrinos. *Phys. Rev.*, D54:3414–3419, 1996.
- [329] David Delepine, Vannia Gonzalez Macias, Shaaban Khalil, and Gabriel Lopez Castro. Probing Majorana neutrino CP phases and masses in neutrino-antineutrino conversion. *Phys. Lett.*, B693:438–442, 2010.
- [330] David Delepine, Vannia Gonzalez Macias, Shaaban Khalil, and Gabriel Lopez Castro. QFT results for neutrino oscillations and New Physics. *Phys. Rev.*, D79:093003, 2009.
- [331] Artur M Ankowski and Camillo Mariani. Systematic uncertainties in long-baseline neutrino-oscillation experiments. *J. Phys.*, G44(5):054001, 2017.
- [332] Ansgar Denner, H. Eck, O. Hahn, and J. Kublbeck. Feynman rules for fermion number violating interactions. *Nucl. Phys.*, B387:467–481, 1992.
- [333] Zhi-zhong Xing. Properties of CP Violation in Neutrino-Antineutrino Oscillations. *Phys. Rev.*, D87(5):053019, 2013.
- [334] Zhi-zhong Xing and Ye-Ling Zhou. Majorana CP-violating phases in neutrino-antineutrino oscillations and other lepton-number-violating processes. *Phys. Rev.*, D88:033002, 2013.
- [335] Andre de Gouvea, Boris Kayser, and Rabindra N. Mohapatra. Manifest cp violation from majorana phases. *Phys. Rev.*, D67:053004, 2003.

- [336] N. Fornengo et al. Probing neutrino non-standard interactions with atmospheric neutrino data. *Phys. Rev.*, D65:013010, 2002.
- [337] Alexander Friedland and Cecilia Lunardini. Two modes of searching for new neutrino interactions at MINOS. *Phys. Rev.*, D74:033012, 2006.
- [338] Mattias Blennow, Tommy Ohlsson, and Julian Skrotzki. Effects of non-standard interactions in the MINOS experiment. *Phys. Lett.*, B660:522–528, 2008.
- [339] M.G. Aartsen et al. Search for Nonstandard Neutrino Interactions with IceCube DeepCore. *Phys. Rev.*, D97(7):072009, 2018.
- [340] P. Adamson et al. Search for flavor-changing nonstandard neutrino interactions using  $\nu_e$  appearance in MINOS. *Phys. Rev.*, D95(1):012005, 2017.
- [341] Jiajun Liao and Danny Marfatia. COHERENT constraints on nonstandard neutrino interactions. *Phys. Lett.*, B775:54–57, 2017.
- [342] Haruna Oki and Osamu Yasuda. Sensitivity of the T2KK experiment to the non-standard interaction in propagation. *Phys. Rev.*, D82:073009, 2010.
- [343] André de Gouvêa and Kevin J. Kelly. Non-standard Neutrino Interactions at DUNE. *Nucl. Phys.*, B908:318–335, 2016.
- [344] Pilar Coloma. Non-Standard Interactions in propagation at the Deep Underground Neutrino Experiment. *JHEP*, 03:016, 2016.
- [345] Mehedi Masud, Animesh Chatterjee, and Poonam Mehta. Probing CP violation signal at DUNE in presence of non-standard neutrino interactions. *J. Phys.*, G43(9):095005, 2016.
- [346] Mattias Blennow, Sandhya Choubey, Tommy Ohlsson, Dipyaman Pramanik, and Sushant K. Raut. A combined study of source, detector and matter non-standard neutrino interactions at DUNE. *JHEP*, 08:090, 2016.

- [347] Katri Huitu, Timo J. Kärkkäinen, Jukka Maalampi, and Sampsia Vihonen. Constraining the nonstandard interaction parameters in long baseline neutrino experiments. *Phys. Rev.*, D93(5):053016, 2016.
- [348] Shinya Fukasawa, Monojit Ghosh, and Osamu Yasuda. Sensitivity of the T2HKK experiment to nonstandard interactions. *Phys. Rev.*, D95(5):055005, 2017.
- [349] Mehedi Masud and Poonam Mehta. Nonstandard interactions spoiling the CP violation sensitivity at DUNE and other long baseline experiments. *Phys. Rev.*, D94:013014, 2016.
- [350] Jiajun Liao, Danny Marfatia, and Kerry Whisnant. Nonstandard neutrino interactions at DUNE, T2HK and T2HKK. *JHEP*, 01:071, 2017.
- [351] Sanjib Kumar Agarwalla, Sabya Sachi Chatterjee, and Antonio Palazzo. Degeneracy between  $\theta_{23}$  octant and neutrino non-standard interactions at DUNE. *Phys. Lett.*, B762:64–71, 2016.
- [352] Pouya Bakhti, Amir N. Khan, and W. Wang. Sensitivities to charged-current nonstandard neutrino interactions at DUNE. *J. Phys.*, G44(12):125001, 2017.
- [353] Ingolf Bischer and Werner Rodejohann. General Neutrino Interactions at the DUNE Near Detector. *Phys. Rev.*, D99(3):036006, 2019.
- [354] K. Eguchi et al. A high sensitivity search for anti-nu/e's from the sun and other sources at kamland. *Phys. Rev. Lett.*, 92:071301, 2004.
- [355] R. N. Mohapatra and J. C. Pati. Left-Right Gauge Symmetry and an Isoconjugate Model of CP Violation. *Phys. Rev.*, D11:566, 1975.
- [356] Gregory Pawloski. The MINOS experiment. *PoS*, HQL2016:004, 2017.
- [357] P. Adamson et al. Measurement of Neutrino and Antineutrino Oscillations Using Beam and Atmospheric Data in MINOS. *Phys. Rev. Lett.*, 110(25):251801, 2013.

- [358] Sacha E. Kopp. Neutrino Spectra and Uncertainties for MINOS. *AIP Conf. Proc.*, 981:142–144, 2008.
- [359] Istvan Danko. First Observation of Accelerator Muon Antineutrinos in MINOS. 2009.
- [360] J. A. Formaggio and G. P. Zeller. From eV to EeV: Neutrino Cross Sections Across Energy Scales. *Rev. Mod. Phys.*, 84:1307–1341, 2012.
- [361] C. Patrignani et al. Review of Particle Physics. *Chin. Phys.*, C40(10):100001, 2016.
- [362] Tommy Ohlsson, He Zhang, and Shun Zhou. Nonstandard interaction effects on neutrino parameters at medium-baseline reactor antineutrino experiments. *Phys. Lett.*, B728:148–155, 2014.
- [363] R. Acquafredda et al. The OPERA experiment in the CERN to Gran Sasso neutrino beam. *JINST*, 4:P04018, 2009.
- [364] Giuliana Galati. Neutrino oscillations with the OPERA experiment. *PoS*, NOW2016:010, 2016.
- [365] N. Agafonova et al. Final Results of the OPERA Experiment on Appearance in the CNGS Neutrino Beam. *Phys. Rev. Lett.*, 120(21):211801, 2018.
- [366] John N. Bahcall, E. Lisi, D. E. Alburger, L. De Braeckeleer, S. J. Freedman, and J. Napolitano. Standard neutrino spectrum from  ${}^8\text{B}$  decay. *Phys. Rev. C*, 54:411–422, Jul 1996.
- [367] M. Hirsch, H. V. Klapdor-Kleingrothaus, and O. Panella. Double beta decay in left-right symmetric models. *Phys. Lett.*, B374:7–12, 1996.
- [368] F. F. Deppisch, M. Hirsch, and H. Pas. Neutrinoless Double Beta Decay and Physics Beyond the Standard Model. *J.Phys.*, G39:124007, 2012.
- [369] Wei-Chih Huang and J. Lopez-Pavon. On neutrinoless double beta decay in the minimal left-right symmetric model. *Eur.Phys.J.*, C74:2853, 2014.

- [370] Chao-Qiang Geng and Da Huang. Large  $\nu$ - $\bar{\nu}$  Oscillations from High-Dimensional Lepton Number Violating Operator. *JHEP*, 03:103, 2017.
- [371] K. Muto, E. Bender, and H. V. Klapdor. Nuclear Structure Effects on the Neutrinoless Double Beta Decay. *Z. Phys.*, A334:187–194, 1989. [,463(1989)].
- [372] M. Agostini et al. Background-free search for neutrinoless double- $\beta$  decay of  $^{76}\text{Ge}$  with GERDA. 2017. [Nature544,47(2017)].
- [373] M. Agostini et al. Improved Limit on Neutrinoless Double- $\beta$  Decay of  $^{76}\text{Ge}$  from GERDA Phase II. *Phys. Rev. Lett.*, 120(13):132503, 2018.
- [374] A. Gando et al. Search for Majorana Neutrinos near the Inverted Mass Hierarchy Region with KamLAND-Zen. *Phys. Rev. Lett.*, 117(8):082503, 2016. [Addendum: Phys. Rev. Lett.117,no.10,109903(2016)].
- [375] G. Adamov et al. COMET Phase-I Technical Design Report. 2018.
- [376] L. Bartoszek et al. Mu2e Technical Design Report. 2014.
- [377] J. Kaulard et al. Improved limit on the branching ratio of mu-  $\rightarrow$  e+ conversion on titanium. *Phys. Lett.*, B422:334–338, 1998.
- [378] Beomki Yeo, Yoshitaka Kuno, MyeongJae Lee, and Kai Zuber. Future experimental improvement for the search of lepton-number-violating processes in the emu sector. *Phys. Rev.*, D96(7):075027, 2017.
- [379] Jeffrey M. Berryman, André de Gouvêa, Kevin J. Kelly, and Andrew Kobach. Lepton-number-violating searches for muon to positron conversion. *Phys. Rev.*, D95(11):115010, 2017.
- [380] Claudio Dib, Vladimir Gribanov, Sergey Kovalenko, and Ivan Schmidt. Lepton number violating processes and Majorana neutrinos. *Part. Nucl. Lett.*, 106:42–55, 2001.
- [381] Tanja Geib, Alexander Merle, and Kai Zuber.  $\mu^- - e^+$  conversion in upcoming LFV experiments. *Phys. Lett.*, B764:157–162, 2017.

- [382] Oscar Naviliat-Cuncic and Martín González-Alonso. Prospects for precision measurements in nuclear  $\beta$  decay at the LHC era. *Annalen Phys.*, 525:600–619, 2013.
- [383] Vardan Khachatryan et al. Search for physics beyond the standard model in final states with a lepton and missing transverse energy in proton-proton collisions at  $\text{sqrt}(s) = 8$  TeV. *Phys. Rev. D*, 91(9):092005, 2015.
- [384] Morad Aaboud et al. Search for heavy Majorana or Dirac neutrinos and right-handed  $W$  gauge bosons in final states with two charged leptons and two jets at  $\sqrt{s} = 13$  TeV with the ATLAS detector. *JHEP*, 01:016, 2019.
- [385] Gary Prezeau and Andriy Kurylov. Neutrino mass constraints on mu-decay and  $\text{pi}0 \rightarrow \text{nu anti-nu}$ . *Phys. Rev. Lett.*, 95:101802, 2005.
- [386] Takeyasu M. Ito and Gary Prezeau. Neutrino mass constraints on beta decay. *Phys. Rev. Lett.*, 94:161802, 2005.
- [387] K. K. Vos, H. W. Wilschut, and R. G. E. Timmermans. Symmetry violations in nuclear and neutron  $\beta$  decay. *Rev. Mod. Phys.*, 87:1483, 2015.
- [388] Steven Weinberg. Infrared photons and gravitons. *Phys. Rev.*, 140:B516–B524, 1965.
- [389] H. van Dam and M. J. G. Veltman. Massive and massless Yang-Mills and gravitational fields. *Nucl. Phys. B*, 22:397–411, 1970.
- [390] Bryce S. DeWitt. Quantum Theory of Gravity. 2. The Manifestly Covariant Theory. *Phys. Rev.*, 162:1195–1239, 1967.
- [391] Bryce S. DeWitt. Quantum Theory of Gravity. 3. Applications of the Covariant Theory. *Phys. Rev.*, 162:1239–1256, 1967.
- [392] Wei-Tou Ni, Sheau-Shi Pan, Hsien-Chi Yeh, Li-Shing Hou, and Ju-Ling Wan. Search for an axionlike spin coupling using a paramagnetic salt with a dc SQUID. *Phys. Rev. Lett.*, 82:2439–2442, 1999.

- [393] Blayne R. Heckel, C. E. Cramer, T. S. Cook, E. G. Adelberger, Stephan Schlamminger, and U. Schmidt. New CP-violation and preferred-frame tests with polarized electrons. *Phys. Rev. Lett.*, 97:021603, 2006.
- [394] S. Baessler, V. V. Nesvizhevsky, K. V. Protasov, and A. Yu. Voronin. A New constraint for the coupling of axion-like particles to matter via ultra-cold neutron gravitational experiments. *Phys. Rev.*, D75:075006, 2007.
- [395] G. D. Hammond, C. C. Speake, C. Trenkel, and A. Pulido Paton. New constraints on short-range forces coupling mass to intrinsic spin. *Phys. Rev. Lett.*, 98:081101, 2007.
- [396] Blayne R. Heckel, E. G. Adelberger, C. E. Cramer, T. S. Cook, Stephan Schlamminger, and U. Schmidt. Preferred-Frame and CP-Violation Tests with Polarized Electrons. *Phys. Rev.*, D78:092006, 2008.
- [397] G. Vasilakis, J. M. Brown, T. W. Kornack, and M. V. Romalis. Limits on new long range nuclear spin-dependent forces set with a K - He-3 co-magnetometer. *Phys. Rev. Lett.*, 103:261801, 2009.
- [398] A. P. Serebrov. New constraints for CP-violating forces between nucleons in the range  $10^{**}(-4)$  cm - 1 cm. *Phys. Lett.*, B680:423–427, 2009.
- [399] V. K. Ignatovich and Y. N. Pokotilovski. Limits on a nucleon-nucleon monopole-dipole coupling from spin relaxation of polarized ultra-cold neutrons in traps. *Eur. Phys. J.*, C64:19–23, 2009.
- [400] A. P. Serebrov et al. Search for macroscopic CP violating forces using a neutron EDM spectrometer. *JETP Lett.*, 91:6–10, 2010.
- [401] S. G. Karshenboim. Precision physics of simple atoms and constraints on a light boson with ultraweak coupling. *Phys. Rev. Lett.*, 104:220406, 2010.
- [402] S. G. Karshenboim. Constraints on a long-range spin-dependent interaction from precision atomic physics. *Phys. Rev.*, D82:113013, 2010.

- [403] A. K. Petukhov, G. Pignol, D. Jullien, and K. H. Andersen. Polarized  $^3He$  as a probe for short-range spin-dependent interactions. *Phys. Rev. Lett.*, 105:170401, 2010.
- [404] S. G. Karshenboim and V. V. Flambaum. Constraint on axion-like particles from atomic physics. *Phys. Rev.*, A84:064502, 2011.
- [405] S. A. Hoedl, F. Fleischer, E. G. Adelberger, and B. R. Heckel. Improved Constraints on an Axion-Mediated Force. *Phys. Rev. Lett.*, 106:041801, 2011.
- [406] Georg Raffelt. Limits on a CP-violating scalar axion-nucleon interaction. *Phys. Rev.*, D86:015001, 2012.
- [407] H. Yan and W. M. Snow. A New Limit on Possible Long-Range Parity-odd Interactions of the Neutron from Neutron Spin Rotation in Liquid  $^4He$ . *Phys. Rev. Lett.*, 110(8):082003, 2013.
- [408] K. Tullney et al. Constraints on Spin-Dependent Short-Range Interaction between Nucleons. *Phys. Rev. Lett.*, 111:100801, 2013.
- [409] P. H. Chu et al. Laboratory search for spin-dependent short-range force from axionlike particles using optically polarized  $^3He$  gas. *Phys. Rev.*, D87(1):011105, 2013.
- [410] M. Bulatowicz, R. Griffith, M. Larsen, J. Mirijanian, T. G. Walker, C. B. Fu, E. Smith, W. M. Snow, and H. Yan. A Laboratory Search for a Long-Range T-odd, P-odd Interaction from Axion-Like Particles using Dual Species Nuclear Magnetic Resonance with Polarized Xe-129 and Xe-131 Gas. *Phys. Rev. Lett.*, 111:102001, 2013.
- [411] Sonny Mantry, Mario Pitschmann, and Michael J. Ramsey-Musolf. Distinguishing axions from generic light scalars using electric dipole moment and fifth-force experiments. *Phys. Rev.*, D90(5):054016, 2014.
- [412] L. R. Hunter and D. Ang. Using Geoelectrons to Search for Velocity-Dependent Spin-Spin Interactions. *Phys. Rev. Lett.*, 112(9):091803, 2014.

- [413] E. J. Salumbides, W. Ubachs, and V. I. Korobov. Bounds on fifth forces at the sub-Angstrom length scale. *J. Molec. Spectrosc.*, 300:65, 2014.
- [414] T. M. Leslie and J. C. Long. Prospects for electron spin-dependent short-range force experiments with rare earth iron garnet test masses. *Phys. Rev.*, D89(11):114022, 2014.
- [415] Asimina Arvanitaki and Andrew A. Geraci. Resonantly Detecting Axion-Mediated Forces with Nuclear Magnetic Resonance. *Phys. Rev. Lett.*, 113(16):161801, 2014.
- [416] Y. V. Stadnik and V. V. Flambaum. Nuclear spin-dependent interactions: Searches for WIMP, Axion and Topological Defect Dark Matter, and Tests of Fundamental Symmetries. *Eur. Phys. J.*, C75(3):110, 2015.
- [417] S. Afach et al. Constraining interactions mediated by axion-like particles with ultracold neutrons. *Phys. Lett.*, B745:58–63, 2015.
- [418] N. Leefer, A. Gerhardus, D. Budker, V. V. Flambaum, and Y. V. Stadnik. Search for the effect of massive bodies on atomic spectra and constraints on Yukawa-type interactions of scalar particles. *Phys. Rev. Lett.*, 117(27):271601, 2016.
- [419] Filip Ficek, Derek F. Jackson Kimball, Mikhail Kozlov, Nathan Leefer, Szymon Pustelny, and Dmitry Budker. Constraints on exotic spin-dependent interactions between electrons from helium fine-structure spectroscopy. *Phys. Rev.*, A95(3):032505, 2017.
- [420] Wei Ji, Changbo Fu, and Haiyan Gao. Searching for New Spin-Dependent Interactions with SmCo<sub>5</sub> Spin Sources and a SERF Comagnetometer. *Phys. Rev.*, D95(7):075014, 2017.
- [421] N. Crescini, C. Braggio, G. Carugno, P. Falferi, A. Ortolan, and G. Ruoso. Improved constraints on monopole-dipole interaction mediated by pseudo-scalar bosons. *Phys. Lett.*, B773:677–680, 2017.

[422] V. A. Dzuba, V. V. Flambaum, and Y. V. Stadnik. Probing low-mass vector bosons with parity nonconservation and nuclear anapole moment measurements in atoms and molecules. *Phys. Rev. Lett.*, 119(22):223201, 2017.

[423] Cedric Delaunay, Claudia Frugueule, Elina Fuchs, and Yotam Soreq. Probing new spin-independent interactions through precision spectroscopy in atoms with few electrons. *Phys. Rev.*, D96(11):115002, 2017.

[424] Y. V. Stadnik, V. A. Dzuba, and V. V. Flambaum. Improved Limits on Axionlike-Particle-Mediated P , T -Violating Interactions between Electrons and Nucleons from Electric Dipole Moments of Atoms and Molecules. *Phys. Rev. Lett.*, 120(1):013202, 2018.

[425] Xing Rong et al. Searching for an exotic spin-dependent interaction with a single electron-spin quantum sensor. *Nature Commun.*, 9(1):739, 2018.

[426] M. S. Safronova, D. Budker, D. DeMille, Derek F. Jackson Kimball, A. Derevianko, and C. W. Clark. Search for New Physics with Atoms and Molecules. *Rev. Mod. Phys.*, 90(2):025008, 2018.

[427] Filip Ficek, Pavel Fadeev, Victor V. Flambaum, Derek F. Jackson Kimball, Mikhail G. Kozlov, Yevgeny V. Stadnik, and Dmitry Budker. Constraints on exotic spin-dependent interactions between matter and antimatter from antiprotonic helium spectroscopy. *Phys. Rev. Lett.*, 120(18):183002, 2018.

[428] Xing Rong, Man Jiao, Jianpei Geng, Bo Zhang, Tianyu Xie, Fazhan Shi, Chang-Kui Duan, Yi-Fu Cai, and Jiangfeng Du. Constraints on a Spin-Dependent Exotic Interaction between Electrons with Single Electron Spin Quantum Sensors. *Phys. Rev. Lett.*, 121(8):080402, 2018.

[429] V. A. Dzuba, V. V. Flambaum, I. B. Samsonov, and Y. V. Stadnik. New constraints on axion-mediated P,T-violating interaction from electric dipole moments of diamagnetic atoms. *Phys. Rev.*, D98(3):035048, 2018.

- [430] Young Jin Kim, Ping-Han Chu, and Igor Savukov. Experimental Constraint on an Exotic Spin- and Velocity-Dependent Interaction in the Sub-meV Range of Axion Mass with a Spin-Exchange Relaxation-Free Magnetometer. *Phys. Rev. Lett.*, 121(9):091802, 2018.
- [431] Tanmay Kumar Poddar, Subhendra Mohanty, and Soumya Jana. Constraints on ultralight axions from compact binary systems. *Phys. Rev. D*, 101(8):083007, 2020.
- [432] R. P. Feynman. Quantum theory of gravitation. *Acta Phys. Polon.*, 24:697–722, 1963. [,272(1963)].
- [433] G. Feinberg and J. Sucher. Long-Range Forces from Neutrino-Pair Exchange. *Phys. Rev.*, 166:1638–1644, 1968.
- [434] G. Feinberg, J. Sucher, and C. K. Au. The Dispersion Theory of Dispersion Forces. *Phys. Rept.*, 180:83, 1989.
- [435] Stephen D. H. Hsu and Pierre Sikivie. Long range forces from two neutrino exchange revisited. *Phys. Rev.*, D49:4951–4953, 1994.
- [436] J. A. Grifols, E. Masso, and R. Toldra. Majorana neutrinos and long range forces. *Phys. Lett.*, B389:563–565, 1996.
- [437] Maurizio Lusignoli and Silvano Petrarca. Remarks on the forces generated by two-neutrino exchange. *Eur. Phys. J.*, C71:1568, 2011.
- [438] Quan Le Thien and Dennis E. Krause. Spin-Independent Two-Neutrino Exchange Potential with Mixing and *CP*-Violation. *Phys. Rev.*, D99(11):116006, 2019.
- [439] Sylvain Fichet. Quantum Forces from Dark Matter and Where to Find Them. *Phys. Rev. Lett.*, 120(13):131801, 2018.
- [440] Giorgio Arcadi, Manfred Lindner, Jessica Martins, and Farinaldo S. Queiroz. New Physics Probes: Atomic Parity Violation, Polarized Electron Scattering and Neutrino-Nucleus Coherent Scattering. 2019.

- [441] Mitrajyoti Ghosh, Yuval Grossman, and Walter Tangarife. Probing the two-neutrino exchange force using atomic parity violation. 2019.
- [442] Alejandro Segarra and Jose Bernabeu. Absolute neutrino mass and the Dirac/Majorana distinction from the weak interaction of aggregate matter. 2020.
- [443] P. Strasser et al. New precise measurements of muonium hyperfine structure at J-PARC MUSE. *EPJ Web Conf.*, 198:00003, 2019.
- [444] Yevgeny V. Stadnik. Probing Long-Range Neutrino-Mediated Forces with Atomic and Nuclear Spectroscopy. *Phys. Rev. Lett.*, 120(22):223202, 2018.
- [445] Alexandria Costantino and Sylvain Fichet. The Neutrino Casimir Force. 2020.
- [446] J. J. Sakurai and Jim Napolitano. *Modern Quantum Mechanics*. Cambridge University Press, 2 edition, 2017.
- [447] Bogdan A. Dobrescu and Irina Mocioiu. Spin-dependent macroscopic forces from new particle exchange. *JHEP*, 11:005, 2006.
- [448] Elizabeth Ellen Jenkins and Aneesh V. Manohar. Baryon chiral perturbation theory using a heavy fermion Lagrangian. *Phys. Lett.*, B255:558–562, 1991.
- [449] Fady Bishara, Joachim Brod, Benjamin Grinstein, and Jure Zupan. Chiral Effective Theory of Dark Matter Direct Detection. *JCAP*, 1702(02):009, 2017.
- [450] David B. Kaplan, Martin J. Savage, and Mark B. Wise. A Perturbative calculation of the electromagnetic form-factors of the deuteron. *Phys. Rev.*, C59:617–629, 1999.
- [451] Frank F. Deppisch. Lepton Flavour Violation and Flavour Symmetries. *Fortsch. Phys.*, 61:622–644, 2013.

- [452] M. B. Gavela, D. Hernandez, T. Ota, and W. Winter. Large gauge invariant non-standard neutrino interactions. *Phys. Rev.*, D79:013007, 2009.
- [453] Sacha Davidson and Martin Gorbahn. Charged lepton flavor change and nonstandard neutrino interactions. *Phys. Rev.*, D101(1):015010, 2020.
- [454] W. Altmannshofer et al. The Belle II Physics Book. *PTEP*, 2019(12):123C01, 2019. [Erratum: PTEP2020,no.2,029201(2020)].
- [455] P. Vilain et al. Measurement of differential cross-sections for muon-neutrino electron scattering. *Phys. Lett.*, B302:351–355, 1993.
- [456] P. Vilain et al. Precision measurement of electroweak parameters from the scattering of muon-neutrinos on electrons. *Phys. Lett.*, B335:246–252, 1994.
- [457] J. Barranco, O. G. Miranda, C. A. Moura, and J. W. F. Valle. Constraining non-standard neutrino-electron interactions. *Phys. Rev.*, D77:093014, 2008.
- [458] F. J. Escrivuela, M. Tortola, J. W. F. Valle, and O. G. Miranda. Global constraints on muon-neutrino non-standard interactions. *Phys. Rev.*, D83:093002, 2011.
- [459] Julien Alcaide, Shankha Banerjee, Mikael Chala, and Arsenii Titov. Probes of the Standard Model effective field theory extended with a right-handed neutrino. *JHEP*, 08:031, 2019.
- [460] Jonathan M. Butterworth, Mikael Chala, Christoph Englert, Michael Spannowsky, and Arsenii Titov. Higgs phenomenology as a probe of sterile neutrinos. *Phys. Rev. D*, 100(11):115019, 2019.
- [461] D. Akimov et al. Observation of Coherent Elastic Neutrino-Nucleus Scattering. *Science*, 357(6356):1123–1126, 2017.
- [462] Daniel Z. Freedman. Coherent Neutrino Nucleus Scattering as a Probe of the Weak Neutral Current. *Phys. Rev.*, D9:1389–1392, 1974.

- [463] Milton Abramowitz. *Handbook of Mathematical Functions, With Formulas, Graphs, and Mathematical Tables*,. Dover Publications, Inc., USA, 1974.
- [464] D. B. Karp and J. L. López. A class of Meijer's G functions and further representations of the generalized hypergeometric functions. *arXiv e-prints*, page arXiv:1801.08670, January 2018.
- [465] E. G. Adelberger, Blayne R. Heckel, and A. E. Nelson. Tests of the gravitational inverse square law. *Ann. Rev. Nucl. Part. Sci.*, 53:77–121, 2003.
- [466] G. R. Dvali, Gregory Gabadadze, and Goran Senjanovic. Constraints on extra time dimensions. pages 525–532, 1999.
- [467] Ignatios Antoniadis, Nima Arkani-Hamed, Savas Dimopoulos, and G. R. Dvali. New dimensions at a millimeter to a Fermi and superstrings at a TeV. *Phys. Lett.*, B436:257–263, 1998.
- [468] F. Ferrer and J. A. Grifols. Long range forces from pseudoscalar exchange. *Phys. Rev. D*, 58:096006, Sep 1998.
- [469] David B. Kaplan and Mark B. Wise. Couplings of a light dilaton and violations of the equivalence principle. *JHEP*, 08:037, 2000.
- [470] Julian Heeck. Unbroken B – L symmetry. *Phys. Lett.*, B739:256–262, 2014.
- [471] D. J. Kapner, T. S. Cook, E. G. Adelberger, J. H. Gundlach, Blayne R. Heckel, C. D. Hoyle, and H. E. Swanson. Tests of the gravitational inverse-square law below the dark-energy length scale. *Phys. Rev. Lett.*, 98:021101, 2007.
- [472] C. D. Hoyle, D. J. Kapner, B. R. Heckel, E. G. Adelberger, J. H. Gundlach, U. Schmidt, and H. E. Swanson. Submillimeter tests of the gravitational inverse-square law. *Phys. Rev. D*, 70:042004, Aug 2004.
- [473] R. Spero, J. K. Hoskins, R. Newman, J. Pellam, and J. Schultz. Test of the gravitational inverse-square law at laboratory distances. *Phys. Rev. Lett.*, 44:1645–1648, Jun 1980.

[474] J. K. Hoskins, R. D. Newman, R. Spero, and J. Schultz. Experimental tests of the gravitational inverse-square law for mass separations from 2 to 105 cm. *Phys. Rev. D*, 32:3084–3095, Dec 1985.

[475] Joshua Long, Hilton Chan, Allison Churnside, Eric Gulbis, Michael Varney, and John Price. Upper limits to submillimetre-range forces from extra space-time dimensions. *Nature*, 421:922–5, 03 2003.

[476] J. Chiaverini, S. J. Smullin, A. A. Geraci, D. M. Weld, and A. Kapitulnik. New experimental constraints on non-newtonian forces below 100  $\mu\text{m}$ . *Phys. Rev. Lett.*, 90:151101, Apr 2003.

[477] S. J. Smullin, A. A. Geraci, D. M. Weld, J. Chiaverini, S. Holmes, and A. Kapitulnik. Constraints on yukawa-type deviations from newtonian gravity at 20 microns. *Phys. Rev. D*, 72:122001, Dec 2005.

[478] E. G. Adelberger, B. R. Heckel, S. Hoedl, C. D. Hoyle, D. J. Kapner, and A. Upadhye. Particle-physics implications of a recent test of the gravitational inverse-square law. *Phys. Rev. Lett.*, 98:131104, Mar 2007.

[479] J. G. Lee, E. G. Adelberger, T. S. Cook, S. M. Fleischer, and B. R. Heckel. New test of the gravitational  $1/r^2$  law at separations down to 52  $\mu\text{m}$ . *Phys. Rev. Lett.*, 124:101101, Mar 2020.

[480] Alexander D. Rider, David C. Moore, Charles P. Blakemore, Maxime Louis, Marie Lu, and Giorgio Gratta. Search for Screened Interactions Associated with Dark Energy Below the 100  $\mu\text{m}$  Length Scale. *Phys. Rev. Lett.*, 117(10):101101, 2016.

[481] Matt Jaffe, Philipp Haslinger, Victoria Xu, Paul Hamilton, Amol Upadhye, Benjamin Elder, Justin Khouri, and Holger Müller. Testing sub-gravitational forces on atoms from a miniature, in-vacuum source mass. *Nature Phys.*, 13:938, 2017.

- [482] Dylan O. Sabulsky, Indranil Dutta, E. A. Hinds, Benjamin Elder, Clare Burrage, and Edmund J. Copeland. Experiment to detect dark energy forces using atom interferometry. *Phys. Rev. Lett.*, 123(6):061102, 2019.
- [483] B. R. Heckel, W. A. Terrano, and E. G. Adelberger. Limits on exotic long-range spin-spin interactions of electrons. *Phys. Rev. Lett.*, 111:151802, Oct 2013.
- [484] W. A. Terrano, E. G. Adelberger, J. G. Lee, and B. R. Heckel. Short-range spin-dependent interactions of electrons: a probe for exotic pseudo-Goldstone bosons. *Phys. Rev. Lett.*, 115(20):201801, 2015.
- [485] W. H. King. Comments on the article “peculiarities of the isotope shift in the samarium spectrum”. *J. Opt. Soc. Am.*, 53(5):638–639, May 1963.
- [486] Cédric Delaunay, Roee Ozeri, Gilad Perez, and Yotam Soreq. Probing atomic higgs-like forces at the precision frontier. *Phys. Rev. D*, 96:093001, Nov 2017.
- [487] Claudia Fruguele, Elina Fuchs, Gilad Perez, and Matthias Schlaffer. Constraining new physics models with isotope shift spectroscopy. *Phys. Rev. D*, 96:015011, Jul 2017.
- [488] Julian C. Berengut et al. Probing New Long-Range Interactions by Isotope Shift Spectroscopy. *Phys. Rev. Lett.*, 120:091801, 2018.
- [489] V. V. Flambaum, A. J. Geddes, and A. V. Viatkina. Isotope shift, nonlinearity of King plots, and the search for new particles. *Phys. Rev.*, A97(3):032510, 2018.
- [490] E. G. Kessler, Jr. The Deuteron Binding Energy and the Neutron Mass. *Phys. Lett.*, A255:221, 1999.
- [491] D. R. Entem and R. Machleidt. Accurate charge dependent nucleon nucleon potential at fourth order of chiral perturbation theory. *Phys. Rev.*, C68:041001, 2003.

[492] A. Ekström, G. R. Jansen, K. A. Wendt, G. Hagen, T. Papenbrock, B. D. Carlsson, C. Forssén, M. Hjorth-Jensen, P. Navrátil, and W. Nazarewicz. Accurate nuclear radii and binding energies from a chiral interaction. *Phys. Rev.*, C91(5):051301, 2015.

[493] Michael I. Eides. Hyperfine Splitting in Muonium: Accuracy of the Theoretical Prediction. *Phys. Lett.*, B795:113–116, 2019.

[494] Michael I. Eides, Howard Grotch, and Valery A. Shelyuto. Theory of light hydrogen - like atoms. *Phys. Rept.*, 342:63–261, 2001.

[495] Peter J. Mohr, David B. Newell, and Barry N. Taylor. CODATA Recommended Values of the Fundamental Physical Constants: 2014. *Rev. Mod. Phys.*, 88(3):035009, 2016.

[496] Michael I. Eides. Weak-interaction contributions to hyperfine splitting and lamb shift. *Phys. Rev. A*, 53:2953–2957, May 1996.

[497] T. Asaka, M. Tanaka, K. Tsumura, and M. Yoshimura. Precision electroweak shift of muonium hyperfine splitting. 2018.

[498] Daisuke Nomura and Thomas Teubner. Hadronic contributions to the anomalous magnetic moment of the electron and the hyperfine splitting of muonium. *Nucl. Phys.*, B867:236–243, 2013.

[499] M1S2S-Collaboration. Measurement of the Muonium 1S-2S Transition Frequency. page physics/9805020, May 1998.

[500] Andrzej Czarnecki, Kirill Melnikov, and Alexander Yelkhovsky. Positronium S state spectrum: Analytic results at  $O(m \alpha^{**6})$ . *Phys. Rev.*, A59:4316, 1999.

[501] V. Meyer, S. N. Bagayev, P. E. G. Baird, P. Bakule, M. G. Boshier, A. Breitrück, S. L. Cornish, S. Dychkov, G. H. Eaton, A. Grossmann, D. Hübl, V. W. Hughes, K. Jungmann, I. C. Lane, Yi-Wei Liu, D. Lucas, Y. Matyugin, J. Merkel, G. zu Putlitz, I. Reinhard, P. G. H. Sandars, R. Santra, P. V.

Schmidt, C. A. Scott, W. T. Toner, M. Towrie, K. Träger, L. Willmann, and V. Yakhontov. Measurement of the  $1s - 2s$  energy interval in muonium. *Phys. Rev. Lett.*, 84:1136–1139, Feb 2000.

[502] Claudia Fruguele, Jesús Pérez-Ríos, and Clara Peset. Current and future perspectives of positronium and muonium spectroscopy as dark sectors probe. *Phys. Rev.*, D100(1):015010, 2019.

[503] Christian G. Parthey, Arthur Matveev, Janis Alnis, Randolph Pohl, Thomas Udem, Ulrich D. Jentschura, Nikolai Kolachevsky, and Theodor W. Hänsch. Precision measurement of the hydrogen-deuterium  $1s - 2s$  isotope shift. *Phys. Rev. Lett.*, 104:233001, Jun 2010.

[504] A. Ishida, T. Namba, S. Asai, T. Kobayashi, H. Saito, M. Yoshida, K. Tanaka, and A. Yamamoto. New Precision Measurement of Hyperfine Splitting of Positronium. *Phys. Lett.*, B734:338–344, 2014.

[505] T Tanaka, M Abe, M Aoki, M Fukao, H Iinuma, Y Ikeda, K Ishida, Takashi Ito, Masahiko Iwasaki, Ryosuke Kadono, O Kamigaito, Sohtaro Kanda, D Kawall, Naritoshi Kawamura, Akihiro Koda, K Kojima, M Kubo, Y Matsuda, T. Mibe, and Tamaki Yoshioka. High precision measurement of muonium hyperfine structure. *Journal of Physics: Conference Series*, 1138:012008, 11 2018.

[506] M. Diermaier, C. B. Jepsen, B. Kolbinger, C. Malbrunot, O. Massiczek, C. Sauerzopf, M. C. Simon, J. Zmeskal, and E. Widmann. In-beam measurement of the hydrogen hyperfine splitting and prospects for antihydrogen spectroscopy. *Nature Communications*, 8:15749, June 2017.

[507] M. Horbatsch and E. A. Hessel. Tabulation of the bound-state energies of atomic hydrogen. , 93(2):022513, February 2016.

[508] D. J. Wineland and N. F. Ramsey. Atomic deuterium maser. *Phys. Rev. A*, 5:821–837, Feb 1972.

[509] N. Kolachevsky, P. Fendel, S. G. Karshenboim, and T. W. Hänsch. 2S hyperfine structure of atomic deuterium. , 70(6):062503, December 2004.

[510] Savel G. Karshenboim and Vladimir G. Ivanov. Hyperfine structure in hydrogen and helium ion. *Phys. Lett.*, B524:259–264, 2002.

[511] R. N. Faustov and A. P. Martynenko. Muonic hydrogen ground state hyperfine splitting. pages 348–354, 2003.

[512] Oleksandr Tomalak. Hyperfine splitting in ordinary and muonic hydrogen. *Eur. Phys. J.*, A54(1):3, 2018.

[513] Aldo Antognini, François Nez, Karsten Schuhmann, F. Amaro, François Biraben, João Cardoso, D. Covita, Andreas Dax, Satish Dhawan, Marc Diepold, Luis Fernandes, Adolf Giesen, A.L. Gouvea, Thomas Graf, Theodor Haensch, Paul Indelicato, Lucile Julien, Cheng-Yang Kao, Paul Knowles, and Randolph Pohl. Proton structure from the measurement of 2s-2p transition frequencies of muonic hydrogen. *Science (New York, N.Y.)*, 339:417–20, 01 2013.

[514] Aldo Antognini, Franz Kottmann, François Biraben, Paul Indelicato, François Nez, and Randolph Pohl. Theory of the 2S-2P Lamb shift and 2S hyperfine splitting in muonic hydrogen. *Annals of Physics*, 331:127–145, April 2013.

[515] Randolph Pohl et al. Laser spectroscopy of muonic deuterium. *Science*, 353(6300):669–673, 2016.

[516] Julian J. Krauth, Marc Diepold, Beatrice Franke, Aldo Antognini, Franz Kottmann, and Randolph Pohl. Theory of the n=2 levels in muonic deuterium. *Annals Phys.*, 366:168–196, 2016.

[517] Michael I. Eides and Valery A. Shelyuto. Light-by-Light Scattering Non-logarithmic Corrections to Hyperfine Splitting in Muonium. *Phys. Rev. D*, 89(1):014034, 2014.

- [518] Michael I. Eides and Valery A. Shelyuto. One More Hard Three-Loop Correction to Parapositronium Energy Levels. *Phys. Rev. D*, 96(1):011301, 2017.
- [519] Simon Bray, Jae Sik Lee, and Apostolos Pilaftsis. Resonant CP violation due to heavy neutrinos at the LHC. *Nucl. Phys.*, B786:95–118, 2007.
- [520] Janusz Gluza, Tomasz Jelinski, and Robert Szafron. Lepton number violation and ‘Diracness’ of massive neutrinos composed of Majorana states. *Phys. Rev.*, D93(11):113017, 2016.
- [521] Arindam Das, P. S. Bhupal Dev, and Rabindra N. Mohapatra. Same Sign versus Opposite Sign Dileptons as a Probe of Low Scale Seesaw Mechanisms. *Phys. Rev.*, D97(1):015018, 2018.
- [522] Susanne Mertens et al. A novel detector system for KATRIN to search for keV-scale sterile neutrinos. *J. Phys.*, G46(6):065203, 2019.
- [523] C. Adams et al. The Long-Baseline Neutrino Experiment: Exploring Fundamental Symmetries of the Universe. 2013.
- [524] P. Hernández, J. Jones-Pérez, and O. Suárez-Navarro. Majorana vs Pseudo-Dirac Neutrinos at the ILC. *Eur. Phys. J.*, C79(3):220, 2019.
- [525] A. Ibarra, E. Molinaro, and S. T. Petcov. Low Energy Signatures of the TeV Scale See-Saw Mechanism. *Phys. Rev.*, D84:013005, 2011.
- [526] A. Ibarra, E. Molinaro, and S.T. Petcov. TeV Scale See-Saw Mechanisms of Neutrino Mass Generation, the Majorana Nature of the Heavy Singlet Neutrinos and  $(\beta\beta)_{0\nu}$ -Decay. *JHEP*, 1009:108, 2010.
- [527] P. S. Bhupal Dev, Rabindra N. Mohapatra, and Yongchao Zhang. CP Violating Effects in Heavy Neutrino Oscillations: Implications for Colliders and Leptogenesis. *JHEP*, 11:137, 2019.
- [528] Wei Chao, Zong-guo Si, Ya-juan Zheng, and Shun Zhou. Testing the Realistic Seesaw Model with Two Heavy Majorana Neutrinos at the CERN Large Hadron Collider. *Phys. Lett.*, B683:26–32, 2010.

- [529] P. S. Bhupal Dev and R. N. Mohapatra. Unified explanation of the  $eejj$ , diboson and dijet resonances at the LHC. *Phys. Rev. Lett.*, 115(18):181803, 2015.
- [530] G. Anamiati, M. Hirsch, and E. Nardi. Quasi-Dirac neutrinos at the LHC. *JHEP*, 10:010, 2016.
- [531] Marco Cirelli, Guido Marandella, Alessandro Strumia, and Francesco Vissani. Probing oscillations into sterile neutrinos with cosmology, astrophysics and experiments. *Nucl.Phys.*, B708:215–267, 2005.
- [532] Anupama Atre, Tao Han, Silvia Pascoli, and Bin Zhang. The Search for Heavy Majorana Neutrinos. *JHEP*, 05:030, 2009.
- [533] Frank F. Deppisch, P. S. Bhupal Dev, and Apostolos Pilaftsis. Neutrinos and Collider Physics. *New J. Phys.*, 17(7):075019, 2015.
- [534] André de Gouvea and Andrew Kobach. Global Constraints on a Heavy Neutrino. *Phys. Rev.*, D93(3):033005, 2016.
- [535] Marcin Chrzaszcz, Marco Drewes, Tomás E. Gonzalo, Julia Harz, Suraj Krishnamurthy, and Christoph Weniger. A frequentist analysis of three right-handed neutrinos with GAMBIT. 2019.
- [536] Georges Aad et al. Search for heavy neutral leptons in decays of  $W$  bosons produced in 13 TeV  $pp$  collisions using prompt and displaced signatures with the ATLAS detector. 2019.
- [537] Albert M Sirunyan et al. Search for heavy neutral leptons in events with three charged leptons in proton-proton collisions at  $\sqrt{s} = 13$  TeV. *Phys. Rev. Lett.*, 120(22):221801, 2018.
- [538] Georges Aad et al. Search for heavy Majorana neutrinos with the ATLAS detector in  $pp$  collisions at  $\sqrt{s} = 8$  TeV. *JHEP*, 07:162, 2015.

- [539] Albert M Sirunyan et al. Search for heavy Majorana neutrinos in same-sign dilepton channels in proton-proton collisions at  $\sqrt{s} = 13$  TeV. *JHEP*, 01:122, 2019.
- [540] A. Abada et al. FCC-hh: The Hadron Collider. *Eur. Phys. J. ST*, 228(4):755–1107, 2019.
- [541] Silvia Pascoli, Richard Ruiz, and Cedric Weiland. Heavy neutrinos with dynamic jet vetoes: multilepton searches at  $\sqrt{s} = 14$  , 27, and 100 TeV. *JHEP*, 06:049, 2019.
- [542] Arindam Das, P. S. Bhupal Dev, and C. S. Kim. Constraining Sterile Neutrinos from Precision Higgs Data. *Phys. Rev.*, D95(11):115013, 2017.
- [543] O. Adriani et al. Search for isosinglet neutral heavy leptons in  $Z_0$  decays. *Phys.Lett.*, B295:371–382, 1992.
- [544] P. Achard et al. Search for heavy isosinglet neutrino in  $e^+e^-$  annihilation at LEP. *Phys.Lett.*, B517:67–74, 2001.
- [545] P. Abreu et al. Search for neutral heavy leptons produced in  $Z$  decays. *Z.Phys.*, C74:57–71, 1997.
- [546] Shankha Banerjee, P. S. Bhupal Dev, Alejandro Ibarra, Tanumoy Mandal, and Manimala Mitra. Prospects of Heavy Neutrino Searches at Future Lepton Colliders. 2015.
- [547] Sabyasachi Chakraborty, Manimala Mitra, and Sujay Shil. Fat Jet Signature of a Heavy Neutrino at Lepton Collider. *Phys. Rev.*, D100(1):015012, 2019.
- [548] Arindam Das, Sudip Jana, Sanjoy Mandal, and S. Nandi. Probing right handed neutrinos at the LHeC and lepton colliders using fat jet signatures. *Phys. Rev.*, D99(5):055030, 2019.
- [549] Alain Blondel, E. Gaverini, N. Serra, and M. Shaposhnikov. Search for Heavy Right Handed Neutrinos at the FCC-ee.

- [550] Subhadeep Mondal and Santosh Kumar Rai. Probing the Heavy Neutrinos of Inverse Seesaw Model at the LHeC. *Phys. Rev.*, D94(3):033008, 2016.
- [551] Stefan Antusch, Oliver Fischer, and A. Hammad. Lepton-Trijet and Displaced Vertex Searches for Heavy Neutrinos at Future Electron-Proton Colliders. 2019.
- [552] Stefan Antusch, Eros Cazzato, and Oliver Fischer. Sterile neutrino searches at future  $e^-e^+$ ,  $pp$ , and  $e^-p$  colliders. *Int. J. Mod. Phys.*, A32(14):1750078, 2017.
- [553] Daniel Dercks, Herbert K. Dreiner, Martin Hirsch, and Zeren Simon Wang. Long-Lived Fermions at AL3X. *Phys. Rev.*, D99(5):055020, 2019.
- [554] Vladimir V. Gligorov, Simon Knapen, Michele Papucci, and Dean J. Robinson. Searching for Long-lived Particles: A Compact Detector for Exotics at LHCb. *Phys. Rev.*, D97(1):015023, 2018.
- [555] Jonathan L. Feng, Iftah Galon, Felix Kling, and Sebastian Trojanowski. ForwArd Search ExpeRiment at the LHC. *Phys. Rev.*, D97(3):035001, 2018.
- [556] Felix Kling and Sebastian Trojanowski. Heavy Neutral Leptons at FASER. *Phys. Rev.*, D97(9):095016, 2018.
- [557] John Paul Chou, David Curtin, and H. J. Lubatti. New Detectors to Explore the Lifetime Frontier. *Phys. Lett.*, B767:29–36, 2017.
- [558] David Curtin et al. Long-Lived Particles at the Energy Frontier: The MATH-USLA Physics Case. *Rept. Prog. Phys.*, 82(11):116201, 2019.
- [559] Mariana Frank, Marc de Montigny, Pierre-Philippe A. Ouimet, James Pinfold, Ameir Shaa, and Michael Staelens. Searching for Heavy Neutrinos with the MoEDAL-MAPP Detector at the LHC. 2019.
- [560] P. S. Bhupal Dev, Apostolos Pilaftsis, and Un-Ki Yang. New Production Mechanism for Heavy Neutrinos at the LHC. *Phys. Rev. Lett.*, 112(8):081801, 2014.

- [561] Apostolos Pilaftsis. Resonant CP violation induced by particle mixing in transition amplitudes. *Nucl. Phys.*, B504:61–107, 1997.
- [562] Juan Carlos Helo, Sergey Kovalenko, and Ivan Schmidt. Sterile neutrinos in lepton number and lepton flavor violating decays. *Nucl. Phys.*, B853:80–104, 2011.
- [563] Marco Drewes, Juraj Klarić, and Philipp Klose. On Lepton Number Violation in Heavy Neutrino Decays at Colliders. *JHEP*, 11:032, 2019. [JHEP19,032(2020)].
- [564] M. Aoki, M. Blecher, D. A. Bryman, S. Chen, M. Ding, L. Doria, P. Gumplinger, C. Hurst, A. Hussein, Y. Igarashi, N. Ito, S. H. Kettell, L. Kurchaninov, L. Littenberg, C. Malbrunot, T. Numao, R. Poutissou, A. Sher, T. Sullivan, D. Vavilov, K. Yamada, and M. Yoshida. Search for massive neutrinos in the decay  $\pi \rightarrow e\nu$ . *Phys. Rev. D*, 84:052002, Sep 2011.
- [565] A. Aguilar-Arevalo et al. Improved search for heavy neutrinos in the decay  $\pi \rightarrow e\nu$ . *Phys. Rev.*, D97(7):072012, 2018.
- [566] D. A. Bryman and R. Shrock. Improved Constraints on Sterile Neutrinos in the MeV to GeV Mass Range. 2019.
- [567] D. A. Bryman and R. Shrock. Constraints on Sterile Neutrinos in the MeV to GeV Mass Range. 2019.
- [568] Eduardo Cortina Gil et al. Search for heavy neutral lepton production in  $K^+$  decays. *Phys. Lett.*, B778:137–145, 2018.
- [569] Marco Drewes, Jan Hajer, Juraj Klaric, and Gaia Lanfranchi. NA62 sensitivity to heavy neutral leptons in the low scale seesaw model. *JHEP*, 07:105, 2018.
- [570] Asmaa Abada, Damir Becirevic, Olcyr Sumensari, Cedric Weiland, and Renata Zukanovich Funchal. Sterile neutrinos facing kaon physics experiments. *Phys. Rev.*, D95(7):075023, 2017.

[571] A. Abashian et al. The Belle Detector. *Nucl. Instrum. Meth.*, A479:117–232, 2002.

[572] D. Liventsev et al. Search for heavy neutrinos at Belle. *Phys. Rev.*, D87(7):071102, 2013.

[573] J. Badier et al. Mass and Lifetime Limits on New Longlived Particles in 300-GeV/c $\pi^-$  Interactions. *Z. Phys.*, C31:21, 1986.

[574] F. Bergsma et al. A Search for Decays of Heavy Neutrinos in the Mass Range 0.5-GeV to 2.8-GeV. *Phys. Lett.*, 166B:473–478, 1986.

[575] P. Vilain et al. Search for heavy isosinglet neutrinos. *Phys. Lett.*, B343:453–458, 1995.

[576] G. Bernardi, G. Carugno, J. Chauveau, F. Dicarlo, M. Dris, et al. FURTHER LIMITS ON HEAVY NEUTRINO COUPLINGS. *Phys. Lett.*, B203:332, 1988.

[577] S.A. Baranov, Yu.A. Batusov, A.A. Borisov, S.A. Bunyatov, V. Yu. Valuev, et al. Search for heavy neutrinos at the IHEP-JINR neutrino detector. *Phys. Lett.*, B302:336–340, 1993.

[578] K. Abe et al. Search for heavy neutrinos with the T2K near detector ND280. 2019.

[579] Igor Krasnov. On DUNE prospects in the search for sterile neutrinos. 2019.

[580] Peter Ballett, Tommaso Boschi, and Silvia Pascoli. Heavy Neutral Leptons from low-scale seesaws at the DUNE Near Detector. 2019.

[581] Sergey Alekhin et al. A facility to Search for Hidden Particles at the CERN SPS: the SHiP physics case. *Rept. Prog. Phys.*, 79(12):124201, 2016.

[582] C. Ahdida et al. Sensitivity of the SHiP experiment to Heavy Neutral Leptons. *JHEP*, 04:077, 2019.

[583] Sergey Kovalenko, Zhun Lu, and Ivan Schmidt. Lepton Number Violating Processes Mediated by Majorana Neutrinos at Hadron Colliders. *Phys.Rev.*, D80:073014, 2009.

[584] Asmaa Abada, Valentina De Romeri, Michele Lucente, Ana M. Teixeira, and Takashi Toma. Effective Majorana mass matrix from tau and pseudoscalar meson lepton number violating decays. *JHEP*, 02:169, 2018.

[585] Medina Ablikim et al. Search for heavy Majorana neutrino in lepton number violating decays of  $D \rightarrow K\pi e^+ e^+$ . *Phys. Rev.*, D99(11):112002, 2019.

[586] Eung Jin Chun, Arindam Das, Sanjoy Mandal, Manimala Mitra, and Nita Sinha. Sensitivity of Lepton Number Violating Meson Decays in Different Experiments. *Phys. Rev. D*, 100(9):095022, 2019.

[587] R. E. Shrock. New Tests For, and Bounds On, Neutrino Masses and Lepton Mixing. *Phys.Lett.*, B96:159, 1980.

[588] K. H. Hiddemann, H. Daniel, and O. Schwentker. Limits on neutrino masses from the tritium beta spectrum. *J. Phys.*, G21:639–650, 1995.

[589] Christine Kraus, Andrej Singer, Kathrin Valerius, and Christian Weinheimer. Limit on sterile neutrino contribution from the Mainz Neutrino Mass Experiment. *Eur. Phys. J.*, C73(2):2323, 2013.

[590] A. I. Belesev, A. I. Berlev, E. V. Geraskin, A. A. Golubev, N. A. Likhovid, A. A. Nozik, V. S. Pantuev, V. I. Parfenov, and A. K. Skasyrskaya. The search for an additional neutrino mass eigenstate in the 2–100 eV region from ‘Troitsk nu-mass’ data: a detailed analysis. *J. Phys.*, G41:015001, 2014.

[591] J. N. Abdurashitov et al. First measeurements in search for keV-sterile neutrino in tritium beta-decay by Troitsk nu-mass experiment. *Pisma Zh. Eksp. Teor. Fiz.*, 105(12):723–724, 2017. [JETP Lett.105,no.12,753(2017)].

[592] F. P. Calaprice and D. J. Millener. Heavy neutrinos and the beta spectra of  $^{35}\text{S}$ ,  $^{18}\text{F}$ , and  $^{19}\text{Ne}$ . *Phys. Rev. C*, 27:1175–1181, Mar 1983.

[593] E. Holzschuh, L. Palermo, H. Stussi, and P. Wenk. The beta-spectrum of S-35 and search for the admixture of heavy neutrinos. *Phys. Lett.*, B482:1–9, 2000.

[594] A. V. Derbin, A. I. Egorov, S. V. Bakhlanov, and V. N. Muratova. Measurement of the Ca-45 beta spectrum in search of deviations from the theoretical shape. *JETP Lett.*, 66:88–92, 1997. [Pisma Zh. Eksp. Teor. Fiz.66,81(1997)].

[595] E. Holzschuh, W. Kundig, L. Palermo, H. Stussi, and P. Wenk. Search for heavy neutrinos in the beta spectrum of Ni-63. *Phys. Lett.*, B451:247–255, 1999.

[596] K. Schreckenbach, G. Colvin, and F. Von Feilitzsch. SEARCH FOR MIXING OF HEAVY NEUTRINOS IN THE BETA+ AND BETA- SPECTRA OF THE CU-64 DECAY. *Phys. Lett.*, 129B:265–268, 1983.

[597] A. V. Derbin, I. S. Drachnev, I. S. Lomskaya, V. N. Muratova, N. V. Pilipenko, D. A. Semenov, L. M. Tukkhonen, E. V. Unzhakov, and A. Kh. Khusainov. Search for a neutrino with a mass of 0.01–1.0 mev in beta decays of 144ce–144pr nuclei. *JETP Letters*, 108(8):499–503, Oct 2018.

[598] M. Galeazzi, F. Fontanelli, F. Gatti, and S. Vitale. Limits on the existence of heavy neutrinos in the range 50–1000 ev from the study of the  $^{187}\text{Re}$  beta decay. *Phys. Rev. Lett.*, 86:1978–1981, Mar 2001.

[599] M. Drewes et al. A White Paper on keV Sterile Neutrino Dark Matter. *JCAP*, 1701(01):025, 2017.

[600] Ruben Saakyan. Determination of Absolute Neutrino Mass Using Quantum Technologies. *Talk given at the UK HEP Forum 2020: Quantum Leaps to the Dark Side*, 2020.

[601] A. I. Derbin, A. V. Chernyi, L. A. Popeko, V. N. Muratova, G. A. Shishkina, and S. I. Bakhlanov. Experiment on anti-neutrino scattering by electrons at

a reactor of the Rovno nuclear power plant. *JETP Lett.*, 57:768–772, 1993. [Pisma Zh. Eksp. Teor. Fiz. 57, 755(1993)].

[602] C. Hagner, M. Altmann, F. v. Feilitzsch, L. Oberauer, Y. Declais, and E. Kajfasz. Experimental search for the neutrino decay  $\nu_3 \rightarrow \nu_j + e^+ + e^-$  and limits on neutrino mixing. *Phys. Rev. D*, 52:1343–1352, Aug 1995.

[603] G. Bellini, J. Benziger, D. Bick, G. Bonfini, D. Bravo, M. Buizza Avanzini, B. Caccianiga, L. Cadonati, F. Calaprice, P. Cavalcante, A. Chavarria, A. Chepurnov, D. D’Angelo, S. Davini, A. Derbin, I. Drachnev, A. Empl, A. Etenko, K. Fomenko, D. Franco, C. Galbiati, S. Gazzana, C. Ghiano, M. Giammarchi, M. Göger-Neff, A. Goretti, L. Grandi, C. Hagner, E. Hungerford, Aldo Ianni, Andrea Ianni, V. Kobychev, D. Koralev, G. Korga, D. Kryn, M. Laubenstein, T. Lewke, E. Litvinovich, B. Loer, F. Lombardi, P. Lombardi, L. Ludhova, G. Lukyanchenko, I. Machulin, S. Manecki, W. Maneschg, G. Manuzio, Q. Meindl, E. Meroni, L. Miramonti, M. Misiaszek, P. Mosteiro, V. Muratova, L. Oberauer, M. Obolensky, F. Ortica, K. Otis, M. Pallavicini, L. Papp, L. Perasso, S. Perasso, A. Pocar, G. Ranucci, A. Razeto, A. Re, A. Romani, N. Rossi, R. Saldanha, C. Salvo, S. Schönert, H. Simgen, M. Skorokhvatov, O. Smirnov, A. Sotnikov, S. Sukhotin, Y. Suvorov, R. Tartaglia, G. Testera, D. Vignaud, R. B. Vogelaar, F. von Feilitzsch, J. Winter, M. Wojcik, A. Wright, M. Wurm, J. Xu, O. Zaimidoroga, S. Zavatarelli, and G. Zuzel. New limits on heavy sterile neutrino mixing in  ${}^8\text{B}$  decay obtained with the borexino detector. *Phys. Rev. D*, 88:072010, Oct 2013.

[604] Feng Peng An et al. Improved Search for a Light Sterile Neutrino with the Full Configuration of the Daya Bay Experiment. *Phys. Rev. Lett.*, 117(15):151802, 2016.

[605] Jeffrey M. Berryman. Constraining Sterile Neutrino Cosmology with Terrestrial Oscillation Experiments. *Phys. Rev.*, D100(2):023540, 2019.

- [606] A. Donini, P. Hernandez, J. Lopez-Pavon, M. Maltoni, and T. Schwetz. The minimal 3+2 neutrino model versus oscillation anomalies. *JHEP*, 1207:161, 2012.
- [607] James Barry, Werner Rodejohann, and He Zhang. Light Sterile Neutrinos: Models and Phenomenology. *JHEP*, 07:091, 2011.
- [608] Asmaa Abada, Giorgio Arcadi, Valerie Domcke, and Michele Lucente. Neutrino masses, leptogenesis and dark matter from small lepton number violation? *JCAP*, 1712(12):024, 2017.
- [609] J. Ashenfelter et al. First search for short-baseline neutrino oscillations at HFIR with PROSPECT. *Phys. Rev. Lett.*, 121(25):251802, 2018.
- [610] A. Abada, C. Biggio, F. Bonnet, M. B. Gavela, and T. Hambye. Low energy effects of neutrino masses. *JHEP*, 12:061, 2007.
- [611] Enrique Fernandez-Martinez, Josu Hernandez-Garcia, and Jacobo Lopez-Pavon. Global constraints on heavy neutrino mixing. *JHEP*, 08:033, 2016.
- [612] Mattias Blennow, Pilar Coloma, Enrique Fernandez-Martinez, Josu Hernandez-Garcia, and Jacobo Lopez-Pavon. Non-Unitarity, sterile neutrinos, and Non-Standard neutrino Interactions. *JHEP*, 04:153, 2017.
- [613] F. del Aguila, J. de Blas, and M. Perez-Victoria. Effects of new leptons in Electroweak Precision Data. *Phys. Rev.*, D78:013010, 2008.
- [614] E. Akhmedov, A. Kartavtsev, M. Lindner, L. Michaels, and J. Smirnov. Improving Electro-Weak Fits with TeV-scale Sterile Neutrinos. *JHEP*, 1305:081, 2013.
- [615] J. de Blas. Electroweak limits on physics beyond the Standard Model. *EPJ Web Conf.*, 60:19008, 2013.
- [616] Wojciech Flieger, Janusz Gluza, and Kamil Porwit. New limits on neutrino non-standard mixings based on prescribed singular values. 2019.

- [617] K. N. Abazajian et al. Light Sterile Neutrinos: A White Paper. 2012.
- [618] Alexey Boyarsky, Oleg Ruchayskiy, and Mikhail Shaposhnikov. The Role of sterile neutrinos in cosmology and astrophysics. *Ann.Rev.Nucl.Part.Sci.*, 59:191–214, 2009.
- [619] Oleg Ruchayskiy and Artem Ivashko. Restrictions on the lifetime of sterile neutrinos from primordial nucleosynthesis. *JCAP*, 1210:014, 2012.
- [620] F. Bezrukov, H. Hettmansperger, and M. Lindner. keV sterile neutrino Dark Matter in gauge extensions of the Standard Model. *Phys. Rev.*, D81:085032, 2010.
- [621] Miha Nemevsek, Goran Senjanovic, and Yue Zhang. Warm Dark Matter in Low Scale Left-Right Theory. *JCAP*, 1207:006, 2012.
- [622] Amr El-Zant, Shaaban Khalil, and Arunansu Sil. Warm dark matter in a  $B - L$  inverse seesaw scenario. *Phys. Rev.*, D91(3):035030, 2015.
- [623] Anirban Biswas, Debasish Borah, and Dibyendu Nanda. keV Neutrino Dark Matter in a Fast Expanding Universe. *Phys. Lett.*, B786:364–372, 2018.
- [624] Aaron C. Vincent, Enrique Fernandez Martinez, Pilar Hernández, Massimiliano Lattanzi, and Olga Mena. Revisiting cosmological bounds on sterile neutrinos. *JCAP*, 1504(04):006, 2015.
- [625] Asmaa Abada, Giorgio Arcadi, and Michele Lucente. Dark Matter in the minimal Inverse Seesaw mechanism. *JCAP*, 1410:001, 2014.
- [626] Kevork N. Abazajian. Sterile neutrinos in cosmology. *Phys. Rept.*, 711–712:1–28, 2017.
- [627] Xiang-Dong Shi and George M. Fuller. A New dark matter candidate: Non-thermal sterile neutrinos. *Phys. Rev. Lett.*, 82:2832–2835, 1999.
- [628] Scott Dodelson and Lawrence M. Widrow. Sterile-neutrinos as dark matter. *Phys. Rev. Lett.*, 72:17–20, 1994.

- [629] E. Bulbul et al. Detection of An Unidentified Emission Line in the Stacked X-ray spectrum of Galaxy Clusters. *Astrophys.J.*, 789:13, 2014.
- [630] A. Boyarsky, O. Ruchayskiy, D. Iakubovskiy, and J. Franse. Unidentified Line in X-Ray Spectra of the Andromeda Galaxy and Perseus Galaxy Cluster. *Phys.Rev.Lett.*, 113(25):251301, 2014.
- [631] A. Boyarsky, J. Franse, D. Iakubovskiy, and O. Ruchayskiy. Checking the dark matter origin of 3.53 keV line with the Milky Way center.
- [632] Kenny C. Y. Ng, Brandon M. Roach, Kerstin Perez, John F. Beacom, Shunsaku Horiuchi, Roman Krivonos, and Daniel R. Wik. New Constraints on Sterile Neutrino Dark Matter from *NuSTAR* M31 Observations. *Phys. Rev.*, D99:083005, 2019.
- [633] Brandon M. Roach, Kenny C. Y. Ng, Kerstin Perez, John F. Beacom, Shunsaku Horiuchi, Roman Krivonos, and Daniel R. Wik. NuSTAR Tests of Sterile-Neutrino Dark Matter: New Galactic Bulge Observations and Combined Impact. 2019.
- [634] A. Neronov and D. Malyshev. Toward a full test of the vMSM sterile neutrino dark matter model with Athena. *Phys. Rev.*, D93(6):063518, 2016.
- [635] K. Hirata et al. Observation of a neutrino burst from the supernova sn1987a. *Phys. Rev. Lett.*, 58:1490–1493, 1987.
- [636] R. M. Bionta et al. Observation of a neutrino burst in coincidence with supernova sn 1987a in the large magellanic cloud. *Phys. Rev. Lett.*, 58:1494, 1987.
- [637] K. Kainulainen, J. Maalampi, and J. T. Peltoniemi. Inert neutrinos in supernovae. *Nucl. Phys.*, B358:435–446, 1991.
- [638] X. Shi and G. Sigl. A Type II supernovae constraint on electron-neutrino - sterile-neutrino mixing. *Phys. Lett.*, B323:360–366, 1994. [Erratum: *Phys. Lett.*B324,516(1994)].

- [639] H. Nunokawa, J. T. Peltoniemi, Anna Rossi, and J. W. F. Valle. Supernova bounds on resonant active sterile neutrino conversions. *Phys. Rev.*, D56:1704–1713, 1997.
- [640] Jun Hidaka and George M. Fuller. Dark matter sterile neutrinos in stellar collapse: Alteration of energy/lepton number transport and a mechanism for supernova explosion enhancement. *Phys. Rev.*, D74:125015, 2006.
- [641] Jun Hidaka and George M. Fuller. Sterile Neutrino-Enhanced Supernova Explosions. *Phys. Rev.*, D76:083516, 2007.
- [642] Irene Tamborra, Georg G. Raffelt, Lorenz Hudepohl, and Hans-Thomas Janka. Impact of eV-mass sterile neutrinos on neutrino-driven supernova outflows. *JCAP*, 1201:013, 2012.
- [643] MacKenzie L. Warren, Matthew Meixner, Grant Mathews, Jun Hidaka, and Toshitaka Kajino. Sterile neutrino oscillations in core-collapse supernovae. *Phys. Rev.*, D90(10):103007, 2014.
- [644] George M. Fuller, Alexander Kusenko, and Kalliopi Petraki. Heavy sterile neutrinos and supernova explosions. *Phys. Lett.*, B670:281–284, 2009.
- [645] Georg G. Raffelt and Shun Zhou. Supernova bound on keV-mass sterile neutrinos reexamined. *Phys. Rev.*, D83:093014, 2011.
- [646] Carlos A. Argüelles, Vedran Brdar, and Joachim Kopp. Production of keV Sterile Neutrinos in Supernovae: New Constraints and Gamma Ray Observables. *Phys. Rev.*, D99(4):043012, 2019.
- [647] L. Oberauer, C. Hagner, G. Raffelt, and E. Rieger. Supernova bounds on neutrino radiative decays. *Astropart. Phys.*, 1:377–386, 1993.
- [648] S. Gariazzo, C. Giunti, M. Laveder, Y. F. Li, and E. M. Zavanin. Light sterile neutrinos. *J. Phys.*, G43:033001, 2016.

- [649] Takehiko Asaka, Mikko Laine, and Mikhail Shaposhnikov. Lightest sterile neutrino abundance within the nuMSM. *JHEP*, 01:091, 2007. [Erratum: *JHEP*02,028(2015)].
- [650] A. D. Dolgov and F. L. Villante. BBN bounds on active sterile neutrino mixing. *Nucl. Phys.*, B679:261–298, 2004.
- [651] Steen Hannestad, Rasmus Sloth Hansen, Thomas Tram, and Yvonne Y. Y. Wong. Active-sterile neutrino oscillations in the early Universe with full collision terms. *JCAP*, 1508(08):019, 2015.
- [652] Alessandro Mirizzi, Gianpiero Mangano, Ninetta Saviano, Enrico Borriello, Carlo Giunti, Gennaro Miele, and Ofelia Pisanti. The strongest bounds on active-sterile neutrino mixing after Planck data. *Phys. Lett.*, B726:8–14, 2013.
- [653] Sarah Bridle, Jack Elvin-Poole, Justin Evans, Susana Fernandez, Paweł Guzowski, and Stefan Soldner-Rembold. A Combined View of Sterile-Neutrino Constraints from CMB and Neutrino Oscillation Measurements. *Phys. Lett.*, B764:322–327, 2017.
- [654] M. Mitra, G. Senjanović, and F. Vissani. Neutrinoless Double Beta Decay and Heavy Sterile Neutrinos. *Nucl. Phys.*, B856:26, 2012.
- [655] J. Lopez-Pavon, S. Pascoli, and Chan-fai Wong. Can heavy neutrinos dominate neutrinoless double beta decay? *Phys. Rev.*, D87(9):093007, 2013.
- [656] Ram Lal Awasthi, M. K. Parida, and Sudhanwa Patra. Neutrino masses, dominant neutrinoless double beta decay, and observable lepton flavor violation in left-right models and SO(10) grand unification with low mass  $W_R, Z_R$  bosons. *JHEP*, 1308:122, 2013.
- [657] Asmaa Abada, Alvaro Hernandez-Cabezudo, and Xabier Marcano. Beta and Neutrinoless Double Beta Decays with KeV Sterile Fermions. *JHEP*, 01:041, 2019.

- [658] Vladimir Tello, Miha Nemevsek, Fabrizio Nesti, Goran Senjanovic, and Francesco Vissani. Left-Right Symmetry: from LHC to Neutrinoless Double Beta Decay. *Phys.Rev.Lett.*, 106:151801, 2011.
- [659] Joydeep Chakrabortty, H. Zeen Devi, Sribabati Goswami, and Sudhanwa Patra. Neutrinoless double- $\beta$  decay in TeV scale Left-Right symmetric models. *JHEP*, 1208:008, 2012.
- [660] James Barry and Werner Rodejohann. Lepton number and flavour violation in TeV-scale left-right symmetric theories with large left-right mixing. *JHEP*, 1309:153, 2013.
- [661] P. S. B. Dev, Sribabati Goswami, Manimala Mitra, and Werner Rodejohann. Constraining Neutrino Mass from Neutrinoless Double Beta Decay. *Phys.Rev.*, D88:091301, 2013.
- [662] Dusan Stefanik, Rastislav Dvornicky, Fedor Simkovic, and Petr Vogel. Reexamining the light neutrino exchange mechanism of the  $0\nu\beta\beta$  decay with left- and right-handed leptonic and hadronic currents. *Phys. Rev.*, C92(5):055502, 2015.
- [663] Mihai Horoi and Andrei Neacsu. Analysis of mechanisms that could contribute to neutrinoless double-beta decay. *Phys. Rev.*, D93(11):113014, 2016.
- [664] Frank F. Deppisch, Chandan Hati, Sudhanwa Patra, Prativa Pritimita, and Utpal Sarkar. Neutrinoless double beta decay in left-right symmetric models with a universal seesaw mechanism. *Phys. Rev.*, D97(3):035005, 2018.
- [665] P. Benes, Amand Faessler, F. Simkovic, and S. Kovalenko. Sterile neutrinos in neutrinoless double beta decay. *Phys.Rev.*, D71:077901, 2005.
- [666] J. Kotila and F. Iachello. Phase space factors for double- $\beta$  decay. *Phys.Rev.*, C85:034316, 2012.
- [667] Sabin Stoica and Mihail Mirea. New calculations for phase space factors involved in double- $\beta$  decay. *Phys. Rev.*, C88(3):037303, 2013.

- [668] M. Mirea, T. Pahomi, and S. Stoica. Phase Space Factors for Double Beta Decay: an up-date. 2014.
- [669] Amand Faessler, Marcela Gonzalez, Sergey Kovalenko, and Fedor Simkovic. Arbitrary mass Majorana neutrinos in neutrinoless double beta decay. *Phys. Rev.*, D90:096010, 2014.
- [670] Juhani Hyvärinen and Jouni Suhonen. Nuclear matrix elements for  $0\nu\beta\beta$  decays with light or heavy majorana-neutrino exchange. *Phys. Rev. C*, 91:024613, Feb 2015.
- [671] J. Barea, J. Kotila, and F. Iachello. Limits on sterile neutrino contributions to neutrinoless double beta decay. *Phys. Rev.*, D92:093001, 2015.
- [672] Mattias Blennow, Enrique Fernandez-Martinez, Jacobo Lopez-Pavon, and Javier Menendez. Neutrinoless double beta decay in seesaw models. *JHEP*, 07:096, 2010.
- [673] Jonathan Engel and Javier Menéndez. Status and Future of Nuclear Matrix Elements for Neutrinoless Double-Beta Decay: A Review. *Rept. Prog. Phys.*, 80(4):046301, 2017.
- [674] J. Barea, J. Kotila, and F. Iachello. Nuclear matrix elements for double- $\beta$  decay. *Phys. Rev.*, C87(1):014315, 2013.
- [675] Lukas Graf, Frank F. Deppisch, Francesco Iachello, and Jenni Kotila. Short-Range Neutrinoless Double Beta Decay Mechanisms. *Phys. Rev.*, D98(9):095023, 2018.
- [676] Robert B. Wiringa, V. G. J. Stoks, and R. Schiavilla. An Accurate nucleon-nucleon potential with charge independence breaking. *Phys. Rev.*, C51:38–51, 1995.
- [677] R. Machleidt. The High precision, charge dependent Bonn nucleon-nucleon potential (CD-Bonn). *Phys. Rev.*, C63:024001, 2001.

[678] Stefano Dell’Oro, Simone Marcocci, Matteo Viel, and Francesco Vissani. Neutrinoless double beta decay: 2015 review. *Adv. High Energy Phys.*, 2016:2162659, 2016.

[679] Xun Chen et al. PandaX-III: Searching for neutrinoless double beta decay with high pressure  $^{136}\text{Xe}$  gas time projection chambers. *Sci. China Phys. Mech. Astron.*, 60(6):061011, 2017.

[680] J. B. Albert et al. Sensitivity and Discovery Potential of nEXO to Neutrinoless Double Beta Decay. *Phys. Rev.*, C97(6):065503, 2018.

[681] N. Abgrall et al. The Large Enriched Germanium Experiment for Neutrinoless Double Beta Decay (LEGEND). *AIP Conf. Proc.*, 1894(1):020027, 2017.

[682] G. Wang et al. CUPID: CUORE (Cryogenic Underground Observatory for Rare Events) Upgrade with Particle IDentification. 2015.

[683] Frank F. Deppisch, Lukas Graf, Werner Rodejohann, and Xun-Jie Xu. Neutrino Self-Interactions and Double Beta Decay. *Phys. Rev. D*, 102(5):051701, 2020.

[684] M. Doi, T. Kotani, and E. Takasugi. Double beta decay and majorana neutrino. *Prog. Theor. Phys. Suppl.*, 83:1, 1985.

[685] W. C. Haxton and G. J. Stephenson. Double beta Decay. *Prog. Part. Nucl. Phys.*, 12:409–479, 1984.

[686] Fedor Šimkovic, Rastislav Dvornický, Dušan Stefník, and Amand Faessler. Improved description of the  $2\nu\beta\beta$  -decay and a possibility to determine the effective axial-vector coupling constant. *Phys. Rev. C*, 97(3):034315, 2018.

[687] P. Gysbers et al. Discrepancy between experimental and theoretical  $\beta$ -decay rates resolved from first principles. *Nature Phys.*, 15(5):428–431, 2019.

[688] M. Tanabashi et al. Review of Particle Physics. *Phys. Rev.*, D98(3):030001, 2018.

[689] Felix Kahlhoefer, Alexander Mück, Stefan Schulte, and Patrick Tunney. Interference effects in dilepton resonance searches for Z bosons and dark matter mediators. *JHEP*, 03:104, 2020.

[690] G. Adhikari et al. nEXO: Neutrinoless double beta decay search beyond  $10^{28}$  year half-life sensitivity. 6 2021.

[691] V. Albanese et al. The SNO+ experiment. *JINST*, 16(08):P08059, 2021.

[692] Michelle J. Dolinski, Alan W. P. Poon, and Werner Rodejohann. Neutrinoless Double-Beta Decay: Status and Prospects. *Ann. Rev. Nucl. Part. Sci.*, 69:219–251, 2019.

[693] M. Agostini et al. Final Results of GERDA on the Search for Neutrinoless Double- $\beta$  Decay. *Phys. Rev. Lett.*, 125:252502, 2020.

[694] Anna Julia Zsigmond. LEGEND: The future of neutrinoless double-beta decay search with germanium detectors. *J. Phys. Conf. Ser.*, 1468(1):012111, 2020.

[695] O. Azzolini et al. Evidence of Single State Dominance in the Two-Neutrino Double- $\beta$  Decay of  $^{82}\text{Se}$  with CUPID-0. *Phys. Rev. Lett.*, 123(26):262501, 2019.

[696] David Waters. Latest Results from NEMO-3 & Status of the SuperNEMO Experiment. *J. Phys. Conf. Ser.*, 888(1):012033, 2017.

[697] R. Arnold et al. Detailed studies of  $^{100}\text{Mo}$  two-neutrino double beta decay in NEMO-3. *Eur. Phys. J. C*, 79(5):440, 2019.

[698] W. R. Armstrong et al. CUPID pre-CDR. 7 2019.

- [699] A. Gando et al. Precision measurement of the  $^{136}\text{Xe}$  two-neutrino  $\beta\beta$  spectrum in KamLAND-Zen and its impact on the quenching of nuclear matrix elements. *Phys. Rev. Lett.*, 122(19):192501, 2019.
- [700] F. Agostini et al. Sensitivity of the DARWIN observatory to the neutrinoless double beta decay of  $^{136}\text{Xe}$ . *Eur. Phys. J. C*, 80(9):808, 2020.
- [701] Pavel Fadeev, Yevgeny V. Stadnik, Filip Ficek, Mikhail G. Kozlov, Victor V. Flambaum, and Dmitry Budker. Revisiting spin-dependent forces mediated by new bosons: Potentials in the coordinate-space representation for macroscopic- and atomic-scale experiments. *Phys. Rev.*, A99(2):022113, 2019.
- [702] S. S. Wilks. The Large-Sample Distribution of the Likelihood Ratio for Testing Composite Hypotheses. *Annals Math. Statist.*, 9(1):60–62, 1938.
- [703] Glen Cowan, Kyle Cranmer, Eilam Gross, and Ofer Vitells. Asymptotic formulae for likelihood-based tests of new physics. *Eur. Phys. J. C*, 71:1554, 2011. [Erratum: Eur.Phys.J.C 73, 2501 (2013)].
- [704] Eric Burns and Wade Fisher. Testing the approximations described in 'Asymptotic formulae for likelihood-based tests of new physics'. 10 2011.